frontiers | Research Topics

Innovators in chemistry
2022

Edited by
Aleksandar Kondinski, Kunyu Wang, Jose Luis Cabellos,
Arjun Singh, Barkat A. Khan, Maxence Wisztorski,
Jafar Soleymani, Citlalli Gaona-Tiburcio,
Tao Wei, Linghui Qian and Muhammad Khurram Tufail

Published in
Frontiers in Chemistry

ISSN 1664-8714
ISBN 978-2-8325-4343-6
DOI 10.3389/978-2-8325-4343-6

Generative AI statement
Any alternative text (Alt text) provided alongside figures in the articles in this ebook has been generated by Frontiers with the support of artificial intelligence and reasonable efforts have been made to ensure accuracy, including review by the authors wherever possible. If you identify any issues, please contact us.

About Frontiers

Frontiers is more than just an open access publisher of scholarly articles: it is a pioneering approach to the world of academia, radically improving the way scholarly research is managed. The grand vision of Frontiers is a world where all people have an equal opportunity to seek, share and generate knowledge. Frontiers provides immediate and permanent online open access to all its publications, but this alone is not enough to realize our grand goals.

Frontiers journal series

The Frontiers journal series is a multi-tier and interdisciplinary set of open-access, online journals, promising a paradigm shift from the current review, selection and dissemination processes in academic publishing. All Frontiers journals are driven by researchers for researchers; therefore, they constitute a service to the scholarly community. At the same time, the *Frontiers journal series* operates on a revolutionary invention, the tiered publishing system, initially addressing specific communities of scholars, and gradually climbing up to broader public understanding, thus serving the interests of the lay society, too.

Dedication to quality

Each Frontiers article is a landmark of the highest quality, thanks to genuinely collaborative interactions between authors and review editors, who include some of the world's best academicians. Research must be certified by peers before entering a stream of knowledge that may eventually reach the public - and shape society; therefore, Frontiers only applies the most rigorous and unbiased reviews. Frontiers revolutionizes research publishing by freely delivering the most outstanding research, evaluated with no bias from both the academic and social point of view. By applying the most advanced information technologies, Frontiers is catapulting scholarly publishing into a new generation.

What are Frontiers Research Topics?

Frontiers Research Topics are very popular trademarks of the *Frontiers journals series*: they are collections of at least ten articles, all centered on a particular subject. With their unique mix of varied contributions from Original Research to Review Articles, Frontiers Research Topics unify the most influential researchers, the latest key findings and historical advances in a hot research area.

Find out more on how to host your own Frontiers Research Topic or contribute to one as an author by contacting the Frontiers editorial office: frontiersin.org/about/contact

Innovators in chemistry: 2022

Citation

Kondinski, A., Wang, K., Cabellos, J. L., Singh, A., Khan, B. A., Wisztorski, M., Soleymani, J., Gaona-Tiburcio, C., Wei, T., Qian, L., Tufail, M. K., eds. (2024). *Innovators in chemistry: 2022*. Lausanne: Frontiers Media SA.
doi: 10.3389/978-2-8325-4343-6

Table of contents

frontiers | Frontiers in Chemistry

TYPE Editorial
PUBLISHED 05 January 2024
DOI 10.3389/fchem.2023.1352328

OPEN ACCESS

EDITED AND REVIEWED BY
Luís D. Carlos,
University of Aveiro, Portugal

*CORRESPONDENCE
Aleksandar Kondinski,
aleksandar@kondinski.com

RECEIVED 08 December 2023
ACCEPTED 12 December 2023
PUBLISHED 05 January 2024

CITATION
Kondinski A (2024), Editorial: Innovators in chemistry: 2022.
Front. Chem. 11:1352328.
doi: 10.3389/fchem.2023.1352328

Editorial: Innovators in chemistry: 2022

Aleksandar Kondinski[1,2]*

[1]Cambridge Centre for Advanced Research and Education in Singapore Ltd, Singapore, Singapore, [2]University of Cambridge, Cambridge, United Kingdom

KEYWORDS

chemical innovation, chemical technology, synthesis, materials, life science

Editorial on the Research Topic
Innovators in chemistry: 2022

The "Innovators in Chemistry 2022" edition showcases the dynamic evolution and critical importance of chemistry in addressing complex challenges across various fields, emphasizing its role in driving sustainable advancements. This issue, curated by a number of young guest editors, assembles a diverse group of both established and emerging researchers whose work significantly impacts the field. Featuring 14 meticulously crafted articles by 80 researchers, the Research Topic spans a wide array of topics in chemical science, including nucleic acid structures, antibiotic resistance, pharmacognosy, green nanotechnology, photocatalysis, ferroelectric materials, protein modification, carbon materials, mass spectrometry, laser technology, luminescent materials, atmospheric chemistry, oil recovery technology, and didactical electrochemistry (Figure 1). It offers a comprehensive view of current trends and future innovations through original research, reviews and opinion articles. This edition not only celebrates recent advancements but also seeks to inspire ongoing exploration and progress in chemistry. Conclusively, "Innovators in Chemistry 2022" highlights the collaborative and intellectual contributions of its participants in steering the future of this central science. The guest editorial team expresses deep gratitude to each author, reviewer, and reader for their invaluable involvement in advancing innovative solutions and understanding of chemistry.

In this edition, we explore a number of exceptional research directions in life sciences. Monsen presents a comprehensive review on G-quadruplexes (G4s), that is four-stranded nucleic acid structures forming in guanine-rich regions of chromatin, particularly in gene promoters. His work discusses the significance of G4s as epigenetic elements in gene transcription and their potential as indirect drug targets in cancer therapies, advocating for research focused on higher-order G4s for more selective molecular targeting, using the human telomerase reverse transcriptase (hTERT) core promoter G-quadruplex as a case study (Monsen). Complementing this, Krco et al. delve into the challenge of antibiotic resistance, with a special focus on metallo-β-lactamases (MBLs) that inactivate β-lactam antibiotics. Their review emphasizes the structure-function relationships of B3-type MBLs, noting their active site diversity and the potential for broader-range inhibitors, as suggested by the inhibition of one B3-type MBL by clavulanic acid (Krco et al.). In a distinct but equally innovative domain, Myklebust et al. report the development of potent bisubstrate inhibitors targeting NAA80, an enzyme crucial for actin N-terminal acetylation in eukaryotic cells. Their optimized compound, CoA-Ac-EDDI-NH_2, combines coenzyme A and a tetrapeptide

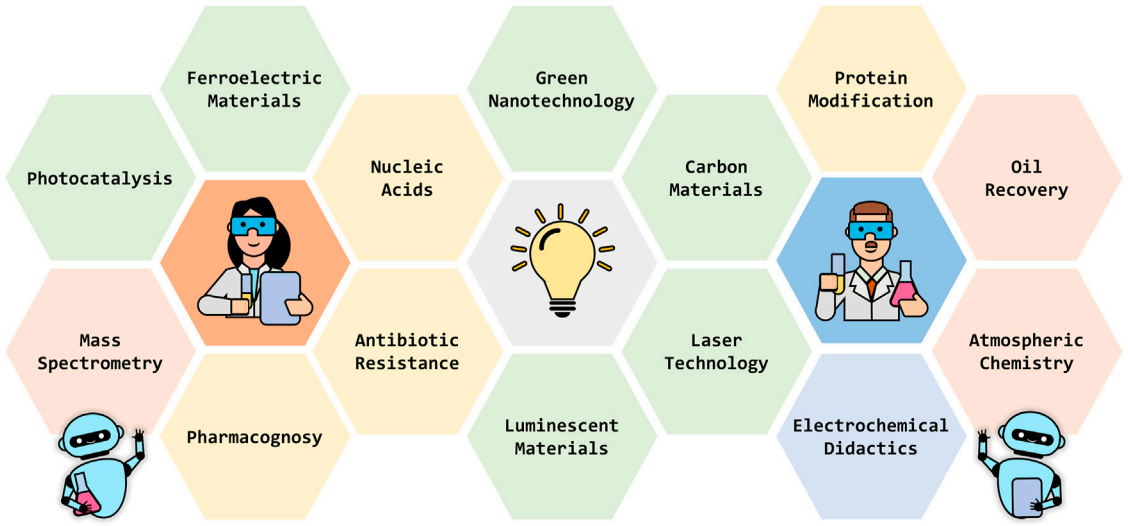

FIGURE 1
Overview of chemical domains covered in the innovators in chemistry 2022.

amide, showing high efficacy and promising insights into the roles of actin and the regulatory functions of NAA80 (Myklebust et al.). Lastly, Shaheen et al. provide a comprehensive analysis of *Xanthium strumarium L.* (XSL) foliage, exploring its antioxidant and anti-diabetic properties. They demonstrate that the ethyl acetate fraction of XSL, with its high phenolic concentration, significantly reduces blood glucose levels in diabetic mice, indicating a link to its traditional use in diabetes treatments (Shaheen et al.).

The landscape of advanced materials technology is rapidly evolving, as demonstrated by a series of recent studies. Zidane et al. exemplify this evolution through their work on eco-friendly nanoparticle synthesis using Purslane leaf extract, marking a significant departure from traditional hazardous chemical methods towards environmentally sustainable practices. This theme of sustainability is further explored by Lu et al., who unveil the potential of transition metal single-atom catalysts supported by red phosphorus to enhance photocatalytic hydrogen production, a crucial aspect in the search for clean energy solutions. The innovative use of materials continues in the realm of biological imaging, as Thornton et al. develop unique macrocyclic lanthanide complexes, opening new avenues in advanced imaging techniques. Expanding the boundaries of material science, Mills et al. delve into the complex effects of doping on the ferroelectric and dielectric properties of barium titanate, emphasizing the complex relationship between material composition and its properties. Concurrently, Ni et al. pose their viewpoint on the advancements in carbon-based materials, highlighting the diverse applications of porous carbon in fields ranging from adsorption and catalysis to energy storage, crucial for tackling current energy and environmental challenges. Finally, the innovative synthesis of two-dimensional transition metal dichalcogenides using laser-assisted techniques, as detailed by Wang et al., showcases a method that promises to trailblaze flexible electronics with its precision and dynamic properties. Collectively, these studies not only reflect the current state of advanced materials technology but also chart a path for future research and applications in this rapidly evolving field.

Recent advancements in chemical analysis and control technologies are highlighted in a series of studies, each focusing on different applications and implications. Reynaud et al. present a significant leap in the field of mass spectrometry (MS) with their development of a compact nano-electro-mechanical system (NEMS) based MS, designed for ultra-high mass analytes. This prototype, operating under higher pressures without compromising on particle focusing or mass measurement quality, demonstrates an improved capability in nanoparticle analysis, a crucial advancement for MS technology. Complementing this, Dash et al. delve into atmospheric chemistry, investigating the formation of methanimine in the troposphere. By exploring the reaction dynamics of the aminomethyl radical with oxygen and considering the influences of ammonia and water, their study sheds light on the complex chemical processes occurring in our atmosphere, contributing to a deeper understanding of tropospheric compound formation. Du et al. address a practical challenge in the oil recovery industry, focusing on the flow resistance characteristics of steam injection in horizontal oil wells. Their experimental approach to evaluating pressure loss and optimizing steam distribution offers a refined method for improving oil recovery, showcasing the application of fluid dynamics and pressure control in an industrial setting.

In response to the increasing importance of electroanalytical chemistry increasing significance, Espinoza-Montero et al. developed a didactical guide on generating hydroxyl radicals ·OH using boron-doped diamond (BDD) in electrochemical oxidation processes. This educational resource elucidates key aspects such as BDD activation, electrolyte response analysis, and overpotential determination for ·OH production through Tafel plots and

voltammetry, along with strategies for radical entrapment. Additionally, their study extends to the practical application of these methods for the efficient and cost-effective degradation of amoxicillin, thereby showcasing the distinct electronic characteristics and stability of BDD in redox reactions (Espinoza-Montero et al.).

On behalf of the involved guest editors and myself, I express our gratitude to the contributors and reviewers who played a vital role in shaping this Research Topic. Gratitude is also extended to the Frontiers team for their invaluable support, making this endeavor both enjoyable and timely. We hope this edition delights the readers of Frontiers in Chemistry and showcases the significant advancements. It is our aspiration that this Research Topic will spark interest, initiate new thoughts, and shed light on uncharted areas of chemical innovation.

Author contributions

AK: Conceptualization, Visualization, Writing–original draft, Writing–review and editing.

Acknowledgments

AK thanks the University of Cambridge and Cambridge Centre for Advanced Research and Education in Singapore (CARES) for their research support.

Conflict of interest

Author AK was employed by Cambridge Centre for Advanced Research and Education in Singapore Ltd.

Publisher's note

frontiers | Frontiers in Chemistry

TYPE Original Research
PUBLISHED 15 December 2022
DOI 10.3389/fchem.2022.1083596

OPEN ACCESS

EDITED BY
Barkat. A. Khan,
Gomal University, Pakistan

REVIEWED BY
J. Uddin,
Coppin State University, United States
M. Hasnat,
Shahjalal University of Science and Technology, Bangladesh

*CORRESPONDENCE
Mohammed L. Tedjani,
medlaidtedjani@gmail.com
Farid Menaa,
menaateam@gmail.com

SPECIALTY SECTION
This article was submitted to Polymer Chemistry, a section of the journal
Frontiers in Chemistry

RECEIVED 29 October 2022
ACCEPTED 28 November 2022
PUBLISHED 15 December 2022

CITATION
Zidane Y, Laouini SE, Bouafia A, Meneceur S, Tedjani ML, Alshareef SA, Almukhlifi HA, Al-Essa K, Al-Essa EM, Rahman MM, Madkhali O and Menaa F (2022), Green synthesis of multifunctional MgO@AgO/Ag_2O nanocomposite for photocatalytic degradation of methylene blue and toluidine blue.
Front. Chem. 10:1083596.
doi: 10.3389/fchem.2022.1083596

Green synthesis of multifunctional MgO@AgO/Ag_2O nanocomposite for photocatalytic degradation of methylene blue and toluidine blue

Younes Zidane[1,2], Salah E. Laouini[1,2], Abderrhmane Bouafia[1,2], Souhaila Meneceur[1,2], Mohammed L. Tedjani[1,2]*, Sohad A. Alshareef[3], Hanadi A. Almukhlifi[3], Khansaa Al-Essa[4], Ethar M. Al-Essa[5], Mohammed M. Rahman[6], Osama Madkhali[7] and Farid Menaa[8]*

[1]Department of Process Engineering, Faculty of Technology, University of El Oued, El-Oued, Algeria, [2]Laboratory of Biotechnology Biomaterial and Condensed Matter, Faculty of Technology, University of El Oued, El-Oued, Algeria, [3]Department of Chemistry, Faculty of Science, University of Tabuk, Tabuk, Saudi Arabia, [4]Department of Chemistry, Jerash University, Jerash, Jordan, [5]Department of Civil Engineering, Isra University, Amman, Jordan, [6]Center of Excellence for Advanced Materials Research (CEAMR) and Chemistry Department, Faculty of Science, King Abdulaziz University, Jeddah, Saudi Arabia, [7]Department of Physics, College of Science, Jazan University, Jazan, Saudi Arabia, [8]Department of Biomedical and Environmental Engineering (BEE), Fluorotronics, Inc.-California Innovations Corporation, San Diego, CA, United States

Introduction: In this paper, MgO@AgO/Ag_2O nanoparticles were greenly synthesized, the current idea is to replace the harmful chemical technique with an ecofriendly synthesis of metal oxide nanoparticles (NPs) utilizing biogenic sources.

Methods: The current investigation was conducted to create silver oxide NPs decorated by MgO NPs (namely, MgO@AgO/Ag_2O nanocom-posite) using the leaves extract of Purslane (*Portulaca Oleracea*) as the reducing and capping agent. The nanopowder was investigated by means of X-ray diffraction, scanning electron mi-croscope, BET surface area, Fourier transform infrared, and UV-vis spectrophotom-eter studies. XRD studies reveal the monophasic nature of these highly crystalline silver nano-particles. SEM studies the shape and morphology of the synthesis AgO/Ag_2O and MgO@AgO/Ag_2O NPs. The presence of magnesium and oxygen was further confirmed by EDS profile.

Results and discussion: The surface area was found to be 9.1787 m^2/g and 7.7166 m^2/g, respectively. FTIR analysis showed the presence of specific functional groups. UV-vis spectrophotometer studies show the absorption band at 450 nm due to surface plasmon resonance. The results have also indicated the high performance of the greenly synthesized AgO/Ag_2O NPs and

Abbreviations: NPs, Nanoparticles; MB, Methylene blue; TB, toluidine blue.

MgO@AgO/Ag_2O NPs for photocatalytic activity dye degradation (methylene blue and toluidine blue).

KEYWORDS

MgO@AgO/Ag2O NPs, green synthesis, *Portulaca oleracea*, photocatalysis, methylene blue, toluidine blue

1 Introduction

With widespread applications in the domains of biology, health, energy, and material science, among others, nanotechnology has emerged as a promising interdisciplinary field of the twenty-first century. Nanomaterials are produced often by a variety of physical and chemical processes that call for high temperatures, vacuum conditions, specialized equipment, and chemical additives (Cai et al., 2022). Due to the use of harmful compounds that remain attached to the synthesized nanoparticles, current improvements in chemical processes for the production of nanomaterials have raised biological dangers to the environment (Yu et al., 2022). Consequently, scientists are presently concentrating on the production of nanomaterials utilizing biogenic sources such as bacteria, algae, and plants. A new age for secure nanobiotechnology has begun because of recent advancements in the green synthesis of nanomaterials, which are rapid, inexpensive, and ecofriendly. Due to their unique physical and chemical features in the domains of biosensors, diagnostic tools, catalysts, anticancer, and antimicrobial agents, metal oxide nanoparticles have recently attracted a lot of attention (Zhang et al., 2020; Ahmad et al., 2021; Wijesinghe et al., 2021a; Wijesinghe et al., 2021b; Gherbi et al., 2022).

In part because of their non-biodegradable and persistent character, the considerable water pollution caused by inorganic (such as heavy metal ions) and organic compounds—such as synthetic organic colors, persistent organic pollutants, antibiotics, etc.—often present significant obstacles. Additionally, these emerging pollutants may have several detrimental effects on human bodies and aquatic microbes (Sharma and Bhattacharya, 2017; Al-Essa and Al-Essa, 2021). The world's use of synthetic dyes now exceeds several million tons, with numerous industrial sectors including the printing and textile industries contributing to this (Mashkoor and Nasar, 2020). Therefore, solutions for wastewater pretreatment are required to reduce these contamination issues. Scientifically, the adsorption process is the most effective and practical method for purifying water is adsorption (Al-Essa, 2018; Bulgariu et al., 2019). Adsorbents should be created from free, sustainable, and locally accessible sources to achieve competitive efficacy (typically, plant resources) (Bulgariu et al., 2019).

Due to their high conductivity, silver oxide nanoparticles (AgONPs) stand out among the competition as a desirable material for metallic-based conductive filler (Stewart et al., 2017), capacity to encourage cell proliferation and osteogenic differentiation facilitate bone repair (Zhang et al., 2015; Xu et al., 2020), in addition to their capacity to prevent the development of microbial biofilm (Hileuskaya et al., 2020) and maybe defeat microorganisms that are resistant to many drugs (Rai et al., 2012). AgONPs were highly sought-after for application in biosensors due to these special characteristics (Zeng et al., 2014; Al Essa et al., 2021), prostheses (Gallo et al., 2016), and dental materials (Ohashi et al., 2004). The resultant AgONPs, however, are inappropriate for biomedicine use due to the common synthesis technique, which frequently employs toxic chemical reducing agents that are dangerous for human (such as sodium borohydride and hydrazine) (Kolarova et al., 2015; Rónavári et al., 2021). Magnesium oxide nanoparticles (MgONPs) are harmless and reasonably simple to synthesize among the many distinct inorganic metal oxides. MgONPs have received approval from the United States Food and Drug Administration as safe materials (21CFR184.1431) (Martinez-Boubeta et al., 2010). MgONPs, for instance, can reduce indigestion, start the post-activation of bone-repair scaffolds, and function as hyperthermia agents in cancer treatment. Both MgO and AgO NPs can be now produced using "green synthesis" techniques, which offer straightforward, affordable, quick, and non-toxic approaches to address these problems. The use of diverse biological entities, such as plant extract, in green synthesis techniques replaces the use of chemical reducing agents. (Ahmadi et al., 2018; Hamouda et al., 2019; Okaiyeto et al., 2019), and bacteria (Hamouda et al., 2019) produce a high output of somewhat uniform-sized metallic nanoparticles by acting as both reducing and capping agents. Due to their accessibility, safety, and simplicity of synthesis, plant-based extracts have drawn more attention. They don't require the preservation of microbial cultures (Roy and Das, 2015). The most often reported use so far has been of various plant fruit and leaf extracts. Purslane is a fascinating possibility for this use among many different plants (Bouafia et al., 2020; Bouafia et al., 2021; Bouafia and Laouini, 2021).

The decor is another method for enhancing photocatalytic activity (Wang et al., 2011; Hunge et al., 2021; Yadav et al., 2021). Surface plasmon resonance (SPR), where Ag, Au, and Pt are typically utilized, is favored by decoration with noble metals (Xing et al., 2017), it has many positive benefits since it promotes the absorption of visible light and the activation of energetic charge carriers, many (Sohrabnezhad and Seifi, 2016), achieves a greater separation of charge, this leads to an increase in redox reactions and a higher formation rate of reactive oxygen species (Ong et al., 2013; Kuriakose et al., 2014; Sohrabnezhad and Seifi, 2016). Previous studies have confirmed the photocatalytic activity of AgO and Mg NPs (Balakrishnan et al., 2020). Moreover, prior studies demonstrated that the decoration of AgONPs with other metals NPs results in a significant improvement in the photocatalytic activity comparing to the nondecorated AgONPs (Laouini et al., 2021).

In this study, the degradation of the methylene blue (MB) and toluidine blue (TB) dyes under sunlight was used to examine the photocatalytic capabilities of AgO/Ag_2O nanoparticles (NPs) coated with MgO. To the best of our knowledge AgO/Ag_2O and $MgO@AgO/Ag_2O$ NPs photocatalytic activity was never tested against MB and TB dyes.

2 Materials and methods

2.1 Reagents

Silver nitrate ($AgNO_3$, 98%), Magnesium chloride hydrates ($MgCl_2$, $6H_2O$, 98%), MB ($C_{16}H_{18}ClN_3S$, 98%), and TB ($C_{15}H_{16}ClN_3S$, 98%) were purchased from Sigma-Aldrich,Germany. The leaves of purslane were collected from local fields in El Oued, Southeast of Algeria. Distilled water was used in all the experiments.

2.2 Preparation of the leaf extract

Fresh and healthy purslane (*Portulaca oleracea*) leaves were collected from nearby farms in the El Oued area (Southeast of Algeria). After properly cleaning them with flowing tap water to get rid of any dirts or other polluted organic materials, they were repeatedly rinsed in de-mineralized water. The fresh leaves were crushed. The leaves components were extracted by mixing 250.0 g of leaves with 900 ml of distilled water in a 1,000 ml glass beaker. The mixture was stirred for 15 min at 70°C. The extract was kept cool and then filtered using the decantation method and stored at 4°C for further use.

2.3 Synthesis of AgO/Ag_2O and $MgO@AgO/Ag_2O$ NPs

The AgO/Ag_2O and $MgO@AgO/Ag_2O$ NPs were synthesized by a green method using plant extract, following modified protocols from previous studies (Abdullah et al., 2020; Bouafia and Laouini, 2020; Bouafia et al., 2021a; Bouafia et al., 2021b; Belaiche et al., 2021; Laid et al., 2021; Laouini et al., 2021; Ben Amor et al., 2022; Daoudi et al., 2022; Djamila et al., 2022; Meneceur et al., 2022; Tedjani et al., 2022). For the synthesis of AgO/Ag_2O NPs filtered extract was taken and diluted to 1,000 ml with deionized water, 1.7 g of $AgNO_3$ was added to 1,000 ml of the extract with continuous stirring, 5 ml diluted hydroxide (0.1 M) was added dropwise to the mixture solution. With controlled and continuous stirring (600 rpm) at 70°C for 4 h, the precursor became brown. The precipitate was then centrifuged and washed several times with deionized water, and dried at 100°C in an oven for 48 h. Finally, the AgO/Ag_2O NPs were manually grinded into a fine powder.

Nanostructured MgO loaded AgO/Ag_2O were simply synthesized. Firstly, nanoparticle solution (AgO/Ag_2O) was prepared by dissolving 0.7 g of (AgO/Ag_2O) in de-ionized water, the solution maintained in continuous stirring at 70°C for 2 h. Then 70 ml (0.01 M) metal ion ($MgCl_2$) solution was added to the nanoparticle solution, mixed thoroughly at 80°C for 2 h, and then dried at 100°C for 48 h.

After drying, the mixture was grinded to obtain a homogeneous powder.

2.4 Material characterizations

The employment of the following methods was necessary for the characterization of generated nanoparticles: X-ray diffractometer (XRD), a scanning electron microscope (SEM), EDS, BET surface area analyzer, Fourier transform infrared (FTIR), and UV-vis spectrophotometer.

Using XRD (Rigaka Miniflex 600) and Cu-K radiation with a wavelength of 0.15406 nm in the 2 range 10–80, the crystalline structure of the produced NPs was determined. The morphology of the prepared AgO/Ag_2O and $MgO@AgO/Ag_2O$ NPs were verified using SEM (TESCAN VEGA 3) with an accelerating voltage of 10 kV. The BET surface area analyzer (micromeritics ASAP 2020 Plus Version 2.00) was used to capture the N_2 adsorption isotherm, associated surface area, and pore parameter. A Nicolet iS5 (Thermo Fisher Scientific) was used to perform FTIR measurements on leaves extract, green synthesis AgO/Ag_2O, and $MgO@AgO/Ag_2O$ NPs to determine the functional groups operating in the region of 4,000 to 400 cm^{-1}. A UV-vis spectrophotometer was used to examine the optical properties of the samples (Shimadzu-1800). The measurement was made at the temperature of 28°C in the 300–900 nm wavelength range. UV-vis spectrometric measurements were performed using a quartz cell and distilled water as a blank solution to determine the stability of AgO/Ag_2O NPs. The optical gap band energy (Egap) of these materials was calculated using the Tauc Equation considering these findings.

2.5 Photocatalytic degradation of MB dye

Based on the samples' capacity to break down the MB dye in the presence of sunlight, the catalytic activity of the samples was evaluated. The experiment was conducted in a lab using sunlight (the samples were not exposed to direct sunlight). MB stock solution (2.5×10^{-5} M) was made. Four samples of 5 ml of dye solution and 5.0 mg of AgO/Ag_2O NPs were combined and exposed to sunlight in. About 2 ml of the suspensions were taken from the reaction mixture every 15, 30, 60, and 120 min while it was exposed to sunlight, and the suspended particles were then extracted using ultracentrifugation. The same test was

conducted using MgO@AgO/Ag_2O. The absorption obtained at 664 nm in a UV-vis spectrophotometer was used to calculate the rate of dye degradation. Based on the formula, the dye degradation % was evaluated using the Eq. 1:

$$\% \textbf{ of degradation} = \frac{C_i - C_t}{C_t} \quad (1)$$

where C_i and C_t (mg/L) are the initial concentration of MB and the concentration of pollutant MB at time t, respectively.

2.6 Photocatalytic degradation of TB dye

The photodegradation of TB dye in aqueous solution was investigated under sunlight in the presence of AgO/Ag_2ONPs and MgO@AgO/Ag_2O as a photocatalyst, A5.0 mg of the catalyst is added to 50 ml of TB dye solution. This solution is prepared in distilled water at a concentration of (4×10^{-3} M). It was then exposed to sunlight at different intervals (10, 20, 30, 40, and 60 min) at a temperature of 28°C and a neutral pH. The catalyst is separated by ultracentrifugation. A spectrophotometer is used for reading the absorbance values at 631 nm.

The equilibrium amount of adsorption is calculated by the Eq. 2:

$$QE = \frac{(C_0 - C_e)V}{m} \quad (2)$$

where, QE (mg/g) is the adsorption capacity at equilibrium, C_0 and C_e (mg/L) are the concentration of TB solutions at the start of reaction and the concentration of pollutant TB at time t, respectively. While V stands for the volume of the solution (L), and m is the mass of adsorbent (g).

3 Results and discussion

3.1 Crystal structure and composition

Portulaca oleracea's medicinal potency is attributed to its complex chemical makeup composition; it is high in primary and secondary metabolites, as well as minerals, vitamins, and other micronutrients.

Purslane is the common name for *Portulaca oleracea L.*, a member of the *Portulaceae* family. A variety of substances have been identified from *Portulaca oleracea*, including flavonoids, alkaloids, polysaccharides, fatty acids, terpenoids, sterols, proteins, vitamins, and minerals. There is a wide range of pharmacological qualities that *Portulaca oleracea* exhibits, including neuroprotective, antibacterial, antidiabetic, antioxidant, anti-inflammatory, antiulcerogenic, and anticancer actions. (Zhou et al., 2015)

To investigate the size and make-up of the crystalline phases, XRD analysis was done.

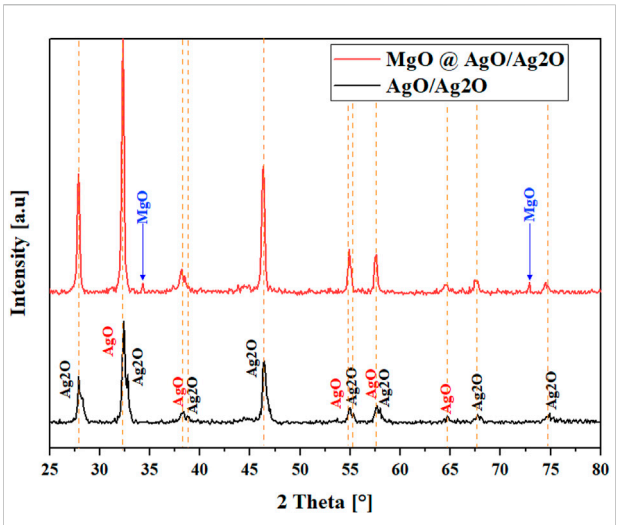

FIGURE 1
XRD patterns of AgO/Ag_2O and MgO@AgO/Ag_2O NPs.

Figure 1 shows the diffraction patterns of AgO/Ag_2O and MgO@AgO/Ag_2O. Similar results have already been described in the literature (Deekshitha and Shetty, 2021), regarding the peaks of Ag_2O. Moreover, It is intriguing to see that there are two distinct peaks that can be attributed to MgO NPs. According to the Debye-Scherrer equation, the crystallite size was determined to be 22.16 nm for AgO/Ag_2O and 21.60 nm for MgO@AgO/Ag_2O NPs, respectively. The results are shown below in Table 1.

3.2 Morphological investigation

SEM was used to study the formation of the prepared AgO/Ag_2O and MgO@AgO/Ag_2O NPs (Figures 2A,C, respectively), and their morphological size (40–50 nm in average) (Figures 2B, D, respectively). The MgO@AgO/Ag_2O NPs were oval and spherical. Most of the MgO@AgO/Ag_2O NPs were placed as aggregated which may explain the slight increase in size of these NPs compared to AgO/Ag_2O NPs; also, a few individual particles were also observed (Gosens et al., 2010).

Further analysis by EDS of the prepared AgO/Ag_2O and MgO@AgO/Ag_2O NPs (Figures 3A,B, respectively). The data associated to MgO@AgO/Ag_2O NPs, confirm the presence of silver, oxygen, and magnesium, with a weight percentage of approximately 87.47% Ag, 12.18% O and 0.35% Mg. It is concluded that all nanoparticles were mixed together. In this way, the aimed ternary oxides nanoparticle system containing MgO, AgO, and Ag_2O NPs was obtained.

The MgO@AgO/Ag_2O NPs sample's EDAX analysis revealed only clear peaks for the elements Ag, Mg, and O; no additional peaks could be observed, proving that the powder was produced without any impurities.

TABLE 1 Quantification and average crystallite size of AgO/Ag_2O and MgO@AgO/Ag_2O NPs.

Crystallite size (nm)	Presented Phases			Lattice parameters	Crystal system	COD Entry	References
	Name	Amount (%)	Formula				
21.60	Magnesium Oxide Periclase	31.1	MgO	Space Group: Fd-3m E a = 8.12 Å α = 90.0000° b = 8.12 Å β = 90.0000° c = 8.12 Å γ = 90.0000°	Cubic	96-500-0226	Freund and Farmer, (1974)
	Silver oxide	15.3	AgO	Space Group: P 1 (#1-1) a = 4.21 Å α = 90.0000° b = 4.21 Å β = 90.0000° c = 4.21 Å γ = 90.0000°	Cubic	01-076-1489	Stehlik et al. (1959)
		55.7	Ag_2O	Space Group: P 1 (#1-1) a = 4.71 Å α = 90.0000° b = 4.71 Å β = 90.0000 c = 4.71 Å γ = 90.0000°	Cubic	00-003-0796	Tulsky and Long, (2001)
22.16	Silver oxide	22%	AgO	Space Group: P 1 (#1-1) a = 4.21 Å α = 90.0000° b = 4.21 Å β = 90.0000 c = 4.21 Å γ = 90.0000°	Cubic	01-076-1489	Stehlik et al. (1959)
		78%	Ag_2O	Space Group: P 1 (#1-1) a = 4.71 Å α = 90.0000 b = 4.71 Å β = 90.0000 c = 4.71 Å γ = 90.0000°	Cubic	00-003-0796	Tulsky and Long, (2001)

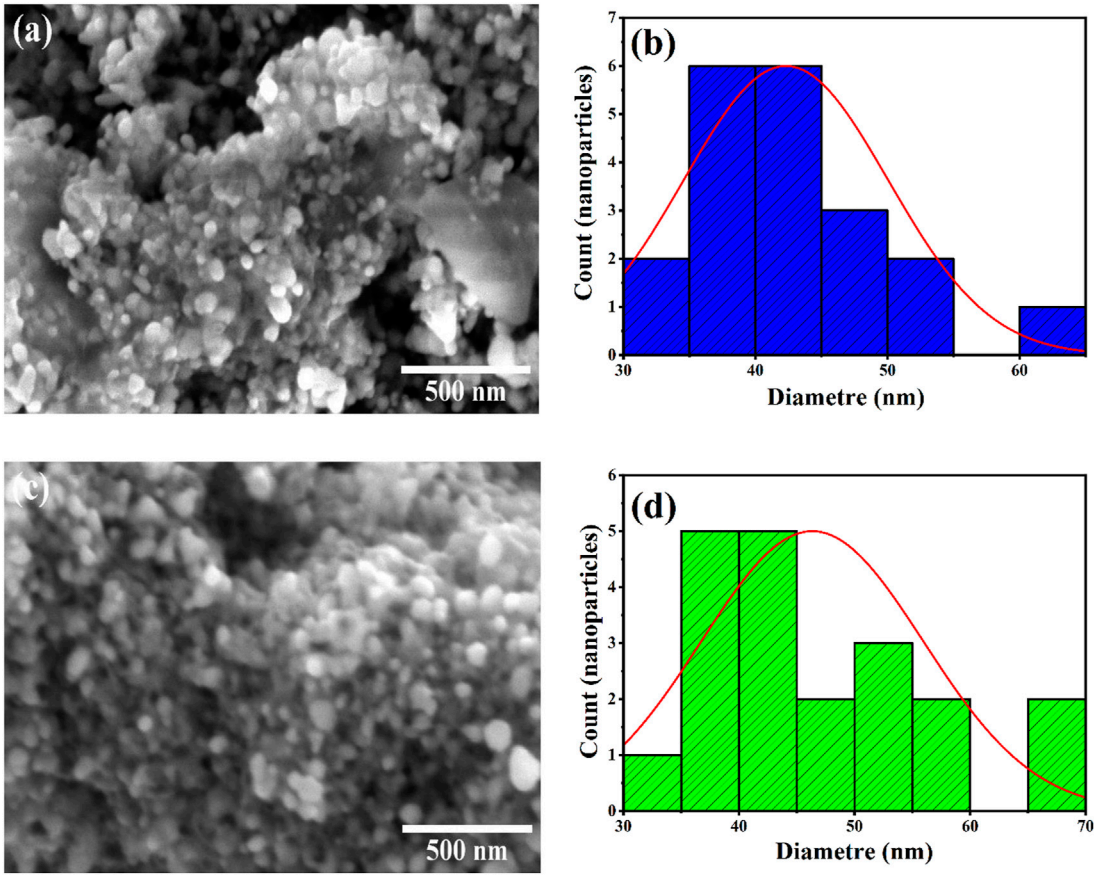

FIGURE 2
SEM images and particle size distributions: **(A,B)** AgO/Ag_2O NPs, **(C,D)** MgO@AgO/Ag_2O NPs.

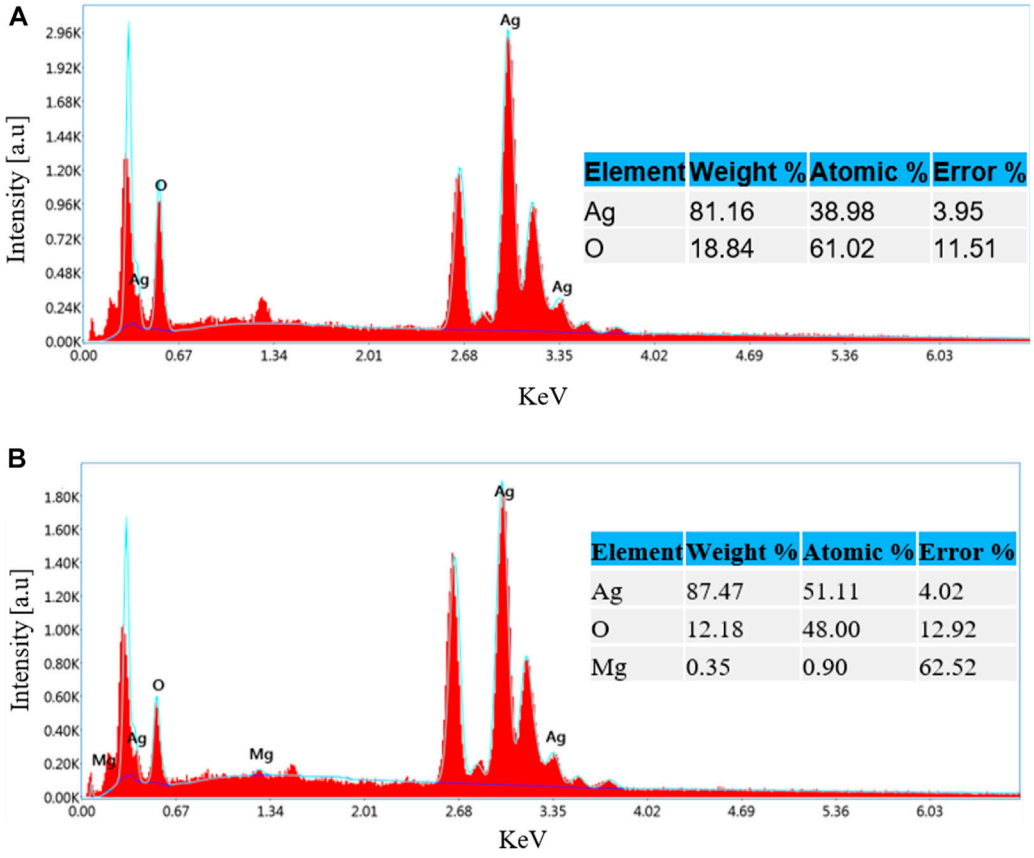

FIGURE 3
EDS of: **(A)** AgO/Ag_2O and **(B)** MgO@AgO/Ag_2O NPs.

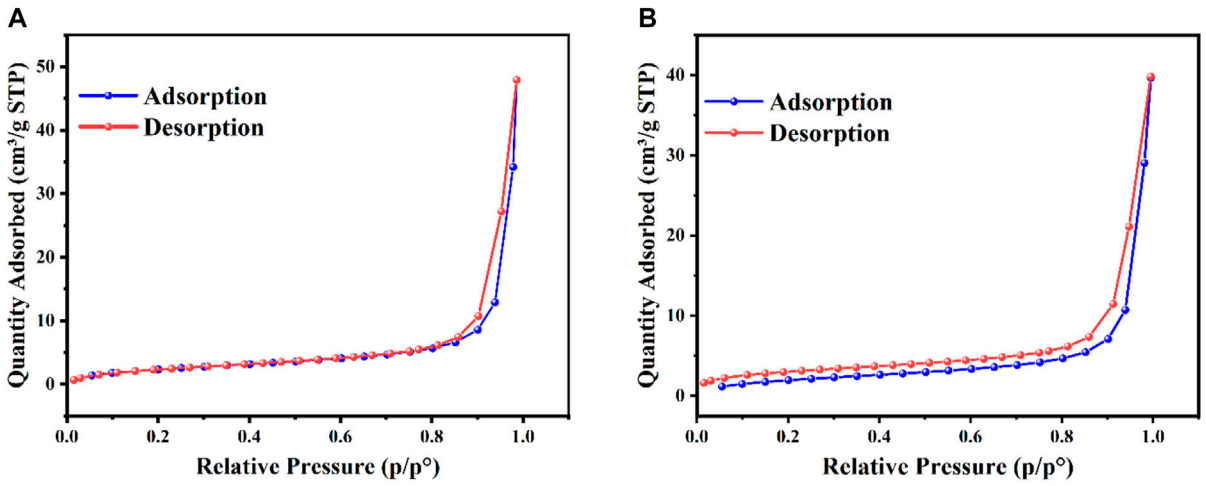

FIGURE 4
Nitrogen adsorption-desorption isotherms: **(A)** AgO/Ag_2O, **(B)** MgO@AgO/Ag_2O NPs.

TABLE 2 BET surface area, porosity, and particle size of AgO/Ag_2O and $MgO@AgO/Ag_2O$ NPs.

Samples		AgO/Ag_2O	$MgO@AgO/Ag_2O$
Surface Area	BET Surface Area	9.1787 m^2/g	7.7166 m^2/g
	Langmuir Surface Area	376.2072 m^2/g	279.6492 m^2/g
Pore Volume	Single point adsorption total pore volume of pores less than 40.3122 nm diameter at p/p° = 0.950000000	0.021557 cm^3/g	0.020119 cm^3/g
	Single point desorption total pore volume of pores less than 40.3122 nm diameter at p/p° = 0.950000000	0.039853 cm^3/g	0.033269 cm^3/g
Pore Size	BJH Adsorption average pore diameter (4V/A)	3.10194 nm	3.15833 nm
	BJH Desorption average pore diameter (4V/A)	2.89018 nm	2.83265 nm
Nanoparticle Size	Average Particle Size	65.3689 nm	77.7541 nm

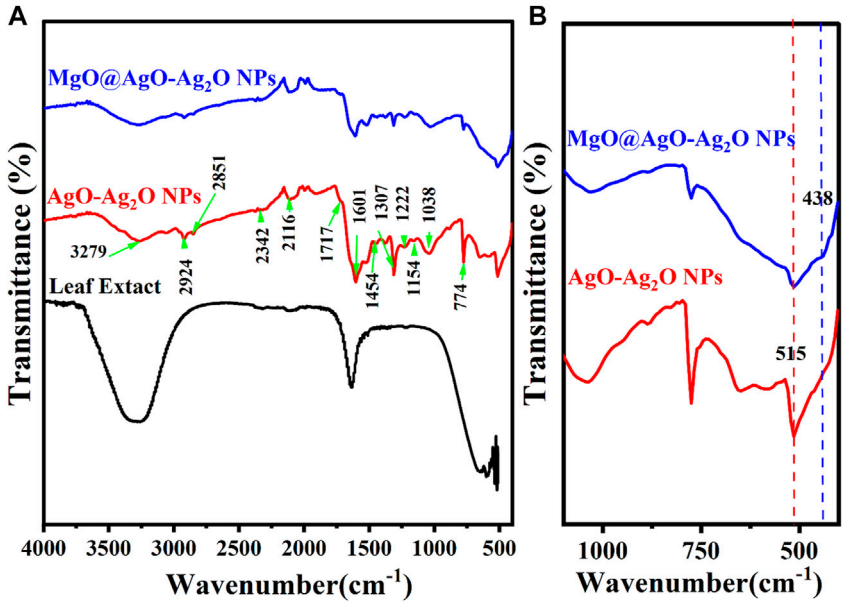

FIGURE 5
(A) FTIR spectra of Purslane (Portulaca Oleracea) leaf extract, AgO/Ag_2O, and $MgO@AgO/Ag_2O$; **(B)** zoomed view range (400 to 1,100 cm^{-1}).

3.3 N_2 adsorption–desorption isotherm

Figure 4 shows the N_2 adsorption-desorption isotherm of 1) AgO/Ag_2O and 2) $MgO@AgO/Ag_2O$ NPs. The specific BET surface area was found to be 9.1787 m^2/g and 7.7166 m^2/g (Table 2). The average pore diameter is 3.1 nm, which demonstrates the existence of mesopores. The pore size between 2.89018 and 2.83265 nm shows that the AgO/Ag_2O and $MgO@AgO/Ag_2O$ NPs, belong to mesoporous materials (2–50 nm), this result can be easily verified by SEM images (Figure 4). The noticeable improvement, in the specific surface area value, proves the enormous photocatalytic activity of the $MgO@AgO/Ag_2O$ NPs.

The figure below presented (Figure 4) depicts the nitrogen adsorption isotherms on the surface of the AgO/Ag_2O and $MgO@AgO/Ag_2O$ NPs. The figures clearly show that:

- All compounds of these nanoparticles belong to mesoporous materials.
- The compound $MgO@AgO/Ag_2O$ NPs presents the best catalytic behavior with concerning the adsorption of N_2.

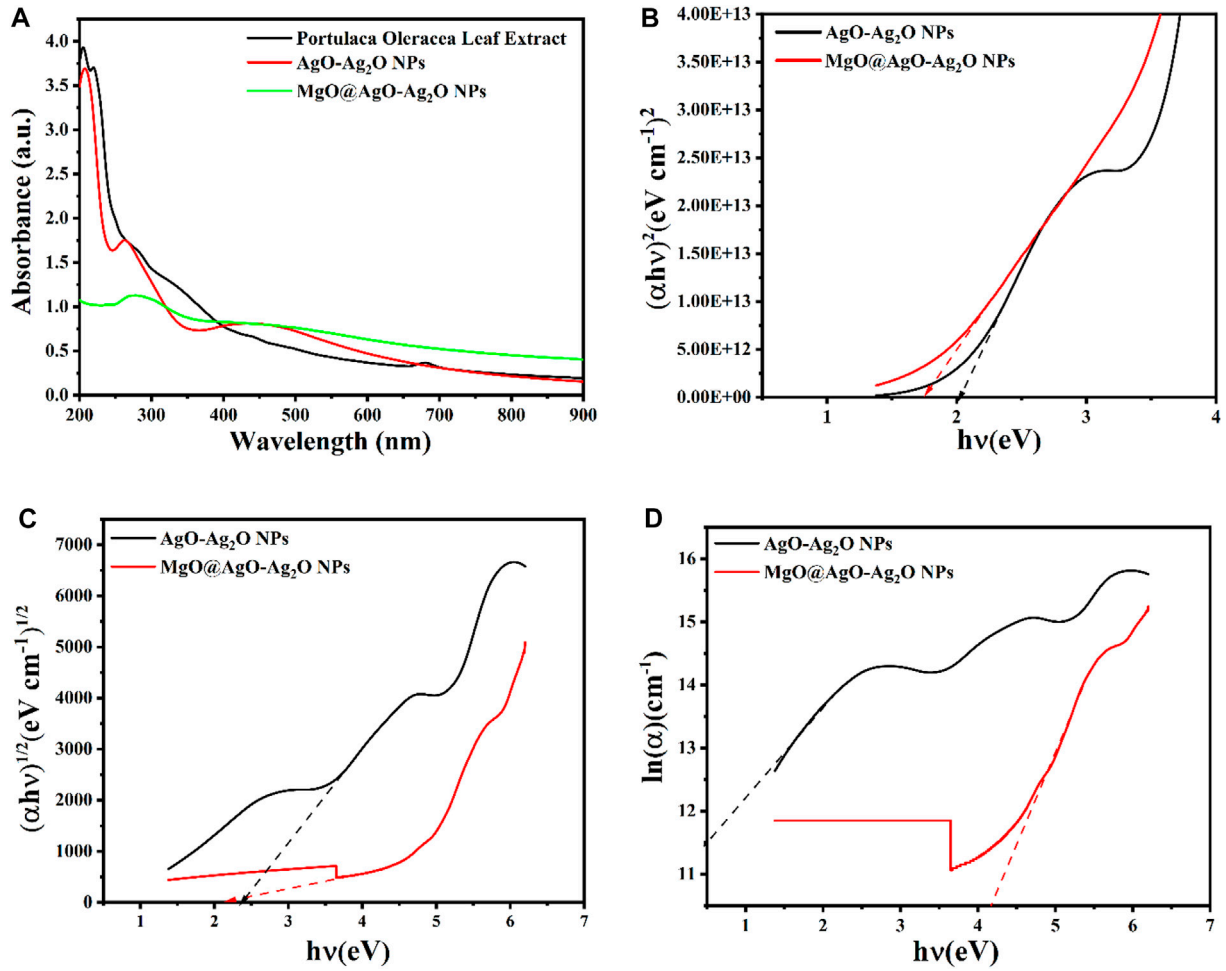

FIGURE 6
UV-vis spectra of **(A)** Extract, AgO/Ag_2O, and MgO@AgO/Ag_2O **(B)** Optical energy gap for direct, **(C)** Indirect transitions, and **(D)** Urbach energy.

3.4 FTIR study

As a result of the aliphatic C-H stretching vibration of hydrocarbon chains and N-H bending vibration, the spectral peaks at 2,924, 2,851, and 1,454 cm^{1-} (Ananthi et al., 2018; Hamouda et al., 2019) are shown in Figure 5.

Peaks centered at 1,340, 1,224, 1,142, and 1,024, and cm^{-1} in the range 1,300–1,000 cm^{-1} are caused by stretching vibrations of C-O groups in anhydrides, esters, ethers, alcohols, and phenols, C-O-H groups in alcohols and phenols, and C-N groups in amines. The vibration of the C=C group of alkenes, the N-H groups of amides, & the amine salts is represented because of the stretch that was seen at 1,603 cm^{-1}. It is possible that the broad stretch in the 3,400–2,400 cm^{-1} range, which is centered at 3,283 cm^{-1}, is caused by the stretching vibrations of amines, amine salts, sulfonamides, alkenes and alkanes, amines' N-H and C-H, and carboxylic acids' C=O. Nitriles, aromatic rings, and aldehydes may all be appeared as other weak bands on the graph Thus, the results of the FTIR investigation show that the main contributing factors to the reduction of Ag^+ ions to Ag^0 nanoparticles in the floral extract were the -C=O (carboxyl), -OH (hydroxyl), and N-H (amine) groups (Chekuri et al., 2015). The interaction of these functional groups with the AgONPs may be responsible for the shifting of these peaks (Hamouda et al., 2019).

The FTIR spectra show that the Mg-O stretching frequency of MgO corresponds to the IR peak at 436 cm^{-1} (Sahoo et al., 2020).

Additionally, the disappearance of the phenolic compound-associated absorbance bands 3,278, 2,924, 2,851, and 1,454 cm^{-1} after the synthesis of MgO@AgO/Ag_2O NPs leads us to conclude that the *Portulaca oleracea L.* leaf extract contains phytochemicals like alcohols, aldehydes, alkanes, epoxy groups, and ether groups that may be responsible for the nucleation process to reduce precursor from M^+ to M^0.

TABLE 3 Direct, indirect optical band gaps, and Urbach energies of synthesized NPs.

Samples	Urbach energy (eV)	Direct optical bandgap (eV)	Indirect optical bandgap (eV)
AgO/Ag_2O	0.379	2.02	2.35
$MgO@AgO/Ag_2O$	0.666	1.75	2.17

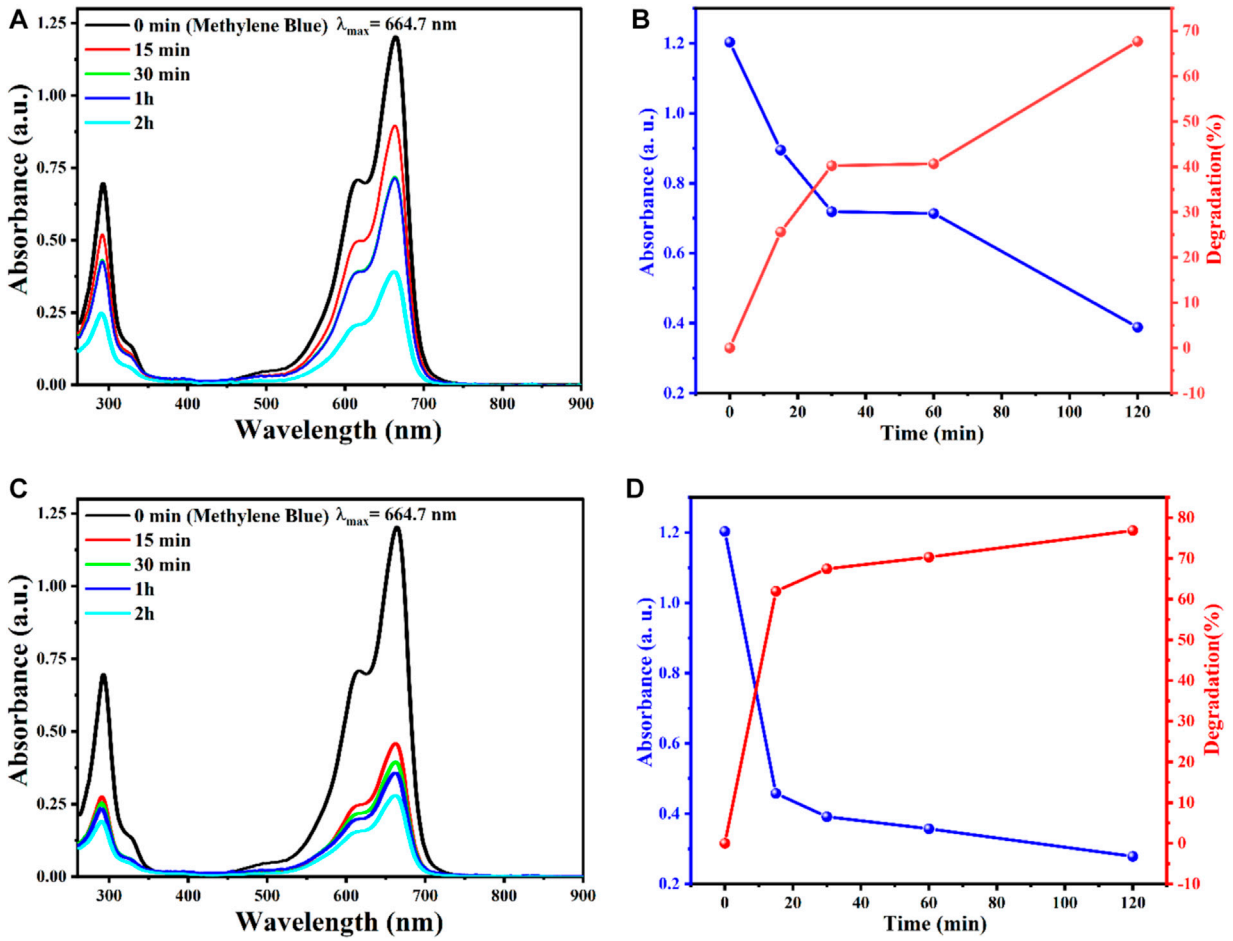

FIGURE 7
The effect reaction time on the degradation of MB, obtained by **(A)** AgO/Ag_2O, Absorbance and degradation versus time: **(B)** AgO/Ag_2O, **(C)** $MgO@AgO/Ag_2O$; **(D)** $MgO@AgO/Ag_2O$ NPs catalyzed degradation of MB dye.

3.5 Optical properties

The formation of AgONPs was achieved within 90 min after adding 1.7 g of $AgNO_3$ to the stirred and heated extract. The process did not require the addition of external additives. In addition, bioactive molecules in leaf extracts interact with silver ions (Ag+) and fuse neighboring small particles into nanoparticles, leading to nucleation of (Ag°) atoms and promoting the nanoparticle growth (Sangar et al., 2019). The formation of AgONPs was confirmed visually by the color change of the reaction mixture from pale green to dark brown. UV-vis spectral scans are commonly implemented to confirm the formation of metal nanoparticles in aqueprobleous solution. Similarly, the product obtained exhibited a surface plasmon resonance (SPR) peak at 240 nm, as a characteristic of AgONPs (Aisida et al., 2019) (Figure 6A). Purslane extract exhibited a peak at approximately 240 nm attributed to the properties of bioactive reducing agent molecules.

To further improve the properties, we synthesized hybrid nanostructures $MgO@AgO/Ag_2O$ containing 10 mM

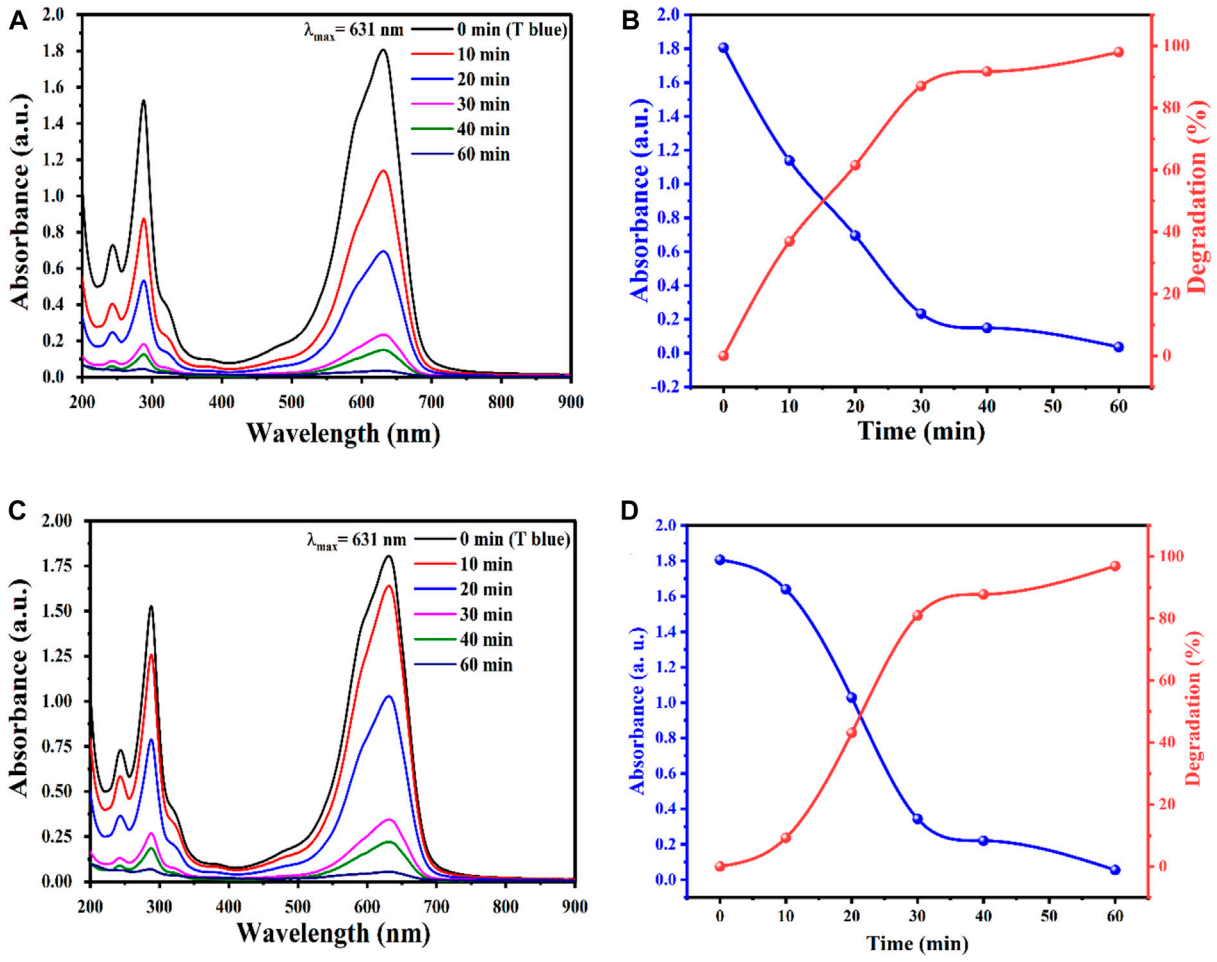

FIGURE 8
The effect of reaction time on degradation of TB, obtained by **(A)** AgO/Ag_2O, Absorbance and degradation versus time: **(B)** AgO/Ag_2O, **(C)** MgO@AgO/Ag_2O; **(D)** MgO@AgO/Ag_2O NPs catalyzed degradation of TB dye.

$MgCl_2$. Magnesium incorporation into the AgO/Ag_2O NPs solution was confirmed by UV-vis spectral analysis. However, the reduced SPR peak intensity is related to confirmation of MgO capping on the AgNP surface (Sathiyaseelan et al., 2020).

The optical band gaps of the biosynthesized NPs were estimated using the absorption spectra of both direct and indirect transitions. The Tauc's equation (Eq. 3) was used to obtain the optical bandgap (Eg) of AgO/Ag_2O and MgO@AgO/Ag_2O NPs (Soltan et al., 2017; Lassoued et al., 2018).

$$(\alpha h\nu) = A\left(h\nu - E_g^{opt}\right)^n \quad (3)$$

According to Lambert–Beer–Bouguer Law, the absorption coefficient (Eq. 4) is given as (Kilic et al., 2019):

$$\alpha = \frac{A}{t}\,2.303 \quad (4)$$

here, a represents the absorbance and t is the of quartz cuvette width (10 mm).

For the direct transition Tauc plots were plotted using $(\alpha h\nu)^2$ against hν, meanwhile $(\alpha h\nu)^{1/2}$ against hν were used to plot the indirect transition graph for each sample. Were hν, *h*, ν and *α* represents the photon energy, Planck's constant, the photon frequency, and the absorption coefficient respectively.

The indirect optical bandgap values of the biosynthesized AgO/Ag_2O and MgO@AgO/Ag_2O NPs varied from 2.35 to 2.17 eV (Figure 6C), while the direct bandgap values varied from 2.02 to 1.75 eV (Figure 6B). The direct optical bandgap of the synthesized sample increased with decoration, while the indirect optical bandgap decreased. Higher bandgap values may indicate the presence of confinement effects in the manufactured product. Such high bandgap values of prepared nanostructures make them suitable for electro-optical devices (Shakir et al., 2009; Shkir et al., 2018).

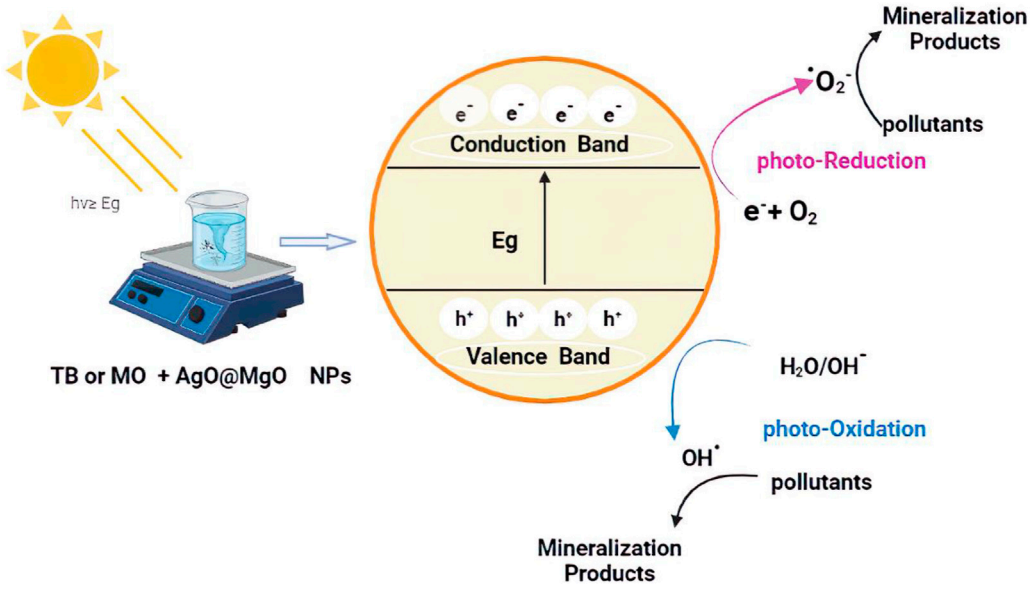

FIGURE 9
MB and TB photocatalytic mineralization mechanism on the surface of AgO/Ag_2O and $MgO@AgO/Ag_2O$.

The Urbach energies (Eq. 5) can be estimated exploiting the slope of the absorption edge in the semi-logarithmic plot (Figure 6D).

$$\ln \alpha = \frac{h\nu}{E_u} + \text{constant } (\ln \alpha_0) \quad (5)$$

here, E_u signifies the Urbach energy.

During our investigation, we observed changes in the Urbach energy of the biosynthesized NPs. These changes occurred due to the influence of MgO. Where an increase in the Urbach energy (from 0.379 to 0.666 eV) was observed upon MgO incorporation, indicating a distortion of the structural order. The Urbach energy characterizes the homogeneity and stability of NPs. The lower the Urbach energy, the more uniform and stable the nanoparticles, and *vice versa*. The increasing AgO addition to the glass structure explains that the structure has become disordered and unstable. This result is consistent with the literature (Table 3) (Işsever et al., 2019).

3.6 Photocatalytic activity of AgO/Ag_2O and $MgO@AgO/Ag_2O$ for azo dye degradation

The organic MB dye was used to measure the catalytic activity of AgO/Ag_2O and $MgO@AgO/Ag_2O$ NPS by measuring the decomposition rate of MB. Selected at 664 nm.

The percentage of MB degradation by AgO/Ag_2O and $MgO@AgO/Ag_2O$ NPs in the presence of sunlight is shown in (Figures 7B, D). The results showed that the percentage MB decomposition values of synthesized AgO/Ag_2O and $MgO@AgO/Ag_2O$ NPs changed from 67.71363% to 76.86329% in the presence of sunlight.

According to (Figures 7A, C), magnesium decoration had a significant effect on the photocatalytic efficiency of AgO/Ag_2O powders. The photocatalytic efficiency of AgO/Ag_2O powder was increased by magnesium decoration. As it can been seen, the photocatalytic efficiency was directly proportional to the exposure duration (time).

This result is caused by surface plasmon resonance (SPR), resulting in increased redox reactions and a higher rate of reactive oxygen species generation. Additionally, heterojunctions structured between AgO/Ag_2O and $MgO@AgO/Ag_2O$ NPs act to increase charge carrier separation, thereby providing highly reactive species that function in photocatalysis (Wang et al., 2011; Ong et al., 2013; Paula et al., 2019).

The effect of photocatalyst decomposition is shown in the Figure 8. Irradiation of NPs affects the degradation of pollutant TB. This effect may be due to the availability of sufficient energy to excite electrons from the valence band to the conduction band. The band gap energy values for AgO/Ag_2O and $MgO@AgO/Ag_2O$ NPs (2.02 eV to 1.75 eV) justify the reduction of the band gap energy. The reaction mechanism is shown in Figure 9.

Wastewater purification remains a major environmental issue due to the increasing and widespread spread of non-degradable pollutants in water, Therefore, this study presents the optimization of photocatalytic degradation of TB dye in an aqueous medium by photocatalyst, under sun irradiation. The

obtained results revealed that most of the TB were removed within 60 min at a rate of 98%.

Photolysis is a chemical reaction in which a chemical substance is broken down by photons, whereas photocatalysis is defined as the acceleration of a photoreaction in the presence of a catalyst. Surface chemistry peculiar to this family of chemicals influences how electron donors and acceptors interact with metal oxide semiconductors. Light is absorbed by an absorption substrate during catalysed photolysis. For electrons to be promoted from the valence band (VB) to the conduction band (CB), forming electron-hole (e^-/h^+) pairs, photocatalyst on semiconducting oxides must absorb photons with energy equal to or greater than the oxide's band gap (Yao et al., 2008; Mittal et al., 2009), as shown in the Eq. 6.

The following steps sum up the mechanism of oxidation for the photodegradation process of the pollutant MB and TB:

Step 1: The radical anion is formed Eq. 6:

$$e^-_{(CB)} + O_2 \xrightarrow{AgO/Ag2O\ or\ MgO@AgO/Ag2O} O_2^{\cdot-} \quad (6)$$

Step 2: The OH radical group appears by the hole (7–11);

$$h^+_{(VB)} + H_2O \xrightarrow{AgO/Ag2O\ or\ MgO@AgO/Ag2O} H^+ + OH^- \quad (7)$$

$$H^+ + \dot{O}_2^- \longrightarrow H\dot{O}_2 \quad (8)$$

$$H\dot{O}_2 + H\dot{O}_2 \longrightarrow H_2O_2 + O_2 \quad (9)$$

$$H_2O_2 \xrightarrow{hv} 2O\dot{H} \quad (10)$$

Step 3: The organic contaminants are oxidized either through direct contact with the holes or by the main radicals and $OH^{\cdot}$ (Eq. 11);

$$\textbf{Toluidine blue or Methylene blue} + OH \xrightarrow{h^+} \textit{Mineralisation products} \quad (11)$$

4 Conclusion

The catalytic activity of AgO/Ag_2O and MgO@AgO/Ag_2O NPs was evaluated based on the rate of degradation of organic dye pollutant. Experimental data illustrated that the percentage of MB degradation values of the synthesized AgO/Ag_2O and MgO@AgO/Ag_2O NPs changed from 67.71 to 76.86%, and 98% of TB degradation. Furthermore, under environmental circumstances, the synthesized AgO/Ag_2O and MgO@AgO/Ag_2O NPs display strong photocatalytic activity for dye degradation of MB and TB stains. AgO/Ag_2O and MgO@AgO/Ag_2O NPs have been found to be useful in the treatment of wastewater (dye degradation). It has proven its ability to purify water from all suspended impurities and remove chemical dyes, and there is a possibility to apply photocatalytic methods to purify water contaminated with hydrocarbons.

Data availability statement

The original contributions presented in the study are included in the article/Supplementary Material, further inquiries can be directed to the corresponding authors.

Author contributions

Conceptualization, writing—original draft preparation: YZ, SL, AB, SM, MT, and FM; methodology, validation, data curation: YZ, SL, AB, SM, MT, SA, HA, KE, EMA-E, MR, OM, and FM; investigation: AB, MT, SM and FM; resources: YZ, AB, AA, KE, EMA-E, MR, and FM; writing—review and editing: AB, SM, MT, SA, HA, KE, EMA-E, MR, and FM; supervision: SL, SM, and FM; Submission: FM. The authors have read and agreed to the published version of the manuscript.

Conflict of interest

Author FM was employed by the company Fluorotronics, Inc.-California Innovations Corporation.

The remaining authors declare that the research was conducted in the absence of any commercial or financial relationships that could be construed as a potential conflict of interest.

Publisher's note

References

Ahmad, M., Rehman, W., Khan, M. M., Qureshi, M. T., Gul, A., Haq, S., et al. (2021). Phytogenic fabrication of ZnO and gold decorated ZnO nanoparticles for photocatalytic degradation of Rhodamine B. *J. Environ. Chem. Eng.* 9, 104725. doi:10.1016/j.jece.2020.104725

Abdullah, J. A. A., Salah Eddine, L., Abderrhmane, B., Alonso-González, M., Guerrero, A., and Romero, A. (2020). Green synthesis and characterization of iron oxide nanoparticles by pheonix dactylifera leaf extract and evaluation of their

antioxidant activity. *Sustain. Chem. Pharm.* 17, 100280. doi:10.1016/j.scp.2020.100280

Ahmadi, O., Jafarizadeh-Malmiri, H., Jodeiri, N. J. G. P., and Synthesis (2018). Eco-friendly microwave-enhanced green synthesis of silver nanoparticles using Aloe vera leaf extract and their physico-chemical and antibacterial studies. *Green Process. Synthesis* 7, 231–240. doi:10.1515/gps-2017-0039

Aisida, S. O., Ugwu, K., Akpa, P. A., Nwanya, A. C., Nwankwo, U., Botha, S. S., et al. (2019). Biosynthesis of silver nanoparticles using bitter leave (Veronica amygdalina) for antibacterial activities. *Surfaces Interfaces* 17, 100359. doi:10.1016/j.surfin.2019.100359

Al Essa, K., Radha, A., and Navrotsky, A. (2021). "Drop solution calorimetric studies of interface enthalpy of cubic silver (I) oxide (Ag2O) nanocrystals," in *Proceedings of the key engineering materials*, 73.

Al-Essa, K. (2018). Activation of Jordanian bentonite by hydrochloric acid and its potential for olive mill wastewater enhanced treatment. *J. Chem.* 2018, 1–10. doi:10.1155/2018/8385692

Al-Essa, K., and Al-Essa, E. M. (2021). Effective approach of activated Jordanian bentonite by sodium ions for total phenolic compounds removal from olive mill wastewater. *J. Chem.* 2021, 1–16. doi:10.1155/2021/7405238

Ananthi, V., Prakash, G. S., Rasu, K. M., Gangadevi, K., Boobalan, T., Raja, R., et al. (2018). Comparison of integrated sustainable biodiesel and antibacterial nano silver production by microalgal and yeast isolates. *J. Photochem. Photobiol. B Biol.* 186, 232–242. doi:10.1016/j.jphotobiol.2018.07.021

Balakrishnan, G., Velavan, R., Mujasam Batoo, K., and Raslan, E. H. (2020). Microstructure, optical and photocatalytic properties of MgO nanoparticles. *Results Phys.* 16, 103013. doi:10.1016/j.rinp.2020.103013

Belaiche, Y., Khelef, A., Laouini, S. E., Bouafia, A., Tedjani, M. L., and Barhoum, A. (2021). Green synthesis and characterization of silver/silver oxide nanoparticles using aqueous leaves extract of Artemisia herba-alba as reducing and capping agents. *Rev. Romana Mater.* 51, 342

Ben Amor, M. L., Zeghdi, S., Laouini, S. E., Bouafia, A., and Meneceur, S. (2022). pH reaction effect on biosynthesis of CuO/Cu_2O nanoparticles by Moringa oleifera leaves extracts for antioxidant activities. *Inorg. Nano-Metal Chem.*, 1–11. doi:10.1080/24701556.2022.2077376

Bouafia, A., and Laouini, E. S. (2021). Plant-Mediated synthesis of iron oxide nanoparticles and evaluation of the antimicrobial activity: A review. *Mini-Reviews Org. Chem.* 18, 725–734. doi:10.2174/1570193X17999200908091139

Bouafia, A., Laouini, S. E., and Ouahrani, M. R. (2020). A review on green synthesis of CuO nanoparticles using plant extract and evaluation of antimicrobial activity. *Asia. Jour. Rese. Chem.* 13, 65–70. doi:10.5958/0974-4150.2020.00014.0

Bouafia, A., Laouini, S. E., Ahmed, A. S. A., Soldatov, A. V., Algarni, H., Feng Chong, K., et al. (2021). The recent progress on silver nanoparticles: Synthesis and electronic applications. *Nanomaterials* 11, 2318. doi:10.3390/nano11092318

Bouafia, A., and Laouini, S. E. (2020). Green synthesis of iron oxide nanoparticles by aqueous leaves extract of Mentha Pulegium L.: Effect of ferric chloride concentration on the type of product. *Mater. Lett.* 265, 127364. doi:10.1016/j.matlet.2020.127364

Bouafia, A., Laouini, S. E., Khelef, A., Tedjani, M. L., and Guemari, F. (2021). Effect of ferric chloride concentration on the type of magnetite (Fe3O4) nanoparticles biosynthesized by aqueous leaves extract of artemisia and assessment of their antioxidant activities. *J. Clust. Sci.* 32, 1033–1041. doi:10.1007/s10876-020-01868-7

Bouafia, A., Laouini, S. E., Tedjani, M. L., Ali, G. A. M., and Barhoum, A. (2021). Green biosynthesis and physicochemical characterization of Fe3O4 nanoparticles using Punica granatum L. fruit peel extract for optoelectronic applications. *Text. Res. J.* 92, 2685–2696. doi:10.1177/00405175211006671

Bulgariu, L., Escudero, L. B., Bello, O. S., Iqbal, M., Nisar, J., Adegoke, K. A., et al. (2019). The utilization of leaf-based adsorbents for dyes removal: A review. *J. Mol. Liq.* 276, 728–747. doi:10.1016/j.molliq.2018.12.001

Cai, J., Li, R., Cao, J., Liu, J., Han, J., and Huang, M. (2022). Plasmonic Au-decorated hierarchical p-NiO/n-ZnO heterostructure arrays for enhanced photoelectrochemical water splitting. *Phys. E Low-dimensional Syst. Nanostructures* 135, 114974. doi:10.1016/j.physe.2021.114974

Chekuri, M., Gangarudraiah, S., Roopavatharam, L. B., Kaphle, A., and Chalimeswamy, A. J. E. C. B. (2015). *Green synthesis of stable silver nanoparticles using flower extract of rosa damascena: Characterization, antimicrobial and anti-oxidant activity study*, 4, 454

Daoudi, H., Bouafia, A., Meneceur, S., Laouini, S. E., Belkhalfa, H., Lebbihi, R., et al. (2022). Secondary metabolite from nigella sativa seeds mediated synthesis of silver oxide nanoparticles for efficient antioxidant and antibacterial activity. *J. Inorg. Organomet. Polym.* 32, 4223–4236. doi:10.1007/s10904-022-02393-y

Deekshitha, D., and Shetty, K. V. (2021). Solar light active biogenic titanium dioxide embedded silver oxide (AgO/Ag2O@TiO2) nanocomposite structures for dye degradation by photocatalysis. *Mater. Sci. Semicond. Process.* 132, 105923. doi:10.1016/j.mssp.2021.105923

Djamila, B., Eddine, L. S., Abderrhmane, B., Nassiba, A., and Barhoum, A. (2022). *In vitro* antioxidant activities of copper mixed oxide (CuO/Cu2O) nanoparticles produced from the leaves of Phoenix dactylifera L. *Biomass Conv. Bioref.*. doi:10.1007/s13399-022-02743-3

Freund, F. (1974). "Ceramics and thermal transformations of minerals," in *The Infrared Spectra of Minerals*. Editor V. C. Farmer (London: Mineralogical Society of Great Britain and Ireland), 462–485. Vol. 4, 0. Available at: https://www.yumpu.com/fr/document/read/16938251/paleontologie-taphonomie-et-prehistoire-227-p/214.

Gallo, J., Panacek, A., Prucek, R., Kriegova, E., Hradilova, S., Hobza, M., et al. (2016). Silver nanocoating technology in the prevention of prosthetic joint infection. *Materials* 9, 337. doi:10.3390/ma9050337

Gherbi, B., Laouini, S. E., Meneceur, S., Bouafia, A., Hemmami, H., Tedjani, M. L., et al. (2022). Effect of pH value on the bandgap energy and particles size for biosynthesis of ZnO nanoparticles: Efficiency for photocatalytic adsorption of methyl orange. *Sustainability* 14, 11300. doi:10.3390/su141811300

Gosens, I., Post, J. A., de la Fonteyne, L. J., Jansen, E. H., Geus, J. W., Cassee, F. R., et al. (2010). Impact of agglomeration state of nano-and submicron sized gold particles on pulmonary inflammation. *Part. Fibre Toxicol.* 7, 37–11. doi:10.1186/1743-8977-7-37

Hamouda, R. A., Hussein, M. H., Abo-Elmagd, R. A., and Bawazir, S. S. J. S. R. (2019). Synthesis and biological characterization of silver nanoparticles derived from the cyanobacterium Oscillatoria limnetica. *Sci. Rep.* 9, 13071–13117. doi:10.1038/s41598-019-49444-y

Hileuskaya, K., Ladutska, A., Kulikouskaya, V., Kraskouski, A., Novik, G., Kozerozhets, I., et al. (2020). 'Green'approach for obtaining stable pectin-capped silver nanoparticles: Physico-chemical characterization and antibacterial activity. *Colloids Surfaces A Physicochem. Eng. Aspects* 585, 124141. doi:10.1016/j.colsurfa.2019.124141

Hunge, Y. M., Uchida, A., Tominaga, Y., Fujii, Y., Yadav, A. A., Kang, S.-W., et al. (2021). Visible light-assisted photocatalysis using spherical-shaped BiVO4 photocatalyst. *Catalysts* 11, 460. doi:10.3390/catal11040460

Işsever, U. G., Kilic, G., Peker, M., Ünaldi, T., and Aybek, A. Ş. J. J. o. M. S. M. i. E. (2019). Effect of low ratio V5+ doping on structural and optical properties of borotellurite semiconducting oxide glasses. *J. Mat. Sci. Mat. Electron.* 30, 15156–15167. doi:10.1007/s10854-019-01889-7

Kilic, G., Issever, U. G., and Ilik, E. J. J. O. M. S. M. I. E. (2019). Characterization of Er3+ doped ZnTeTa semiconducting oxide glass. *J. Mat. Sci. Mat. Electron.* 30, 8920–8930. doi:10.1007/s10854-019-01220-4

Kolarova, K., Vosmanska, V., Rimpelova, S., Ulbrich, P., and Svorcik, V. J. J. O. N. (2015). Silver nanoparticles stabilized using chitosan films: Preparation, properties and antibacterial activity. *J. Nanosci. Nanotechnol.* 15, 10120–10126. doi:10.1166/jnn.2015.11697

Kuriakose, S., Choudhary, V., Satpati, B., and Mohapatra, S. J. B. (2014). Enhanced photocatalytic activity of Ag–ZnO hybrid plasmonic nanostructures prepared by a facile wet chemical method. *Beilstein J. Nanotechnol.* 5, 639–650. doi:10.3762/bjnano.5.75

Laid, T. M., Abdelhamid, K., Eddine, L. S., and Abderrhmane, B. (2021). Optimizing the biosynthesis parameters of iron oxide nanoparticles using central composite design. *J. Mol. Struct.* 1229, 129497. doi:10.1016/j.molstruc.2020.129497

Laouini, S. E., Bouafia, A., Soldatov, A. V., Algarni, H., Tedjani, M. L., Ali, G. A. M., et al. (2021). Green synthesized of Ag/Ag2O nanoparticles using aqueous leaves extracts of phoenix dactylifera L. And their azo dye photodegradation. *Membranes* 11, 468. doi:10.3390/membranes11070468

Lassoued, A., Lassoued, M. S., Dkhil, B., Ammar, S., and Gadri, A. J. P. (2018). Synthesis, structural, morphological, optical and magnetic characterization of iron oxide (α-Fe 2 O 3) nanoparticles by precipitation method: Effect of varying the nature of precursor. *Phys. E Low-dimensional Syst. Nanostructures* 97, 328–334. doi:10.1016/j.physe.2017.12.004

Martinez-Boubeta, C., Balcells, L., Cristòfol, R., Sanfeliu, C., Rodríguez, E., Weissleder, R., et al. (2010). Self-assembled multifunctional Fe/MgO nanospheres for magnetic resonance imaging and hyperthermia. *Nanomedicine Nanotechnol. Biol. Med.* 6, 362–370. doi:10.1016/j.nano.2009.09.003

Mashkoor, F., and Nasar, A. J. J. O. M. (2020). Magsorbents: Potential candidates in wastewater treatment technology – a review on the removal of methylene blue dye. *J. Magnetism Magnetic Mater.* 500, 166408. doi:10.1016/j.jmmm.2020.166408

Meneceur, S., Hemmami, H., Bouafia, A., Laouini, S. E., Tedjani, M. L., Berra, D., et al. (2022). Photocatalytic activity of iron oxide nanoparticles synthesized by different plant extracts for the degradation of diazo dyes Evans blue and Congo red. *Biomass Conv. bioref.* doi:10.1007/s13399-022-02734-4

Mittal, N., Shah, A., Punjabi, P. B., and Sharma, V. K. (2009). Photodegradation of rose bengal using MnO_2 (manganese dioxide). *Rasayan J. Chem.* 2, 516–520.

Ohashi, S., Saku, S., and Yamamoto, K. J. J. O. R. (2004). Antibacterial activity of silver inorganic agent YDA filler. *J. Oral Rehabil.* 31, 364–367. doi:10.1111/j.1365-2842.2004.01200.x

Okaiyeto, K., Ojemaye, M. O., Hoppe, H., Mabinya, L. V., and Okoh, A. I. J. M. (2019). Phytofabrication of silver/silver chloride nanoparticles using aqueous leaf extract of Oedera genistifolia: Characterization and antibacterial potential. *Molecules* 24, 4382. doi:10.3390/molecules24234382

Ong, W. L., Natarajan, S., Kloostra, B., and Ho, G. W. J. N. (2013). Metal nanoparticle-loaded hierarchically assembled ZnO nanoflakes for enhanced photocatalytic performance. *Nanoscale* 5, 5568–5575. doi:10.1039/c3nr00043e

Paula, C., Andrade Neto, N., Garcia, L., Nascimento, R., Paskocimas, C., Bomio, M., et al. (2019). Increased degradation capacity of methylene blue dye using Mg-doped ZnO nanoparticles decorated by Ag0 nanoparticles. *J. Elec. Materi.* 48, 3017–3025. doi:10.1007/s11664-019-07059-z

Rai, M. K., Deshmukh, S., Ingle, A., and Gade, A. J. J. O. A. M. (2012). Silver nanoparticles: The powerful nanoweapon against multidrug-resistant bacteria. *J. Appl. Microbiol.* 112, 841–852. doi:10.1111/j.1365-2672.2012.05253.x

Rónavári, A., Igaz, N., Adamecz, D. I., Szerencsés, B., Molnar, C., Kónya, Z., et al. (2021). Green silver and gold nanoparticles: Biological synthesis approaches and potentials for biomedical applications. *Molecules* 26, 844. doi:10.3390/molecules26040844

Roy, S., and Das, T. K. J. I (2015). *Plant mediated green synthesis of silver nanoparticles*, 3, 1044

Sahoo, S. K., Dhal, J. P., and Panigrahi, G. K. J. C. C. (2020). Magnesium oxide nanoparticles decorated iron oxide nanorods: Synthesis, characterization and remediation of Congo red dye from aqueous media. *Compos. Commun.* 22, 100496. doi:10.1016/j.coco.2020.100496

Sangar, S., Sharma, S., Vats, V. K., Mehta, S., and Singh, K. J. J. O. C. P. (2019). Biosynthesis of silver nanocrystals, their kinetic profile from nucleation to growth and optical sensing of mercuric ions. *J. Clean. Prod.* 228, 294–302. doi:10.1016/j.jclepro.2019.04.238

Sathiyaseelan, A., Saravanakumar, K., Mariadoss, A. V. A., and Wang, M.-H. J.(2020). Biocompatible fungal chitosan encapsulated phytogenic silver nanoparticles enhanced antidiabetic, antioxidant and antibacterial activity. *Int. J. Biol. Macromol.* 153, 63–71. doi:10.1016/j.ijbiomac.2020.02.291

Shakir, M., Kushwaha, S., Maurya, K., Bhagavannarayana, G., and Wahab, M. J. S. S. C. (2009). Characterization of ZnSe nanoparticles synthesized by microwave heating process. *Solid State Commun.* 149, 2047–2049. doi:10.1016/j.ssc.2009.08.021

Sharma, S., and Bhattacharya, A. J. A. W. S. (2017). Drinking water contamination and treatment techniques. *Appl. Water Sci.* 7, 1043–1067. doi:10.1007/s13201-016-0455-7

Shkir, M., Yahia, I., Ganesh, V., Bitla, Y., Ashraf, I., Kaushik, A., et al. (2018). A facile synthesis of Au-nanoparticles decorated PbI2 single crystalline nanosheets for optoelectronic device applications. *Sci. Rep.* 8, 13806–13810. doi:10.1038/s41598-018-32038-5

Sohrabnezhad, S., and Seifi, A. J. A. S. S. (2016). The green synthesis of Ag/ZnO in montmorillonite with enhanced photocatalytic activity. *Appl. Surf. Sci.* 386, 33–40. doi:10.1016/j.apsusc.2016.05.102

Soltan, W. B., Nasri, S., Lassoued, M. S., and Ammar, S. J. (2017). Structural, optical properties, impedance spectroscopy studies and electrical conductivity of SnO2 nanoparticles prepared by polyol method. *J. Mat. Sci. Mat. Electron.* 28, 6649–6656. doi:10.1007/s10854-017-6356-1

Stehlik, B., Weidenthaler, P., and Vlach, J. (1959). Kristallstruktur von Silber(II)-oxyd. *Collect. Czech. Chem. Commun.* 24, 1416–1419. doi:10.1135/cccc19591416

Stewart, I. E., Kim, M. J., and Wiley, B. J. J. A. A. M. (2017). Interfaces Effect of morphology on the electrical resistivity of silver nanostructure films. *ACS Appl. Mat. Interfaces* 9, 1870–1876. doi:10.1021/acsami.6b12289

Tedjani, M. L., Khelef, A., Laouini, S. E., Bouafia, A., and Albalawi, N. (2022). Optimizing the antibacterial activity of iron oxide nanoparticles using central composite design. *J. Inorg. Organomet. Polym.* 32, 3564–3584. doi:10.1007/s10904-022-02367-0

Tulsky, E. G., and Long, J. R. (2001). Dimensional reduction: A practical formalism for manipulating solid structures. *Chem. Mat.* 13, 1149–1166. doi:10.1021/cm0007858

Wang, Y., Shi, R., Lin, J., Zhu, Y. J. E., and Science, E. (2011). Enhancement of photocurrent and photocatalytic activity of ZnO hybridized with graphite-like C 3 N 4. *Energy Environ. Sci.* 4, 2922–2929. doi:10.1039/c0ee00825g

Wijesinghe, U., Thiripuranathar, G., Iqbal, H., and Menaa, F. (2021). Biomimetic synthesis, characterization, and evaluation of fluorescence resonance energy transfer, photoluminescence, and photocatalytic activity of zinc oxide nanoparticles. *Sustainability* 13, 2004. doi:10.3390/su13042004

Wijesinghe, U., Thiripuranathar, G., Menaa, F., Iqbal, H., Razzaq, A., and Almukhlifi, H. (2021). Green synthesis, structural characterization and photocatalytic applications of ZnO nanoconjugates using Heliotropium indicum. *Catalysts* 11, 831. doi:10.3390/catal11070831

Xing, Y.-Z., Zhang, H., Liu, X.-B., and Zheng, Y.-M. J. N. P. A. (2017). Pau li-blocking effect in two-body collisions dominates the in-medium effects in heavy-ion reactions near Fermi energy. *Nucl. Phys. A* 957, 135–143. doi:10.1016/j.nuclphysa.2016.08.006

Xu, L., Wang, Y.-Y., Huang, J., Chen, C.-Y., Wang, Z.-X., and Xie, H. J. T. (2020). Silver nanoparticles: Synthesis, medical applications and biosafety. *Theranostics* 10, 8996–9031. doi:10.7150/thno.45413

Yadav, A. A., Kang, S.-W., and Hunge, Y. M. (2021). Photocatalytic degradation of Rhodamine B using graphitic carbon nitride photocatalyst. *J. Mat. Sci. Mat. Electron.* 32, 15577–15585. doi:10.1007/s10854-021-06106-y

Yao, Y., Li, G., Ciston, S., Lueptow, R. M., and Gray, K. A. (2008). Photoreactive TiO_2/carbon nanotube composites: Synthesis and reactivity. *Environ. Sci. Technol.* 42, 4952–4957. doi:10.1021/es800191n

Yu, X., Yang, H., and Wang, H. (2022). A cleaner biocementation method of soil via microbially induced struvite precipitation: A experimental and numerical analysis. *J. Environ. Manag.* 316, 115280. doi:10.1016/j.jenvman.2022.115280

Zeng, S., Baillargeat, D., Ho, H.-P., and Yong, K.-T. J. C. S. R. (2014). Nanomaterials enhanced surface plasmon resonance for biological and chemical sensing applications. *Chem. Soc. Rev.* 43, 3426–3452. doi:10.1039/c3cs60479a

Zhang, J., Ding, E., Xu, S., Li, Z., Fakhri, A., and Gupta, V. K. (2020). Production of metal oxides nanoparticles based on poly-alanine/chitosan/reduced graphene oxide for photocatalysis degradation, anti-pathogenic bacterial and antioxidant studies. *Int. J. Biol. Macromol.* 164, 1584–1591. doi:10.1016/j.ijbiomac.2020.07.291

Zhang, R., Lee, P., Lui, V. C., Chen, Y., Liu, X., Lok, C. N., et al. (2015). Biology; Medicine. Silver nanoparticles promote osteogenesis of mesenchymal stem cells and improve bone fracture healing in osteogenesis mechanism mouse model. *Nanomedicine Nanotechnol. Biol. Med.* 11, 1949–1959. doi:10.1016/j.nano.2015.07.016

Zhou, Y.-X., Xin, H.-L., Rahman, K., Wang, S.-J., Peng, C., and Zhang, H. (2015). *Portulaca oleracea* L.: A review of phytochemistry and pharmacological effects. *BioMed Res. Int.* 2015, 925631–925711. doi:10.1155/2015/925631

frontiers | Frontiers in Chemistry

TYPE Mini Review
PUBLISHED 25 April 2023
DOI 10.3389/fchem.2023.1195640

OPEN ACCESS

EDITED BY
Tao Wei,
University of Erlangen Nuremberg, Germany

REVIEWED BY
Muqing Chen,
University of Science and Technology of China, China

*CORRESPONDENCE
Xuewen Wang,
iamxwwang@nwpu.edu.cn

†These authors have contributed equally to this work

RECEIVED 28 March 2023
ACCEPTED 10 April 2023
PUBLISHED 25 April 2023

CITATION
Wang H, Xu M, Ji H, He T, Li W, Zheng L and Wang X (2023), Laser-assisted synthesis of two-dimensional transition metal dichalcogenides: a mini review. *Front. Chem.* 11:1195640. doi: 10.3389/fchem.2023.1195640

Laser-assisted synthesis of two-dimensional transition metal dichalcogenides: a mini review

Hanxin Wang[1†], Manzhang Xu[1,2,3†], Hongjia Ji[1], Tong He[4,5], Weiwei Li[1,2,3], Lu Zheng[1,2,3] and Xuewen Wang[1,2,3,6*]

[1]Frontiers Science Center for Flexible Electronics (FSCFE), Institute of Flexible Electronics (IFE), Northwestern Polytechnical University, Xi'an, China, [2]MIIT Key Laboratory of Flexible Electronics (KLoFE), Northwestern Polytechnical University, Xi'an, China, [3]Shaanxi Key Laboratory of Flexible Electronics (KLoFE), Northwestern Polytechnical University, Xi'an, China, [4]Institute of Basic and Translational Medicine, Xi'an Medical University, Xi'an, China, [5]School of Chemistry and Chemical Engineering, Shaanxi Normal University, Xi'an, China, [6]Key Laboratory of Flexible Electronics of Zhejiang Province, Ningbo Institute of Northwestern Polytechnical University, Ningbo, China

The atomically thin two-dimensional (2D) transition metal dichalcogenides (TMDCs) have attracted the researcher's interest in the field of flexible electronics due to their high mobility, tunable bandgaps, and mechanical flexibility. As an emerging technique, laser-assisted direct writing has been used for the synthesis of TMDCs due to its extremely high preparation accuracy, rich light–matter interaction mechanism, dynamic properties, fast preparation speed, and minimal thermal effects. Currently, this technology has been focused on the synthesis of 2D graphene, while there are few literatures that summarize the progress in direct laser writing technology in the synthesis of 2D TMDCs. Therefore, in this mini-review, the synthetic strategies of applying laser to the fabrication of 2D TMDCs have been briefly summarized and discussed, which are divided into top-down and bottom-up methods. The detailed fabrication steps, main characteristics, and mechanism of both methods are discussed. Finally, prospects and further opportunities in the booming field of laser-assisted synthesis of 2D TMDCs are addressed.

KEYWORDS

laser, two-dimensional materials, transition metal dichalcogenides, synthesis methods, mechanism

1 Introduction

Flexible electronics is a disruptive science and technology based on a high degree of interdisciplinary integration, which provides novel opportunities for the development of the next generation of the information technology revolution and the era of intelligent manufacturing (Zheng et al., 2022; Li et al., 2023). The two-dimensional materials, especially transition metal dichalcogenides have become trending research topics of flexible electronics due to their unique structure, mechanical flexibility, tunable bandgaps, and high mobility (Mak et al., 2010; Fan et al., 2015; Kim et al., 2015; Leong, 2020; Yu et al., 2020; Liu et al., 2021; Wu et al., 2022).

Currently, significant research has been focused on the efficient synthesis of high-quality large-scale 2D TMDCs with simple crafts and low costs, owing to the prerequisite and key factor for their diverse advanced industrial application (Lee et al., 2012; Lei et al., 2013; Mahjouri Samani et al., 2014; Shim et al., 2014; Xia et al., 2014; Xu et al., 2021b). Various synthesis techniques, such as chemical vapor deposition (CVD), metal–organic chemical

TABLE 1 Summary of preparation methods of 2D TMDCs.

Method	Advantage	Disadvantage
Mechanical exfoliation	High quality, simple	Low yield, challenging to mass production
Liquid-phase exfoliation	High preparation efficiency, simple	Small lateral size, low yield
Physical vapor deposition	High quality, low cost	Low repetition rate, complex process
Atomic layer deposition	High repetition rate	High cost, complex process
Hydrothermal	High yield, low cost	Low controllability, unstable grain size, low quality
CVD	Low cost, high quality, possible to mass production	High preparation temperature, low repetition rate
MOCVD	High deposition rate, high quality	Chemical pollution, high cost, long production cycle
MBE	Atomic-level control, high purity	Rigorous conditions, expensive equipment
Laser-assisted synthesis	Low cost, high repetition rate, patternable	Hardly achieve nanometer-level resolution, numerous defects

vapor deposition (MOCVD), and molecular beam epitaxy (MBE), have been used to control the growth of 2D TMDCs on different substrates and show great potential in growing high-quality crystalline 2D TMDCs under high temperature (Yu et al., 2017; Gao et al., 2021). However, patterning TMDCs cannot be achieved in the synthesis process, and an additional patterning process is still required during the device fabrication (Mak et al., 2010). In recent years, direct laser writing technology has been widely used in the synthesis of materials because of the ability to minimize thermal effects, rich light–matter interaction mechanism, kinetic properties, the high fabrication accuracy, and fast preparation speed (Lu et al., 2014; Jung et al., 2019; Park et al., 2020a; Park et al., 2020b; Hu et al., 2020). In addition, maskless and lithography-free properties of laser patterning can enable one-step fabrication of the desired specific patterns, avoiding material contamination while reducing the process flow (Cao et al., 2013; Mohapatra et al., 2020). All preparation methods of synthesizing 2D TMDCs and their advantages and disadvantages are shown in Table 1, which shows the salient features of direct laser writing technology from multiple perspectives.

In this mini-review, we systematically summarize the latest studies on the laser-assisted synthesis of 2D TMDCs. Basically, there are essentially two classes of synthetic strategies: top-down and bottom-up methods. With regard to top-down methods, the advantages and mechanisms of the laser–material interactions are discussed, including laser exfoliation, laser thinning, and laser-driven phase transition. With regard to bottom-up methods, the growth mechanisms are discussed, including direct laser writing, laser heterostructures, and laser doping. Finally, prospects and further opportunities in the laser-assisted synthesis of 2D TMDCs are also addressed.

2 Top-down synthesis methods

Top-down synthesis methods generally require synthesizing the 2D TMDC crystal first, followed by further processing via laser–material interactions to improve the morphology or properties. Specifically, it can be classified into laser stripping, laser thinning, and laser-driven phase transition.

2.1 Laser exfoliation

The unique characteristics of the laser, such as ultra-high-peak power density and short pulse duration, far exceed conventional heating methods, such as electric or gas heating, thus making it possible to exfoliate monolayers of two-dimensional materials. The van der Waals interaction between the layers of TMDC materials can be broken by the laser, which enables the efficient and controllable preparation of TMDCs with a specific number of layers in a relatively short time. In addition, this technique has now been used to exfoliate a variety of 2D TMDC materials such as MoS_2, $MoSe_2$, and WS_2 under different conditions (Schuffenhauer et al., 2005; Hu et al., 2006; An et al., 2018; Gao et al., 2019; Zhai et al., 2021; Zuo et al., 2021; Kimiagar and Abrinaei, 2023).

TMDCs are layered materials that form an MX_2 crystal structure composed of strongly covalently bonded X-M-X sandwiches, and the X-M-X layers are held together by weak van der Waals forces (An et al., 2018). Zhai et al. (2021) created a method for exfoliating 2H-phase MoS_2 (2H-MoS_2), that is, both efficient and free from contaminants, and also the exfoliation process can be directly observed by optical microscopy (Figure 1A). Compared to other exfoliation techniques, this method is significantly faster and easier. The thickness of the irradiated region underwent a reduction approximately from 100 nm to 5 nm, and the area of the peeled region is also much larger than the diameter of the laser spot used. They believed that the light illumination and water medium are essential for the laser exfoliation of 2D TMDCs. When 2H-MoS_2 layers are exposed to laser irradiation, the rapid vaporization of water molecules between the layers results in the exfoliation of MoS_2 sheets, and the exfoliation process can be controlled by applying a bias voltage. The related research results indicated that water molecules could be incorporated into the interlayer spaces of 2H-MoS_2 sheets (Levita and Righi, 2017; Ma et al., 2018). The phase transition may accompany the exfoliation process. Gao et al. (2019) achieved a one-step exfoliating bulk 2H-MoS_2 into 2H and 1T MoS_2 nanosheets using pulsed laser irradiation. Figure 1B shows a conceptual model of this experimental mechanism, suggesting that the 2H-phase MoS_2 can be reversed into 1T MoS_2 with the assistance of the chemically doped Fe^{3+} ions. In addition, the capability of the protic solvent also provides the proton to the reaction environment and plays a crucial role in triggering the phase transition.

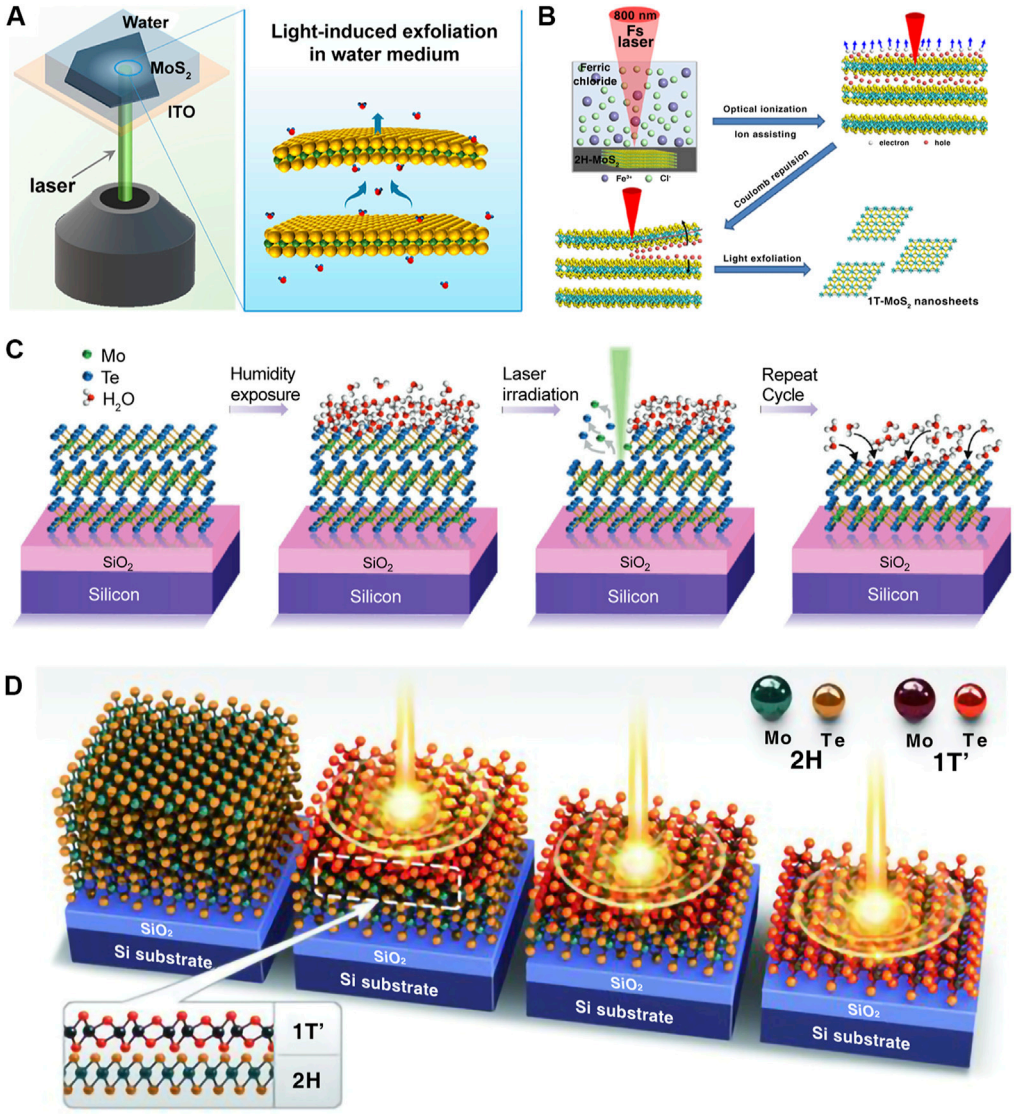

FIGURE 1
Top-down synthesis methods. **(A)** Schematic of the laser exfoliation device for 2H-MoS_2 flakes in aqueous media (Zhai et al., 2021) (Copyright 2021, American Chemical Society). **(B)** Schematic of the preparation of MoS_2 nanosheets through femtosecond laser exfoliation (Zuo et al., 2021) (Copyright 2021, American Chemical Society). **(C)** Schematic of the mechanism for laser thinning of $MoTe_2$ (Nagareddy et al., 2018) (Copyright 2018, Wiley-VCH). **(D)** Schematic of the laser-driven phase patterning process of $MoTe_2$ from 2H to 1T′ (Cho et al., 2015) (Copyright 2015, American Association for the Advancement of Science).

2.2 Laser thinning

Laser thinning techniques have provided a direct and site-specific method for removing layers and obtaining "on-demand" 2D TMDCs (Castellanos Gomez et al., 2012; Lu et al., 2014; Sunamura et al., 2016; Kim et al., 2017; Park et al., 2017; Gong et al., 2018; Nagareddy et al., 2018; Rho et al., 2019; Tran-Khac et al., 2019; Wang et al., 2020; Kang et al., 2021). Unlike the traditional gas or plasma etching thinning method, laser thinning shows high accuracy on thinned layers, flexible programmable patterning mode, and high thinning efficiency. Nagareddy et al. (2018) demonstrated an efficient laser thinning method, which was constructed by the Raman spectroscopy and coupled with an atomic force microscope. The experimental setup was placed in an airtight environment with strictly controlled humidity. Using ultra-low laser power, the thickness of $MoTe_2$ film can be controlled layer by layer from multilayer to monolayer, as shown in Figure 1C. In addition, the thickness reduction shows the linear correlation between the thickness reduction and the number of scans. The laser thinning process is achieved through the sublimation of the top layer, mainly caused by the conversion of light absorbed by the material into heat energy (Lu et al., 2014). The heat generated by the conversion of absorbed laser into energy is difficult to dissipate through the substrate due to the poor coupling between TMDC thin layers that are mediated by van der Waals forces (Su et al., 2021). Thus, until the laser power is increased, the bottom layer remains in close contact with the SiO_2/Si substrate, acting as a heat sink to prevent removal.

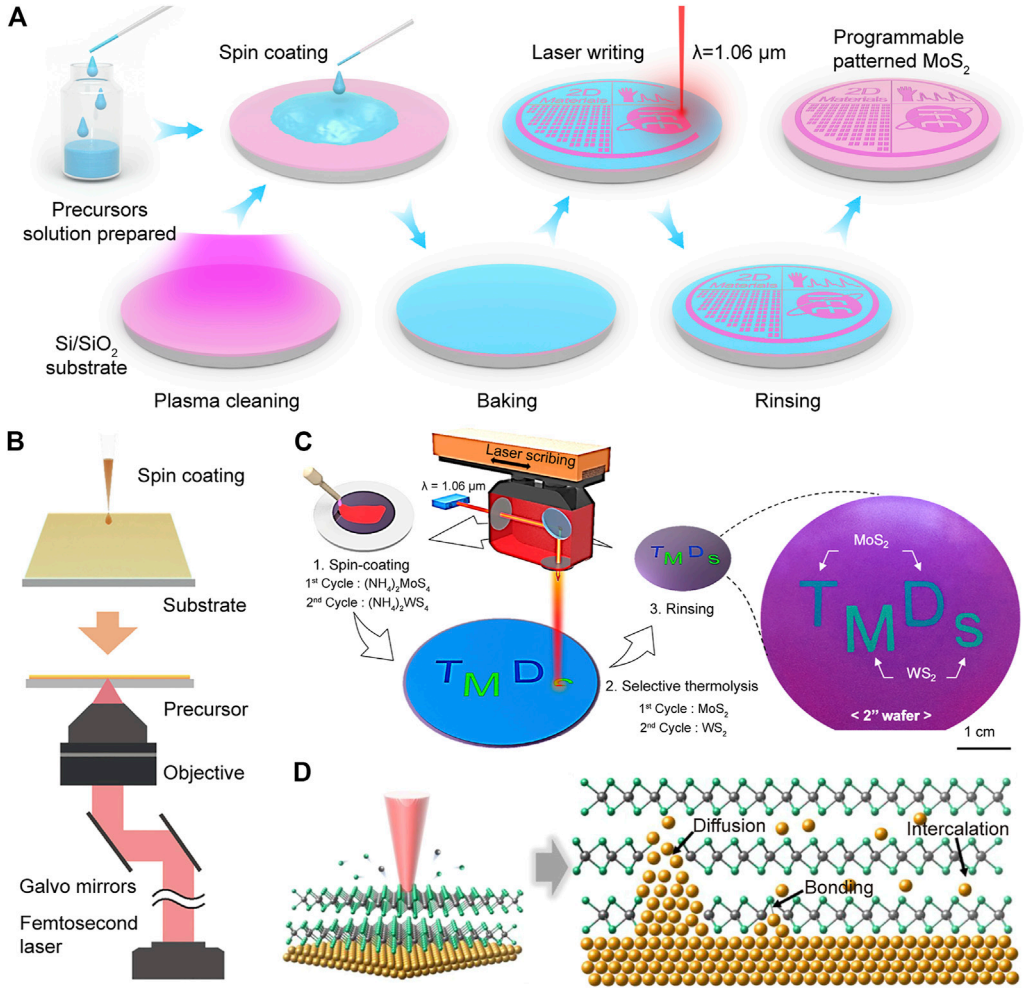

FIGURE 2
Bottom-up synthesis methods. **(A)** Flow diagram of direct laser writing, a method for the laser-directed synthesis of MoS_2 on the SiO_2/Si wafer (Xu et al., 2021a) (Copyright 2021, Elsevier). **(B)** Schematic of MoS_2 synthesized by femtosecond laser (Xu et al., 2022) (Copyright 2022, American Chemical Society). **(C)** Schematic of the layer synthesis of MoS_2–WS_2 heterostructure (Park et al., 2020a) (Copyright 2020, American Chemical Society). **(D)** Schematic of Au-doped MoS_2 (Huo et al., 2021) (Copyright 2021, American Chemical Society).

2.3 Laser driven phase

The exploration and manipulation of a novel phase of matter is a primary pursuit for materials research. The emergence of atomically 2D TMDCs has enabled the examination of diffusive, displacive, and quantum phase transitions. Cho et al. (2015) demonstrated a novel method of localized polymorph engineering and realized the laser-induced phase transition of $MoTe_2$. The multilayer 2H-$MoTe_2$ flake with about 30 layers was obtained by mechanical exfoliation. The schematic diagram of the phase transition mechanism is illustrated in Figure 1D. Under laser irradiation, the thickness of the irradiated region in 2H-$MoTe_2$ decreased by a few layers and transformed to 1T′ phase. During the irradiation process, the 1T′ $MoTe_2$ layer remained due to the heat sink effect of the SiO_2 substrate. It should be noticed that the phase transition is irreversible from 1T′ to 2H phase even under the higher energy or intensity of the laser. The driving force for the one-way phase transition is caused by the irreversible Te vacancy created under laser irradiation. Compared with conventional methods such as heat treatment, strain engineering, charge transfer, and plasma irradiation, laser-induced phase transition engineering allows for specific phase transition sites and patterned processing without impurities during the phase transition (Chen Z. R. et al., 2019).

3 Bottom-up synthesis methods

Unlike the top-down synthesis method, the bottom-up synthesis method is more efficient and cost-effective in the synthesis of 2D TMDC materials because it does not require the preparation of precursors using other methods. With the assistance of a laser, large-area patterned TMDCs, heterostructure, and atom doping can be realized.

3.1 Laser directed synthesis

Direct laser writing technology can directly pattern 2D TMDC materials without mask and lithography, reducing the process flow of device fabrication and the risk of chemical contamination. Generally, the fiber laser (1.06 μm), carbon dioxide laser (10.6 μm), and femtosecond laser (780 nm) have been adopted for the synthesis of 2D TMDCs (Hu et al., 2018). Xu et al. (2021a) reported a method for the efficient synthesis of wafer-scale MoS_2 using a direct laser writing technique, and the workflow is shown in Figure 2A. With heating by a 1.06 μm commercial fiber laser, the MoS_2 can be programmable with text, lines, patterns, and matrices in a few minutes. The laser interacts with the precursor, and the reaction temperature facilitates the thermal decomposition of $(NH_4)_2MoS_4$ into MoS_2. Apart from the thermal decomposition, the photochemical reaction induced by two-photon absorption can also be adopted for synthesizing 2D TMDCs. As shown in Figure 2B, the femtosecond direct laser writing was carried out to synthesize MoS_2 under an objective lens. Molybdenum acetylacetonate and carbon disulfide were adopted as the molybdenum and sulfur sources. The two-photon absorption occurs in the focal point, synthesizing MoS_2 from the molybdenum metal complex via a photochemical reaction. With the assistance of a femtosecond laser, a minimal line width of approximately 780 nm can be achieved.

3.2 Laser heterostructure

The direct laser writing technique allows the fabrication of single 2D TMDCs and the direct preparation of 2D TMDC heterostructures. Compared with the transfer method, the laser heterostructure process can be programmable patterned, avoiding material damage and pollution (Li et al., 2020). In addition, the synthesis efficiency of heterostructures is greatly improved compared with CVD. Park et al. (2020a) successfully prepared WS_2–MoS_2 heterostructures vertically by two-step laser scribing, as shown in Figure 2C. The MoS_2 layer was first synthesized by the thermal decomposition of $(NH_4)_2MoS_4$ when the temperature increased over 700°C under laser irradiation. While for the heterostructures, due to the different optical absorption coefficients, the MoS_2 layer shows a minor temperature increase, and only the $(NH_4)_2WS_4$ layer absorbed the laser energy and selectively decomposed into WS_2. Thus, the selective growth process by laser effectively produces layer-by-layer 2D TMDC heterostructures in a programmable pattern.

3.3 Laser doping

The impurity atom can modulate the physical and chemical properties of semiconductors such as electrical and optical. A small amount of elemental doping could affect the energy bands enhancing semiconductor conductivity. However, doping elements in 2D TMDCs are relatively difficult and generate more defects in the 2D TMDCs. In addition, the weak interaction will result in unstable interfaces due to the interaction between doped elements and 2D TMDCs (Mak et al., 2010). Laser provides a simple way for 2D TMDC doping, which is promising for future electronic applications (Chen J. et al., 2019). One way to achieve laser doping in 2D TMDCs is by dissolving the doping substance in the precursor, which results in doping during formation (Hu et al., 2020). In addition, doping of elements in preprepared 2D TMDCs can also be accomplished by introducing gas molecules or solids containing the desired doping atoms (Afaneh et al., 2018; Rho et al., 2019; Huo et al., 2021). For example, Huo et al. (2021) reported an Au-doped MoS_2 process by doping a solid source, as shown in Figure 2D. MoS_2 was transferred to the Au electrode, and with femtosecond laser irradiation, the Au atom can be intercalated and diffused into MoS_2. The interface diffusion and chemical bonding of Au reduced the Schottky barrier of the metal–semiconductor interfaces, which could enhance the performance of the devices.

4 Conclusion and outlook

This mini-review summarized the top-down and bottom-up methods for the laser synthesis of 2D TMDCs. Compared with the traditional methods, the laser synthesis methods have the advantages of flexibility, convenience, efficiency, and controllability. Laser synthesis technology can directly produce large-area, high-quality TMDCs, alloys, and heterostructure, which is a promising sign for future industrial-scale manufacturing.

Laser synthesis of 2D TMDCs is an emerging field, and some issues need to be further addressed, especially for the laser–reactive matter interaction. In addition, the synthesis of sulfides in the atmospheric environment is the focus of attention, while the atmosphere protection and hydrogen participation would be focused while synthesizing selenide and telluride. In addition, recent works on laser synthesis of 2D TMDCs constructed on the rigid substrate (such as SiO_2/Si) or liquid environments and direct laser synthesis on flexible substrates (such as polyimide, polydimethylsiloxane, polyethylene terephthalate, and polyethylene naphthalene) have not been realized yet, which would offer another chance for realizing applications in flexible electronics.

Author contributions

HW: investigation, methodology, visualization, and writing—original draft. MX: investigation, methodology, writing—original draft, writing—review and editing, visualization, and funding acquisition. HJ: investigation, writing—original draft, writing—review and editing, and visualization. TH: investigation, methodology, and conceptualization. WL: methodology, writing—review and editing, and funding acquisition. LZ: methodology, conceptualization, writing—review and editing, and funding acquisition. XW: conceptualization, methodology, writing—review and editing, supervision, project administration, and funding acquisition.

Funding

The authors gratefully acknowledge financial support from the National Key Research and Development Program of China (2020YFB2008501), the National Natural Science Foundation of China (11904289), the Key Research and Development Program of Shaanxi Province (2020ZDLGY04-08 and 2020GXLH-Z-027), the Natural Science Foundation of Shaanxi Province (2023-JC-YB-495, 2022JQ-659, and 2022JQ-552), the Natural Science Foundation of Ningbo (202003N4003), the Fundamental Research Funds for the Central Universities (3102019PY004, 31020190QD010, and 3102019JC004), the start-up funds from Northwestern Polytechnical University, and the Open Research Fund of the State Key Laboratory of Organic Electronics and Information Displays.

Conflict of interest

The authors declare that the research was conducted in the absence of any commercial or financial relationships that could be construed as a potential conflict of interest.

Publisher's note

All claims expressed in this article are solely those of the authors and do not necessarily represent those of their affiliated organizations, or those of the publisher, the editors, and the reviewers. Any product that may be evaluated in this article, or claim that may be made by its manufacturer, is not guaranteed or endorsed by the publisher.

References

Afaneh, T., Sahoo, P. K., Nobrega, I. A. P., Xin, Y., and Gutiérrez, H. R. (2018). Laser-assisted chemical modification of monolayer transition metal dichalcogenides. *Adv. Funct. Mater.* 28 (37), 1802949. doi:10.1002/adfm.201802949

An, S. J., Kim, Y. H., Lee, C., Park, D. Y., and Jeong, M. S. (2018). Exfoliation of transition metal dichalcogenides by a high-power femtosecond laser. *Sci. Rep.* 8 (1), 12957. doi:10.1038/s41598-018-31374-w

Cao, L. J., Yang, S. B., Gao, W., Liu, Z., Gong, Y. J., Ma, L. L., et al. (2013). Direct laser-patterned micro-supercapacitors from paintable MoS_2 films. *Small* 9 (17), 2905–2910. doi:10.1002/smll.201203164

Castellanos Gomez, A., Barkelid, M., Goossens, A. M., Calado, V. E., van der Zant, H. S. J., and Steele, G. A. (2012). Laser-thinning of MoS_2: On demand generation of a single-layer semiconductor. *Nano Lett.* 12 (6), 3187–3192. doi:10.1021/nl301164v

Chen, J., Wang, Q. Y., Sheng, Y. C., Cao, G. Q., Yang, P., Shan, Y. B., et al. (2019a). High-performance WSe_2 photodetector based on a laser-induced p–n junction. *ACS Appl. Mater. Interfaces* 11 (46), 43330–43336. doi:10.1021/acsami.9b13948

Chen, Z. R., Nan, H. Y., Liu, Z., Wang, X. Y., Gu, X. F., and Xiao, S. Q. (2019b). Effect of thermal conductivity of substrate on laser-induced phase transition of $MoTe_2$. *J. Raman Spectrosc.* 50 (5), 755–761. doi:10.1002/jrs.5559

Cho, S., Kim, S., Kim, J. H., Zhao, J., Seok, J., Keum, D. H., et al. (2015). Phase patterning for ohmic homojunction contact in $MoTe_2$. *Science* 349 (6248), 625–628. doi:10.1126/science.aab3175

Fan, X. B., Xu, P. T., Zhou, D. K., Sun, Y. F., Li, Y. C., Nguyen, M. A. T., et al. (2015). Fast and efficient preparation of exfoliated 2H MoS_2 nanosheets by sonication-assisted lithium intercalation and infrared laser-induced 1T to 2H phase reversion. *Nano Lett.* 15 (9), 5956–5960. doi:10.1021/acs.nanolett.5b02091

Gao, Q. G., Zhang, C. F., Yang, K. Q., Pan, X. J., Zhang, Z., Yang, J. J., et al. (2021). High-performance CVD bilayer MoS_2 radio frequency transistors and gigahertz mixers for flexible nanoelectronics. *Micromachines* 12 (4), 451. doi:10.3390/mi12040451

Gao, Z. W., Liu, M. J., Zheng, W. R., Zhang, X. D., and Lee, L. Y. S. (2019). Surface engineering of MoS_2 via laser-induced exfoliation in protic solvents. *Small* 15 (44), 1903791. doi:10.1002/smll.201903791

Gong, L. L., Zhang, Q., Wang, L. J., Wu, J. F., Han, C., Lei, B., et al. (2018). Emergence of photoluminescence on bulk MoS_2 by laser thinning and gold particle decoration. *Nano Res.* 11 (9), 4574–4586. doi:10.1007/s12274-018-2037-5

Hu, J. J., Zabinski, J. S., Sanders, J. H., Bultman, J. E., and Voevodin, A. A. (2006). Pulsed laser syntheses of layer-structured WS_2 nanomaterials in water. *J. Phys. Chem. B* 110 (18), 8914–8916. doi:10.1021/jp0611471

Hu, Y. S., Zeng, X. B., Ren, T. T., Wu, S. X., Wang, W. Z., Zeng, Y., et al. (2018). Preparation of controllable-thickness 1T@2H-MoS_2 thin films by pulsed laser-induced synthesis and the selective separation of the 1T phase. *J. Mater. Chem. C* 6 (43), 11651–11658. doi:10.1039/C8TC03815E

Hu, Y. S., Zeng, X. B., Ren, T. T., Xiao, Y. H., Zeng, Y., Wang, W. Z., et al. (2020). One-step growth of centimeter-scale doped multilayer MoS_2 films by pulsed laser-induced synthesis. *J. Mater. Chem. C* 8 (20), 6900–6905. doi:10.1039/C9TC06908A

Huo, J. P., Xiao, Y., Sun, T. M., Zou, G. S., Shen, D. Z., Feng, B., et al. (2021). Femtosecond laser irradiation-mediated MoS_2–metal contact engineering for high-performance field-effect transistors and photodetectors. *ACS Appl. Mater. Interfaces* 13 (45), 54246–54257. doi:10.1021/acsami.1c12685

Jung, J., Lee, J., Kim, Y., Bark, H., and Lee, C. (2019). Ultrafast and low-temperature synthesis of patternable MoS_2 using laser irradiation. *J. Phys. D Appl. Phys.* 52 (18), 18LT01. doi:10.1088/1361-6463/ab0724

Kang, S., Won, D., Yang, H., Lin, C. H., Ku, C. S., Chiang, C. Y., et al. (2021). Phase-controllable laser thinning in $MoTe_2$. *Appl. Surf. Sci.* 563, 150282. doi:10.1016/j.apsusc.2021.150282

Kim, S. J., Choi, K., Lee, B., Kim, Y., and Hong, B. H. (2015). Materials for flexible, stretchable electronics: Graphene and 2D materials. *Annu. Rev. Mater. Res.* 45 (1), 63–84. doi:10.1146/annurev-matsci-070214-020901

Kim, S., Kim, J. H., Kim, D., Hwang, G., Baik, J., Yang, H., et al. (2017). Post-patterning of an electronic homojunction in atomically thin monoclinic $MoTe_2$. *2D Mater.* 4 (2), 024004. doi:10.1088/2053-1583/aa5b0e

Kimiagar, S., and Abrinaei, F. (2023). Laser-assisted hydrothermal synthesis of MoS_2 nanosheets under different laser energies and potential application in nonlinear optics. *Optik* 272, 170305. doi:10.1016/j.ijleo.2022.170305

Lee, Y. H., Zhang, X. Q., Zhang, W., Chang, M. T., Lin, C. T., Chang, K. D., et al. (2012). Synthesis of large-area MoS_2 atomic layers with chemical vapor deposition. *Adv. Mater.* 24 (17), 2320–2325. doi:10.1002/adma.201104798

Lei, S. D., Ge, L. H., Liu, Z., Najmaei, S., Shi, G., You, G., et al. (2013). Synthesis and photoresponse of large GaSe atomic layers. *Nano Lett.* 13 (6), 2777–2781. doi:10.1021/nl4010089

Leong, W. S. (2020). Versatile strategy for making 2D materials. *Nature* 577 (7791), 477–478. doi:10.1038/d41586-020-00094-5

Levita, G., and Righi, M. C. (2017). Effects of water intercalation and tribochemistry on MoS_2 lubricity: An ab initio molecular dynamics investigation. *ChemPhysChem* 18 (11), 1475–1480. doi:10.1002/cphc.201601143

Li, J., Yang, X. D., Liu, Y., Huang, B. L., Wu, R. X., Zhang, Z. W., et al. (2020). General synthesis of two-dimensional van der Waals heterostructure arrays. *Nature* 579 (7799), 368–374. doi:10.1038/s41586-020-2098-y

Li, W. W., Xu, M. Z., Gao, J. W., Zhang, X. S., Huang, H., Zhao, R. Q., et al. (2023). Large-scale ultra-robust MoS_2 patterns directly synthesized on polymer substrate for flexible sensing electronics. *Adv. Mater.* 35 (8), 2207447. doi:10.1002/adma.202207447

Liu, Y., Duan, X. D., Shin, H. J., Park, S., Huang, Y., and Duan, X. F. (2021). Promises and prospects of two-dimensional transistors. *Nature* 591 (7848), 43–53. doi:10.1038/s41586-021-03339-z

Lu, J. P., Lu, J. H., Liu, H. W., Liu, B., Chan, K. X., Lin, J. D., et al. (2014). Improved photoelectrical properties of MoS_2 films after laser micromachining. *ACS Nano* 8 (6), 6334–6343. doi:10.1021/nn501821z

Ma, H., Shen, Z. G., and Ben, S. (2018). Understanding the exfoliation and dispersion of MoS_2 nanosheets in pure water. *J. Colloid Interface Sci.* 517, 204–212. doi:10.1016/j.jcis.2017.11.013

Mahjouri Samani, M., Tian, M. K., Wang, K., Boulesbaa, A., Rouleau, C. M., Puretzky, A. A., et al. (2014). Digital transfer growth of patterned 2D metal chalcogenides by confined nanoparticle evaporation. *ACS Nano* 8 (11), 11567–11575. doi:10.1021/nn5048124

Mak, K. F., Lee, C., Hone, J., Shan, J., and Heinz, T. F. (2010). Atomically thin MoS_2: A new direct-gap semiconductor. *Phys. Rev. Lett.* 105 (13), 136805. doi:10.1103/PhysRevLett.105.136805

Mohapatra, P. K., Ranganathan, K., and Ismach, A. (2020). Selective area growth and transfer of high optical quality MoS_2 layers. *Adv. Mater. Interfaces* 7 (24), 2001549. doi:10.1002/admi.202001549

Nagareddy, V. K., Octon, T. J., Townsend, N. J., Russo, S., Craciun, M. F., and Wright, C. D. (2018). Humidity-controlled ultralow power layer-by-layer thinning, nanopatterning and bandgap engineering of $MoTe_2$. *Adv. Funct. Mater.* 28 (52), 1804434. doi:10.1002/adfm.201804434

Park, J., Kim, M. S., Cha, E., Kim, J., and Choi, W. (2017). Synthesis of uniform single layer WS_2 for tunable photoluminescence. *Sci. Rep.* 7 (1), 16121. doi:10.1038/s41598-017-16251-2

Park, S., Lee, A., Choi, K. H., Hyeong, S. K., Bae, S., Hong, J. M., et al. (2020a). Layer-selective synthesis of MoS_2 and WS_2 structures under ambient conditions for customized electronics. *ACS Nano* 14 (7), 8485–8494. doi:10.1021/acsnano.0c02745

Park, S., Park, J., Kim, Y. g., Bae, S., Kim, T. W., Park, K. I., et al. (2020b). Laser-directed synthesis of strain-induced crumpled MoS_2 structure for enhanced triboelectrification toward haptic sensors. *Nano Energy* 78, 105266. doi:10.1016/j.nanoen.2020.105266

Rho, Y., Pei, J., Wang, L., Su, Z., Eliceiri, M., and Grigoropoulos, C. P. (2019). Site-selective atomic layer precision thinning of MoS_2 via laser-assisted anisotropic chemical etching. *ACS Appl. Mater. Interfaces* 11 (42), 39385–39393. doi:10.1021/acsami.9b14306

Schuffenhauer, C., Parkinson, B. A., Jin-Phillipp, N. Y., Joly-Pottuz, L., Martin, J.-M., Popovitz-Biro, R., et al. (2005). Synthesis of fullerene-like tantalum disulfide nanoparticles by a gas-phase reaction and laser ablation. *Small* 1 (11), 1100–1109. doi:10.1002/smll.200500133

Shim, G. W., Yoo, K., Seo, S. B., Shin, J., Jung, D. Y., Kang, I. S., et al. (2014). Large-area single-layer $MoSe_2$ and its van der Waals heterostructures. *ACS Nano* 8 (7), 6655–6662. doi:10.1021/nn405685j

Su, B. W., Zhang, X. L., Xin, W., Guo, H. W., Zhang, Y. Z., Liu, Z. B., et al. (2021). Laser-assisted two dimensional material electronic and optoelectronic devices. *J. Mater. Chem. C* 9 (8), 2599–2619. doi:10.1039/D0TC05540A

Sunamura, K., Page, T. R., Yoshida, K., Yano, T. a., and Hayamizu, Y. (2016). Laser-induced electrochemical thinning of MoS_2. *J. Mater. Chem. C* 4 (15), 3268–3273. doi:10.1039/C5TC04409J

Tran-Khac, B. C., White, R. M., DelRio, F. W., and Chung, K. H. (2019). Layer-by-layer thinning of MoS_2 via laser irradiation. *Nanotechnology* 30 (27), 275302. doi:10.1088/1361-6528/ab11ad

Wang, M. M., Li, D. W., Liu, K., Guo, Q. T., Wang, S. M., and Li, X. (2020). Nonlinear optical imaging, precise layer thinning, and phase engineering in $MoTe_2$ with femtosecond laser. *ACS Nano* 14 (9), 11169–11177. doi:10.1021/acsnano.0c02649

Wu, R. X., Tao, Q. Y., Li, J., Li, W., Chen, Y., Lu, Z. Y., et al. (2022). Bilayer tungsten diselenide transistors with on-state currents exceeding 1.5 milliamperes per micrometre. *Nat. Electron.* 5 (8), 497–504. doi:10.1038/s41928-022-00800-3

Xia, J., Huang, X., Liu, L. Z., Wang, M., Wang, L., Huang, B., et al. (2014). CVD synthesis of large-area, highly crystalline $MoSe_2$ atomic layers on diverse substrates and application to photodetectors. *Nanoscale* 6 (15), 8949–8955. doi:10.1039/C4NR02311K

Xu, M. Z., Gao, J. W., Song, J. C., Wang, H. X., Zheng, L., Wei, Y., et al. (2021a). Programmable patterned MoS_2 film by direct laser writing for health-related signals monitoring. *iScience* 24 (11), 103313. doi:10.1016/j.isci.2021.103313

Xu, M. Z., Tang, B. J., Lu, Y. H., Zhu, C., Lu, Q. B., Zhu, C., et al. (2021b). Machine learning driven synthesis of few-layered WTe_2 with geometrical control. *J. Am. Chem. Soc.* 143 (43), 18103–18113. doi:10.1021/jacs.1c06786

Xu, Y. N., Jiao, B. Z., Wang, Y. C., Xue, S. Y., Gao, H., Yu, K. W., et al. (2022). Rapid *in-situ* synthesis and patterning of edge-unsaturated MoS_2 by femtosecond laser-induced photochemical reaction. *ACS Appl. Mater. Interfaces* 14 (4), 5558–5566. doi:10.1021/acsami.1c20293

Yu, H., Liao, M., Zhao, W., Liu, G., Zhou, X. J., Wei, Z., et al. (2017). Wafer-scale growth and transfer of highly-oriented monolayer MoS_2 continuous films. *ACS Nano* 11 (12), 12001–12007. doi:10.1021/acsnano.7b03819

Yu, J. D., Wang, L., Hao, Z. B., Luo, Y., Sun, C. Z., Wang, J., et al. (2020). Van der Waals epitaxy of III-nitride semiconductors based on 2D materials for flexible applications. *Adv. Mater.* 32 (15), 1903407. doi:10.1002/adma.201903407

Zhai, X. T., Zhang, R. X., Sheng, H. X., Wang, J., Zhu, Y. M., Lu, Z. C., et al. (2021). Direct observation of the light-induced exfoliation of molybdenum disulfide sheets in water medium. *ACS Nano* 15 (3), 5661–5670. doi:10.1021/acsnano.1c00838

Zheng, L., Wang, X. W., Jiang, H. J., Xu, M. Z., Huang, W., and Liu, Z. (2022). Recent progress of flexible electronics by 2D transition metal dichalcogenides. *Nano Res.* 15 (3), 2413–2432. doi:10.1007/s12274-021-3779-z

Zuo, P., Jiang, L., Li, X., Tian, M. Y., Ma, L., Xu, C. Y., et al. (2021). Phase-reversed MoS_2 nanosheets prepared through femtosecond laser exfoliation and chemical doping. *J. Phys. Chem. C* 125 (15), 8304–8313. doi:10.1021/acs.jpcc.1c00235

frontiers | Frontiers in Chemistry

TYPE Mini Review
PUBLISHED 07 June 2023
DOI 10.3389/fchem.2023.1211512

OPEN ACCESS

EDITED BY
Arjun Singh,
Memorial Sloan Kettering Cancer Center, United States

REVIEWED BY
Soumitra Basu,
Kent State University, United States
Domenica Musumeci,
University of Naples Federico II, Italy
Dmitry N. Kaluzhny,
Engelhardt Institute of Molecular Biology (RAS), Russia

*CORRESPONDENCE
Robert C. Monsen,
rcmons01@louisville.edu

RECEIVED 24 April 2023
ACCEPTED 30 May 2023
PUBLISHED 07 June 2023

CITATION
Monsen RC (2023), Higher-order G-quadruplexes in promoters are untapped drug targets.
Front. Chem. 11:1211512.
doi: 10.3389/fchem.2023.1211512

Higher-order G-quadruplexes in promoters are untapped drug targets

Robert C. Monsen*

Department of Medical Oncology and Hematology, UofL Health Brown Cancer Center, University of Louisville, Louisville, KY, United States

G-quadruplexes (G4s) are four-stranded nucleic acid secondary structures that form within guanine-rich regions of chromatin. G4 motifs are abundant in the genome, with a sizable proportion (~40%) existing within gene promoter regions. G4s are proven epigenetic features that decorate the promoter landscape as binding centers for transcription factors. Stabilizing or disrupting promoter G4s can directly influence adjacent gene transcription, making G4s attractive as indirect drug targets for hard-to-target proteins, particularly in cancer. However, no G4 ligands have progressed through clinical trials, mostly owing to off targeting effects. A major hurdle in G4 drug discovery is the lack of distinctiveness of the small monomeric G4 structures currently used as receptors. This mini review describes and contrasts monomeric and higher-order G-quadruplex structure and function and provides a rationale for switching focus to the higher-order forms as selective molecular targets. The human telomerase reverse transcriptase (hTERT) core promoter G-quadruplex is then used as a case study that highlights the potential for higher-order G4s as selective indirect inhibitors of hard-to-target proteins in cancer.

KEYWORDS

G-quadruplex (G4), higher-order G4, DNA, promoter, drug target

1 G-quadruplex structures in promoters: monomeric vs. higher-order forms

1.1 Intramolecular monomeric promoter G-quadruplexes

G-quadruplexes (G4s) are four-stranded secondary structures created from the stacking of two or more guanine tetrads ("G-tetrads") (Spiegel et al., 2020). Each G-tetrad is composed of four guanine bases arranged in a square planar configuration, that is, stabilized by Hoogsteen hydrogen bonding (Figure 1A). Monovalent cations are coordinated within the G-tetrad column central channel by the inward facing carbonyl groups, providing stabilization from coordinate bonding and neutralization of the partially negative charges (Lane et al., 2008). A commonly used sequence motif to describe a monomeric G-quadruplex is $G_{3\text{-}4}L_{1\text{-}7}G_{3\text{-}4}L_{1\text{-}7}G_{3\text{-}4}L_{1\text{-}7}G_{3\text{-}4}$, where G indicates a guanine tract and L designates any nucleotide in the intervening loop. Historically, the largest loop length has been taken to be seven nucleotides because of the destabilizing effect of large loops *in vitro* (Spiegel et al., 2020; Ravichandran et al., 2021).

G-rich sequences in specific gene promoter regions can adopt G4 structures with a surprisingly diverse array of topological conformations for the intramolecular monomeric G4 *in vitro*, depending on the sequence composition, loop lengths, ionic environment, and hydration (Chen and Yang, 2012; Miller et al., 2010; Bhattacharyya et al., 2016). The most

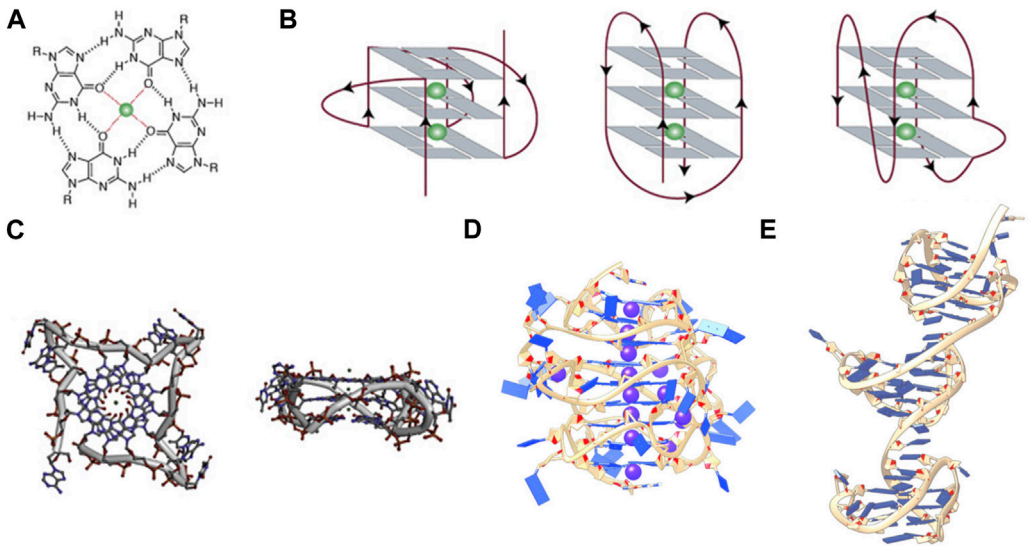

FIGURE 1
(A) Structure of a G-tetrad, **(B)** From left to right, schematic representations of **(A)** parallel, antiparallel, and mixed hybrid with bulge, **(C)** Top and side views of a parallel monomeric G-quadruplex, **(D)** side view of a stacked intramolecular all-parallel higher-order G-quadruplex, and **(E)** side view of an intramolecular higher-order all-hybrid G-quadruplex in a beads-on-a-string arrangement. **(C–E)** are not to scale. Figures 1A–C, are adapted from (Spiegel et al., 2020), **(D)** is adapted from (Monsen et al., 2020), and **(C)** is adapted from (Monsen et al., 2021).

frequent topologies are: antiparallel, in which two out of four G-tracts run in the same direction; hybrid, in which three G-tracts run in the same direction; and parallel, in which all G-tracts run in the same direction (Figure 1B) (Spiegel et al., 2020). This review is primarily concerned with promoter G4s that are necessarily intramolecular and flanked on either end by single- or double-stranded regions. In the context of a promoter bubble (Shirude et al., 2007; Monsen et al., 2023), as well as when promoter G4 sequences are flanked by single-stranded regions (this can be realized *in vitro,* for example, by adding two residues on either end of the monomer G4 motif: $L_2G_xL_nG_xL_nG_xL_nG_xL_2$), the parallel topology is preferred (Chen et al., 2021). The biological preference for parallel promoter G4 conformations is supported by the extensive immunofluorescence seen across chromosomes stained with the parallel-favoring anti-G4 antibody "BG4" (Biffi et al., 2013; Javadekar et al., 2020). The first ever near-atomic structural study of a G4 in a near-native duplex bubble has shown that duplex end-stacking at the G-tetrad interface may be a key factor to promoter G4 stability, suggesting that antiparallel and hybrid topologies could be sterically prohibited (Monsen et al., 2023). Overall, *in vitro* monomeric promoter G4 sequences adopt a variety of topological configurations when isolated, but when placed in their biological context prefer the parallel form.

1.2 Intramolecular higher-order promoter G-quadruplexes

Intramolecular higher-order promoter G4s (xG4s) consist of two or more connected monomeric G4 domains. The xG4 motif is degenerate compared to the lower order G4 motif and is of the general form $(G_{2\text{-}4}L_{1\text{-}12}G_{2\text{-}4}L_{1\text{-}12}G_{2\text{-}4}L_{1\text{-}12}G_{2\text{-}4}L_{\geq 0})_n$ (Monsen et al., 2022a), where the length of the 3′ connecting loop can be zero and $n \geq 2$. The xG4 motif becomes substantially more degenerate when accounting for mismatches and/or bulges (i.e., non-guanine nucleotides within a putative G-tract) (Berselli et al., 2020). The xG4 motif is notable for multiple reasons. First, the zero-nucleotide connecting loop presents the possible situation where the last guanine of the 3′ G-tetrad of the first G4 domain and the first guanine of the 5′ G-tetrad of the second G4 domain create a continuous G-tetrad column that spans the entire macromolecule. If both G4s are parallel, this would facilitate formation of a single continuous medium groove spanning the two domains with a favorable locked 3′ to 5′ G-tetrad stacked interface (Kogut et al., 2019). A second, less obvious feature of the xG4 motif is that it accounts for two-tetrad G4s, in which there are only two guanines in the G-tracts. Two-tetrad monomeric G4s cannot exist as stable parallel conformations *in vitro* when isolated (Kejnovska et al., 2021), but have been seen in higher-order G4 assemblies (Monsen et al., 2022a) [we note that stable antiparallel two-tetrad G4s are seen *in vitro* (Lim et al., 2009)]. This is an important feature, as it reveals that biologically relevant xG4s have an expanded structural repertoire compared to the monomeric sequences. Lastly, xG4s seem to tolerate much longer loops (1-12+ nucleotides), both within and between the G4 domains (Berselli et al., 2020; Monsen et al., 2020; Monsen et al., 2022a). This may be the result of tertiary interactions that stabilize either across the G4-G4 domain by loop interactions (Rigo and Sissi, 2017), symmetry in the loop giving rise to a stabilizing hairpin moiety (Berselli et al., 2020), or arise from the stability imparted on the G4 cores from head-to-tail stacking (Kogut et al., 2019).

Structural characterizations of intramolecular promoter xG4s to date have revealed an overwhelming preference for stacked arrangements (Micheli et al., 2010; Rigo and Sissi, 2017; Monsen

et al., 2020; Monsen et al., 2022a), with the highest resolution models showing a preference for an all-parallel stacked globular configuration (Figure 1D) (Monsen et al., 2020; Monsen et al., 2022a). Importantly, all reported putative xG4 sequences that have been investigated form stable G4 structures *in vitro*. In some cases, the presence of long loops (>7 nucleotides) result in hairpins (Monsen et al., 2022a) that contribute to the stability of the individual domains (Ravichandran et al., 2021) while also creating structurally unique interfaces. In contrast to promoter xG4s, other higher-order intramolecular G4s reported, such as the human telomere (Monsen et al., 2021), the insulin-linked polymorphic region (ILPR) minisatellite (Schonhoft et al., 2009), and the CEB25 minisatellite locus (Amrane et al., 2012), show mixed antiparallel and hybrid topologies that are better described as dumbbell shaped or beads-on-a-string configurations. Figure 1 contrasts the structures of a monomer G4 in the parallel conformation, a higher-order all-parallel stacked G4, and a higher-order all-hybrid beads-on-a-string.

The selective binding interface of the xG4s is not imparted by the G-tetrad columns, but rather the specific G4-G4 interaction interfaces, loop sequence, size, and configurations. Figure 1C reveals that there is little targetable real estate associated with the monomeric parallel G4 (Monsen et al., 2023). Conversely, Figures 1D, E reveals multiple putative binding sites that would be large enough and distinct enough for specific protein or drug interaction. Biochemical support for this idea comes from a recent pull-down study conducted by Ceschi et al. (Ceschi et al., 2022). In this study, the authors used a variety of higher-order G4 sequences (such as those in Figures 1D, E) to enrich for tightly interacting proteins from cell lysates that are specific to higher-order G4s over the lower order forms. Surprisingly, the intermediate filament Vimentin was shown to have a selective nanomolar affinity to higher-order G4 structures with no apparent binding to lower order species. While the mechanism of recognition is still unclear, this study supports the hypothesis that xG4s offer unique recognition sites that could be useful in selective targeting.

2 G-quadruplex distribution and function in promoters

2.1 Biological distribution and function of promoter G4s

Promoter G-quadruplexes are prevalent epigenetic regulatory elements. Current estimates show more than 700,000 monomeric G4 motifs across the human genome (Hansel-Hertsch et al., 2017). Huppert and Balasaubramanian, using the canonical sequence motif $G_{3+}L_{1-7}G_{3+}L_{1-7}G_{3+}L_{1-7}G_{3+}$, showed that more than 40% of gene promoters have at least one monomeric G4 motif (Huppert and Balasubramanian, 2007). More recently, Hänsel-Hertsch and colleagues have used a chromatin immunoprecipitation (ChIP)-sequencing direct capture approach to show that thousands of G4 structures, not just motifs, are enriched in highly transcribed gene promoters, specifically many involved in cancer (Hansel-Hertsch et al., 2016). Promoter quadruplexes overall appear to be acting as general transcription factor (TF) "binding hubs", coinciding with regions of open chromatin and high transcriptional activity (Spiegel et al., 2021).

At a more granular level, promoter G4s act in concert with transcriptional proteins to affect gene transcription in multiple ways. Initially, promoter G4s were thought to only act as simple physical barriers to polymerases, acting as "on/off" switches of transcription (Sarkies et al., 2010). However, studies have now shown that G4s can directly recruit transcription factors with some level of specificity. For instance, two zinc fingers, SP1 and MAZ (Myc-associated zinc finger), show G4 structure-dependent recognition. In the former case, Raiber and colleagues, using pull-down experiments with the transcription factor SP1, showed that 36% of the sequences lacked consensus SP1 binding motifs (Raiber et al., 2012). They went on to show that 77% of those sequences lacking the SP1 consensus motif were putative G-quadruplexes and that, overall, SP1 binding had 87% overlap with G4 sequence motifs. In the latter case, Cogoi and colleagues have shown that MAZ recognizes a G4 formed within the *kRas* promoter and showed that stabilizing the *kRas* G4 with a small molecule could promote MAZ binding and increase transcription, while mutations that destabilized the G4 reduced MAZ binding and transcription (Cogoi et al., 2010).

G4s can also serve as transcriptional repressors. The classical case for this is the G4 formed within the *c-Myc* promoter. In their seminal study, Siddiqui-Jain et al. showed that a G-rich region in the nuclease hypersensitivity element III (NHEIII) of the c-Myc P1 promoter forms one or more monomeric G4s (Siddiqui-Jain et al., 2002). Through mutational destabilization, they showed that there is a 3-fold increase in c-Myc expression, indicating that the G4 acts as a transcriptional repressor. They showed that stabilization of the G4 with a small molecule could further reduce transcription to below the basal level. Later studies on the protein nucleolin, a multifaceted and abundant protein found in the nucleolus (Tajrishi et al., 2011), have shown that it can help the folding of promoter G4s like a molecular chaperone (Tosoni et al., 2015). Nucleolin was shown to fold the c-Myc NHEIII G4, promoting transcriptional downregulation in cells (Gonzalez and Hurley, 2010). Altogether, these studies show that promoter G4s are important epigenetic regulators of genes, and that their stability and interaction with transcription factors can influence transcription.

2.2 Biological distribution and function of promoter xG4s

Promoter xG4s are also abundant across the genome. Berselli and colleagues recently developed QPARSE (13), the first algorithm capable of finding xG4s in the genome that accounts for mismatches and bulges in G-tracts (see Figure 1B for a G4 with a bulge). In the study, the authors used their degenerate G4 motif algorithm to find monomeric, dimeric, and trimeric G4 sequences in the range of −200 to +600 of the transcriptional start sites (TSS) across the annotated human genome [GENCODE (Harrow et al., 2012)]. They found that 49%, 15%, and 4% of TSS regions had monomer, dimer, and trimer G4 repeats, respectively, and show that this enrichment cannot entirely be attributed to high GC content. Ceschi et al. have recently used the same algorithm to search just the first 100 bp upstream of the TSS of gene promoters in GENCODE, finding

1,478 dimer and trimer promoter xG4s (Ceschi et al., 2022) (~4% of the 38,404 annotated genes in GENCODE v34).

Parsing out the *in vivo* function of a particular xG4 compared to their monomeric counterparts is a challenging task. At one end you have bioinformatic and G4-or G4-ChIP-sequencing approaches that lack the spatial resolution to distinguish between monomer, dimer, trimer, and other higher-order G4 effects (Park, 2009; Mahony and Pugh, 2015). For instance, the ChIP-sequencing studies mentioned above should, in theory, encompass promoter sites enriched with xG4s. At the other end, there is a dearth of tools that allow direct probing of the effects of monomer versus higher-order G4s. Specifically, there are no reports to date that have convincingly shown selective (de)stabilization of a single G4 domain among a higher-order promoter G4 assembly (Frasson et al., 2022). Mutational reporter assays are the current best approach to parsing out the functionality of xG4s within a cellular context (Siddiqui-Jain et al., 2002; Cogoi et al., 2010), but these come at the risk of altering protein recognition motifs (Bell et al., 2015).

The most thorough investigation of a promoter xG4 to date was conducted in 2019 by Ducani and colleagues on an xG4 found in the promoter of the proto-oncogene *c-Kit* (Ducani et al., 2019). The *c-Kit* gene encodes for a transmembrane tyrosine kinase receptor (c-Kit or CD117) that, after activation by stem cell factor (SCF), transduces signals that promote cell proliferation, differentiation, and migration (Liang et al., 2013). Excessive signaling by continued stimulation or mutation has been implicated in a variety of cancers, such as gastrointestinal stromal tumors (GISTs), pancreatic cancer, melanoma, and hematological neoplastic diseases (Gregory-Bryson et al., 2010; Abbaspour Babaei et al., 2016). Since c-Kit has a tyrosine kinase domain, these cancers are typically treated with tyrosine kinase inhibitors (TKIs) tailored to the mutation type (Abbaspour Babaei et al., 2016). Unfortunately, treating c-Kit-driven cancers with TKIs is often followed with a rapid switch to drug-resistance through mutation (Demetri et al., 2002; Loughrey et al., 2006; Abbaspour Babaei et al., 2016). Therefore, understanding how the *c-Kit* promoter xG4 regulates its transcription is important for drug development efforts. The c-Kit xG4 consists of three monomeric G4 motifs, designated K2, SP, and K1 (from 5′ to 3′) connected by a single dA loop and a hexanucleotide dGCGCAG loop, respectively. Each separate G4 domain has been structurally and/or functionally examined (Rankin et al., 2005; Phan et al., 2007; Hsu et al., 2009; Kuryavyi et al., 2010; Raiber et al., 2012; Kotar et al., 2019), and the higher-order structural assembly of domains K2-SP confirmed by integrative structural biology approaches (Rigo and Sissi, 2017; Monsen et al., 2022a). Both structural studies show that the K2-SP regions interact through stacking, although the two studies differ slightly in the size of the sequence examined. Based on circular dichroism of the full-length sequence used by Ducani, however, the full-length K2-SP-K1 sequence adopts an all-parallel conformation, which is consistent with the promoter xG4s structurally verified to date (Monsen et al., 2020; Monsen et al., 2022a). To investigate the biological function of such an arrangement, Ducani and colleagues conducted luciferase assays to test the effect of disrupting all combinations of the G4 regions by mutating guanines essential for structural integrity. They show in the leukemia cell line HEL92.1.7 that the K1 G4 (alone) and K2-SP G4s (together as a higher-order feature) have opposing roles in transcriptional regulation, with the former acting repressively and the latter acting to stimulate transcription. Further, they show that each G4 unit is significantly affected by the formation or disruption of the others, signifying G4-G4 crosstalk within a cellular context. The readout from each mutational state was more of a continuous distribution, rather than an all or nothing response. Overall, this study suggests that xG4s play a very nuanced role in governing transcriptional activation or repression. It remains to be seen whether a K2-SP disrupting small molecule, or SP-K1 stabilizing small molecule will act as an indirect c-Kit inhibitor.

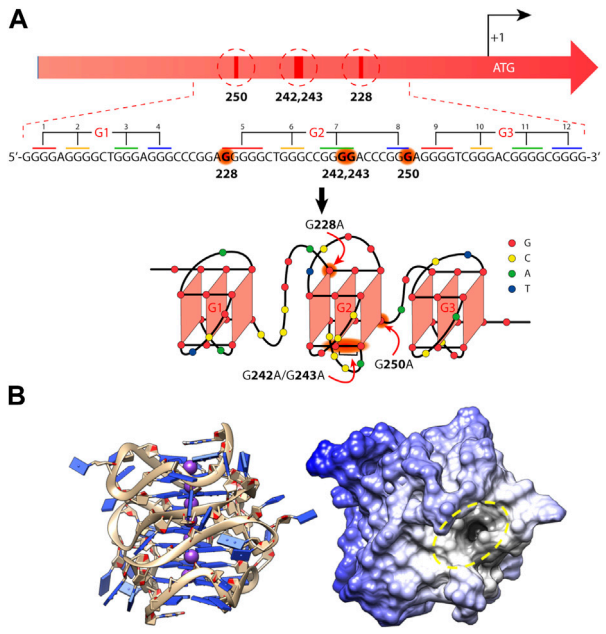

FIGURE 2
Mutations and folding of the hTERT core promoter G-quadruplex. **(A)** Cancer-specific mutations in the hTERT promoter's primary structure that generate *de novo* binding sites for the ETS transcription factors and putative structure that was proposed for the G-rich (noncoding) strand of the hTERT promoter. Below is the sequence of the WT hTERT G4 motif and one conceivable way of G4 folding. The assignment of G-tracts (numbered) to three G4-motifs (G1, G2, and G3) is presented. Common mutation sites are shown in red in the hTERT G-rich sequence and in red arrows in the structural model. **(B)** The folded all-parallel hTERT xG4 represented with sugar-phosphate backbone as ribbons and nucleobases as slabs (left) and surface representation showing a large binding pocket (dark area inside of yellow dashed oval) at the junction between the first and second G4s. **(A)** was adapted from (Pavlova et al., 2022) and **(B)** was adapted from (Monsen and Trent, 2018).

3 Case study: targeting the hTERT core promoter xG4

One of the most studied xG4s to date is found within the *hTERT* core promoter region. *hTERT* encodes the protein catalytic subunit of telomerase, the ribonucleoprotein primarily responsible for maintaining telomere length homeostasis (Bryan and Cech, 1999). Although typically undetectable in somatic cells, hTERT is aberrantly over-expressed in more than 90% of aggressive cancers (Shay and Bacchetti, 1997), making it a long sought after cancer-specific target. The *hTERT* gene was first identified as harboring a putative xG4 in its promoter by Palumbo et al. (2009). The hTERT xG4 sequence consists of twelve G-tracts of three or more guanines that enable the maximum formation of three contiguous G4s (Figure 2).

Since its discovery, the tertiary structure of the *hTERT* xG4 has been intensely disputed. In the original work, Palumbo et al. showed by CD that the *hTERT* sequence was entirely parallel (Palumbo et al., 2009), although, based on their DMS footprinting results, they proposed a model consisting of a parallel G4 unit connected to an antiparallel G4 unit connected by a ~26 nucleotide hairpin loop. About a year after, Micheli et al. (2010) independently proposed that the hTERT xG4 formed three parallel G4 units that were contiguous and stacked 3′ to 5′ based on CD and Taq polymerase stop assays. Later studies using an experimental small molecule and DMS footprinting assays reported yet another, slightly different, G4-hairpin arrangement (Song et al., 2019). However, structural studies of the sequence using a combination of CD, hydrodynamics, NMR, modeling, and small-angle X-ray scattering (SAXS) have since confirmed that the most consistent model is one in which three parallel G4s are tightly stacked in a stacked 3′ to 5′ arrangement (Figure 2) (Monsen et al., 2020). A recent DMS footprinting experiment confirms the all-parallel model as correct (Pavlova et al., 2022).

The *hTERT* xG4 is a potentially selective, transcriptionally repressive structure. The *hTERT* core promoter region has multiple non-coding mutations that are seen across many cancer types, with the two most prominent denoted "G228A" and "G250A", that coincide with a robust increased telomerase activity (Killela et al., 2013). These mutations exist within G-tracts that form the central G4 unit of the three stacked all-parallel xG4 model (see Figure 2) (Micheli et al., 2010; Chaires et al., 2014; Monsen et al., 2020). Using luciferase expression assays of the wild type (WT) promoter versus mutant promoters of either G228A or G250A, Bell and colleagues showed that a robust increase in promoter activity is gained with either mutant (Bell et al., 2015). Further investigation showed that either G- > A mutation creates a *de novo* ETS (Erythroblast Transformation Specific) transcription factor consensus motif that is recognized by the transcription factor GABP (GA-binding protein). However, the creation of an ETS motif has been shown to be insufficient to fully explain the transcriptional changes seen in mutant cells (Kang et al., 2016).

Early investigations by Micheli et al. showed that the central G4, which encompasses either G- > A mutation, is unstable as an isolated monomeric G4, and only forms stably as a higher-order G4 assembly through stacking with both 5′ and 3′ G4 regions (Micheli et al., 2010). The destabilizing effects of the mutants on the overall xG4 have since been confirmed (Pavlova et al., 2022). A G4 ligand reported to refold and stabilize the hTERT xG4 WT structure (with or without G- > A mutations) was able to restore its repressive effects and showed good selectivity for the hTERT promoter over other genes with known promoter G4s (Kang et al., 2016). More recently, Monsen et al., (2022b) used a virtual screening approach to target the loop and G4-junctional regions of the all-parallel hTERT xG4 (Figure 2). Using a variety of *in vitro* binding and competition assays, the authors were able to find a drug-like small molecule that stabilized across the second and third G4 regions that showed high selectivity over duplex DNA and moderate selectivity over all other forms of DNA tested. In both cases, repression of hTERT expression was confirmed in breast cancer cell lines. Collectively, these studies reveal that the *hTERT* xG4 is an indirect target for down-regulating hTERT in cells. Further, these studies show for the first time that a higher-order promoter G4 can be targeted with selectivity using the unique features imparted from G4-G4 domains.

4 Discussion

Higher-order G-quadruplexes have emerged as selective targets in the promoters of thousands of annotated genes across the human genome. While xG4s offer some of the same protein binding recognition that monomeric G4s do, promoter xG4s also appear to encode for transcriptional status, possibly acting as titratable "dimmer switches" of gene activity. Structurally, xG4s offer a much richer drug targeting landscape consisting of G4-G4 interaction junctions adorned with protein-like binding pockets formed among sequence-specific loop features. This is emphasized by the decade-long pursuit targeting the *hTERT* core promoter xG4 which has resulted in both a unique receptor and the first drug-like small molecule targeting an xG4 with selectivity.

While xG4 studies to date have led to exciting new insight into their structural arrangements and potential regulatory mechanisms, there is still much to be understood. One of the major hurdles in studying xG4s is their recalcitrance to the traditional structural biology techniques NMR and X-ray diffraction. To date, all structural models have been derived from medium-to low-resolution integrative structural strategies and/or footprinting methods (Palumbo et al., 2009; Micheli et al., 2010; Rigo and Sissi, 2017; Monsen et al., 2020; Monsen et al., 2021; Monsen et al., 2022a; Pavlova et al., 2022). Cryo-EM is emerging as a possible solution to this problem (Monsen et al., 2023); however, atomic resolution of relatively small, potentially heterogeneous [e.g., G-tract isomers (Harkness and Mittermaier, 2017; Hennecker et al., 2022)] or flexible systems (e.g., inter-domain movements or long flexible loops) (Monsen et al., 2021; Monsen et al., 2022a; Monsen et al., 2023) is still a considerable challenge in the field (Herzik et al., 2019) [although scaffolds might offer a solution (Wu and Rapoport, 2021)]. A second major hurdle, as touched on above, is determining their biological mechanism. Molecular tools, such as xG4-specific fluorescent molecules (Summers et al., 2021) or antibodies (Biffi et al., 2013), should aid in revealing their spatial and temporal formation. Recently, the zinc finger-containing transcription factor Yin Yang-1 (YY1) was shown to bind G4s and bring two G4 domains into proximity through its dimerization (Li et al., 2021), offering a potential tool for investigating biological function of xG4s in a more biologically relevant context.

Author contributions

RM conceptualized the topic, researched, and analyzed the literature, and wrote the manuscript.

Funding

This research received no specific grant from any funding agency in the public, commercial, or not-for-profit sectors.

Acknowledgments

The author thanks John O. Trent for his suggested use of "xG4" for higher-order promoter G4s, J. Brad Chaires for providing the

inspiration for the topic and proofreading, and Robert D. Gray for proofreading the review.

Conflict of interest

The authors declare that the research was conducted in the absence of any commercial or financial relationships that could be construed as a potential conflict of interest.

Publisher's note

References

Abbaspour Babaei, M., Kamalidehghan, B., Saleem, M., Huri, H. Z., and Ahmadipour, F. (2016). Receptor tyrosine kinase (c-Kit) inhibitors: A potential therapeutic target in cancer cells. *Drug Des. Devel Ther.* 10, 2443–2459. doi:10.2147/dddt.s89114

Amrane, S., Adrian, M., Heddi, B., Serero, A., Nicolas, A., Mergny, J. L., et al. (2012). Formation of pearl-necklace monomorphic G-quadruplexes in the human CEB25 minisatellite. *J. Am. Chem. Soc.* 134 (13), 5807–5816. doi:10.1021/ja208993r

Bell, R. J., Rube, H. T., Kreig, A., Mancini, A., Fouse, S. D., Nagarajan, R. P., et al. (2015). The transcription factor GABP selectively binds and activates the mutant TERT promoter in cancer. *Science* 348 (6238), 1036–1039. doi:10.1126/science.aab0015

Berselli, M., Lavezzo, E., and Toppo, S. (2020). Qparse: Searching for long-looped or multimeric G-quadruplexes potentially distinctive and druggable. *Bioinformatics* 36 (2), 393–399. doi:10.1093/bioinformatics/btz569

Bhattacharyya, D., Mirihana Arachchilage, G., and Basu, S. (2016). Metal cations in G-quadruplex folding and stability. *Front. Chem.* 4, 38. doi:10.3389/fchem.2016.00038

Biffi, G., Tannahill, D., McCafferty, J., and Balasubramanian, S. (2013). Quantitative visualization of DNA G-quadruplex structures in human cells. *Nat. Chem.* 5 (3), 182–186. doi:10.1038/nchem.1548

Bryan, T. M., and Cech, T. R. (1999). Telomerase and the maintenance of chromosome ends. *Curr. Opin. Cell. Biol.* 11 (3), 318–324. doi:10.1016/s0955-0674(99)80043-x

Ceschi, S., Berselli, M., Cozzaglio, M., Giantin, M., Toppo, S., Spolaore, B., et al. (2022). Vimentin binds to G-quadruplex repeats found at telomeres and gene promoters. *Nucleic Acids Res.* 50 (3), 1370–1381. doi:10.1093/nar/gkab1274

Chaires, J. B., Trent, J. O., Gray, R. D., Dean, W. L., Buscaglia, R., Thomas, S. D., et al. (2014). An improved model for the hTERT promoter quadruplex. *PLoS One* 9 (12), e115580. doi:10.1371/journal.pone.0115580

Chen, J., Cheng, M., Salgado, G. F., Stadlbauer, P., Zhang, X., Amrane, S., et al. (2021). The beginning and the end: Flanking nucleotides induce a parallel G-quadruplex topology. *Nucleic Acids Res.* 49 (16), 9548–9559. doi:10.1093/nar/gkab681

Chen, Y., and Yang, D. (2012). Sequence, stability, and structure of G-quadruplexes and their interactions with drugs. *Curr. Protoc. Nucleic Acid. Chem.* 50, nc1705s50. doi:10.1002/0471142700.nc1705s50

Cogoi, S., Paramasivam, M., Membrino, A., Yokoyama, K. K., and Xodo, L. E. (2010). The KRAS promoter responds to Myc-associated zinc finger and poly(ADP-ribose) polymerase 1 proteins, which recognize a critical quadruplex-forming GA-element. *J. Biol. Chem.* 285 (29), 22003–22016. doi:10.1074/jbc.m110.101923

Demetri, G. D., von Mehren, M., Blanke, C. D., Van den Abbeele, A. D., Eisenberg, B., Roberts, P. J., et al. (2002). Efficacy and safety of imatinib mesylate in advanced gastrointestinal stromal tumors. *N. Engl. J. Med.* 347 (7), 472–480. doi:10.1056/nejmoa020461

Ducani, C., Bernardinelli, G., Hogberg, B., Keppler, B. K., and Terenzi, A. (2019). Interplay of three G-quadruplex units in the KIT promoter. *J. Am. Chem. Soc.* 141 (26), 10205–10213. doi:10.1021/jacs.8b12753

Frasson, I., Pirota, V., Richter, S. N., and DoriaG-quadruplexes, F. (2022). Multimeric G-quadruplexes: A review on their biological roles and targeting. *Int. J. Biol. Macromol.* 204, 89–102. doi:10.1016/j.ijbiomac.2022.01.197

Gonzalez, V., and Hurley, L. H. (2010). The C-terminus of nucleolin promotes the formation of the c-MYC G-quadruplex and inhibits c-MYC promoter activity. *Biochemistry* 49 (45), 9706–9714. doi:10.1021/bi100509s

Gregory-Bryson, E., Bartlett, E., Kiupel, M., Hayes, S., and Yuzbasiyan-Gurkan, V. (2010). Canine and human gastrointestinal stromal tumors display similar mutations in c-KIT exon 11. *BMC Cancer* 10, 559. doi:10.1186/1471-2407-10-559

Hansel-Hertsch, R., Beraldi, D., Lensing, S. V., Marsico, G., Zyner, K., Parry, A., et al. (2016). G-quadruplex structures mark human regulatory chromatin. *Nat. Genet.* 48 (10), 1267–1272. doi:10.1038/ng.3662

Hansel-Hertsch, R., Di Antonio, M., and Balasubramanian, S. (2017). DNA G-quadruplexes in the human genome: Detection, functions and therapeutic potential. *Nat. Rev. Mol. Cell. Biol.* 18 (5), 279–284. doi:10.1038/nrm.2017.3

Harrow, J., Frankish, A., Gonzalez, J. M., Tapanari, E., Diekhans, M., Kokocinski, F., et al. (2012). Gencode: The reference human genome annotation for the ENCODE project. *Genome Res.* 22 (9), 1760–1774. doi:10.1101/gr.135350.111

Hennecker, C., Yamout, L., Zhang, C., Zhao, C., Hiraki, D., Moitessier, N., et al. (2022). Structural polymorphism of guanine quadruplex-containing regions in human promoters. *Int. J. Mol. Sci.* 23 (24), 16020. doi:10.3390/ijms232416020

Herzik, M. A., Jr., Wu, M., and Lander, G. C. (2019). High-resolution structure determination of sub-100 kDa complexes using conventional cryo-EM. *Nat. Commun.* 10 (1), 1032. doi:10.1038/s41467-019-08991-8

Hsu, S. T., Varnai, P., Bugaut, A., Reszka, A. P., Neidle, S., and Balasubramanian, S. (2009). A G-rich sequence within the c-kit oncogene promoter forms a parallel G-quadruplex having asymmetric G-tetrad dynamics. *J. Am. Chem. Soc.* 131 (37), 13399–13409. doi:10.1021/ja904007p

Huppert, J. L., and Balasubramanian, S. (2007). G-quadruplexes in promoters throughout the human genome. *Nucleic Acids Res.* 35 (2), 406–413. doi:10.1093/nar/gkl1057

Javadekar, S. M., Nilavar, N. M., Paranjape, A., Das, K., and Raghavan, S. C. (2020). Characterization of G-quadruplex antibody reveals differential specificity for G4 DNA forms. *DNA Res.* 27 (5), dsaa024. doi:10.1093/dnares/dsaa024

Kang, H. J., Cui, Y., Yin, H., Scheid, A., Hendricks, W. P. D., Schmidt, J., et al. (2016). A pharmacological chaperone molecule induces cancer cell death by restoring tertiary DNA structures in mutant hTERT promoters. *J. Am. Chem. Soc.* 138 (41), 13673–13692. doi:10.1021/jacs.6b07598

Kejnovska, I., Stadlbauer, P., Trantirek, L., Renciuk, D., Gajarsky, M., Krafcik, D., et al. (2021). G-quadruplex formation by DNA sequences deficient in guanines: Two tetrad parallel quadruplexes do not fold intramolecularly. *Chemistry* 27 (47), 12115–12125. doi:10.1002/chem.202100895

Killela, P. J., Reitman, Z. J., Jiao, Y., Bettegowda, C., Agrawal, N., Diaz, L. A., Jr., et al. (2013). TERT promoter mutations occur frequently in gliomas and a subset of tumors derived from cells with low rates of self-renewal. *Proc. Natl. Acad. Sci. U. S. A.* 110 (15), 6021–6026. doi:10.1073/pnas.1303607110

Kogut, M., Kleist, C., and Czub, J. (2019). Why do G-quadruplexes dimerize through the 5'-ends? Driving forces for G4 DNA dimerization examined in atomic detail. *PLOS Comput. Biol.* 15 (9), e1007383. doi:10.1371/journal.pcbi.1007383

Kotar, A., Rigo, R., Sissi, C., and Plavec, J. (2019). Two-quartet kit* G-quadruplex is formed via double-stranded pre-folded structure. *Nucleic Acids Res.* 47 (5), 2641–2653. doi:10.1093/nar/gky1269

Kuryavyi, V., Phan, A. T., and Patel, D. J. (2010). Solution structures of all parallel-stranded monomeric and dimeric G-quadruplex scaffolds of the human c-kit2 promoter. *Nucleic Acids Res.* 38 (19), 6757–6773. doi:10.1093/nar/gkq558

Lane, A. N., Chaires, J. B., Gray, R. D., and Trent, J. O. (2008). Stability and kinetics of G-quadruplex structures. *Nucleic Acids Res.* 36 (17), 5482–5515. doi:10.1093/nar/gkn517

Li, L., Williams, P., Ren, W., Wang, M. Y., Gao, Z., Miao, W., et al. (2021). YY1 interacts with guanine quadruplexes to regulate DNA looping and gene expression. *Nat. Chem. Biol.* 17 (2), 161–168. doi:10.1038/s41589-020-00695-1

Liang, J., Wu, Y. L., Chen, B. J., Zhang, W., Tanaka, Y., and Sugiyama, H. (2013). The C-kit receptor-mediated signal transduction and tumor-related diseases. *Int. J. Biol. Sci.* 9 (5), 435–443. doi:10.7150/ijbs.6087

Lim, K. W., Amrane, S., Bouaziz, S., Xu, W., Mu, Y., Patel, D. J., et al. (2009). Structure of the human telomere in K+ solution: A stable basket-type G-quadruplex with only two G-tetrad layers. *J. Am. Chem. Soc.* 131 (12), 4301–4309. doi:10.1021/ja807503g

Loughrey, M. B., Waring, P. M., Dobrovic, A., Demetri, G., Kovalenko, S., and McArthur, G. (2006). Polyclonal resistance in gastrointestinal stromal tumor treated with sequential kinase inhibitors. *Clin. Cancer Res.* 12 (20), 6205–6206. doi:10.1158/1078-0432.ccr-06-1079

Mahony, S., and Pugh, B. F. (2015). Protein-DNA binding in high-resolution. *Crit. Rev. Biochem. Mol. Biol.* 50 (4), 269–283. doi:10.3109/10409238.2015.1051505

Micheli, E., Martufi, M., Cacchione, S., De Santis, P., and Savino, M. (2010). Self-organization of G-quadruplex structures in the hTERT core promoter stabilized by polyaminic side chain perylene derivatives. *Biophys. Chem.* 153 (1), 43–53. doi:10.1016/j.bpc.2010.10.003

Miller, M. C., Buscaglia, R., Chaires, J. B., Lane, A. N., and Trent, J. O. (2010). Hydration is a major determinant of the G-quadruplex stability and conformation of the human telomere 3' sequence of d(AG3(TTAG3)3). *J. Am. Chem. Soc.* 132 (48), 17105–17107. doi:10.1021/ja105259m

Monsen, R. C., Chakravarthy, S., Dean, W. L., Chaires, J. B., and Trent, J. O. (2021). The solution structures of higher-order human telomere G-quadruplex multimers. *Nucleic Acids Res.* 49 (3), 1749–1768. doi:10.1093/nar/gkaa1285

Monsen, R. C., Chua, E. Y. D., Hopkins, J. B., Chaires, J. B., and Trent, J. O. (2023). Structure of a 28.5 kDa duplex-embedded G-quadruplex system resolved to 7.4 Aresolution with cryo-EM. *Nucleic Acids Res.* 51 (4), 1943–1959. doi:10.1093/nar/gkad014

Monsen, R. C., DeLeeuw, L., Dean, W. L., Gray, R. D., Sabo, T. M., Chakravarthy, S., et al. (2020). The hTERT core promoter forms three parallel G-quadruplexes. *Nucleic Acids Res.* 48 (10), 5720–5734. doi:10.1093/nar/gkaa107

Monsen, R. C., DeLeeuw, L. W., Dean, W. L., Gray, R. D., Chakravarthy, S., Hopkins, J. B., et al. (2022). Long promoter sequences form higher-order G-quadruplexes: An integrative structural biology study of c-myc, k-ras and c-kit promoter sequences. *Nucleic Acids Res.* 50 (7), 4127–4147. doi:10.1093/nar/gkac182

Monsen, R. C., Maguire, J. M., DeLeeuw, L. W., Chaires, J. B., and Trent, J. O. (2022). Drug discovery of small molecules targeting the higher-order hTERT promoter G-quadruplex. *PLoS One* 17 (6), e0270165. doi:10.1371/journal.pone.0270165

Monsen, R. C., and Trent, J. O. (2018). G-Quadruplex virtual drug screening: A review. *Biochimie* 152, 134–148. doi:10.1016/j.biochi.2018.06.024

Palumbo, S. L., Ebbinghaus, S. W., and Hurley, L. H. (2009). Formation of a unique end-to-end stacked pair of G-quadruplexes in the hTERT core promoter with implications for inhibition of telomerase by G-quadruplex-interactive ligands. *J. Am. Chem. Soc.* 131 (31), 10878–10891. doi:10.1021/ja902281d

Park, P. J. (2009). ChIP-seq: Advantages and challenges of a maturing technology. *Nat. Rev. Genet.* 10 (10), 669–680. doi:10.1038/nrg2641

Pavlova, A. V., Savitskaya, V. Y., Dolinnaya, N. G., Monakhova, M. V., Litvinova, A. V., Kubareva, E. A., et al. (2022). G-quadruplex formed by the promoter region of the hTERT gene: Structure-driven effects on DNA mismatch repair functions. *Biomedicines* 10 (8), 1871. doi:10.3390/biomedicines10081871

Phan, A. T., Kuryavyi, V., Burge, S., Neidle, S., and Patel, D. J. (2007). Structure of an unprecedented G-quadruplex scaffold in the human c-kit promoter. *J. Am. Chem. Soc.* 129 (14), 4386–4392. doi:10.1021/ja068739h

Raiber, E. A., Kranaster, R., Lam, E., Nikan, M., and Balasubramanian, S. (2012). A non-canonical DNA structure is a binding motif for the transcription factor SP1 *in vitro*. *Nucleic Acids Res.* 40 (4), 1499–1508. doi:10.1093/nar/gkr882

Rankin, S., Reszka, A. P., Huppert, J., Zloh, M., Parkinson, G. N., Todd, A. K., et al. (2005). Putative DNA quadruplex formation within the human c-kit oncogene. *J. Am. Chem. Soc.* 127 (30), 10584–10589. doi:10.1021/ja050823u

Ravichandran, S., Razzaq, M., Parveen, N., Ghosh, A., and Kim, K. K. (2021). The effect of hairpin loop on the structure and gene expression activity of the long-loop G-quadruplex. *Nucleic Acids Res.* 49 (18), 10689–10706. doi:10.1093/nar/gkab739

Rigo, R., and Sissi, C. (2017). Characterization of G4-G4 crosstalk in the c-KIT promoter region. *Biochemistry* 56 (33), 4309–4312. doi:10.1021/acs.biochem.7b00660

Harkness, R. W., and Mittermaier, A. K. (2017). G-quadruplex dynamics. *Biochim. Biophys. Acta Proteins Proteom* 1865 (11), 1544–1554. doi:10.1016/j.bbapap.2017.06.012

Sarkies, P., Reams, C., Simpson, L. J., and Sale, J. E. (2010). Epigenetic instability due to defective replication of structured DNA. *Mol. Cell.* 40 (5), 703–713. doi:10.1016/j.molcel.2010.11.009

Schonhoft, J. D., Bajracharya, R., Dhakal, S., Yu, Z., Mao, H., and Basu, S. (2009). Direct experimental evidence for quadruplex-quadruplex interaction within the human ILPR. *Nucleic Acids Res.* 37 (10), 3310–3320. doi:10.1093/nar/gkp181

Shay, J. W., and Bacchetti, S. (1997). A survey of telomerase activity in human cancer. *Eur. J. Cancer* 33 (5), 787–791. doi:10.1016/s0959-8049(97)00062-2

Shirude, P. S., Okumus, B., Ying, L., Ha, T., and Balasubramanian, S. (2007). Single-molecule conformational analysis of G-quadruplex formation in the promoter DNA duplex of the proto-oncogene c-kit. *J. Am. Chem. Soc.* 129 (24), 7484–7485. doi:10.1021/ja070497d

Siddiqui-Jain, A., Grand, C. L., Bearss, D. J., and Hurley, L. H. (2002). Direct evidence for a G-quadruplex in a promoter region and its targeting with a small molecule to repress c-MYC transcription. *Proc. Natl. Acad. Sci. U. S. A.* 99 (18), 11593–11598. doi:10.1073/pnas.182256799

Song, J. H., Kang, H. J., Luevano, L. A., Gokhale, V., Wu, K., Pandey, R., et al. (2019). Small-molecule-targeting hairpin loop of hTERT promoter G-quadruplex induces cancer cell death. *Cell. Chem. Biol.* 26 (8), 1110–1121.e4. doi:10.1016/j.chembiol.2019.04.009

Spiegel, J., Adhikari, S., and Balasubramanian, S. (2020). The structure and function of DNA G-quadruplexes. *Trends Chem.* 2 (2), 123–136. doi:10.1016/j.trechm.2019.07.002

Spiegel, J., Cuesta, S. M., Adhikari, S., Hansel-Hertsch, R., Tannahill, D., and Balasubramanian, S. (2021). G-quadruplexes are transcription factor binding hubs in human chromatin. *Genome Biol.* 22 (1), 117. doi:10.1186/s13059-021-02324-z

Summers, P. A., Lewis, B. W., Gonzalez-Garcia, J., Porreca, R. M., Lim, A. H. M., Cadinu, P., et al. (2021). Visualising G-quadruplex DNA dynamics in live cells by fluorescence lifetime imaging microscopy. *Nat. Commun.* 12 (1), 162. doi:10.1038/s41467-020-20414-7

Tajrishi, M. M., Tuteja, R., and Tuteja, N. (2011). Nucleolin: The most abundant multifunctional phosphoprotein of nucleolus. *Commun. Integr. Biol.* 4 (3), 267–275. doi:10.4161/cib.4.3.14884

Tosoni, E., Frasson, I., Scalabrin, M., Perrone, R., Butovskaya, E., Nadai, M., et al. (2015). Nucleolin stabilizes G-quadruplex structures folded by the LTR promoter and silences HIV-1 viral transcription. *Nucleic Acids Res.* 43 (18), 8884–8897. doi:10.1093/nar/gkv897

Wu, X., and Rapoport, T. A. (2021). Cryo-EM structure determination of small proteins by nanobody-binding scaffolds (Legobodies). *Proc. Natl. Acad. Sci. U. S. A.* 118 (41), e2115001118. doi:10.1073/pnas.2115001118

frontiers | Frontiers in Chemistry

TYPE Original Research
PUBLISHED 14 June 2023
DOI 10.3389/fchem.2023.1197010

OPEN ACCESS

EDITED BY
Kunyu Wang,
Texas A and M University, United States

REVIEWED BY
Yiou Wang,
Beijing Institute of Technology, China
Zaiwang Zhao,
Inner Mongolia University, China

*CORRESPONDENCE
Bolong Huang,
bhuang@polyu.edu.hk

RECEIVED 31 March 2023
ACCEPTED 06 June 2023
PUBLISHED 14 June 2023

CITATION
Lu L, Sun M, Wu T, Lu Q, Chen B, Chan CH, Wong HH and Huang B (2023), Transition metal anchored on red phosphorus to enable efficient photocatalytic H_2 generation. *Front. Chem.* 11:1197010. doi: 10.3389/fchem.2023.1197010

Transition metal anchored on red phosphorus to enable efficient photocatalytic H_2 generation

Lu Lu[1], Mingzi Sun[1], Tong Wu[1], Qiuyang Lu[1], Baian Chen[1], Cheuk Hei Chan[1], Hon Ho Wong[1] and Bolong Huang[1,2]*

[1]Department of Applied Biology and Chemical Technology, The Hong Kong Polytechnic University, Kowloon, Hong Kong SAR, China, [2]Research Centre for Carbon-Strategic Catalysis, The Hong Kong Polytechnic University, Kowloon, Hong Kong SAR, China

Transition metal (TM) single atom catalysts (SACs) are of great potential for photocatalytic H_2 production because of their abundant catalytic active sites and cost-effectiveness. As a promising support material, red phosphorus (RP) based SACs are still rarely investigated. In this work, we have carried out systematic theoretical investigations by anchoring TM atoms (Fe, Co, Ni, Cu) on RP for efficient photocatalytic H_2 generation. Our density functional theory (DFT) calculations have revealed that 3d orbitals of TM locate close to the Fermi level to guarantee efficient electron transfer for photocatalytic performances. Compared with pristine RP, the introduction of single atom TM on the surface exhibit narrowed bandgaps, resulting in easier spatial separation for photon-generated charge carriers and an extended photocatalytic absorption window to the NIR range. Meanwhile, the H_2O adsorptions are also highly preferred on the TM single atoms with strong electron exchange, which benefits the subsequent water-dissociation process. Due to the optimized electronic structure, the activation energy barrier of water-splitting has been remarkably reduced in RP-based SACs, revealing their promising potential for high-efficiency H_2 production. Our comprehensive explorations and screening of novel RP-based SACs will offer a good reference for further designing novel photocatalysts for high-efficiency H_2 generation.

KEYWORDS

red phosphorus, single-atom catalysts, transition metals, photocatalysis, H_2 generation

1 Introduction

Hydrogen energy is a clean and renewable energy, attracting increasing research attention in recent years. Especially, it has a high gravimetric energy density, and the product of H_2 combustion is only pure water, making it a promising candidate to cope with the fossil energy crisis and meet the challenge of peak carbon dioxide emission limitation. (Wang S. et al., 2019; Pan et al., 2021; Xue et al., 2022). However, the high cost of H_2 production as well as safety issues in storage and transportation have greatly restricted its commercial applications. Without additional electric power consumption, solar energy-driven catalytic water splitting has been considered as an eco-friendly strategy for low-cost H_2 production. Currently, photocatalytic H_2 evolution has not been broadly adopted in large-scale industrial production since it still suffers from the low solar-to-hydrogen (STH) conversion rate, which is caused by intrinsic unfavorable thermodynamics and sluggish kinetics of solar-driven catalytic water splitting reaction. (Chen et al., 2020; Bie et al., 2022). In recent decades, to improve the catalytic activity of photocatalysts, researchers have tried a

series of modulation strategies to enhance surface reactivity, reduce the activation energy barrier, and restrain the intrinsic fast recombination of photoinduced charge carriers.

Previously, phosphorus has been treated as an effective heteroatom dopant for the band structure engineering of TiO_2-based photocatalysts. (Yu et al., 2003; Wang et al., 2012a; Hu et al., 2017; Zhu et al., 2019; Huang et al., 2022). Afterwards, it has been discovered that phosphorus itself can also act as an efficient photocatalyst for hydrogen evolution through water-splitting. (Shen et al., 2014; Hu et al., 2017; Liu et al., 2019; Chen et al., 2022). Among its three allotropes (black, P_4-white, and red phosphorus), red phosphorus (RP) is the most available form and has excellent chemical stability at room temperature, and it has been treated as a promising semiconductor material in the construction of photocatalytic platforms. (Wang et al., 2012a; Xia et al., 2015; Hu et al., 2017; Liu et al., 2019; Chen et al., 2022; Fung et al., 2022). It has been reported that RP is a durable photocatalyst with the stable catalytic activity of H_2 evolution for more than 90 h under visible light irradiation. (Wang et al., 2012a; Wang et al., 2012b). Though RP has good absorption of visible light at about 700 nm, the overall water-splitting efficiency of pristine RP is relatively limited due to its low conductivity, poor electron-hole separation efficiency, and sluggish charge-carrier mobility. (Zhu et al., 2019; Wang M. et al., 2020; Wu et al., 2021; Chen et al., 2022).

Since RP has good lattice compatibility, it is possible to modify the catalytic surface through the doping method or heterostructure construction. As a result, the electronic structures of RP can be well-manipulated to benefit the photocatalytic reaction. (Li et al., 2019; Zhu et al., 2020a; Huang et al., 2022; Wang et al., 2022; Jia et al., 2023). With the assistance of appropriate active co-catalyst atoms such as Pt, the overall photocatalytic H_2 production performance of RP is greatly improved. (Wang et al., 2012a). In consideration of material cost and future industrial applications, developing non-precious metals based catalysts is of great significance for the popularization of hydrogen energy. In particular, 3d transition metals (TMs) are the most commonly studied candidates to replace noble-metal catalysts due to their high catalytic activity. By suitable tuning strategies, the novel non-noble metal catalysts can also achieve comparable or even superior catalytic activity to noble metal catalysts. Scientists have reported that both morphological and scale controls are effective for the electronic property tuning of semiconductor materials. (Zhu et al., 2020b; Wu et al., 2020; Khandelwal et al., 2022). By downsizing the material scale from the nanoscale to the cluster scale and then finally the atomic scale, an enhanced inter-atomic strain is induced, leading to the modulations in geometrical structure and electronic structures. (Liu and Corma, 2018; Khandelwal et al., 2022). Hence, developing single-atom catalysts (SACs) is a potential method for the modulation of catalytic activity on the atomic scale. The atomic dispersion of active metal atoms on the RP surface will maximumly improve the atomic utilization rate, offering maximum photocatalytic active sites to enable the light adsorption and activation of H_2O molecules with a minimum consumption of metal atoms. (Wang B. et al., 2019; Gao et al., 2020). In previous studies, the Ni-anchored RP SACs have been proven to be very efficient photocatalysts for water splitting, with a greatly improved catalytic activity than the pristine RP. (Wang et al., 2022; Jia et al., 2023). However, the detailed photocatalytic reaction mechanisms of Ni-RP SACs and the potential of other 3d TMs SACs still lack sufficient studies.

In this work, we have conducted comprehensive calculations of the electronic structures of commonly used TMs-based SACs (TM = Fe, Co, Ni, and Cu) on RP support (denote as TMs-RP) to predict their performances of photocatalytic H_2 generation. Based on the band structures and work functions, the thermodynamic driving force for hydrogen and oxygen evolution reaction (HER and OER) of each TMs-RP SACs is obtained and the pH tuning is also realized based on the Nernst equations. Besides, the kinetics for water adsorption and activation, the energy barrier for H adsorption, and the activation barrier of H_2 evolution are demonstrated in detail. This work will offer an atomic scale insight into the reaction mechanisms of TMs-RP SACs based photocatalytic H_2 evolution. Meanwhile, the detailed theoretical explorations also serve as fundamental theoretical references for the rational design of TMs-based SACs with enhanced photocatalytic performances in the future.

2 Calculation setup

In this work, we have conducted density functional theory (DFT) calculations within the CASTEP module. (Clark et al., 2005). The geometry optimizations and single-point energy calculations for all models have been conducted based on the GGA-PBE (Perdew et al., 1992; Perdew et al., 1996; Hasnip and Pickard, 2006) functional, ultrasoft pseudopotentials, and the BFGS algorithm. To guarantee the electronic minimization and convergence requirement, we have adopted the ensemble DFT method of Marzari et al. for the solution of the Kohn-Sham equation. (Marzari et al., 1997). The cutoff energy has been applied with the ultrafine quality, which is set as 380 eV for RP and Fe-RP, Co-RP, Ni-RP, and 440 eV for Cu-RP. The k-point set is 2 × 2×1 for all the energy minimizations. The convergence parameters are set up as follows: the SCF tolerance is 5.0×10^{-7} eV/atom; the Max. Hellmann-Feynman force per atom is 0.01 eV/Å; the Max. stress is 0.02 GPa; and the Max. displacement is 5.0×10^{-4} Å. According to previous experimental studies, the [001]-oriented Hittorf's phosphorus has been proven to be very efficient for water-splitting. (Zhu et al., 2020a). Thus, in this work, we choose the RP (001) surface to act as the supporting host to stabilize the single-atom (SA) TMs. The RP (001) facet is built from relaxed bulk Hittorf's phosphorus, (Thurn and Krebs, 1966), with a thickness of two layers including 84 atoms (Supplementary Figure S1A). The top view of pristine RP (001) and TMs-RP (Fe, Co, Ni, and Cu) catalysts are demonstrated in Supplementary Figures S1B–F. The lattice parameter is 9.27 Å and 9.21 Å for length A and B-orientations, respectively. The vacuum thickness is set to be 20 Å, resulting in a length of 40.95 Å in C-orientation to ensure sufficient space for geometry optimizations. During the adsorption of H_2O and H on different TMs-RP in this work, the SAC surfaces have been constrained in order to highlight the behaviors of key adsorbates. The H-adsorption free energy (ΔG_{H^*}) serves as a key descriptor for the prediction of HER activity, which can be calculated based on the following equation (Nørskov et al., 2005; Kerketta et al., 2022):

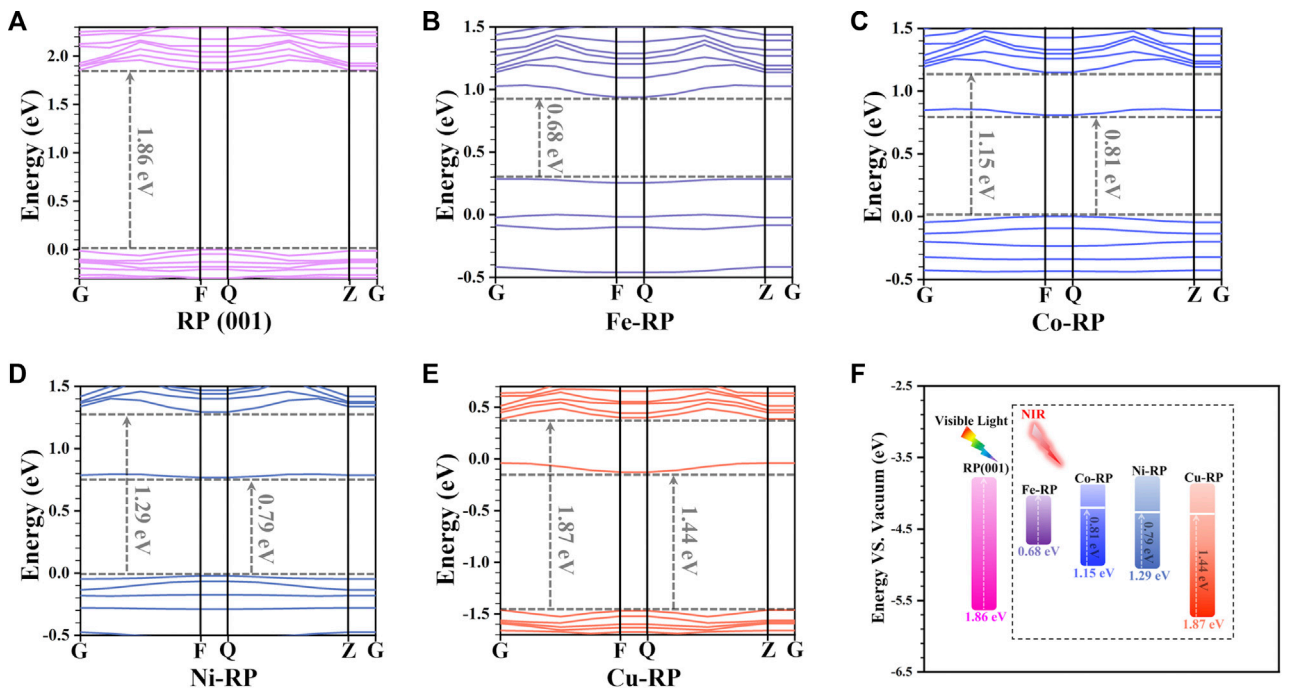

FIGURE 1
Band structures of **(A)** RP (001), **(B)** Fe-RP, **(C)** Co-RP, **(D)** Ni-RP, and **(E)** Cu-RP, respectively. **(F)** Summarized bandgap positions and values for pristine-RP (001) as well as Fe-, Co-, Ni-, and Cu-anchored RP.

$$\Delta E_H = E_{H^*} - E^* - 1/2E(H_2) \quad (1)$$

In this equation, * indicates the un-adsorbed pure surface, and H* stands for the surface adsorbed with H.

3 Results and discussions

3.1 Electronic structures of TMs-RP

For photocatalytic reactions, the excitation energy required for electron-hole separation is largely decided by the bandgap value of the semiconductor photocatalyst. To make the most use of solar energy, the bandgap of the photocatalysts is expected to be located within the spectrum of sunlight, namely, from the UV to NIR range. In fact, most of the solar energy (nearly 95%) is constituted by visible light (43%) and NIR (52%). To match the Vis-NIR excitation window of sunlight, the bandgap of the candidate photocatalyst is expected to be less than 3.10 eV. And based on the redox potential of water, to drive the water splitting reaction, the bandgap value is projected to be wider than 1.23 eV with the location of VBM lower than the oxidation level of O_2/H_2O and CBM higher than the reduction level of H_2/H^+. Thus, the bandgap values and band positions of photocatalysts can largely reflect their absorption window toward sunlight, and the relative positions of VBM and CBM with reference to standard hydrogen electrode potential can be used to predict the redox tendency for water splitting.

To evaluate the bandgap matching degree of the TMs-RP, we have first compared the band structure of pristine RP (Figure 1A) with Fe-, Co-, Ni-, Cu-anchored RP, respectively (Figures 1B–E) to reveal the anchoring effect from different TM atoms. For the pristine RP (001) surface, the bandgap is calculated to be 1.86 eV,

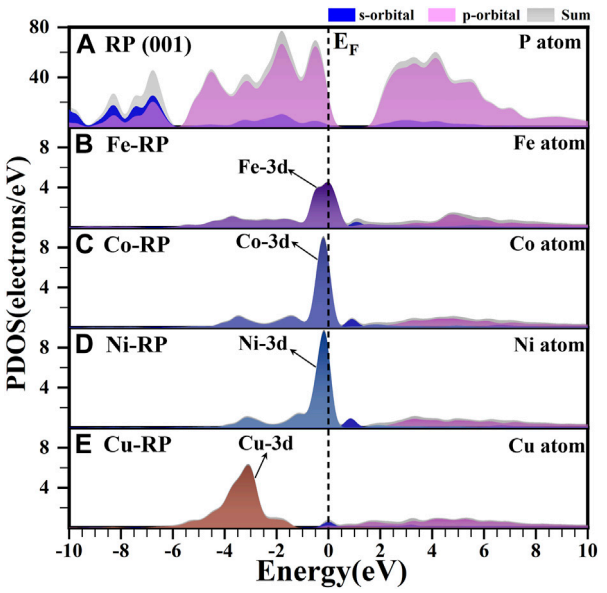

FIGURE 2
The calculated PDOS results of **(A)** P atom in RP (001), **(B)** Fe atom in Fe-RP **(C)** Co atom in Co-RP, **(D)** Ni atom in Ni-RP, and **(E)** Cu atom in Cu-RP respectively. The dashed line means the Fermi level.

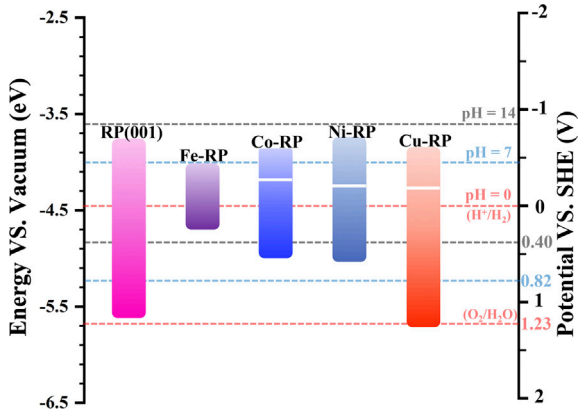

FIGURE 3
Band structure alignments in the scale of Vacuum (left) and SHE (right) for pristine-RP (001), Fe-RP, Co-RP, Ni-RP, and Cu-RP, with reference to the redox pairs of H^+/H_2 and O_2/H_2O. Red dashed lines indicate pH = 0, blue dashed lines represent pH = 7, and black dashed lines stand for pH = 14.

corresponding to an excitation energy of 667 nm in the red-light range. For Fe-, Co-, and Ni-anchored RP, we find additional TM states generated upper to the valence band maximum (VBM) and below the conduction band minimum (CBM), resulting in a narrowed bandgap of 0.68 eV, 1.15 eV, and 1.29 eV, respectively. Notably, the bandgap of Cu-RP is not affected by Cu single atoms, which still remains 1.87 eV. In particular, owing to the states appeared below CBM in Co-RP (0.81 eV) and Ni-RP (0.79 eV), the excitation energy required for the generation of photon-induced charge carriers has largely shifted to the NIR range (1531 nm–1824 nm), as indicated in Figure 1F. For Cu-RP, there is an obvious downshifting of both VB and CB, which shows only one mid-gap state with a distance of 1.44 eV from the VBM, which reduces the absorption energy to a lower NIR window (861 nm).

Besides band structures, the calculated partial density of states (PDOS) is another important indicator of electronic structures. In Figure 2, we focus on the analysis of the d-orbital property of each TM since the d-band center is also strongly related to the photocatalytic activity and the electron transfer efficiency. (Zhou et al., 2022). The pristine RP shows an evident bandgap between CBM and VBM, which are both dominated by the P-3p orbitals (Figure 2A). For Fe-, Co-, and Ni-anchored RP, the localized d orbitals locate very close to the Fermi level (E_F) and VBM (Figures 2B–D). Especially, Co-RP and Ni-RP both display very sharp 3d orbitals with higher electron density near E_F, exhibiting better performance for electron transmission. In contrast, the 3d orbitals of Cu-RP have significantly moved to a lower position of VB, which is far from the E_F (Figure 2E). This results in a wider gap for the transition of photo-induced charge carriers during photocatalysis. The band edge is mainly contributed by the p-orbitals of P with overlapping of 3d orbitals of TMs, which induces the p-d coupling effect to further facilitate charge-carrier transfer. For all four TMs-RP catalysts, we notice the contribution of s-orbital to the CBM, which serve as a ladder to lower the excitation energy for electron excitation from VB to CB. For Cu-RP, the s-orbital dominates the E_F, which only limitedly compensates for low electron transfer density near the VBM. Overall, the PDOS results have revealed that the single-atom TM anchored in RP, especially Co- and Ni-, brings great improvements in both separations and transportations of photo-generated charge carriers during photocatalysis.

3.2 Band structure alignment analysis

The electron-transition capacity of valence electrons is decided by the energy gap between E_F and vacuum level. (Zhou et al., 2022). Thus, the work function has been treated as a key descriptor for electron transition and charge flow in heterojunction structure, and it can be obtained from the calculated electrostatic potential. (Qin et al., 2020; Ruan et al., 2022). As discussed above, besides the bandgap values, the relative position of the bandgap with a reference to standard hydrogen electrode potential is also critical to predict photocatalytic activity. For the construction of the band alignment diagram (Figure 3), the electrostatic potential for each TM-RP type studied in this work has been calculated to indicate the distance between the Fermi level and vacuum level (Supplementary Figures 2A–E). The thermodynamic driving force for photocatalysis is mainly affected by the relative potential position of CBM and VBM of the semiconductor as well as the redox potential of the corresponding reversible reaction. (Li et al., 2016). More negative CBM means stronger reduction reaction tendency, while more positive VBM potential signifies stronger oxidation reaction driving force. Therefore, besides a bandgap value of more than 1.23 eV, the band edges (both VBM and CBM) of the photocatalyst candidates need to cover both the standard potentials of OER and HER to guarantee the high performances of water-splitting. (Mortazavi et al., 2021).

In the acidic condition (pH = 0 in aqueous solution), the CBM of pristine RP and TM-anchored RP are all located above the reduction level of H_2/H^+, exhibiting a high hydrogen evolution tendency (Supplementary Figure S3). However, based on the energy gap between CBM and H_2/H^+ level, the TMs-RP all exhibit a relatively weaker hydrogen evolution tendency than the pristine RP surface except Ni-RP. According to the large gap value from Ni-RP CBM to the H_2/H^+ level, we propose that the anchoring Ni atom offers a stronger driving force for the hydrogen evolution reaction. Meanwhile, the VBM positions of pristine RP and TM-RP (except Cu-RP) are located above O_2/H_2O level, theoretically indicating the weak capability for oxygen evolution. Previous works have revealed the slight mismatching of bandgaps and work functions between theoretical calculations and experimental data. (Wang et al., 2009; Wang et al., 2012a). By considering the calculated SHE as a reference, the pristine RP and Cu-RP are also able to achieve oxygen evolution in the acidic condition.

Since standard redox potentials of H_2O are sensitive to pH variation, the photocatalytic driving force for HER and OER can be well tuned by the pH manipulation based on the following Nernst equations: (Shojaei et al., 2020; Mortazavi et al., 2021):

$$E^{HER}(H^+/H_2) = -4.44\,eV + pH \times 0.059\,eV \quad (2)$$

$$E^{OER}(O_2/H_2O) = -5.67\,eV + pH \times 0.059\,eV \quad (3)$$

The pH variation also impacts the band positions, which has been verified in experiments that the slope of E_{CB} (−0.033 eV/pH) does not follow the Nernstian dependence on pH (−0.059 eV/pH). (Simon et al., 2014). The slope of Nernstian dependence on pH for H_2O redox potentials is steeper. However, in this work, the pH value influences on the corresponding band positions are not included. In our work, the model is built in a vacuum environment with the mainly related elements (H_2O, H, or OH) adsorbed on the catalytic surface in HER. The corresponding band positions are stationary with redox potentials of H_2O in different pH values to reveal the reaction tendency for HER and OER. (Zhang et al., 2021; Yang et al., 2018; Makaremi et al., 2018; da Silva et al., 2019; Shahid et al., 2020). In the neutral condition (pH = 7), the H_2/H^+ level and O_2/H_2O level move up to a more negative position (with reference to SHE) at −0.41 eV and 0.82 eV, respectively (Supplementary Figure S4). Accordingly, for the pristine RP and TMs-RP photocatalysts, the driving force for HER declines while the tendency for OER increases. RP and Cu-RP still cover both potential levels of HER and OER, indicating their photocatalytic activity towards the full water splitting under neutral conditions. In addition, in the highly alkaline environment (pH = 14), pristine RP and TMs-RP nearly lose their HER capability in terms of thermodynamics (Supplementary Figure S5). Thus, we can predict that in the design of photocatalytic heterojunction, Ni-RP is a possible candidate to serve as an efficient HER photocatalyst in wide pH environments.

3.3 Water adsorption comparison

Besides thermodynamic driving force, many other factors such as microstructures at the micro or nanoscale, adsorption energy, surface/interface morphological properties, and coupling effects with cocatalyst components also have significant influence on photocatalytic performance. (Li et al., 2015). For a better explanation of the reaction mechanism and the prediction of the catalytic activity of a potential photocatalyst, the adsorption of reactants and the reaction energy should also be included. The complex charge-carrier dynamics as well as surface-reaction interactions should be fully investigated since they can largely affect the apparent quantum efficiency in multi-stage heterogeneous photocatalytic reactions. (Li et al., 2016).

The H_2O adsorption energy has a great influence on interfacial charge transfer, and decides the aggregation extent of H_2O molecules near the catalytic active sites, which further triggers the concentration effect and results in more H* generated from water splitting. (Wang F. et al., 2020). The adsorption strength of H_2O molecules is greatly affected by the structural stability of single atoms anchored catalytic surface. In particular, the interactions between the anchored SA-TMs and supporting P atoms have been investigated regarding the iso-surface of charge density difference (Supplementary Figure S6) and the Mulliken charge (Supplementary Table S1). The RP stabilized SA-atoms have an obvious electron exchange with coordinated P atoms. Notably, we discover that the Fe atoms (0.27 e) have a stronger interaction with surrounding P atoms than those of Co-RP (0.24 e) and Ni-RP (0.18 e) counterparts. The stable anchoring site on the RP surface of SA-Cu is different from the other three TMs-RP, which is not in the center of the hexatomic ring formed by P atoms. SA-Cu shows a relatively larger average net charge loss of 0.30 e. The electron flow between the stabilized SA-TM atoms and supporting atoms indicates the modification of electronic structures on the RP surface, which verifies the feasibility of doping TMs for photocatalytic activity modulation.

From the charge density difference diagram in Figures 4A–E, H_2O molecules have a much stronger interaction with TMs-RP when compared to pristine RP surfaces. We can see the electron loss in active metals SA sites and adsorbed O atoms (from adsorbed H_2O). Then, the electrons aggregate between TM and H_2O with the formation of an obvious adsorption bond. According to the calculated H_2O adsorption energy values in Figure 4F, H_2O adsorption processes in pristine-RP and TMs-RP are all exothermic, indicating spontaneous adsorption trends. By the loading of TMs SA atoms on the RP surface, the water adsorption capacity has been improved remarkably. Among the four TM-based SACs, Fe-RP (−0.61 eV), Co-RP (−0.67 eV), and Ni-RP (−0.60 eV) exhibit better H_2O affinity than Cu-RP (−0.45 eV). If the H_2O adsorption is too strong, the over-adsorption induces poison effects on the catalytic surface. (Sravan Kumar et al., 2020). Overall, the adsorption energies of Fe-, Co-, Ni-, and Cu-RP are not too negative, indicating less possibility for catalyst poisoning effect during the photocatalysis.

3.4 Reaction energy change of H_2 generation

Besides the water adsorption comparisons, H adsorption is another determinant factor in HER, where both too negative and too positive values are not beneficial for the HER. Based on the adsorption sites, the calculations for H-adsorption reaction energy change are classified into two different types (Figure 5). One considers that H atoms are adsorbed on the SA-metal atoms (Figure 5A), and the other one demonstrates the adsorption of H atoms on the coordinated P atoms to the SA-metal atom (Figure 5B). To guarantee satisfactory computational accuracy, consistent calculation parameters have been set for all the models. For the situations that H atoms adsorbed on SA-metal atoms (H-TMs), the 4 TM SA (Fe-, Co-, Ni-, and Cu-) anchored RP catalysts all have much smaller energy barriers (0.06 eV, −0.25 eV, 0.30 eV, and −0.29 eV, respectively) than that of pristine RP (1.49 eV). As for H adsorbed on coordinated P atoms (H-P-TMs), it can be discovered that the energy barriers of H-P-TMs are slightly larger than those in H-TMs, 0.33 eV (Fe-RP), 0.35 eV (Co-RP), 0.89 eV (Ni-RP), 0.67 eV (Cu-RP, P_1 site), 0.89 eV (Cu-RP, P_2 site), and 1.27 eV (Cu-RP, P_3 site) respectively, but their calculated ΔE_H values are still much less than that of pristine-RP. To sum up, under an acidic environment, the H* is mainly from H^+ in the solution, where the adsorption energy of H* on the catalyst surface is the main influence factor for HER. Based on the calculated ΔE_H, in both situations, H adsorbed on TM atoms (Fe-RP < Co-RP < Cu-RP < Ni-RP < RP) or on coordinated P atoms (Fe-RP < Co-RP < H-P_1-Cu < Ni-RP = H-P_2-Cu < H-P_3-Cu < RP), SA TMs-RP have much lower energy barriers than pristine-RP for HER. It is worth noting that in the acidic condition, Fe-RP exhibits the lowest energy HER barrier in both H-adsorption sites discussed above.

For the photocatalytic mechanism in neutral and alkaline environments, H* is mainly from water dissociation. The energy

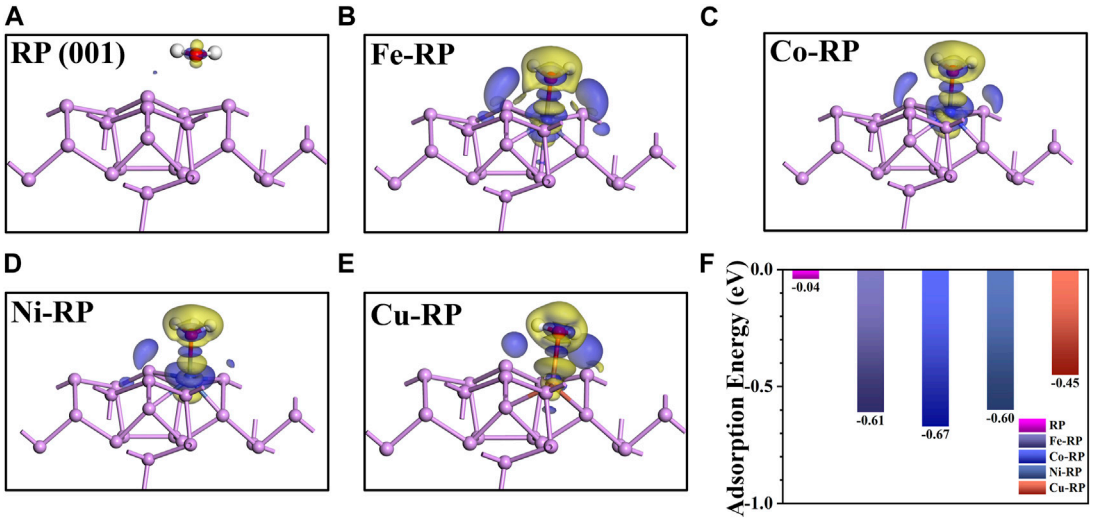

FIGURE 4
The charge density difference for the net flow of charge between active P/TM atom and O atom in H_2O for **(A)** RP (001), **(B)** Fe-RP, **(C)** Co-RP, **(D)** Ni-RP and **(E)** Cu-RP. The blue color and red color mean the gain and loss of electrons, respectively. **(F)** The comparison of water adsorption energy.

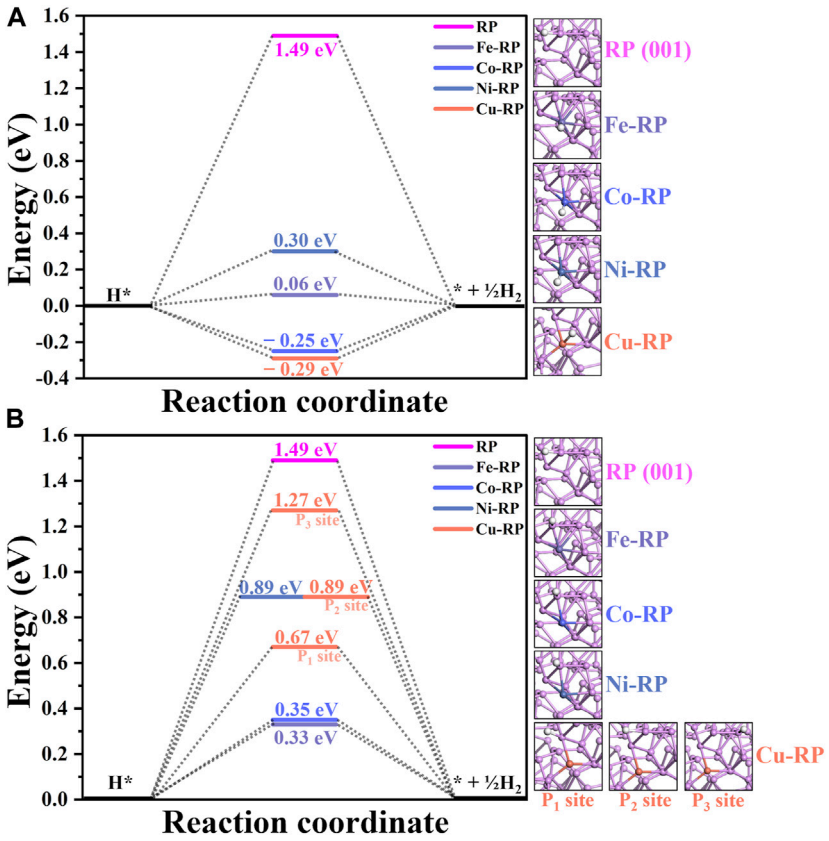

FIGURE 5
The activation barrier for H adsorption on RP (001) and single atom TM anchored RP surface: **(A)** H adsorbed on transition metal atoms. **(B)** H adsorbed on coordinated P atoms.

10.3389/fchem.2023.1197010

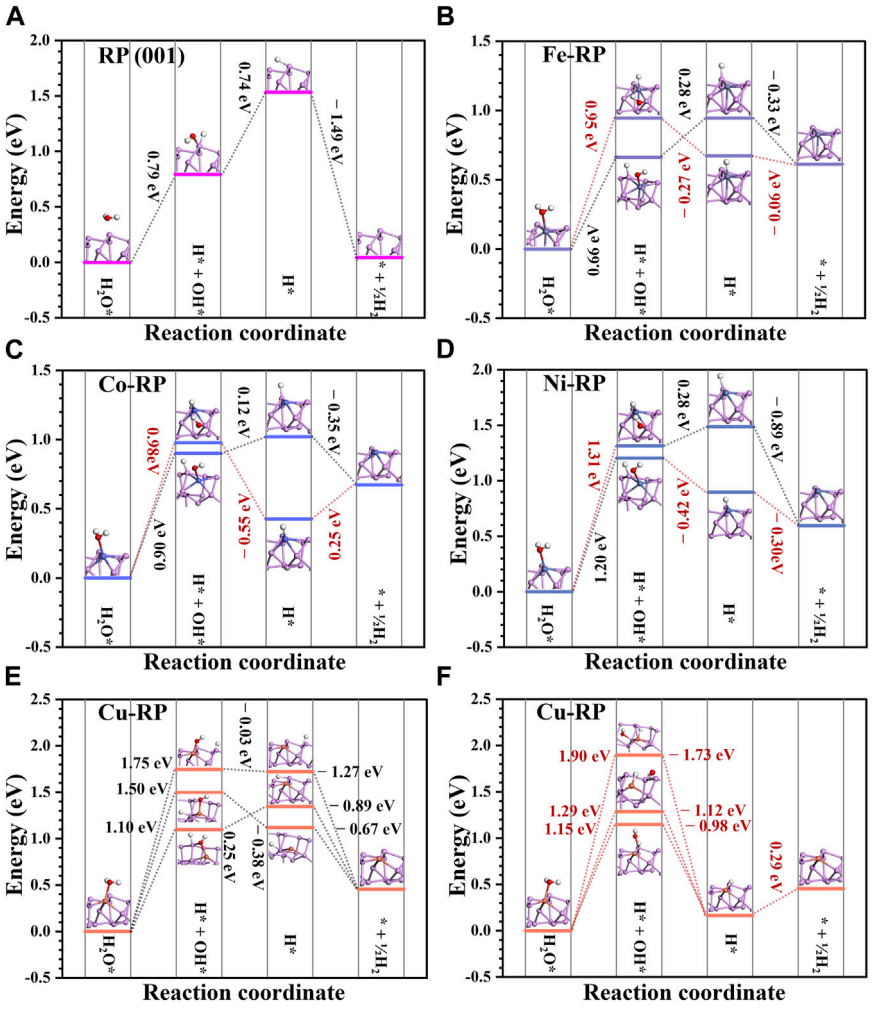

FIGURE 6
The reaction energy change of hydrogen generation on **(A)** RP (001), **(B)** Fe-RP, **(C)** Co-RP, **(D)** Ni-RP, and **(E–F)** Cu-RP surface. The black dashed lines labeled reaction paths indicate the OH adsorbed on TM atoms and H adsorbed on neighboring P atoms while the red dashed lines labeled paths demonstrate OH adsorbed on coordinated P atoms and H adsorbed on TM atoms during the water dissociation process.

barrier for the dissociation of H_2O molecules and the desorption of OH^- are important influence factors in reaction energy changes. As shown in Figures 6A–F, the energy change for the whole reaction towards H_2 generation is compared. For all the catalysts, the water dissociation step requires the largest energy costs as the rate-determining step. We have considered two different situations for water dissociation to compare the reaction energy barriers. For the adsorption of OH and H on TM atoms and neighboring P atoms, respectively, the Co-RP and Ni-RP show an energy barrier of 0.90 eV and 1.20 eV, respectively. Different from other TMs-RP types, the anchored single-atom Cu is not symmetrically located in the hexatomic ring of supporting P atoms, which leads to three possible P sites for water dissociations with a water dissociation energy of 1.50 eV, 1.10 eV, and 1.75 eV, respectively (Figure 6E). For water dissociation, Co-RP, Ni-RP, and Cu-RP exhibit higher energy barriers than that of pristine RP (0.79 eV). Notably, Fe-RP shows the smallest energy barrier (0.66 eV) during water dissociation process among all the candidate catalysts. After H_2O dissociation, if the OH is adsorbed on coordinated P atoms and H is adsorbed on TM atoms, the activation energy barriers needed are relatively higher than the former path discussed above, indicating a lower HER efficiency. While the following desorption of OH^- becomes much easier on the TMs-RP surface, which requires much lower energy barriers (<0.28 eV) or even becomes spontaneous. In comparison, the pristine RP exhibits a much higher energy cost for the OH^- desorption, which leads to the poisoning effect of active sites and lowers the overall photocatalysis performances. Moreover, only Cu-RP and Co-RP (H adsorbed on Co atoms) show endothermic trends for the direct H_2 formation step while other TMs-RP all show the exothermic trend.

For TMs-RP, the energy barriers for OH* desorption are relatively small. In neutral and alkaline environments, since the H* is mainly from the dissociation products (H* and OH*) of adsorbed H_2O* molecules, the water adsorption energy and dissociation energy are the two main influencing factors for HER. The water adsorption energy follows the order of Co-RP < Fe-RP < Ni-RP < Cu-RP < RP, while the water dissociation energy, which is the largest energy barrier, follows the order of Fe-RP < RP < Co-

RP < Cu-RP < Ni-RP. Less H_2O molecules tend to be gathered around the active catalytic sites on pristine RP surface because its adsorption energy is only −0.04 eV. Thus, although pristine-RP has a relatively small energy barrier for water dissociation, its HER activity will be limited due to the inadequate gathering of reactant H_2O molecules on the catalytic surface. The adsorption energies of water molecules on Fe-RP, Co-RP, and Ni-RP are much lower than that of pristine-RP and Cu-RP, leading to more efficient accumulation of H_2O molecules on these three catalyst surfaces, which will benefit the following water dissociation process. Further taking the order of water dissociation energy into consideration, the activation barriers of Ni-RP and Cu-RP are relatively larger. Overall, in neutral and alkaline conditions, the Fe-RP and Co-RP can potentially offer superior HER performance.

Combining the band alignment and reaction energy, we have proposed photocatalyst candidates for different environments. For the acidic solution, Fe-RP, Co-RP, and Cu-RP are the most promising candidates. For the neutral environments, Fe-RP delivers better performances than other TMs-RP, indicating novel selections to achieve even superior performances than the reported Ni-RP catalysts. (Wang et al., 2022; Jia et al., 2023). In a weak alkaline environment, only Ni-RP is possible to satisfy the requirement of band alignments. As we further consider the electronic structure analysis, the much larger bandgap of RP and Cu-RP significantly lowers the charge separation and transfer process after light excitation, which largely affects their photocatalysis performances. Therefore, we propose that Fe-RP and Co-RP are promising candidates for photocatalysis of H_2 generation.

4 Conclusion

In this work, we have conducted comprehensive investigations on photocatalytic activity regarding the electronic properties, adsorption properties, and reaction energy change for four kinds of SACs by anchoring TM (Fe, Co, Ni, and Cu) single atoms on RP. With the introduction of the single-atom TM anchored on the surface, the sunlight absorption window is extended from red light to a higher NIR region, which potentially improves the utilization rate of solar energy. The electronic structures indicate that Co-RP and Ni-RP show highly catalytic active 3d orbitals to benefit the electron transfer during photocatalysis. Considering the band alignments of photocatalysts, Ni-RP indicates its superiority in supporting HER capability over a wide pH range. Under the acidic environment, Cu-RP, Fe-RP, and Co-RP demonstrate the most preferred proton binding to promote H_2 generation. For the neutral and alkaline solution, all TMs-RP catalysts exhibit much stronger H_2O adsorption than pristine RP, which promotes the following dissociation to supply sufficient proton. In particular, Fe-RP and Co-RP has shown the lowest energy barriers for H_2 generation. Overall, we notice that there is no TMs-RP that has superiority in all pH environments, where different TMs have their specific merits. Based on the comprehensive investigations of different parameters, we think that the TMs-RP possesses great potential and flexibility to achieve efficient H_2 generation in different environments. This work has supplied important theoretical references and opened great opportunities for experimental researchers to further optimize the photocatalytic activity in advanced and novel SACs.

Data availability statement

The original contributions presented in the study are included in the article/Supplementary Material, further inquiries can be directed to the corresponding author.

Author contributions

BH conceived this project and supervised this study. LL and BH carried out the model building and data analysis. MS, TW, QL, BC, CHC, and HHW contributed to the data analysis. LL wrote the first draft of the manuscript. MS, TW, QL, BC, CHC, HHW, and BH contributed to the revision of the article. All the authors approved the submitted version.

Funding

The authors gratefully acknowledge the support from the National Key R&D Program of China (2021YFA1501101), the National Natural Science Foundation of China/Research Grant Council of Hong Kong Joint Research Scheme (N_PolyU502/21), National Natural Science Foundation of China/Research Grants Council (RGC) of Hong Kong Collaborative Research Scheme (CRS_PolyU504_22), the funding for Projects of Strategic Importance of The Hong Kong Polytechnic University (Project Code: 1-ZE2V), Shenzhen Fundamental Research Scheme-General Program (JCYJ20220531090807017), the Natural Science Foundation of Guangdong Province (2023A1515012219), and Departmental General Research Fund (Project Code: ZVUL) from The Hong Kong Polytechnic University.

Acknowledgments

The authors also thank the support from Research Centre for Carbon-Strategic Catalysis (RC-CSC), Research Institute for Smart Energy (RISE), and Research Institute for Intelligent Wearable Systems (RI-IWEAR) of the Hong Kong Polytechnic University.

Conflict of interest

The authors declare that the research was conducted in the absence of any commercial or financial relationships that could be construed as a potential conflict of interest.

Publisher's note

Supplementary material

The Supplementary Material for this article can be found online at: https://www.frontiersin.org/articles/10.3389/fchem.2023.1197010/full#supplementary-material

References

Bie, C., Wang, L., and Yu, J. (2022). Challenges for photocatalytic overall water splitting. *Chem* 8 (6), 1567–1574. doi:10.1016/j.chempr.2022.04.013

Chen, F., Sun, S., Mu, K., Li, Y., Shen, Z., and Zhan, S. (2022). *In-situ*-formed red phosphorus nanosheet on bulk red phosphorus for boosting charge separation in photocatalysis: The role of multiple interfacial effects. *Appl. Catal. B Environ.* 312, 121373. doi:10.1016/j.apcatb.2022.121373

Chen, Y., Feng, X., Liu, Y., Guan, X., Burda, C., and Guo, L. (2020). Metal oxide-based tandem cells for self-biased photoelectrochemical water splitting. *ACS Energy Lett.* 5 (3), 844–866. doi:10.1021/acsenergylett.9b02620

Clark, S. J., Segall, M. D., Pickard, C. J., Hasnip, P. J., Probert, M. I. J., Refson, K., et al. (2005). First principles methods using CASTEP. *Z. für Kristallogr. - Cryst. Mater.* 220 (5-6), 567–570. doi:10.1524/zkri.220.5.567.65075

da Silva, R., Barbosa, R., Mançano, R. R., Durães, N., Pontes, R. B., Miwa, R. H., et al. (2019). Metal chalcogenides janus monolayers for efficient hydrogen generation by photocatalytic water splitting. *ACS Appl. Nano Mater.* 2 (2), 890–897. doi:10.1021/acsanm.8b02135

Fung, C-M., Er, C-C., Tan, L-L., Mohamed, A. R., and Chai, S-P. (2022). Red phosphorus: An up-and-coming photocatalyst on the horizon for sustainable energy development and environmental remediation. *Chem. Rev.* 122 (3), 3879–3965. doi:10.1021/acs.chemrev.1c00068

Gao, C., Low, J., Long, R., Kong, T., Zhu, J., and Xiong, Y. (2020). Heterogeneous single-atom photocatalysts: Fundamentals and applications. *Chem. Rev.* 120 (21), 12175–12216. doi:10.1021/acs.chemrev.9b00840

Hasnip, P. J., and Pickard, C. J. (2006). Electronic energy minimisation with ultrasoft pseudopotentials. *Comput. Phys. Commun.* 174 (1), 24–29. doi:10.1016/j.cpc.2005.07.011

Hu, Z., Shen, Z., and Yu, J. C. (2017). Phosphorus containing materials for photocatalytic hydrogen evolution. *Green Chem.* 19 (3), 588–613. doi:10.1039/c6gc02825j

Huang, G., Ye, W., Lv, C., Butenko, D. S., Yang, C., Zhang, G., et al. (2022). Hierarchical red phosphorus incorporated TiO_2 hollow sphere heterojunctions toward superior photocatalytic hydrogen production. *J. Mater. Sci. Technol.* 108, 18–25. doi:10.1016/j.jmst.2021.09.026

Jia, G., Sun, M., Wang, Y., Cui, X., Huang, B., and Yu, J. C. (2023). Enabling efficient photocatalytic hydrogen evolution via *in situ* loading of Ni single atomic sites on red phosphorus quantum dots. *Adv. Funct. Mater.* 33 (10), 2212051. doi:10.1002/adfm.202212051

Kerketta, U., Tesler, A. B., and Schmuki, P. (2022). Single-atom Co-catalysts employed in titanium dioxide photocatalysis. *Catalysts* 12 (10), 1223. doi:10.3390/catal12101223

Khandelwal, A., Maarisetty, D., and Baral, S. S. (2022). Fundamentals and application of single-atom photocatalyst in sustainable energy and environmental applications. *Renew. Sustain. Energy Rev.* 167, 112693. doi:10.1016/j.rser.2022.112693

Li, J., Liu, X., Tan, L., Liang, Y., Cui, Z., Yang, X., et al. (2019). Light-activated rapid disinfection by accelerated charge transfer in red phosphorus/ZnO heterointerface. *Small Methods* 3 (3), 1900048. doi:10.1002/smtd.201900048

Li, X., Yu, J., and Jaroniec, M. (2016). Hierarchical photocatalysts. *Chem. Soc. Rev.* 45 (9), 2603–2636. doi:10.1039/c5cs00838g

Li, X., Yu, J., Low, J., Fang, Y., Xiao, J., and Chen, X. (2015). Engineering heterogeneous semiconductors for solar water splitting. *J. Mater. Chem. A* 3 (6), 2485–2534. doi:10.1039/c4ta04461d

Liu, F., Shi, R., Wang, Z., Weng, Y., Che, C-M., and Chen, Y. (2019). Direct Z-scheme hetero-phase junction of black/red phosphorus for photocatalytic water splitting. *Angew. Chem. Int. Ed.* 58 (34), 11917–11921. doi:10.1002/ange.201906416

Liu, L., and Corma, A. (2018). Metal catalysts for heterogeneous Catalysis: From single atoms to nanoclusters and nanoparticles. *Chem. Rev.* 118 (10), 4981–5079. doi:10.1021/acs.chemrev.7b00776

Makaremi, M., Grixti, S., Butler, K. T., Ozin, G. A., and Singh, C. V. (2018). Band engineering of carbon nitride monolayers by N-type, P-type, and isoelectronic doping for photocatalytic applications. *ACS Appl. Mater. Interfaces* 10 (13), 11143–11151. doi:10.1021/acsami.8b01729

Marzari, N., Vanderbilt, D., and Payne, M. C. (1997). Ensemble density-functional theory for ab initio molecular dynamics of metals and finite-temperature insulators. *Phys. Rev. Lett.* 79 (7), 1337–1340. doi:10.1103/physrevlett.79.1337

Mortazavi, B., Javvaji, B., Shojaei, F., Rabczuk, T., Shapeev, A. V., and Zhuang, X. (2021). Exceptional piezoelectricity, high thermal conductivity and stiffness and promising photocatalysis in two-dimensional $MoSi_2N_4$ family confirmed by first-principles. *Nano Energy* 82, 105716. doi:10.1016/j.nanoen.2020.105716

Nørskov, J. K., Bligaard, T., Logadottir, A., Kitchin, J. R., Chen, J. G., Pandelov, S., et al. (2005). Trends in the exchange current for hydrogen evolution. *J. Electrochem. Soc.* 152 (3), J23. doi:10.1149/1.1856988

Pan, S., Li, R., Zhang, Q., Cui, C., Wang, M., Shi, B., et al. (2021). An over 20% solar-to-hydrogen efficiency system comprising a self-reconstructed NiCoFe-based hydroxide nanosheet electrocatalyst and monolithic perovskite/silicon tandem solar cell. *J. Mater. Chem. A* 9 (24), 14085–14092. doi:10.1039/d1ta03126k

Perdew, J. P., Burke, K., and Ernzerhof, M. (1996). Generalized gradient approximation made simple. *Phys. Rev. Lett.* 77 (18), 3865–3868. doi:10.1103/physrevlett.77.3865

Perdew, J. P., Chevary, J. A., Vosko, S. H., Jackson, K. A., Pederson, M. R., Singh, D. J., et al. (1992). Atoms, molecules, solids, and surfaces: Applications of the generalized gradient approximation for exchange and correlation. *Phys. Rev. B* 46 (11), 6671–6687. doi:10.1103/physrevb.46.6671

Qin, Y., Li, H., Lu, J., Feng, Y., Meng, F., Ma, C., et al. (2020). Synergy between van der waals heterojunction and vacancy in $ZnIn_2S_4$/g-C_3N_4 2D/2D photocatalysts for enhanced photocatalytic hydrogen evolution. *Appl. Catal. B Environ.* 277, 119254. doi:10.1016/j.apcatb.2020.119254

Ruan, X., Cui, X., Cui, Y., Fan, X., Li, Z., Xie, T., et al. (2022). Favorable energy band alignment of TiO_2 anatase/rutile heterophase homojunctions yields photocatalytic hydrogen evolution with quantum efficiency exceeding 45.6. *Adv. Energy Mater.* 12 (16), 2200298. doi:10.1002/aenm.202200298

Shahid, I., Ahmad, S., Shehzad, N., Yao, S., Nguyen, C. V., Zhang, L., et al. (2020). Electronic and photocatalytic performance of boron phosphide-blue phosphorene vdW heterostructures. *Appl. Surf. Sci.* 523, 146483. doi:10.1016/j.apsusc.2020.146483

Shen, Z., Hu, Z., Wang, W., Lee, S-F., Chan, D. K. L., Li, Y., et al. (2014). Crystalline phosphorus fibers: Controllable synthesis and visible-light-driven photocatalytic activity. *Nanoscale* 6 (23), 14163–14167. doi:10.1039/c4nr04250f

Shojaei, F., Mortazavi, B., Zhuang, X., and Azizi, M. (2020). Silicon diphosphide (SiP_2) and silicon diarsenide ($SiAs_2$): Novel stable 2D semiconductors with high carrier mobilities, promising for water splitting photocatalysts. *Mater. Today Energy* 16, 100377. doi:10.1016/j.mtener.2019.100377

Simon, T., Bouchonville, N., Berr, M. J., Vaneski, A., Adrović, A., Volbers, D., et al. (2014). Redox shuttle mechanism enhances photocatalytic H_2 generation on Ni-decorated CdS nanorods. *Nat. Mater.* 13 (11), 1013–1018. doi:10.1038/nmat4049

Sravan Kumar, K. B., Whittaker, T. N., Peterson, C., Grabow, L. C., and Chandler, B. D. (2020). Water poisons H_2 activation at the Au-TiO_2 interface by slowing proton and electron transfer between Au and titania. *J. Am. Chem. Soc.* 142 (12), 5760–5772. doi:10.1021/jacs.9b13729

Thurn, H., and Krebs, H. (1966). Die Kristallstruktur des Hittorfschen Phosphors. *Angew. Chem.* 78 (24), 1101–1102. doi:10.1002/ange.19660782408

Wang, B., Cai, H., and Shen, S. (2019b). Single metal atom photocatalysis. *Small Methods* 3 (9), 1800447. doi:10.1002/smtd.201800447

Wang, F., Li, C., Li, Y., and Yu, J. C. (2012b). Hierarchical P/YPO_4 microsphere for photocatalytic hydrogen production from water under visible light irradiation. *Appl. Catal. B Environ.* 119-120, 267–272. doi:10.1016/j.apcatb.2012.03.011

Wang, F., Ng, W. K. H., Yu, J. C., Zhu, H., Li, C., Zhang, L., et al. (2012a). Red phosphorus: An elemental photocatalyst for hydrogen formation from water. *Appl. Catal. B Environ.* 111-112, 409–414. doi:10.1016/j.apcatb.2011.10.028

Wang, F., Xiao, L., Chen, J., Chen, L., Fang, R., and Li, Y. (2020b). Regulating the electronic structure and water adsorption capability by constructing carbon-doped CuO hollow spheres for efficient photocatalytic hydrogen evolution. *ChemSusChem* 13 (21), 5711–5721. doi:10.1002/cssc.202001884

Wang, M., Qin, Z., Diao, Z., Li, R., Zhong, J., Ma, D., et al. (2020a). Red phosphorus/carbon nitride van der Waals heterostructure for photocatalytic pure water splitting under wide-spectrum light irradiation. *ACS Sustain. Chem. Eng.* 8 (35), 13459–13466. doi:10.1021/acssuschemeng.0c04372

Wang, M., Xu, S., Zhou, Z., Dong, C-L., Guo, X., Chen, J-L., et al. (2022). Atomically dispersed janus nickel sites on red phosphorus for photocatalytic overall water splitting. *Angew. Chem. Int. Ed.* 61 (29), e202204711. doi:10.1002/anie.202204711

Wang, S., Liu, G., and Wang, L. (2019a). Crystal facet engineering of photoelectrodes for photoelectrochemical water splitting. *Chem. Rev.* 119 (8), 5192–5247. doi:10.1021/acs.chemrev.8b00584

Wang, X., Maeda, K., Thomas, A., Takanabe, K., Xin, G., Carlsson, J. M., et al. (2009). A metal-free polymeric photocatalyst for hydrogen production from water under visible light. *Nat. Mater.* 8 (1), 76–80. doi:10.1038/nmat2317

Wu, C., Jing, L., Deng, J., Liu, Y., Li, S., Lv, S., et al. (2021). Elemental red phosphorus-based photocatalysts for environmental remediation: A review. *Chemosphere* 274, 129793. doi:10.1016/j.chemosphere.2021.129793

Wu, J., Xiong, L., Zhao, B., Liu, M., and Huang, L. (2020). Densely populated single atom catalysts. *Small Methods* 4 (2), 1900540. doi:10.1002/smtd.201900540

Xia, D., Shen, Z., Huang, G., Wang, W., Yu, J. C., and Wong, P. K. (2015). Red phosphorus: An earth-abundant elemental photocatalyst for "green" bacterial inactivation under visible light. *Environ. Sci. Technol.* 49 (10), 6264–6273. doi:10.1021/acs.est.5b00531

Xue, Z-H., Luan, D., Zhang, H., and Lou, X. W. (2022). Single-atom catalysts for photocatalytic energy conversion. *Joule* 6 (1), 92–133. doi:10.1016/j.joule.2021.12.011

Yang, H., Li, J., Yu, L., Huang, B., Ma, Y., and Dai, Y. (2018). A theoretical study on the electronic properties of in-plane CdS/ZnSe heterostructures: Type-II band alignment for water splitting. *J. Mater. Chem. A* 6 (9), 4161–4166. doi:10.1039/c7ta10624f

Yu, J. C., Zhang, L., Zheng, Z., and Zhao, J. (2003). Synthesis and characterization of phosphated mesoporous titanium dioxide with high photocatalytic activity. *Chem. Mater.* 15 (11), 2280–2286. doi:10.1021/cm0340781

Zhang, W. X., Yin, Y., and He, C. (2021). Spontaneous enhanced visible-light-driven photocatalytic water splitting on novel type-II GaSe/CN and Ga_2SSe/CN vdW heterostructures. *J. Phys. Chem. Lett.* 12 (21), 5064–5075. doi:10.1021/acs.jpclett.1c01023

Zhou, Y., Qin, W., Sun, X., Zhu, Y., and Niu, J. (2022). Synergistic effects on d-band center via coordination sites of M-N_3P_1 (M = Co and Ni) in dual single atoms that enhances photocatalytic dechlorination from tetrachlorobispheonl A. *J. Hazard. Mater.* 430, 128419. doi:10.1016/j.jhazmat.2022.128419

Zhu, Y., Li, J., Dong, C-L., Ren, J., Huang, Y-C., Zhao, D., et al. (2019). Red phosphorus decorated and doped TiO_2 nanofibers for efficient photocatalytic hydrogen evolution from pure water. *Appl. Catal. B Environ.* 255, 117764. doi:10.1016/j.apcatb.2019.117764

Zhu, Y., Lv, C., Yin, Z., Ren, J., Yang, X., Dong, C-L., et al. (2020a). A [001]-Oriented hittorf's phosphorus nanorods/polymeric carbon nitride heterostructure for boosting wide-spectrum-responsive photocatalytic hydrogen evolution from pure water. *Angew. Chem. Int. Ed.* 59 (2), 868–873. doi:10.1002/anie.201911503

Zhu, Y., Ren, J., Zhang, X., and Yang, D. (2020b). Elemental red phosphorus-based materials for photocatalytic water purification and hydrogen production. *Nanoscale* 12 (25), 13297–13310. doi:10.1039/d0nr01748e

frontiers | Frontiers in Chemistry

TYPE Original Research
PUBLISHED 20 June 2023
DOI 10.3389/fchem.2023.1202501

OPEN ACCESS

EDITED BY
Linghui Qian,
Zhejiang University, China

REVIEWED BY
Wesley Wang,
The Scripps Research Institute, United States
Anna Kashina,
University of Pennsylvania, United States

*CORRESPONDENCE
Thomas Arnesen,
thomas.arnesen@uib.no
Bengt Erik Haug,
bengt-erik.haug@uib.no

RECEIVED 08 April 2023
ACCEPTED 08 June 2023
PUBLISHED 20 June 2023

CITATION
Myklebust LM, Baumann M, Støve SI, Foyn H, Arnesen T and Haug BE (2023), Optimized bisubstrate inhibitors for the actin N-terminal acetyltransferase NAA80.
Front. Chem. 11:1202501.
doi: 10.3389/fchem.2023.1202501

Optimized bisubstrate inhibitors for the actin N-terminal acetyltransferase NAA80

Line M. Myklebust[1], Markus Baumann[1,2], Svein I. Støve[1], Håvard Foyn[3], Thomas Arnesen[1,3,4]* and Bengt Erik Haug[2]*

[1]Department of Biomedicine, University of Bergen, Bergen, Norway, [2]Department of Chemistry and Centre for Pharmacy, University of Bergen, Bergen, Norway, [3]Department of Biological Sciences, University of Bergen, Bergen, Norway, [4]Department of Surgery, Haukeland University Hospital, Bergen, Norway

Acetylation of protein N-termini is one of the most common protein modifications in the eukaryotic cell and is catalyzed by the N-terminal acetyltransferase family of enzymes. The N-terminal acetyltransferase NAA80 is expressed in the animal kingdom and was recently found to specifically N-terminally acetylate actin, which is the main component of the microfilament system. This unique animal cell actin processing is essential for the maintenance of cell integrity and motility. Actin is the only known substrate of NAA80, thus potent inhibitors of NAA80 could prove as important tool compounds to study the crucial roles of actin and how NAA80 regulates this by N-terminal acetylation. Herein we describe a systematic study toward optimizing the peptide part of a bisubstrate-based NAA80 inhibitor comprising of coenzyme A conjugated onto the N-terminus of a tetrapeptide amide via an acetyl linker. By testing various combinations of Asp and Glu which are found at the N-termini of β- and γ-actin, respectively, CoA-Ac-EDDI-NH_2 was identified as the best inhibitor with an IC_{50} value of 120 nM.

KEYWORDS

bisubstrate inhibitor, N-terminal acetylation, acetyltransferase, NAA80, actin, cytoskeleton, coenzyme A

1 Introduction

N-terminal (Nt) acetylation is a highly abundant protein modification, occurring on approximately 80% of the human proteome (Arnesen et al., 2009; Aksnes et al., 2015). The process is catalyzed by Nt acetyltransferases (NATs), transferring an acetyl group from Acetyl CoA to the amino group of the first amino acid in the protein sequence. To date seven NATs have been found in human cells, NatA-NatF, and NatH, having distinctive features in terms of subunit composition, subcellular localization and substrate specificity (Aksnes et al., 2019). Some NATs, NatA, NatB and NatC, have broad substrate pools and act co-translationally. Other NATs have a very specific substrate pool, such as NatD co-translationally acetylating histones H2A and H4 (Songkyu et al., 2003; Hole et al., 2011), NatF post-translationally acetylating transmembrane proteins (Van Damme et al., 2011; Aksnes et al., 2015), or NatH/NAA80 post-translationally acetylating actins (Drazic et al., 2018).

The first catalytic mechanism of a human NAT (Evjenth et al., 2012), as well as the first structures of a NAT and NAT-complex bound to its peptide substrate, have been presented (Liszczak et al., 2011; Liszczak et al., 2013; Støve et al., 2016). Taking advantage of this information, we and others have developed peptidic NAT inhibitors that are based on

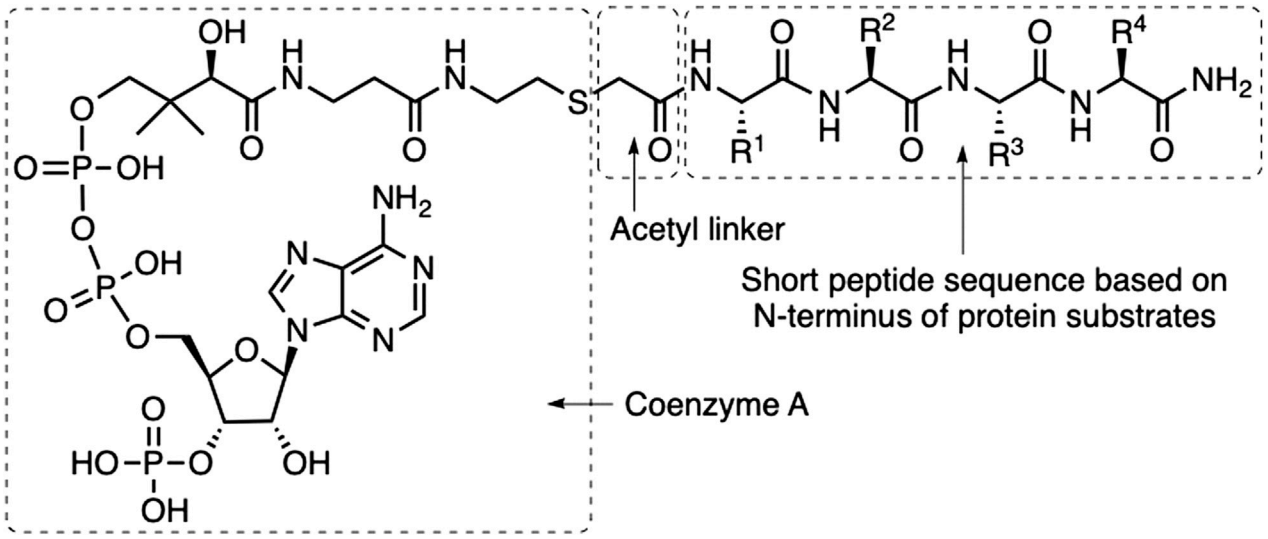

FIGURE 1
Structure of bisubstrate inhibitors. The bisubstrate inhibitors are constructed as conjugates of Coenzyme A coupled via an acetamide linker to a tetrapeptide amide. The amino acids in the peptide sequence were exchanged systematically to identify improved NAA80 inhibition.

covalently linking mimics of the two substrates of the biochemical reaction, i.e., coenzyme A (CoA) and a short peptide carrying an N-terminal bromoacetyl group (Figure 1) giving a thioether-linked acetyl moiety (Foyn et al., 2013; Støve et al., 2016; Goris et al., 2018; Deng et al., 2021). In these studies it has been found that it is sufficient to use the four amino acids from the N-terminus of the protein substrates to obtain potent bisubstrate inhibitors.

Such bisubstrate inhibitors demonstrate specificity and significant inhibitory potential with IC_{50} and K_i in the low μM/nM range. For NatD, increasing the length of the acetyl linker to propionyl has proven beneficial for the design of highly potent inhibitors (Deng et al., 2021). Further, for most NATs, access to bisubstrate inhibitors has led to significant advances in the field by enabling the determination of protein crystal structures (Liszczak et al., 2013; Støve et al., 2016; Hong et al., 2017; Goris et al., 2018; Deng et al., 2020; Deng et al., 2023).

Actin is a major component of the cytoskeleton and cytoskeletal dynamics are important for several cellular activities such as cell motility, division, and intracellular trafficking (Pollard and Cooper, 2009). The cellular activity of actin is connected to its dynamic transition between monomeric (G-actin) and filamentous (F-actin) forms. This is regulated in cells by actin-binding proteins as well as by post-translational modifications. It was established 4 decades ago that animal actins undergo a unique Nt-maturation process (Redman and Rubenstein, 1981; Rubenstein and Martin, 1983). Now we know that this involves the following steps (Arnesen and Aksnes, 2023): a) a general Nt-processing step for all eukaryotic proteins of co-translational N-terminal acetylation (Aksnes et al., 2019) (preceded by methionine excision for muscle actins), b) a unique animal actin-specific post-translational cleavage of the Nt-acetylated residue by ACTMAP (Haahr et al., 2022) and finally c) an animal actin-specific post-translational Nt-acetylation by NAA80/NatH to generate acidic actin Nt-termini (Drazic et al., 2018; Goris et al., 2018; Wiame et al., 2018). NAA80 binding to profilin, specifically PFN2, primes the interaction with actin monomers and the acetylation of actin's N-terminus which sticks out from the folded actin monomer (Rebowski et al., 2020; Ree et al., 2020). In human cells lacking NAA80, actin is not Nt-acetylated (near 0% Nt-acetylation) while in the presence of NAA80, actin is acetylated to a near 100% stoichiometry (Drazic et al., 2018; Drazic et al., 2022). This suggests that actin Nt-acetylation is essential for optimal actin functionality in humans. Indeed, human NAA80-KO cells where actin is unacetylated display fragmentation of the Golgi apparatus, altered cytoskeletal organization including decreased G-actin/F-actin ratio, increased F-actin, increased cell size, increased filopodia and lamellopodia and increased cell migration (Aksnes et al., 2018; Drazic et al., 2018; Beigl et al., 2020). The physiological impact of actin Nt-acetylation is not fully understood due to the lack of NAA80 KO animal models. However, two brothers carrying a homozygous *NAA80* variant resulting in a partial reduction in cellular actin Nt-acetylation were recently presented (Muffels et al., 2021). These individuals showed hearing loss, mild muscle weakness and developmental delay.

Bisubstrate inhibitors of NAT enzymes could potentially be used as tools to study the effects of inhibiting Nt-acetylation to shed more light on the roles of Nt-acetylation in the cell. NAA80 inhibitors could specifically be applied to manipulate cytoskeletal dynamics and to increase cell migration. Herein we describe the optimization of a bisubstrate inhibitor for NAA80.

2 Material and methods

2.1 Synthesis of bisubstrate inhibitors

Bisubstrate inhibitors were synthesised manually or on an Initiator + Alstra (Biotage) automated microwave peptide synthesizer using Fmoc-based solid phase peptide synthesis and ChemMatrix Rink Amide resin (0.44 mmol/g loading) on a 0.25 mmol scale. 2-(6-Chloro-1*H*-benzotriazole-1-yl)-1,1,3,3-tetramethylaminium hexafluorophosphate (HCTU) and

10.3389/fchem.2023.1202501

TABLE 1 Analytical data for bisubstrate inhibitors.

Inhibitors	Purity (%)[a]	MS obs. $[M-2H]^{2-}$	MS calcd. $[M-2H]^{2-}$	MS obs. $[M-H]^{-}$	MS calcd. $[M-H]^{-}$
CoA-Ac-DDEI-NH_2	98.4	647.3	647.2	1,295.4	1,295.3
CoA-Ac-DEEL-NH_2	97.9	654.3	654.2	1,309.3	1,309.3
CoA-Ac-DEEI-NH_2	95.5	654.3	654.2	1,309.4	1,309.3
CoA-Ac-EEEL-NH_2	94.1	661.3	661.2	1,323.4	1,323.3
CoA-Ac-EDEI-NH_2	95.2	654.3	654.2	1,309.3	1,309.3
CoA-Ac-EDEL-NH_2	94.7	654.3	654.2	1,309.4	1,309.3
CoA-Ac-EEDI-NH_2	95.1	654.3	654.2	1,309.4	1,309.3
CoA-Ac-EEDL-NH_2	97.0	654.3	654.2	1,309.4	1,309.3
CoA-Ac-EDDI-NH_2	93.5	647.3	647.2	1,295.3	1,295.3
CoA-Ac-ESEL-NH_2	96.8	640.4	640.2	1,281.6	1,281.3
CoA-Ac-EDQL-NH_2	100	653.8	653.7	1,308.3	1,308.3
CoA-Ac-PDEL-NH_2	97.3	638.3	638.2	1,277.3	1,277.3

[a]Based on RP-HPLC analysis with monitoring at 220 nm

TABLE 2 Inhibitory activity.

Inhibitor	IC_{50} (μM)[a]
CoA-DDDI-NH_2[b]	0.38 ± 0.10
CoA-EEEI-NH_2[b]	1.16 ± 0.11
CoA-MDEL-NH_2[b]	1.26 ± 0.10
CoA-DEEI-NH_2	1.22 ± 0.33
CoA-EDEI-NH_2	0.76 ± 0.18
CoA-EEDI-NH_2	0.17 ± 0.04
CoA-DEEL-NH_2	4.73 ± 1.43
CoA-EDEL-NH_2	0.15 ± 0.02
CoA-EDQL-NH_2	0.85 ± 0.05
CoA-ESEL-NH_2	11.5 ± 3.23
CoA-PDEL-NH_2	13.4 ± 2.24
CoA-EEDL-NH_2	1.76 ± 0.52
CoA-EEEL-NH_2	1.16 ± 0.12
CoA-DDEI-NH_2	2.67 ± 0.67
CoA-EDDI-NH_2	0.12 ± 0.05

[a]All measurements were performed in triplicates. IC_{50} values are given with standard deviation.
[b]Data taken from Goris *et al.* (Goris et al., 2018)

N,*N*-diisopropylethylamine (DIPEA) were used to couple each amino acid (3–5 equivalents) in dimethylformamide (DMF). When the automated microwave peptide synthesizer was used, the coupling process took place with microwave heating at 75 C for 5 min, while manual coupling was performed at room temperature for 30 min. The peptidyl-resin was treated with 20% piperidine in DMF for removal of the Fmoc-protecting group at room temperature for 3 + 10 min. After Fmoc-deprotection of the N-terminal amino acid, the peptidyl-resin was treated with bromoacetic acid (8 eq.) and *N*,*N*′-diisopropylcarbodiimide (DIC) in DMF for 1 h. The resin was then treated with a mixture of trifluoroacetic acid, triisopropylsilane and water (95:2.5:2.5, v/v/v) for 2 h. The suspension was filtered, and the filtrate was concentrated under reduced pressure until ~5 mL of the solution remained. The crude product was precipitated by adding cold diethyl ether and after removal of the ether layer, the precipitate was triturated with fresh diethyl ether twice. The crude bromoacetyl peptide was dried under

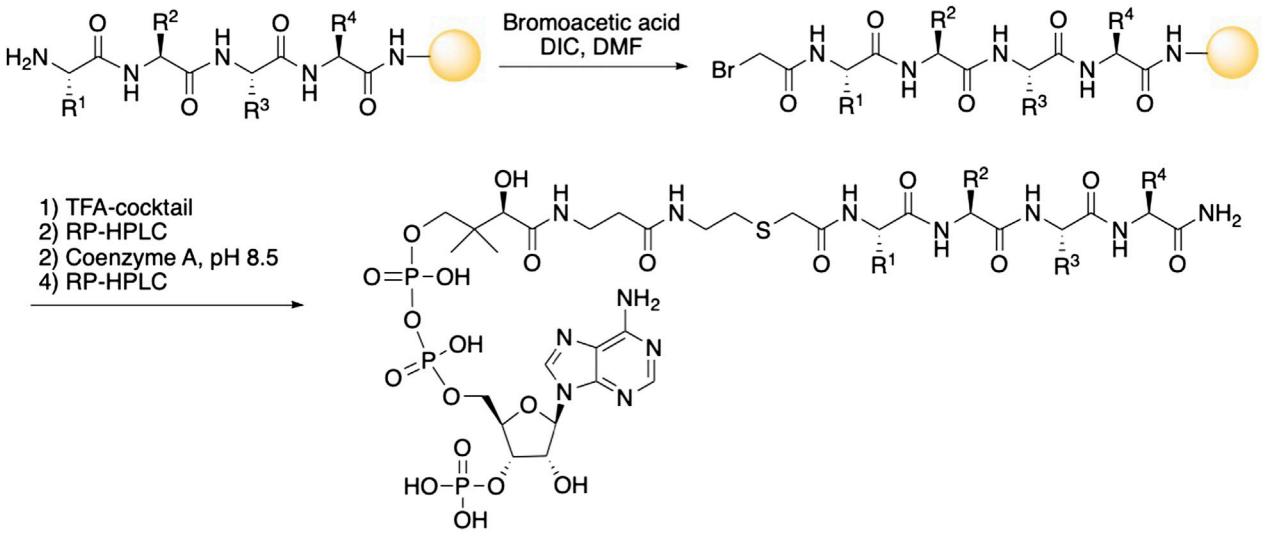

SCHEME 1
Synthesis of bisubstrate inhibitors. The peptide sequence was assembled using solid-phase Fmoc-based peptide synthesis with a bromoacetyl group at the N-terminal. Cleavage from the solid support and conjugation with Coenzyme A followed by purification gave the bisubstrate inhibitors.

vacuum, purified by semi-preparative RP-HPLC and lyophilised. Purified bromoacetyl peptides and coenzyme A trilithium salt (2 eq.) were dissolved in triethylammonium bicarbonate buffer (1 M, pH 8.5) and left at room temperature overnight. Purification by RP-HPLC and lyophilisation gave the desired CoA-Ac peptides as colorless powders.

2.2 Recombinant protein expression and purification of HsNAA80

HsNAA80/nNat6 (NCBI gene ID:24,142) was subcloned as described by Drazic *et al.* (Drazic et al., 2018) into pETM41 vector. HsNAA80 fused to the maltose binding protein (MBP), was expressed in *Escherichia coli* BL21 star cells at 20°C overnight and lysed with sonication in lysis buffer (300 mM NaCl, 50 mM TrisHCl (pH 8.5), 1 mM DTT, 1x EDTA-free protease mixture). The recombinantly expressed MBP-hsNAA80 was further purified as described by Goris *et al.* (Goris et al., 2018)

2.3 *In vitro* acetyltransferase activity assay

The enzymatic activity of MBP-hNAA80 was measured using a 5,5′-dithiobis-(2-nitrobenzoic acid, DTNB) assay as described previously by Foyn *et al.* (Foyn et al., 2017) and Drazic *et al.* (Drazic et al., 2018) Briefly, the thiol group exposed in the enzymatic product CoA cleaves DTNB and produces 2-nitro-5-thiobenzonate (TNB^-) which ionize to TNB^{2-} in neutral or alkaline pH and is readily quantified by measuring the absorbance at 412 nm.

2.3.1 Nt-acetyltransferase inhibitor assays

An *in vitro* DTNB assay with enzyme (10–600 nM), 300 μM Ac-CoA, 300 μM substrate peptide, acetylation buffer (Tris, pH 8.5), and at least nine different inhibitor concentrations ranging from 0 to 500 μM was used to calculate the IC_{50} value for each bisubstrate inhibitor applied in the assay. The reaction was carried out as previously described (Drazic et al., 2018; Goris et al., 2018), and within a timeframe of 15–50 min. All measurements were performed in triplicates.

IC_{50} values were determined using GraFit 7 software and the results are summarized in Table 2.

3 Results and discussion

The NATs constitute an important class of enzymes and potent inhibitors can prove to be useful as tool compounds to study their roles both *in vitro* and *in vivo*. To identify such a tool compound for NAA80, we have in this work optimized the earlier identified bisubstrate inhibitor CoA-Ac-DDDI-NH_2 (see Figure 1 for general structure). In our earlier work we tested the *in vitro* activity of NAA80 toward a broad library of potential substrates such as amino acids, nucleosides, coenzymes, various amines (e.g., serotonin and spermidine), vitamins and a number of 24-mer peptides representing the N-terminal part of proteins (Goris et al., 2018). In these substartes, the four N-terminal amino acids were varied while the remaining peptide sequence was kept constant. We found that for all of these potential substrates, NAA80 only acetylated three peptides, $MDEL_{24}$, $DDDI_{24}$ and $EEEI_{24}$. $DDDI_{24}$ and $EEEI_{24}$ correspond to the N-terminal part of β- and γ-actin in their cytosolic processed forms, respectively, while $MDEL_{24}$ represents the unprocessed N-terminal part of the protein p65. The level of product formation for actylation of $MDEL_{24}$, $DDDI_{24}$ and $EEEI_{24}$ was determined to be 119 ± 5.61 μM, 50.5 ± 1.0 μM, and 42.4 ± 0.95 μM, respectively (Goris et al., 2018). In our inhibitor design, we decided to continue using a tetrapeptide for the protein-mimicking part as previous studies have shown that these are the most important

10.3389/fchem.2023.1202501

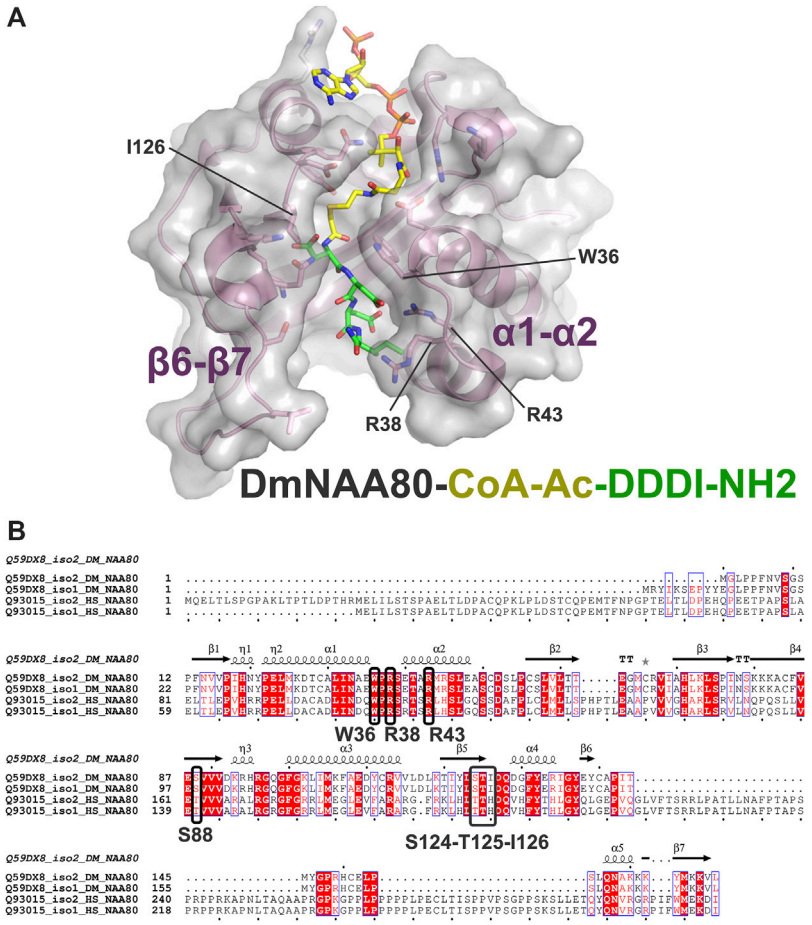

FIGURE 2
Structure of the binary *Drosophila melanogaster* (DM)NAA80/CoA-Ac-DDDI-NH_4 complex and similarities between *Drosophila* and human NAA80 protein sequences. **(A)** The structure of DmNaa80 is represented with transparent grey surface and pink secondary structures. Side chains involved in binding of the peptide is indicated with sticks, while the bisubstrate inhibitor is highlighted as colored sticks. Key regions (α1- α2, β6-β7) and amino acids (W36, R38, R43, and I126) involved in the peptide binding of the inhibitor are labelled. **(B)** Sequence alignment of DmNAA80 and *Homo sapiens* (Hs) NAA80. The blue boxes represent sequence conservation while highly conserved residues are shown in red. Strickly conserved residues are white on a red background. Important residues directly involved in peptide inhibitor binding are marked in bold black and with black boxes. Secondary structures and sequence numbering are shown above for the DmNAA80 iso2 sequence. The alignment was made using Clustal T-Coffee and ESPript 3.0.

residues for inhibitory activity (Liszczak et al., 2011; Foyn et al., 2013; Liszczak et al., 2013; Støve et al., 2016; Hong et al., 2017; Goris et al., 2018; Deng et al., 2020; Deng et al., 2021; Deng et al., 2023). Co-crystal structures of NAT-bisubstrate inhibitor complexes typically show that these four amino acids are most important for protein-inhibitor binding interactions. All inhibitors were prepared with the C-terminal carboxylic acid capped as amides to avoid the negative charge of a C-terminal carboxylic acid and better mimic a protein N-terminal.

The peptide part of all inhibitors was prepared using Fmoc-based solid phase peptide synthesis where the C-terminal amino acid was loaded onto a Rink amide resin (Scheme 1). After removal of the Fmoc-group of the N-terminal amino acid, coupling with bromoacetic acid introduced the acetyl-linker. The bromoacetyl peptide was then deprotected and cleaved from the resin and purified by RP-HPLC. Next, triethylammonium bicarbonate buffer (pH 8.5) was used to facilitate the conjugation of CoA to the bromoacetyl peptide. The final bisubstrate inhibitors were purified by RP-HPLC and characterized by MS and NMR to confirm their structures (see Table 1; Supplementary Table S1).

We have already reported that bisubstrate inhibitors based on the N-terminus of processed β- and γ-actin (DDDI and EEEI) display IC_{50} values of 0.38 and 1.16 μM, respectively (Table 2). The difference in inhibitory potency was somewhat higher than was expected based on the small difference in how well NAA80 acetylated the 24-mer peptides $DDDI_{24}$ and $EEEI_{24}$ as their four N-terminal amino acids. Surprisingly, while the $MDEL_{24}$ peptide showed a higher degree of acetylation than the $DDDI_{24}$ and $EEEI_{24}$ peptides when we screened for potential substrates, we found that the inhibitor based on the MDEL sequence was less potent and displayed an IC_{50} value of 1.26 μM.

To elucidate inhibitor binding we have previously solved the crystal structure of DmNAA80 bound to a DDDI bisubstrate inhibitor (Goris et al., 2018). This structure revealed that mainly the α1-α2 region of NAA80 contributed to peptide binding in the inhibitor, while the β6-β7 loop which is important for peptide binding in many of the other NATs, is slightly shifted away from the peptide without contributing to inhibitor binding (Figure 2A). More specifically, D1 of the inhibitor was stabilised by a hydrogen bond from the backbone oxygen of D1 to the backbone nitrogen in S88, while the D1 side chain was stabilized by hydrogen

bonds to the side chain of S124, and through a water-mediated hydrogen bond to T125 and I126. D2 of the inhibitor formed a hydrogen bond with W36 and a salt bridge with R43. Further, D3 made a water-mediated contact with R43 and hydrogen bonds with S46 and S48 and finally, the backbone oxygen of I4 formed a hydrogen bonds with R38. As can be seen from the multiple sequence alignments of DmNAA80 and hNAA80 (Figure 2B), most of the key contributing residues to binding in the DmNAA80-DDDI structure and hNAA80-profilin-actin ternary complex (W36, R43, R38 in DmNAA80 iso2 (Goris et al., 2018) corresponding to W105, R107 and R112 in hNAA80 iso 2 (Rebowski et al., 2020) is conserved. However, a key difference between the two is the extended region around the β6-β7 loop in hNAA80, a region that has shown importance for substrate binding in other NATs (Liszczak et al., 2011; Liszczak et al., 2013; Støve et al., 2016; Hong et al., 2017; Goris et al., 2018), and likely further contributes to optimimal binding of the peptide part of the bisubstrate analogue and increased potency of these inhibitors.

Since the DDDI-inhibitor was found to be significantly more potent that the EEEI-inhibitor, we decided to investigate whether the introduction of Asp into the EEEI sequence would increase inhibitory activity. It turned out that the introduction of Asp in position three was the most beneficial and the inhibitor based on the EEDI sequence showed almost ten-fold higher inhibitor activity compared to EEEI (Table 2). The EEDI sequence also proved to outperform DDDI and was found to inhibit NAA80 with an IC_{50} of 0.17 μM. Inhibitors based on the DEEI and EDEI sequences gave comparable or slightly improved IC_{50} values respectively compared to the EEEI inhibitor.

We also tested replacing the Ile residue with a Leu and found that the EEEI and EEEL sequences gave inhibitors with equal potency. On the other hand, the DEEL and EEDL sequences gave however a loss of activity compared to DEEI and EEDI while the inhibitor based on EDEL showed a four-to five-fold increase in potency compared to EDEI. Replacing Glu in position three of the EDEL sequence with a Gln residue led to an increase in IC_{50} from 0.15 μM to 0.85 μM and the replacement of the Asp residue with Ser led to a dramatic loss of potency. Interestingly, a PDEL sequence proved to give only slightly lower inhibitory potency compared to the ESEL sequence.

The introduction of two Asp residues into the EEEI sequence gave inhibitors with a large difference in inhibitory potency as the DDEI sequence gave an IC_{50} of 2.67 μM, where CoA-Ac-EDDI-NH_2 turned out to be the most potent inhibitor with an IC_{50} of 0.12 μM.

The NAA80/NatH is a particular case among the NAT enzymes in having actin as its sole substrate. The various cytoplasmic and muscle actin substrates all have different combinations of Asp and Glu in the first N-terminal positions (Aksnes et al., 2019). Here, we show that using specific combinations of Asp and Glu in the peptide sequence makes us able to identify a highly potent NAA80 inhibitor. In conclusion, we have found that for NAA80, the choice of acidic residue at different positions of the peptide part of bisubstrate inhibitors is important and varying these has led to an optimized inhibitor with up to 3 fold higher inhibitory activity compared to those previously described. The CoA-Ac-EDDI-NH_2 was the most potent NAA80 bisubstrate inhibitor with an IC_{50} of 0.12 μM. This inhibitor should be useful in further *in vivo* studies by micro injection in *Danio rerio* and for cell-based studies by micro injection into human cells to elucidate NAA80 function and the effects upon Nt-acetylation of actin.

Data availability statement

The original contributions presented in the study are included in the article/Supplementary Materials, further inquiries can be directed to the corresponding authors.

Author contributions

LMM, MB, SIS and HF designed and performed experiments. TA and BEH designed and supervised experiments. LMM, SIS, TA and BEH prepared figures and wrote the manuscript. All authors contributed to the article and approved the submitted version.

Funding

The peptide synthesis laboratory at the Department of Chemistry at the University of Bergen is funded by the Trond Mohn Foundation. The Norwegian NMR Platform (NNP) is funded by the Research Council of Norway (226244/F50). This work was supported by grants from the Trond Mohn Foundation to LM.M, the Research Council of Norway (RCN) (FRIPRO Grants 249843 and 325142 to TA), the Norwegian Health Authorities of Western Norway (F-12540 to TA), the Norwegian Cancer Society (171752-PR-2009-0222 to TA), and the European Research Council (ERC) under the European Union Horizon 2020 Research and Innovation Program (Grant 772039 to TA).

Acknowledgments

The authors would like to thank associate professor Jarl Underhaug for assistance with running NMR experiments.

Conflict of interest

The authors declare that the research was conducted in the absence of any commercial or financial relationships that could be construed as a potential conflict of interest.

Publisher's note

Supplementary material

The Supplementary Material for this article can be found online at: https://www.frontiersin.org/articles/10.3389/fchem.2023.1202501/full#supplementary-material

References

Aksnes, H., Marie, M., Arnesen, T., and Drazic, A. (2018). Actin polymerization and cell motility are affected by NAA80-mediated posttranslational N-terminal acetylation of actin. *Commun. Integr. Biol.* 11 (4), e1526572. doi:10.1080/19420889.2018.1526572

Aksnes, H., Ree, R., and Arnesen, T. (2019). Co-Translational, post-translational, and non-catalytic roles of N-terminal acetyltransferases. *Mol. Cell* 73 (6), 1097–1114. doi:10.1016/j.molcel.2019.02.007

Aksnes, H., Van Damme, P., Goris, M., Starheim, K. K., Marie, M., Støve, S. I., et al. (2015). An organellar nα-acetyltransferase, Naa60, acetylates cytosolic N termini of transmembrane proteins and maintains Golgi integrity. *Cell Rep.* 10 (8), 1362–1374. doi:10.1016/j.celrep.2015.01.053

Arnesen, T., and Aksnes, H. (2023). Actin finally matures: Uncovering machinery and impact. *Trends Biochem. Sci.* [Internet]. 2023 Feb 17[cited 2023 Mar 20]; Available from: https://www.sciencedirect.com/science/article/pii/S0968000423000361.

Arnesen, T., Van Damme, P., Polevoda, B., Helsens, K., Evjenth, R., Colaert, N., et al. (2009). Proteomics analyses reveal the evolutionary conservation and divergence of N-terminal acetyltransferases from yeast and humans. *Proc. Natl. Acad. Sci.* 106 (20), 8157–8162. doi:10.1073/pnas.0901931106

Beigl, T. B., Hellesvik, M., Saraste, J., Arnesen, T., and Aksnes, H. (2020). N-terminal acetylation of actin by NAA80 is essential for structural integrity of the Golgi apparatus. *Exp. Cell Res.* 390 (2), 111961. doi:10.1016/j.yexcr.2020.111961

Deng, S., Gardner, S. M., Gottlieb, L., Pan, B., Petersson, E. J., and Marmorstein, R. (2023). Molecular role of NAA38 in thermostability and catalytic activity of the human NatC N-terminal acetyltransferase. *Structure* 31 (2), 166–173.e4. doi:10.1016/j.str.2022.12.008

Deng, S., Pan, B., Gottlieb, L., Petersson, E. J., and Marmorstein, R. (2020). Molecular basis for N-terminal alpha-synuclein acetylation by human NatB. *eLife* 9, e57491. doi:10.7554/elife.57491

Deng, Y., Deng, S., Ho, Y. H., Gardner, S. M., Huang, Z., Marmorstein, R., et al. (2021). Novel bisubstrate inhibitors for protein N-terminal acetyltransferase D. *J. Med. Chem.* 64 (12), 8263–8271. doi:10.1021/acs.jmedchem.1c00141

Drazic, A., Aksnes, H., Marie, M., Boczkowska, M., Varland, S., Timmerman, E., et al. (2018). NAA80 is actin's N-terminal acetyltransferase and regulates cytoskeleton assembly and cell motility. *PNAS* 115 (17), 4399–4404. doi:10.1073/pnas.1718336115

Drazic, A., Timmerman, E., Kajan, U., Marie, M., Varland, S., Impens, F., et al. (2022). The final maturation state of β-actin involves N-terminal acetylation by NAA80, not N-terminal arginylation by ATE1. *J. Mol. Biol.* 434 (2), 167397. doi:10.1016/j.jmb.2021.167397

Evjenth, R. H., Brenner, A. K., Thompson, P. R., Arnesen, T., Frøystein, N. Å., and Lillehaug, J. R. (2012). Human protein N-terminal acetyltransferase hNaa50p (hNAT5/hSAN) follows ordered sequential catalytic mechanism: Combined kinetic and NMR study. *J. Biol. Chem.* 287 (13), 10081–10088. doi:10.1074/jbc.m111.326587

Foyn, H., Jones, J. E., Lewallen, D., Narawane, R., Varhaug, J. E., Thompson, P. R., et al. (2013). Design, synthesis, and kinetic characterization of protein N-terminal acetyltransferase inhibitors. *ACS Chem. Biol.* 8 (6), 1121–1127. doi:10.1021/cb400136s

Foyn, H., Thompson, P. R., and Arnesen, T. (2017). DTNB-based quantification of *in vitro* enzymatic N-terminal acetyltransferase activity. *Methods Mol. Biol.* 1574, 9–15. doi:10.1007/978-1-4939-6850-3_2

Goris, M., Magin, R. S., Foyn, H., Myklebust, L. M., Varland, S., Ree, R., et al. (2018). Structural determinants and cellular environment define processed actin as the sole substrate of the N-terminal acetyltransferase NAA80. *Proc. Natl. Acad. Sci.* 115 (17), 4405–4410. doi:10.1073/pnas.1719251115

Haahr, P., Galli, R. A., van den Hengel, L. G., Bleijerveld, O. B., Kazokaitė-Adomaitienė, J., Song, J. Y., et al. (2022). Actin maturation requires the ACTMAP/C19orf54 protease. *Science* 377 (6614), 1533–1537. doi:10.1126/science.abq5082

Hole, K., Van Damme, P., Dalva, M., Aksnes, H., Glomnes, N., Varhaug, J. E., et al. (2011). The human N-Alpha-Acetyltransferase 40 (hNaa40p/hNatD) is conserved from yeast and N-terminally acetylates histones H2A and H4. *PLoS ONE* 6 (9), e24713. doi:10.1371/journal.pone.0024713

Hong, H., Cai, Y., Zhang, S., Ding, H., Wang, H., and Han, A. (2017). Molecular basis of substrate specific acetylation by N-terminal acetyltransferase NatB. *Structure* 25 (4), 641–649.e3. doi:10.1016/j.str.2017.03.003

Liszczak, G., Arnesen, T., and Marmorstein, R. (2011). Structure of a ternary Naa50p (NAT5/SAN) N-terminal acetyltransferase complex reveals the molecular basis for substrate-specific acetylation. *J. Biol. Chem.* 286 (42), 37002–37010. doi:10.1074/jbc.m111.282863

Liszczak, G., Goldberg, J. M., Foyn, H., Petersson, E. J., Arnesen, T., and Marmorstein, R. (2013). Molecular basis for N-terminal acetylation by the heterodimeric NatA complex. *Nat. Struct. Mol. Biol.* 20 (9), 1098–1105. doi:10.1038/nsmb.2636

Muffels, I. J. J., Wiame, E., Fuchs, S. A., Massink, M. P. G., Rehmann, H., Musch, J. L. I., et al. (2021). NAA80 bi-allelic missense variants result in high-frequency hearing loss, muscle weakness and developmental delay. *Brain Commun.* 3 (4), fcab256. doi:10.1093/braincomms/fcab256

Pollard, T. D., and Cooper, J. A. (2009). Actin, a central player in cell shape and movement. *Science* 326 (5957), 1208–1212. doi:10.1126/science.1175862

Rebowski, G., Boczkowska, M., Drazic, A., Ree, R., Goris, M., Arnesen, T., et al. (2020). Mechanism of actin N-terminal acetylation. *Sci. Adv.* 6 (15), eaay8793. doi:10.1126/sciadv.aay8793

Redman, K., and Rubenstein, P. A. (1981). NH2-terminal processing of *Dictyostelium discoideum* actin *in vitro*. *J. Biol. Chem.* 256 (24), 13226–13229. doi:10.1016/s0021-9258(18)43032-3

Ree, R., Kind, L., Kaziales, A., Varland, S., Dai, M., Richter, K., et al. (2020). PFN2 and NAA80 cooperate to efficiently acetylate the N-terminus of actin. *J. Biol. Chem.* 295 (49), 16713–16731. doi:10.1074/jbc.ra120.015468

Rubenstein, P. A., and Martin, D. J. (1983). NH2-terminal processing of actin in mouse L-cells *in vivo*. *J. Biol. Chem.* 258 (6), 3961–3966. doi:10.1016/s0021-9258(18)32761-3

Songkyu, O., Wang, X., Waterborg, J. H., and Sternglanz, R. (2003). An N α-acetyltransferase responsible for acetylation of the N-terminal residues of histones H4 and H2A. *J. Biol. Chem.* 278 (40), 38109–38112. doi:10.1074/jbc.c300355200

Støve, S. I., Magin, R. S., Foyn, H., Haug, B. E., Marmorstein, R., and Arnesen, T. (2016). Crystal structure of the golgi-associated human nα-acetyltransferase 60 reveals the molecular determinants for substrate-specific acetylation. *Structure* 24 (7), 1044–1056. doi:10.1016/j.str.2016.04.020

Van Damme, P., Hole, K., Pimenta-Marques, A., Helsens, K., Vandekerckhove, J., Martinho, R. G., et al. (2011). NatF contributes to an evolutionary shift in protein N-terminal acetylation and is important for normal chromosome segregation. *PLoS Genet.* 7 (7), e1002169. doi:10.1371/journal.pgen.1002169

Wiame, E., Tahay, G., Tyteca, D., Vertommen, D., Stroobant, V., Bommer, G. T., et al. (2018). NAT6 acetylates the N-terminus of different forms of actin. *FEBS J.* 285 (17), 3299–3316. doi:10.1111/febs.14605

frontiers | Frontiers in Chemistry

TYPE Mini Review
PUBLISHED 20 June 2023
DOI 10.3389/fchem.2023.1196073

OPEN ACCESS

EDITED BY
Aleksandar Kondinski,
University of Cambridge, United Kingdom

REVIEWED BY
Mohammad Abrar Alam,
Arkansas State University, United States
Marian Breuer,
Maastricht University, Netherlands
Malcolm Page,
University of Basel, Switzerland

*CORRESPONDENCE
Gerhard Schenk,
schenk@uq.edu.au
Marc T. Morris,
marc.morris@uq.edu.au

†These authors have contributed equally to this work and share first authorship

RECEIVED 29 March 2023
ACCEPTED 05 June 2023
PUBLISHED 20 June 2023

CITATION
Krco S, Davis SJ, Joshi P, Wilson LA, Monteiro Pedroso M, Douw A, Schofield CJ, Hugenholtz P, Schenk G and Morris MT (2023), Structure, function, and evolution of metallo-β-lactamases from the B3 subgroup—emerging targets to combat antibiotic resistance. *Front. Chem.* 11:1196073. doi: 10.3389/fchem.2023.1196073

Structure, function, and evolution of metallo-β-lactamases from the B3 subgroup—emerging targets to combat antibiotic resistance

Stefan Krco [1,2†], Samuel J. Davis [1,2†], Pallav Joshi [1], Liam A. Wilson [3], Marcelo Monteiro Pedroso[1,2], Andrew Douw [1], Christopher J. Schofield [3], Philip Hugenholtz [1,2], Gerhard Schenk [1,2,4,5*] and Marc T. Morris [1,2*]

[1]School of Chemistry and Molecular Biosciences, The University of Queensland, Brisbane, QLD, Australia, [2]Australian Centre for Ecogenomics, The University of Queensland, Brisbane, QLD, Australia, [3]Chemistry Research Laboratory, Department of Chemistry, The Ineos Oxford Institute for Antimicrobial Research, Oxford University, Oxford, United Kingdom, [4]Sustainable Minerals Institute, The University of Queensland, Brisbane, QLD, Australia, [5]Australian Institute of Bioengineering and Nanotechnology, The University of Queensland, Brisbane, QLD, Australia

β-Lactams are the most widely employed antibiotics in clinical settings due to their broad efficacy and low toxicity. However, since their first use in the 1940s, resistance to β-lactams has proliferated to the point where multi-drug resistant organisms are now one of the greatest threats to global human health. Many bacteria use β-lactamases to inactivate this class of antibiotics via hydrolysis. Although nucleophilic serine-β-lactamases have long been clinically important, most broad-spectrum β-lactamases employ one or two metal ions (likely Zn^{2+}) in catalysis. To date, potent and clinically useful inhibitors of these metallo-β-lactamases (MBLs) have not been available, exacerbating their negative impact on healthcare. MBLs are categorised into three subgroups: B1, B2, and B3 MBLs, depending on their sequence similarities, active site structures, interactions with metal ions, and substrate preferences. The majority of MBLs associated with the spread of antibiotic resistance belong to the B1 subgroup. Most characterized B3 MBLs have been discovered in environmental bacteria, but they are increasingly identified in clinical samples. B3-type MBLs display greater diversity in their active sites than other MBLs. Furthermore, at least one of the known B3-type MBLs is inhibited by the serine-β-lactamase inhibitor clavulanic acid, an observation that may promote the design of derivatives active against a broader range of MBLs. In this Mini Review, recent advances in structure-function relationships of B3-type MBLs will be discussed, with a view to inspiring inhibitor development to combat the growing spread of β-lactam resistance.

KEYWORDS

antibiotic resistance, β-Lactamase, Metallo-β-Lactamase superfamily, classification, structure, function, evolution, drug development

1 Introduction

The spread of antibiotic resistance is arguably one of the greatest current threats to global health, with multidrug-resistant pathogenic strains increasingly encountered in clinical settings (World Health Organization, 2014). Concerningly, resistance is also being discovered in environmental bacteria that seemingly have not yet been subjected to the same levels of selective pressure as medically relevant pathogenic microbes (though antibiotics are very widely used in farming) (Miraula et al., 2016; Selleck et al., 2020; Wilson et al., 2021).

One of the primary mechanisms of resistance to β-lactams, the most widely employed class of antibiotics (Bush and Bradford, 2016), is *via* hydrolysis by β-lactamases, which are divided into four Ambler classes: A, B, C, and D (Bush, 2013). Classes A, C and D are serine-β-lactamases (SBLs), which employ a conserved nucleophilic serine residue during hydrolysis of the β-lactam ring. Class B β-lactamases are metallo-β-lactamases (MBLs) that accommodate one or two zinc ions in their active site, which activate a metal ion-bound hydroxide to initiate β-lactam hydrolysis, though at least some MBLs can employ other divalent metal ions (Bahr et al., 2021). Based on their overall sequences, active site residues, mechanisms, substrate preferences, and phylogenetic relationships, MBLs are further subdivided into three subgroups. While evolutionary analyses indicate that subgroups B1 and B2 form a monophyletic group, B3 MBLs appear to have branched independently, suggesting a convergent evolution to acquire the ability to operate on β-lactam substrates (Hall et al., 2004; Bahr et al., 2021). In addition to being distinct from B1 and B2 MBLs, B3 MBLs also display extensive intra-subgroup diversity, notably with active site variations not observed within the B1 and B2 subgroups (Figures 1, 2) (Hall et al., 2004; Pedroso et al., 2020; Bahr et al., 2021).

The MBL-fold, named after its initial discovery in the MBL BcII (Carfi et al., 1995), has a distinctive αββα core fold (Figure 1) and is observed in a wide diversity of bimetallic metallohydrolases (Bahr et al., 2021). Together, these form the wider MBL superfamily, with members including phosphatases (*e.g.*, nucleases, phytases), pesticide-degrading esterases, sulfatases (Barbeyron et al., 1995; Hagelueken et al., 2006), lactonases (Fernandez et al., 2011; Miraula et al., 2016), dehalogenases (Wang et al., 2010), oxidases (Muok et al., 2019) and the true β-lactam-degrading members, which form only a small subset within the MBL superfamily (Bebrone, 2007; Bahr et al., 2021). Some MBL fold enzymes also display non-hydrolytic reactions, such as the ethylmalonic encephalopathy 1 protein (ETHE1) that catalyses the iron and oxygen-dependent oxidation of glutathione persulfide (GSSH) to give persulfite and glutathione (Tan et al., 2017; Au et al., 2021; Vašková et al., 2023). Interestingly, there is emerging evidence that many of these diverse activities are observed promiscuously throughout the family (Miraula et al., 2016; Diene et al., 2019; Lee et al., 2019; Perez-Garcia et al., 2021). Notably, a number of recent studies have reported promiscuous enzymatic activities in different members of the MBL superfamily, including human nucleases or glyoxalases with β-lactamase activity (Miraula et al., 2016; Tan et al., 2017; Diene et al., 2019; Lee et al., 2019; Au et al., 2021; Perez-Garcia et al., 2021). Promiscuous enzymes with the MBL-fold could thus represent an as-yet overlooked reservoir from which novel sources of antibiotic resistance may arise under appropriate evolutionary pressures.

Most Class B MBLs are extended-spectrum β-lactamases (ESBLs) and effectively inactivate representatives from each of the three most important groups of β-lactam antibiotics, *i.e.*, penicillins, cephalosporins and carbapenems (Hou et al., 2017; Sidjabat et al., 2018; Bahr et al., 2021). Note, however, that monobactams, such as aztreonam, are not MBL substrates. The strong activity of MBLs against carbapenems, or so-called 'last-resort' antibiotics, is of particular clinical concern (Hou et al., 2017; Sidjabat et al., 2018; Bahr et al., 2021). Recently, infections from *Pseudomonas aeruginosa*-mediated carbapenem resistance have proliferated and are now a leading cause of death in critically ill and immunocompromised patients (Amsalu et al., 2021; Thaden et al., 2016). The discovery of a highly efficient B3 MBL, Adelaide Imipenemase (AIM-1) in *P. aeruginosa*, with catalytic efficiencies for the inactivation of a broad range of representatives from each of the three major classes of β-lactam antibiotics that is superior to the most effective B1 MBL known to date, NDM-1, demonstrates that the B3 subgroup of MBLs pose a significant but as-of-yet underestimated risk factor to global healthcare (Yong et al., 2012; Selleck et al., 2016; Hou et al., 2017; McGeary et al., 2017). Moreover, while numerous inhibitors for MBLs have been developed (Mohamed et al., 2011; Hussein et al., 2012; McGeary et al., 2014; Arjomandi et al., 2016; McGeary et al., 2017; Krajnc et al., 2019; Palacios et al., 2020; Wachino et al., 2020; Farley et al., 2021) none have yet been used in clinical applications, further exacerbating the threat of MBLs to global health (Mojica et al., 2022). By contrast, potent clinical inhibitors are available for SBLs including the well-established inhibitors clavulanic acid, tazobactam, sulbactam, as well as the more recently developed avibactam and vaborbactam, all of which are used in combination with a β-lactam antibiotic (Hecker et al., 2015; Bush and Bradford, 2016). However, none of the SBL inhibitors are clinically (Bush and Bradford, 2016) effective against MBLs. A major challenge for the development of inhibitors with high specificity for the true MBLs stems from the inherent structural and mechanistic similarity they share with other enzymes from the MBL superfamily [*e.g.*, glyoxalases and some nucleases such as the human enzymes MBLAC1, CPSF73, and HAGH (Pettinati et al., 2016)] as well as enzymes from other families that accommodate bimetallic metal centres that fulfill essential roles in metabolism [e.g. Purple Acid Phosphatases or Phosphodieterases (Mitić et al., 2006; Azevedo et al., 2014)]. The recent discovery of an MBL from the B3 subgroup, CSR-1 from *Cronobacter sakazakii*, that is inhibited by clavulanic acid may thus present a promising avenue to modify existing anti serine-β-lactamase drugs to become broader spectrum therapeutics (Pedroso et al., 2020).

The majority of characterized B3-type MBLs are from environmental bacteria (Hernandez Valladares et al., 2000; Allen et al., 2009; Miraula et al., 2015; Gudeta et al., 2016a; Gudeta et al., 2016b; Pedroso et al., 2017; Rodríguez et al., 2017; Selleck et al., 2020; Wilson et al., 2021) but are increasingly associated with pathogenic organisms as well (*e.g.*, *C. sakazakii*) (Ullah et al., 1998; Yum et al., 2010; Zhou et al.,

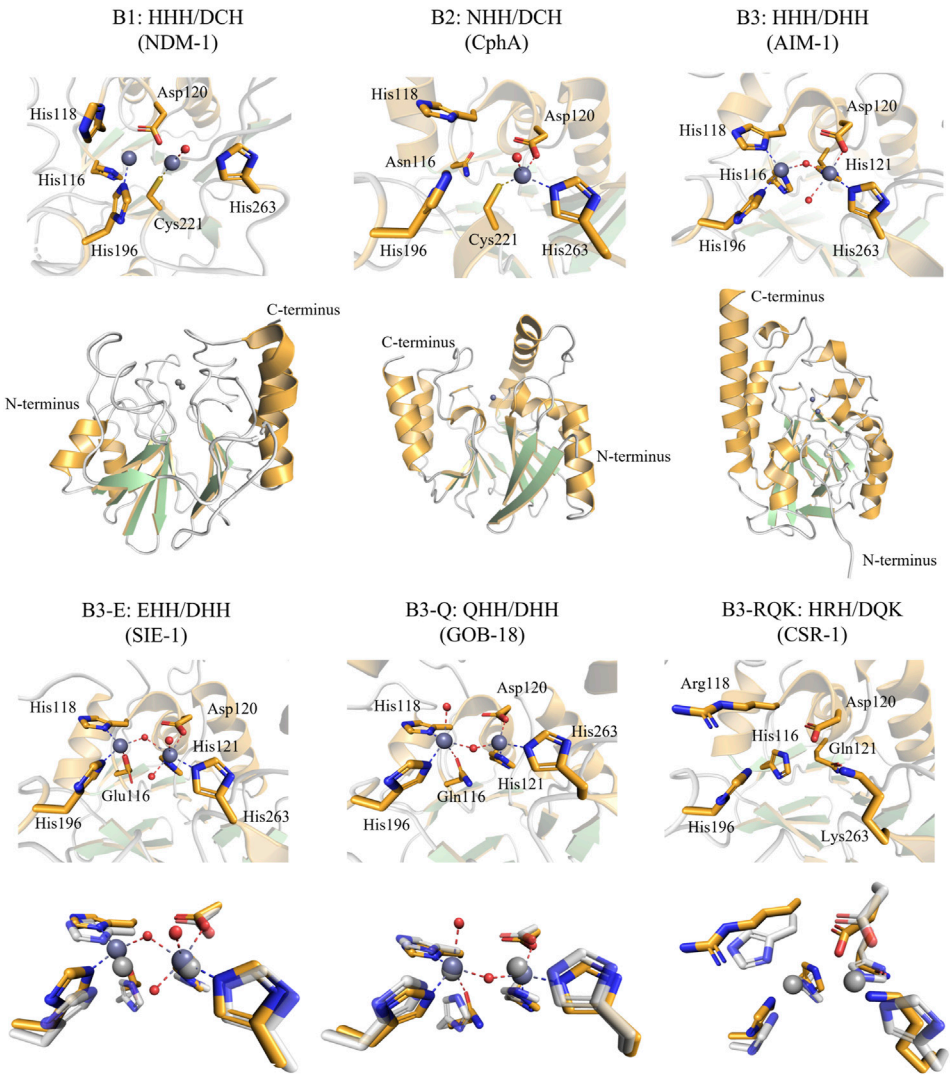

FIGURE 1
Active site and overall structure views of Class B MBLs ("true MBLs") from the B1, B2, and B3 subfamilies. Residues are numbered according to the BBL numbering scheme (Garau et al., 2004). Note that the B1 and B3 MBLs employ two active site metal ions and the B2 MBLs only one metal ion (dark grey spheres: zinc ions). The structures of SIE-1, GOB-18, and CSR-1 were each structurally aligned with AIM-1 (shown in white, 20% transparency, light grey zinc ions) for comparison. The figures were generated using the Pymol visualisation software (Schrödinger, 2015). PDB IDs—NDM-1, a B1 MBL: 3S0Z, CphA, a B2 MBL: 1X8G, and the B3 MBLs: AIM-1: 4P62, SIE-1: 7LUU, GOB-18: 5K0W, CSR-1: 6DN4.

2019). This mini review highlights recent advances in our understanding of this emerging health threat.

2 Discussion

2.1 Diversity among antibiotic-degrading MBLs

The B1 subgroup has received by far the most attention amongst studies on the Class B MBLs; it contains some of the most notorious agents that confer resistance to antibiotics. B1 subgroup members include enzymes such as NDM-1, IMP-1, and VIM-2 (Crowder et al., 2006), which have been extensively reviewed previously (Mojica et al., 2016; Bahr et al., 2021). B1-type MBLs are characterised by a conserved HHH/DCH active site motif [i.e., His116, His118, His196 and Asp120, Cys221, His263, as per the BBL numbering scheme (Galleni et al., 2001; Garau et al., 2004)]. The two sets of conserved amino acid side chains provide the ligands that coordinate two zinc ions (*i.e.*, the Zn1 and Zn2 sites, respectively), both of which are required for catalysis (Mitić et al., 2014; Bahr et al., 2021); although it cannot be ruled out that divalent metal ions other than zinc are relevant for MBL activity *in vivo* (Cahill et al., 2016).

The B2-type MBLs constitute the smallest Class B subgroup, of which the best-known member is CphA (Hernandez Valladares et al., 2000). B2 MBLs display the highest degree of substrate selectivity within MBLs, only effectively inactivating carbapenems (Felici et al., 1993; Hernandez Valladares et al., 2000). B2 MBLs are characterised by their NHH/DCH active site motif, corresponding to the Zn1 and Zn2 sites, respectively; however, only one zinc ion, in the Zn2 site, is required for catalysis (Bahr

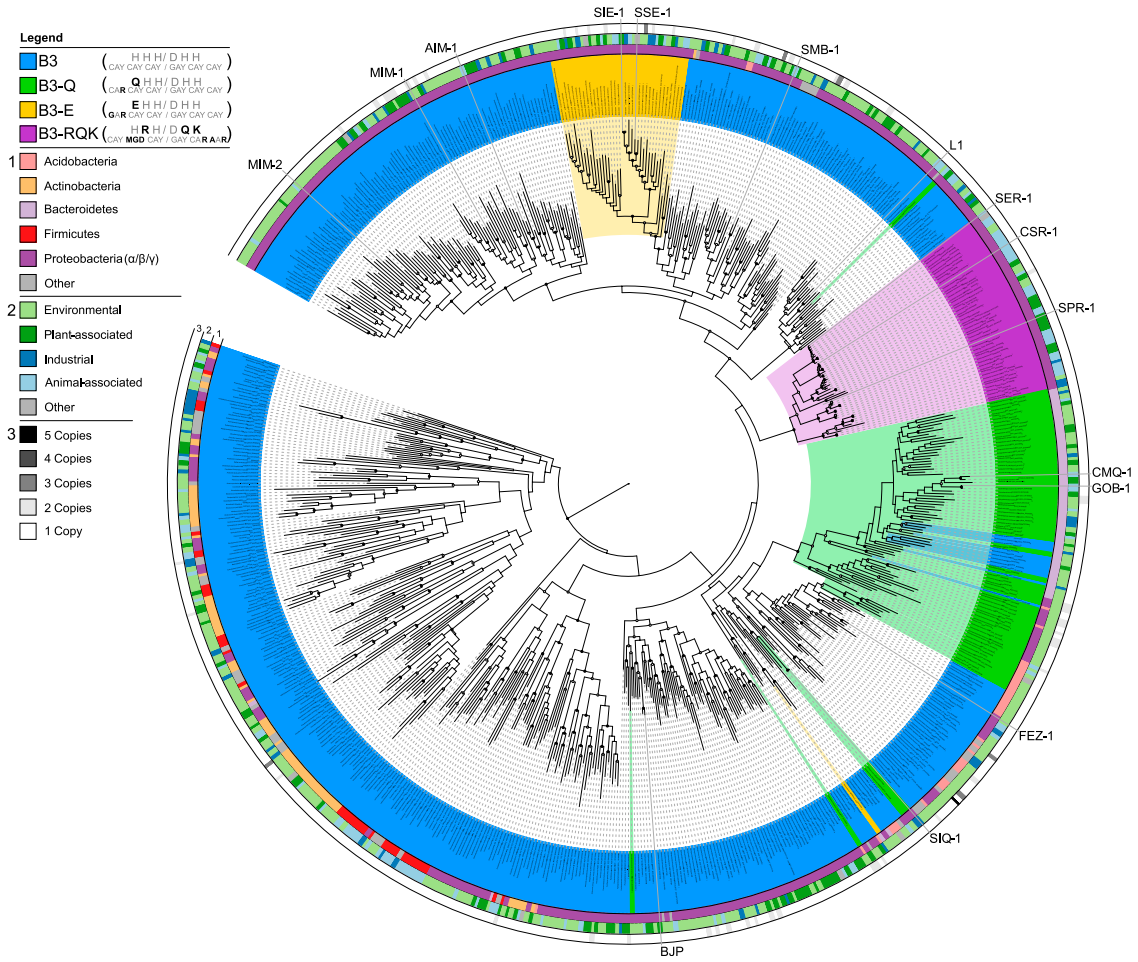

FIGURE 2
Phylogenetic analysis of MBLs belonging to the B3 subgroup, highlighting the different active site variants. B3 active site variants are highlighted in different colours according to the figure legend in the top left. The inner circle 1) represents the phylum-level affiliations of bacteria containing B3 MBLs; the middle circle 2) represents the source of the B3-containing bacteria; the outer circle 3) represents B3 MBL gene copy number in each genome. Reproduced with permission from Pedroso et al. (2020).

et al., 2021). Indeed, the presence of a Zn(II) in the Zn1 site leads to inhibition (Mitić et al., 2014; Bottoni et al., 2016; Bahr et al., 2021).

The B3 MBL subgroup contains mostly MBLs detected in environmental organisms and is the most divergent group among the Class B β-lactamases, both from phylogenetic and structural perspectives (Pedroso et al., 2020; Fröhlich et al., 2021).

While the B1 and B2 subgroups seem to have a common evolutionary origin, the B3 subgroup likely evolved independently within the overall MBL superfamily, sharing less than 20% sequence similarity with B1 and B2 MBLs (Hall et al., 2004; Bebrone, 2007; Pedroso et al., 2020; Bahr et al., 2021). Furthermore, the diversity internal to the B3 subgroup seems greater than within the B1 and B2 subgroups, with pairwise similarities being as low as 15% (Pedroso et al., 2020). However, B3-type MBLs possess an active site that can accommodate up two Zn(II) ions, and as for B1 MBLs both Zn(II) ions appear to be needed for full catalytic activity (Selleck et al., 2016). The canonical B3 active site motif is HHH/DHH for the Zn1 and Zn2 binding sites, respectively. However, unlike the B1 and B2 subgroups there is considerable diversity within the active site motif of the B3 subgroup (Pedroso et al., 2020). Sequence analyses suggest that there are at least four distinct variants that have evolved within the B3 clade, *i.e.*, the canonical form with the HHH/DHH active site motif, and three less abundant forms (Figure 2) (Pedroso et al., 2020). Two of these variants have a substitution of residue 116 of the Zn1 site, replacing the canonical histidine by either a glutamine (Q) or a glutamic acid (E), resulting in the B3-Q (**Q**HH/DHH) or B3-E (**E**HH/DHH) active site motifs, respectively (Figures 1, 2). The glutamine substitution, in contrast to the glutamate mutation, appears to have occurred independently on multiple occasions within the B3 subfamily (Figure 2) (Pedroso et al., 2020). The least abundant and most intriguing variant, characterised by the B3-RQK active site motif, has three mutations relative to the canonical HHH/DHH motif, *i.e.*, a histidine to arginine of residue 118 of the Zn1 site, and histidine to glutamine and

histidine to lysine in residues 121 and 263 of the Zn2 site, respectively, resulting in the H**R**H/D**QK** active site motif (Vella et al., 2013; Pedroso et al., 2020) (Figures 1, 2). This variant appears to form a monophyletic group, having evolved from a single evolutionary event within the B3 MBL subgroup (Figure 2) (Pedroso et al., 2020).

2.2 Structures and catalytic properties of MBLs from the B3 subgroup

a) B3 variants with the canonical HHH/DHH motif. The most studied representatives from the B3 MBL subgroup are L1 from *S. maltophilia* (Simm et al., 2002; Aitha et al., 2016; Kim et al., 2020) and AIM-1 from *P. aeruginosa* (Selleck et al., 2016), with the latter posing a major threat to healthcare due to its high catalytic efficiency towards a broad range of β-lactam antibiotics (Supplementary Table S1). The metal ion in the Zn1 site is tetrahedrally coordinated by the three histidine ligands of the active site motif, as well as the oxygen from the hydroxide that in the resting enzyme bridges the two metal ions and which acts as the nucleophile that initiates the hydrolysis of the β-lactam bond. The Zn2 site usually adopts a distorted trigonal bipyramidal geometry where His121 and His263 from the active site motif and the metal ion-bridging nucleophilic hydroxide form the equatorial plane, and Asp120 and an additional water ligand occupy axial positions (Figure 1). Overall, the active site geometry of AIM-1 is similar to that of most of the characterised B1-type MBLs, including that of NDM-1 (King and Strynadka, 2011) or IMP-1 (Concha et al., 2000; Yamaguchi et al., 2021).

MBLs from the B3 subgroup have received far less attention than representatives from the B1 subgroup, largely because they have historically been less often associated with human pathogens. However, they are increasingly being identified in clinical settings and likely pose an underestimated threat to global health (Ullah et al., 1998; Yum et al., 2010; Zhou et al., 2019). For example, AIM-1, originally isolated from a patient from a hospital in Adelaide, Australia, is expressed by bacteria such as *P. aeruginosa* and *K. pneumoniae* (Zhou et al., 2019) and is located on a mobile genetic element (Yong et al., 2012). A recent shotgun genomic sequencing and phylogenetics analysis of wastewater samples from different locations has revealed that, although the gene encoding for AIM-1 may have originated from the non-pathogenic, environmental species *Pseudoxanthomonas mexicana*, it is now widely distributed across the globe (Amsalu et al., 2021).

Furthermore, AIM-1 is highly efficient in inactivating representatives from each of the three major groups of β-lactam antibiotics. In fact, it is considerably more reactive against most of those substrates than NDM-1, one of the most effective agents in antibiotic-resistant isolates around the globe (World Health Organization, 2014; Mojica et al., 2022). In particular, AIM-1 is highly efficient in inactivating "last-resort" carbapenems, with k_{cat}/K_M ratios as high as 18 $s^{-1}\mu M^{-1}$, nearly 100-fold higher than the corresponding values reported for NDM-1 (Supplementary Table S1). Mechanistic studies have shown, that like the B1 MBLs, AIM-1 operates most effectively with two Zn(II) bound to the active site (Selleck et al., 2016).

b) B3 variants with the QHH/DHH motif (B3-Q). The best characterised members of the B3-Q MBL variants are the GOB family of MBLs, although several other B3 members have been recovered from environmental soil metagenomes (*e.g.*, LRA-12 or PEDO-1) (Gudeta et al., 2016a; Gudeta et al., 2016b; Rodríguez et al., 2017). GOB-1 was discovered in the opportunistically pathogenic bacterial species *E. meningoseptica* (Horsfall et al., 2011), but numerous GOB variants have since been discovered in *E. meningoseptica* and other *Elizabethkingia* species (Yum et al., 2010; Pedroso et al., 2020; Bahr et al., 2021).

Structural data are available only for one GOB variant, GOB-18 (PDB: 5K0W), and provide evidence that the histidine to glutamine substitution in position116 of the Zn1 motif does not greatly affect the geometry of the active site when compared with that of AIM-1 (Morán-Barrio et al., 2016). However, a noteworthy difference between GOB-18 and AIM-1 is the inversion in the coordination geometries of the Zn1 and Zn2 sites within GOB-18, with Zn2 adopting a tetrahedral and the Zn1 a trigonal bipyramidal geometry (including an axial water ligand) (Figure 1) (Morán-Barrio et al., 2016; Wilson et al., 2021). Similarly to AIM-1, GOB-1 is also effective against a broad range of β-lactam antibiotics, in particular carbapenems, with k_{cat}/K_M ratios as high as 8 $s^{-1}\mu M^{-1}$ (Supplementary Table S1). It is reported that GOB-18 may occur both in mono- and bi-metallic form, similar to the B1-type MBL BsII from *Bacillus subtilis*, and it may thus be possible that GOB MBLs are active in both states (Morán-Barrio et al., 2007; Lisa et al., 2010). Indeed, the monometallic form may be particularly active against carbapenem substrates, using a mechanism similar to B2-type MBLs that almost exclusively operate on these substrates (Garau et al., 2005; Fonseca et al., 2011).

c) 3 variants with the EHH/DHH motif (B3-E). Only one member of the B3-E variants has been characterised to date, SIE-1 from *Sphingobium indicum* (Wilson et al., 2021), but sequences of other putative B3 MBLs sharing this active site motif have been reported (Pedroso et al., 2020; Bahr et al., 2021). The replacement of the histidine in position 116 of the canonical Zn1 motif by a glutamate does not lead to significant structural changes when compared to AIM-1, preserving a tetrahedral Zn1 and a trigonal bipyramidal Zn2 site (Figure 1) (Wilson et al., 2021). The largest structural difference between the active sites of SIE-1 and canonical B3 MBLs (*e.g.*, AIM-1) or B3-Q (*i.e.*, GOB-18) is that the Zn1-Zn2 distance is longer in SIE-1 (3.75Å) than in AIM-1 (3.48Å) or GOB-18 (3.5Å) (Wilson et al., 2021).

Like other B3 MBLs, SIE-1 is catalytically active against all major classes of β-lactams (Supplementary Table S1). While generally less efficient than the canonical AIM-1 or the B3-Q enzyme GOB-18, SIE-1 has catalytic parameters comparable to those of the B1-type MBL NDM-1 (Wilson et al., 2021). Interestingly, SIE-1 shows increased selectivity toward cephalosporin substrates (with k_{cat}/K_M ratios as high as ~1.3 $s^{-1}\mu M^{-1}$) and is thus more efficient against such substrates than penicillins, an infrequent characteristic amongst B3 MBLs (Wilson et al., 2021) (Supplementary Table S1). From the limited data currently available, it appears that B3-E variants likely employ a mechanism

involving two Zn(II) ions in the active site, similar to AIM-1 (Wilson et al., 2021).

d) B3 variants with the HRH/DQK motif (B3-RQK). The B3-RQK subfamily is the most divergent and least represented among the B3 MBL variants, with substitutions in both the Zn1 and Zn2 sites (Figure 2). To date representatives of the B3-RQK variants have been discovered in and characterised from *Serratia proteamaculans* (SPR-1) (Vella et al., 2013), *C. sakazakii* (CSR-1) (Pedroso et al., 2020) and *Salmonella enterica* (SER-1) (Pedroso et al., 2020). Members of the B3-RQK class are not only unusual because they have the largest number of substitutions in their active sites, but also because two of the canonical histidine residues were replaced by arginine and lysine residues, both very rare ligands in metal ion-dependent enzymes. Due to their high pK_a values, these residues are likely to be protonated at pH values optimal for MBL activity, and thus unlikely to coordinate to metal ions effectively. This interpretation is in agreement with initial studies of SPR-1, which indicated that it may have only one Zn(II) bound in the resting state, but that a catalytically active di-Zn(II) centre is formed upon the addition of a substrate (Vella et al., 2013). This substrate-promoted activation mechanism is similar to that proposed for the pesticide-degrading diesterase GpdQ (Hadler et al., 2009; Hadler et al., 2010; Paul et al., 2018; Sharma et al., 2019; Sharma et al., 2020) and indicates an inherent plasticity in the mechanism and potentially the functionality of these enzymes.

Indeed, a high-resolution structure and binding studies of the B3-RQK enzyme CSR-1 reveals that its active site has a strongly decreased metal ion affinity when compared to AIM-1 (Pedroso et al., 2020). Furthermore, while CSR-1 is active against substrates from each of the three major groups of β-lactam antibiotics, it is considerably less efficient than other MBLs (Supplementary Table S1). It has been demonstrated that, at least for some sets of MBLs, that the active site metal ion affinity correlates with catalytic efficiency, in particular for the Zn2 site. In the case of CSR-1 replacement of its arginine in position 118 by the canonical histidine enhances metal ion binding affinity at the Zn1 site with a modest improvement in catalytic efficiency (Supplementary Table S2). However, replacing both the glutamine and lysine residues in the CSR-1 Zn2 site with their canonical histidine counterparts enhances the affinities of both Zn(II) ions and drastically improves the catalytic efficiency to a level comparable to that of other B3 MBLs (Supplementary Table S2). Given that B3-RQK variants evolved from within the B3 MBL subgroup (Figure 2), it is possible that these enzymes indeed represent a functional adaptation, even though no alternative substrates for them have yet been identified.

2.3 Inhibition of B3-RQK MBLs may provide an avenue to combat antibiotic resistance

Given the rise of antibiotic resistance, the lack of clinical inhibitors for MBLs is of pressing concern. A range of SBL inhibitors have been tested to no avail against numerous MBLs, such as penams (*e.g.*, sulbactam and tazobactam), diazabicyclooctanones (*e.g.*, avibactam and relebactam) (Wang et al., 2016; Lang Pauline et al., 2021), and some boronates (*e.g.*, vaborbactam) (Bush and Bradford, 2016; Cahill et al., 2017; Bahr et al., 2021). Some newer agents such as next-generation boronates (*e.g.*, taniborbactam or xeruborbactam, which are being tested in clinical trials) (Krajnc et al., 2019; Hamrick et al., 2020; Hecker et al., 2020; Liu et al., 2020; Bahr et al., 2021; Brem et al., 2022; Yang et al., 2023), thiol-based compounds (Brem et al., 2016; Tehrani and Martin, 2017) [*e.g.*, captopril (Heinz et al., 2003)], carboxylate-based compounds (Concha et al., 2000; Hinchliffe et al., 2018; Brem et al., 2022), phosphonate-based compounds (Yang et al., 2013; Pemberton et al., 2019), or pyrazoles (Alam, 2022) hold some promise as MBL inhibitors. The recent observation that the commonly used serine-β-lactamase inhibitor clavulanic acid (a clavam) inhibits B3-RQK MBLs may be leveraged to broaden the application scope of this widely used therapeutic. Clavulanic acid is a known inhibitor of serine-β-lactamases (Drawz and Bonomo, 2010), especially those belonging to Classes A and D with K_i values ranging from 20 to 200 μM (Pedroso et al., 2020).

While ineffective against all known MBLs associated with antibiotic resistance in clinical isolates, clavulanic acid inhibits B3-RQK with a K_i of 200–350 μM (Pedroso et al., 2020). A combination of docking and mutagenesis studies with CSR-1 demonstrated that the lysine residue in position 263 of the Zn2 active site motif may play a crucial role in the binding of clavulanic acid by enabling it to outcompete the catalytically essential Zn(II) in this site (Pedroso et al., 2020). Replacing this lysine with the canonical histidine favours the binding of the metal ion and thus prevents inhibition by clavulanic acid. Considering the overall similarity of the active site geometry in the metal binding pocket of MBLs it may thus be possible to modify clavulanic acid so that its affinity to the Zn2 site will be greater than that of the metal ion.

3 Future perspectives

MBLs have emerged as a major threat to global health, compounded by a lack of clinically suitable inhibitors. The most prevalent MBL subgroup associated with antibiotic resistance is B1, which have highly conserved active site geometries around the catalytically essential Zn(II) ions. However, in recent years an increasing number of MBLs from the B3 subgroup have been identified and characterised. To date, most B3 MBLs are associated with environmental microorganisms that are not pathogenic for humans, but a growing number have been found in more concerning bacteria such as *K. pneumoniae*.

Recent studies have shown that B3 MBLs are evolutionarily related to enzymes with distinct functions, in particular different types of nucleases (Diene et al., 2019), and they have also been identified in several viral genomes. It is thus plausible that B3 MBLs have evolved from a different ancestral functionality and acquired β-lactamase activity in response to environmental pressure. Considering the abundance of such B3 MBLs in diverse microbial organisms it may be only a matter of time before more of these agents accumulate in human pathogens, thus presenting a

new threat to healthcare. It is therefore imperative to think about inhibition strategies to combat them now.

Furthermore, the B3 subgroup is more diverse in terms of active site geometry, mechanism, reactivity, substrate selectivity, and inhibition than the B1 and B2 MBL subgroups. There is a thus a risk that inhibitors developed solely against the currently most important B1 MBL subgroup, which contains the notorious but relatively recently discovered NDM (discovered, 2009), VIM (1999), and IMP (1991) MBLs" to "recently discovered NDM- (discovered, 2009), VIM- (1999), and IMP-type (1991) MBLs, will be become less effective due to a future rise in B3 (and B2) MBLs, against which they may not be active. Interestingly, one active site variant among the B3 MBLs is inhibited by the widely used SBL inhibitor clavulanic acid, by a mechanism involving displacement of the Zn2 metal ion in the active site for which interactions with residue 263 appear to be particularly important. This observation suggests that it may be possible to modify clavulanic acid or related compounds to possess enhanced affinity for the Zn2 site. Along with reports on bicyclic boronates (Cahill et al., 2017; Krajnc et al., 2019), it may be within reach to generate very broad spectrum β-lactamase inhibitors.

Author contributions

SK, SD, PJ, MMP, and AD were responsible for writing the preliminary draft of the manuscript, with support from MTM and GS. CS, LW, and PH were responsible for the critical evaluation of the later versions of the manuscript. GS and MTM were involved in the conceptualization of the manuscript, as well as the final preparation for submission. All authors contributed to the article and approved the submitted version.

Funding

The authors acknowledge support from the National Health and Medical Research Council from Australia in form of the Ideas Grant ID 2010390.

Conflict of interest

The authors declare that the research was conducted in the absence of any commercial or financial relationships that could be construed as a potential conflict of interest.

The reviewer MP declared a past co-authorship with the author CS to the handling editor.

Publisher's note

Supplementary material

The Supplementary Material for this article can be found online at: https://www.frontiersin.org/articles/10.3389/fchem.2023.1196073/full#supplementary-material

References

Aitha, M., Al-Adbul-Wahid, S., Tierney, D. L., and Crowder, M. W. (2016). Probing substrate binding to the metal binding sites in metallo-β-lactamase L1 during catalysis. *Medchemcomm* 7 (1), 194–201. doi:10.1039/c5md00358j

Alam, M. A. (2022). Antibacterial pyrazoles: Tackling resistant bacteria. *Future Med. Chem.* 14 (5), 343–362. doi:10.4155/fmc-2021-0275

Allen, H. K., Moe, L. A., Rodbumrer, J., Gaarder, A., and Handelsman, J. (2009). Functional metagenomics reveals diverse beta-lactamases in a remote Alaskan soil. *Isme J.* 3 (2), 243–251. doi:10.1038/ismej.2008.86

Amsalu, A., Sapula, S. A., Whittall, J. J., Hart, B. J., Bell, J. M., Turnidge, J., et al. (2021). Worldwide distribution and environmental origin of the Adelaide imipenemase (AIM-1), a potent carbapenemase in *Pseudomonas aeruginosa*. *Microb. Genom* 7 (12), 000715. doi:10.1099/mgen.0.000715

Arjomandi, O. K., Hussein, W. M., Vella, P., Yusof, Y., Sidjabat, H. E., Schenk, G., et al. (2016). Design, synthesis, and *in vitro* and biological evaluation of potent amino acid-derived thiol inhibitors of the metallo-β-lactamase IMP-1. *Eur. J. Med. Chem.* 114, 318–327. doi:10.1016/j.ejmech.2016.03.017

Au, S. X., Dzulkifly, N. S., Muhd Noor, N. D., Matsumura, H., Raja Abdul Rahman, R. N. Z., and Normi, Y. M. (2021). Dual activity BLEG-1 from Bacillus lehensis G1 revealed structural resemblance to B3 metallo-β-lactamase and glyoxalase II: An insight into its enzyme promiscuity and evolutionary divergence. *Int. J. Mol. Sci.* 22 (17), 9377. doi:10.3390/ijms22179377

Azevedo, M. F., Faucz, F. R., Bimpaki, E., Horvath, A., Levy, I., de Alexandre, R. B., et al. (2014). Clinical and molecular genetics of the phosphodiesterases (PDEs). *Endocr. Rev.* 35 (2), 195–233. doi:10.1210/er.2013-1053

Bahr, G., González, L. J., and Vila, A. J. (2021). Metallo-β-lactamases in the age of multidrug resistance: From structure and mechanism to evolution, dissemination, and inhibitor design. *Chem. Rev.* 121 (13), 7957–8094. doi:10.1021/acs.chemrev.1c00138

Barbeyron, T., Potin, P., Richard, C., Collin, O., and Kloareg, B. (1995). Arylsulphatase from alteromonas carrageenovora. *Microbiol. Read.* 141 (11), 2897–2904. doi:10.1099/13500872-141-11-2897

Bebrone, C. (2007). Metallo-β-lactamases (classification, activity, genetic organization, structure, zinc coordination) and their superfamily. *Biochem. Pharmacol.* 74 (12), 1686–1701. doi:10.1016/j.bcp.2007.05.021

Bottoni, C., Perilli, M., Marcoccia, F., Piccirilli, A., Pellegrini, C., Colapietro, M., et al. (2016). Kinetic studies on CphA mutants reveal the role of the P158-P172 loop in activity versus carbapenems. *Antimicrob. Agents Chemother.* 60 (5), 3123–3126. doi:10.1128/AAC.01703-15

Brem, J., Panduwawala, T., Hansen, J. U., Hewitt, J., Liepins, E., Donets, P., et al. (2022). Imitation of β-lactam binding enables broad-spectrum metallo-β-lactamase inhibitors. *Nat. Chem.* 14 (1), 15–24. doi:10.1038/s41557-021-00831-x

Brem, J., van Berkel, S. S., Zollman, D., Lee, S. Y., Gileadi, O., McHugh, P. J., et al. (2016). Structural basis of metallo-β-lactamase inhibition by captopril stereoisomers. *Antimicrob. Agents Chemother.* 60 (1), 142–150. doi:10.1128/aac.01335-15

Bush, K., and Bradford, P. A. (2016). β-Lactams and β-lactamase inhibitors: An overview. *Cold Spring Harb. Perspect. Med.* 6 (8), a025247. doi:10.1101/cshperspect.a025247

Bush, K. (2013). The ABCD's of β-lactamase nomenclature. *J. Infect. Chemother.* 19 (4), 549–559. doi:10.1007/s10156-013-0640-7

Cahill, S. T., Cain, R., Wang, D. Y., Lohans, C. T., Wareham, D. W., Oswin, H. P., et al. (2017). Cyclic boronates inhibit all classes of β-lactamases. *Antimicrob. Agents Chemother.* 61 (4), 022600–e2316. doi:10.1128/aac.02260-16

Cahill, S. T., Tarhonskaya, H., Rydzik, A. M., Flashman, E., McDonough, M. A., Schofield, C. J., et al. (2016). Use of ferrous iron by metallo-β-lactamases. *J. Inorg. Biochem.* 163, 185–193. doi:10.1016/j.jinorgbio.2016.07.013

Carfi, A., Pares, S., Duée, E., Galleni, M., Duez, C., Frère, J. M., et al. (1995). The 3-D structure of a zinc metallo-beta-lactamase from Bacillus cereus reveals a new type of protein fold. *Embo J.* 14 (20), 4914–4921. doi:10.1002/j.1460-2075.1995.tb00174.x

Concha, N. O., Janson, C. A., Rowling, P., Pearson, S., Cheever, C. A., Clarke, B. P., et al. (2000). Crystal structure of the IMP-1 metallo β-lactamase from *Pseudomonas aeruginosa* and its complex with a mercaptocarboxylate inhibitor: Binding determinants

of a potent, broad-spectrum inhibitor. *Biochemistry* 39 (15), 4288–4298. doi:10.1021/bi992569m

Crowder, M. W., Spencer, J., and Vila, A. J. (2006). Metallo-beta-lactamases: Novel weaponry for antibiotic resistance in bacteria. *Acc. Chem. Res.* 39 (10), 721–728. doi:10.1021/ar0400241

Diene, S. M., Pinault, L., Keshri, V., Armstrong, N., Khelaifia, S., Chabrière, E., et al. (2019). Human metallo-β-lactamase enzymes degrade penicillin. *Sci. Rep.* 9 (1), 12173. doi:10.1038/s41598-019-48723-y

Drawz, S. M., and Bonomo, R. A. (2010). Three decades of β-lactamase inhibitors. *Clin. Microbiol. Rev.* 23 (1), 160–201. doi:10.1128/CMR.00037-09

Farley, A. J. M., Ermolovich, Y., Calvopiña, K., Rabe, P., Panduwawala, T., Brem, J., et al. (2021). Structural basis of metallo-β-lactamase inhibition by N-Sulfamoylpyrrole-2-carboxylates. *ACS Infect. Dis.* 7 (6), 1809–1817. doi:10.1021/acsinfecdis.1c00104

Felici, A., Amicosante, G., Oratore, A., Strom, R., Ledent, P., Joris, B., et al. (1993). An overview of the kinetic parameters of class B beta-lactamases. *Biochem. J.* 291 (1), 151–155. doi:10.1042/bj2910151

Fernandez, F. J., Garces, F., López-Estepa, M., Aguilar, J., Baldomà, L., Coll, M., et al. (2011). The UlaG protein family defines novel structural and functional motifs grafted on an ancient RNase fold. *BMC Evol. Biol.* 11 (1), 273. doi:10.1186/1471-2148-11-273

Fonseca, F., Bromley, E. H., Saavedra, M. J., Correia, A., and Spencer, J. (2011). Crystal structure of Serratia fonticola sfh-I: Activation of the nucleophile in mono-zinc metallo-β-lactamases. *J. Mol. Biol.* 411 (5), 951–959. doi:10.1016/j.jmb.2011.06.043

Fröhlich, C., Chen, J. Z., Gholipour, S., Erdogan, A. N., and Tokuriki, N. (2021). Evolution of β-lactamases and enzyme promiscuity. *Protein Eng. Des. Sel.* 34, gzab013. doi:10.1093/protein/gzab013

Galleni, M., Lamotte-Brasseur, J., Rossolini, G. M., Spencer, J., Dideberg, O., and Frère, J. M. (2001). Standard numbering scheme for class B beta-lactamases. *Antimicrob. Agents Chemother.* 45 (3), 660–663. doi:10.1128/aac.45.3.660-663.2001

Garau, G., Bebrone, C., Anne, C., Galleni, M., Frère, J. M., and Dideberg, O. (2005). A metallo-beta-lactamase enzyme in action: Crystal structures of the monozinc carbapenemase CphA and its complex with biapenem. *J. Mol. Biol.* 345 (4), 785–795. doi:10.1016/j.jmb.2004.10.070

Garau, G., García-Sáez, I., Bebrone, C., Anne, C., Mercuri, P., Galleni, M., et al. (2004). Update of the standard numbering scheme for class B beta-lactamases. *Antimicrob. Agents Chemother.* 48 (7), 2347–2349. doi:10.1128/aac.48.7.2347-2349.2004

Gudeta, D. D., Bortolaia, V., Amos, G., Wellington, E. M., Brandt, K. K., Poirel, L., et al. (2016a). The soil microbiota harbors a diversity of carbapenem-hydrolyzing β-lactamases of potential clinical relevance. *Antimicrob. Agents Chemother.* 60 (1), 151–160. doi:10.1128/aac.01424-15

Gudeta, D. D., Bortolaia, V., Pollini, S., Docquier, J. D., Rossolini, G. M., Amos, G. C., et al. (2016b). Expanding the repertoire of carbapenem-hydrolyzing metallo-ß-lactamases by functional metagenomic analysis of soil microbiota. *Front. Microbiol.* 7, 1985. doi:10.3389/fmicb.2016.01985

Hadler, K. S., Mitić, N., Ely, F., Hanson, G. R., Gahan, L. R., Larrabee, J. A., et al. (2009). Structural flexibility enhances the reactivity of the bioremediator glycerophosphodiesterase by fine-tuning its mechanism of hydrolysis. *J. Am. Chem. Soc.* 131 (33), 11900–11908. doi:10.1021/ja903534f

Hadler, K. S., Mitić, N., Yip, S. H., Gahan, L. R., Ollis, D. L., Schenk, G., et al. (2010). Electronic structure analysis of the dinuclear metal center in the bioremediator glycerophosphodiesterase (GpdQ) from Enterobacter aerogenes. *Inorg. Chem.* 49 (6), 2727–2734. doi:10.1021/ic901950c

Hagelueken, G., Adams Thorsten, M., Wiehlmann, L., Widow, U., Kolmar, H., Tümmler, B., et al. (2006). The crystal structure of SdsA1, an alkylsulfatase from *Pseudomonas aeruginosa*, defines a third class of sulfatases. *Proc. Natl. Acad. Sci.* 103 (20), 7631–7636. doi:10.1073/pnas.0510501103

Hall, B. G., Salipante, S. J., and Barlow, M. (2004). Independent origins of subgroup Bl + B2 and subgroup B3 metallo-beta-lactamases. *J. Mol. Evol.* 59 (1), 133–141. doi:10.1007/s00239-003-2572-9

Hamrick, J. C., Docquier, J. D., Uehara, T., Myers, C. L., Six, D. A., Chatwin, C. L., et al. (2020). VNRX-5133 (taniborbactam), a broad-spectrum inhibitor of serine- and metallo-β-lactamases, restores activity of cefepime in enterobacterales and *Pseudomonas aeruginosa*. *Antimicrob. Agents Chemother.* 64 (3), 019633–e2019. doi:10.1128/aac.01963-19

Hecker, S. J., Reddy, K. R., Lomovskaya, O., Griffith, D. C., Rubio-Aparicio, D., Nelson, K., et al. (2020). Discovery of cyclic boronic acid QPX7728, an ultrabroad-spectrum inhibitor of serine and metallo-β-lactamases. *J. Med. Chem.* 63 (14), 7491–7507. doi:10.1021/acs.jmedchem.9b01976

Hecker, S. J., Reddy, K. R., Totrov, M., Hirst, G. C., Lomovskaya, O., Griffith, D. C., et al. (2015). Discovery of a cyclic boronic acid β-lactamase inhibitor (RPX7009) with utility vs class A serine carbapenemases. *J. Med. Chem.* 58 (9), 3682–3692. doi:10.1021/acs.jmedchem.5b00127

Heinz, U., Bauer, R., Wommer, S., Meyer-Klaucke, W., Papamichaels, C., Bateson, J., et al. (2003). Coordination geometries of metal ions in d- or l-captopril-inhibited metallo-beta-lactamases. *J. Biol. Chem.* 278 (23), 20659–20666. doi:10.1074/jbc.M212581200

Hernandez Valladares, M., Kiefer, M., Heinz, U., Soto, R. P., Meyer-Klaucke, W., Nolting, H. F., et al. (2000). Kinetic and spectroscopic characterization of native and metal-substituted beta-lactamase from Aeromonas hydrophila AE036. *FEBS Lett.* 467 (2-3), 221–225. doi:10.1016/s0014-5793(00)01102-9

Hinchliffe, P., Tanner, C. A., Krismanich, A. P., Labbé, G., Goodfellow, V. J., Marrone, L., et al. (2018). Structural and kinetic studies of the potent inhibition of metallo-β-lactamases by 6-Phosphonomethylpyridine-2-carboxylates. *Biochemistry* 57 (12), 1880–1892. doi:10.1021/acs.biochem.7b01299

Horsfall, L. E., Izougarhane, Y., Lassaux, P., Selevsek, N., Liénard, B. M. R., Poirel, L., et al. (2011). Broad antibiotic resistance profile of the subclass B3 metallo-β-lactamase GOB-1, a di-zinc enzyme. *FEBS J.* 278 (8), 1252–1263. doi:10.1111/j.1742-4658.2011.08046.x

Hou, C. F. D., Liu, J. W., Collyer, C., Mitić, N., Pedroso, M. M., Schenk, G., et al. (2017). Insights into an evolutionary strategy leading to antibiotic resistance. *Sci. Rep.* 7 (1), 40357. doi:10.1038/srep40357

Hussein, W. M., Fatahala, S. S., Mohamed, Z. M., McGeary, R. P., Schenk, G., Ollis, D. L., et al. (2012). Synthesis and kinetic testing of tetrahydropyrimidine-2-thione and pyrrole derivatives as inhibitors of the metallo-β-lactamase from Klebsiella pneumonia and *Pseudomonas aeruginosa*. *Chem. Biol. Drug Des.* 80 (4), 500–515. doi:10.1111/j.1747-0285.2012.01440.x

Kim, Y., Maltseva, N., Wilamowski, M., Tesar, C., Endres, M., and Joachimiak, A. (2020). Structural and biochemical analysis of the metallo-β-lactamase L1 from emerging pathogen Stenotrophomonas maltophilia revealed the subtle but distinct di-metal scaffold for catalytic activity. *Protein Sci.* 29 (3), 723–743. doi:10.1002/pro.3804

King, D., and Strynadka, N. (2011). Crystal structure of New Delhi metallo-β-lactamase reveals molecular basis for antibiotic resistance. *Protein Sci.* 20 (9), 1484–1491. doi:10.1002/pro.697

Krajnc, A., Brem, J., Hinchliffe, P., Calvopiña, K., Panduwawala, T. D., Lang, P. A., et al. (2019). Bicyclic boronate VNRX-5133 inhibits metallo- and serine-β-lactamases. *J. Med. Chem.* 62 (18), 8544–8556. doi:10.1021/acs.jmedchem.9b00911

Lang Pauline, A., Leissing Thomas, M., Page Malcolm, G. P., Schofield Christopher, J., and Brem, J. (2021). Structural investigations of the inhibition of *Escherichia coli* AmpC β-lactamase by diazabicyclooctanes. *Antimicrob. Agents Chemother.* 65 (2), e02073-20–e02020. doi:10.1128/AAC.02073-20

Lee, J. H., Takahashi, M., Jeon, J. H., Kang, L. W., Seki, M., Park, K. S., et al. (2019). Dual activity of PNGM-1, a metallo-β-lactamase and tRNase Z, pinpoints the evolutionary origin of subclass B3 metallo-β-lactamases. bioRxiv, 575373. doi:10.1101/575373

Lisa, M. N., Hemmingsen, L., and Vila, A. J. (2010). Catalytic role of the metal ion in the metallo-beta-lactamase GOB. *J. Biol. Chem.* 285 (7), 4570–4577. doi:10.1074/jbc.M109.063743

Liu, B., Trout, R. E. L., Chu, G. H., McGarry, D., Jackson, R. W., Hamrick, J. C., et al. (2020). Discovery of taniborbactam (VNRX-5133): A broad-spectrum serine- and metallo-β-lactamase inhibitor for carbapenem-resistant bacterial infections. *J. Med. Chem.* 63 (6), 2789–2801. doi:10.1021/acs.jmedchem.9b01518

McGeary, R. P., Schenk, G., and Guddat, L. W. (2014). The applications of binuclear metallohydrolases in medicine: Recent advances in the design and development of novel drug leads for purple acid phosphatases, metallo-β-lactamases and arginases. *Eur. J. Med. Chem.* 76, 132–144. doi:10.1016/j.ejmech.2014.02.008

McGeary, R. P., Tan, D. T. C., Selleck, C., Monteiro Pedroso, M., Sidjabat, H. E., and Schenk, G. (2017). Structure-activity relationship study and optimisation of 2-aminopyrrole-1-benzyl-4,5-diphenyl-1H-pyrrole-3-carbonitrile as a broad spectrum metallo-β-lactamase inhibitor. *Eur. J. Med. Chem.* 137, 351–364. doi:10.1016/j.ejmech.2017.05.061

Miraula, M., Schenk, G., and Mitić, N. (2016). Promiscuous metallo-β-lactamases: MIM-1 and MIM-2 may play an essential role in quorum sensing networks. *J. Inorg. Biochem.* 162, 366–375. doi:10.1016/j.jinorgbio.2015.12.014

Miraula, M., Whitaker, J. J., Schenk, G., and Mitić, N. (2015). β-Lactam antibiotic-degrading enzymes from non-pathogenic marine organisms: A potential threat to human health. *J. Biol. Inorg. Chem.* 20 (4), 639–651. doi:10.1007/s00775-015-1250-x

Mitić, N., Miraula, M., Selleck, C., Hadler, K. S., Uribe, E., Pedroso, M. M., et al. (2014). Catalytic mechanisms of metallohydrolases containing two metal ions. *Adv. Protein Chem. Struct. Biol.* 97, 49–81. doi:10.1016/bs.apcsb.2014.07.002

Mitić, N., Smith, S. J., Neves, A., Guddat, L. W., Gahan, L. R., and Schenk, G. (2006). The catalytic mechanisms of binuclear metallohydrolases. *Chem. Rev.* 106 (8), 3338–3363. doi:10.1021/cr050318f

Mohamed, M. S., Hussein, W. M., McGeary, R. P., Vella, P., Schenk, G., and Abd El-Hameed, R. H. (2011). Synthesis and kinetic testing of new inhibitors for a metallo-β-lactamase from Klebsiella pneumonia and *Pseudomonas aeruginosa*. *Eur. J. Med. Chem.* 46 (12), 6075–6082. doi:10.1016/j.ejmech.2011.10.030

Mojica, M. F., Bonomo, R. A., and Fast, W. (2016). B1-Metallo-β-Lactamases: Where do we stand? *Curr. Drug Targets* 17 (9), 1029–1050. doi:10.2174/1389450116666151001105622

Mojica, M. F., Rossi, M. A., Vila, A. J., and Bonomo, R. A. (2022). The urgent need for metallo-β-lactamase inhibitors: An unattended global threat. *Lancet Infect. Dis.* 22 (1), e28–e34. doi:10.1016/s1473-3099(20)30868-9

Morán-Barrio, J., González, J. M., Lisa, M. N., Costello, A. L., Peraro, M. D., Carloni, P., et al. (2007). The metallo-beta-lactamase GOB is a mono-Zn(II) enzyme with a novel active site. *J. Biol. Chem.* 282 (25), 18286–18293. doi:10.1074/jbc.M700467200

Morán-Barrio, J., Lisa, M. N., Larrieux, N., Drusin Salvador, I., Viale Alejandro, M., Moreno Diego, M., et al. (2016). Crystal structure of the metallo-β-lactamase GOB in the periplasmic dizinc form reveals an unusual metal site. *Antimicrob. Agents Chemother.* 60 (10), 6013–6022. doi:10.1128/AAC.01067-16

Muok, A. R., Deng, Y., Gumerov, V. M., Chong, J. E., DeRosa, J. R., Kurniyati, K., et al. (2019). A di-iron protein recruited as an Fe[II] and oxygen sensor for bacterial chemotaxis functions by stabilizing an iron-peroxy species. *Proc. Natl. Acad. Sci.* 116 (30), 14955–14960. doi:10.1073/pnas.1904234116

Palacios, A. R., Rossi, M. A., Mahler, G. S., and Vila, A. J. (2020). Metallo-β-Lactamase inhibitors inspired on snapshots from the catalytic mechanism. *Biomolecules* 10 (6), 854. doi:10.3390/biom10060854

Paul, T. J., Schenk, G., and Prabhakar, R. (2018). Formation of catalytically active binuclear center of glycerophosphodiesterase: A molecular dynamics study. *J. Phys. Chem. B* 122 (22), 5797–5808. doi:10.1021/acs.jpcb.8b02046

Pedroso, M. M., Selleck, C., Enculescu, C., Harmer, J. R., Mitić, N., Craig, W. R., et al. (2017). Characterization of a highly efficient antibiotic-degrading metallo-β-lactamase obtained from an uncultured member of a permafrost community. *Metallomics* 9 (8), 1157–1168. doi:10.1039/c7mt00195a

Pedroso, M. M., Waite, D. W., Melse, O., Wilson, L., Mitić, N., McGeary, R. P., et al. (2020). Broad spectrum antibiotic-degrading metallo-β-lactamases are phylogenetically diverse. *Protein & Cell.* 11 (8), 613–617. doi:10.1007/s13238-020-00736-4

Pemberton, O. A., Jaishankar, P., Akhtar, A., Adams, J. L., Shaw, L. N., Renslo, A. R., et al. (2019). Heteroaryl phosphonates as noncovalent inhibitors of both serine- and metallocarbapenemases. *J. Med. Chem.* 62 (18), 8480–8496. doi:10.1021/acs.jmedchem.9b00728

Perez-Garcia, P., Kobus, S., Gertzen, C. G. W., Hoeppner, A., Holzscheck, N., Strunk, C. H., et al. (2021). A promiscuous ancestral enzyme´s structure unveils protein variable regions of the highly diverse metallo-β-lactamase family. *Commun. Biol.* 4 (1), 132. doi:10.1038/s42003-021-01671-8

Pettinati, I., Brem, J., Lee, S. Y., McHugh, P. J., and Schofield, C. J. (2016). The chemical Biology of human metallo-β-lactamase fold proteins. *Trends Biochem. Sci.* 41 (4), 338–355. doi:10.1016/j.tibs.2015.12.007

Rodríguez, M. M., Herman, R., Ghiglione, B., Kerff, F., D'Amico González, G., Bouillenne, F., et al. (2017). Crystal structure and kinetic analysis of the class B3 di-zinc metallo-β-lactamase LRA-12 from an Alaskan soil metagenome. *PLOS ONE* 12 (7), e0182043. doi:10.1371/journal.pone.0182043

Schrödinger, L. L. C. (2015). The PyMOL molecular graphics system. Version 1.8.

Selleck, C., Larrabee, J. A., Harmer, J., Guddat, L. W., Mitić, N., Helweh, W., et al. (2016). AIM-1: An antibiotic-degrading metallohydrolase that displays mechanistic flexibility. *Chem. – A Eur. J.* 22 (49), 17704–17714. doi:10.1002/chem.201602762

Selleck, C., Pedroso, M. M., Wilson, L., Krco, S., Knaven, E. G., Miraula, M., et al. (2020). Structure and mechanism of potent bifunctional β-lactam- and homoserine lactone-degrading enzymes from marine microorganisms. *Sci. Rep.* 10 (1), 12882. doi:10.1038/s41598-020-68612-z

Sharma, G., Hu, Q., Jayasinghe-Arachchige, V. M., Paul, T. J., Schenk, G., and Prabhakar, R. (2019). Investigating coordination flexibility of glycerophosphodiesterase (GpdQ) through interactions with mono-di-and triphosphoester (NPP, BNPP, GPE, and paraoxon) substrates. *Phys. Chem. Chem. Phys.* 21 (10), 5499–5509. doi:10.1039/C8CP07031H

Sharma, G., Jayasinghe-Arachchige, V. M., Hu, Q., Schenk, G., and Prabhakar, R. (2020). Effect of chemically distinct substrates on the mechanism and reactivity of a highly promiscuous metallohydrolase. *ACS Catal.* 10 (6), 3684–3696. doi:10.1021/acscatal.9b04847

Sidjabat, H. E., Gien, J., Kvaskoff, D., Ashman, K., Vaswani, K., Reed, S., et al. (2018). The use of SWATH to analyse the dynamic changes of bacterial proteome of carbapanemase-producing *Escherichia coli* under antibiotic pressure. *Sci. Rep.* 8 (1), 3871. doi:10.1038/s41598-018-21984-9

Simm, A. M., Higgins, C. S., Carenbauer, A. L., Crowder, M. W., Bateson, J. H., Bennett, P. M., et al. (2002). Characterization of monomeric L1 metallo-beta -lactamase and the role of the N-terminal extension in negative cooperativity and antibiotic hydrolysis. *J. Biol. Chem.* 277 (27), 24744–24752. doi:10.1074/jbc.M201524200

Tan, S. H., Normi, Y. M., Leow, A. T. C., Salleh, A. B., Murad, A. M. A., Mahadi, N. M., et al. (2017). Danger lurking in the "unknowns": Structure-to-function studies of hypothetical protein Bleg1_2437 from Bacillus lehensis G1 alkaliphile revealed an evolutionary divergent B3 metallo-beta-lactamase. *J. Biochem.* 161 (2), 167–186. doi:10.1093/jb/mvw058

Tehrani, K., and Martin, N. I. (2017). Thiol-containing metallo-β-lactamase inhibitors resensitize resistant gram-negative bacteria to meropenem. *ACS Infect. Dis.* 3 (10), 711–717. doi:10.1021/acsinfecdis.7b00094

Thaden, J. T., Pogue, J. M., and Kaye, K. S. (2005). Role of newer and re-emerging older agents in the treatment of infections caused by carbapenem-resistant Enterobacteriaceae. *Virulence* 8 (4), 403–416. doi:10.1080/21505594.2016.1207834

Ullah, J. H., Walsh, T. R., Taylor, I. A., Emery, D. C., Verma, C. S., Gamblin, S. J., et al. (1998). The crystal structure of the L1 metallo-β-lactamase from Stenotrophomonas maltophilia at 1.7 å resolution 1 1Edited by K. Nagai. *J. Mol. Biol.* 284 (1), 125–136. doi:10.1006/jmbi.1998.2148

Vašková, J., Kočan, L., Vaško, L., and Perjési, P. (2023). Glutathione-related enzymes and proteins: A review. *Molecules* 28 (3), 1447. doi:10.3390/molecules28031447

Vella, P., Miraula, M., Phelan, E., Leung, E. W. W., Ely, F., Ollis, D. L., et al. (2013). Identification and characterization of an unusual metallo-β-lactamase from Serratia proteamaculans. *JBIC J. Biol. Inorg. Chem.* 18 (7), 855–863. doi:10.1007/s00775-013-1035-z

Wachino, J. I., Jin, W., Kimura, K., Kurosaki, H., Sato, A., and Arakawa, Y. (2020). Sulfamoyl heteroarylcarboxylic acids as promising metallo-β-lactamase inhibitors for controlling bacterial carbapenem resistance. *mBio* 11 (2), 031444–e3219. doi:10.1128/mBio.03144-19

Wang, D. Y., Abboud, M. I., Markoulides, M. S., Brem, J., and Schofield, C. J. (2016). The road to avibactam: The first clinically useful non-β-lactam working somewhat like a β-lactam. *Future Med. Chem.* 8 (10), 1063–1084. doi:10.4155/fmc-2016-0078

Wang, G., Li, R., Li, S., and Jiang, J. (2010). A novel hydrolytic dehalogenase for the chlorinated aromatic compound chlorothalonil. *J. Bacteriol.* 192 (11), 2737–2745. doi:10.1128/jb.01547-09

Wilson, L. A., Knaven, E. G., Morris, M. T., Monteiro Pedroso, M., Schofield, C. J., Brück, T. B., et al. (2021). Kinetic and structural characterization of the first B3 metallo-β-lactamase with an active-site glutamic acid. *Antimicrob. Agents Chemother.* 65 (10), 00936211–e100921. doi:10.1128/AAC.00936-21

World Health Organization (2014). *Antimicrobial resistance: Global report on surveillance.* Geneva: World Health Organization.

Yamaguchi, Y., Kato, K., Ichimaru, Y., Jin, W., Sakai, M., Abe, M., et al. (2021). Crystal structures of metallo-β-lactamase (IMP-1) and its D120E mutant in complexes with citrate and the inhibitory effect of the benzyl group in citrate monobenzyl ester. *J. Med. Chem.* 64 (14), 10019–10026. doi:10.1021/acs.jmedchem.1c00308

Yang, K. W., Feng, L., Yang, S. K., Aitha, M., LaCuran, A. E., Oelschlaeger, P., et al. (2013). New β-phospholactam as a carbapenem transition state analog: Synthesis of a broad-spectrum inhibitor of metallo-β-lactamases. *Bioorg Med. Chem. Lett.* 23 (21), 5855–5859. doi:10.1016/j.bmcl.2013.08.098

Yang, Y., Yan, Y. H., Schofield, C. J., McNally, A., Zong, Z., and Li, G. B. (2023). Metallo-β-lactamase-mediated antimicrobial resistance and progress in inhibitor discovery. *Trends Microbiol.* doi:10.1016/j.tim.2023.01.013

Yong, D., Toleman Mark, A., Bell, J., Ritchie, B., Pratt, R., Ryley, H., et al. (2012). Genetic and biochemical characterization of an acquired subgroup B3 metallo-β-lactamase gene, blaAIM-1, and its unique genetic context in *Pseudomonas aeruginosa* from Australia. *Antimicrob. Agents Chemother.* 56 (12), 6154–6159. doi:10.1128/AAC.05654-11

Yum, J. H., Lee, E. Y., Hur, S. H., Jeong, S. H., Lee, H., Yong, D., et al. (2010). Genetic diversity of chromosomal metallo-beta-lactamase genes in clinical isolates of Elizabethkingia meningoseptica from Korea. *J. Microbiol.* 48 (3), 358–364. doi:10.1007/s12275-010-9308-5

Zhou, H., Guo, W., Zhang, J., Li, Y., Zheng, P., and Zhang, H. (2019). Draft genome sequence of a metallo-β-lactamase (bla(AIM-1))-producing *Klebsiella pneumoniae* ST1916 isolated from a patient with chronic diarrhoea. *J. Glob. Antimicrob. Resist* 16, 165–167. doi:10.1016/j.jgar.2019.01.010

frontiers | Frontiers in Chemistry

TYPE Opinion
PUBLISHED 11 July 2023
DOI 10.3389/fchem.2023.1205280

OPEN ACCESS

EDITED BY
Aleksandar Kondinski,
University of Cambridge, United Kingdom

REVIEWED BY
Bingan Lu,
Hunan University, China

*CORRESPONDENCE
Mei Ni,
nimei@cfri.edu.cn

RECEIVED 14 April 2023
ACCEPTED 26 June 2023
PUBLISHED 11 July 2023

CITATION
Ni M, Zhou L, Liu Y and Ni R (2023), Advances in the synthesis and applications of porous carbon materials. *Front. Chem.* 11:1205280. doi: 10.3389/fchem.2023.1205280

Advances in the synthesis and applications of porous carbon materials

Mei Ni[1]*, Lei Zhou[2,3], Yancen Liu[1] and Runtao Ni[4]

[1]Department of Basic Courses, China Fire and Rescue Institute, Beijing, China, [2]Yangtze Delta Region Institute, University of Electronic Sciences and Technology of China, Huzhou, China, [3]Institute of Fundamental and Frontiers Sciences, University of Electronic Sciences and Technology of China, Chengdu, China, [4]Administration for Market Regulation of Zhengding, Shijiazhuang, China

KEYWORDS

porous carbon materials, synthesis, adsorption, energy storage, catalysis

1 Introduction

The progress of human civilization depends on the development of all kinds of materials. The establishment of modern science has led to the rapid development of synthetic materials. However, increasing energy demand and environmental pollution urgently require the search for new materials to solve the energy and environmental crisis.

Carbon is an extremely abundant element in nature and provides the basis for all life on Earth (Li et al., 2008; Toth et al., 2016). The carbon atom has six electrons outside the nucleus, and its outermost electron arrangement is $2s^2 2p^2$, which shows a strong ability to form covalent bonds (Krueger, 2010). Porous carbon materials have advantages such as chemical stability, low density, high thermal conductivity, high electrical conductivity, and high mechanical strength (Gallo, 2017). Porous carbon materials also have a large specific surface area, adjustable pore size, and functional groups and can be prepared from a wide range of precursors at relatively low cost.

In recent years, a large number of researchers have been devoted to the synthesis and application of porous carbon (Ang, 2019; Liu, 2019; Liu, 2020a; Hwang, 2020; Raj, 2021). Depending on the pore size distribution, the pore structure of carbon materials can be divided into three categories, namely, micropores (pore size <2 nm), mesopores (2 nm < pore size <50 nm), and macropores (pore size >50 nm) (Vu, 2012). The size of the pore structure of porous carbon materials has a significant impact on their performance in practical applications.

Due to these advantages, carbon materials are widely used in the fields of adsorption (He, 2019), catalysis (Dong et al., 2020), and energy storage (Peng, 2019). This paper mainly introduces the synthesis and application of carbon materials and describes the main improvement ideas for current carbon materials (Figure 1). Importantly, the future direction of carbon materials is further discussed.

2 Synthesis methods of carbon materials

2.1 Activation method

Many designs are currently focused on how to increase the specific surface area of carbon materials, which include heat treatment, physical activation, and chemical activation. The physical activation method refers to the use of CO_2, water vapor, O_2, and other gases as activation media for the preparation of activated carbon under high-temperature conditions (Sevilla, 2014; Rashidi, 2019; Ma, 2020). The CO_2 molecules move at a slower rate thermally compared to water vapor activation, resulting in a larger specific surface area and a higher

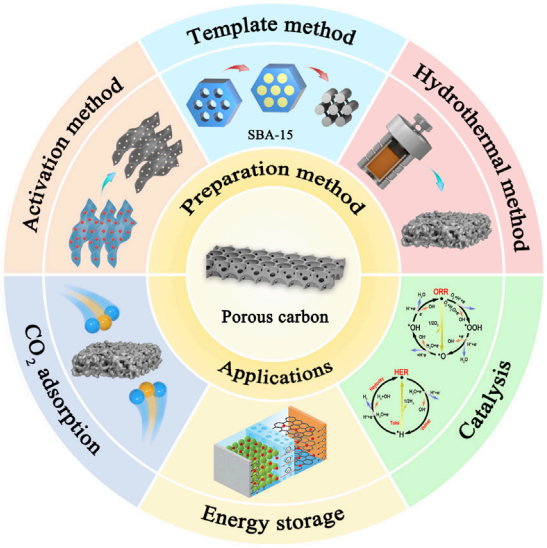

FIGURE 1
Schematic illustration of the synthesis and application of porous carbon materials.

volume of microporous material. However, the small size and low activation of the activating molecules with a single activator result in a large number of blind pores and an ineffective specific surface area of the carbon material (Kim, 2017).

Chemical activation is the reaction of chemical reagents with the carbon source during pyrolysis, commonly known as KOH, NaOH, H_3PO_4, and $ZnCl_2$ (Molina, 1995; Lillo, 2003). The main factors influencing the preparation of porous carbon materials by chemical activation include the composition of the precursor material, the activation temperature, the activator, and the impregnation ratio (Maia, 2018). A high impregnation ratio (raw material/activator) allows the formation of activated carbon with a high specific surface area, usually between 1:1 and 5:1 (Rashidi, 2016). KOH is the most commonly used activator, and the pore structure of the prepared material is well developed. Prasankumar converted Tasmanian blue gum tree bark into activated carbons through a simple KOH activationand carbonization method. The generated activated carbons have a hierarchically connected mesoporous structure and a surface area of 971 $m^2 g^{-1}$ with an average pore size of 2.2 nm (Thibeorchews, 2022).

Activated carbon is mainly derived from various organic precursors rich in carbon (bitumen, coal, polymers, etc.). Due to the environmentally unfriendly nature of fossil fuels, a large number of activated carbons prepared from biomass as precursors have attracted a great deal of attention in recent years. They are prepared from natural substances such as walnut shell powder (Pang, 2016; Jiang, 2022), banana stem fibers (Taer, 2021), American poplar fruit (Kumar, 2020), bamboo (Khuong, 2022), castor seed (Neme, 2022), and lotus seed shell (Hu, 2018), synthesizing activated carbons with a high specific surface area.

2.2 Template method

Specific surface area and pore size distribution are key factors that affect the properties of carbon materials. The template method is considered to be an effective method for achieving controlled mesoporous structures. The template method can be divided into the hard template method and the soft-template method. The former involves thorough mixing of the hard template with the precursor materials, carbonization, and subsequent removal of the template. The synthesis of porous carbon materials using various structural silica templates, such as SBA-15 (Yan, 2020) and 3D cubic KIT-6 (Karthikeyan, 2022), has been reported in recent years. The pore size and pore volume of the obtained porous carbon materials can be systematically adjusted by changing the size of the template (Sang, 2011). In addition, porous carbon can also be prepared using $CaCO_3$, MgO, $Mg(OH)_2$, magnesium acetate, magnesium citrate, or magnesium gluconate as templates (Wei, 2019; Zhou, 2020), which can be subsequently removed with dilute hydrochloric acid. Liu found a new solvent-free method for the preparation of mesoporous carbon using mesoporous silica KIT-6 as a hard template for the preparation of mesoporous carbon, overcoming the disadvantages of the conventional filling process (Liu, 2019).

The soft-template method involves the self-assembly and co-condensation of a soft template with a precursor to produce a material with a specific structure (Zhang, 2009). The advantages of the soft-template method are that the template does not require subsequent processing and the experimental steps are simple and environmentally friendly. Soft templates include various triblock copolymers, such as F127 and F108. Peng prepared a unique hierarchical porous N-, O-, and S-enriched carbon foam via a combination of a soft-template method, freeze-drying, and chemical etching (Peng, 2019). The structure offers not only an ultra-high specific surface area but also a network of multiple-scale channels.

2.3 Hydrothermal carbonization method

Hydrothermal carbonization is a process in which carbon precursors are gradually hydrolyzed, dehydrated, condensed, and aromatized under high temperature and pressure using water as a solvent and eventually converted into carbon materials. This method is milder and allows for autonomous control of product morphology and better regulation of pore size distribution. In the hydrothermal carbonization process, there are many factors that influence the properties of the carbon material, such as the hydrothermal temperature, the rate of temperature increase, and the holding time. The specific surface area of the carbon material produced is generally low, and the pores are not well developed, so it is often used in combination with activation to obtain porous carbon materials with a high specific surface area.

Liu prepared nitrogen-doped porous carbon materials with a specific surface area of up to 2,864 $m^2 g^{-1}$ and a total pore volume of 1.6 $cm^3 g^{-1}$ by hydrothermal treatment of biomass raw materials and the addition of an activator, KOH, to the aqueous solution, followed by high-temperature pyrolysis and activation (Liu, 2016). Veltri prepared a nitrogen–oxygen co-doped biomass-based carbon material by hydrothermal charring of orange juice with a specific surface area of 1,725 $m^2 g^{-1}$ (Veltri, 2020). The pore structure tended to be reasonable, and the mass fractions of nitrogen and oxygen were as high as 5.65% and 5.38%

3 Applications

3.1 Application of porous carbons in adsorption

The International Panel on Climate Change (IPCC) report shows that the atmospheric concentrations of greenhouse gases (mainly CO_2) continue to increase (Lunn, 2021). Porous carbon has a wide range of sources, stable physical and chemical properties, and fast adsorption and desorption rates. It is a kind of CO_2 adsorption material with great potential for application.

The carbonized coconut shell was modified with urea at 350°C and activated with K_2CO_3 to produce a nitrogen-doped carbon material with good CO_2 adsorption properties (Yue, 2018). He used polydopamine and melamine as carbon sources and $CaCO_3$ nanoparticles as templating agents to synthesize porous carbon materials, which showed high CO_2 adsorption capacity and selectivity at room temperature (He, 2019). Pluronic P123 as a soft template was polymerized with D-glucose by the hydrothermal method and activated by CO_2 to produce a porous adsorbent with high microporous content (Nicolae, 2020). The CO_2/N_2 adsorption selectivity of 9 was achieved at 6.00 mmol g^{-1}.

3.2 Application of porous carbon in energy storage

In order to mitigate climate change and environmental pollution caused by excessive use of fossil energy, clean and sustainable alternative energy sources are urgently needed around the world (Weigelt, 2016; Azcárate, 2017). In the past decades, a large number of researchers have been devoted to the development of new types of energy storage (Gondal, 2017; McKone, 2017). Carbon is widely used in energy storage and has the advantages of a large specific surface area, well-developed pores, good electrical conductivity, good electrolyte wetting, high chemical stability, and a wide potential window (Luo. 2020; Kim, 2021). The electrochemical properties of porous carbon electrode materials are a key factor affecting their energy storage properties.

Porous carbon materials are often used as anodes in batteries due to their good electrolyte wetting. The formation of uniform and elastic solid electrolyte interphase (SEI) or the use of tailored electrolytes can improve the stability of the SEI on the carbon surface, thereby increasing the safety and cyclability of the batteries (Fan, 2023; Gu, 2023). The porous carbon used as an electrode in a supercapacitor achieves a high specific capacitance and superior rate capability. Sun prepared nitrogen and sulfur co-doped carbon materials by chemical vapor deposition using magnesium hydroxide as a template, which had a large specific surface area (674 m^2 g^{-1}) and a porous interleaved network with a high level of heteroatom doping (Miao, 2019). As an anode material for Li-ion batteries, it shows a very high reversible capacity and excellent cycling stability.

3.3 Application of porous carbons in catalysis

The development of highly selective, catalytic, stable, green, and economically accessible catalysts is extremely important in industrial production. Carbon materials are often used as catalysts in CO_2 electroreduction, oxygen reduction reactions (ORRs), and hydrogen evolution reactions (HERs) due to their abundance of sources and their excellent chemical properties.

Chen proposed an NH_3 heat treatment strategy to completely remove pyrrole nitrogen and pyridine nitrogen dopants, and the prepared porous carbon material could efficiently electroreduce CO_2, achieving a CO Faraday efficiency of 95.2% at a current density of −2.84 mA cm^{-2} (Dong et al., 2020). Saravanan treated peanut shells using a simple pyrolysis technique assisted by chemical activation and explored the HER properties of peanut shell-derived carbon nanosheets in acidic media (Saravanan, 2019). The nitrogen-doped carbon nanosheets with a high specific surface area and a large number of active sites showed excellent HER catalytic activity in aqueous electrolysis devices (Liu, 2020b). Lai synthesized two-dimensional porous disordered-layer carbon nanowebs with a large number of N-doped C defects using an aromatic ring as the carbon source and urea as the nitrogen source in a novel molecular design strategy (Lai, 2020). It was shown that carbon edge defects doped with graphitic N atoms could lead to materials exhibiting excellent ORR catalytic properties.

4 Discussions

Due to their high specific surface area, tunable physicochemical properties, low cost, and accessibility, porous carbon materials have shown a wide range of applications in areas such as catalysts, adsorbents, and energy storage. Previously, various methods were used to produce porous carbon materials with different pore structures, but most of the preparation was carried out in the laboratory with complex methods and processes, which made it difficult to meet the requirements of industrial preparation. Moreover, in order to regulate and optimize the structure of porous carbon materials at a more microscopic level and to point the way to the design and preparation of materials, further research on the mechanisms of action of carbon materials in their applications is needed. Thus, with the increasing energy shortage and environmental pollution, the further enhancement of the development of simple, clean, and cost-effective porous carbon materials could make a huge difference in a wider range of areas.

Author contributions

MN conceived and designed the entire review and wrote the manuscript. LZ, YL, and RN edited the manuscript. All authors contributed to the article and approved the submitted version.

Funding

This work was supported by the Sichuan Science and Technology Program (No. 2023NSFSC0972).

Conflict of interest

The authors declare that the research was conducted in the absence of any commercial or financial relationships that could be construed as a potential conflict of interest.

Publisher's note

References

Ang, F., Wang, C. Z., Pei, F., Cui, J. Q., Fang, X. L., and Zheng, N. F. (2019). Recent advances in hollow porous carbon materials for lithium-sulfur batteries. *Small* 15, 1804786. doi:10.1002/smll.201804786

Azcárate, C., Mallor, F., and Mateo, P. (2017). Tactical and operational management of wind energy systems with storage using a probabilistic forecast of the energy resource. *Renew. Energy* 102, 102445–102456. doi:10.1016/j.renene.2016.10.064

Dong, Y., Zhang, Q., Tian, Z., Li, B., Yan, W., Wang, S., et al. (2020). Ammonia thermal treatment toward topological defects in porous carbon for enhanced carbon dioxide electroreduction. *Adv. Mater.* 32 (28), 2001300. doi:10.1002/adma.202001300

Fan, L., Xie, H., Hu, Y., Cai, Z., Apparao, M. R., Zhou, J., et al. (2023). A tailored electrolyte for safe and durable potassium ion batteries. *Energy Environ. Sci.* 16, 305–315. doi:10.1039/D2EE03294E

Gallo, S. C., Li, X. Y., Fütterer, K., Charitidis, C. A., and Dong, H. (2017). Carbon nanofibers functionalized with active screen plasma-deposited metal nanoparticles for electrical energy storage devices. *ACS Appl. Mater. Interfaces* 9, 23195–23201. doi:10.1021/acsami.7b05567

Gondal, I. A., Masood, S. A., and Amjad, M. (2017). Review of geothermal energy development efforts in Pakistan and way forward. Renew. *Sustain. Energy Rev.* 71, 687–696. doi:10.1016/j.rser.2016.12.097

Gu, M., Apparao, M. R., Zhou, J., and Lu, B. (2023). *In situ* formed uniform and elastic SEI for high-performance batteries. *Energy Environ. Sci.* 16, 1166–1175. doi:10.1039/D2EE04148K

He, X., Liu, J., Jiang, Y., Yassen, M., Guan, H., Sun, J., et al. (2019). 'Useful'template synthesis of N-doped acicular hollow porous carbon/carbon-nanotubes for enhanced capture and selectivity of CO_2. *Chem. Eng. J.* 361, 278–285. doi:10.1016/j.cej.2018.12.031

Hu, L., Zhu, Q., Wu, Q., Li, D., An, Z., and Xu, B. (2018). Natural biomass-derived hierarchical porous carbon synthesized by an *in situ* hard template coupled with NaOH activation for ultrahigh rate supercapacitors. *ACS Sustain. Chem. Eng.* 6, 13949–13959. doi:10.1021/acssuschemeng.8b02299

Hwang, J., Aleksander, E., Ralph, F., Joanna, G., Bernhard, V. K., and Schmidt, J. (2020). Controlling the morphology of metal–organic frameworks and porous carbon materials: Metal oxides as primary architecture-directing agents. *Chem. Soc. Rev.* 49, 3348–3422. doi:10.1039/c9cs00871c

Jiang, Y., Chen, J., Zeng, Q., Zou, Z., Li, J., Zeng, L., et al. (2022). Facile method to produce sub-1 nm pore-rich carbon from biomass wastes for high performance supercapacitors. *J. Colloid Interface Sci.* 612, 213–222. doi:10.1016/j.jcis.2021.12.144

Karthikeyan, G. G., Ramani, V., Muthusankar, E., and Pandurangan, A. (2022). Simple and efficient CVD synthesis of graphitic P-doped 3D cubic ordered mesoporous carbon at low temperature with excellent supercapacitor performance. *Adv. Powder Technol.* 33 (3), 103439. doi:10.1016/j.apt.2022.103439

Khuong, D. A., Trinh, K. T., Nakaoka, Y., Tsubota, T., Tashima, D., Nguyen, H. N., et al. (2022). The investigation of activated carbon by K_2CO_3 activation: Micropores- and macropores-dominated structure. *Chemosphere* 299, 134365. doi:10.1016/j.chemosphere.2022.134365

Kim, D., Kil, H., Nakabayashi, K., Yoon, S., and Miyawaki, J. (2017). Structural elucidation of physical and chemical activation mechanisms based on the microdomain structure model. *Carbon* 114, 98–105. doi:10.1016/j.carbon.2016.11.082

Kim, J., Park, J., Lee, J., Lim, W., Jo, C., and Lee, J. (2021). Biomass-derived P,N self doped hard carbon as bifunctional oxygen electrocatalyst and anode material for seawater batteries. *Adv. Funct. Mater.* 31 (22), 2010882. doi:10.1002/adfm.202010882

Krueger, A. (2010). *Carbon material and nanotechnology*. Hoboken, New Jersey, United States: John Wiley & Sons.

Kumar, T. R., Raja, A., Pan, Z., Pan, J., and Sun, Y. A. (2020). Tubular-like porous carbon derived from waste American poplar fruit asadvanced electrode material for high-performance supercapacitor. *J. Energy Storage* 32, 101903–101914. doi:10.1016/j.est.2020.101903

Lai, Q. X., Zheng, J., Tang, Z. M., Bi, D., Zhao, J. X., and Liang, Y. Y. (2020). Optimal configuration of N-doped carbon defects in 2D turbostratic carbon nanomesh for advanced oxygen reduction electrocatalysis. *Angew. Chem. Int. Ed.* 59, 11999–12006. doi:10.1002/ange.202000936

Li, X., Zhang, G., Bai, X., Sun, X., Wang, X., Wang, E., et al. (2008). Highly conducting graphene sheets and Langmuir-Blodgett films. *Nat. Nanotech* 3, 538–542. doi:10.1038/nnano.2008.210

Lillo, R. M., Cazorla, A. D., and Linares, S. A. (2003). Understanding chemical reactions between carbons and NaOH and KOH: An insight into the chemical activation mechanism. *Carbon* 41 (2), 267–275. doi:10.1016/S0008-6223(02)00279-8

Liu, B., Zhou, X. H., Chen, H. B., Liu, Y. J., and Li, H. M. (2016). Promising porous carbons derived from lotus seedpods with outstanding supercapacitance performance. *Electrochimica Acta* 208, 55. doi:10.1016/j.electacta.2016.05.020

Liu, H. G., Wu, S. Q., Tian, N., Yan, F. X., You, C. Y., and Yang, Y. (2020a). Carbon foams: 3D porous carbon materials holding immense potential. *J. Mater. Chem. A* 8, 23699–23723. doi:10.1039/D0TA08749A

Liu, S., Wang, Z., Han, T., Fei, T., Zhang, T., and Zhang, H. Y. (2019). Solvent-free synthesis of mesoporous carbon employing KIT-6 as hard template for removal of aqueous Rhodamine B. *J. Porous Mater.* 26 (4), 941–950. doi:10.1007/s10934-018-0692-2

Liu, Z., Zhou, Q. L., Zha, B., Li, S. L., Xiong, Y. Q., and Xu, W. J. (2020b). Few-layer N-doped porous carbon nanosheets derived from corn stalks as a bi-functional electrocatalyst for overall water splitting. *Fuel* 280, 118567. doi:10.1016/j.fuel.2020.118567

Lunn, J., and Peeva, N. (2021). Communications in the IPCC's sixth assessment report cycle. *Clim. Change* 169 (1), 1–10. doi:10.1007/s10584-021-03233-7

Luo, X., Yang, Q., Dong, Y., Huang, X., Kong, D., Wang, B., et al. (2020). Maximizing pore and heteroatom utilization within N, P codoped polypyrrole-derived carbon nanotubes for high performance supercapacitors. *J. Mater. Chem. A* 8 (34), 17558–17567. doi:10.1039/D0TA06238C

Ma, M., Ying, H., Cao, F., Wang, Q., and Ai, N. (2020). Adsorption of Congo red on mesoporous activated carbon prepared by CO_2 physical activation. *Chin. J. Chem. Eng.* 28 (4), 1069–1076. doi:10.1016/j.cjche.2020.01.016

Maia, D., Oliveira, D., Nazzarro, M., Sapag, K., Lopez, R., Lucena, S., et al. (2018). CO_2 gas-adsorption calorimetry applied to the study of chemically activated carbons. *Chem. Eng. Res. Des.* 136, 753–760. doi:10.1016/j.cherd.2018.06.034

McKone, J. R., DiSalvo, F. J., and Abruña, H. D. (2017). Solar energy conversion, storage, and release using an integrated solar-driven redox flow battery. *J. Mater. Chem. A* 5, 5362–5372. doi:10.1039/C7TA00555E

Miao, X., Sun, D. F., Zhou, X. Z., and Lei, Z. Q. (2019). Designed formation of nitrogen and sulfur dual-doped hierarchically porous carbon for long-life lithium and sodium ion batteries. *Chem. Eng. J.* 364, 208–216. doi:10.1016/j.cej.2019.01.158

Molina, S. M., Rodriguez, R. F., Caturla, F., and Selles, M. (1995). Porosity in granular carbons activated with phosphoric acid. *Carbon* 33 (8), 1105–1113. doi:10.1016/0008-6223(95)00059-M

Neme, I., Gonfa, G., and Masi, C. (2022). Preparation and characterization of activated carbon from castor seed hull by chemical activation with H_3PO_4. *Results Mater* 15, 100304. doi:10.1016/j.rinma.2022.100304

Nicolae, S. A., Szilágyi, P. Á., and Titirici, M. M. (2020). Soft templating production of porous carbon adsorbents for CO_2 and H_2S capture. *Carbon* 169, 193–204. doi:10.1016/j.carbon.2020.07.064

Pang, L. Y., Zou, B., Han, X., Cao, L. Y., Wang, W., and Guo, Y. P. (2016). One-step synthesis of high-performance porous carbon from corn starch for supercapacitor. *Mater. Lett.* 184, 88–91. doi:10.1016/j.matlet.2016.07.147

Peng, H., Yao, B., Wei, X., Liu, T., Kou, T., Xiao, P., et al. (2019). Pore and heteroatom engineered carbon foams for supercapacitors. *Adv. Energy Mater.* 9, 1803665. doi:10.1002/aenm.201803665

Raj, C., Manikandan, R., Rajesh, M., Sivakumar, P., Jung, H., Das, S., et al. (2021). Corn husk mesoporous activated carbon electrodes and seawater electrolyte: The sustainable sources for assembling retainable supercapacitor module. *J. Power Sources* 490, 229518. doi:10.1016/j.jpowsour.2021.229518

Rashidi, N. A., and Yusup, S. (2019). Production of palm kernel shell-based activated carbon by direct physical activation for carbon dioxide adsorption. *Environ. Sci. Pollut. Res.* 26 (33), 33732–33746. doi:10.1007/s11356-018-1903-8

Rashidi, N., and Yusup, S. (2016). An overview of activated carbons utilization for the post-combustion carbon dioxide capture. *J. CO_2 Util.* 13, 1–16. doi:10.1016/j.jcou.2015.11.002

Sang, L. C., Vinu, A., and Coppens, M. O. (2011). Ordered mesoporous carbon with tunable, unusually large pore size and well-controlled particle morphology. *J. Mater. Chem.* 21 (20), 7410–7417. doi:10.1039/C1JM10683J

Saravanan, K., Peabu, N., Sasidharanmand Maduraiveeran, G. (2019). Nitrogen-self doped activated carbon nanosheets derived from peanut shells for enhanced hydrogen evolution reaction. *Appl. Surf. Sci.* 489, 725–733. doi:10.1016/j.apsusc.2019.06.040

Sevilla, M., and Mokaya, R. (2014). Energy storage applications of activated carbons: Supercapacitors and hydrogen strorage. *Energy & Environ. Sci.* 7 (4), 1250–1280. doi:10.1039/C3EE43525C

Taer, E., Afdal, Y. D., Amri, A., Awitdrus., Rika, T., Apriwandi, et al. (2021). The synthesis of activated carbon made from banana stem ffbers as the supercapacitor electrodes. *Mater. Today Proc.* 44, 3346–3349. doi:10.1016/j.matpr.2020.11.645

Thibeorchews, P., Devashish, S., Sohini, B., Kaaviah, M., Ram, M., Mata, M., et al. (2022). Biomass derived hierarchical porous carbon for supercapacitor application and dilute stream CO_2 capture. *Carbon* 199 (31), 249–257. doi:10.1016/j.carbon.2022.07.057

Toth, P. S., Velický, M., Bissett, M. A., Slater, T. J. A., Savjani, N., Aminu, K. R., et al. (2016). Asymmetric MoS_2/graphene/metal sandwiches: Preparation, characterization, and application. *Adv. Mater* 28, 8256–8264. doi:10.1002/adma.201600484

Veltri, F., Alessandro, F., Scarcello, A., Beneduci, A., Polanco, M., Perez, D., et al. (2020). Porous carbon materials obtained by the hydrothermal carbonization of orange juice. *Nanomaterials* 10 (4), 655. doi:10.3390/nano10040655

Vu, A., Qian, Y., and Stein, A. (2012). Porous electrode materials for lithium-ion batteries-how to prepare them and what makes them special. *Adv. Energy Mater.* 2, 1056–1085. doi:10.1002/aenm.201200320

Wei, F., Zhang, H., He, X., Ma, H., Dong, S., Xie, X., et al. (2019). Synthesis of porous carbons from coal tar pitch for high-performance supercapacitors. *New Carbon Mater.* 34 (2), 132–138. doi:10.1016/S1872-5805(19)60006-5

Weigelt, C., and Shittu, E. (2016). Competition, regulatory policy, and firms' resource investments: The case of renewable energy technologies. *Acad. Manag. J.* 59 (2), 678–704. doi:10.5465/amj.2013.0661

Yan, S., Tang, C., Yang, Z., Wang, X., Zhang, H., Liu, S., et al. (2020). Hierarchical porous electrospun carbon nanofibers with nitrogen doping as binder-free electrode for supercapacitor. *J. Mater. Sci. Mater. Electron.* 31 (19), 16247–16259. doi:10.1007/s10854-020-04173-1

Yue, L. M., Xia, Q. Z., Wang, L. W., Wang, L. L., Dacosta, H., Yang, J., et al. (2018). CO_2 adsorption at nitrogen doped carbons prepared by K_2CO_3 activation of urea-modified coconut shell. *J. Colloid Interface Sci.* 511, 259–267. doi:10.1016/j.jcis.2017.09.040

Zhang, L. L., and Zhao, X. S. (2009). Carbon-based materials as supercapacitor electrodes. *Chem. Soc. Rev.* 38 (9), 2520–2531. doi:10.1039/B813846J

Zhou, Y., Ren, X., Du, Y., Jiang, Y., Wan, J., and Ma, F. (2020). *In-situ* template cooperated with urea to construct pectin-derived hierarchical porous carbon with optimized pore structure for supercapacitor. *Electrochimica Acta* 355, 136801. doi:10.1016/j.electacta.2020.136801

frontiers | Frontiers in Chemistry

TYPE Original Research
PUBLISHED 31 July 2023
DOI 10.3389/fchem.2023.1232690

OPEN ACCESS

EDITED BY
Aleksandar Kondinski,
University of Cambridge, United Kingdom

REVIEWED BY
Carlos D. S. Brites,
University of Aveiro, Portugal
Dimitrije Mara,
Institute of General and Physical Chemistry, Serbia

*CORRESPONDENCE
Louise S. Natrajan,
louise.natrajan@manchester.ac.uk

RECEIVED 01 June 2023
ACCEPTED 17 July 2023
PUBLISHED 31 July 2023

CITATION
Thornton ME, Hemsworth J, Hay S, Parkinson P, Faulkner S and Natrajan LS (2023), Heterometallic lanthanide complexes with site-specific binding that enable simultaneous visible and NIR-emission.
Front. Chem. 11:1232690.
doi: 10.3389/fchem.2023.1232690

Heterometallic lanthanide complexes with site-specific binding that enable simultaneous visible and NIR-emission

Matthew E. Thornton[1], Jake Hemsworth[1], Sam Hay[2], Patrick Parkinson[3], Stephen Faulkner[4] and Louise S. Natrajan[1]*

[1]Department of Chemistry, Faculty of Science and Engineering, The University of Manchester, Manchester, United Kingdom, [2]Department of Chemistry, Faculty of Science and Engineering, Manchester Institute of Biotechnology, The University of Manchester, Manchester, United Kingdom, [3]Department of Physics and Astronomy and the Photon Science Institute, Faculty of Science and Engineering, The University of Manchester, Manchester, United Kingdom, [4]Department of Chemistry, Chemistry Research Laboratory, The University of Oxford, Oxford, United Kingdom

Macrocyclic lanthanide complexes have become widely developed due to their distinctive luminescence characteristics and wide range of applications in biological imaging. However, systems with sufficient brightness and metal selectivity can be difficult to produce on a molecular scale. Presented herein is the stepwise introduction of differing lanthanide ions in a bis-DO3A/DTPA scaffold to afford three trinuclear bimetallic [Ln_2Ln'] lanthanide complexes with site-specific, controlled binding [(Yb_2Tb), (Eu_2Tb), (Yb_2Eu)]. The complexes display simultaneous emission from all Ln^{III} centers across the visible (Tb^{III}, Eu^{III}) and near infra-red (Yb^{III}) spectrum when excited *via* phenyl ligand sensitization at a wide range of temperatures and are consequently of interest for exploiting imaging in the near infra-red II biological window. Analysis of lifetime data over a range of excitation regimes reveals intermetallic communication between Tb^{III} and Eu^{III} centers and further develops the understanding of multimetallic lanthanide complexes.

KEYWORDS

Lanthanide, luminescence, energy transfer, NIR emission, Macrocycle

1 Introduction

The photophysical properties of lanthanide ions in the common +III oxidation state (Ln^{III}) has become a wide and complex field of research across multiple disciplines and applications, particularly Ln^{III} luminescence for bioimaging (Bünzli and Piguet, 2005; Bünzli, 2010; Monteiro, 2020). Previous works have exploited "windows" of attenuation in the absorption profiles of biological tissues at near-infrared (NIR) wavelengths, allowing deeper penetration of such wavelengths and therefore enhanced imaging (Hemmer et al., 2016; Fan and Zhang, 2019). The Ln^{III} ions are of particular interest due to their characteristic line-like emission across the visible and NIR range, low autofluorescence and photobleaching and high signal-to-noise ratios in comparison to classic organic fluorophores. A caveat to their use is intrinsically poor extinction coefficient as a result of partially-forbidden *f-f* transitions, which is mitigated by sensitization strategies *via* organic chromophores (the antenna effect) or *d*- and *f*-block metal complexes (Faulkner and Pope, 2003; Natrajan et al., 2009). Furthermore, *X*-H (*X* = O, N, C) oscillators are well documented in their ability to

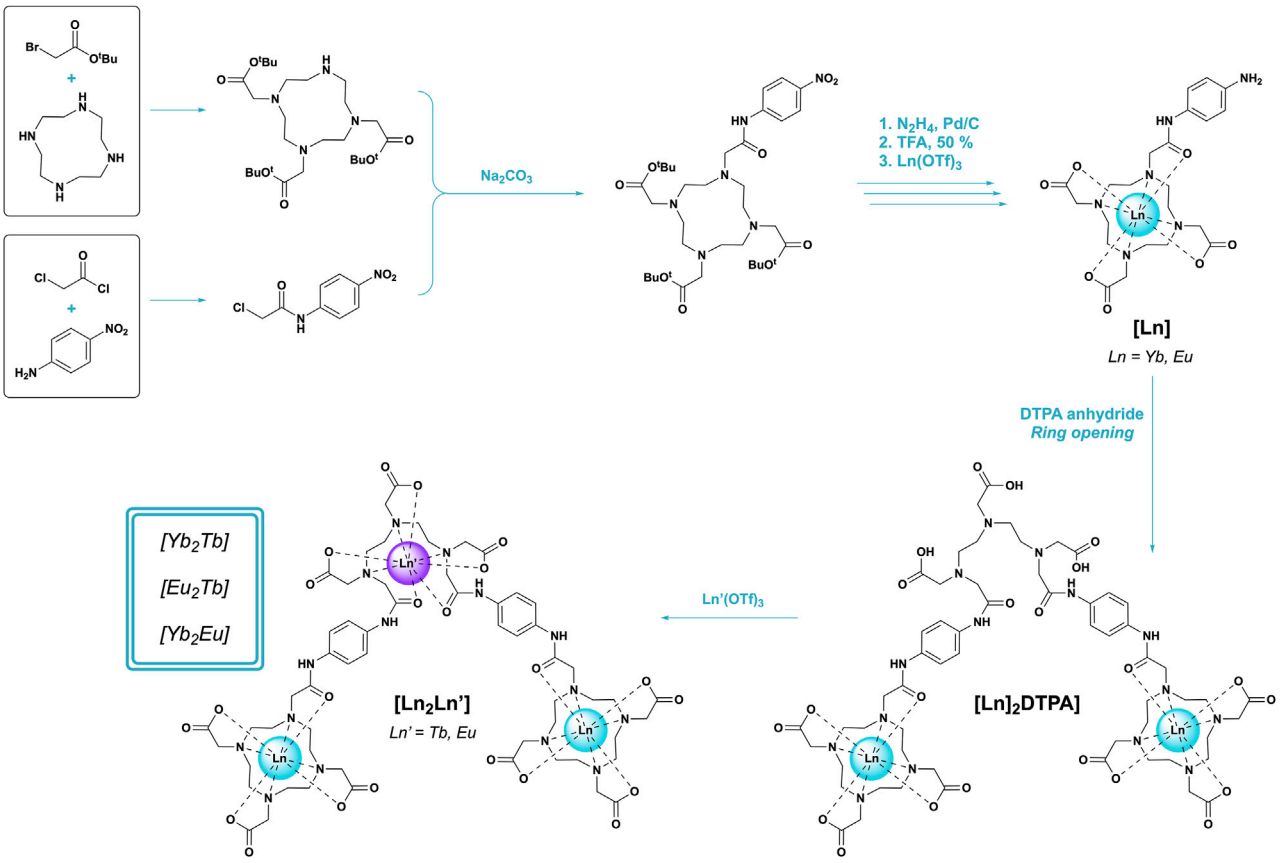

FIGURE 1
Synthetic scheme of the stepwise approach used in synthesis of [Ln_2Ln'] trinuclear bimetallics.

vibrationally quench Ln^{III} excited states due to significant overlap between vibrational overtones of these bonds and emissive Ln^{III} energy levels (Doffek et al., 2012).

This work further develops a previously designed ligand based on a multi-macrocyclic architecture of 1,4,7,10-tetraazacyclododecane-1,4,7-triacetic acid (DO3A) and diethylenetriaminepentaacetic acid (DTPA) (Faulkner and Pope, 2003). Polyamino carboxylate ligands are well known to securely bind lanthanides in a range of environments and have displayed the ability to act as trinuclear heterometallic binding ligands in a site-selective [TbYbTb] arrangement. Herein, we develop the scaffold to include two [LnTbLn] complexes (Ln^{III} = Yb^{III}, Eu^{III}) and a complementary [YbEuYb] species (Figure 1) and further investigate the photophysical capabilities of the ligand across various temperature windows and excitation regimes. The metal selection results in clear Ln^{III}–centred emission across the visible (Tb^{III}, Eu^{III}) and NIR (Yb^{III}) spectrum, which overlaps with both NIR-I (650–950 nm) and NIR-II (1000–1350 nm) imaging windows and therefore invites application in imaging technologies (Foucault-Collet et al., 2013; Jin et al., 2022). The simultaneous response from both Ln^{III} centres has further application as a dual-modal device; the unique magnetic and photophysical behaviour of these metals facilitates use as both MRI contrast agents and optical probes (Rivas et al., 2013; Xu et al., 2013).

Low temperature, solid-state and deuterated media measurements are prioritized to mitigate non-emissive quenching mechanisms. These experiments were also designed to facilitate observation of energy transfer (ET) between metal centers; the relative excited state energies of the chosen metal combinations have been exploited for ET processes in numerous multimetallic Ln^{III} systems (Bispo-Jr et al., 2018; Abad Galán et al., 2021). This work contributes toward the growing library of bimetallic trinuclear Ln^{III} systems that have been studied to elucidate the characteristics of intermetallic communication in discrete molecular complexes (Aboshyan-Sorgho et al., 2012; Zaïm et al., 2014; Tropiano et al., 2015; Maniaki et al., 2023). Finally, the presence of ET in molecular Ln^{III} systems is also useful for imaging applications such as those employing two-photon processes like upconversion (Aboshyan-Sorgho et al., 2011; Nonat et al., 2019).

2 Materials and methods

2.1 Synthesis and characterization

The overall synthesis of target complexes [Yb_2Tb], [Eu_2Tb], and [Yb_2Eu] was adapted and modified from a previously reported literature procedure (Natrajan et al., 2009). Experimental procedures and characterization are detailed on pages S2-S41.

1,4,7,10-tetraazacyclododecane (cyclen) was purchased from CheMatech and used without further purification. All other

reagents and solvents were purchased from Sigma-Aldrich, Fluorochem Ltd. or Apollo Scientific Ltd. and used without further purification. Electrospray +/− (ES-MS) spectra were recorded on a Thermo Orbitrap Exactive Plus mass spectrometer. MALDI-TOF spectra were recorded on a Shimadzu Biotech Axima Confidence mass spectrometer. FT-IR spectra were recorded on a Bruker ALPHA I FT-IR spectrometer. Elemental analysis data were recorder using a Thermo Scientific FlashSmart Elemental Analyzer.

NMR spectra were recorded on a Bruker AVIII HD 500 MHz spectrometer (BBFO inverse probe) in deuterated chloroform, deuterium oxide or deuterated methanol and analyzed using MestReNova 14.1.0. Chemical shifts in parts per million (ppm–δ) are reported relative to residual proton resonances and an internal tetramethylsilane reference. Splitting abbreviations: s: singlet, br. s: broad singlet, d: doublet, dd: doublet of doublets, t: triplet, dt: doublet of triplets, m: multiplet. Blank sections of spectra or those containing solvent resonances are omitted in certain spectra for clarity. Due to complex isomerism between the square and twisted square antiprismatic (SAP ↔ TSAP) forms of multi-macrocyclic cyclen compounds, ^{1}H NMR assignments were often achieved *via* correlation with 2D COSY, HSQC and HMBC data where possible (Miller et al., 2010; Tircso et al., 2011). ^{1}H NMR data for compounds containing paramagnetic atoms (Yb^{III}, Tb^{III}, Eu^{III}) were processed using a line broadening/apodization factor of 1.5–5 Hz and baseline corrected using a multipoint baseline correction with a Whittaker, cubic spline or segment algorithm. The chemical shift values of the ^{1}H resonances in all the lanthanide (III) complexes are reported without assignment due to the complex nature of the paramagnetic NMR assignment of polyaminocarboxylate lanthanide compounds (Sørensen et al., 2017). ^{13}C data could not be collected for the same paramagnetic compounds.

Energy minimization of crystal structures was carried out using Avogadro 1.2.0. Compound structures were downloaded as mol2 files from the Cambridge Crystallographic Data Centre (CCDC) and Ln···C distances measured directly from crystallographic data without any further modification to the structure. The superimposed Yb^{III}—Gd^{III} structure was achieved *via* manual manipulation of each structure to minimize steric clash and bonding of the two structures. Bond angles and lengths were maintained during any new bond formation. The auto optimization tool was then used to minimize the energy of the new structure (UFF force field, steepest descent algorithm). Intermetallic measurements were then conducted on this new, minimzed structure.

2.2 Luminescence spectroscopy

Luminescence spectra were recorded on an Edinburgh Instruments FLS1000 Photoluminescence Spectrometer. Solid-state and low temperature spectra were recorded using a cryostat attachment with the sample deposited on a fused silica slide and were the default method of measurement unless stated otherwise. Solution measurements were recorded using a Hellma quartz glass 3.5 mL cuvette with a 1 cm path length and a sample absorbance of 0.1. UV-VIS spectra were recorded using a Mettler-Toledo UV5Bio spectrometer. Samples were excited using a 450 W Xe lamp with a long-pass filter on the detection arm and emission captured by PMT-900 (visible) and PMT-1700 (NIR) detectors. Any direct comparison of spectra used identical settings; excitation/emission monochromator slit widths and post-collection processing were identical for all. Lifetime measurements were collected using a microsecond flash lamp operating at 40 Hz (Tb^{III}, Eu^{III} data) or 100 Hz (Yb^{III} data). Plotting, fitting and analysis of data was carried out using Origin 2019b. All data were fitted with exponential decay models starting with the fewest terms (mono-, bi-exponential) until sufficiently good fit residuals were achieved. In particular, 2-component fits were always compared against tri-exponential alternatives and found to better fit the data *via* residual, visual, Chi^2 and R^2 analysis.

Shorter–lived lifetimes from Yb^{III} emission require consideration of the instrument response function (IRF) of the excitation source, both of which are on a microsecond timescale. An IRF trace was recorded at 100 Hz in line with the procedure detailed by the instrument manufacturer (Edinburgh Instruments) by matching excitation and detection wavelengths (λ = 280 nm) and recording the decay. This was repeated across different temperatures, both with the sample present and separately using milk powder to provide scatter (in both solid and solution-state). The variation in IRF trace between different variables is minimal. Detector response of the (NIR) PMT-1700 was also considered by recording a pseudo-IRF detecting scattered 2λ light from visible excitation (λ_{ex} = 600 nm, λ_{em} = 1200 nm), to provide a similar result. The convolution tool in Origin was used to generate a decay trace with the appropriate IRF taken into consideration, which was then fitted to an exponential decay profile in the same manner as all other lifetime fits. Fitting of Tb^{III} and Eu^{III} signals used the IRF as a benchmark to ensure fitting parameters were only applied after the instrument response had decayed to background and therefore could not contribute to the resulting lifetime.

3 Results

3.1 Photophysical properties of the near infra-red-visible emitting complex [Yb_2Tb]

Initial excitation *via* the phenyl linker (λ_{ex} = 280 nm) affords sensitized visible emission from the Tb^{III} metal center $^{5}D_4 \rightarrow {}^{7}F_J$ (J = 6, 5, 4, 3) transitions. Additional wavelengths selected to directly probe the $^{5}D_3$ (λ_{ex} = 366 nm) and $^{5}D_4$ (λ_{ex} = 488 nm) energy levels of Tb^{III} also result in emission, however at a lower intensity due to poor extinction coefficients at these wavelengths. Only the primary $^{7}F_5$ transition is visible at λ_{ex} = 488 nm. Solid-state variable temperature spectra at 20, 77, 150, and 298 K highlights an increased intensity and resolution of m_j state crystal field splitting at lower temperatures, most notably in the central 545 nm $^{5}D_4 \rightarrow {}^{7}F_5$ transition (Figure 2A, Supplementary Figure S2.1).

Simultaneous NIR Yb^{III} emission from the $^{2}F_{5/2} \rightarrow {}^{2}F_{7/2}$ transition (~980 nm) and the associated 4-fold splitting of the Kramer ground state are present under the same set of excitation regimes across a range of temperatures, with an expected loss in resolution, intensity and broadening of signal at higher temperatures (Figure 2B, Supplementary Figure S2.2). The relationship between emission intensity and excitation wavelength is not concordant between the Yb^{III} and Tb^{III} centers. The signal intensity of the

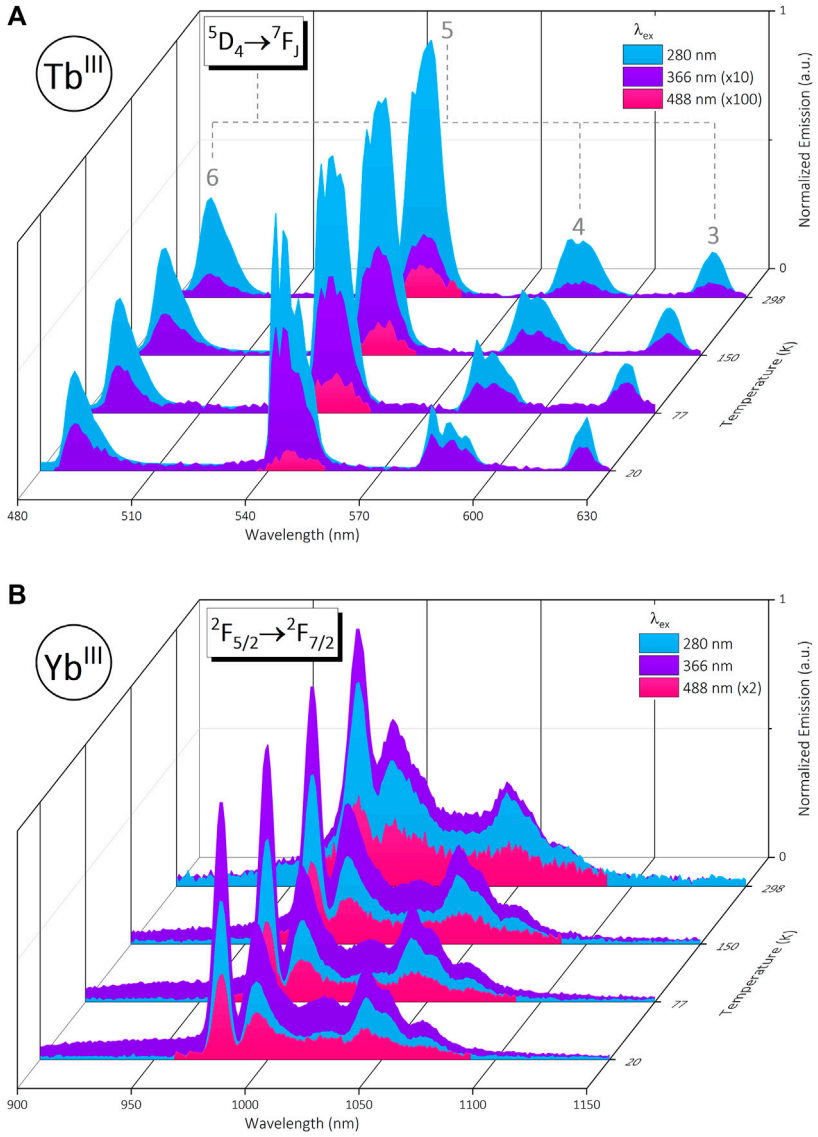

FIGURE 2
(A): Normalized visible emission of trinuclear bimetallic [Yb_2Tb] under 280 nm (blue), 366 nm (purple) and 488 nm (pink) excitation in the solid state from 20—298 K. **(B)**: Simultaneous normalized NIR emission from [Yb_2Tb] under the same conditions. Data are normalized at each temperature relative to the emission maximum (~545 nm @ λ_{ex} = 280 nm for 2A, ~980 nm @ λ_{ex} = 366 nm for 2B).

Yb^{III} $^2F_{7/2}$ transition increases at λ_{ex} = 366 nm; the intended Tb^{III} $^5D_3$ state excitation. However, this is not unique to the trinuclear [Yb_2Tb] species as the mono and bimetallic Yb^{III} precursors [Yb] and [Yb]$_2$DTPA display the same behavior (Supplementary Figures S2.3, S2.4). Inspection of solid-state excitation profiles for the series at 980 nm (Supplementary Figure S2.5) show a broad ligand-centered band with a hypsochromic shift across the series from [Yb] (λ_{max} = 331 nm) to [Yb_2Tb] (λ_{max} = 311 nm) and further again for the Tb^{III} center (λ_{em} = 545 nm, λ_{max} = 296 nm). Solution-state excitation spectra for the series (Supplementary Figure S2.6) identify this primarily as a solid state effect and present a narrowing of each profile (λ_{max} = 285 nm) with a similar ~15 nm shift for Tb^{III} excitation (λ_{max} = 270 nm). UV-VIS absorption data show minimal change in signal when comparing complexes and resemble solution-state profiles (Supplementary Figure S2.7).

Solid-state lifetime measurements of the primary Tb^{III} emission at 545 nm fit a bi-exponential decay profile across all temperatures and λ_{ex}, determined *via* analysis of R^2 values and fit residuals (Supplementary Figures S2.8–S2.10). For simplicity, we report the global fluorescence lifetime, τ_n, of each decay component which is an average across variable λ_{ex} (280, 366, 488 nm) and temperature (20, 77, 150, and 298 K). This value for the two exponents of Tb^{III} decay are 0.14 ± 0.01 ms and 0.70 ± 0.03 ms for τ_1 and τ_2 respectively (fitting after the IRF). The relative contribution of each component varies marginally across the variable excitation and temperature series, but the long-lived τ_2 component remains the most significant (Supplementary Table S2). Calculation of the average lifetime, τ_{avg}, considers the variation in percentage contribution from each τ_n component toward an overall average value (Supplemetary equations S1, S2). Factoring in all data across the excitation and

10.3389/fchem.2023.1232690

TABLE 1 Solid-state lifetimes of Ln^{III} centers at multiple temperatures from the [Yb] complex series including trinuclear bimetallic [Yb_2Tb], averaged across variable excitation wavelengths (298 K: dark red, 150 K: light red, 77 K: dark blue, 20 K: light blue). Tb^{III} values are calculated average lifetimes from a bi-exponential fit.

Lifetime		Yb^{III} τ (μs)			Tb^{III} τ_{avg} (ms)
Complex		[Yb] (± *0.98 μs*)	$[Yb]_2$DTPA (± *1.2 μs*)	[Yb_2Tb] (± *1.3 μs*)	[Yb_2Tb] (± *0.03 ms*)
Temperature (K)	298	7.6	10	8.1	0.56
	150	7.7	9.9	8.4	0.57
	77	8.0	10	8.7	0.56
	20	8.5	11	9.2	0.51

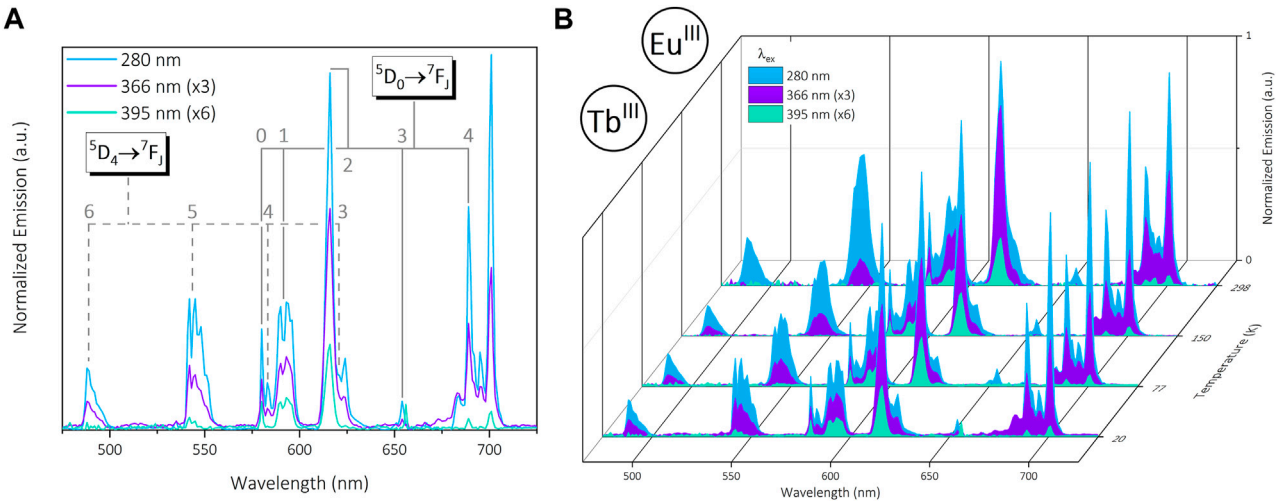

FIGURE 3
(A): Normalized visible emission of trinuclear bimetallic [Eu_2Tb] under 280 nm (blue), 366 nm (purple) and 395 nm (green) excitation in the solid state at 20 K. **(B)**: Normalized visible emission from [Eu_2Tb] at 20—298 K across the same set of excitations. Data are normalized at each temperature relative to the emission maximum (~701 nm @ λ_{ex} = 280 nm).

temperature range results in τ_{avg} = 0.55 ± 0.03 m for the Tb^{III} center (Table 1).

The 980 nm–centered Yb^{III} emission fits a mono-exponential decay following convolution with the IRF signal (Supplemetary Figures S2.11—S2.14) and has a global fluorescence lifetime τ = 8.6 ± 0.4 μs across variable λ_{ex} and temperature. This is comparable to lifetime values for Yb^{III} precursors (±0.4 μs); τ [Yb] = 7.9 μs, τ $[Yb]_2$DTPA = 10 μs (Table 1).

3.2 Emission behavior of the dual-visible emitting complex [Eu_2Tb]

Insertion of Eu^{III} into the DO3A binding pocket results in strong visible emission (480—700 nm) from the same ^7F_J Tb^{III} transitions present in [Yb_2Tb], in addition to the $^5D_0 \rightarrow {}^7F_J$ (J = 0–4) transitions from Eu^{III}. As above, excitation of the phenyl linker at λ_{ex} = 280 nm results in simultaneous sensitized emission from the two metal centers (Figure 3A). Direct excitation of the Tb^{III} $^5D_3$ band (λ_{ex} = 366 nm) again yields emission from both metals proportional to respective excitation profiles. The second direct Tb^{III} excitation ($^5D_4$, λ_{ex} = 488 nm) employed in [Yb_2Tb] is relatively weak in this complex, meaning no significant emission was observed. Alternatively, direct excitation of the Eu^{III} $^5L_6$ level (λ_{ex} = 395 nm) can be used to selectively produce Eu^{III}–centered emission and minimize Tb^{III} spectral features, namely, the J = 4, 3 transitions (Figure 3A). Variable temperature emission spectra highlight the consistency of this wavelength–selective visible emission in addition to crystal field splitting at lower temperatures, in particular the Eu^{III} $^7J_1$ and $^7J_2$ signals (Figure 3B, Supplementary Figure S2.15). The lack of splitting in the $^5D_0 \rightarrow {}^7F_0$ transition is indicative of a singular Eu^{III} environment due to the non-degeneracy of both states, as expected from equivalent [Eu^{III}(DO3A)] sites (Binnemans, 2015). Additionally, the hypersensitive $^7F_2$ transition known to be highly dependent on coordination environment remains consistent throughout. Analysis of λ_{ex} against temperature shows an appreciable change in intensity at 701 nm (Eu^{III} $^7F_4$ state) when changing from sensitized (λ_{ex} = 280 nm) to direct excitation (λ_{ex} = 395 nm) (Supplementary Figure S2.16). However, the relative intensity of the $^7F_4$ signal is strong overall which is in agreement with the square antiprismatic geometry expected of macrocyclic species such as DO3A (Binnemans, 2015).

TABLE 2 Solid-state lifetimes of Ln^{III} centers at multiple temperatures from the [Eu] complex series, averaged across variable excitation wavelengths (298 K: dark red, 150 K: light red, 77 K: dark blue, 20 K: light blue). Both Eu^{III} and Tb^{III} values are calculated average lifetimes from a bi-exponential fit.

Lifetime		Eu^{III} τ_{avg} (ms)			Tb^{III} τ_{avg} (ms)
Complex		[Eu] (± *0.05 ms*)	$[Eu]_2$DTPA (± *0.03 ms*)	$[Eu_2Tb]$ (± *0.02 ms*)	$[Eu_2Tb]$ (± *0.02 ms*)
Temperature (K)	298	0.58	0.76	0.15	0.23
	150	1.1	0.88	0.21	0.35
	77	1.2	0.88	0.23	0.34
	20	1.2	0.89	0.24	0.38

Fitting of the 545 nm Tb^{III} decay results in a bi-exponential fit analogous to the $[Yb_2Tb]$ species (τ_1 = 0.11 ± 0.01 ms, τ_2 = 0.56 ± 0.07 ms). The percentage contribution of each lifetime component is more evenly distributed than in the corresponding $[Yb_2Tb]$ complex, resulting in a shorter τ_{avg} value of 0.33 ± 0.02 ms (Table 2). However, comparison of the longer-lived τ_2 component in both Tb^{III}-containing complexes highlights similarity between the two (Supplementary Table S3).

The Eu^{III} lifetimes were measured by fitting the decay of the primary 615 nm emission ($^5D_0 \rightarrow {}^7F_2$) at various temperatures and fit with a bi-exponential equation also (Supplementary Figures S2.17—S2.19) (τ_1 = 82 ± 5 µs, τ_2 = 0.36 ± 0.04 ms). The contribution of each component toward τ_{avg} is largely independent of λ_{ex} and differs from Tb^{III} bi-exponential fits as the longer-lived τ_2 component no longer dominates (Supplementary Table S4). Each τ_n component has appreciable significance, yielding a τ_{avg} value of 0.21 ± 0.02 ms. Comparison of component-weighted τ_{avg} Eu^{III} lifetimes from [Eu] and $[Eu]_2$DTPA shows they are longer across the series when compared to the final $[Eu_2Tb]$ bimetallic compound (τ_{avg} = 1.0 ± 0.3 ms and 0.85 ± 0.06 ms respectively, Table 2).

Comparison of Eu^{III} precursors [Eu] and $[Eu]_2$DTPA with the trinuclear target species $[Eu_2Tb]$ highlights significant differences in solid-state excitation profiles arising from 615 nm emission (Supplementary Figure S2.20). The DO3A complex [Eu] displays strong absorption bands corresponding to $^5D_4 \leftarrow {}^7F_0$ (362 nm), $^5D_4 \leftarrow {}^7F_1$ (375 nm), $^5L_6 \leftarrow {}^7F_0$ (395 nm), $^5L_6 \leftarrow {}^7F_1$ (400 nm) and $^5D_2 \leftarrow {}^7F_0$ (465 nm) Eu^{III} transitions. Phenyl ligand absorption (λ_{ex} max ≈280 nm) begins to dominate in the following $[Eu]_2$DTPA compound, coupled with the loss of the $^5D_4$ band at 375 nm. $[Eu_2Tb]$ follows the trend with increased ligand-centered absorption and further absence of the other $^5D_4$ feature at 362 nm; Eu^{III} series spectra exhibit general solid-state broadening analogous to $[Yb_2Tb]$. Solution-state excitation scans in D_2O are ligand-centered across the series, with a marginal shift between samples ($\Delta\lambda_{max}$ = 20 nm) and a minor $^5L_6$ feature at 395 nm (Supplementary Figure S2.21) and are in agreement with UV-VIS spectra (Supplementary Figure S2.22).

3.3 Photophysical properties of the near infra-red-visible emitting complex $[Yb_2Eu]$

Synthesis of the $\{Yb(DO3A)\}_2$-{Eu (DTPA)} complex $[Yb_2Eu]$ results in simultaneous NIR and visible emission from the two metals (λ_{ex} = 280, 366 and 395 nm) analogous to $[Yb_2Tb]$ and $[Eu_2Tb]$, with an expected decrease in emission intensity at higher temperatures (Supplementary Figures S2.23, S2.24). Excitation at 366 nm was investigated despite the absence of Tb^{III} to generate results comparable with other data sets. The Eu^{III} $^7F_2$ transition displays a minor spectral shift, and the $^7F_4$ presents a change in splitting pattern compared to $[Eu_2Tb]$, both of which are sensitive to coordination environment and suggest Eu^{III} is selectively bound in the DTPA site (Figure 4A). The Eu^{III} center exhibits a greater response at λ_{ex} = 395 nm compared to $[Eu_2Tb]$, which is consistent across a range of temperatures (Figure 4B). Solid-state excitation spectra (λ_{em} = 615 nm) show a large ligand-centered signal in addition to distinct Eu^{III} bands analogous to [Eu] and rationalize this behavior (Supplementary Figure S2.25). Solution-state excitation spectra of $[Yb_2Eu]$ present $^5D_4 \leftarrow {}^7F_0$, $^7F_1$ Eu^{III} excitation signals which are absent in solution measurements of the other Eu^{III} complexes (Supplementary Figure S2.26).

The Yb^{III} emission intensity from the $^2F_{5/2} \rightarrow {}^2F_{7/2}$ transition shows an increased temperature-wavelength relationship compared to other Yb^{III} complexes but maintains maximum emission at λ = 366 nm (Supplementary Figure S2.27). At T = 298 K both ligand and Eu^{III} excitation (λ_{ex} = 280 nm and 395 nm, respectively) result in similar emission intensity, however the latter begins to dominate at lower temperatures (T ≤ 150 K). Solid and solution-state excitation spectra at 980 nm exhibit the same relationship as $[Yb_2Tb]$ with a ~40 nm blue shift between the two metal centers and UV-VIS spectra is comparable to other Eu^{III} species (Supplementary Figure S2.28).

Lifetime data for Eu^{III} emission in $[Yb_2Eu]$ is similar to previous samples with τ_1 = 0.17 ± 0.02 ms, τ_2 = 0.74 ± 0.03 ms across the temperature and excitation range. The individual component contribution reflects the previous DTPA-bound metal (Tb^{III} $[Yb_2Tb]$), with a clear dominance of the long-lived τ_2 decay (Supplementary Table S5) which gives rise to a longer τ_{avg} value of 0.63 ± 0.09 ms. Yb^{III} lifetimes remain on the same order of magnitude as previous measurements; τ = 9.8 ± 0.6 µs across variable λ_{ex} and temperature. A summary of temperature-dependent lifetime data for each Ln^{III} across the trinuclear bimetallic series is presented in Table 3 and highlights the general observation of longer lifetimes at lower temperatures.

3.4 Solution-state measurements

Solution-state measurements in water and D_2O result in lifetimes with mono-exponential decay profiles for all metals; the shorter-lived τ_1 component in the bi-exponential Tb^{III} and Eu^{III} solids are not present. Solution measurements are likely

10.3389/fchem.2023.1232690

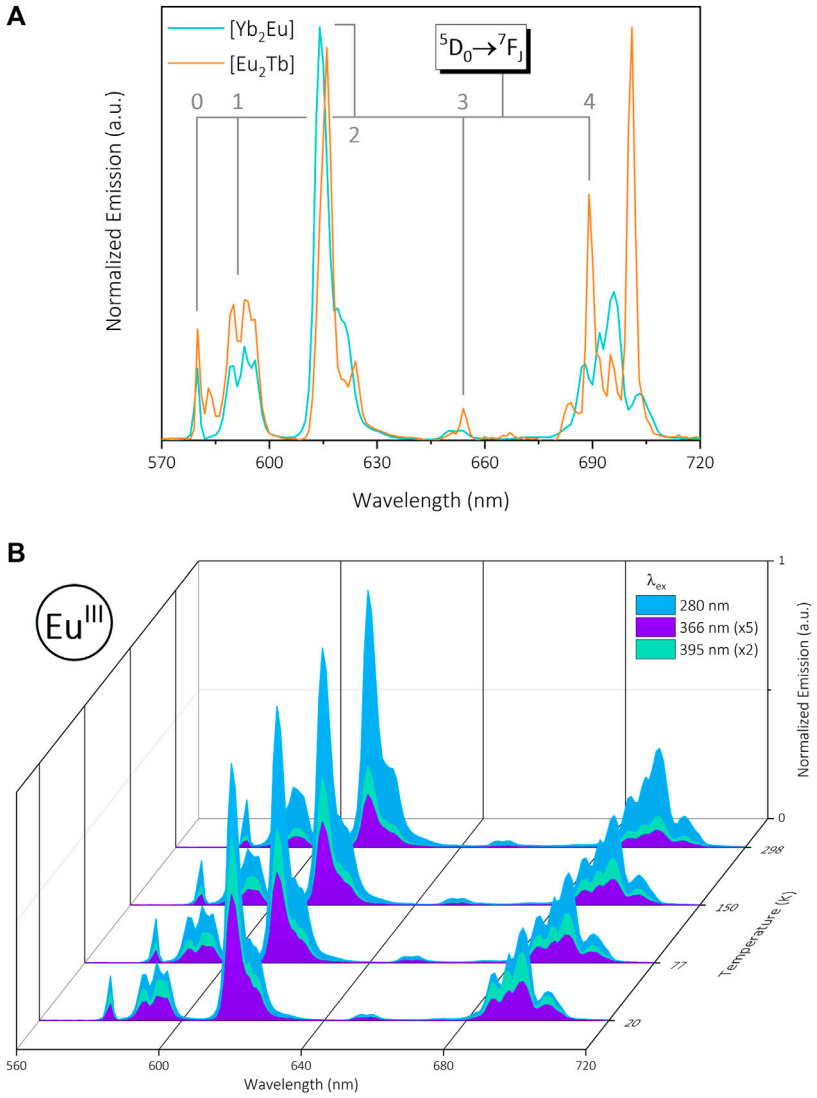

FIGURE 4
(A): Normalized visible emission of trinuclear bimetallic [Yb_2Eu] (green) and [Eu_2Tb] (orange) under 280 nm excitation in the solid state at 20 K. Data are normalized for each complex relative to the emission maximum. **(B)**: Normalized visible emission from [Yb_2Eu] at 20—298 K under 280 nm (blue), 366 nm (purple) and 395 nm (green) excitation in the solid state (normalized to ~615 nm @ λ_{ex} = 280 nm).

probing an average lifetime arising from minor changes in hydration state and exchange between the square and twisted square antiprismatic (SAP ↔ TSAP) isomers of the DO3A macrocycles (Miller et al., 2010; Tircso et al., 2011; Nielsen and Sørensen, 2019). Consequently, solution experiments exhibit significantly longer lifetimes on average, with significant gains in deuterated solvent due to reduced energetic overlap of *X*–D oscillators with emissive Ln^{III} states (Supplementary Figures S2.29—S2.31) (Doffek et al., 2012). The number of bound solvent molecules can be calculated *via* the inner sphere hydration parameter, *q*, using a modified Horrocks equation (Supplementary Equation S3, Supplementary Table S1) (Beeby et al., 1999). This calculation takes into account the degree of vibrational quenching by proximate *X*-H (*X* = C, N, O) groups for each metal; O-H oscillators contribute significantly for all three, however the significance of N-H groups is relevant for Eu^{III} only and is negligible in magnitude for Tb^{III} and Yb^{III} systems. Whilst C-H quenching arising from the acetate methylene and DO3A ring groups has a considerable influence on the luminescent lifetimes of near infra-red emitting lanthanides, in the case of Yb^{III} this contribution is small when compared to closely diffusing O-H oscillators and mostly unobserved, due to the long *X*-H . . . Ln^{III} distances of these species and a $1/r^6$ dependence for quenching *via* energy transfer. This enables the estimation of *q* by a modified Horrock's equation (Beeby et al., 1999).

Comparison of the luminescence decay in water and D_2O (Table 4) shows *q* values change depending on both metal choice and binding environment, with the lowest arising from DO3A-bound Yb^{III} in [Yb_2Tb] (*q* = 0.21) and [Yb_2Eu] (*q* = 0.29). The small size of Yb^{III} due to the lanthanide contraction and availability of hard Lewis basic N- and O- donors in the

TABLE 3 Solid-state lifetimes of Ln^{III} centers at multiple temperatures from the [Ln_2Ln'] complex series, averaged across variable excitation wavelengths ([Yb_2Tb] = orange, [Eu_2Tb] = green, [Yb_2Eu] = blue). Both Eu^{III} and Tb^{III} values are calculated average lifetimes from a bi-exponential fit.

Lifetime		Yb^{III} τ (μs)		Tb^{III} τ_{avg} (ms)		Eu^{III} τ_{avg} (ms)	
Complex		[Yb_2Tb]	[Yb_2Eu]	[Yb_2Tb]	[Eu_2Tb]	[Eu_2Tb]	[Yb_2Eu]
Temperature (K)	**298**	8.1	9.1	0.56	0.23	0.15	0.60
	150	8.4	9.7	0.57	0.35	0.21	0.65
	77	8.7	10	0.56	0.34	0.23	0.66
	20	9.2	11	0.51	0.38	0.24	0.62
Global τ		**8.6** ± *0.4*	**9.8** ± *0.6*	**0.55** ± *0.03*	**0.33** ± *0.06*	**0.21** ± *0.02*	**0.63** ± *0.09*

TABLE 4 Solution-state lifetimes of Ln^{III} centers in [Ln_2Ln'] complexes and associated *q* values for each, at 298 K (λ_{ex} = 280 nm, λ_{em} = 980 nm (Yb^{III}), 545 nm (Tb^{III}), 615 nm (Eu^{III}).

Complex	[Yb_2Tb]		[Eu_2Tb]		[Yb_2Eu]	
Metal	Yb^{III}	Tb^{III}	Eu^{III}	Tb^{III}	Yb^{III}	Eu^{III}
τ_{H_2O} (ms)	0.0019	1.7	0.60	1.0	0.0016	0.58
τ_{D_2O} (ms)	0.0078	3.0	1.9	2.4	0.0080	2.3
q	**0.2**	**1.1**	**1.0**	-	**0.3**	**1.1**

octadentate DO3A precludes access to nearby solvent molecules (Faulkner and Pope, 2003). In complex [Yb_2Tb], the neighboring DTPA-bound Tb^{III} is more readily accessible due to a larger ionic radius and reduction in kinetic stability of the DTPA binding pocket, resulting in ~1 bound water molecule (Idée et al., 2009; Sørensen and Faulkner, 2018). Similarly, in the complex [Eu_2Tb], *q* = 1.0 for the DO3A Eu^{III} center as a result of the slightly larger 9 coordinate ionic radius (Sastri et al., 2003) which competes with the steric bulk of the DO3A macrocycle to allow inclusion of 1 solvent donor. In the case of the Tb^{III}(DTPA) centre in [Eu_2Tb], an apparent *q* value of 2.4 is determined. However, in the case of substantial energy transfer from the assumedly $^5D_4$ excited state of Tb^{III} to the $^5D_0$ state of Eu^{III} occuring, phonon assisted energy transfer processes through the O-H vibrational manifold are in direct competition with those that act to quench the $^5D_4 \rightarrow {}^7F_J$ transitions. Given that both of these quenching pathways will possess different rate constants, it follows that Horrocks equation is no longer appropriate (Beeby et al., 1999). Analysis of lifetime data for the analogous [Yb_2Eu] complex indicates that any competitive intermolecular energy transfer from the $^5D_0$ Eu^{III} excited state to the $^7F_{5/2}$ excited state of Yb^{III} is inconsequential, and *q* of Eu^{III} bound in the DTPA coordination pocket is calculated as 1.1 as expected.

4 Discussion

The potential of this molecular scaffold to facilitate energy transfer between two bound Ln^{III} ions was a key factor in both the ligand and experimental design. Measurement of the Gd-(DO3A)-aminophenyl acetamide complex [Gd] (analogous to [Yb] and [Eu]) facilitates characterization of the triplet state T_1 of the phenyl linker. The primary Gd $^6P_{7/2}$ state is too high in energy to be sensitized, therefore emission of [Gd] is entirely ligand-centered. Solid-state measurements at 298 K display broad fluorescence (λ_{em} = 431 nm), while phosphorescence from the triplet state is observed at 20 K (λ_{em} = 476 nm, Supplementary Figure S2.32). Crucially, this is high enough in energy to sensitize Tb^{III}, Eu^{III} and Yb^{III} emissive states (T_1 = 21,008 cm^{-1}, Tb^{III} $^5D_4$ = 20,453 cm^{-1}, Eu^{III} $^5D_0$ = 17,227 cm^{-1}, Yb^{III} $^2F_{7/2}$ = 2924 cm^{-1}) (Carnall et al., 1968b; 1968a; Sastri et al., 2003) (Figure 5). Additionally, the relative energies and stoichiometry of potential donor and acceptor states (2:1 acceptor:donor ratio) of the metal centers are conducive toward intermetallic ET pathways in [Yb_2Tb] (Tb^{III} $^5D_4 \rightarrow Yb^{III}$ $^2F_{5/2}$) and [Eu_2Tb] (Tb^{III} $^5D_4 \rightarrow Eu^{III}$ $^5D_0$). The potential [Yb_2Eu] pathway (Eu^{III} $^5D_0 \rightarrow Yb^{III}$ $^2F_{5/2}$) requires too great an energy mismatch to be a competing process, even when considering phonon assistance *via* the vibrational manifold of O-H oscillators, as is possibly the case in the $Tb^{III} \rightarrow Yb^{III}$ systems.

Existence of energy transfer between bound metals is often strongly correlated with changes in the luminescence lifetime of excited states, where an energetic pathway from the donor excited state to an acceptor results in an overall reduction in lifetime in the former. An observed reduction in lifetime is apparent as temperature increases for each metal site due to increased *X*-H (*X* = C, N, O) vibrations and therefore quenching of excited states. Recorded lifetimes for the potential Tb^{III} $^5D_4$ donor state are largely consistent across a range of excitation bands. There is however a marked decrease in Tb^{III} τ_{avg} values between target complexes [Yb_2Tb] and [Eu_2Tb] (0.55 ms vs. 0.33 ms). There is also a significant reduction of Eu^{III} τ_{avg} in [Eu_2Tb] compared to the Eu^{III} complex series (0.64 ms, ~75%) which is not present in the analogous Yb^{III}(DO3A) acceptor series, suggesting the existence of an relaxation pathway present in [Eu_2Tb] that is absent in [Yb_2Tb]. Furthermore, Table 3 indicates a 48% decrease in Eu^{III} τ_{avg} from [Yb_2Eu] to [Eu_2Tb] and supports evidence toward a Eu^{III}-Tb^{III} interaction. This is illustrated more clearly when considering the observed rate constants k_{obs} ($1/\tau_{avg}$), for Eu^{III} emission in various systems. There is an increase in k_{obs} upon addition of Tb^{III} compared to the Eu^{III}–only complex series ([Eu] k_{obs} = 1000 μs^{-1} $[Eu]_2$DTPA k_{obs} = 1180 μs^{-1} [Eu_2Tb] k_{obs} = 4762 μs^{-1}). Estimation of the potential energy transfer rate constant k_{ET} can be calculated as the difference between the rate radiative decay from Eu^{III} in the presence and absence of a Tb^{III} transfer partner ($k_{ET} = k_{EuTb} - k_{Eu}$), using data from [$Eu_2Tb$] and $[Eu]_2$DTPA, respectively. Calculation with τ_{avg} values for these compounds yield a value of k_{ET} = 3582 μs^{-1}. Analogous

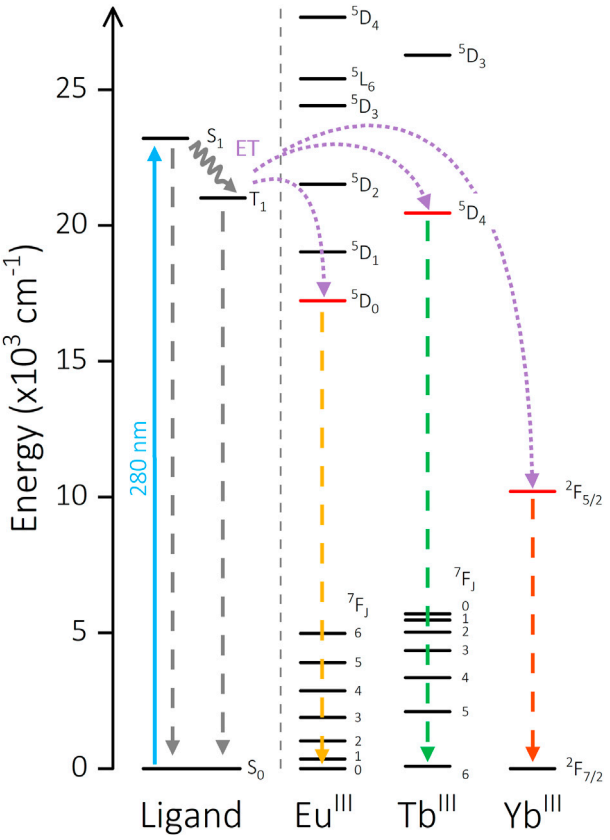

FIGURE 5
Energy level diagram showing the sensitization pathways of [Ln_2Ln'] complexes. Solid arrow: excitation, waved arrow: non-radiative decay, dashed arrow: emission, dotted arrow: energy transfer pathway. Ligand energy levels are calculated from [Gd] measurements. Eu^{III}, Tb^{III}, and Yb^{III} energies are taken from literature for comparison (Carnall et al., 1968a; Carnall et al., 1968b; Sastri et al., 2003).

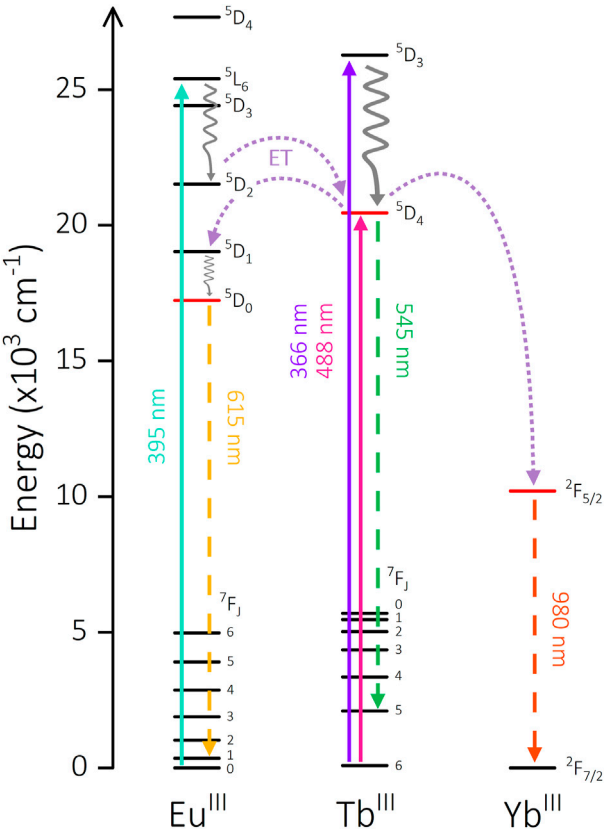

FIGURE 6
Energy level diagram showing potential intermetallic energy transfer mechanisms in [Ln_2Ln'] complexes. Solid arrow: excitation, waved arrow: non-radiative decay, dashed arrow: emission, dotted arrow: energy transfer pathway.

changes in lifetime are not observed in complexes where either metal is paired with Yb^{III}. Additionally, DO3A-bound Yb^{III} and Eu^{III} complexes show minimal variations in lifetime when paired with a spectroscopically silent Lu^{III} in the central DTPA pocket ([Yb_2Lu][Eu_2Lu], Supplementary Table S6).

Indeed, the ^5D_J energy levels of Tb^{III} (J = 4) and Eu^{III} (J = 2, 1, 0) exhibit appreciable energetic overlap. The 395 nm excitation feature in [Eu_2Tb] populates a Eu^{III} $^5L_6$ state which is energetically higher than the Tb^{III} $^5D_4$ level (ΔE = 4947 cm^{-1}) and can populate the latter *via* non-radiative decay to $^5D_2$ and subsequent ET (Figure 6) (Bispo et al., 2018). Additionally, there is the possibility of phonon-assisted ET facilitated by proximate *X*-H oscillators. The manifold provided by vibrational overtones of O-H and O-D oscillators can provide an alternate energetic pathway to populate ^7F_J states of Tb^{III} from direct Eu^{III} $^5L_6$ population. Irrespective of these pathways, the emissive states of both Tb^{III} and Eu^{III} are higher in energy than the ^7F_J states of either metal (Supplementary Figure S2.33) and have been reported to communicate in similar systems (Zaïm et al., 2014). The simultaneous reduction in lifetime of both Eu^{III} and Tb^{III} is exclusive to [Eu_2Tb] and is not present in the parent complexes. The ability of each to act as both donor and acceptor when paired together appears to facilitate a series of ET and possibly back energy transfer (BET) processes between the metal centers.

Despite evidence of solvent interactions and consequent vibrational quenching, solution lifetimes are comparable or often longer than those in the solid state. The additional components in solid-state data likely arise from a combination of SAP ↔ TSAP isomerism and intermolecular quenching between emissive centers in two or more molecules. Solid-state quenching effects appear to play a significant role in the ability of the complex to facilitate energy transfer, as preliminary evidence of Tb^{III}-sensitized Yb^{III} emission has previously been reported in solution (Faulkner and Pope, 2003). However, intermetallic distance is another contributing factor and is especially pertinent in solution-state measurements (Sørensen et al., 2017). Single crystal X-ray diffraction structures reported for aminophenyl trifluoromethyl Yb^{III}(DO3A) (CCDC ID: EGOWUV) and bis-aminocarboxyphenyl Gd^{III}(DTPA) (CCDC ID: QEZGIM) complexes with analogous phenyl moieties allow approximate calculation of these distances *via* superimposition and preliminary energy minimization. Crystal structures were used without modification and manipulated into a feasible geometry

before undergoing optimization in Avogadro to yield an average Yb^{III}–Gd^{III} distance of 11.9 Å (Supplementary Figure S2.34) (Dutta et al., 2006; Pujales-Paradela et al., 2019). Examples of multimetallic architectures that exhibit intermetallic energy transfer often report shorter distances (≤10 Å) (Natrajan et al., 2009; Maniaki et al., 2023). The significant r^{-6} distance dependence of dipolar ET processes and the innate flexibility of molecular lanthanide systems both act to quench any potential intermetallic communication.

5 Conclusion

A series of three trinuclear bimetallic lanthanide complexes have been synthesized with selective introduction of metals into specific DO3A and DTPA binding sites. All three species exhibit strong sensitized emission when excited *via* a phenyl linker and represent a broad spectral range, from visible to NIR depending on the metal combination selected. Extensive photophysical measurements investigating the effects of temperature and excitation wavelength revealed communication between Eu^{III} and Tb^{III} centers when closely bound within the same complex, highlighting the potential for energy transfer between metals. The absence of evidence of intermetallic communication in the Yb^{III} heterometallics emphasizes the impact of solid-state quenching and solution-state molecular motion on multimetallic lanthanide scaffolds that could facilitate energy transfer. Further work on optimizing the distance between metal centers and varying Ln^{III} selection will be investigated in the future, with the aim of observing energy transfer and therefore accessing more intricate photophysics and applications.

Data availability statement

The datasets presented in this study can be found in online repositories. The names of the repository/repositories and accession number(s) can be found in the article/Supplementary Material.

Author contributions

MET conducted all synthesis, characterization, measurements and analysis for compounds [Yb_2Tb] and [Yb_2Eu]. Initial synthesis and characterization of [Eu_2Tb] was completed by JH and photophysical measurements finished by MET. LSN, SH, and PP secured funding and provided supervision and discussion. LSN and SF initiated the research and facilitated creation of the project. All authors contributed to the article and approved the submitted version.

Funding

The BBSRC Doctoral Training Partnership 2 BB/M011208/1 for studentship funding. PP is funded under the UKRI Future Leaders Fellowship scheme [MR/T021519/1].

Acknowledgments

MET and LSN thank the University of Manchester for access to facilities including the Centre for Radiochemistry Research National Nuclear User's Facility (NNUF, EP/T011289/1).

Conflict of interest

The authors declare that the research was conducted in the absence of any commercial or financial relationships that could be construed as a potential conflict of interest.

Publisher's note

Supplementary material

The Supplementary Material for this article can be found online at: https://www.frontiersin.org/articles/10.3389/fchem.2023.1232690/full#supplementary-material

References

Abad Galán, L., Aguilà, D., Guyot, Y., Velasco, V., Roubeau, O., Teat, S. J., et al. (2021). Accessing lanthanide-to-lanthanide energy transfer in a family of site-resolved [LnIIILnIII′] heterodimetallic complexes. *Chem. Eur. J.* 27, 7288–7299. doi:10.1002/chem.202005327

Aboshyan-Sorgho, L., Besnard, C., Pattison, P., Kittilstved, K. R., Aebischer, A., Bünzli, J.-C. G., et al. (2011). Near-Infrared→Visible light upconversion in a molecular trinuclear d–f–d complex. *Angew. Chem. Int. Ed.* 50, 4108–4112. doi:10.1002/anie.201100095

Aboshyan-Sorgho, L., Nozary, H., Aebischer, A., Bu, J.-C. G., Morgantini, P.-Y., Kittilstved, K. R., et al. (2012). Optimizing millisecond time scale near-infrared emission in polynuclear chrome(III)–Lanthanide(III) complexes. *J. Am. Chem. Soc.* 134 (30), 12675–12684. doi:10.1021/ja304009b

Beeby, A., Clarkson, I. M., Dickins, R. S., Faulkner, S., Parker, D., Royle, L., et al. (1999). Non-radiative deactivation of the excited states of europium, terbium and ytterbium complexes by proximate energy-matched OH, NH and CH oscillators: An improved luminescence method for establishing solution hydration states. *J. Chem. Soc. Perkin Trans.* 2 (3), 493–504. doi:10.1039/a808692c

Binnemans, K. (2015). Interpretation of europium(III) spectra. *Coord. Chem. Rev.* 295, 1–45. doi:10.1016/j.ccr.2015.02.015

Bispo, A. G., Lima, S. A. M., and Pires, A. M. (2018). Energy transfer between terbium and europium ions in barium orthosilicate phosphors obtained from sol-gel route. *J. Lumin.* 199, 372–378. doi:10.1016/j.jlumin.2018.03.057

Bünzli, J. C. G. (2010). Lanthanide luminescence for biomedical analyses and imaging. *Chem. Rev.* 110 (5), 2729–2755. doi:10.1021/cr900362e

Bünzli, J. C. G., and Piguet, C. (2005). Taking advantage of luminescent lanthanide ions. *Chem. Soc. Rev.* 34, 1048–1077. doi:10.1039/b406082m

Carnall, W. T., Fields, P. R., and Rajnak, K. (1968a). Electronic energy levels of the trivalent lanthanide aquo ions. III. Tb^{3+}. *J. Chem. Phys.* 49, 4447–4449. doi:10.1063/1.1669895

Carnall, W. T., Fields, P. R., and Rajnak, K. (1968b). Electronic energy levels of the trivalent lanthanide aquo ions. IV. Eu^{3+}. *J. Chem. Phys.* 49, 4450–4455. doi:10.1063/1.1669896

Doffek, C., Alzakhem, N., Bischof, C., Wahsner, J., Güden-Silber, T., Lügger, J., et al. (2012). Understanding the quenching effects of aromatic C-H- and C-D-oscillators in near-IR lanthanoid luminescence. *J. Am. Chem. Soc.* 134, 16413–16423. doi:10.1021/ja307339f

Dutta, S., Kim, S. K., Eun, J. L., Kim, T. J., Kang, D. S., Chang, Y., et al. (2006). Synthesis and magnetic relaxation properties of paramagnetic Gd-complexes of new DTPA-bis-amides. The X-ray crystal structure of $[Gd(L)(H_2O)]\cdot 3H_2O$ (L = DTPA-bis(4-carboxylicphenyl)amide). *Bull. Korean Chem. Soc.* 27, 1038–1042. doi:10.5012/bkcs.2006.27.7.1038

Fan, Y., and Zhang, F. (2019). A new generation of NIR-II probes: Lanthanide-based nanocrystals for bioimaging and biosensing. *Adv. Opt. Mater.* 7, 1801417. doi:10.1002/adom.201801417

Faulkner, S., and Pope, S. J. A. (2003). Lanthanide-sensitized lanthanide luminescence: Terbium-sensitized ytterbium luminescence in a trinuclear complex. *J. Am. Chem. Soc.* 125, 10526–10527. doi:10.1021/ja035634v

Foucault-Collet, A., Gogick, K. A., White, K. A., Villette, S., Pallier, A., Collet, G., et al. (2013). Lanthanide near infrared imaging in living cells with Yb3+ nano metal organic frameworks. *Proc. Natl. Acad. Sci. U. S. A.* 110, 17199–17204. doi:10.1073/pnas.1305910110

Hemmer, E., Benayas, A., Légaré, F., and Vetrone, F. (2016). Exploiting the biological windows: Current perspectives on fluorescent bioprobes emitting above 1000 nm. *Nanoscale Horiz.* 1, 168–184. doi:10.1039/c5nh00073d

Idée, J. M., Port, M., Robic, C., Medina, C., Sabatou, M., and Corot, C. (2009). Role of thermodynamic and kinetic parameters in gadolinium chelate stability. *J. Mag. Res. Imag.* 30, 1249–1258. doi:10.1002/jmri.21967

Jin, G. Q., Sun, D., Xia, X., Jiang, Z. F., Cheng, B., Ning, Y., et al. (2022). Bioorthogonal lanthanide molecular probes for near-infrared fluorescence and mass spectrometry imaging. *Angew. Chem. Int. Ed.* 61, 202208707. doi:10.1002/anie.202208707

Maniaki, D., Sickinger, A., Barrios Moreno, L. A., Aguilà, D., Roubeau, O., Settineri, N. S., et al. (2023). Distributive Nd-to-Yb energy transfer within pure [YbNdYb] heterometallic molecules. *Inorg. Chem.* 62, 3106–3115. doi:10.1021/acs.inorgchem.2c03940

Miller, K. J., Saherwala, A. A., Webber, B. C., Wu, Y., Sherry, A. D., and Woods, M. (2010). The population of SAP and TSAP isomers in cyclen-based lanthanide(III) chelates is substantially affected by solvent. *Inorg. Chem.* 49, 8662–8664. doi:10.1021/ic101489t

Monteiro, J. H. S. K. (2020). Recent advances in luminescence imaging of biological systems using lanthanide(III) luminescent complexes. *Molecules* 25 (9), 2089. doi:10.3390/molecules25092089

Natrajan, L. S., Villaraza, A. J. L., Kenwright, A. M., and Faulkner, S. (2009). Controlled preparation of a heterometallic lanthanide complex containing different lanthanides in symmetrical binding pockets. *Chem. Commun.* 40, 6020–6022. doi:10.1039/b913702e

Nielsen, L. G., and Sørensen, T. J. (2019). Including and declaring structural fluctuations in the study of lanthanide(III) coordination Chemistry in solution. *Inorg. Chem.* 59 (1), 94–105. doi:10.1021/acs.inorgchem.9b01571

Nonat, A., Bahamyirou, S., Lecointre, A., Przybilla, F., Mély, Y., Platas-Iglesias, C., et al. (2019). Molecular upconversion in water in heteropolynuclear supramolecular Tb/Yb assemblies. *J. Am. Chem. Soc.* 141, 1568–1576. doi:10.1021/jacs.8b10932

Pujales-Paradela, R., Savić, T., Pérez-Lourido, P., Esteban-Gómez, D., Angelovski, G., Botta, M., et al. (2019). Lanthanide complexes with ^{1}H paraCEST and ^{19}F response for magnetic resonance imaging applications. *Inorg. Chem.* 58, 7571–7583. doi:10.1021/acs.inorgchem.9b00869

Rivas, C., Stasiuk, G. J., Gallo, J., Minuzzi, F., Rutter, G. A., and Long, N. J. (2013). Lanthanide(III) complexes of rhodamine-DO3A conjugates as agents for dual-modal imaging. *Inorg. Chem.* 52, 14284–14293. doi:10.1021/ic402233g

Sastri, V. S., Bünzli, J.-C., Rao, V. R., Rayudu, G. V. S., and Perumareddi, J. R. (2003). "Spectroscopy of lanthanide complexes," in *Modern aspects of rare earths and their complexes* (United States: American Chemical Society), 569–731. doi:10.1016/B978-044451010-5/50022-5

Sørensen, T. J., and Faulkner, S. (2018). Multimetallic lanthanide complexes: Using kinetic control to define complex multimetallic arrays. *Acc. Chem. Res.* 51, 2493–2501. doi:10.1021/acs.accounts.8b00205

Sørensen, T. J., Tropiano, M., Kenwright, A. M., and Faulkner, S. (2017). Triheterometallic lanthanide complexes prepared from kinetically inert lanthanide building blocks. *Eur. J. Inorg. Chem.* 2017, 2165–2172. doi:10.1002/ejic.201700027

Tircso, G., Webber, B. C., Kucera, B. E., Young, V. G., and Woods, M. (2011). Analysis of the conformational behavior and stability of the SAP and TSAP isomers of lanthanide(III) NB-DOTA-type chelates. *Inorg. Chem.* 50, 7966–7979. doi:10.1021/ic2012843

Tropiano, M., Blackburn, O. A., Tilney, J. A., Hill, L. R., Just Sørensen, T., and Faulkner, S. (2015). Exploring the effect of remote substituents and solution structure on the luminescence of three lanthanide complexes. *J. Lumin.* 167, 296–304. doi:10.1016/j.jlumin.2015.06.035

Xu, W., Alam Bony, B., Rong Kim, C., Su Baeck, J., Chang, Y., Eun Bae, J., et al. (2013). Mixed lanthanide oxide nanoparticles as dual imaging agent in biomedicine. *Sci. Rep.* 3, 3210. doi:10.1038/srep03210

Zaïm, A., Eliseeva, S. V., Guénée, L., Nozary, H., Petoud, S., and Piguet, C. (2014). Lanthanide-to-Lanthanide energy-transfer processes operating in discrete polynuclear complexes: Can trivalent europium Be used as a local structural probe? *Chem. Eur. J.* 20, 12172–12182. doi:10.1002/chem.201403206

frontiers | Frontiers in Chemistry

TYPE Original Research
PUBLISHED 07 September 2023
DOI 10.3389/fchem.2023.1238674

OPEN ACCESS

EDITED BY
Maxence Wisztorski,
Université de Lille, France

REVIEWED BY
Zhanchen Guo,
Nanjing University, China
Meiyong Liao,
National Institute for Materials Science, Japan

*CORRESPONDENCE
Christophe Masselon,
christophe.masselon@cea.fr

RECEIVED 12 June 2023
ACCEPTED 21 August 2023
PUBLISHED 07 September 2023

CITATION
Reynaud A, Trzpil W, Dartiguelongue L, Çumaku V, Fortin T, Sansa M, Hentz S and Masselon C (2023), Compact and modular system architecture for a nano-resonator-mass spectrometer.
Front. Chem. 11:1238674.
doi: 10.3389/fchem.2023.1238674

Compact and modular system architecture for a nano-resonator-mass spectrometer

Adrien Reynaud[1], Wioletta Trzpil[1], Louis Dartiguelongue[2,3], Vaitson Çumaku[2,3], Thomas Fortin[2,3], Marc Sansa[1], Sebastien Hentz[1] and Christophe Masselon[2,3]*

[1]Université Grenoble Alpes, CEA-Leti, Grenoble, France, [2]Université Grenoble Alpes, CEA, Institut de Recherche Interdisciplinaire de Grenoble, Grenoble, France, [3]INSERM UA13 Biosciences et bioingénérie pour la santé, Grenoble, France

Mass measurements in the mega-to giga-Dalton range are essential for the characterization of natural and synthetic nanoparticles, but very challenging to perform using conventional mass spectrometers. Nano-electro-mechanical system (NEMS) based MS has demonstrated unique capabilities for the analysis of ultra-high mass analytes. Yet, system designs to date included constraints transferred from conventional MS instruments, such as ion guides and high vacuum requirements. Encouraged by other reports, we investigated the influence of pressure on the performances of the NEMS sensor and the aerodynamic focusing lens that equipped our first-generation instrument. We thus realized that the NEMS spectrometer could operate at significantly higher pressures than anticipated without compromising particle focusing nor mass measurement quality. Based on these observations, we designed and constructed a new NEMS-MS prototype considerably more compact than our original system, and which features an improved aerodynamic lens alignment concept, yielding superior particle focusing. We evaluated this new prototype by performing nanoparticle deposition to characterize aerodynamic focusing, and mass measurements of calibrated gold nanoparticles samples. The particle capture efficiency showed nearly two orders of magnitude improvement compared to our previous prototype, while operating at two orders of magnitude greater pressure, and without compromising mass resolution.

KEYWORDS

mass spectrometry, NEMS, aerodynamic lens, resonator, single particle

1 Introduction

The characterization of large supra-molecular species is attracting growing interest in biology and analytical chemistry (Keifer et al., 2017; Erdogan et al., 2022). Mass spectrometry (MS) in the MDa to GDa range is especially interesting for the analysis of viral particles and synthetic nanoparticles (Dominguez-Medina et al., 2018; Lai et al., 2021). In this mass range, conventional MS becomes challenged by sample heterogeneity associated with the presence of variant species, chemical modifications, as well as salt or solvent adducts (Rolland and Prell, 2022). This creates highly convoluted m/z patterns that cannot be straightforwardly converted into the original analyte's mass. Several technologies based on single particle mass

determination methods have emerged to circumvent this issue, namely charge detection MS (CDMS) (Jarrold, 2022), nano-electro-mechanical system-based mass spectrometry (NEMS-MS) (Sage et al., 2015) and mass photometry (Young et al., 2018).

Nano-electro-mechanical system-based mass spectrometry (NEMS-MS) has unique capabilities to analyze ultra-high mass analytes in the MDa to GDa mass range regardless of their charge (Hanay et al., 2012; Sage et al., 2015). Earliest NEMS-based mass spectrometers consisted of modified MS architectures in which the detector was replaced by a nano-resonator (Naik et al., 2009; Hanay et al., 2012). Employing NEMS allowed decreasing the number of components because it works as both detector and analyzer. Moreover, as NEMS-MS does not require charging of the particles, analytes focusing could also rely on particle inertia, while mass is measured directly. These features make NEMS-MS insensitive to mass to charge convolution generated by similar species with differing charge states, enabling a simplified architecture that could ultimately become integrated as tiny instruments. However, as the technique is relatively young (Naik et al., 2009), many features and components still require optimization.

The first NEMS-MS prototype (Naik et al., 2009) consisted of an electrospray ionization source (ESI), a two-stage differentially pumped hexapole ion optics driven at radio frequency, and a NEMS mass sensor localized 2 m below the source. The NEMS resonator was operated at a pressure of 10^{-8} mbar and cooled to 40 K. This prototype achieved the first demonstration of NEMS-based MS of single biological molecules. Subsequent research on NEMS-MS focused on simplifying the measurement and the mass spectrometer's architecture, as well as developing more effective methods to focus the analyte on the NEMS mass analyzer/detector. A significant milestone was independently proposed by Hentz and Masselon (2016) and by Malvar et al. (2016). They proposed NEMS-MS systems devoid of ion guides, allowing them to create prototypes with somewhat relaxed pumping requirements. These systems consisted of series of chambers with decreasing pressures: a nebulization stage operating at ambient pressure, a heated capillary inlet with a first pressure drop to 10–100 mbar, a pressure-limiting orifice that could optionally be followed by a series of focusing orifices (aerodynamic lens), and a resonator chamber operating in the 10^{-3} to 10^{-5} mbar regime. These systems allowed decreasing the apparatus size, pumping requirements, and complexity of the system. However, the prototypes were still characterized by modest particle capture efficiency defined as the ratio of the number of detected over emitted particles. In the work by Malvar et al. 1 particle per 5×10^8 was detected, with event rates of ~0.3 particle per minute. Dominguez-Medina et al. (2018) reported the detection of 1 viral particle per 2.6×10^8 with an event rate of 0.8–1.35 particle per minute on a 20 resonators array. Recently, Hannay's group proposed a NEMS-MS system operating under ambient conditions while providing improved particle focusing (Erdogan et al., 2022). As a result, they achieved higher capture efficiency detecting 1 particle per 1.85×10^5 20 nm gold nanoparticles (GNP) and 1 particle per 4.97×10^5 40 nm GNP on one device. However, the atmospheric pressure measurement decreased NEMS performance and mass resolution. Consequently, measurements performed with their prototype on gold nanoparticles and viral particles exhibited substantial mass dispersion.

On the basis of literature reports, we hypothesized that there must exist a favorable operating pressure range that would allow reducing pumping requirements without affecting measurement performance. The goal of the present study was to establish this range through theoretical study and numerical simulation, an eventually demonstrate it experimentally. Ultimately, we applied our findings to develop a new NEMS-MS prototype characterized by decreased pumping requirements, superior focusing performances and improved particle capture efficiency over our previous system (Dominguez-Medina et al., 2018).

2 Materiel and methods

2.1 Working principle of NEMS-MS

Along the development iterations, the core of the NEMS-MS architecture remained unchanged (see Figure 1). It consists of four main parts: a nebulization and desolvation stage, an aerodynamic focusing lens followed by a skimmer, and an array of sensing elements.

The NEMS-MS technique analyzes particles from the gas phase, and thus an aerosol must be generated when the analytes are in solution. Two aerosolization methods are typically used: Surface Acoustic Wave Nebulization (SAWN) and nano ElectroSpray Ionization (nESI). The two methods are suitable for biological samples (e.g. viruses, virus-like particles) in small volume (<ml) of buffer solutions. SAWN produces lower kinetic energy droplets, promoting particle sampling through the inlet capillary. Nanoparticles can also be generated using a constant output atomizer, in order to produce larger amount of aerosol required to test system transmission and focusing. The nebulized particle stream passes through a stainless-steel inlet capillary which can be heated up to 250°C in order to dry particles and prevent solvent influence on the mass measurement (Clement et al., 2021). The inlet capillary typically is 250 µm in diameter, and 11 cm long and drives pressure levels in the following chambers of the instrument. Once the solvent excess has been removed, the aerosol must be focused to optimize individual particles capture and detection by the nano-resonator array. An aerodynamic lens is used to perform inertial focusing, producing a narrow particle beam. The longitudinal shape of the particle beam being a cone, the particle number flux (particle/m^2/s) decreases with the distance from the lens outlet. Consequently, one of the key parameters of the design is the lens-to-sensor distance, which shall be kept as small as possible. More details about the aerodynamic lens physical principle, simulation and characterization are provided in Section 2.3. Finally, the analyte stream reaches an array of 20 NEMS resonators fabricated from silicon on insulator (SOI) wafers using very large scale (VLSI) integration process (Mile et al., 2010). As the beams are 300 nm wide and their length is about 10 µm, their active area is exceedingly small. An analyte particle reaching a resonator's active surface induces simultaneous shifts in its resonance frequencies, which can be directly related to the mass and position of the landed particle (Sage et al., 2018).

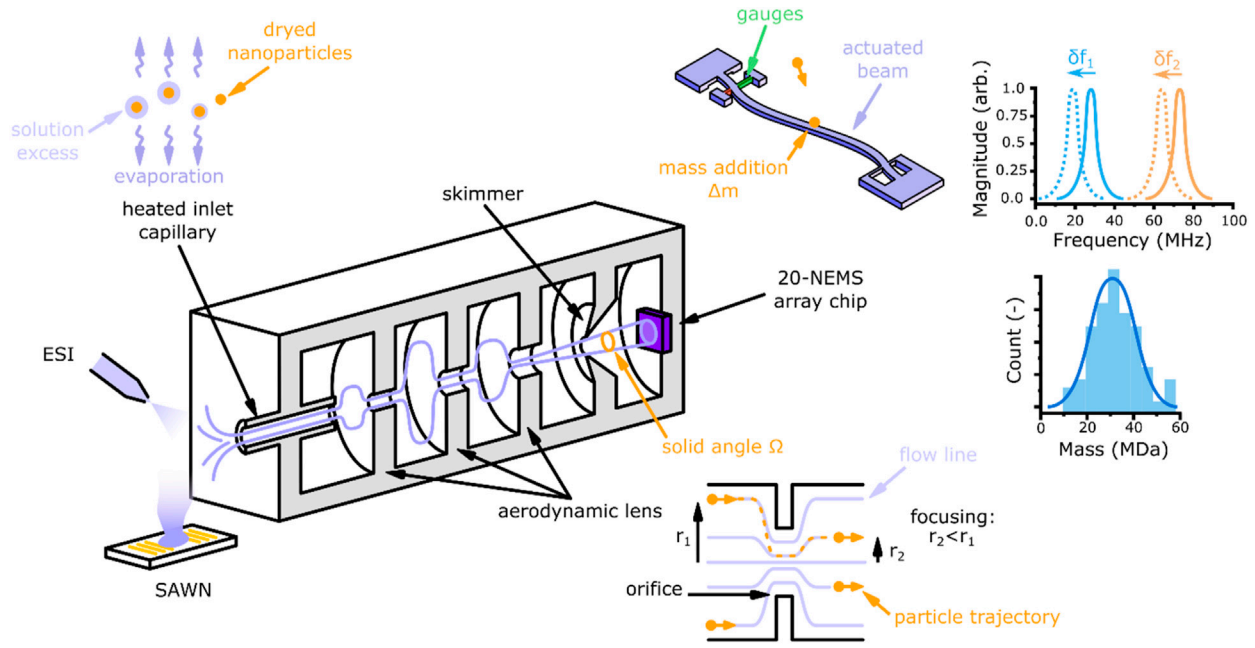

FIGURE 1
Overall scheme of NEMS-MS system architecture.

TABLE 1 Length, resonance frequency and quality factors for 3 nano resonators.

NEMS ID	Length [μm]	Mode 1		Mode 2	
		f [MHz]	*Q* [-]	*f* [MHz]	*Q* [-]
1	9.04	26.75	4000	73.47	2200
10	8.07	34.80	3600	95.10	1900
20	7.61	44.45	3000	122.00	1700

2.2 NEMS quality factor measurement

2.2.1 Doubly clamped nano resonators

Each NEMS within the array comprises a doubly-clamped vibrating beam electrostatically actuated at its resonance frequency. Two piezoresistive nano gauges near one end of the beam compress and stretch due to the it's displacement, generating a differential signal at the beam's oscillation frequency (see Figure 1). The resonators composing the array were designed with different lengths (see Table 1) in order to be addressed using different resonance frequencies, as shown in Figure 2. They all are 160 nm thick and 300 nm wide and their respective lengths are reported in the Supplementary Material; Section 9.

Resonator-based MS measurements require retrieving the frequency information from each individual resonator. Initial resonance frequencies and phase references are recorded for every resonator in the array (*cf.* Figure 2). Then, a phase-locked loop (PLL) is locked onto a given resonator to monitor and register frequency data for two modes successively for a given period, called idling time τ_{PLL}, after which it switches to the next resonator. Any landing particle event results in a mass addition Δm and causes quasi-instantaneous shift in the n-th mode resonance frequency Δf_n. The following relationship describes how Δf_n and Δm are interrelated:

$$\Delta m = M \frac{\Delta f_n}{f_n} \frac{\alpha_n}{\phi_n^2(x)} \tag{1}$$

Where M is the total mass of the beam, f_n the resonance frequency of the n-th mode, x the particle landing position, $\phi_n(x)$ the n-th mode shape and α_n a constant defined by $\alpha_n = -2\int_{x'=0}^{x'=1} \phi_n^2(x')dx'$. Equation 1 contains two unknowns: the particle mass Δm and its landing location x; thus, a two-equations system must be solved. In practice, the nano-resonator beams are actuated at their first and second modes so the two variables can be derived. The frequency jumps are considered as actual particle landing events when the frequencies shift by amounts larger than 5 times the average frequency noise in each mode (*cf.* Supplementary Material; Section 5). As a consequence, a crucial parameter for particle mass determination is the frequency stability over the measurement period, which must be as high as possible at the time scale of τ_{PLL}.

2.2.2 Characterizing NEMS for various pressures

The nano-resonators used as sensors can be described by several characteristics, one of which is the quality factor (Q factor), which captures information about energy dissipation in the system. The most significant dissipation for NEMS resonator operating in ambient conditions is caused by viscous damping (Li et al., 2007). To minimize energy losses and therefore maximize the quality factor of the sensor, NEMS are typically operated in a vacuum environment. However, it has been suggested that, as

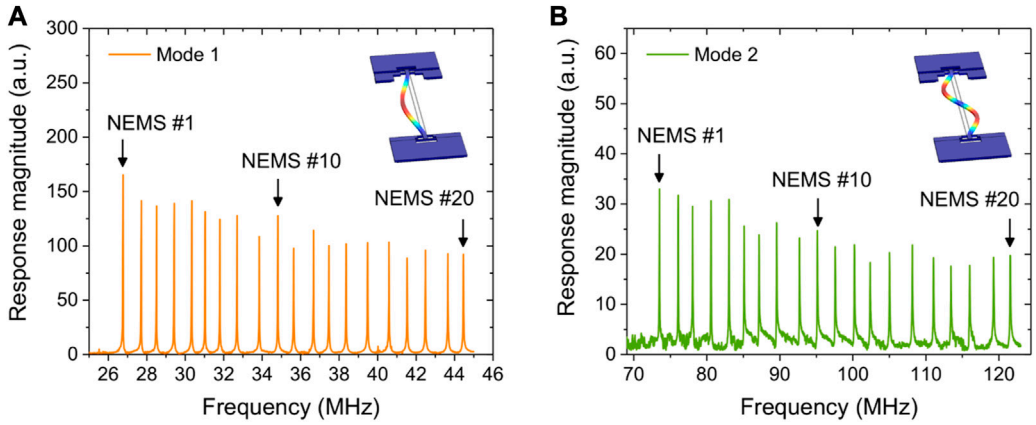

FIGURE 2
Frequency response of a 20 NEMS array for **(A)** mode 1 and **(B)** mode 2. Insets of each panel present the mode of vibration obtained using COMSOL simulation, and represented with exaggerated amplitudes for the sake of visualization. Each peak corresponds to the resonance of a single NEMS resonator. The length of resonators NEMS #1, NEMS #10, NEMS #20 are 9.04, 8.7, and 7.61 µm, respectively.

their critical dimensions approach the mean free path of gas molecules at ambient pressure, the Q factor of nanoscale devices is only marginally reduced while transitioning from high vacuum to atmospheric pressure (Li et al., 2007). Because our goal was to rationalize our system, one possible way entailed relaxing pumping requirements. To evaluate this possibility, we studied the effect of the pressure on NEMS resonance frequencies, their quality factor, and frequency stability. The experimental apparatus used to measure the relevant metrics (i.e., resonance frequency, Q factor and frequency stability) consisted in a vacuum chamber connected to a primary pump and equipped with a 925 micro-Pirani gauge. In order to vary the pressure inside the chamber, a valve was used to create a nitrogen leak allowing to perform measurements in the range 10^{-3} – 10^{3} *mbar*.

2.3 Aerodynamic lens

2.3.1 Inertial focusing

Aerodynamic lenses for aerosol sampling and focusing have been developed since the 1990s (Liu et al., 1995). They use particle drag force and inertia in order to manipulate particles through flow contractions induced by a series of orifices. This produces sudden changes in particle's motion that result in radial particle shifts, for particles having relaxation time higher than the obstacle characteristic time. In aerosol physics, this phenomenon is often characterized using the Stokes number, which is the ratio between particle's inertia and the drag force to which they are subjected, given by:

$$\mathrm{St} = \frac{\rho_p d_p^2 C_c(d_p) u}{18 \eta L} \tag{2}$$

Where ρ_p is the particle density, d_p its diameter, u the fluid velocity and C_c the Cunningham correction slip coefficient used to correct the drag force expression as a function of the flow regime (molecular, transition, continuum). η is the fluid viscosity and L is the obstacle characteristic length. When the Stokes number is close to unity, particles deviate from their trajectory due to their inertia but are quickly reattached to a flow line closer to the axis than their previous radial location. This describes how particles should behave when passing through one aerodynamic lens orifice. Since the Stokes number is a function of particle diameter and mass, an aerodynamic lens usually consists of several orifices focusing different particle sizes. Forcing particles to pass through multiple orifices therefore results in a narrower particle beam for a range of particle sizes.

2.3.2 Numerical model

Several authors modelled how nanoparticles behave within an aerodynamic lens (Zhang et al., 2002; Wang et al., 2005a; Abouali et al., 2009). A common approach is based on lagrangian tracking of the particles through the aerodynamic lens, ultimately allowing computation of the particle beam solid angle. COMSOL Multiphysics was used to solve steady, compressible, viscous, laminar Navier-Stokes equations. For computation efficiency's sake, an axisymmetric geometric domain was used. When it comes to boundary conditions, no slip boundary was used for walls, and both the downstream pressure and the throughput mass flow were computed using a macroscopic vacuum system model (cf. Supplementary Material; Section 3). As for the lagrangian part of the simulation, two forces were taken into account: the drag force and the Langevin force used to model brownian motion. The analytical formulations of both forces feature the Cunningham correction slip factor, depending itself on the flow regime (i.e., the Knudsen number) which had to be updated due to the pressure gradient particles are travelling through. The physical model was solved using the velocity Verlet algorithm with an adaptative time step and was written in Python.

2.3.3 Characterization

First, the aerodynamic lens focusing ability was characterized based on polystyrene nanoparticle deposition on a silicon target located at the same position than the detector. The polystyrene 100 nm nanoparticles colloidal solution (Magsphere, Pasadena,

California, United States) concentration was 1×10^{11} particles/ml and was nebulized using nESI at a flowrate of 8 $\mu l/min$ for 30 min. The inlet capillary was heated at 85°C. In order to estimate the diameter of the deposition pattern, the target was observed using binocular loupe and the resulting picture was processed by analyzing pixel intensity profiles (*cf.* Supplementary Material; Section 7).

The second approach aimed at validating the transmission efficiency of the focusing lens by using the NEMS sensors, and comparing first and second NEMS-MS prototypes characteristics. In this approach, three gold nanoparticles colloidal solutions were investigated. 20 and 40 nm diameter GNP were purchased from BBI Solutions (Crumlin, Wales, UK) and the nm diameter GNP were purchased from Sigma Aldrich (Saint-Louis, Missouri, United States). GNP were sprayed using SAWN or nESI. The mass spectra—Converted into geometric diameter—And event counts per minute and per active NEMS devices were evaluated.

2.4 Pumping requirements

As our overall objective was to decrease the pumping requirements, the design phase included a pressure calculation step. A mass conservation model (cf. Supplementary Material; Section 3) was used to compute the pressure in each chamber based on a given pumping speed. It helped finding design parameters (inlet capillary length and diameter, lens orifice diameters, skimmer diameters) matching NEMS and aerodynamic lens compatible pressure ranges. This model was a keystone in the iterating process for simulating several pumping setups. Importantly, the optimal pressure range for pump performance was also taken into account, as turbomolecular pumps capacity steeply degrades below 10^{-3} mbar.

3 Results and discussion

One of the key parameter to downsize NEMS-MS prototype was the operating pressure: turbo-molecular pumps are large and heavy and require cumbersome vacuum chambers and frame. However, limiting the pressure is necessary to avoid the nano-resonator dampening leading to degradation of the quality factor and thus poorer mass resolution. Furthermore, the operating pressure of the aerodynamic lens, linked to a large extent to the analytical throughput, also plays a role in the quality of the inertial focusing. As a consequence, both of these aspects had to be addressed independently in order to determine the suitable operating pressure range.

3.1 Nano-resonators in moderate vacuum

We studied the dependence of the quality factor (Q factor) of several resonators with respect to the operating pressure. In order to cover the various beam dimensions from our 20 resonators arrays, we selected three different beams (i.e. the ones with smallest, largest and median length) and characterized their mechanical parameters—Resonance frequency, quality factor, and frequency stability—As a function of pressure.

Figure 3 displays the Q factors as a function of operating pressure for the three selected resonators. Before reaching high pressures, Q factors are constant and are, for resonators 1, 10 and 20: 4000, 3600 and 3000 for the first mode. For the second mode, their values are 2200, 1900, and 1700, respectively. A loss of 10% of the maximum value (highlighted by dashed lines) was observed at 2, 3, and 4 mbar for the first mode and at 10, 20, and 25 mbar for the second mode for NEMS number 1, 10 and 20 respectively. The trend presented by quality factor as a function of pressure has been previously reported (Li et al., 2007; Gavan et al., 2009), and our results confirm prior observations for our specific devices. A model based on the hydrodynamic function with comparisons to other models was described in (Aoust et al., 2015). The manifestation of the minor effect of the pressure on the quality factor can be given by the flow regime. It can be determined by the Knudsen number $Kn = \lambda/L_c$, which is the ratio between the molecule mean free path λ and a resonator characteristic dimension L_c. In our case, the width of the beams (300 nm) can be considered to estimate the Knudsen regime (Gavan et al., 2009). If the mean free path λ is larger than L_c (when $Kn > 10$), the probability that the beam encounters a gas molecule is small, leading to a null viscous damping. In this regime, the damping is mainly caused by thermoelastic effects and energy transfer into the support (clamps). In our case, the most significant losses are connected with energy dissipation into the support (cf. Supplementary Material; Section 6). Viscous damping is introduced for a Knudsen number $Kn < 10$, leading to decrease of the quality factor. The vertical line on the graph Figure 3A was plotted to delimit the relevant Knudsen regimes. For devices with characteristic dimensions in the hundreds of nanometers, this regime shifts toward higher pressure values, and the operating pressure may be increased without sacrificing performance.

Another parameter that can determine the flow regime is the Weissenberg number $Wi = \tau/T$, which is a ratio of the characteristic time scale T to the relaxation time τ in the medium. It has been shown (Karabacak et al., 2007) that increasing the resonance frequency of nano-resonators allows to reach the molecular flow regime where viscous damping becomes negligible. This may explain why, for the second mode of vibration, the quality factor was less influenced by a comparable increase in pressure than the first mode. Moreover, for the same mode of vibration, smaller resonators (i.e. having a higher frequency) are characterized by a lesser quality factor reduction as a function of pressure, which was also consistent with previous observations (Karabacak et al., 2007).

Frequency stability is a key performance parameter for nano-resonators used in mass spectrometry as the particle masses are deduced from frequency shifts. Lower frequency stability causes higher noise level and degraded mass resolution. The frequency stability was characterized using Allan deviation and was measured as a function of pressure from the closed loop frequency trace of an individual resonator. We show that this parameter remains constant until a pressure of $\sim 0.5\,mbar$ (cf. Figure 4), showing that mass resolution and hence measurement performance remain stable up to this value. Other Allan deviation plots are reported in the Supplementary Material; Section 1.

Our investigations showed that our nano-resonators could operate in a pressure regime as high as $0.5\,mbar$ without sacrificing mass resolution. Moreover, they confirmed that using

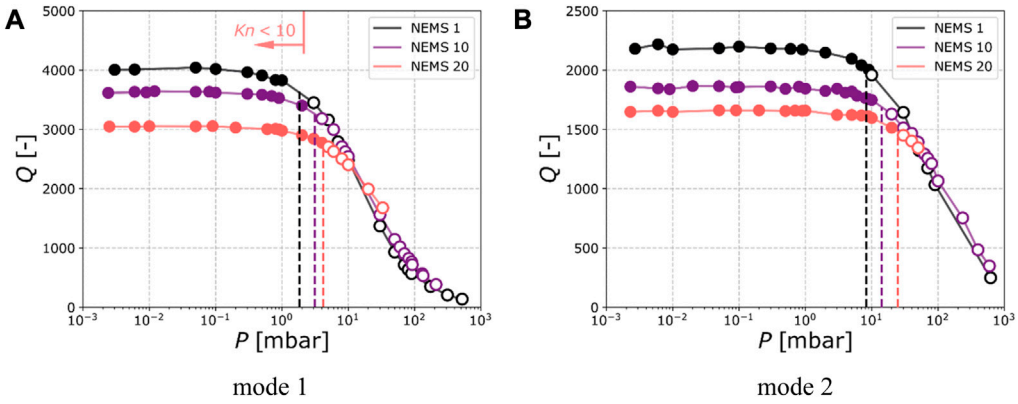

FIGURE 3
Resonance quality factor of the first **(A)** and second **(B)** modes for the NEMS number 1, 10 and 20 when operated in at various pressures. This three NEMS have different lengths and thus different resonance frequencies (see Table 1). The dashed vertical lines indicate pressures at which the quality factor loses 10% of its maximum value.

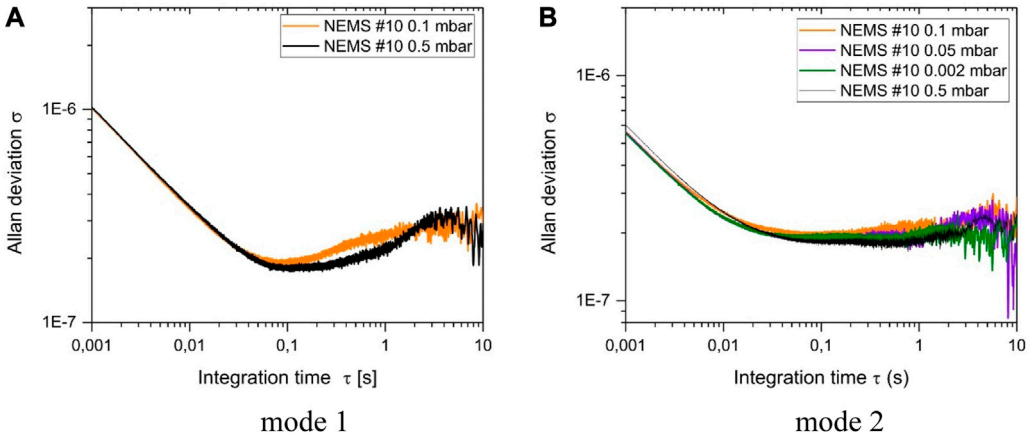

FIGURE 4
Allan deviation of the first **(A)** and second **(B)** modes for the NEMS number 10.

smaller NEMS would allow further reduction of the pumping requirements and thus limit the apparatus footprint.

3.2 Aerodynamic focusing

The ability to operate nano-resonators at a relatively high pressure (or low Knudsen number) is the foundation of the NEMS-MS prototype downsizing. Yet, another important aspect of the instrument depends on pressure: particle transport to the NEMS detector. Therefore, we had to also validate the operation of the aerodynamic lens at higher pressure.

The first NEMS-MS prototype (Dominguez-Medina et al., 2018) integrated an aerodynamic lens which was designed using (Wang et al., 2005b) guidelines. It was optimized to collimate virus-like nanoparticles of diameter in the 100 nm range and unit density. It was experimentally characterized with 45 nm polystyrene particles at an upstream pressure of 10^2 mbar and a downstream pressure of 10^{-2} mbar. The resulting deposit at the NEMS location was measured to be 1.5 mm diameter. Since this performance matches the targeted NEMS-MS applications, we decided to retain the same aerodynamic lens design and investigate its focusing abilities at higher pressure.

As described earlier, the selected approach was based on the particle lagrangian tracking through the aerodynamic lens because it could directly provide the particle beam solid angle. Boundary conditions, including mass flow and downstream pressures, were computed using the vacuum system model (cf. Section 2.4; Supplementary Material; Section 3). Ultimately, calculated pressures were compared with actual measurements and found to be in good agreement.

Figures 5A–D present particles trajectories inside the aerodynamic lens computed with an exit pressure of 1.33 mbar for particles of different diameters and a density of 1.06 g/cm^3, which corresponds to polystyrene and is close to that of viral samples for which the lens was initially designed. Based on these results, both the

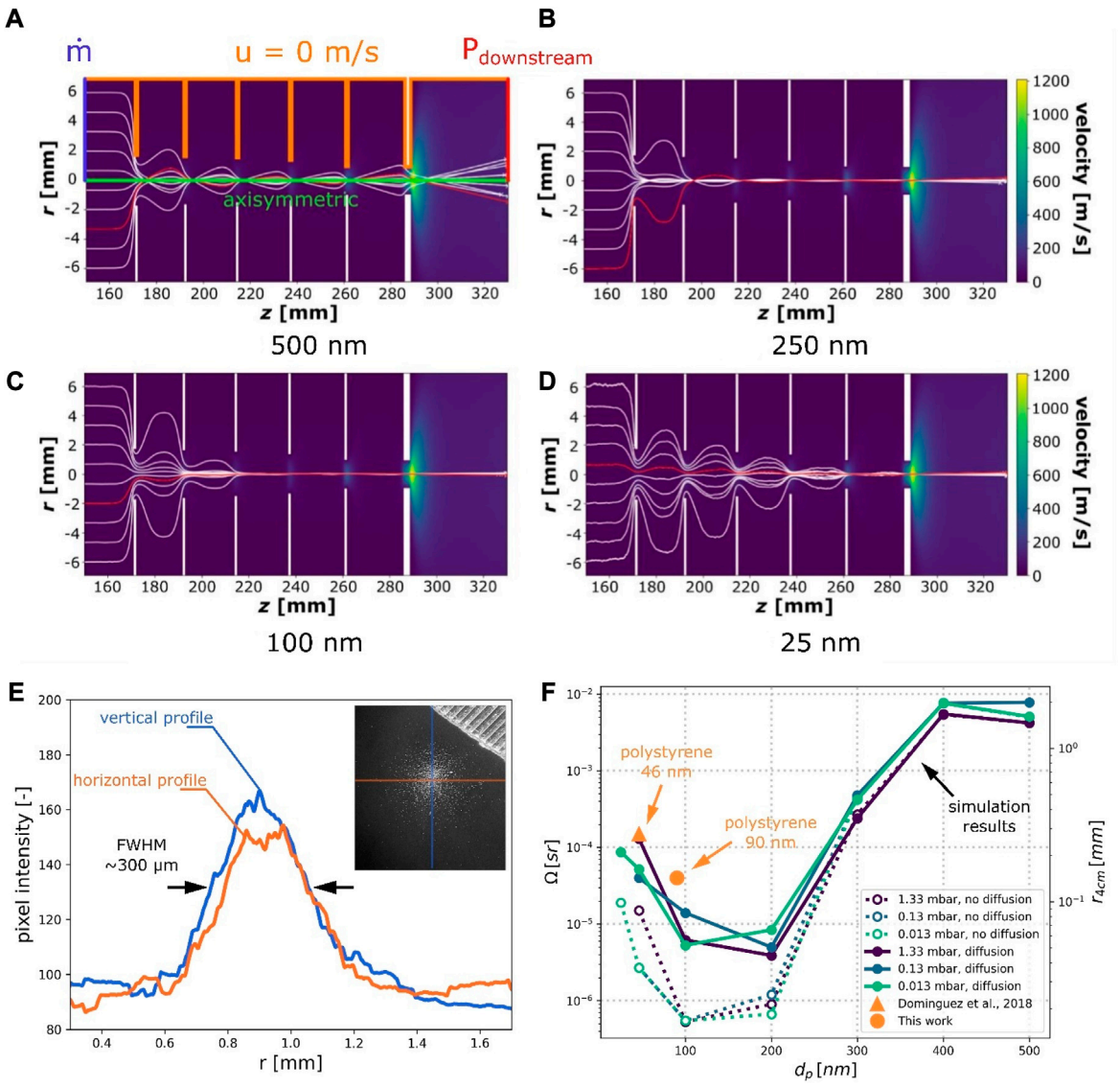

FIGURE 5
Particle trajectories through the lens simulated for different particle diameters: **(A)** 500 nm, **(B)** 250 nm, **(C)** 100 nm and **(D)** 25 nm. **(E)** Pixel intensity profiles of the deposit photograph along two axes, located by the orange and blue lines on the inset. **(F)** Solid angle Ω and particle beam radius at 4 cm downstream the lens (location of the NEMS sensor) computed for several downstream pressures. Orange points represent experimental data and dots are simulation results.

solid angle Ω and the particle beam radius 4 cm downstream the aerodynamic lens (written r_{4cm}) were derived for different particle diameter d_p. The 4 cm distance corresponds to the location of the NEMS array in the new mechanical architecture. The results reported in Figure 5F show how the solid angle behaves depending on particle diameter and that the solid angle remains optimal for the range $100 - 200\,nm$. Moreover, the addition of the Langevin force used to model diffusion plays a significant role only for particles smaller than $300\,nm$ and yields more realistic predictions when compared to experimental results (orange dots). Finally, within the investigated pressure range ($1.33 \times 10^{-2} - 1.33$ mbar), the model showed that the impact of diffusion remained relatively constant and pressure had a limited influence on the resulting particle beam's solid angle.

We verified the numerically computed focusing of the aerodynamic lens by exposing silicon targets to a ~90 nm average diameter polystyrene nanoparticle beam. Using a binocular loupe and image processing, the deposit diameter was estimated to be approximately $300\,\mu m$ (*cf.* Figure 5E). This value was reported on Figure 5F and is consistent with the numerical model predictions. It is worth noting that this represents a factor 5 improvement over the previous system generation (Dominguez-Medina et al., 2018) in terms of beam diameter. This is mainly due to the smaller lens-to-detector distance which used in the novel design (4 *vs.* 8 cm). According to these results, as for the NEMS sensor, the aerodynamic lens may be used without performance degradation over the studied pressures for the size range of

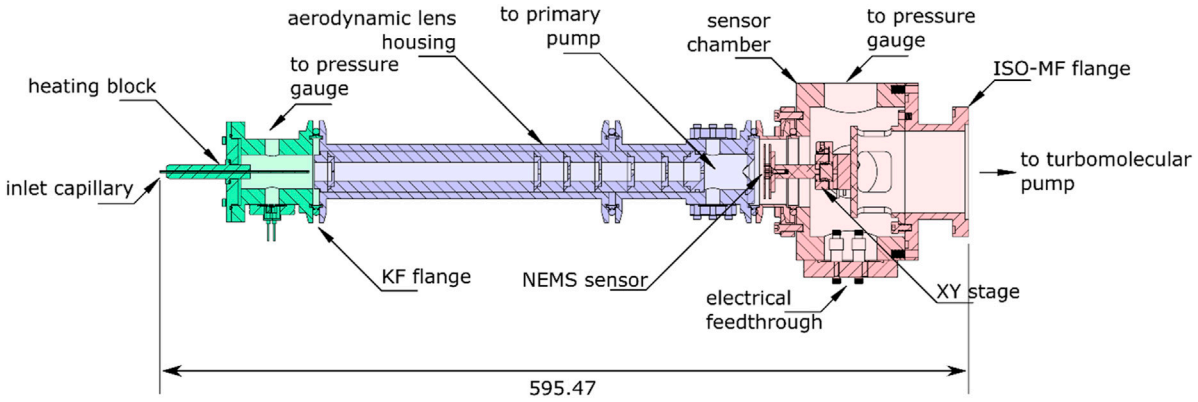

FIGURE 6
Mechanical compact and modular design of the NEMS-MS prototype. The green parts are the inlet section, the blue parts comprise the aerodynamic lens and the skimmer. The red parts are the sensor chamber, designed to hold the turbo molecular pump and the XY actuated stages.

interest, confirming that the NEMS-MS architecture is compatible with a substantial reduction of the pumping system.

3.3 Compact and modular NEMS-MS design

Following the aerodynamic lens study and the NEMS performance analysis over a wide pressure range, the vacuum system was modelled as described in Section 2.4 and a new pumping strategy was defined to maintain a 0.1 slm mass flow and related pressures of 2.7 mbar downstream the lens and 1.3×10^{-2} mbar inside the sensor chamber. Instead of the two turbomolecular pumps (450 l/s and 250 l/s) used to pump the system downstream of the aerodynamic lens and in the sensor chamber respectively, a single smaller turbo-molecular pump (TwisTorr 74FS, Agilent Technologies, Les Ullis, and France) was used to pump down the sensor chamber. A backing primary scroll pump (IDP-3, Agilent Technologies, Les Ullis, and France) was also used to pump the chamber downstream of the aerodynamic lens and back up the turbo-molecular pump.

One of the objectives underlying the reduced pumping is to downsize the NEMS-MS bench in order to make it more practical to use. Thus, this second-generation prototype was engineered considering not only the dimensions, but also the modularity of the instrument. This will allow future users facing novel challenges to upgrade the instrument. Therefore, each function (particle intake, aerosol focusing and particle mass measurement) has been attributed a different mechanical module, as shown on Figure 6. Having opted to limit the diameter of the instrument, the mechanical cohesion of the assembly could be ensured by KF50 flanges, which are easier to mount, open and close. Moreover, the overall system was mounted on a rail, keeping the sensor chamber fixed and allowing the inlet chamber and the aerodynamic lens to slide away from the nano-resonator housing to access and replace the sensor's chip.

Because of the heavy pumps operated on the first-generation prototype, heavy vacuum components were used to support the weight and to prevent mechanical vibrations. Large hardware parts made the aerodynamic lens-to-detector distance optimization difficult and constrained the sensing area to deposit area ratio. Moreover, large mechanical parts being complex and expensive to machine, a built-in alignment solution could not be implemented, and a port aligner as well as a XY stage were used to align the lens outlet and the NEMS array respectively. As a result, one of the most time-consuming tasks to perform when replacing a NEMS chip was the alignment process, which was required to keep the sensor at the center of the particle beam produced by the aerodynamic lens. This operation was facilitated in the new system by designing a native alignment between the inlet capillary, the aerodynamic lens housing and the skimmer. Henceforth, the alignment step reduces to positioning the sensor within the particle beam area instead of aligning multiple parts aerodynamic lens and sensor as in the previous NEMS-MS prototype.

Finally, since the novel NEMS-MS prototype may host various sensor technologies—Nano-electromechanical as well as nano-optomechanical devices—The sensor chamber was designed accordingly, guaranteeing an easy and compact alignment solution whatever the type of chip used. The sensor itself is packaged onto a printed circuit board which is mounted on a motorized XY stage (Agilis AG-LS25, Newport, Irvine, California, United States), which could be used to monitor the sensor location and scan the particle beam.

3.4 Gold nano particles mass spectra

Eventually, to assess the new-generation compact and modular NEMS-MS system, we performed mass analysis of a series of calibrated samples of GNP of sizes 20, 30, and 40 nm. Nanoparticle colloidal suspensions were diluted in methanol, achieving concentrations of 4.50×10^{10} to 3.50×10^{11} particle/ml depending on nanoparticle diameter. Figure 7 presents examples of frequency traces obtained in both resonance modes during exposition to 20 nm GNP. The amplitudes of the observed frequency discontinuities can be translated into the mass-position domain, allowing the production of a particle mass distribution (PMD) (cf. Section 2.2.1). The distributions obtained for the three sampled analyzed in this study are shown in Figure 8.

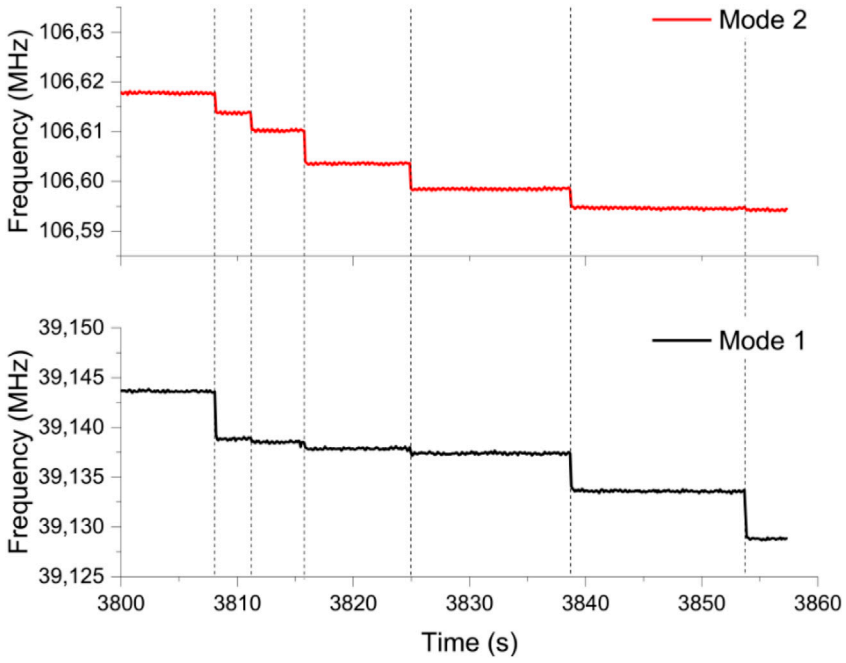

FIGURE 7
Phase-locked loop raw frequency traces for one resonator as a function of time during the deposition of 20 nm GNP produced by nanoESI. Black and red lines represent first and second mode, respectively. Dashed lines indicate mass deposition events.

Since GNP manufacturers characterized the batches by measuring nanoparticle diameters, the PMD were translated into mass equivalent diameters, assuming perfect sphericity and homogeneous density equal to that of bulk gold ($\rho_{gold} = 19.3\, g/cm^3$). Gaussian functions were used to fit masses and diameters histograms. Fitting parameters are reported in Table 2 and show good agreement with manufacturer's data (diameter measured by SEM), the relative difference in size ranging from 0.3% to 16% depending on the sample, and from 8.0% to 11.9% in mass. The standard deviation also compared well with manufacturer's data. Moreover, it should be highlighted that even if this comparison allowed to quantify the difference between NEMS-MS mass measurement and SEM size measurement, these techniques do not determine the same metric. Indeed, in order to compute the diameter of a particle, SEM is based on 2D image processing and NEMS-MS performs a mass-to-size conversion. Thus, both techniques assume the sphericity of particles, but the different metrics may induce different error factors. Finally, one might keep in mind that nano-resonator mass measurement has its own uncertainty as investigated previously by Clement et al. (2021).

In addition to characterizing mass measurement accuracy and precision, these experiments allowed to estimate the particle capture efficiency, which is useful for comparison with the previous system. Particle capture efficiency, as defined as the ratio between the number of detected particles to the number of GNP nebulized from solution during the measurement, was determined for one single NEMS among the 20 resonators of the array. The measurement details (i.e., flow rate, duration, initial concentration) are presented in the Supplementary Material (Section 8). The particle capture efficiencies were computed for each GNP sample and are reported in Table 3. These values are compared with those reported by Dominguez-Medina et al. (2018), performed with ESI nebulization technique, showing an improvement factor of 20–200. The detection efficiency improvement could partly be attributed to the reduction in aerodynamic lens-to-sensor distance which has been halved (4 cm *vs.* 8 cm). Another possible reason may be that the new prototype is less affected by pump vibrations as the lens housing and the skimmer are mounted contiguously. Moreover, the lens housing is also aligned with the rest of the mechanical parts of the system, and has no degrees of freedom. These mechanical optimizations indirectly benefited from the pumping requirements downsizing, which allowed to reduce every dimension of the system, and were not possible on the first-generation prototype due to the cumbersome vacuum hardware components.

The interest in analyzing large sample fractions grows when the amount of available sample volume is small, which is often the case for biological samples, or for broad mass distributions that require a lot of events to acquire adequate statistics. To pursue the same objective (Erdogan et al., 2022), chose to dispense with vacuum system altogether and performed on-chip electrostatic focusing at ambient pressure. The main benefit of this technique was to reduce the volume and the cost of the apparatus while achieving a particle capture efficiency of 1 per 1.85×10^5 particle to 1 per 4.97×10^5 particle for one device. At this point, it should be stressed that particle capture efficiency comparisons are complicated due to potentially different raw resonance frequency postprocesses.

10.3389/fchem.2023.1238674

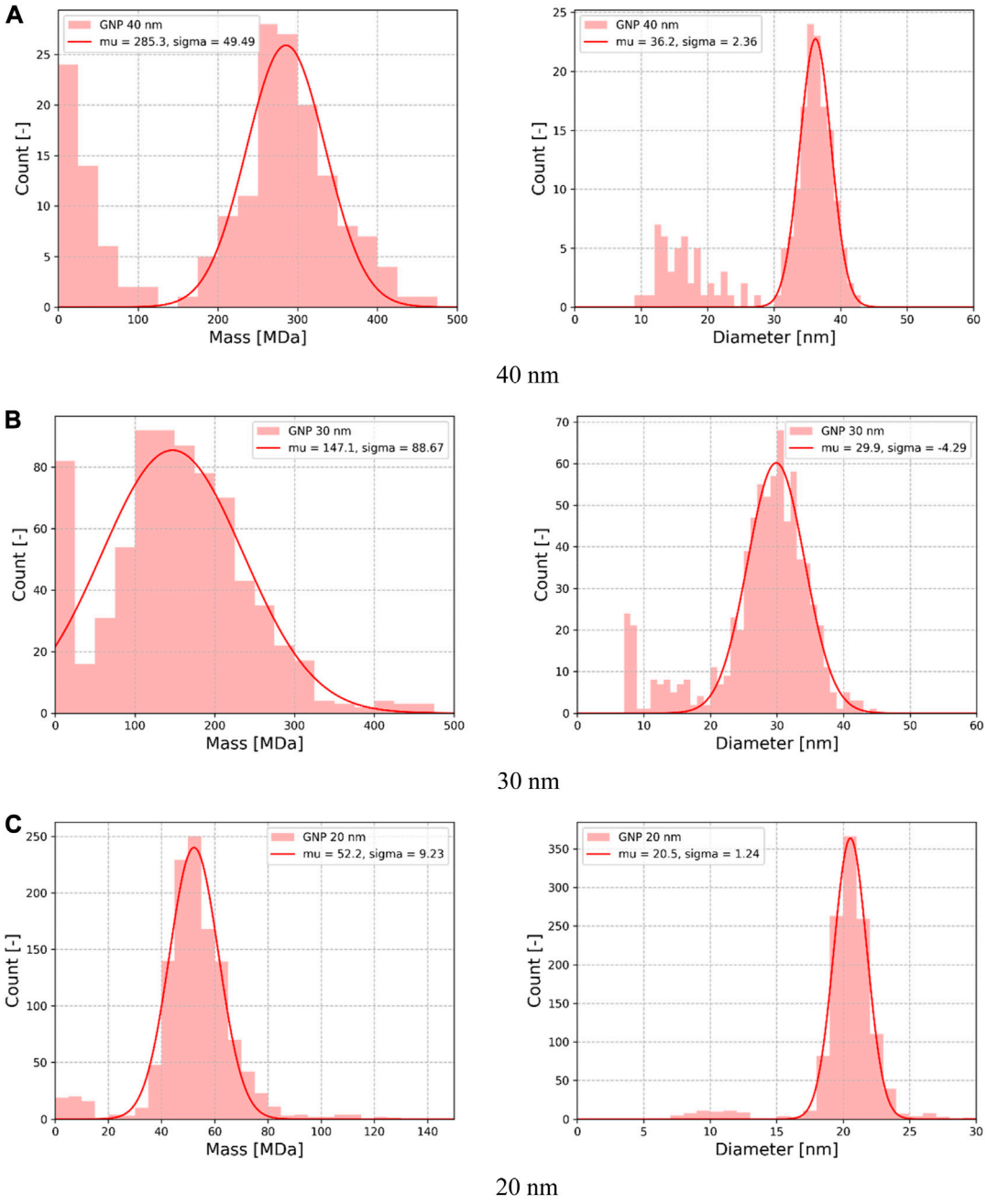

FIGURE 8
Histogram of the mass measurement performed during 60 min of acquisition time retrieved from the frequency shifts for gold NP of diameter **(A)** 40 nm **(B)** 30 nm **(C)** 20 nm.

TABLE 2 Gaussian fit parameters (mean and dispersion) compared with manufacturer data.

Sample	Mass			Diameter		
	NEMS-MS $\bar{m}$ (σ_m)	SEM $\bar{m}$	Relative difference	NEMS-MS $\overline{d_p}$ (σ_{d_p})	SEM $\overline{d_p}$	Relative difference
	[MDa]	[MDa]	[–]	[nm]	[nm]	[–]
20 nm (BBI)	52.2 (9.2)	46	11.9%	20.5 (1.2)	19.6 (<1.6)	4.4%
30 nm (Sigma-Aldrich)	147.1 (88.7)	164	11.5%	29.9 (4.3)	30 (2)	0.3%
40 nm (BBI)	285.3 (49.5)	308	8.0%	36.2 (2.4)	37–42 (N/A)	2.2%–16%

TABLE 3 Capture efficiency computed for the gold nanoparticles. [1]Range computed based on the upper and lower capture efficiency reported by (Dominguez-Medina et al., 2018), namely 1 per ~2×10^9 and 1 per ~1×10^{10} sprayed particle, respectively. [2] Capture efficiency expressed as 1 detected particle per N nebulized particles.

GNP sample	Sprayed particles	Number of NEMS	Event count	Capture efficiency[2]	Capture efficiency for 1 NEMS[2]	Improvement factor[1]
	[$\times 10^9$ NP]	[-]	[-]	[-]	[-]	[-]
20 nm (BBI)	12.3	9	1220	1 per 4.5×10^6	1 per 9.0×10^7	22–111
30 nm (Sigma-Aldrich)	3.12	12	739	1 per 2.5×10^6	1 per 5.1×10^7	40–198
40 nm (BBI)	1.58	9	183	1 per 3.9×10^6	1 per 7.8×10^7	26–129

4 Conclusion

In order to downsize the first generation NEMS-MS prototype without compromising mass measurement quality, the impact of an increase in operating pressure was analyzed. For this purpose, we separately addressed the NEMS and the aerodynamic lens. NEMS devices were characterized experimentally over a wide pressure range (10^{-3}–10^3 mbar) and it was shown that their performance was unaffected at pressures up to 0.5 mbar. The aerodynamic lens was simulated numerically over an operating downstream pressure range of 1.3×10^{-2}–1.3 mbar for particle within the range of 25–500 nm and did not show to be significantly affected by this parameter.

Based on these results, a new vacuum system has been designed with a single turbomolecular pump (74 L/s), replacing the two larger pumps used in the previous-generation assembly (450 L/s and 250 L/s). This radical optimization led to a more compact, lightweight, modular and easy to operate mechanical design. Moreover, it allowed to position the NEMS sensor closer to the aerodynamic lens outlet, improving the particle transfer from the source to the sensor. Performance improvement was quantified using two approaches: the particle beam area at the sensor has been measured to be approximately 5 times smaller than in the previous design, and the particle capture efficiency has been increased by a factor of 20–200. The prototype, based on arrays of NEMS operated with a frequency-addressing scheme, was validated with mass measurements of standard nanoparticle samples and showed excellent agreement with predicted values.

Particle capture efficiency being one of the main limitations of NEMS-based MS, it was one of the main motivations underlying this design optimization. Improving it allows to perform analysis faster: the data used to plot the spectra reported on Figure 8 were registered during 60 min experiments and would have required more than 10 hours on the previous setup. Overall, the NEMS-MS technique presents a trade-off between particle capture efficiency and mass resolution: increasing the NEMS exposition to aerosol seems to imply an increase in pressure, which in return affects the mass resolution. In our system, the trade-off to keep a 0.1 MDa mass resolution (Clement et al., 2021) seems to be, pressure-wise, at 0.5 mbar (cf. Figure 3). However, this threshold might not be suitable for smaller particles as the diffusion could cause the divergence of the particle beam downstream the aerodynamic lens (Wang and McMurry, 2006).

Although the presented NEMS-MS prototype yielded significantly enhanced performance, there is still potential for improvement. For instance, the size of the aerodynamic lens can be decreased, as it is the longest component in this prototype. Moreover, due to pumping considerations, the actual NEMS operating pressure (1×10^{-2} mbar) is still lower than the identified limit of operation (5×10^{-1} mbar), which opens the way to further developments using even smaller pumps or inlets with larger intake. Furthermore, detection efficiency could be further increased by NEMS and aerodynamic lens architecture, while sensitivity and mass range could be enhanced by NEMS sensor geometry. For the latter purpose, nano-optomechanical sensor might be implemented in this apparatus, which offer larger sensitive area and mass determination independently of particle landing position and physical properties (stiffness, size, and shape) (Sansa et al., 2020). These optimizations will eventually lead to new iterations of this NEMS-MS prototype, which will be greatly facilitated by its modularity.

Data availability statement

The raw data supporting the conclusion of this article will be made available by the authors, without undue reservation.

Author contributions

AR, CM, and SH conceived and designed the novel instrument. AR, LD, VÇ, and WT built and tested the instrument. AR, CM, MS, SH, and WT conceived and designed the simulations and experiments. AR, LD, VÇ, and WT performed the simulations and experiments. AR, CM, LD, MS, TF, and WT processed, analyzed, and interpreted the data. AR, CM, and WT drafted the manuscript. All authors contributed to the article and approved the submitted version.

Funding

This work was funded in part by the European Union through the ERC ENLIGHTENED project (GA # 616251), by the Cross-Disciplinary Program on Instrumentation and Detection of the French Alternative Energies and Atomic Energy Commission [CEA] (VIA-NEMS) and by the French National Research Agency [ANR] through the AERONEMS project (ANR-21-CE42-0028-01). VÇ

acknowledges funding from the Grenoble Alliance for Integrated Structural and Cell Biology (ANR-17-EURE-0003).

Acknowledgments

We gratefully acknowledge M. Michel Boujard from CEA Technilab for the fabrication of system parts, as well as Katell Aldrin and Dr Vincent Agache from CEA LETI/DTBS for the generous gift of 40 nm GNP. We also express our thanks to Dr Bastien Pellegrin and Dr Sébastien Artous from CEA LITEN, as well as Dr Mehrzad Roudini and Andreas Winkler from IFW Dresden for helpful discussions.

Conflict of interest

CM and SH are co-inventors of patents US9506852B2, EP2779209A1, and JP6352004B2.

The remaining authors declare that the research was conducted in the absence of any commercial or financial relationships that could be construed as a potential conflict of interest.

Publisher's note

All claims expressed in this article are solely those of the authors and do not necessarily represent those of their affiliated organizations, or those of the publisher, the editors and the reviewers. Any product that may be evaluated in this article, or claim that may be made by its manufacturer, is not guaranteed or endorsed by the publisher.

Supplementary material

The Supplementary Material for this article can be found online at: https://www.frontiersin.org/articles/10.3389/fchem.2023.1238674/full#supplementary-material

References

Abouali, O., Nikbakht, A., Ahmadi, G., and Saadabadi, S. (2009). Three-dimensional simulation of brownian motion of nano-particles in aerodynamic lenses. *Aerosol Sci. Technol.* 43, 205–215. doi:10.1080/02786820802587888

Aoust, G., Levy, R., Bourgeteau, B., and Le Traon, O. (2015). Viscous damping on flexural mechanical resonators. *Sens. Actuators Phys.* 230, 126–135. doi:10.1016/j.sna.2015.04.004

Clement, K., Reynaud, A., Defoort, M., Vysotskyi, B., Fortin, T., Lai, S. H., et al. (2021). Requirements and attributes of nano-resonator mass spectrometry for the analysis of intact viral particles. *Anal. Bioanal. Chem.* 413, 7147–7156. doi:10.1007/s00216-021-03511-4

Dominguez-Medina, S., Fostner, S., Defoort, M., Sansa, M., Stark, A. K., Halim, M. A., et al. (2018). Neutral mass spectrometry of virus capsids above 100 megadaltons with nanomechanical resonators. *Science* 362, 918–922. doi:10.1126/science.aat6457

Erdogan, R. T., Alkhaled, M., Kaynak, B. E., Alhmoud, H., Pisheh, H. S., Kelleci, M., et al. (2022). Atmospheric pressure mass spectrometry of single viruses and nanoparticles by nanoelectromechanical systems. *ACS Nano* 16, 3821–3833. doi:10.1021/acsnano.1c08423

Gavan, K. B., van der Heijden, J., van der Drift, E. W. J. M., and van der Zant, H. S. J. (2009). "Effect of pressure on the Q factor and the resonance frequency of SiN microcantilevers," in 2009 4th IEEE International Conference on Nano/Micro Engineered and Molecular Systems, Shenzhen, China, 05-08 January 2009 (IEEE), 380–384. doi:10.1109/NEMS.2009.5068600

Hanay, M. S., Kelber, S., Naik, A. K., Chi, D., Hentz, S., Bullard, E. C., et al. (2012). Single-protein nanomechanical mass spectrometry in real time. *Nat. Nanotechnol.* 7, 602–608. doi:10.1038/nnano.2012.119

Hentz, S., and Masselon, C. (2016). Device for determining the mass of a particle in suspension or in solution in a fluid. US9506852B2.

Jarrold, M. F. (2022). Applications of charge detection mass spectrometry in molecular biology and biotechnology. *Chem. Rev.* 122, 7415–7441. doi:10.1021/acs.chemrev.1c00377

Karabacak, D. M., Yakhot, V., and Ekinci, K. L. (2007). High-frequency nanofluidics: An experimental study using nanomechanical resonators. *Phys. Rev. Lett.* 98, 254505. doi:10.1103/PhysRevLett.98.254505

Keifer, D. Z., Pierson, E. E., and Jarrold, M. F. (2017). Charge detection mass spectrometry: Weighing heavier things. *Analyst* 142, 1654–1671. doi:10.1039/C7AN00277G

Lai, S. H., Tamara, S., and Heck, A. J. R. (2021). Single-particle mass analysis of intact ribosomes by mass photometry and Orbitrap-based charge detection mass spectrometry. *iScience* 24, 103211. doi:10.1016/j.isci.2021.103211

Li, M., Tang, H. X., and Roukes, M. L. (2007). Ultra-sensitive NEMS-based cantilevers for sensing, scanned probe and very high-frequency applications. *Nat. Nanotechnol.* 2, 114–120. doi:10.1038/nnano.2006.208

Liu, P., Ziemann, P. J., Kittelson, D. B., and McMurry, P. H. (1995). Generating particle beams of controlled dimensions and divergence: I. Theory of particle motion in aerodynamic lenses and nozzle expansions. *Aerosol Sci. Technol.* 22, 293–313. doi:10.1080/02786829408959748

Malvar, O., Ruz, J. J., Kosaka, P. M., Domínguez, C. M., Gil-Santos, E., Calleja, M., et al. (2016). Mass and stiffness spectrometry of nanoparticles and whole intact bacteria by multimode nanomechanical resonators. *Nat. Commun.* 7, 13452. doi:10.1038/ncomms13452

Mile, E., Jourdan, G., Bargatin, I., Labarthe, S., Marcoux, C., Andreucci, P., et al. (2010). In-plane nanoelectromechanical resonators based on silicon nanowire piezoresistive detection. *Nanotechnology* 21, 165504. doi:10.1088/0957-4484/21/16/165504

Naik, A. K., Hanay, M. S., Hiebert, W. K., Feng, X. L., and Roukes, M. L. (2009). Towards single-molecule nanomechanical mass spectrometry. *Nat. Nanotechnol.* 4, 445–450. doi:10.1038/nnano.2009.152

Rolland, A. D., and Prell, J. S. (2022). Approaches to heterogeneity in native mass spectrometry. *Chem. Rev.* 122, 7909–7951. doi:10.1021/acs.chemrev.1c00696

Sage, E., Brenac, A., Alava, T., Morel, R., Dupré, C., Hanay, M. S., et al. (2015). Neutral particle mass spectrometry with nanomechanical systems. *Nat. Commun.* 6, 6482. doi:10.1038/ncomms7482

Sage, E., Sansa, M., Fostner, S., Defoort, M., Gély, M., Naik, A. K., et al. (2018). Single-particle mass spectrometry with arrays of frequency-addressed nanomechanical resonators. *Nat. Commun.* 9, 3283. doi:10.1038/s41467-018-05783-4

Sansa, M., Defoort, M., Brenac, A., Hermouet, M., Banniard, L., Fafin, A., et al. (2020). Optomechanical mass spectrometry. *Nat. Commun.* 11, 3781. doi:10.1038/s41467-020-17592-9

Wang, X., Gidwani, A., Girshick, S. L., and McMurry, P. H. (2005a). Aerodynamic focusing of nanoparticles: II. Numerical simulation of particle motion through aerodynamic lenses. *Aerosol Sci. Technol.* 39, 624–636. doi:10.1080/02786820500181950

Wang, X., Kruis, F. E., and McMurry, P. H. (2005b). Aerodynamic focusing of nanoparticles: I. Guidelines for designing aerodynamic lenses for nanoparticles. *Aerosol Sci. Technol.* 39, 611–623. doi:10.1080/02786820500181901

Wang, X., and McMurry, P. H. (2006). An experimental study of nanoparticle focusing with aerodynamic lenses. *Int. J. Mass Spectrom.* 258, 30–36. doi:10.1016/j.ijms.2006.06.008

Young, G., Hundt, N., Cole, D., Fineberg, A., Andrecka, J., Tyler, A., et al. (2018). Quantitative mass imaging of single biological macromolecules. *Science* 360, 423–427. doi:10.1126/science.aar5839

Zhang, X., Smith, K. A., Worsnop, D. R., Jimenez, J., Jayne, J. T., and Kolb, C. E. (2002). A numerical characterization of particle beam collimation by an aerodynamic lens-nozzle system: Part I. An individual lens or nozzle. *Aerosol Sci. Technol.* 36, 617–631. doi:10.1080/02786820252883856

frontiers | Frontiers in Chemistry

TYPE Original Research
PUBLISHED 14 September 2023
DOI 10.3389/fchem.2023.1249968

OPEN ACCESS

EDITED BY
Tao Wei,
University of Erlangen Nuremberg, Germany

REVIEWED BY
Lakshmi Narayanan Mosur Saravana Murthy,
Intel, United States
Subodh G.,
University of Kerala, India
Peiwen Lv,
Chinese Academy of Sciences (CAS), China

*CORRESPONDENCE
Sara C. Mills,
sara.mills@nrl.navy.mil

RECEIVED 29 June 2023
ACCEPTED 28 August 2023
PUBLISHED 14 September 2023

CITATION
Mills SC, Patterson EA and Staruch ML (2023), Effect of sub-micron grains and defect-dipole interactions on dielectric properties of iron, cobalt, and copper doped barium titanate ceramics.
Front. Chem. 11:1249968.
doi: 10.3389/fchem.2023.1249968

Effect of sub-micron grains and defect-dipole interactions on dielectric properties of iron, cobalt, and copper doped barium titanate ceramics

Sara C. Mills[1,2]*, Eric A. Patterson[1] and Margo L. Staruch[1]

[1]U.S. Naval Research Laboratory, Materials Science and Technology Division, Washington, DC, United States, [2]American Society for Engineering Education (ASEE), Washington, DC, United States

Introduction: Dilutely doped ferroelectric materials are of interest, as engineering these materials by introducing point defects via doping often leads to unique behavior not otherwise achievable in the undoped material. For example, B-site doping with transition metals in barium titanate ($BaTiO_3$, or BTO) creates defect dipoles via oxygen vacancies leading enhanced polarization, strain, and the ability to tune dielectric properties. Though defect dipoles should lead to dielectric property enhancements, the effect of grain size in polycrystalline ferroelectrics such as BTO plays a significant role in those properties as well.

Methods: Herein, doped BTO with 1.0% copper (Cu), iron (Fe), or cobalt (Co) was synthesized using traditional solid-state processing to observe the contribution of both defect-dipole formation and grain size on the ferroelectric and dielectric properties.

Results and discussion: 1.0% Cu doped BTO showed the highest polarization and strain (9.3 $\mu C/cm^2$ and 0.1%, respectively) of the three doped BTO samples. While some results, such as the aforementioned electrical properties of the 1.0% Cu doped BTO can be explained by the strong chemical driving force of the Cu atoms to form defect dipoles with oxygen vacancies and copper's consistent +2 valency leading to stable defect-dipole formation (versus the readily mixed valency states of Fe and Co at +2/+3), other properties cannot. For instance, all three T_c values should fall below that of undoped BTO (typically 120°C–135°C), but the T_c of 1.0% Cu BTO actually exceeds that range (139.4°C). Data presented on the average grain size and distribution of grain sizes provides insight allowing us to decouple the effect of defect dipoles and the effect of grain size on properties such as T_c, where the 1.0% Cu BTO was shown to possess the largest overall grains, leading to its increase in T_c.

Conclusion/future work: Overall, the 1% Cu BTO possessed the highest polarization, strain, and T_c and is a promising dopant for engineering the performance of the material. This work emphasizes the challenge of extricating one effect (such as defect-dipole formation) from another (grain size modification) inherent to doping polycrystalline BTO.

KEYWORDS

barium titanate, doping, ferroelectric, grain size, ceramic processing

1 Introduction

Engineering ferroelectric ceramics by purposefully introducing point defects has a profound effect on the material's behavior, such as unusual ferroelectric properties and high electric field induced strain (Zhao et al., 2019). Examples of point defects include dopant or impurity ions as well as vacancies, which can lead to defect dipoles arising from oxygen vacancies and ionized acceptors (Ren, 2004; Maier et al., 2015). For perovskites (ABO_3 structure), dilute doping at the B site leads to a distribution of oxygen vacancies to achieve charge neutrality, which form defect complexes with the doped acceptor ion (Vani and Kumar, 2012; Maier et al., 2015). The oxygen vacancies have an intrinsic mobility, which is affected by the dopant itself, the concentration of dopant, and the transition metal's valence state. Barium titanate ($BaTiO_3$, BTO) is a ubiquitous ferroelectric oxide with low dielectric loss, chemical stability, and is lead-free with low toxicity, and has been widely and commonly doped at the Ti^{4+} site with various transition metals, including iron (Fe), manganese (Mn), cobalt (Co), and copper (Cu) (Rani et al., 2016). Although there are a multitude of studies on such dopants, these works focus on dopant concentrations that lead to hexagonal BTO, do not include polarization/strain curves in addition to permittivity and loss measurements, study ferromagnetic or optical properties, are processed under different thermal profiles, and do not attempt to directly compare three different dopants in the same work (Langhammer et al., 2003; Cheng et al., 2005; Dang et al., 2011; Deka et al., 2014; Langhammer et al., 2015; Langhammer et al., 2016; Rani et al., 2016; Krimech and Sayouri, 2020; Althobaiti, 2023).

In perovskites, such as dilutely doped BTO, both the ionic radius and valency of the dopant is highly important in determining the site of doping (either A or B site). This is closely related to how effective the particular dopant will be at trapping oxygen vacancies, which is highly influenced by the valence state and the charge neutrality conditions of the composition (Eichel, 2008; Schie et al., 2014). In addition, the concentration of oxygen vacancies is influenced by the concentration and specific element chosen as the dopant (Huang et al., 2014). B-site dopants with a lower valency than Ti^{4+} (i.e. 2+ or 3+) can then form stable defect dipoles with oxygen vacancies along the <001> direction, the same direction as the spontaneous polarization direction (Zhao et al., 2019). These particular defect-dipole complexes have been shown to have a profound effect on the ferroelectric and piezoelectric behavior of materials such as barium titanate. The moment of the defect dipole induces an internal bias field, which can increase the polarization of the material by producing large crystal field anisotropy in the vicinity of the dopant and, when poled in the direction of the defect dipole, can also increase the strain experienced in the material (Maier et al., 2015). The orientation of the dipoles takes place during oxygen vacancy diffusion on the scale of several unit cells, which occurs at room temperature and leads to a recoverable domain wall configuration and "pinched" hysteresis loops with decreased remnant polarization (Kamel and de With, 2008; Zhao et al., 2019). Overall, a dopant cation has a direct effect over the range of several unit cells on the association and migration energies, i.e., the energies of oxygen vacancy—dopant association and activation energy of vacancy motion away from the dopant, respectively (Schie et al., 2014). This can significantly impact the formation of these complexes and thus the bulk ferroelectric properties.

Although our previous work (Patterson et al., 2023) and several other works discussed above focus on single crystals, for polycrystalline samples another important influence on the ferroelectric and piezoelectric properties of both doped and undoped BTO is grain size. It has been reported that several electrical properties such as the piezoelectric constant (d_{33}), polarization, and relative permittivity are affected by grain size, typically with a decrease in these properties with a decrease in grain size as grains approach the nanometer scale (Zhao et al., 2004; Guo et al., 2012; Huan et al., 2014). This is predicted to be due to a change in domain density and non-uniformities at grain boundaries (Huan et al., 2014). It has also been observed that non-uniformities such as aluminum segregation at grain boundaries can be partially responsible for ferroelectric aging behavior even when no second phase is detected, separate from impacts of volume of domain walls (Carl and Hardtl, 1977). Overall, domain configuration has a large impact on macroscopic dielectric properties, which in turn is substantially affected by the microstructure (Eichel, 2008). However, it is imperative to attempt to separate the effects of microstructure and intrinsic effects on the dielectric properties of polycrystalline ferroelectrics.

In this work, dielectric materials properties will be investigated (polarization, strain, and relative permittivity/loss) and reported with respect to polycrystalline BTO ceramics doped with 1.0 mol% of Fe, Co or Cu, synthesized via traditional solid-state processing. These results will then be discussed with respect to the grain size, determined from cross-sectional scanning electron microscopy (SEM) images. Comparisons between the dielectric properties of the three different doped BTO samples show the importance of considering all of the various contributions from the dopant that can affect the dielectric properties. These can be due to defect-dipole formation, grain growth/growth inhibition, oxygen vacancy diffusion, or a complex contribution from a subset or all of these. The challenge of extricating one effect from the other will be emphasized, along with the need for these in-depth studies.

2 Materials and methods

Ceramic powders of $BaTi_{1-x}Me_xO_3$ (with Me = Fe, Co, or Cu) were prepared using traditional solid state synthesis methods with x = 0.01 mol. Precursor oxides of $BaCO_3$, TiO_2, Fe_2O_3, $CoCO_3$, and CuO (99.9+%) were mixed in ethanol and ball milled for 8 h with proper stoichiometric amounts of the Fe, Co or Cu precursor added. The mixed powders were dried and then calcined at 1,150°C for 2 h and milled and dried again as before. Pellets of each composition were then uniaxially pressed in a 12.7 mm diameter die after mixing the calcined powder with 4-5 wt% binder (Paraloid B-72 resin mixed with acetone). The pressed pellets were sintered at 1,250°C in air for 4 h. The density of the sintered pellets was greater than 91% theoretical density for all samples in this study. The phase of the pellets was confirmed with X-ray diffraction (XRD) using a Rigaku SmartLab Rigaku X-ray powder diffractometer with Cu Kα radiation at 40 kV and 200 mA for a 2θ range from 20° to 80° with a 0.02° step size.

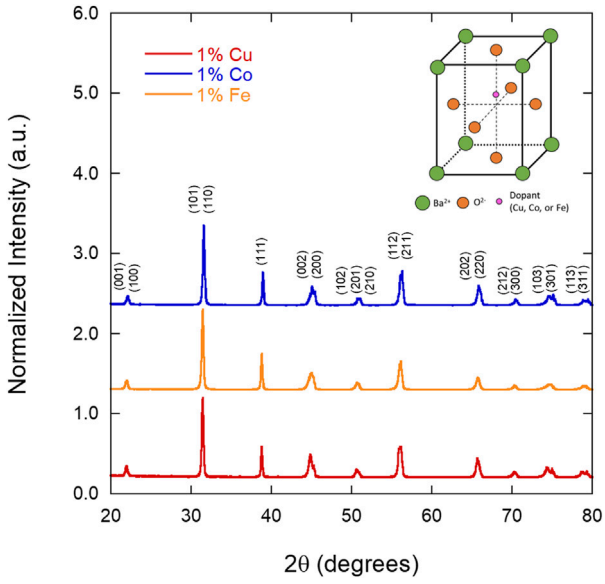

FIGURE 1
X-ray diffraction patterns of the 1% Fe, Co, and Cu-doped BTO powders measured after calcination at 1150°C, showing the tetragonal phase of BTO and no evidence of a hexagonal phase impurity (indexed with respect to PDF# 04-012-8129). The crystal structure of tetragonal BTO is shown in the top right corner.

The sintered pellets were then ground down to a thickness of approximately 800 μm and masked and sputtered with gold electrodes for synchronous ferroelectric and piezoelectric measurements, which were performed with a self-constructed Sawyer-Tower system and a linear variable differential transformer (LVDT) connected to a lock-in amplifier. The electrical measurements were performed on samples in three different states with increasing applied voltages from 0.1 kV up to 1.4 kV at 1 Hz (all data shown in this work is at 1.4 kV) as the properties are well-understood to strongly depend on the defect configuration, which can be modified through temperature or electric field. Therefore, the thermal and electrical history of the sample are important factors in discussing the dielectric behavior. The three states to be measured are referred hereafter as: as-sintered, aged, and poled. All samples were thermally reset at 300°C for 4 h after the initial sintering and allowed to cool to room temperature. This default "as-sintered" state was then tested. The "aged" subset of these samples were then aged at 80°C for 24 h to allow for diffusion of oxygen vacancies prior to characterization. Finally, the "poled" subset of samples were poled at a DC bias of 1.5 kV for 1 h at room temperature and tested.

Simultaneous capacitance and tan δ measurements were performed using two different methods in order to determine the relative permittivity and dielectric loss of the samples under different conditions. All samples for these measurements were tested in the "as-sintered state." First, an Agilent E4980A precision LCR meter was used to sweep between frequencies of 200 Hz and 2 MHz to determine the permittivity and loss at room temperature. Second, a Thermal Product Solutions (TPS) Tenney Environmental Test Chamber was used to measure the capacitance and loss from −30°C to 155°C at four different frequencies: 0.1, 1, 10, and 100 kHz. The frequency was generated from an HP 4284A Precision LCR meter, which also measured the capacitance and loss at each frequency over the temperature range. A self-assembled LCR test interface was used to connect the LCR meter to the sample holder inside the environmental test chamber, which was accompanied by a National Instruments thermocouple placed close to the sample to more accurately monitor temperature.

Cross-sectional scanning electron microscopy (SEM) images were taken of the polished, fractured surface of each composition using a Thermo Scientific Quattro S at an accelerating voltage of 10 keV. Images were taken across different regions of the cross-section, and were analyzed by ImageJ software. Ten images were used to determine the average grain size via the linear intercept method, whereby five lines were drawn per image to obtain an average grain size for one image, resulting in 50 total lines drawn with ten average values of grain size for each particular sample.

3 Results and discussion

3.1 X-ray diffraction

Sintered pellets of 1% Fe, Co, and Cu-doped BTO were analyzed via XRD to determine if the concentration of Fe affected the presence of the expected ferroelectric, tetragonal phase, as some studies have observed the formation of the hexagonal phase at as low as 1% Fe (Langhammer et al., 2020). Figure 1 shows that across the three samples, the calcined powders are of the ferroelectric tetragonal phase with no other phases present, demonstrating that doping in this study with Fe, Co, or Cu does not induce a detectable phase change at x = 1%. The lattice parameters and c/a ratios obtained from a whole pattern fit of each diffraction pattern (indexed with respect to tetragonal BTO, PDF# 04-012-8129) is included in Table 1. The c/a ratio of undoped BTO, 1.01, is slightly higher than that of the Co, Fe, and Cu-doped BTO samples (1.008, 1.007, and 1.008, respectively). Doping with 1% Co and Fe has been shown to slightly decrease the c/a ratio, which was observed here for all three dopants (Buscaglia et al., 2000).

3.2 Ferroelectric and piezoelectric testing

Polarization and strain of the three compositions in all three conditions were measured at 1.4 kV, which translates to a field of approximately 1.5 kV/mm. Figure 2 shows polarization (Figure 2A) and strain loops (Figure 2B) for the "as-sintered" condition measured at 1.4 kV. Note that all samples were tested at applied voltages between 0.1 and 1.4 kV at 1 Hz, but only the 1.4 kV results are shown here. The polarization and strain loops for the samples that were aged (80°C, 24 h) and poled (1.5 kV, 1 h at 2.4 kV) can be found in the Supplementary Material (Supplementary Figures S1, S2). Measuring samples after aging and poling was performed to determine the extent that temperature and field cycling affects the polarization and strain of these differently doped materials. The 1.0% Fe-doped BTO sample showed an increase in strain from ~0.025% to ~0.04% after aging, and the 1.0% Cu BTO sample showed a decrease in polarization from ~9 to ~5 μC/cm^2 (Supplementary Figure S1). In order to fully realize the effect on

TABLE 1 Lattice parameters, dielectric properties, average grain sizes, and densities for the three doped BTO samples.

	Lattice parameters			@ 10 kHz					
	a,b	c	c/a	ε_r	tan δ	T_{c_H} (°C)	T_{c_C} (°C)	Avg. grain size (μm)	Relative density (%)
1% Co BTO	4.002	4.033	1.008	1830	0.017	107.1	90.2	0.62 ± 0.2	95.2
								2.29 ± 0.3	
1% Fe BTO	4.005	4.033	1.007	2240	0.012	99.8	61.2	0.88 ± 0.2	96.9
								49.19 ± 13.5	
1% Cu BTO	4.004	4.036	1.008	2150	0.026	139.4	103.6	4.73 ± 1.1	91.4
								14.35 ± 4.4	
								32.57 ± 3.8	

Dielectric properties are reported for samples measured at 10 kHz, and the Curie temperature is reported both on heating (T_{c_H}) and on cooling (T_{c_C}). Lattice parameters were obtained from a whole pattern fit of the XRD patterns of each sample. Grain size was measured using the linear-intercept method. Density was measured using the Archimedes method.

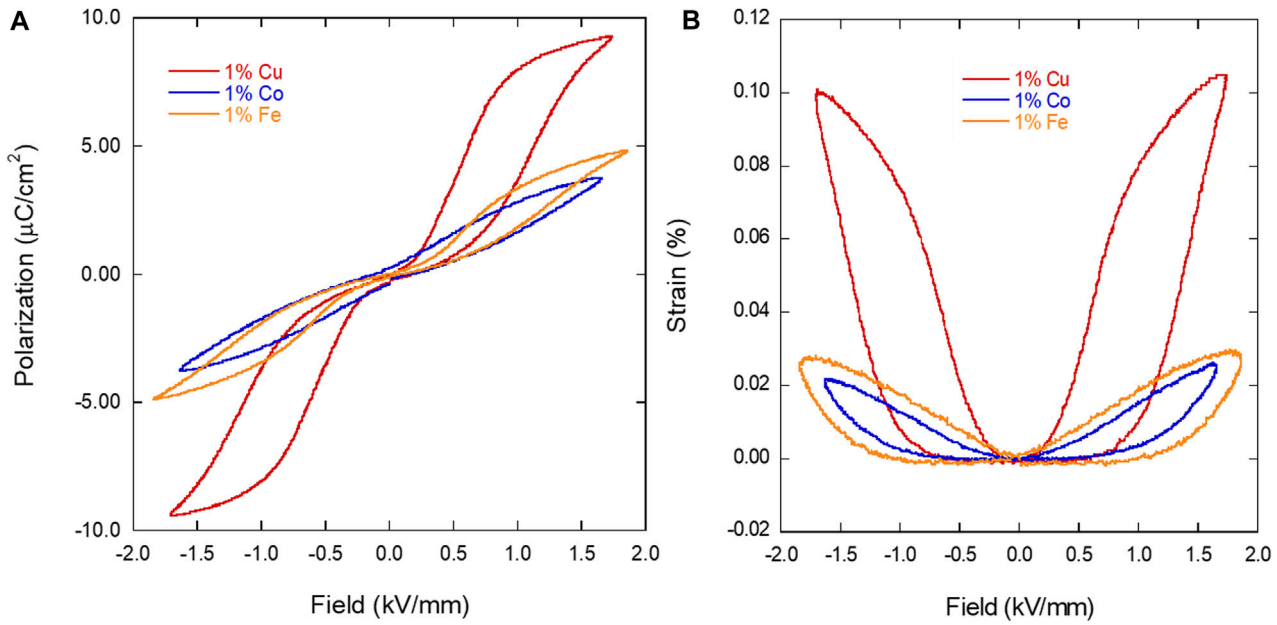

FIGURE 2
Polarization **(A)** and strain **(B)** loops for the thermally reset (300°C) 1% Fe, Co and Cu-doped BTO samples measured at 1.4 kV.

the polarization and strain after poling, the poled samples were measured at 2.4 kV (Supplementary Figure S2), showing multiple changes in polarization and strain behaviour. It is important to not compare their maximum values without considering that the field level is nearly twice as high as in the as-sintered and aged state. With that in mind, the 1.0% Cu BTO sample displayed no further enhancement compared to the "as-sintered" value of polarization and the pinched portion of the polarization hysteresis loop disappears in favor of a traditional ferroelectric shape. The strain also takes on a more butterfly shape with negative strain at the coercive field. Additionally, the polarization loops of the 1.0% Co and Fe samples have become asymmetric, indicating a high internal electric field (Supplementary Figure S2A). This is supported by the offset in the field of the 1.0% Co and Fe BTO strain loops (Supplementary Figure S2B). The poled strain loops also show a general improvement of strain for all three samples that approaches 0.1%, albeit at higher fields as mentioned. Aging and poling can have extreme effects on the polarization and strain behaviour of ferroelectric materials via domain/defect-dipole orientations (Kamel and de With, 2008). While the effects that both aging or poling have on the polarization and strain of the material via an external, post-processing method are quite large, in these samples they were found to be repeatably reversible following a 300°C heat treatment. Importantly, the hysteresis loops always returned to the "as-sintered" state, so it is from this baseline condition that comparisons will be focused on in this discussion.

In the "as-sintered" state, the 1.0% Cu-doped BTO yields the highest polarization (~9.3 μC/cm^2) and strain (~0.1%) when compared to the 1.0% Fe and Co-doped BTO, with polarizations of 4.8 and 3.7 μC/cm^2 and strains of 0.03% and 0.025%, respectively.

In comparison, undoped BTO sintered at similar conditions yield polarizations between 15 and 18 μC/cm^2 (Tan et al., 2015; Malyshkina et al., 2020). Additionally, Figure 2B shows that all three dopants yielded little to no negative strain, showing recoverable strain across each dopant. The presence of the pinched polarization loops of the 1.0% Fe and Cu-doped BTO samples (Figure 2A) is a good indication of defect dipole formation pinning domain walls in those samples.

There is an obvious improvement in the ferroelectric properties with respect to the 1.0% Cu-doped BTO when compared to the 1.0% Fe and Co. Looking at each dopant, however, it does not seem at first glance that ionic radius plays a part, as the difference between the ionic radii for the various oxidation states of each transition metal are relatively similar when compared to Ti^{4+} (0.61) (listed in Å): 0.75 (Co^{2+}), 0.55 (Co^{3+}), 0.77 (Cu^{+}), 0.73 (Cu^{2+}), 0.78 (Fe^{2+}), and 0.65 (Fe^{3+}) (Shannon, 1976). Therefore, doping with any of these three elements for Ti^{4+} should not play a role in one composition more than another. It is important to note, however, that the valence state of the incorporated ion is dependent on a number of factors, such as initial precursors and the oxidizing/reducing conditions during synthesis. Therefore, we should expect a mix of these valence states for some if not all of the dopants chosen in this work.

While the valence states of the incorporated dopants will not significantly distort the lattice, the valency of the ions can influence the intrinsic ferroelectric behaviour. Co and Fe are both stable at a 2+ or 3+ state, while Cu is commonly found in a 2+ state. The mixed valence of the Co and Fe may play a role in achieving charge neutrality (via different amounts of oxygen vacancies and other free charges) which then affects the ferroelectric and piezoelectric properties of the material. This difference in valence is proposed to directly affect the establishment of defect-dipoles, formed between the dopant and induced oxygen vacancies. Using Kröger-Vink notation, the defect-dipole complexes for the three different dopants are the following: $(Fe'_{Ti}\text{–}V_O^{\cdot\cdot})^{\cdot}$, $(Co'_{Ti}\text{–}V_O^{\cdot\cdot})^{\cdot}$, and $(Cu''_{Ti}\text{–}V_O^{\cdot\cdot})^{X}$. The charge states of the three different defect dipole complexes are based on the assumption that Fe and Co are both in a 3+ state and Cu is 2+. This was assumed because it has been shown that, for Fe and Co, oxidation from the 2+ to 3+ state is more energetically favourable in comparison to the incorporation of those two elements in their divalent state (Buscaglia et al., 2001). Due to the charged nature of the defect-dipole complexes for Fe and Co in the 3+ state, there are additional mechanisms for charge compensation that may take place, including free electrons trapped in the lattice (Eichel, 2008). This excess charge can give rise to a screening effect that ultimately causes ferroelectric instability, which could explain the decreased polarization and strain in the 1% Fe and Co-BTO samples when compared to the 1% Cu sample (Wang et al., 2012). Additionally, work by Erhart et al. (2007) suggests that there is a very strong chemical driving force between copper dopants and oxygen vacancies in lead titanate, which theoretically leads to all copper ions complexed with an oxygen vacancy.

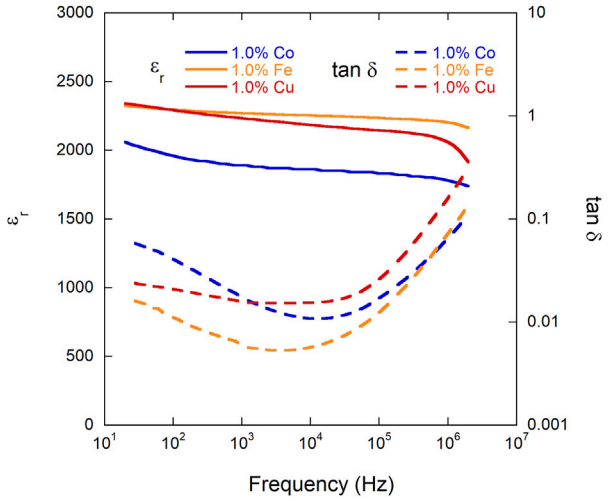

FIGURE 3
Relative permittivity (ε_r) (solid lines) and loss tangent (tan δ) (dashed lines) of each composition (1% Co, Cu, and Fe BTO) measured at room temperature with respect to frequency after samples were thermally reset at 300°C for 4 h.

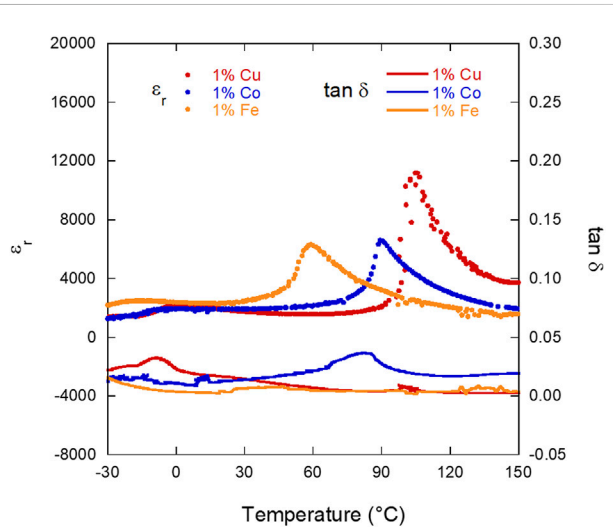

FIGURE 4
Relative permittivity (ε_r) (solid lines) and loss tangent (tan δ) (dashed lines) of each composition (1% Co, Cu, and Fe BTO) with respect to temperature, measured at 10 kHz in the "as-sintered" state (thermally reset at 300°C for 4 h after sintering). Only the cooling curves are shown in this plot.

3.3 Other dielectric measurements

3.3.1 Relative permittivity (ε_r)/tan δ vs. frequency (room temperature)

The relative permittivity (ε_r) and loss tangent (tan δ) of as-sintered samples of each composition were measured at room temperature with respect to frequency, shown in Figure 3 and reported in Table 1. When compared to the typical relative permittivity of barium titanate (ε_r~3,000-6,000), all three of the doped BTO samples exhibit a lower value than undoped BTO, which is due to the fact that in comparison to Ti^{4+}, all three dopants (Co^{3+}, Cu^{2+}, and Fe^{3+}) are more conductive and less polarizable, decreasing the relative permittivity, as expected (Rani et al., 2016). More specifically, undoped BTO at similar processing conditions yields a relative permittivity similar to the reported ranged of BTO, ranging

from ~3,000 to 6,500 at 1 kHz (Hoshina et al., 2008; Tan et al., 2015). However, the permittivity of all three doped BTO samples remains fairly constant up to 2 MHz, due to the failure of the dipoles to follow the fast alternating electric field (Rani et al., 2016). With regards to tan δ at 10 kHz, each doped sample exhibited a loss of ~0.01, a relatively low value of loss due to the dopant's ability to reduce leakage current in the sample (Imai et al., 2002). All samples showed an increase in loss in the MHz, frequency range and the 1% Cu doped BTO sample nominally yielded the highest loss at 2 MHz. The Cu doped sample, however, showed the most frequency-stable loss at the intermediate to lower frequencies (with the increase starting at 100 kHz).

3.3.2 Relative permittivity (ε_r)/tan δ vs. temperature (variable frequency)

As-sintered samples of 1% Co, Cu, and Fe doped BTO were loaded into an LCR test interface and the ε_r and tan δ were measured between −30°C and 155°C at 0.1, 1, 10, and 100 kHz. Data from the cooling curves for each sample at 10 kHz are shown in Figure 4 with Curie temperatures measured both on heating (T_{c_H}) and cooling (T_{c_C}) are reported in Table 1. Plots of ε_r and tan δ with respect to temperature at all four frequencies are included in the Supplementary Material (Supplementary Figure S3). The magnitude of ε_r is highest at the Curie temperature for 1% Cu (~7,200) and is similar for 1% Co and 1% Fe (~5,520). Additionally, the T_{c_H} of the 1.0% Cu-doped BTO (139.4°C) is higher than both the 1.0% Co (107.1°C) and 1.0% Fe (99.8°C) samples. One can also observe that there is a slight increase in tan δ at T_{c_H} for all three dopants, and that the loss is consistently highest in the 1% Co sample. To further explore the differences in T_c values of the three dopants, the difference between the T_c on heating and cooling ($\Delta T_{Ch\text{-}Cc}$) have been calculated as 16.9, 38.6, and 35.8°C for Co, Fe, and Cu doped BTO, respectively. The smaller $\Delta T_{Ch\text{-}Cc}$ of the 1% Co and the similar $\Delta T_{Ch\text{-}Cc}$ values of the 1% Fe and Cu doped BTO samples could be due to the relative abilities of each dopant to trap vacancies in the sample, which would lead either more or less thermal energy needed to complete the phase transition between the tetragonal and cubic phases.

With respect to the T_{c_H} of the three samples, it is important to note that the accepted value of T_c for undoped BTO lies between 120°C and 135°C, with samples processed under comparable conditions yielding Curie temperatures ranging between 120°C and 130°C (Tan et al., 2015; Malyshkina et al., 2020). It is generally expected that doping BTO with these cations or ones of similar valency will decrease the T_c due to oxygen vacancy formation (Tewatia et al., 2021). The 1.0% Co and 1.0% Fe samples follow this trend in lower T_{c_H} than the reported value of undoped BTO: 1.0% Co (107.1°C) and 1.0% Fe (99.8°C). The similarity in T_{c_H} of the 1.0% Co and Fe samples follows the similarity of their trends in other properties, such as polarization and strain, which could be due to their similarities in valence (3+), which would lead to similar defect-dipole formation and subsequent effects on ferroelectric properties as a result. In contrast, the T_{c_H} of 1.0% Cu BTO was 139.4°C, higher than the maximum of the accepted range of T_c of undoped BTO. This suggests that there may be another factor at play that is driving the T_{c_H} higher, as the introduction of oxygen vacancies should decrease the T_c. One such factor is the grain size in the material. Properties such as polarization and relative permittivity are affected by grain size, with a decrease in these properties as grains approach the nanometer scale.

3.4 Grain size measurement

In order to measure the grain sizes of the three samples, cross-sections of a pellet of each dopant were polished and then imaged via SEM. Grain size was then determined by the linear intercept method, utilizing ten SEM images to obtain average grain sizes for the different grain size distributions within each sample. Schematics of each sample illustrating the grain structure of each sample can be seen in Figures 5A, B, F for Co, Fe and Cu dopants, respectively. Micrographs from different sub-sections of these representative cross-section schematics are also included in Figures 5C–E, G–I. The average grain size values can be found in Table 1.

The cross-section of the 1.0% Co sample (Figures 5A, C) had a minor but distinctly bimodal distribution of grains (0.62 ± 0.2 and 2.29 ± 0.3 μm), revealing a population of submicron grains. These two groups of grains were equally distributed throughout the cross-section of the sample, as illustrated in Figure 5A. Next, the 1.0% Fe sample (schematically shown in Figure 5B) also had a bimodal distribution of grains (0.88 ± 0.2 and 49.19 ± 13.5 μm), but here the subset of larger grains were substantially bigger compared to the Co sample. For clarity, it is important to note that the larger grains of this sample were measured individually (measuring 175 grains to obtain the average), while the smaller grains were measured by the linear intercept method. Unlike 1.0% Co BTO, 1.0% Fe BTO had clusters of these large grains surrounded by the smaller, submicron grains, shown in the SEM images in Figures 5D, E, which are representative of what was observed along the entirety of the cross-section. Finally, the 1.0% Cu sample (illustrated in Figure 5F) had three distinct areas along the cross-section (Figures 5G–I) and three different populations of grain sizes (4.73 ± 1.1, 14.35 ± 4.4, and 32.57 ± 3.8 μm). Overall, 1.0% Cu had the largest grains of the three different dopants, albeit not distributed evenly over the cross-section. Upon electron dispersive spectroscopy (EDS) analysis, there was a lack of apparent dopant segregation into grain boundaries or secondary phases in the cross-sections of the doped samples. Undoped BTO sintered under similar conditions have grains averaging approximately 4 μm in diameter, the size of which is very dependent on the sintering temperature and time (Hoshina et al., 2008; Tan et al., 2015; Malyshkina et al., 2020). The choice of dopant itself is likely driving the observed differences in grain sizes between the three samples, since they were sintered intentionally under the same conditions to achieve similar high density (>91%) rather than optimizing the sintering conditions to create a specific grain size. In previous doping studies, for instance, Co has been used to control grain sizes in ceramics to ~1 μm by inhibiting grain growth, and Cu was added as a sintering aid to encourage grain growth (Cheng et al., 2005; Mahmoudi et al., 2019).

This grain size analysis, then, can potentially inform some of the differences in dielectric properties between the three samples. Although doping should theoretically decrease the Curie temperature, this was not observed in the 1.0% Cu sample. This

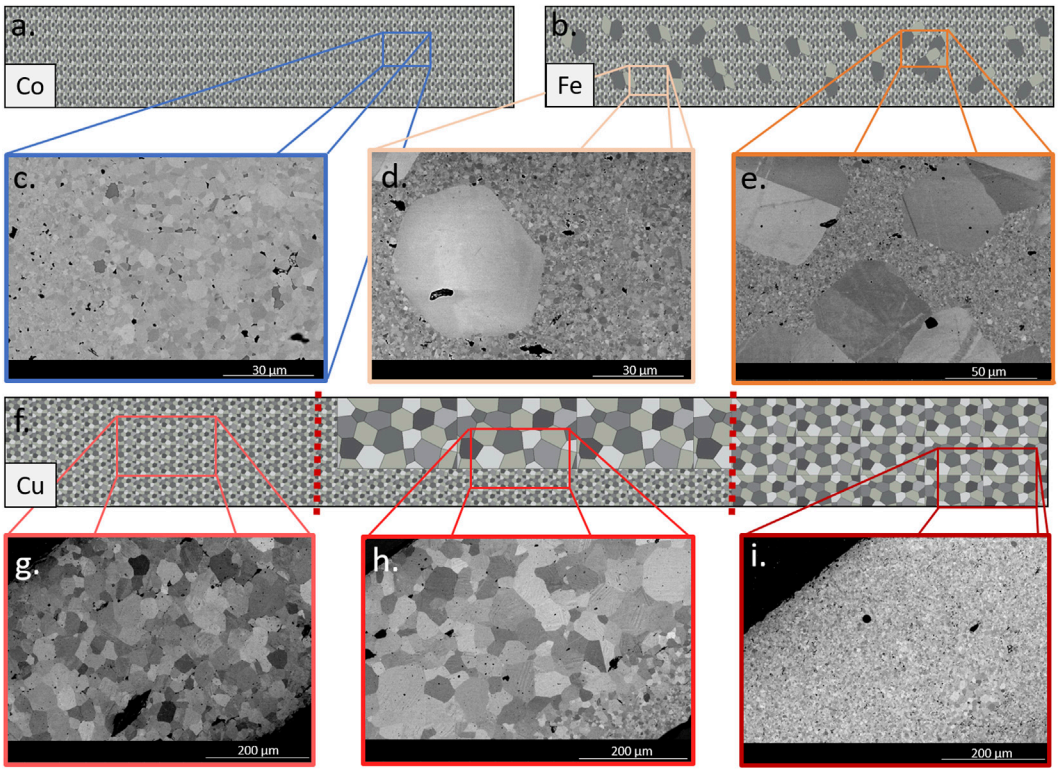

FIGURE 5
Schematics illustrating the grain structure of cross sections of 1.0% Co BTO **(A)**, 1.0% Fe BTO **(B)** and 1.0% Cu BTO **(F)** samples. Magnified areas are SEM images from each sample [1.0% Co **(C)**, 1.0% Fe **(D,E)**, and 1.0% Cu **(G–I)**] showing the grain structure and size distribution along the length of the cross section.

increase in T_c could then be contributed, in part, to the larger average grain size, as it has been shown that T_c increases as grain size increases (Tewatia et al., 2021). Additionally, although there are larger grains present in 1.0% Fe BTO, the dominant small grains of this sample and that of the 1.0% Co sample could explain the lower T_c, polarization, and strain values when compared to 1.0% Cu BTO. The permittivity values do not follow this trend, as the 1.0% Cu and Fe samples have similar values, while the 1.0% Co BTO possesses the lowest ε_r. However, since these values are not vastly different (Table 1) and do fall below that of undoped BTO (ranging from 3,000 to 6,000), it may not be a significant indicator of the dependence of this value on either dopant or grain size alone. This analysis, though, does highlight the importance of considering both the defect dipole and grain size effects on dielectric properties. Although some dopants are typically classified as more or less effective than others, such as if a dopant's valency and/or quantity added should lead to positive enhancements via defect dipole formation, the effect of grain size can outweigh the benefit of the defect dipoles with respect to dielectric properties.

4 Conclusion

In this work, we have studied the dielectric properties of polycrystalline B-site doped BTO with 1.0% copper (Cu), iron (Fe), and cobalt (Co), synthesized using traditional solid-state processing, to observe the contribution of both defect-dipole formation and grain size on the ferroelectric and dielectric properties. 1.0% Cu doped BTO showed the highest polarization and strain (9.3 $\mu C/cm^2$ and 0.1%, respectively) of the three dopants in and a very clearly pinched hysteresis and recoverable strain behavior in the as-sintered state, with some changes in polarization and strain to all three doped samples after aging or poling. Additionally, 1.0% Cu BTO showed the highest Curie temperature (Tc) (139.4°C). With respect to defect dipole formation, these results suggested that the strong chemical driving force of the Cu atoms to form defect dipoles with charge neutrality induced oxygen vacancies leads to improved polarization and strain. However, since this would not explain the high Tc of the 1.0% Cu; the average grain size and distribution of grain sizes provided insight for this parameter instead. The 1.0% Cu BTO possessed the largest overall grains, which leads to an increased Tc. Grain size cannot be the only contributor to the improvement of properties, though, as the larger grain size would not account for the type of pinching in the polarization loop and increased strain, which we attribute to defect-dipole formation. Overall, this work emphasizes the challenge attributing a singular contribution, such as defect dipole formation via doping or grain size to dielectric properties of polycrystalline, doped BTO. Instead, it is critical to obtain a more comprehensive view of the material as a whole in order to inform causation and conclusions.

Data availability statement

The raw data supporting the conclusion of this article will be made available by the authors, without undue reservation.

Author contributions

SM carried out the majority of the experiments outlined in the manuscript, EP also contributed to the experimental efforts. SM, EP, and MS conceived of the ideas, and SM and MS were in charge of overall planning. SM drafted the manuscript with support from EP and MS. All authors contributed to the article and approved the submitted version.

Funding

This work was supported by the Office of Naval Research through the Naval Research Laboratory's Basic Research Program.

Conflict of interest

The authors declare that the research was conducted in the absence of any commercial or financial relationships that could be construed as a potential conflict of interest.

Publisher's note

All claims expressed in this article are solely those of the authors and do not necessarily represent those of their affiliated organizations, or those of the publisher, the editors and the reviewers. Any product that may be evaluated in this article, or claim that may be made by its manufacturer, is not guaranteed or endorsed by the publisher.

Supplementary material

The Supplementary Material for this article can be found online at: https://www.frontiersin.org/articles/10.3389/fchem.2023.1249968/full#supplementary-material

References

Althobaiti, S., Alghamdi, M., Alamri, B., and Madani, A. (2023). Structural and optical investigations of Nd and Cu doped $BaTiO_3$ prepared by solid state reaction. *Optik* 275, 170534. doi:10.1016/j.ijleo.2023.170534

Buscaglia, M. T., Buscaglia, V., Viviani, M., and Nanni, P. (2001). Atomistic simulation of dopant incorporation in barium titanate. *J. Am. Ceram. Soc.* 84, 376–384. doi:10.1111/j.1151-2916.2001.tb00665.x

Buscaglia, M. T., Buscaglia, V., Viviani, M., Nanni, P., and Hanuskova, M. (2000). Influence of foreign ions on the crystal structure of $BaTiO_3$. *J. Eur. Ceram. Soc.* 20 (12), 1997–2007. doi:10.1016/S0955-2219(00)00076-5

Carl, K., and Hardtl, K. H. (1977). Electrical after-effects in $Pb(Ti,Zr)O_3$ ceramics. *Ferroelectrics* 17, 473–486. doi:10.1080/00150197808236770

Cheng, B. L., Button, T. W., Gabbay, M., Fantozzi, G., and Maglione, M. (2005). Oxygen vacancy relaxation and domain wall hysteresis motion in cobalt-doped barium titanate ceramics. *J. Am. Ceram. Soc.* 88, 907–911. doi:10.1111/j.1551-2916.2005.00167.x

Dang, N. V., Thanh, T. D., Hong, L. V., Lam, V. D., and Phan, T.-L. (2011). Structural, optical and magnetic properties of polycrystalline $BaTi_{1-x}Fe_xO_3$ ceramics. *J. Appl. Phys.* 110, 043914. doi:10.1063/1.3625235

Deka, B., Ravi, S., Perumal, A., and Pamu, D. (2014). Ferromagnetism and ferroelectricity in Fe doped $BaTiO_3$. *Phys. B Condens. Matter* 448, 204–206. doi:10.1016/j.physb.2014.03.069

Eichel, R.-A. (2008). Characterization of defect structure in acceptor-modified piezoelectric ceramics by multifrequency and multipulse electron paramagnetic resonance spectroscopy. *J. Am. Ceram. Soc.* 91, 691–701. doi:10.1111/j.1551-2916.2008.02303.x

Erhart, P., Eichel, R.-A., Träskelin, P., and Albe, K. (2007). Association of oxygen vacancies with impurity metal ions in lead titanate. *Phys. Rev. B* 76, 174116. doi:10.1103/PhysRevB.76.174116

Guo, Y. Y., Yan, Z. B., Zhang, N., Cheng, W. W., and Liu, J.-M. (2012). Ferroelectric aging behaviors of $BaTi_{0.995}Mn_{0.005}O_3$ ceramics: Grain size effects. *Appl. Phys. A* 107, 243–248. doi:10.1007/s00339-011-6750-0

Hoshina, T., Takizawa, K., Li, J., Kasama, T., Kakemoto, H., and Tsurumi, T. (2008). Domain size effect on dielectric properties of barium titanate ceramics. *Jpn. J. Appl. Phys.* 47, 7607–7611. doi:10.1143/JJAP.47.7607

Huan, Y., Wang, X., Fang, J., and Li, L. (2014). Grain size effect on piezoelectric and ferroelectric properties of $BaTiO_3$ ceramics. *J. Eur. Ceram. Soc.* 34, 1445–1448. doi:10.1016/j.jeurceramsoc.2013.11.030

Huang, F., Jiang, Z., Lu, X., Ti, R., Wu, H., Kan, Y., et al. (2014). Nonmonotonic variation of aging behavior in Fe-doped $BaTiO_3$ ceramics. *Appl. Phys. Lett.* 105, 022904. doi:10.1063/1.4890383

Imai, K., Takeno, S., and Nakamura, K. (2002). Effect of Fe doping of thin $(Ba,Sr)TiO_3$ films on increase in dielectric constant. *Jpn. J. Appl. Phys.* 41, 6060–6064. doi:10.1143/JJAP.41.6060

Kamel, T. M., and de With, G. (2008). Poling of hard ferroelectric PZT ceramics. *J. Eur. Ceram. Soc.* 28, 1827–1838. doi:10.1016/j.jeurceramsoc.2007.11.023

Krimech, F., and Sayouri, S. (2020). Structure and dielectric behavior of Cu-doped $BaTiO_3$ ceramics. *Mater. Today Proc.* 30, 909–917. doi:10.1016/j.matpr.2020.04.349

Langhammer, H. T., Böttcher, R., Müller, T., Walther, T., and Ebbinghaus, S. G. (2015). Defect properties of cobalt-doped hexagonal barium titanate ceramics. *J. Phys. Condens. Matter* 27, 295901. doi:10.1088/0953-8984/27/29/295901

Langhammer, H. T., Müller, T., Böttcher, R., and Abicht, H.-P. (2003). Crystal structure and related properties of copper-doped barium titanate ceramics. *Solid State Sci.* 5, 965–971. doi:10.1016/S1293-2558(03)00087-6

Langhammer, H. T., Müller, T., Walther, T., Böttcher, R., Hesse, D., Pippel, E., et al. (2016). Ferromagnetic properties of barium titanate ceramics doped with cobalt, iron, and nickel. *J. Mater. Sci.* 51, 10429–10441. doi:10.1007/s10853-016-0263-3

Langhammer, H. T., Walther, T., Böttcher, R., and Ebbinghaus, S. G. (2020). On the incorporation of iron into hexagonal barium titanate: II. Magnetic moment, electron paramagnetic resonance (EPR) and optical transmission. *J. Phys. Condens. Matter* 32, 385702. doi:10.1088/1361-648X/ab9345

Mahmoudi, P., Nemati, A., and Maleki Shahraki, M. (2019). Grain growth kinetics and electrical properties of CuO doped SnO_2-based varistors. *J. Alloys Compd.* 770, 784–791. doi:10.1016/j.jallcom.2018.08.201

Maier, R. A., Pomorski, T. A., Lenahan, P. M., and Randall, C. A. (2015). Acceptor-oxygen vacancy defect dipoles and fully coordinated defect centers in a ferroelectric perovskite lattice: Electron paramagnetic resonance analysis of Mn^{2+} in single crystal $BaTiO_3$. *J. Appl. Phys.* 118, 164102. doi:10.1063/1.4934505

Malyshkina, O. V., Shishkov, G. S., Martyanov, A. A., and Ivanova, A. I. (2020). Effect of sintering temperature on dielectric properties of barium titanate ceramics and composite. *Mod. Electron. Mater.* 6, 141–146. doi:10.3897/j.moem.6.4.65576

Patterson, E. A., Finkel, P., Cain, M. G., Thompson, P., Lucas, C., and Staruch, M. (2023). Rejuvenation of giant electrostrain in doped barium titanate single crystals. *Apl. Mater* 11, 041109. doi:10.1063/5.0142103

Rani, A., Kolte, J., Vadla, S. S., and Gopalan, P. (2016). Structural, electrical, magnetic and magnetoelectric properties of Fe doped $BaTiO_3$ ceramics. *Ceram. Int.* 42, 8010–8016. doi:10.1016/j.ceramint.2016.01.205

Ren, X. (2004). Large electric-field-induced strain in ferroelectric crystals by point-defect-mediated reversible domain switching. *Nat. Mater.* 3, 91–94. doi:10.1038/nmat1051

Schie, M., Waser, R., and De Souza, R. A. (2014). A simulation study of oxygen-vacancy behavior in strontium titanate: Beyond nearest-neighbor interactions. *J. Phys. Chem. C* 118, 15185–15192. doi:10.1021/jp504436t

Shannon, R. D. (1976). Revised effective ionic radii and systematic studies of interatomic distances in halides and chalcogenides. *Acta Cryst.* 32, 751–767. doi:10.1107/S0567739476001551

Tan, Y., Zhang, J., Wu, Y., Wang, C., Koval, V., Shi, B., et al. (2015). Unfolding grain size effects in barium titanate ferroelectric ceramics. *Sci. Rep.* 5, 9953. doi:10.1038/srep09953

Tewatia, K., Sharma, A., Sharma, M., and Kumar, A. (2021). Factors affecting morphological and electrical properties of barium titanate: A brief review. *Mater. Today Proc.* 44, 4548–4556. doi:10.1016/j.matpr.2020.10.813

Vani, K., and Kumar, V. (2012). Influence of defect mobility on electrostrain in acceptor-doped $Ba_{0.80}Sr_{0.20}TiO_3$. *AIP Adv.* 2, 042177. doi:10.1063/1.4770325

Wang, Y., Liu, X., Burton, J. D., Jaswal, S. S., and Tsymbal, E. Y. (2012). Ferroelectric instability under screened coulomb interactions. *Phys. Rev. Lett.* 109, 247601. doi:10.1103/PhysRevLett.109.247601

Zhao, D., Lenz, T., Gelinck, G. H., Groen, P., Damjanovic, D., de Leeuw, D. M., et al. (2019). Depolarization of multidomain ferroelectric materials. *Nat. Commun.* 10, 2547. doi:10.1038/s41467-019-10530-4

Zhao, Z., Buscaglia, V., Viviani, M., Buscaglia, M. T., Mitoseriu, L., Testino, A., et al. (2004). Grain-size effects on the ferroelectric behavior of dense nanocrystalline $BaTiO_3$ ceramics. *Phys. Rev. B* 70, 024107. doi:10.1103/PhysRevB.70.024107

frontiers | Frontiers in Chemistry

TYPE Original Research
PUBLISHED 21 September 2023
DOI 10.3389/fchem.2023.1243235

OPEN ACCESS

EDITED BY
Jose Luis Cabellos,
Polytechnic University of Tapachula, Mexico

REVIEWED BY
Andrea Maranzana,
University of Turin, Italy
Ana María Mendoza Wilson,
Centro de Investigacion en Alimentacion y Desarrollo A.C., Mexico

*CORRESPONDENCE
Mohamad Akbar Ali,
akbar.mohamad@ku.ac.ae

RECEIVED 20 June 2023
ACCEPTED 01 September 2023
PUBLISHED 21 September 2023

CITATION
Dash MR and Ali MA (2023), Can a single ammonia and water molecule enhance the formation of methanimine under tropospheric conditions?: kinetics of $^{\bullet}CH_2NH_2 + O_2$ (+NH_3/H_2O). *Front. Chem.* 11:1243235. doi: 10.3389/fchem.2023.1243235

Can a single ammonia and water molecule enhance the formation of methanimine under tropospheric conditions?: kinetics of $\cdot CH_2NH_2 + O_2$ (+NH_3/H_2O)

Manas Ranjan Dash[1] and Mohamad Akbar Ali[2,3]*

[1]Department of Chemistry, School of Physical Sciences, DIT University, Dehradun, Uttarakhand, India, [2]Department of Chemistry, College of Art and Science, Khalifa University of Science and Technology, Abu Dhabi, United Arab Emirates, [3]Advanced Materials Chemistry Center (AMCC), Khalifa University of Science and Technology, Abu Dhabi, United Arab Emirates

The aminomethyl ($\bullet CH_2NH_2$) radical is generated from the photo-oxidation of methylamine in the troposphere and is an important precursor for new particle formation. The effect of ammonia and water on the gas-phase formation of methanimine (CH_2NH) from the $^{\bullet}CH_2NH_2 + O_2$ reaction is not known. Therefore, in this study, the potential energy surfaces for $^{\bullet}CH_2NH_2 + O_2$ (+NH_3/H_2O) were constructed using *ab initio*//DFT, i.e., *coupled-cluster theory* (CCSD(T))//hybrid-density functional theory, i.e., M06-2X with the 6-311++G (3df, 3pd) basis set. The Rice–Ramsperger–Kassel–Marcus (RRKM)/master equation (ME) simulation with Eckart's asymmetric tunneling was used to calculate the rate coefficients and branching fractions relevant to the troposphere. The results show 40% formation of CH_2NH at the low-pressure (<1 bar) and 100% formation of $CH_2NH_2OO^{\bullet}$ at the high-pressure limit (HPL) condition. When an ammonia molecule is introduced into the reaction, there is a slight increase in the formation of CH_2NH; however, when a water molecule is introduced into the reaction, the increase in the formation of CH_2NH was from 40% to ~80%. The calculated rate coefficient for $^{\bullet}CH_2NH_2 + O_2$ (+NH_3) [1.9×10^{-23} cm^3 $molecule^{-1}$ s^{-1}] and for $CH_2NH_2 + O_2$ (+H_2O) [3.3×10^{-17} cm^3 $molecule^{-1}$ s^{-1}] is at least twelve and six order magnitudes smaller than those for free $^{\bullet}CH_2NH_2 + O_2$ (2×10^{-11} cm^3 $molecule^{-1}$ s^{-1} at 298 K) reactions, respectively. Our result is consistent with that of previous experimental and theoretical analysis and in good agreement with its isoelectronic analogous reaction. The work also provides a clear understanding of the formation of tropospheric carcinogenic compounds, i.e., hydrogen cyanide (HCN).

KEYWORDS

aminomethyl radical, O_2 radical, methanimine, *ab initio*/DFT, RRKM/ME, H_2O and NH_3, HCN, catalysis

1 Introduction

Methylamine is a simple organic nitrogen compound that is released into the atmosphere from a range of sources, for example, food industries, animal husbandry, marine sources, and biomass burning (Schade and Crutzen, 1995; Ge et al., 2011a; Ge et al., 2011b; Zhang et al., 2012; Almeida et al., 2013). Methylamine forms a particulate salt when reacting with acids such as H_2SO_4, HNO, and CH_3COOH; therefore, it plays a vital role in enhancing

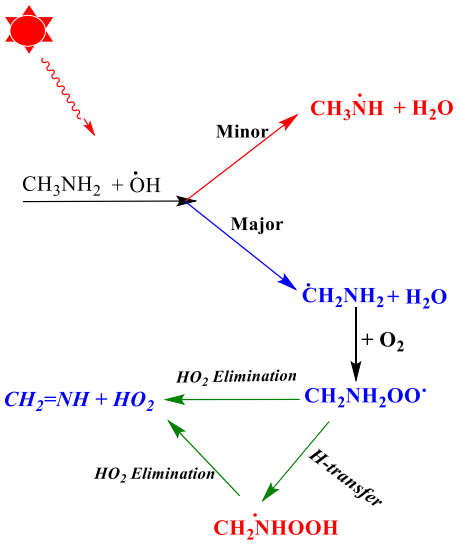

FIGURE 1
Photo-oxidation mechanism of methylamine (Gonza´lez et al., 2022; Onel et al., 2014; Rissanen et al., 2014; Ashraful and Silva, 2020).

atmospheric cloud nucleation (Murphy et al., 2007; Lee and Wexler, 2013). The reaction of methylamine with various tropospheric oxidants such as O_3, OH, and NO_3 radicals leads to the formation of semi-volatile and non-volatile chemical species, consequently leading to the formation of secondary organic aerosols (Schade and Crutzen, 1995; Murphy et al., 2007; Ge et al., 2011a; Nielsen et al., 2012; Qiu and Zhang, 2013). Methylamine is also expected to be present in the interstellar medium (ISM), which leads to the formation of amino acids (Altwegg et al., 2016; Elsila et al., 2009; Gonza´lez et al., 2022). Although glycine ($HO_2CCH_2NH_2$) has not yet been identified in the ISM medium, it is detected in different comets (Elsila et al., 2009; Altwegg et al., 2016). Methylamines are also possible atmospheric precursors of hydrogen cyanide and nitrous oxide (N_2O) (Nielsen et al., 2012). N_2O is a greenhouse gas and the potential source of stratospheric NOx production. To know the significance of methylamine reactions in the two drastically different environments, several researchers have investigated their atmospheric significance and sinks in both the gas phase and solid phase (Schade and Crutzen, 1995; Ge et al., 2011a; Ge et al., 2011b; Almeida et al., 2013).

Once CH_3NH_2 is released into the Earth's atmosphere, it reacts with the OH radical via the H-abstraction reaction, leading to the formation of a carbon-centered aminomethyl ($^{\bullet}CH_2NH_2$) radical, which is observed as a major product, and nitrogen-centered methyl amino radical ($CH_3NH^{\bullet}$), which is observed as a minor product (Figure 1) (Gonza´lez et al., 2022; Onel et al., 2014; Rissanen et al., 2014; Ashraful and Silva, 2020).

As suggested in the previous studies (Gonza´lez et al., 2022; Onel et al., 2014; Rissanen et al., 2014; Ashraful and Silva, 2020), $^{\bullet}CH_2NH_2$ predominantly reacts with molecular oxygen (O_2), which can lead to the formation of methanimine (CH_2NH) and the hydroperoxy radical (HO_2) as major reaction products via a hydrogen atom transfer (HAT) mechanism (Gonza´lez et al., 2022; Onel et al., 2014; Rissanen et al., 2014; Ashraful and Silva, 2020). The chemical kinetics studies on the $^{\bullet}CH_2NH_2 + O_2$ reaction system have been investigated by various researcher groups (Masaki et al., 1995; Jansen et al., 1999; Rissanen et al., 2014; Ashraful and Silva, 2020; Glarborg et al., 2020). Jansen et al. (1999) used pulse radiolysis and UV-absorption detection to analyze the chemical kinetics of the $^{\bullet}CH_2NH_2 + O_2$ reaction at 298 K and 1 atm of SF_6 as a bath gas. Masaki et al. (1995) investigated the kinetics of the same reaction by employing the photoionization mass spectrometry technique at 298 K and a few torr pressure of N_2. Rissanen et al. (2014) used the laser flash photolysis technique in combination with photoionization mass spectrometry to determine the rate coefficients of the $^{\bullet}CH_2NH_2 + O_2$ reaction. They observed negative temperature-dependent rate coefficients from 267 K to 363 K, independent of the pressure between 0.5 Torr and 2.5 Torr (Rissanen et al., 2014). The reported rate coefficients fall in the range of $(2–8) \times 10^{-11}$ cm^3 $molecule^{-1}$ s^{-1} (Rissanen et al., 2014; Mallick et al., 2018; Ashraful and Silva, 2020; Kumar et al., 2020). Rissanen et al. (2014) also performed quantum chemical calculations coupled with ME simulation to predict the product branching fractions. Their modeling results reproduce the experimentally observed negative temperature dependence and validated the production of CH_2NH under low-pressure conditions. Recently, a chemical kinetic model for the oxidation of methylamine has been characterized by Glarborg et al. (2020) and validated against the results obtained from shock tube experiments. In their work, the potential energy surface of several reactions was studied theoretically starting from the isomerization of CH_3NH and the reactions of $CNHx$ (x = 3–5) molecules with O_2 using the quantum chemistry composite method. In this study, the rate coefficients for $^{\bullet}CH_2NH_2 + O_2$ were re-investigated at high-level quantum chemical calculations with similar statistical rate theories to validate the finding for the role of ammonia and water and molecules in the same reaction. To the best of our knowledge, the branching ratios and temperature- and pressure-dependent rate coefficients have not been available until now.

Concerning the gas-phase reactivity of $^{\bullet}CH_2NH_2$ toward O_2 in the role of ammonia and water, several studies in the past few years have proposed the role of different species such as H_2O, NH_3, formic acid, and CO_2 on important atmospheric reactions (Vöhringer-Martinez et al., 2007; Iuga et al., 2010; Buszek et al., 2012; Iuga et al., 2011; Thomsen et al., 2012; Jonas et al., 2013; Zhang et al., 2013; Zhang et al., 2014; Jara-Toro et al., 2017; Ali et al., 2018; Inaba, 2018; Mallick et al., 2018; Ali, 2019; Ali et al., 2019; Ali, 2020; Kumar et al., 2020; Wu et al., 2020; Zhang et al., 2020; Ali et al., 2021; Ali and Balaganesh, 2022; Ali et al., 2022; Dash and Ali, 2022). It is well-known that ammonia (NH_3) is highly alkaline and is one of the most common chemicals used in the agriculture sector, and as a fertilizer, it is the major source in the atmosphere. Ammonia is mainly produced industrially and exists naturally as a product of the decomposition of organic matter. It is also used as a refrigerant gas and in the production of plastics, textiles, dyes, explosives, and other chemicals. The emissions of NH_3 into the Earth's atmosphere have been increasing over the last few decades. The change in NH_3 concentration has essential implications for air quality and the ecosystem. To ascertain the significant influence of NH_3 on many atmospheric reactions, several researchers have investigated the role of NH_3 on many important atmospheric reactions

(Jonas et al., 2013; Mallick et al., 2018; Ali, 2019; Kumar et al., 2020; Zhang et al., 2020; Ali et al., 2021). To this end, it is essential to clearly understand the reaction between $^{\bullet}CH_2NH_2$ and O_2 in the presence of NH_3, given its similar catalytic efficiency to water.

Water vapor is an environmentally significant constituent of the Earth's atmosphere. Numerous investigations have been carried out to determine the catalytic role of a single H_2O molecule in many atmospheric and combustion reaction systems (Vöhringer-Martinez et al., 2007; Iuga et al., 2010; Buszek et al., 2012; Iuga et al., 2011; Thomsen et al., 2012; Zhang et al., 2013; Zhang et al., 2014; Jara-Toro et al., 2017; Ali et al., 2018; Inaba, 2018; Ali et al., 2019; Ali, 2020; Wu et al., 2020; Ali and Balaganesh, 2022; Ali et al., 2022; Dash and Ali, 2022). These studies reveal that water-catalyzed reactions are energetically more favorable than other catalyzed reactions due to the formation of many hydrogen-bonded intermediates and transition states. However, water does not enhance the reaction's rate coefficients under tropospheric conditions due to its high concentration and lower entropic contribution compared to a free reaction (Ali et al., 2019; Ali, 2020; Ali and Balaganesh, 2022; Dash and Ali, 2022).

In this paper, we have investigated the rate coefficients for the effect of NH_3 and H_2O molecules on the important atmospheric and combustion prototype reactions, i.e., $^{\bullet}CH_2NH_2 + O_2$, for the first time. Using the RRKM/ME simulation, the temperature- and pressure-dependent rate coefficients were calculated between 200 K and 400 K and pressure ranges of 0.0001–1000 atm. The role of enthalpy and entropy contributions on hydrogen-bonded species on the effect of ammonia and water on the $^{\bullet}CH_2NH_2 + O_2$ reaction has been discussed to understand the chemical kinetic behavior of these complexes. In these situations, we have been inspired to model a gas-phase ternary reaction system, $^{\bullet}CH_2NH_2 \cdots O_2 \cdots X$ (X = NH_3, H_2O), where H_2O and NH_3 can act as catalysts (*vide Infra*). To assess the accuracy of the data provided in this work, we have compared the energies and re-calculated rate coefficients and compared them with the available literature data for $^{\bullet}CH_2NH_2 + O_2$ and its isoelectronic similar reaction, i.e., $^{\bullet}CH_2OH + O_2$ (Dash and Ali, 2022). We hope that this study will strengthen the chemical kinetic database for global modeling and provide a thorough understanding for further study on analogous reaction systems.

2 Theoretical and computational methodology

2.1 Quantum chemical calculations

All the electronic structure calculations were carried out with the Gaussian 09 suite of programs (Frisch, 2013). The stationary points on potential energy surfaces (PESs) for $^{\bullet}CH_2NH_2 + O_2$, $^{\bullet}CH_2NH_2 + O_2$ (+NH_3), and $^{\bullet}CH_2NH_2 + O_2$ (+H_2O) reactions were computed using the hybrid-density functional method, i.e., M06-2X (Zhao and Truhlar, 2008) with the Pople 6-311++G (3df, 3pd) basis set (Frisch et al., 1984) and tabulated in Supplementary Table S1. The M06-2X is a frequently used preeminent functional to investigate the non-covalent interactions of transition states, intermediates, and post-intermediates for investigating chemical systems that encounter hydrogen bonding. To add corrections from the van der Waals interaction on M06-2X (Zhao and Truhlar, 2008), the Grimme empirical dispersion "GD3" was used (Grimme et al., 2010). Normal modes of the vibrational frequency for each optimized species were carried out to obtain the zero-point energy (ZPE) and to calculate the rotational–vibrational partition functions. The transition state (TS) shows a single imaginary frequency, whereas reactants, intermediates, and products all show positive vibrational frequencies (see Supplementary Table S2). Intrinsic reaction coordinate (IRC) calculations (Fukui, 1981) were performed to confirm the identity of intermediates and post-intermediates for each TS. The IRC calculation was performed in both directions with the maxpoints=50 and the step size set to 3. The internal degrees of freedom of all species involved in the reaction were treated as harmonic oscillators and rigid rotor approximations, as suggested in previous studies for similar reaction systems (Ali et al., 2018; Dash and Ali, 2022). To improve the accuracy of energy, the single-point energy calculations were carried out at CCSD(T)/6-311++G (3df, 3dp)//M06-2X/6-311++G (3df, 3dp)+GD3 (Frisch et al., 1984; Raghavachari et al., 1989; Zhao and Truhlar, 2008). The result provides values that are accurate enough up to ~1 kcal/mol, as validated in our previous studies (Ali et al., 2019; Ali, 2020; Ali and Balaganesh, 2022; Dash and Ali, 2022). To check the qualitative contribution of the single-reference wave function, we have carried out the T1 diagnostic calculation at CCSD(T)/6-311++G (3df, 3pd). The calculated T1 diagnostic was found to be ≤ 0.03, which is an acceptable range for a single reference wave function. To understand the spin contamination for each species, the spin expectation value $<S^2>$ was calculated and found to be in the range of ~0.75–0.77, which indicates that spin contamination was negligible.

2.2 State-of-the-art kinetics calculations

All the kinetics calculations were carried out using a software tool in the MultiWell suite of the program (Barker, 2009; Barker, 2011; Barker, 2023). The "*me*" codes in MultiWell programs calculate the unimolecular rate coefficients $k(E)$ based on the RRKM/master equation as follows (Forst, 2003):

$$k(E) = \left[\frac{m^{\neq}}{m}\frac{\sigma_{ext}}{\sigma_{ext}^{\neq}}\right]\frac{g_e^{\neq}}{g_e}\frac{1}{h}\frac{G^{\neq}(E-E_{0,0})}{\rho(E)}. \quad (1)$$

To avoid repetition from the previous studies, the details of each term of the equation are given in Supplementary Material S1. To calculate temperature- and pressure-dependent rate coefficients and branching fractions, N_2 bath gases were used with an approximate value of the energy transfer process $<\Delta E>_{down}$ = 200 × $(T/300)^{0.85}$ cm^{-1} (Goldsmith et al., 2012). The Lennard–Jones parameters for collider gases (N_2) εk_B, $\sigma(N_2)$ = 3.74 Å, and $\varepsilon/k_B(N_2)$ = 82 K were obtained from Hippler et al. (1983). The Lennard–Jones parameters of $NH_2CH_2O_2$ and $NH_2CH_3O_2$ were approximated based on Rissanen et al. (2014). The double arrays used in *me* simulations consisted of 1500 array elements with 10 cm^{-1} energy grains using a quasi-continuum regime, which is evaluated up to 85,000 cm^{-1}. At each pressure and temperature value, ME simulations were carried out using the chemical activation energy distribution, which is appropriate for association reactions. The RRKM/ME simulations consisted of 10^5 stochastic trials, each with a simulated time duration corresponding to an average of 100 collisions.

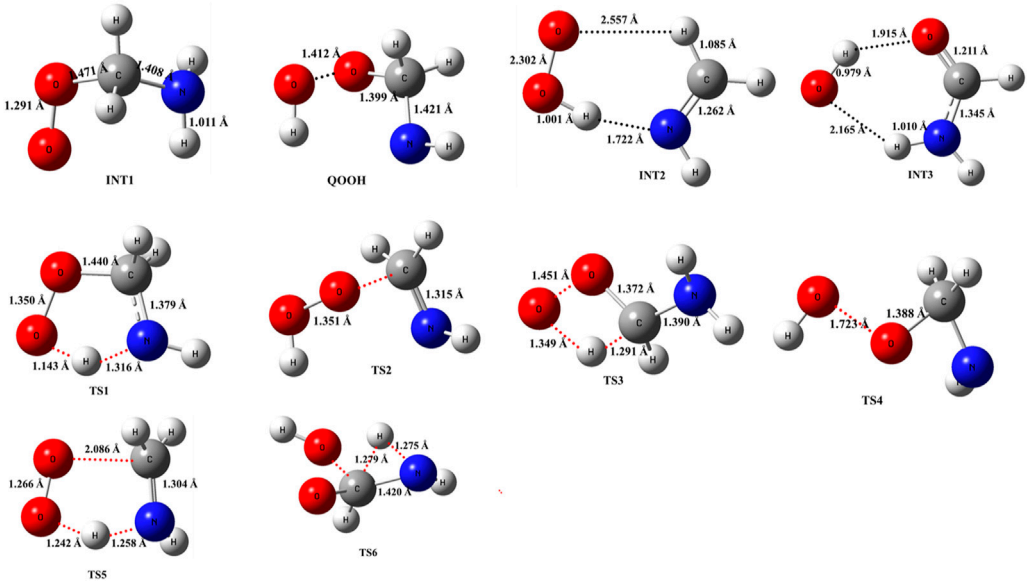

FIGURE 2
Structural and geometrical changes during the $^{\bullet}CH_2NH_2$ + O_2 reaction calculated using M06-2X/6-311++G (3df, 3pd).

The pressure-dependent total rate coefficients $k^{bimol}(T, M)$ for $^{\bullet}CH_2NH_2 + O_2$ were calculated using (Ali, 2020; Dash and Ali, 2022)

$$k^{bimol}(T, M) = \Gamma K_{eq} \times k_{\infty}^{uni}\left(1 - f_{CH_2NH_2+O_2}\right), \quad (2)$$

where (Γ) is the quantum mechanical tunneling correction to the microcanonical rate coefficients *k(E)*. Γ was implemented in the MultiWell master equation code, which is based on the 1-D Eckart asymmetric barrier. The *k(E)* calculated using the modified sums of states of the transition state reflect the tunneling effects. Tunneling was used to initialize the chemical activation distribution if both the "CHEMACT" and "TUN" keywords were selected. The $f_{CH_2NH_2+O_2}$ is the branching fraction (*f*) of the reaction going back to the reactants, and k_{∞}^{uni} is a high-pressure limit rate coefficient. The *fall-off* behavior of rate coefficients from (pressure = 1000 bar, P→∞) toward the low-pressure limit (*p* = 0.0001 bar, P→0) was considered.

For the barrierless reactions, i.e., $^{\bullet}CH_2NH_2 + O_2 \rightarrow CH_2NH_2OO$, $^{\bullet}CH_2NH_2 \ldots H_2O + O_2 \rightarrow CH_2NH_2OO \ldots H_2O$, $^{\bullet}CH_2NH_2 \ldots NH_3 + O_2 \rightarrow {}^{\bullet}CH_2NH_2OO \ldots NH_3$, the inverse Laplace transform (ILT) method was used. Since the rate coefficients for association reactions are usually weak and dependent on temperature, the activation energy for the recombination reaction was assumed to be equal to 0. As suggested in many similar reactions (Rissanen et al., 2014), this approach is good, and Arrhenius's activation energy can be equal to the reaction critical energy (E_0). MultiWell input for ILT calls for only two parameters E_0 and A-factor. In this work, we use statistical rate theories, which do not account for non-statistical effects, such as slow intramolecular vibrational energy redistribution (IVR), as suggested by Ali et al. (2023).

The equilibrium constant (K_{eq}) for the formation of $^{\bullet}CH_2NH_2 + O_2 \rightarrow CH_2NH_2OO^{\bullet}$, $^{\bullet}CH_2NH_2 \ldots H_2O \rightarrow CH_2NH_2OO \ldots H_2O$, $^{\bullet}CH_2NH_2 \ldots NH_3 \rightarrow {}^{\bullet}CH_2NH_2OO \ldots NH_3$, $^{\bullet}CH_2NH_2 \ldots H_2O + O_2 \rightarrow CH_2NH_2OO \ldots H_2O$ and $^{\bullet}CH_2NH_2 \ldots NH_3 + O_2 \rightarrow {}^{\bullet}CH_2NH_2OO \ldots NH_3$ was calculated using the "THERMO" code as given: (Barker, 2009; Barker, 2011; Barker, 2023)

$$K_{eq} = \frac{Q_{INT}}{Q_R} exp\left(-\frac{E_{INT} - E_R}{k_B T}\right). \quad (3)$$

The equilibrium constants (K_{eq}) for the formation of two-body and three-body complexes calculated by Eq. 3 are tabulated in Supplementary Tables S3, S4. The Q_{INT} and Q_R are total partition functions of the intermediates and reactants, respectively; $E_{INT} - E_R$ is the zero-point corrected energy difference between intermediates and reactants. The calculated rate coefficients in the high-pressure limit (k_{∞}) were fitted to the modified Arrhenius expression $k_{\infty}(T) = A \times T^n \times exp(\frac{-E_a}{RT})$ in the temperature range of 200 K–400 K.

3 Results and discussion

3.1 Geometries and Energies

3.1.1 Reaction channels for $^{\bullet}CH_2NH_2 + O_2$

The optimized structures of intermediates and transition states are shown in Figure 2. The zero-point corrected PES for the $^{\bullet}CH_2NH_2 + O_2$ reaction is depicted in Figure 3, and enthalpies values are given in Table 1. In the current reaction system, the O_2 molecule attacks the radical carbon atom, which leads to the formation of the intermediate $^{\bullet}OO\text{-}CH_2NH_2$ (INT1). Several conformational isomers of INT1 were observed, and for simplicity, we have considered the lowest energy conformer in our calculation. The calculated stabilization energy for INT1 is −31.7 kcal mol^{-1}, which is in very good agreement with the reported values by Rissanen et al. (2014) and Zhang et al. (2020) This value is also in very good agreement with its isoelectronic reactions, i.e., the O_2 + $^{\bullet}CH_2OH$ value (−31.9 kcal/mol) (Dash and Ali, 2022). The

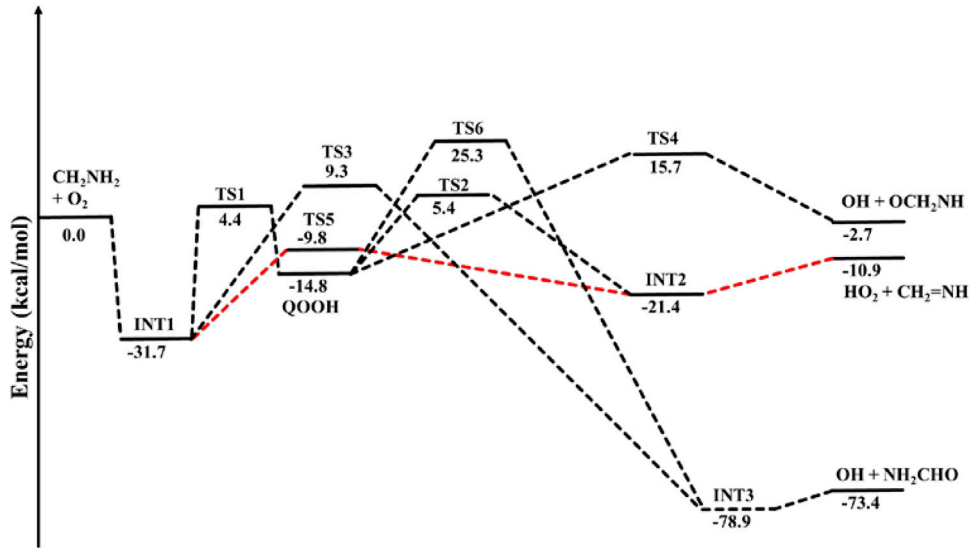

FIGURE 3
Potential energy surface for the $^{\bullet}CH_2NH_2 + O_2$ reaction obtained using CCSD(T)/6-311++G (3df, 3pd)//M06-2X/6-311++G (3df, 3pd). The energies shown in the figure include the zero-point energy.

TABLE 1 Comparison of enthalpies (in kcal mol^{-1}) of each species for the $^{\bullet}CH_2NH_2 + O_2$ reaction with those found in previous studies and its isoelectronic analogs.

$^{\bullet}CH_2NH_2 + O_2 \rightarrow$	*This Work*	*Previous works.* Rissanen et al. (2014); Glarborg et al. (2020)	$^{\bullet}CH_2OH + O_2 \rightarrow$	*Previous Work* (Dash and Ali, 2022)	$\Delta S_{r,298K}$
H_2NCH_2OO (INT1)	−31.7	−33.3[a],-32.5[b]	$HOCH_2OO$ (Int-1)	−31.9	−37.3
H···$NHCH_2OO$ (TS1)	4.4	2.5[a]	H···OCH_2OO (TS-1)	−7.4	−39.6
HO_2···CH_2NH (TS2)	5.4	2.7[a]	HO_2···CH_2O (TS-2)	2.8	−36.2
H···$CHNH_2OO$ (TS3)	9.3	6.2[a]	HO···HCOOH (TS-3)	8.6	−38.0
HO···OCH_2NH (TS4)	15.7	12.4[a]	HO···OCH_2O (TS-4)	24.0	−35.3
H···$NHCH_2$···OO (TS5)	−9.8	−10.2[a],-12.0[b]	H···O_2··CH_2O (TS-5)	−18.5	−38.9
H···NHCHO···OH (TS6)	25.3	21.8[a]	-	-	−35.9
HO···OCH_2NH (QOOH)	−14.8	−16.1[a]	HO···OCH_2O	−14.2	−37.6
OOH···$NHCH_2$ (INT2)	−21.4	−22.8[a],22.0[b]	OOH···OCH_2 (Int-2)	−25.6	−29.2
HO···NH_2CHO (INT3)	−78.9	−77.2[a]	-	-	−29.3
$CH_2NH + HO_2$	−10.9	−12.2[a],-10.6[b]	$CH_2O + HO_2$	−17.9	1.8
$NH_2CHO + OH$	−73.4	−73.1[a]			−2.0
$OCH_2NH + OH$	−2.7	−2.9[a]	$OCH_2O + OH$	−15.0	−5.5

[a]Rissanen et al. (2014).
[b]Glarborg et al. (2020).

unpaired electron in INT1 resides at the terminal O-atom, which can be decomposed differently. The lowest energy channel is an isomerization process where the terminal O-atom attacks the H-atoms of the NH_2 group via five- and six-membered cyclic transition states (TS5 and TS1), leading to hydrogen-bonded five- and six-membered cyclic complexes, i.e., INT2 and QOOH, respectively. The calculated barrier heights for TS5 and TS1 are 21.9 and 36.1 kcal mol^{-1}, respectively, with respect to INT1, indicating that the isomerization reaction going through TS5,

leading to the formation of INT2, is energetically more favorable than that going through TS1 to QOOH. Supplementary Figure S1 provides an IRC scan that confirms the connectivity of TS5 with INT2 and CH_2NH + HO_2 at the M06-2X/6-311++G (3df, 3pd). It is noted that the influence of the formation of hydrogen-bonded cyclic complexes may change the energetics and kinetics of the reaction system. In INT2, two strong hydrogen bonds are formed between the H-atom of the HO_2 and the N-atom of the CH_2NH (1.72 Å) and O-atom of the HO_2 radical and the H-atom of the CH_2NH (2.55 Å), which leads to the formation of a stable six-membered ring planar cyclic structure. In QOOH, a five-membered ring cyclic structure with one hydrogen bond is formed between the terminal O and H-atoms (2.47 Å). Therefore, INT2 is energetically 6.6 kcal mol^{-1} more stable than QOOH. QOOH can further dissociate via TS2 and TS4 to form HO_2 + CH_2NH and OH + OCH_2NH, respectively. Because the barrier height for the formation of QOOH is very high, the formation of CH_2NH and OCH_2NH via QOOH may be negligible under tropospheric conditions. The terminal O-atom of INT1 can also attack the H-atom of a nearby C-atom, leading to the formation of a hydrogen-bonded six-membered cyclic intermediate, INT3, via a four-membered ring transition state (TS3) and subsequently dissociating to form OH + NH_2CHO. In INT3, two strong hydrogen bonds are formed between the H-atom of the OH radical and the O-atom of the NH_2CHO (1.91 Å) and the O-atom of the OH radical and the H-atom of the NH_2CHO (2.16 Å). INT3 is energetically the most stable structure in the PES, with a stabilization energy of −78.9 kcal mol^{-1} from the reactants. The barrier height of this reaction channel is 41 kcal mol^{-1}, which is 20 kcal mol^{-1} higher than that of the TS5 and may not contribute to the overall reaction kinetics (*vide infra*).

The other reaction channel, such as the conversion from QOOH to INT3 via H-atom shift (C to N) through a three-membered transition state, TS6 (41 kcal mol^{-1}), is expected to have a negligible impact on the total rate coefficient due to its high energy barriers.

The enthalpies of reaction (ΔH_{rxn} (0 K) for $^{\bullet}CH_2NH_2$ + O_2 → CH_2NH + $^{\bullet}HO_2$ (−10.9 kcal mol^{-1}) are in very good agreement with those found in the most accurate active thermochemical database (ATcT) (−11.42 kcal mol^{-1}) (Ruscic et al., 2004; Ruscic and Bross, 2020) and in good agreement with the theoretically calculated value in Rissanen et al. (2014) (−12.2 kcal mol^{-1}). The computed PES for the $^{\bullet}CH_2NH_2$ + O_2 reaction is also consistent with its isoelectronic analogous reaction system, i.e., $^{\bullet}CH_2OH$ + O_2 reported by Dash and Ali (2022) using CCSD(T)//ωB97XD/6-311++G (3df, 3pd) level of theory. The enthalpy values obtained in their calculations are also given in Table 1. The reaction energies for $CH_3NH^{\bullet}$ + O_2 → CH_2NH + HO_2 (−17.3 kcal/mol) are also calculated and found to be in very good agreement with that in the ATcT (−17.9 kcal/mol) (Ruscic et al., 2004; Ruscic and Bross, 2020). The energies obtained for most of the structures of the $^{\bullet}CH_2OH$ + O_2 system (Ali, 2020) along the reaction paths are very close to those of the current system, indicating the reliability of the data presented here. However, the barrier heights for the isomerization pathways Int-1→TS-1 (−7.4 kcal/mol)→QOOH and Int-1 →TS-5 (−18.5 kcal/mol) Int-2 in the CH_2OH + O_2 system (Dash and Ali, 2022) are quite low and more stable compared to those in the same pathways in the current system with respect to the reactant's energy (Table 1). Moreover, the barrier height for the reaction proceeding from HO···OCH_2O to OCH_2O + OH (Dash and Ali, 2022) is 24 kcal/mol (TS-4), and the stabilization energy for the products is −15 kcal/mol, whereas in the current system, the corresponding energies are 8.3 and 12.3 kcal/mol less stable than the former ones, respectively. These differences in barrier energies can affect the overall rate coefficients between the two systems.

3.1.2 Role of the ammonia molecule on $^{\bullet}CH_2NH_2$ + O_2

When a single ammonia molecule is introduced in $^{\bullet}CH_2NH_2$ + O_2, the simultaneous collision between $^{\bullet}CH_2NH_2$, O_2, and NH_3 is very unlikely to occur; therefore, the probability of a trimolecular reaction is very small under real conditions. Hence, the first step is the formation of a CH_2NH_2···NH_3 complex, followed by collision with O_2. The CH_2NH_2···NH_3 complex (−2.2 kcal/mol) is assumed to be more important than CH_2NH_2···O_2 and NH_3···O_2 due to its lower binding energy (<1 kcal/mol). As discussed in our previous work, we have also used a similar approach for ammonia-assisted reactions (Ali et al., 2019; Ali, 2020; Ali and Balaganesh, 2022; Dash and Ali, 2022). The geometrical changes in ammonia-assisted intermediates and transition states are shown in Figure 4, and the zero-point corrected PES for the ammonia-assisted $^{\bullet}CH_2NH_2$ + O_2 reaction is given in Figure 5. The energy of all the stationary points, i.e., reactants, intermediates (INTs), and transition states, is tabulated in Table 2.

Figure 5 shows that the effect of the ammonia reaction proceeds via similar reaction pathways as a free reaction. For simplicity, only the most stable structures are shown in the PES. As shown in Figure 5, O_2 attacks the bimolecular complex $^{\bullet}CH_2NH_2$···NH_3 to form a trimolecular hydrogen-bonded complex (INT1n) (Figure 4), whose stabilization energy is −36.1 kcal mol^{-1}. The resulting ammonia-assisted intermediate (INT1n) is 4.4 kcal mol^{-1} more stable than the corresponding ammonia-free intermediate, i.e., INT1. This is due to the formation of strong hydrogen bonds between the terminal O-atom of H_2NCH_2OO and one of the H-atoms of NH_3 (2.20 Å) and the H-atom of H_2NCH_2OO (2.08 Å) with the N-atom of NH_3, whereas no such effect is observed in INT1. On the other hand, Table 2 shows that INT1 is entropically more favorable than INT1n with respect to reactants. This is due to the fact that the hydrogen-bonded complex decreases the entropy of the system. Similar to uncatalyzed reaction pathways, the terminal O-atom intra-molecularly attacks the H-atoms in the NH_2 group in the presence of NH_3, leading to the formation of INT2n and QOOH-n via five-membered cyclic transition states (TS5n/TS7n and TS1n, respectively). The difference in the barrier heights between two isomeric transition states, TS5n and TS7n, is 2.1 kcal mol^{-1}. TS5n seems to be more stable than TS7n because, in the case of TS5n, all three hydrogen atoms of ammonia face toward the molecular center, leading to the formation of a six-membered ring hydrogen-bonded cyclic structure, whereas in the case of TS7n, hydrogen atoms of ammonia are away from the molecular center, leading to the formation of a similar six-membered ring hydrogen-bonded cyclic structure. Entropy data also support that TS5n is more disordered than TS7n.

Supplementary Figure S2 provides an IRC scan at the same level that confirms that TS5n bridges the $OCH_2C(O)OOH$ radical (INT2n) and CH_2NH + HO_2 +NH_3. The IRC scan confirms that the only stationary point between INT2h and the trimolecular products is that associated. The barrier height of TS1n is 2.5 kcal mol^{-1} lower than that of the corresponding ammonia-free transition state TS1. This is due to the formation of two strong hydrogen bonds (H-atoms of ammonia with N and O atoms of the cyclic ring) in TS1n (1.93 and 2.14 Å). On

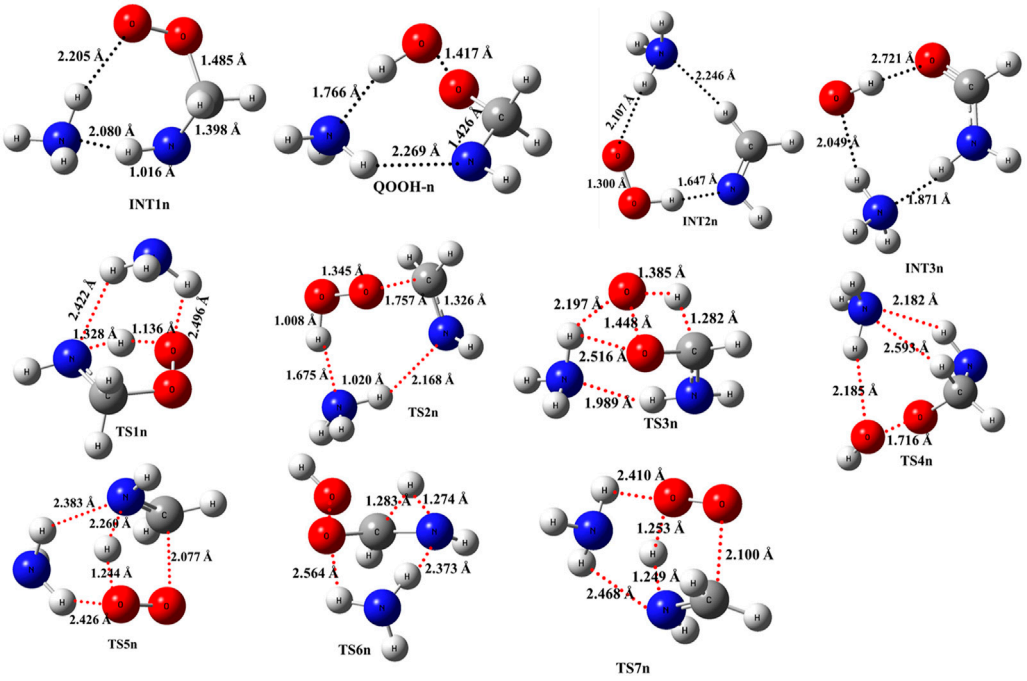

FIGURE 4
Structural and geometrical changes for the ammonia-assisted $^{\bullet}CH_2NH_2$ + O_2 reaction calculated using M06-2X/6−311++G (3df, 3pd).

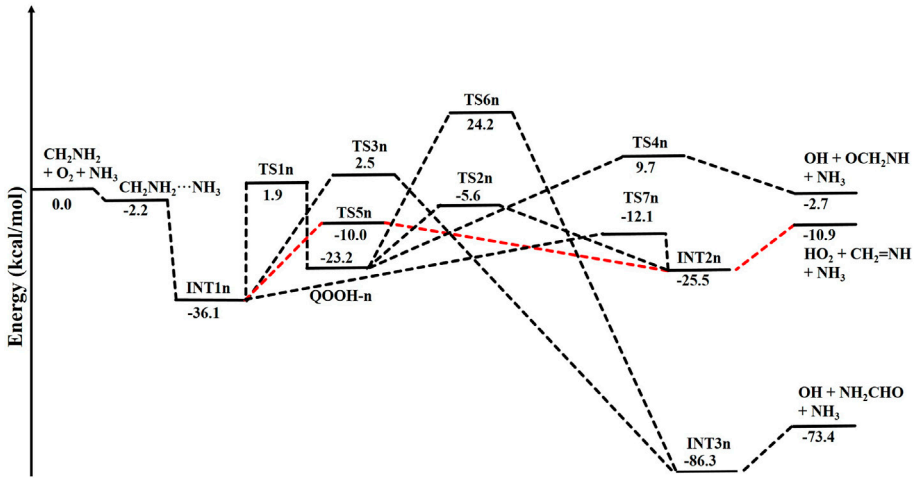

FIGURE 5
Potential energy surface for the role of ammonia on the $^{\bullet}CH_2NH_2$ + O_2 reaction obtained using CCSD(T)/6-311++G (3df, 3pd)//M06-2X/6-311++G (3df, 3pd). The energies shown in the figure include the zero-point energy.

the other hand, the barrier height of TS5n is almost similar to that of TS5, although hydrogen bonds are present in TS5n. The differences in the barrier height can be explained by the formation of two adjacent cyclic ring structures (five- and six-membered), as aforementioned in TS5n, making it sterically hindered compared to only one ring structure in TS5. The stabilization energies of ammonia-assisted QOOH and INT2 are calculated to be −23.3 and −25.5 kcal mol^{-1}, respectively, which are 8.4 and 4.1 kcal mol^{-1} lower than those of the corresponding free-ammonia structures. This can be explained similarly by comparing the presence of hydrogen bonds in the respective structures. In QOOH-n, the formation of two strong hydrogen bonds between the H-atom of ammonia with N atom QOOH (2.26 Å) and N atom NH_3 and terminal H atom of QOOH (1.76 Å) leads to a seven-membered ring-like structure rather than only one hydrogen bond in the case of free QOOH. Similarly, the stability of INT2n can be explained by the formation of an eight-membered ring with three hydrogen bonds, H of HO_2 and N of CH_2NH (1.64 Å), O of HO_2 and N of NH_3 (2.1 Å), and H of CH_2NH

TABLE 2 Enthalpies (in kcal mol^{-1}) and entropies (in cal K^{-1} mol^{-1}) due to the effect of NH_3 on each species involved for the $^{\bullet}CH_2NH_2 + O_2$ reaction.

$^{\bullet}CH_2NH_2 + O_2$ (+NH_3) →	ΔH_{rxn} (0 K)	ΔS_{rxn} (298 K)
$CH_2NH_2\cdots NH_3$	−2.2	−28.2
$H_2NCH_2OO\cdots NH_3$ (INT1n)	−36.1	−66.3
$H\cdots NHCH_2OO\cdots NH_3$ (TS1n)	1.9	−68.9
$HO_2\cdots CH_2NH\cdots NH_3$ (TS2n)	−5.6	−70.4
$H\cdots CHNH_2OO\cdots NH_3$ (TS3n)	2.5	−70.9
$HO\cdots OCH_2NH\cdots NH_3$ (TS4n)	9.7	−66.7
$H\cdots NHCH_2\cdots OO\cdots NH_3$ (TS5n)	−10.0	−68.6
$H\cdots NHCHO\cdots OH\cdots NH_3$ (TS6n)	24.2	−66.5
$H\cdots NHCH_2\cdots OO\cdots NH_3$ (TS7n)	−12.1	−69.6
$HO\cdots OCH_2NH\cdots NH_3$ (QOOH-n)	−23.2	−68.8
$OOH\cdots NHCH_2\cdots NH_3$ (INT2n)	−25.5	−55.5
$HO\cdots NH_2CHO$ (INT3n)	−86.3	−61.2

TABLE 3 Enthalpies (in kcal mol^{-1}) and entropies (in cal K^{-1} mol^{-1}) due to the effect of H_2O on each species involved for the $^{\bullet}CH_2NH_2 + O_2$ reaction.

$^{\bullet}CH_2NH_2 + O_2$ (+H_2O) →	ΔH_{rxn} (0 K)	ΔS_{rxn} (298 K)
$CH_2NH_2\cdots H_2O$	−2.7	−27.9
$H_2NCH_2OO\cdots H_2O$ (INT1h)	−36.1	−70.3
$H\cdots NHCH_2OO\cdots H_2O$ (TS1h)	1.5	−71.7
$HO_2\cdots CH_2NH\cdots NH_3$ (TS2h)	−5.0	−71.5
$H\cdots CHNH_2OO\cdots NH_3$ (TS3h)	2.0	−72.0
$HO\cdots OCH_2NH\cdots NH_3$ (TS4h)	9.3	−70.9
$H\cdots NHCH_2\cdots OO\cdots NH_3$ (TS5h)	−11.8	−70.4
$H\cdots NHCHO\cdots OH\cdots NH_3$ (TS6h)	21.4	−66.2
$HO\cdots OCH_2NH\cdots NH_3$ (QOOH-h)	−22.3	−71.4
$OOH\cdots NHCH_2\cdots NH_3$ (INT2h)	−27.1	−60.1
$HO\cdots NH_2CHO$ (INT3h)	−88.6	−64.1

and N of NH_3 (2.24 Å) compared to a six-membered ring with two hydrogen bonds in the case of INT2. On the other hand, the structures of QOOH-n and INT2n are entropically less favorable compared to those of uncatalyzed QOOH and INT2n.

QOOH-n further dissociates to INT2n (via TS2n) and INT3n (via TS6n) and then subsequently forms HO_2+CH_2NH + NH_3 and OH + OCH_2NH + NH_3 via TS4n and OH + NH_2CHO + NH_3. INT2n and INT3n are eight-membered ring hydrogen-bonded structures, and their stabilization energies are 4.1 kcal mol^{-1} and 7.4 of kcal mol^{-1} lower than those of the corresponding uncatalyzed intermediates. Ammonia-assisted intermediates are more stable than ammonia-free ones because of the formation of an eight-membered ring structure with three strong hydrogen bonds between $HO_2\cdots NH_3$ (2.1 Å), $NH_3\cdots CH_2NH$ (2.24 Å), and $HO_2\cdots CH_2NH$ (1.64 Å) in INT2n and $OH\cdots NH_3$ (2.04 Å), $NH_3\cdots NH_2CHO$ (1.87 Å), and $HO\cdots NH_2CHO$ (1.72 Å) in INT3n. The barrier heights of TS2n (−5.6 kcal mol^{-1}), TS3n (2.5 kcal mol^{-1}), TS4n (9.7 kcal mol^{-1}), and TS6n (24.2 kcal mol^{-1}) were also consistently lower than those of the corresponding ammonia-free transition states due to similar hydrogen bonding interactions. Overall, the reaction in the presence of an ammonia-assisted intermediate is thermodynamically more favorable than the free reaction, and *vice versa* entropically.

3.1.3 Role of the water molecule on $^{\bullet}CH_2NH_2 + O_2$

As previously discussed in the case of ammonia reactions, we have also employed a similar approach for water reactions. When a single H_2O molecule is added to $^{\bullet}CH_2NH_2 + O_2$, the first step is the formation of a $CH_2NH_2\cdots H_2O$ complex, followed by collision with O_2. The $CH_2NH_2\cdots H_2O$ (-2.7 kcal/mol) is assumed to be more important than $CH_2NH_2\cdots O_2$ and $H_2O\cdots O_2$ (<1 kcal/mol) due to lower binding energy. The geometrical changes in water-assisted intermediates and transition states are shown in Figure 6 and the Cartesian coordinates of all the optimized geometries are given in Supplementary Table S1.

The zero-point-corrected PES for the water-assisted $^{\bullet}CH_2NH_2 + O_2$ reaction is given in Figure 7, and the energy of all the stationary points, i.e., reactants, INTs, and TSs, is tabulated in Table 3. As shown in Figure 6 and Figure 7, the O_2 molecule attacks the bimolecular complex $^{\bullet}CH_2NH_2\cdots H_2O$ to form a trimolecular hydrogen-bonded complex (INT1h) with a stabilization energy of −36.1 kcal mol^{-1}. The INT1h is 4.4 kcal mol^{-1} lower than that of the water-free intermediate (INT1) and identical to the energy of ammonia-assisted INT1n. The result indicates water- and ammonia-assisted reactions are energetically more favorable than free reactions.

In INT1h, two strong hydrogen bonds are observed between the terminal O-atom of H_2NCH_2OO and one of the H-atoms of H_2O (1.91 Å) and O-atom H_2O and terminal H-atom H_2NCH_2OO (2.12 Å) (see Figure 6). On the other hand, Table 3 and Table 1 show that INT1h is entropically least favored than INT1n and INT1. Similar to the free reaction, the terminal O-atom of INT1h intra-molecularly attacks the H-atoms in the NH_2 group, leading to the formation of cyclic structures, i.e., INT2h and QOOH-h, via five-membered cyclic transition states, i.e., TS5h and TS1h, respectively. The barrier heights of TS5h and TS1h are 2 kcal mol^{-1} and 3 kcal mol^{-1} lower than those of water-free transition states TS5 and TS1, respectively. In a similar manner, TS5h and TS1h are 1.8 kcal mol^{-1} and 0.4 kcal mol^{-1} lower than TS5n and TS1n, respectively. These differences in barrier heights indicate that water-assisted transition states are energetically more stable than ammonia-assisted and water-free species. The stabilization energies of water-assisted QOOH-h and INT2h are calculated to be −22.3 kcal mol^{-1} and −27.1 kcal mol^{-1}, which are 7.8 kcal mol^{-1} and 5.7 kcal mol^{-1} lower than those of the corresponding free structures. This can be understood by comparing the presence of hydrogen bonds in the respective structures. Supplementary Figure S3 provides an IRC scan at the same level that confirms TS5h bridges the $OCH_2C(O)OOH$ radical (INT2h) and CH_2NH + H_2O + HO_2 products. The IRC scan confirms that the only stationary point between INT2h and the trimolecular products is that associated. In QOOH-h, the formation of two strong hydrogen bonds between the H-atom of water with the N atom of QOOH (1.95 Å) and the O atom of H_2O and the terminal H atom of QOOH (1.82 Å) led to the formation of a seven-membered ring-like structure. Similarly, the stability of INT2h can be found by the formation of an eight-membered cyclic ring with three hydrogen bonds, H of HO_2 and

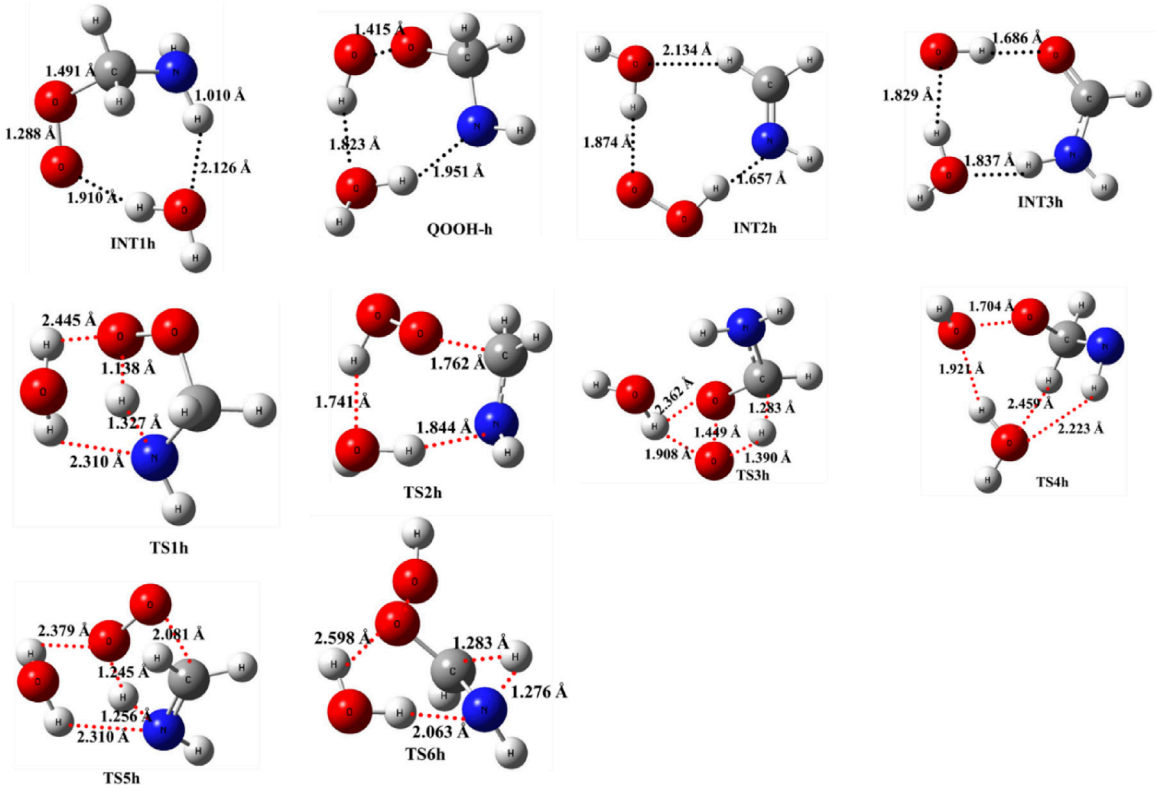

FIGURE 6
Optimized structures of water-assisted intermediates and transition states were obtained using M06-2X/6-311++G (3df, 3pd).

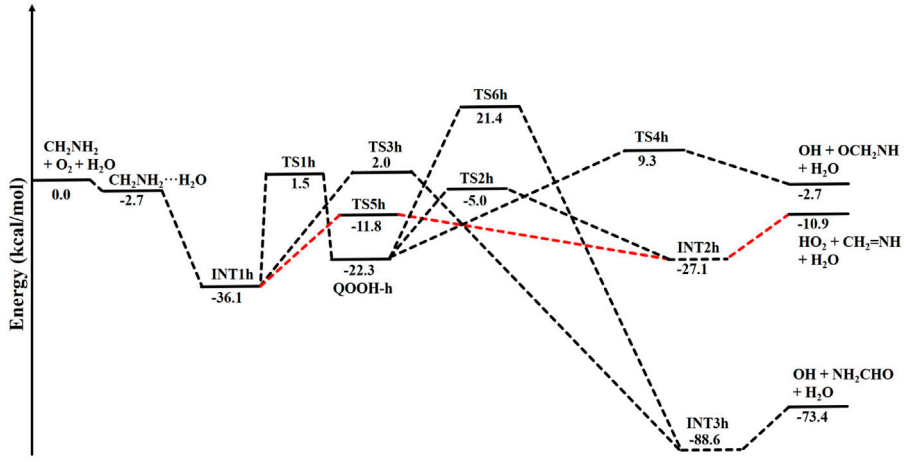

FIGURE 7
Potential energy surface for the role of water on the $^{\bullet}CH_2NH_2 + O_2$ reaction obtained using CCSD(T)/6-311++G (3df, 3pd)//M06-2X/6-311++G (3df, 3pd). The energies shown in the figure include the zero-point correction.

N of CH_2NH (1.65 Å), O of HO_2 and H of H_2O (1.87 Å), and H of CH_2NH and O of H_2O (2.13 Å), which are compared to that of a six-membered ring with two hydrogen bonds, as indicated in the case of INT2. Between water- and ammonia-catalyzed QOOH and INT2, QOOH-n is more stable than QOOH-h and INT2h is more stable than INT2n.

In general, the water-free pathways are entropically more favorable than water-free ones. The QOOH further dissociates to INT2h (via TS2h) and INT3h (via TS6h) and then subsequently forms HO_2+ CH_2NH + H_2O, OH + OCH_2NH + H_2O via TS4h, and OH + NH_2CHO + H_2O. In general, the water-assisted reaction channels are thermodynamically more favorable and entropically

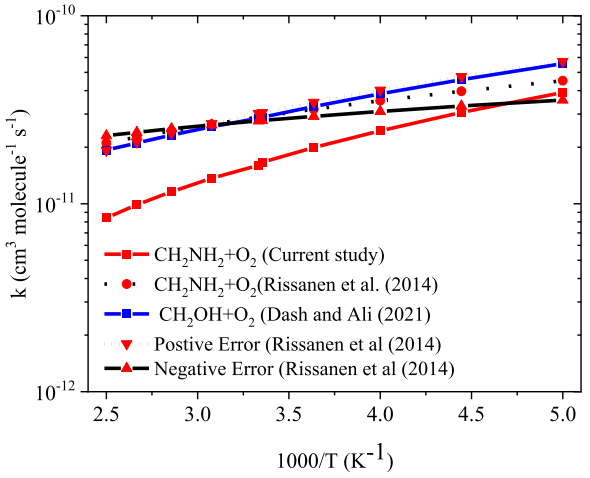

FIGURE 8
Rate coefficients for the $^{\bullet}CH_2NH_2$ +O_2 reaction at 1 bar pressure.

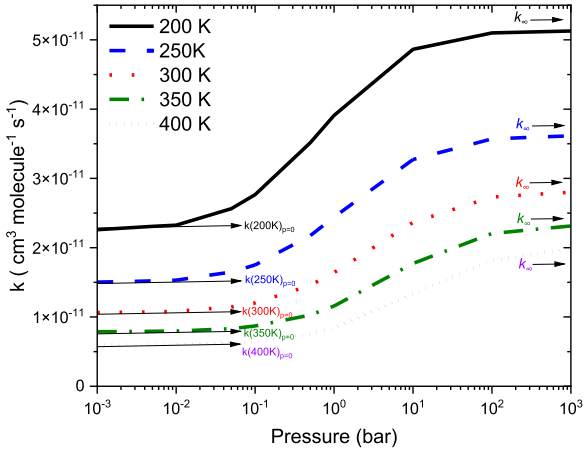

FIGURE 9
Total rate coefficients as a function in the fall-off regions for the $^{\bullet}CH_2NH_2$ +O_2 reaction.

less favorable than the free reaction. It is also clear from Table 3 that all other pathways are thermodynamically less important compared to R + O_2→INT1h→TS5h→INT2h→ CH_2NH + HO_2+H_2O, whose barrier height is the lowest with respect to reactants. Therefore, the other reaction channels may have less contribution under tropospheric conditions.

3.2 Kinetics

3.2.1 Rate coefficients for the $^{\bullet}CH_2NH_2$ + O_2 reaction

To obtain the rate coefficients for $^{\bullet}CH_2NH_2$ + O_2 in temperatures between 200 K and 400 K and pressures from 0.000001 bar to 1000 bar, the RRKM/ME simulation has been used. The rate coefficients as a function of the temperature at 1 bar pressure are shown in Figure 8. The rate coefficients for the formation of O_2-CH_2NH and CH_2NH are observed to be pressure-dependent and negative temperature-dependent. This result is consistent with that of the previous reports by Rissanen et al. (2014) and a similar reaction system, i.e., $^{\bullet}CH_2OH$ + O_2 (Dash and Ali, 2022). The calculated rate coefficient at 300 K (1.6×10^{-11} cm^3 molecule^{-1} s^{-1}) is a factor of ~2 lower than the experimentally measured ones (3.2×10^{-11} cm^3 molecule^{-1} s^{-1}) (Rissanen et al., 2014). The calculated value is in good agreement with the lower temperature range <250 K when the positive error is considered. In light of the expected errors in computed thermochemistry, which may be up to 1 kcal/mol, we believe that this level of accuracy is sufficient for these purposes. A recent study by Ali et al. (2023) indicates that the barrier heights of similar reactions are very sensitive to quantum chemical calculations. The computed rate coefficients are compared with previously reported values and also with its isoelectronic analogous reaction system, i.e., $^{\bullet}CH_2OH$ + O_2 (see Figure 8) (Dash and Ali, 2022). The calculated values at 300 K are a factor of 2 lower than the theoretically calculated values (Dash and Ali, 2022). The presence of the N atom in CH_2NH and the O atom $^{\bullet}CH_2OH$ can explain this, leading to the development of various chemical kinetics conclusions.

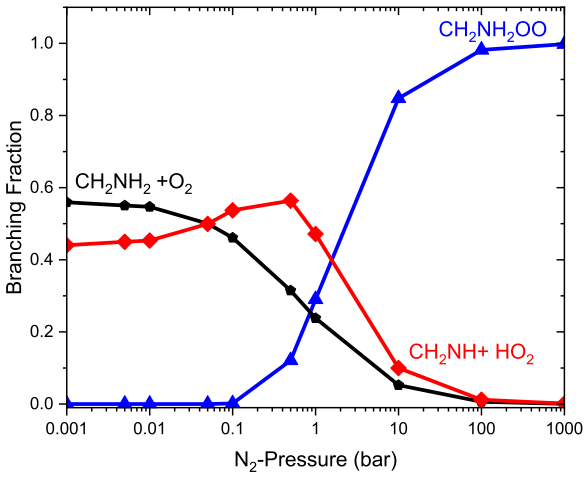

FIGURE 10
Pressure-dependent branching fractions for the $^{\bullet}CH_2NH$ + O_2 reaction at 300 K.

Figure 9 reports the rate coefficients in the fall-off regions for the $^{\bullet}CH_2NH_2$ + O_2 reaction at different temperatures. The rate coefficients increase as pressure increases, and the HPL condition is observed at ~100 bar. As shown in Figure 9, the largest difference between the two limits occurs at about 250 K, which reaches a factor of 2. However, at 200 K, the difference between the two regimes is about a factor of 2. To provide more detailed insights, the relative branching fractions of these channels were determined at 200 K, 300 K, and 400 K and shown in Supplementary Figure S4. For simplicity, the branching fraction at different pressures and at 300 K is shown in Figure 10. At all temperatures and pressures, the branching fractions of QOOH are almost negligible; therefore, they are not shown in Figure 10. The branching fraction for the formation CH_2NH/HO_2 contributes 40% at 300 K and increases as temperature increases to 400 K. The formation of CH_2NH decreases

TABLE 4 Calculated rate coefficients for the $^{\bullet}CH_2NH_2 + O_2$, $^{\bullet}CH_2NH_2 + O_2 (+NH_3)$, and $^{\bullet}CH_2NH_2 + O_2 (+H_2O)$ in the temperature range of 200 K–400 K at 1 bar pressure.

Temperature	$^{\bullet}CH_2NH_2 + O_2$	Exp. value Rissanen et al. (2014)	$^{32}CH_2OH + O_2$	$^{\bullet}CH_2NH_2 + O_2 (+NH_3)$	$^{\bullet}CH_2NH_2 + O_2 (+H_2O)$
200	3.9×10^{-11}	1.9×10^{-11}	5.6×10^{-11}	1.9×10^{-22}	9.8×10^{-20}
225	3.1×10^{-11}	2.2×10^{-11}	4.6×10^{-11}	8.6×10^{-23}	7.8×10^{-19}
250	2.4×10^{-11}	2.4×10^{-11}	3.8×10^{-11}	4.8×10^{-23}	3.7×10^{-18}
275	2.0×10^{-11}	2.7×10^{-11}	3.3×10^{-11}	3.0×10^{-23}	1.3×10^{-17}
298	1.7×10^{-11}	2.9×10^{-11}	2.8×10^{-11}	1.9×10^{-23}	3.3×10^{-17}
300	1.6×10^{-11}	2.8×10^{-11}	2.85×10^{-11}	1.9×10^{-23}	3.3×10^{-17}
325	1.4×10^{-11}	3.1×10^{-11}	2.6×10^{-11}	1.4×10^{-23}	7.4×10^{-17}
350	1.2×10^{-11}	3.4×10^{-11}	2.3×10^{-11}	1.1×10^{-23}	1.4×10^{-16}
375	0.9×10^{-11}	3.6×10^{-11}	2.1×10^{-11}	8.7×10^{-24}	2.3×10^{-16}
400	0.8×10^{-11}	3.8×10^{-11}	1.9×10^{-11}	7.4×10^{-24}	4.0×10^{-16}
$k = AT^n$	$A = 0.02$		$A = 1.0 \times 10^{-09}$	$A = 4.8 \times 10^{-31}$	$A = 3.5 \times 10^{5}$
	$n = -3.4$		$n = -0.75$	$n = 2.0$	$n = -6.0$
$\exp(-B/T)$	$B = 323$		$B = -222$	$B = -1858$	$B = 4958$

to 0% as pressure increases to 100 bar. At the same time, the formation of CH_2NH_2OO increases as pressure increases to 100 bar (100%). The plot shows that backward reaction to regenerate reactants is prominent at <0.01 bar. These results are also consistent with the previously reported branching ratio by Rissanen et al. (2014). At all the pressure rates, it is more advantageous to lose HO_2 via the formation of CH_2NH rather than through OH loss via formamide formation due to an energetically favorable pathway (see Figure 10). As temperature increases from 300 K to 400 K, the product branching ratio increases (see Supplementary Figure S4). The result is due to the fact that the relevant stationary points on the respective potential energy surfaces have a dominant entropy factor over the enthalpy factor.

3.2.2 Rate coefficients for $^{\bullet}CH_2NH_2+O_2$ $(+NH_3)$

As discussed in the previous section, only the entry channel $^{\bullet}CH_2NH \cdots NH_3 + O_2$ is considered for the rate coefficient calculations.

$$CH_2NH_2 + O_2 + NH_3 \underset{k_{-1n}}{\overset{k_{1n}}{\rightleftharpoons}} CH_2NH_2 - - - NH_3 + O_2$$

$$\underset{k_{-2n}}{\overset{k_{2n}}{\rightleftharpoons}} O_2 - CH_2NH_2 - - - NH_3 \xrightarrow{k_{uni-n}} CH_2NH + HO_2 + NH_3$$

The equation to calculate the effective pressure-dependent rate coefficients $k_{eff}^{bimol}(T, M)$ is as follows:

$$k_{eff}^{bimol}(T, M) = K_{eq-1n} \times [NH_3] \times K_{eq-2n} \times k_{\infty}^{uni}\left[1 - f_{(\bullet CH_2NH_2 \ldots NH_3 + O_2)}\right], \quad (4)$$

where $K_{eq-1h} = \frac{k_{1n}}{k_{-1n}}$ *and* and $K_{eq-2n} = \frac{k_{2n}}{k_{-2n}}$ are equilibrium constants of each pathway involved in a reaction, $[NH_3]$ is the concentration, and f is the branching fraction for the reaction proceeding to the reactant. The ammonia concentration used at 10 ppbv is based on the observations from previous studies (Ali et al., 2021). The rate coefficients for the ammonia-assisted reaction are almost similar to those of $^{\bullet}CH_2NH_2 + O_2$ in the temperature range of 200 K–400 K (see Table 4). In fact, some lower values were obtained at higher temperatures. The catalytic behavior does not take place if step 0 is not included in the reaction mechanism. The result could be due to the lower entropy change in the reaction. The total effective rate coefficient for $^{\bullet}CH_2NH_2 + O_2$ (2.7×10^{-21} cm^3 molecule^{-1} s^{-1} at 300 K) is ~12 orders of magnitude lower than that for the $^{\bullet}CH_2NH + O_2$ reaction (8.8×10^{-13} cm^3 molecule^{-1} s^{-1}). This result is due to the fact that the ammonia-assisted pathway depends on the ammonia concentration (see Table 4).

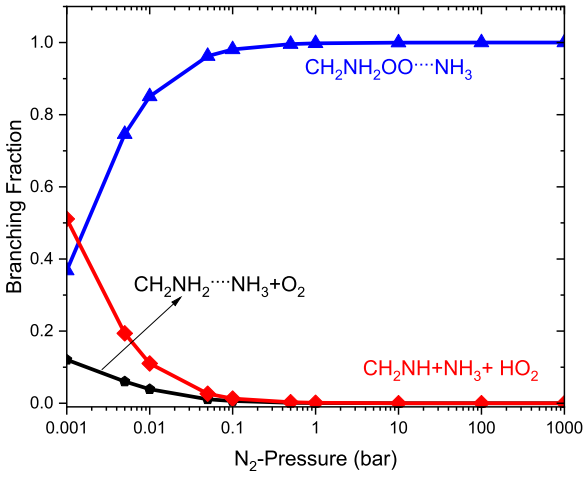

FIGURE 11
Pressure-dependent branching fractions for the $^{\bullet}CH_2NH_2 \ldots NH_3 + O_2$ reaction at 300 K.

The relative branching fractions of these channels determined at 200 K, 300 K, and 400 K are shown in Supplementary Figure S5. For

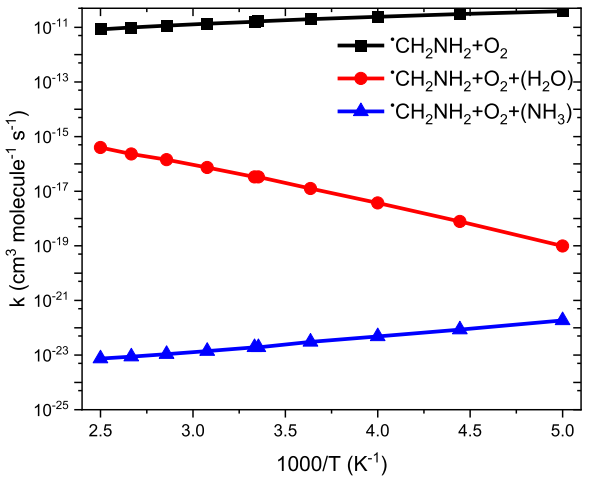

FIGURE 12
Comparison between rate coefficients for $^{\bullet}CH_2NH_2 + O_2$, $^{\bullet}CH_2NH_2 + O_2$ (+NH_3), and $^{\bullet}CH_2NH_2 + O_2$ (+H_2O) in the temperature range of 200 K–400 K at 1 bar pressure.

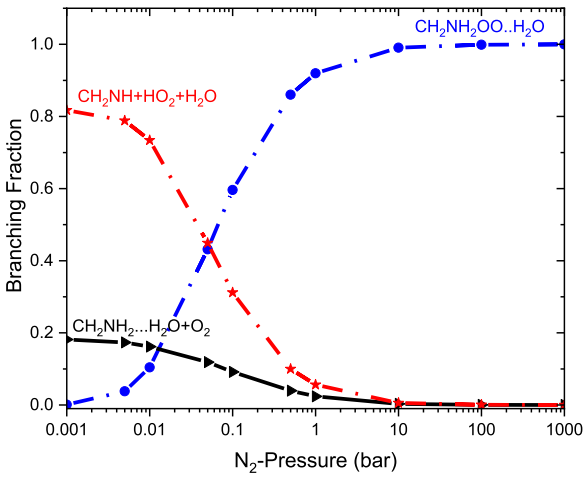

FIGURE 13
Pressure-dependent branching fractions for the $^{\bullet}CH_2NH_2$ ... H_2O+ O_2 reaction at 300 K.

simplicity, the branching fraction at 300 K is shown in Figure 11. The branching fraction for the formation of CH_2NH/HO_2 contributes 50% at 300 K, and almost the same temperature increases to 400 K (see Supplementary Figure S5). At the same time, the formation of CH_2NH_2OO ... NH_3 increases as the pressure increases to 100 bar (100%). The plot shows the back-reaction that regenerates $^{\bullet}CH_2NH_2$ ... $NH_3 + O_2$. When the results are compared with those of the free reaction, it is easier to lose HO_2 via the formation of CH_2NH than through OH loss via formamide formation. We can say that the effect of ammonia has a negligible impact on the product branching ratios, and the results are almost similar to those of a free reaction, except at very low pressure (Supplementary Figure S5).

3.2.3 Rate constant for $^{\bullet}CH_2NH_2 + O_2$ (+H_2O)

The scheme for the formation of INT1h, CH_2NH, and HO_2 from $^{\bullet}CH_2NH_2 + O_2$ reactions with the effect of a water can be written as follows.

$$CH_2NH_2 + O_2 + H_2O \underset{k_{-1h}}{\overset{k_{1h}}{\rightleftharpoons}} CH_2NH_2 - - - H_2O + O_2$$

$$\underset{k_{-2h}}{\overset{k_{2h}}{\rightleftharpoons}} O_2 - CH_2NH_2 - - - H_2O \xrightarrow{k_{uni-h}} CH_2NH + HO_2 + H_2O$$

The equation to calculate the effective pressure-dependent rate coefficients $k_{eff}^{bimol}(\exp(-B/T))$ is as follows:

$$k_{eff}^{bimol}(T,M) = K_{eq-1h} \times [H_2O] \times K_{eq-2h} \times k_{\infty}^{uni}[1 - f_{(\bullet CH_2NH_2...H_2O+O_2)}], \quad (5)$$

where $K_{eq(1)h} = \frac{k_{1h}}{k_{-1h}}$ and $K_{eq-2h} = \frac{k_{2h}}{k_{-2h}}$ are the equilibrium constants of each reaction pathway involved in equation (iii), $[H_2O]$ is the concentration, and f is the branching fraction for the reaction proceeding to the reactants. The $[H_2O]$ is calculated using a typical humidity concentration, as discussed in the previous paper (Dash and Ali, 2022). The rate coefficients were also calculated using different water concentrations, as shown in Supplementary Figure S6. The effect of relative humidity from 20% to 100% on calculated rate coefficients is a factor of 10 difference. The effective rate coefficient calculated based on Eq. 4 (2.04×10^{-17} cm^3 molecule^{-1} s^{-1} at 298 K) is ~six to seven orders of magnitude lower than that of the water-free $^{\bullet}CH_2NH_2 + O_2$ reaction (~2.2×10^{-11} cm^3 molecule^{-1} s^{-1} at 298 K). This is due to the fact that the water-assisted pathway depends parametrically on water concentration and entropy reduces the rate coefficients. Our results are also consistent with the previously reported values for similar reaction systems (Ali et al., 2022; Dash and Ali, 2022).

Our calculation shows that the total effective rate coefficients for systems $^{\bullet}CH_2NH_2 + O_2$ (+NH_3) (~10^{-11} order) and $^{\bullet}CH_2NH_2 + O_2$ (+H_2O) (6 order) are smaller than that of the free reaction (see Figure 12).

It is clear that the geometries of INT and TSs are different in $^{\bullet}CH_2NH_2 + O_2$ (+NH_3) reaction systems compared to their isoelectronic analogous $^{\bullet}CH_2NH_2 + O_2$ (+H_2O) reactions, resulting in different computed enthalpies and rate coefficients. Because of this, the kinetics of $^{\bullet}CH_2NH_2 + O_2$ (+NH_3) is quite different from those of $^{\bullet}CH_2NH_2 + O_2$ (+H_2O) reaction systems. In the case of free reactions and ammonia, the rate coefficients exhibit negative temperature dependence, whereas in the case of water, positive temperature dependence was observed. This may be due to the fact that water concentration is highly dependent on temperature, and ammonia concentration is nearly independent of temperature. The branching fractions for the formation of $^{\bullet}OOCH_2NH_2$ and $^{\bullet}CH_2NH$ and the reaction going back to $^{\bullet}CH_2NH_2 + O_2$ with the effect of a single water molecule at 300 K and pressure range 0.001 bar–1000 bar are shown in Figure 13, and a comparison of branching fractions for $^{\bullet}CH_2NH_2 + O_2$, $^{\bullet}CH_2NH_2 + O_2$ (+NH_3), and $^{\bullet}CH_2NH_2 + O_2$ (+H2O) at 200 K, 300 K, and 400 K is shown in Supplementary Figure S7.

As previously discussed in water- and ammonia-free reactions, the product branching ratios for the formation of $CH_2NH + HO_2$ decrease, and the reaction goes back to the reactants, i.e., $^{\bullet}CH_2NH_2 + O_2$, when the pressure increases from 0.1 bar. When a water molecule is added to the reaction, the product branching ratio changes significantly (~80%), and a single water reaction favors

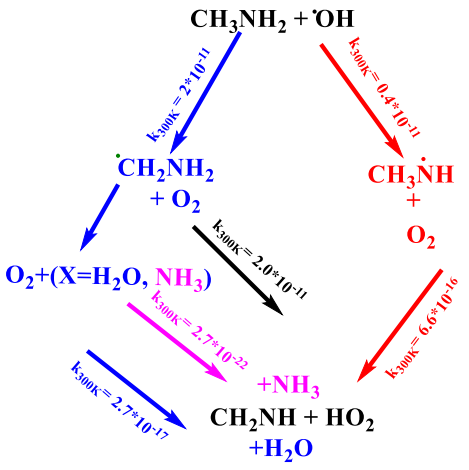

FIGURE 14
Atmospheric degradation reaction of CH_3NH_2 with and without ammonia/water molecules.

the formation of CH_2NH + HO_2 at a temperature of <300 K; however, the effect of ammonia favors only ~10%. Despite the slower water reaction, our ME calculations indicate that a favorable CH_2NH + HO_2 formation is observed under tropospheric conditions.

3.3 Atmospheric fate of methylamine and methanimine

The atmospheric degradation of CH_3NH_2 with and without ammonia and water molecules is shown in Figure 14. The atmospheric lifetime (τ) because of its interaction with OH and species $^{\bullet}CH_2NH_2$ with O_2 radicals is calculated as follows:

$$\tau = \frac{1}{k_{[X=OH,O2]} \times [X]}. \quad (6)$$

The average OH radical concentration at tropospheric conditions 225 K and <1 bar is ~1 × 10^6 cm^3 $molecule^{-1}$ $s^{-1,}$ and a concentration of [O_2] = 1 × 10^{16} molecules cm^{-3} was used, which is based on a previous study (Dash and Ali, 2022). We can say that the photo-oxidation lifetime of methylamine to the sink of $^{\bullet}CH_2NH_2$ is nearly 13–14 h. Based on current data and previous results, we can say that the CH_3NH_2 + OH/O_2 → CH_2O + HO_2 via $^{\bullet}CH_2NH_2$ leading to the formation of CH_2NH is both kinetically and thermodynamically more favorable than the CH_3NH_2 + OH/O_2 → CH_3NH + HO_2 via $CH_3NH^{\bullet}$ under tropospheric conditions. This result is also consistent with its isoelectronic analogous (Ali et al., 2019) reaction $^{\bullet}CH_2OH$ + OH/O_2 → CH_2O+ HO_2. Generally, the effective rate coefficients for the role of water and ammonia reactions are smaller than those of the free $^{\bullet}CH_2NH_2$ + O_2 reaction system in the temperature range of 200 K–400 K. Therefore, the effect of $^{\bullet}CH_2NH_2$ + O_2 with H_2O/NH_3 is less important for the sink of $^{\bullet}CH_2NH_2$ in a gas-phase atmospheric reaction.

To understand the impact of INT1 in budget calculations, we have calculated the atmospheric lifetime of ~3 microseconds of $^{\bullet}CH_2NH_2$ with its reaction O_2, indicating that the formation of CH_2NH is fast under tropospheric conditions (i.e., at 225 K and an altitude of ~10–11 km) when taking an average concentration of O_2 radicals in the upper troposphere of ~1 × 10^{16} molecule cm^{-3}. It is of interest to know whether HO_2···CH_2NH_2···H_2O can be produced from the reaction of CH_2NH···H_2O + O_2 reaction under atmospheric conditions. For this purpose, we calculated the pseudo-first-order rate coefficients of decay of $^{\bullet}CH_2NH_2$···H_2O+ O_2 at 300 K using concentration [O_2] = 1 × 10^{16} molecules cm^{-3}. The decay rate of INT2h producing CH_2NH_2+H_2O-HO_2 was found to be 8 × 10^{-3} s^{-1}, which led to the 2 min of the lifetime of HO_2···CH_2NH_2···H_2O. Therefore, we can say that under tropospheric conditions, HO_2···CH_2NH_2···H_2O can be produced from the reaction of $^{\bullet}CH_2NH_2$ + O_2 (+H_2O).

To understand the fate of the $CH_3NH^{\bullet}$ radical with its reaction with O_2 under the PES (see Supplementary Figure S8), rate coefficients for the addition of O_2 to $CH_3NH^{\bullet}$ are investigated using the RRKM/ME simulation. The O_2 radical mildly reacts with $CH_3NH^{\bullet}$ with the ~6 kcal/mol below the reactants. Unlike the formation of common aminoperoxy radicals, O_2 addition to $CH_3NH^{\bullet}$ proceeds with a transition state TS1a with ~5 kcal/mol of barriers, leading to the formation of Int2 and dissected to Int-2 via a five-membered ring transition state with the barrier height of ~13 kcal/mol (with respect to Int-ad) and dissociated with barrierless process to CH_2NH + HO_2. We predicted the rate coefficients using the direct reaction, i.e., $CH_3NH^{\bullet}$ + O_2→TS2a→CH_2NH + HO_2 (Supplementary Figure S8, in blue), and the indirect reaction, i.e., $CH_3NH^{\bullet}$ + O_2 →TS1a→CH_3NHOO→TS2a→Int2→CH_2NH + HO_2 (Supplementary Figure S8, in black). The calculated rate coefficient for the direct formation of CH_2NH + HO_2 is 7 × 10^{-16} cm^3 $molecule^{-1}$ s^{-1}, which is at least two orders of magnitude smaller than the indirect reaction. Based on our ME calculation, we can say that the formation of CH_2NH does not come from the $CH_3NH^{\bullet}$ +O_2 reaction because the reaction is quite slow under tropospheric conditions.

The mechanistic and kinetic analysis suggests the formation of these two $^{\bullet}CH_2NH_2$ and $CH_3NH^{\bullet}$, and our overall understanding of atmospheric and interstellar oxygen chemistry remained uncertain. Although many experimental and computational efforts over the past decade on reaction rate coefficients and branching ratios have been made, our knowledge of the chemical pathways theorized for the O_2 reaction in two different environments is not clear. Therefore, as suggested in a previous study, at a low temperature, i.e., <100 K, the formation of $CH_3NH^{\bullet}$ is dominated over the formation of $^{\bullet}CH_2NH_2$ under an interstellar cold medium (Gonza´lez et al., 2022). We have performed the RRKM/ME simulation at below 100 K and found that the formation of CH_3NOO is dominated under high-pressure limit conditions, i.e., >10 bar and below 100 K. Under low pressure and low temperature, the reaction goes back to the reactant. The formation of CH_3NOO in the ISM medium is not clear, but our analysis suggests that the reaction $CH_3NH^{\bullet}$+O_2 does nothing under ISM conditions. We have also carried out our RRKM/ME simulation under combustion conditions (>1000 K and HPL), and our analysis suggests that the formation of $CH_3NOO^{\bullet}$ and CH_2NH is even negligible. It may also be suggested that such a reaction might take place in a more polluted situation.

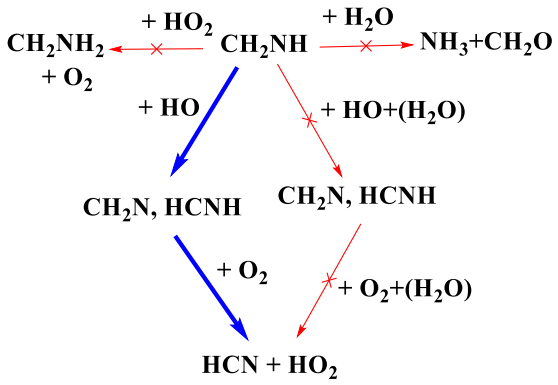

FIGURE 15
Atmospheric degradation of CH_2NH with various possible atmospheric species.

There has been considerable speculation about what will happen after the formation of CH_2NH (Rissanen et al., 2014; Ali et al., 2018; Ali, 2020). Figure 15 shows the atmospheric degradation reaction of CH_2NH with various possible atmospheric species. The result in the figure shown is based on our previous calculation, except for the reaction of $CH_3NH^{\bullet} + O_2$, which is re-calculated. As shown in Figure 15, we can see that the reaction with water does not lead to the formation of NH_3 and CH_2O as suggested in our previous work under tropospheric conditions (Ali, 2020). We also tried to find out if the backward reaction was favorable; for that, we have set up an ME simulation and predicted that this reaction would do nothing in the troposphere (Ali et al., 2016). We also calculated the rate coefficients for the reaction of CH_2NH + OH radicals, and the mechanism has already been discussed in our previous work (Ali and Barker, 2015). The results show the formation of $CH_2N^{\bullet}$+ and $^{\bullet}$CHNH as major products and show a similarity between isoelectronic analogous systems, i.e., CH_2O and CH_2CH_2. As suggested in Rissanen et al. (2014) and Ashraful and Silva (2020), water may favor the formation of $CH_2N^{\bullet}$ and $^{\bullet}$CHNH; therefore, we have also analyzed the effect of water molecules on the CH_2NH + OH reaction (Ali et al., 2019). We have found that the reaction rate coefficients increase when the concentration of water molecules is not included in the calculation and decrease in the presence of water (Ali et al., 2019). Based on our current and previous findings, we propose that the formation of HCN could be the major product when O_2 radicals react with $^{\bullet}$CHNH radicals. We also suggest that the gas-phase formation of CH_2NH from the $CH_2N^{\bullet} + O_2$ reaction will be even slower, as shown in the previous degradation mechanism (see Figure 14). Again, this is due to less favorable N—O-O bond formation than C—O-O bond formation. We can also suggest that the formation of HCN in its presence may be unimportant under tropospheric conditions. Our calculation suggests that oxidation pathways may also contribute to the HO_x abundance under the tropospheric conditions, as shown in the degradation reaction mechanism (Figure 15 and Figure 14). Such state-of-the-art kinetics provides a clue to the formation of HCN under tropospheric conditions. Our result may be helpful in setting up an experimental analysis for the formation of HCN under tropospheric conditions.

4 Conclusion

In this work, the rate coefficients and branching fraction for $^{\bullet}CH_2NH_2 + O_2$, $^{\bullet}CH_2NH_2 + O_2$ (+H_2O), and $^{\bullet}CH_2NH_2 + O_2$ (+NH_3) for the formation of methanimine (CH_2NH) and HO_2 have been investigated using CCSD(T)//M06-2X/6-311++G (3df, 3pd) coupled with the RRKM/ME simulation. The results show that $^{\bullet}CH_2NH_2 + O_2$ leads to the formation of CH_2NH at temperatures <300 K and goes back to reactants ($^{\bullet}CH_2OH + O_2$) at high temperatures (>300 K). When the water/ammonia molecule is added to the $^{\bullet}CH_2NH_2 + O_2$ reaction, it favors the formation of CH_2NH at a temperature <300 K. The NH_3- and H_2O- assisted rate coefficients are at least 10^{10}–10^{12} (Gonza´lez et al., 2022) and 10^6 times, respectively, smaller than those of the free reaction; thus, we can say that the effect of NH_3/H_2O on $^{\bullet}CH_2NH_2 + O_2$ has less importance in the troposphere. Under tropospheric conditions, the reaction $CH_3NH_2 + OH/O_2 \rightarrow CH_2NH + HO_2$ via $^{\bullet}CH_2NH_2$ leading to form $CH_2NH + HO_2$ is both kinetically and thermodynamically more favorable than reaction $CH_3NH_2 + OH/O_2 \rightarrow CH_2NH + HO_2$ via $^{\bullet}CH_3NH$. The mechanism indicates that a single NH_3/H_2O molecule has the potential to increase the branching fraction in a gas-phase reaction at a lower temperature <300 K and slower reaction at a higher temperature. Such results are promising, and chemical kinetic data can be beneficial for the future implementation of ammonolysis and hydrolysis of other carbon-centered hydroxyl compounds. In previous studies, researchers stated that the reaction CH_2NH may be favorable in water; our study demonstrated that water increases the formation of CH_2NH. Our results also indicate the formation of HCN may have come from the reaction going via a carbon-centered radical instead of an N-centered radical. Experimental analysis is required to validate this finding. Such chemical kinetic analysis is interesting; chemical kinetics details can be useful to understand the bigger amine/imine that may lead to the formation of HCN, and N_2O may increase the reaction rate.

Data availability statement

The original contributions presented in the study are included in the article/Supplementary Material; further inquiries can be directed to the corresponding author.

Author contributions

MD and MA completed all the electronic structure calculations, and MA completed the chemical kinetic calculations. MD and MA prepared the draft of the manuscript. All authors contributed to the article and approved the submitted version.

Funding

The work is supported by the faculty startup grant # 8474000461 at Khalifa University Abu Dhabi UAE.

Acknowledgments

MA thanks the Department of Chemistry at College of Art and Science at Khalifa University of Science and Technology, Abu Dhabi UAE, to carry out the research. MA thanks the supercomputer facility computational support at Khalifa University of Science and Technology, at Abu Dhabi, UAE. The authors thank reviewers for their valuable suggestions.

Conflict of interest

The authors declare that the research was conducted in the absence of any commercial or financial relationships that could be construed as a potential conflict of interest.

Publisher's note

All claims expressed in this article are solely those of the authors and do not necessarily represent those of their affiliated organizations, or those of the publisher, the editors, and the reviewers. Any product that may be evaluated in this article, or claim that may be made by its manufacturer, is not guaranteed or endorsed by the publisher.

Supplementary material

The Supplementary Material for this article can be found online at: https://www.frontiersin.org/articles/10.3389/fchem.2023.1243235/full#supplementary-material

References

Ali, M. A., and Balaganesh, M. (2023). Effect of formic acid on O_2 + OHCHOH =HCOOH + HO_2 reaction under tropospheric condition: Kinetics of cis and trans isomers. *Phys. Chem. Chem. Phys.* 25, 9965–9978. doi:10.1039/D2CP05874J

Ali, M. A., Balaganesh, M., Al-Odail, F. A., and Lin, K. C. (2021). Effect of ammonia and water molecule on OH + CH3OH reaction under tropospheric condition. *Sci. Rep.* 11, 12185. doi:10.1038/s41598-021-90640-6

Ali, M. A., and Balaganesh, M. (2022). Effect of water and formic acid on ·OH + CH4 reaction: An ab initio/DFT study. *Catalysts* 12, 133. doi:10.3390/catal12020133

Ali, M. A., Balaganesh, M., and Jang, S. (2019). Can a single water molecule catalyze the OH+CH2CH2 and OH+CH2O reactions? *Atmos. Environ.* 207, 82–92. doi:10.1016/j.atmosenv.2019.03.025

Ali, M. A., Balaganesh, M., and Lin, K. C. (2018). Catalytic effect of a single water molecule on the OH + CH2NH reaction. *Phys. Chem. Chem. Phys.* 20, 4297–4307. doi:10.1039/C7CP07091H

Ali, M. A., and Barker, J. R. (2015). Comparison of three isoelectronic multiple-well reaction systems: OH + CH2O, OH + CH2CH2, and OH + CH2NH. *J. Phys. Chem. A* 19, 7578–7592. doi:10.1021/acs.jpca.5b00910

Ali, M. A. (2020). Computational studies on the gas phase reaction of methylenimine (CH2NH) with water molecules. *Sci. Rep.* 10, 10995. doi:10.1038/s41598-020-67515-3

Ali, M. A., Dash, M. R., and Latifah, M. Al M. (2022). Catalytic effect of CO_2 and H_2O molecules on CH_3 + $^3O_2$ reaction. *Catalyst* 12, 699. doi:10.3390/catal12070699

Ali, M. A., Sonk, A. S., and Barker, J. R. (2016). Predicted chemical activation rate constants for HO2 + CH2NH: The dominant role of a hydrogen-bonded pre-reactive complex. *J. Phys. Chem. A* 120, 7060–7070. doi:10.1021/acs.jpca.6b06531

Ali, M. A. (2019). Theoretical study on the gas phase reaction of CH_2O + NH_3: the formation of $CH_2O\cdots NH_3$, NH_2CH_2OH, or CH_2NH + H_2O. *Phys. Chem. Chem. Phys.* 21, 19242–19251. doi:10.1039/C9CP02777G

Almeida, Schobesberger, S., Kürten, A., Ortega, I. K., Kupiainen-Määttä, O., Praplan, A. P., et al. (2013). Molecular understanding of sulphuric acid–amine particle nucleation in the atmosphere. *Nature* 502, 359–363. doi:10.1038/nature12663

Altwegg, K., Balsiger, H., Bar-Nun, A., Berthelier, J. J., Bieler, A., Bochsler, P., et al. (2016). Prebiotic chemicals—Amino acid and phosphorus—In the coma of comet 67P/Churyumov-Gerasimenko. *Sci. Adv.* 2, 1–6. doi:10.1126/sciadv.1600285

Ashraful, A. M., and Silva, G. da. (2020). A detailed chemical kinetic model for the supercritical water oxidation of methylamine: The importance of imine formation. *Int. J. Chem. Kinet.* 52, 701–711. doi:10.1002/kin.21393

Barker, J. R. (2009). Energy transfer in master equation simulations: A new approach. *Int. J. Chem. Kinet.* 41, 232–245. doi:10.1002/kin.1017

Barker, J. R. (2011). Multiple-well, multiple-path unimolecular reaction systems. I. MultiWell computer program suite. *Int. J. Chem. Kinet.* 33, 232–245. doi:10.1002/kin.1017

Barker, J. R. (2023). *MultiWell-2023 software*. Ann Arbor: University of Michigan.

Buszek, R. J., Torrent-Sucarrat, M., Anglada, J. M., and Francisco, J. S. (2012). Effects of a single water molecule on the OH + H2O2 reaction. *J. Phys. Chem. A* 116, 5821–5829. doi:10.1021/jp2077825

Dash, M. R., and Ali, M. A. (2022). Effect of a single water molecule on ˙CH2OH + 3O2 reaction under atmospheric and combustion conditions. *Phys. Chem. Chem. Phys.* 24, 1510–1519. doi:10.1039/D1CP03911C

Elsila, J. E., Glavin, D. P., and Dworkin, J. P. (2009). Cometary glycine detected in samples returned by Stardust. *Meteorit. Planet. Sci.* 44, 1323–1330. doi:10.1111/j.1945-5100.2009.tb01224.x

Forst, W. (2003). *Unimolecular reactions*. Cambridge: A Concise Introduction Cambridge University Press.

Frisch, M. J. (2013). *Gaussian 09, revision D.01*. Wallingford, CT: Gaussian, Inc.

Frisch, M. J., Pople, J. A., and Binkley, J. S. (1984). Self-consistent molecular orbital methods 25. Supplementary functions for Gaussian basis sets. *J. Chem. Phys.* 80, 3265–3269. doi:10.1063/1.447079

Fukui, K. (1981). The path of chemical reactions-the IRC approach. *Acc. Chem. Res.* 14, 363–368. doi:10.1021/ar00072a001

Ge, X., Wexler, A. S., and Clegg, S. L. (2011a). Atmospheric amines – Part I. A review. *Atmos. Environ.* 45, 524–546. doi:10.1016/j.atmosenv.2010.10.012

Ge, X., Wexler, A. S., and Clegg, S. L. (2011b). Atmospheric amines – Part II. Thermodynamic properties and gas/particle partitioning. *Atmos. Environ.* 45, 561–577. doi:10.1016/j.atmosenv.2010.10.013

Glarborg, P., Andreasen, C. S., Hashemi, H., Qian, R., and Marshall, P. (2020). Oxidation of methylamine. *Int. J. Chem. Kinet.* 52, 893–906. doi:10.1002/kin.21408

Goldsmith, C. F., Green, W. H., and Klippenstein, S. J. (2012). Role of O_2 + QOOH in low-temperature ignition of propane. 1. Temperature and pressure dependent rate coefficients. *J. Phys. Chem. A* 116, 3325–3346. doi:10.1021/jp210722w

Gonza´lez, D., Lema-Saavedra, A., Espinosa, S., Martı´nez-Nu´ñez, E., Ferna´ndez-Ramos, A., Canosa, A., et al. (2022). Reaction of OH radicals with CH3NH2 in the gas phase: Experimental (11.7–177.5 K) and computed rate coefficients (10–1000 K). *Phys. Chem. Chem. Phys.* 24, 23593–23601. doi:10.1039/d2cp03414j

Grimme, S., Antony, J., Ehrlich, S., and Krieg, H. (2010). A consistent and accurate *ab initio* parametrization of density functional dispersion correction (DFT-D) for the 94 elements H-Pu. *J. Chem. Phys.* 132, 154104. doi:10.1063/1.3382344

Hippler, J., Troe, J., and Wendelken, H. J. (1983). Collisional deactivation of vibrationally highly excited polyatomic molecules. II. Direct observations for excited toluene. *J. Chem. Phys.* 78, 6709–6717. doi:10.1063/1.444670

Inaba, S. (2018). Catalytic role of H2O molecules in oxidation of CH3OH in water. *Catalysts* 8, 157. doi:10.3390/catal8040157

Iuga, C., Alvarez-Idaboy, J. R., Reyes, L., and Vivier-Bunge, A. (2010). Can a single water molecule really catalyze the acetaldehyde OH reaction in tropospheric conditions? *J. Phys. Chem. Lett.* 1, 3112–3115. doi:10.1021/jz101218n

Iuga, C., Alvarez-Idaboy, J. R., and Vivier-Bunge, A. (2011). On the possible catalytic role of a single water molecule in the acetone + OH gas phase reaction: A theoretical pseudo-second-order kinetics study. *Theor. Chem. Acc.* 129, 209–217. doi:10.1007/s00214-011-0921-0

Jansen, T. C., Trabjerg, I., Rettrup, S., Pagsberg, P., Sillesen, A., Mønsted, O., et al. (1999). Experimental and theoretical investigation of the UV spectrum and kinetics of the amino methyl radical, CH2NH2. *Acta Chem. Scand.* 53, 1054–1058. doi:10.3891/acta.chem.scand.53-1054

Jara-Toro, R. A., Hernández, F. J., Taccone, R. A., Lane, S. I., and Pino, G. A. (2017). Water catalysis of the reaction between methanol and OH at 294 K and the atmospheric implications. *Angew. Chem. Int. Ed.* 56, 2166–2170. doi:10.1002/anie.201612151

Jonas, E., Bilde, M., and Mikkelsen, K. V. (2013). Influence of nucleation precursors on the reaction kinetics of methanol with the OH radical. *J. Phys. Chem. A* 117, 6695–6701. doi:10.1021/jp4051269

Kumar, A., Mallick, S., Mishra, B. M., and Kumar, P. (2020). Effect of ammonia and formic acid on the $CH_3O^{\cdot} + O_2$ reaction: A quantum chemical investigation. *Phys. Chem. Chem. Phys.* 22, 2405–2413. doi:10.1039/C9CP04612G

Lee, D., and Wexler, A. S. (2013). Atmospheric amines – Part III: Photochemistry and toxicity. *Atmos. Environ.* 71, 95–103. doi:10.1016/j.atmosenv.2013.01.058

Mallick, S., Sarkar, S., Bandyopadhyay, B., and Kumar, P. (2018). Effect of ammonia and formic acid on the OH· + HCl reaction in the troposphere: Competition between single and double hydrogen atom transfer pathways. *J. Phys. Chem. A* 122, 350–363. doi:10.1021/acs.jpca.7b09889

Masaki, A., Tsunashima, S., and Washida, N. (1995). Rate constants for reactions of substituted methyl radicals (CH2OCH3, CH2NH2, CH2I, and CH2CN) with O2. *J. Phys. Chem.* 99, 13126–13131. doi:10.1021/j100035a014

Murphy, S. M., Sorooshian, A., Kroll, J. H., Ng, N. L., Chhabra, P., Tong, C., et al. (2007). Secondary aerosol formation from atmospheric reactions of aliphatic amines. *Atmos. Chem. Phys.* 7, 2313–2337. doi:10.5194/acp-7-2313-2007

Nielsen, C. J., Hermann, H., and Weller, C. (2012). Atmospheric chemistry and environmental impact of the use of amines in carbon capture and storage (CCS). *Chem. Soc. Rev.* 41, 6684–6704. doi:10.1039/C2CS35059A

Onel, L., Blitz, M., Dryden, M., Thonger, L., and Seakins, P. (2014). Branching ratios in reactions of OH radicals with methylamine, dimethylamine, and ethylamine. *Environ. Sci. Technol.* 48, 9935–9942. doi:10.1021/es502398r

Qiu, C., and Zhang, R. (2013). Multiphase chemistry of atmospheric amines. *Phys. Chem. Chem. Phys.* 15, 5738–5752. doi:10.1039/C3CP43446J

Raghavachari, K., Trucks, G. W., Pople, J. A., and Head-Gordon, M. (1989). A fifth-order perturbation comparison of electron correlation theories. *Chem. Phys. Lett.* 157, 479–483. doi:10.1016/S0009-2614(89)87395-6

Rissanen, M. P., Eskola, A. J., Nguyen, T. L., Barker, J. R., Liu, J., Liu, J., et al. (2014). CH2NH2 +O2 and CH3CHNH2 +O2 reaction kinetics: Photoionization mass spectrometry experiments and master equation calculations. *J. Phys. Chem. A* 118, 2176–2186. doi:10.1021/jp411238e

Ruscic, B., and Bross, D. H. (2020). *Active thermochemical tables (ATcT) values based on ver. 1.122p of the thermochemical network*. Available at: https://atct.anl.gov/.

Ruscic, B., Pinzon, R. E., Morton, M. L., Laszewski, G. von., Bittner, S., Nijsure, S. G., et al. (2004). Introduction to active thermochemical tables: Several "key" enthalpies of formation revisited. *J. Phys. Chem. A* 108, 9979–9997. doi:10.1021/jp047912y

Schade, G. W., and Crutzen, P. J. (1995). Emission of aliphatic amines from animal husbandry and their reactions: Potential source of N2O and HCN. *J. Atm. Chem.* 22, 319–346. doi:10.1007/BF00696641

Thomsen, D., Kurtén, T., Jørgensen, S., Wallington, T., Baggesen, S., Aalling, C., et al. (2012). On the possible catalysis by single water molecules of gas-phase hydrogen abstraction reactions by OH radicals. *Phys. Chem. Chem. Phys.* 14, 12992–12999. doi:10.1039/C2CP40795G

Vöhringer-Martinez, E., Hansmann, B., Hernandez, H., Francisco, J. S., Troe, J., and Abel, B. (2007). Water catalysis of a radical-molecule gas-phase reaction. *Science* 315, 496–501. doi:10.1126/science.1134494

Wu, J., Gao, L. G., Varga, Z., Xu, X., Ren, W., and Truhlar, D. G. (2020). Water catalysis of the reaction of methanol with OH radical in the atmosphere is negligible. *Angew. Chem. Int. Ed.* 59, 10918–10922. doi:10.1002/ange.202001065

Zhang, G., Bi, X., Chan, L. Y., Li, L., Wang, X., Feng, J., et al. (2012). Enhanced trimethylamine-containing particles during fog events detected by single particle aerosol mass spectrometry in urban Guangzhou, China. *Atmos. Environ.* 55, 121–126. doi:10.1016/j.atmosenv.2012.03.038

Zhang, T., Wang, W., Li, C., Du, Y., and Lu, J. (2013). Catalytic effect of a single water molecule on the atmospheric reaction of HO2 + OH: Fact or fiction? A mechanistic and kinetic study. *RSC Adv.* 3, 7381–7391. doi:10.1039/C3RA40341F

Zhang, T., Wen, M., Zeng, Z., Lu, Y., Wang, Y., Wang, W., et al. (2020). Effect of NH_3 and HCOOH on the $H_2O_2 + HO \rightarrow HO_2 + H_2O$ reaction in the troposphere: Competition between the one-step and stepwise mechanisms. *RSC Adv.* 10, 9093–9102. doi:10.1039/D0RA00024H

Zhang, W., Du, B., and Qin, Z. (2014). Catalytic effect of water, formic acid, or sulfuric acid on the reaction of formaldehyde with OH radicals. *J. Phys. Chem. A* 118, 4797–4807. doi:10.1021/jp502886p

Zhao, Y., and Truhlar, D. G. (2008). The M06 suite of density functionals for main group thermochemistry, thermochemical kinetics, noncovalent interactions, excited states, and transition elements: Two new functionals and systematic testing of four M06-class functionals and 12 other functionals. *Theor. Chem. Acc.* 120, 215–241. doi:10.1007/s00214-007-0310-x

frontiers | Frontiers in Chemistry

TYPE Original Research
PUBLISHED 02 November 2023
DOI 10.3389/fchem.2023.1276691

OPEN ACCESS

EDITED BY
Arjun Singh,
Memorial Sloan Kettering Cancer Center, United States

REVIEWED BY
Mingwei Zhao,
China University of Petroleum, China
Zhenyuan Yin,
Tsinghua University, China

*CORRESPONDENCE
Mingzhong Li,
limingzhong_upc@hotmail.com

RECEIVED 12 August 2023
ACCEPTED 16 October 2023
PUBLISHED 02 November 2023

CITATION
Du Q, Li M and Liu C (2023), Experimental study on flow resistance characteristics of the uniform steam injection outflow control device.
Front. Chem. 11:1276691.
doi: 10.3389/fchem.2023.1276691

Experimental study on flow resistance characteristics of the uniform steam injection outflow control device

Qiuying Du, Mingzhong Li* and Chenwei Liu

School of Petroleum Engineering, China University of Petroleum, Qingdao, China

Introduction: Multi-point steam injection technology is a new completion method for heavy oil horizontal wells to solve the uneven distribution of the intake profile in the horizontal section. It is equipped with the flow control device to achieve the effect of balanced steam injection.

Methods: The steady-state experiment method was adopted; Considering the variable mass complex flow of the steam–liquid two-phase flow in the downhole flow device, the pressure loss of downhole tools through uniform steam injection with different steam–liquid compositions was tested, the influencing factors of the pressure drop were analyzed, and a more reliable pressure drop calculation method was established.

Results: The overflow pressure drop can be adjusted by changing the aperture, steam dryness, and fluid flow of the downhole outflow control device (OCD).

Discussion: By comparing the experimental and theoretical results, the calculation method of the overflow resistance of single-phase and steam–liquid two-phase fluids in OCD is given, and the error is within the usable range.

KEYWORDS

outflow control device, two-phase fluids, uniform steam injection, flow resistance characteristics, pressure drop

1 Introduction

In the process of steam injection in long horizontal wells, due to reservoir heterogeneity, heel–toe effect, and natural fractures in the reservoir, the suction profile of steam injection wells is difficult to maintain a balanced development, and steam channeling is easy to occur, and the heel end, high permeability interval, and fractures of wells are prone to premature water/steam. Due to low water/vapor viscosity, once water/gas coning occurs in the well, it will quickly form a channel at the coning point, thereby inhibiting oil production elsewhere (Mozaffari et al., 2013).

In order to reduce this non-uniformity, the flow control device, outflow control device (OCD), can be installed at the completion interval to inhibit the flow through the high-speed interval and generate additional pressure drop so as to increase the flow rate of the wellbore interval with high flow resistance, eliminate the non-uniform flow caused by the heel effect of the horizontal well and the non-uniformity of permeability, and ensure the uniform spread of the suction profile along the horizontal well (Parappilly, and Zhao, 2009; Gu et al., 2014a; Dong et al., 2014a; Dong et al., 2014b). The combination of a packer and OCD is usually used in production, which can achieve uniform oil drainage in heterogeneous reservoirs and

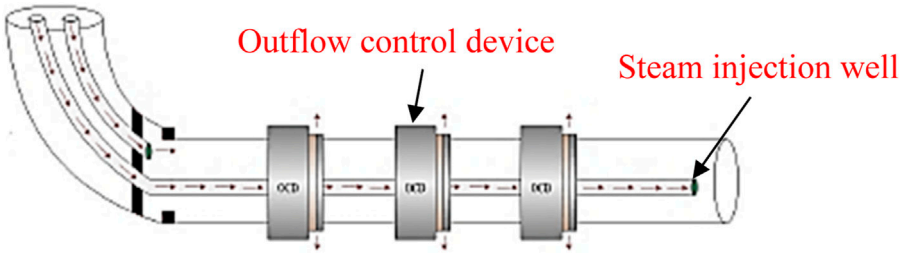

FIGURE 1
Schematic diagram of the outflow control device.

maintain liquid output balance by limiting different oil production indexes in each section so as to delay bottom water coning, prolong anhydrous or bottom water oil production period, and improve oil and gas well production and recovery efficiency (Sun et al., 2018a; Sun et al., 2019). It is an advanced measure to stabilize oil and water and control water.

At present, a variety of OCDs has been developed in China. According to the mechanism of action, it can be divided into nozzle, spiral channel, and nozzle types (Huang et al., 2018a). The current limiting mechanism of nozzle-type OCD is that the throttle pressure drop is generated by the contraction of the flow channel when the fluid passes through the device (Kumar et al., 2010; Huang et al., 2018b). The spiral-channel-type OCD wraps one or more flow channels around the tubing to generate an additional pressure drop using friction (Rivas and Gates, 2018; Dong et al., 2020a; Dong et al., 2020b). Unlike the instantaneous pressure drop produced by the nozzle, this design produces a segmented pressure drop over a relatively long area, which is more resistant to the erosion and clogging of fluid particles during the drilling fluid cycle (Dong et al., 2020a). The nozzle-type OCD has a limited flow in a long nozzle. Compared with the nozzle-type OCD, owing to its longer spray irrigation, the resistance loss along the path is larger and the local resistance loss is smaller at the same strength (Hasan and Kabir, 1994; Hasan et al., 1998; Sun et al., 2018b). Therefore, compared with the three OCDs, the nozzle-type OCD is more resistant to the erosion and blockage of fluid particles (Hasan and Kabir, 2005; Caetano, 1985). Compared with the spiral-channel-type OCD, the resistance loss along the nozzle-type OCD plays a minor role in the pressure drop composition of the nozzle-type OCD, so the nozzle-type OCD is less sensitive to viscosity (Caetano et al., 1992; Gu et al., 2014b; Gu et al., 2015). The installation position of OCD on the horizontal steam injection well is shown in Figure 1.

Aiming at the completion characteristics of horizontal well OCD, this paper established a mathematical model of horizontal well variable mass flow under the condition of OCD installation based on the equivalent diameter model of the target well section, heterogeneous reservoir skin factor model, horizontal wellbore variable mass flow pressure drop model, and OCD pressure drop model by applying the principle of potential superposition. The effects of OCD aperture, steam dryness, and steam injection speed on the pressure drop were compared, and the OCD structure parameters and steam injection parameters were optimized. This method provides a new optimal control method for horizontal well uniform steam injection (Yin et al., 2019; Liu et al., 2022; Yin and Linga, 2019) and offers technical support for OCD completion optimization design and oil increase and water control in the horizontal well.

2 Experimental scheme

The main research content of this experiment is to measure the pressure drop of the fluid passing through the downhole flow control device and to establish a set of calculation methods of flow control resistance through the study of fluid resistance law so as to determine a reasonable OCD design method to achieve the purpose of uniform steam injection (Least et al., 2013; Yu et al., 2010). In order to study and analyze the flow resistance of different components of fluid that passes through the flow control device and analyze the influence of gas–liquid composition on the pressure drop, the pressure drop of single-phase liquid passing through the control device was first tested, and the pressure drop of fluid passing through the control device was analyzed by changing the flow rate, hole diameter, and fluid flow rate of the control device (Chesney et al., 2015). Then, the influence of the mixture flow rate and mass gas content on the pressure drop was analyzed by changing the mass gas content (Temizel et al., 2019).

2.1 Experimental apparatus and materials

The downhole tool flow resistance test system mainly comprises five parts: the gas supply system, liquid supply system, outflow control device (OCD) simulation system, measurement system (Gai et al., 2010), and data acquisition system (Figure 2). The fluid supply system consists of a liquid pump, inverter, air compressor, and gas pressure-reducing valve (Luo et al., 2015). The liquid pump uses a non-pulse screw pump. Its head measures 180 m, and the displacement range is 0–45 m^3/h (Wang et al., 2016); the maximum pressure of the air compressor is 1.8 MPa, the maximum displacement is 5.1 m^3/min, and the noise is 56 db; the gas storage tank volume is 1.5 m^3, and working pressure is 0.8 MPa; it is made of Q345 material, equipped with a 1 MPa safety valve, and facilitates spray treatment. The gas-reducing valve is of YK43X type, with the maximum pressure of 1.6 MPa and output pressure range of

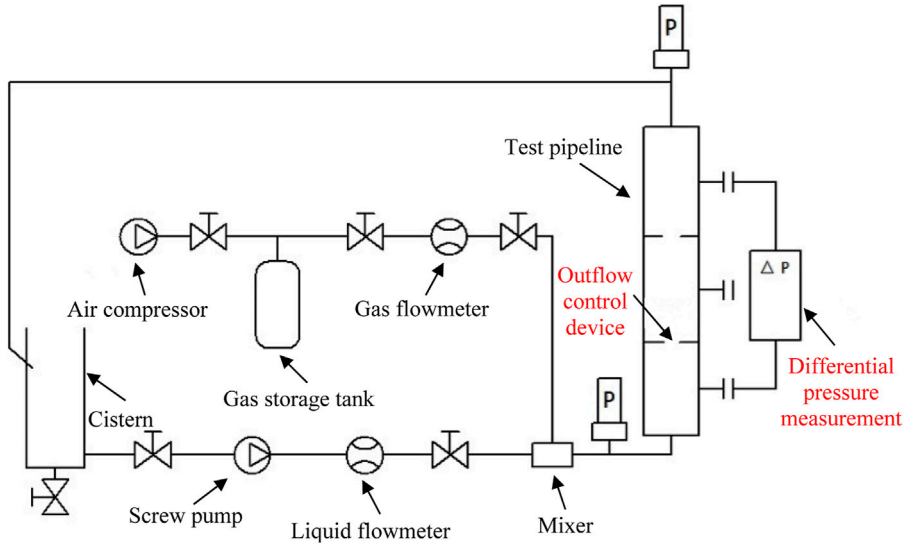

FIGURE 2
Schematic diagram of the downhole tool flow resistance test device.

FIGURE 3
Flow control device simulator.

0.1–1 MPa. The accuracy of the pressure transmitter is 0.25% F.s, and the measuring ranges are 0–5 MPa and 0–1.6 MPa, respectively (Prakasa et al., 2019). The accuracy of the temperature sensor is class A, with a measuring range of 0°C–150°C, the flow sensor accuracy of 0.2%–0.5%, liquid flowmeter range of 0–16 m^3/h, and gas flowmeter of 0–5.0 m^3/min. The sensor can communicate with the computer through the A/D conversion board. The nozzle-type OCD is installed on the test completion string. The data acquisition and processing system comprises digital acquisition card, computer, and software. It carries out real-time data acquisition and post-processing and prepares original data reports, analysis reports, and curves, creates output database files, indicates the real-time display of control elements' working status, and displays and prompts users to each stage of the workflow and pressure upper limit alarm.

2.2 Test procedure

Due to the nozzle-type flow control device used in the FluxRite™ completion string in the Mackay River oil sand, the fluid pressure drop through the flow control device was studied only under the conditions of single-phase liquid and high gas–liquid ratios (dryness).

First, eight sizes of simulated nozzles were made according to the nozzle sizes of the FluxRite™ flow control device (2.5 mm, 4.0 mm), and four of them (2.5 mm, 3.0 mm, 4.0 mm, and 5.0 mm) were selected to conduct pressure difference loss experiments on single-phase liquid flow resistance (Figure 3). The test medium was tap water, with reference to the hot water injection flow of horizontal wells in Canada's Mackay River block (0.3 m^3/h), and the flow rates were 0.15 m^3/h, 0.2 m^3/h, 0.25 m^3/h, 0.3 m^3/h, 0.35 m^3/h, and 0.4 m^3/h. The pressure drop of the fluid through the simulated

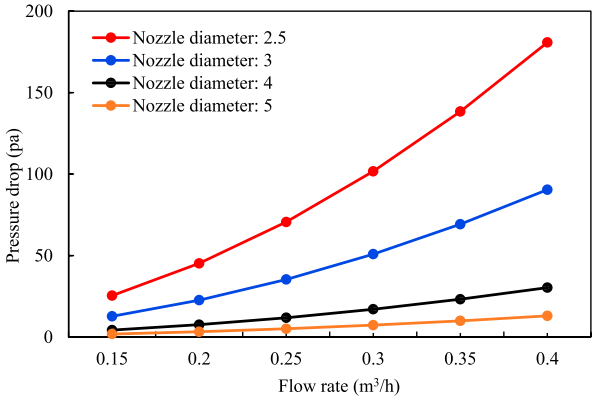

FIGURE 4
Single-phase liquid flow resistance calculation.

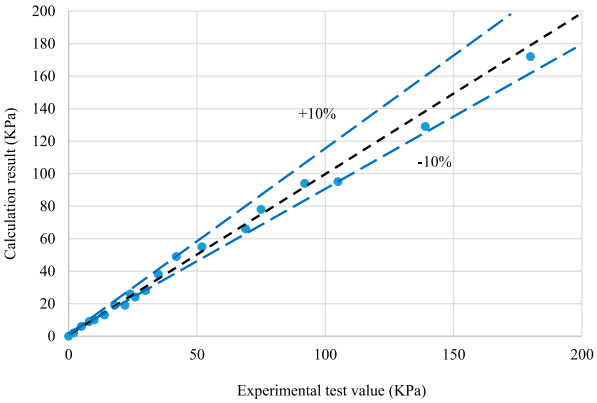

FIGURE 5
Fitting results of single-phase liquid flow resistance data.

nozzle was recorded by the data acquisition system, and the relationship between the pressure drop and flow rate was analyzed.

Then, three nozzles of sizes 2.5 mm, 3.0 mm, and 4.0 mm were selected to carry out the resistance characteristic experiment of the gas–liquid two-phase flow through simulated nozzles. The gas–liquid mixture consisted of air and water, with reference to the flow rate of wet steam injection in horizontal wells in Canada's Mackay River block (60 kg/h), and its mass flow rate was 50 kg/h, 55 kg/h, 60 kg/h, 65 kg/h, and 70 kg/h. Considering that the steam-assisted gravity drainage (SAGD) steam injection process is a relatively high-dryness flow process, the dryness of the gas–liquid mixture (that is, the mass content of the gas in the mixture) was set to 0.9, 0.8, and 0.7. The pressure difference of the fluid through the simulated nozzle is recorded by the data acquisition system, and the relationship between the pressure drop and the flow rate and the dryness of the mixture is analyzed.

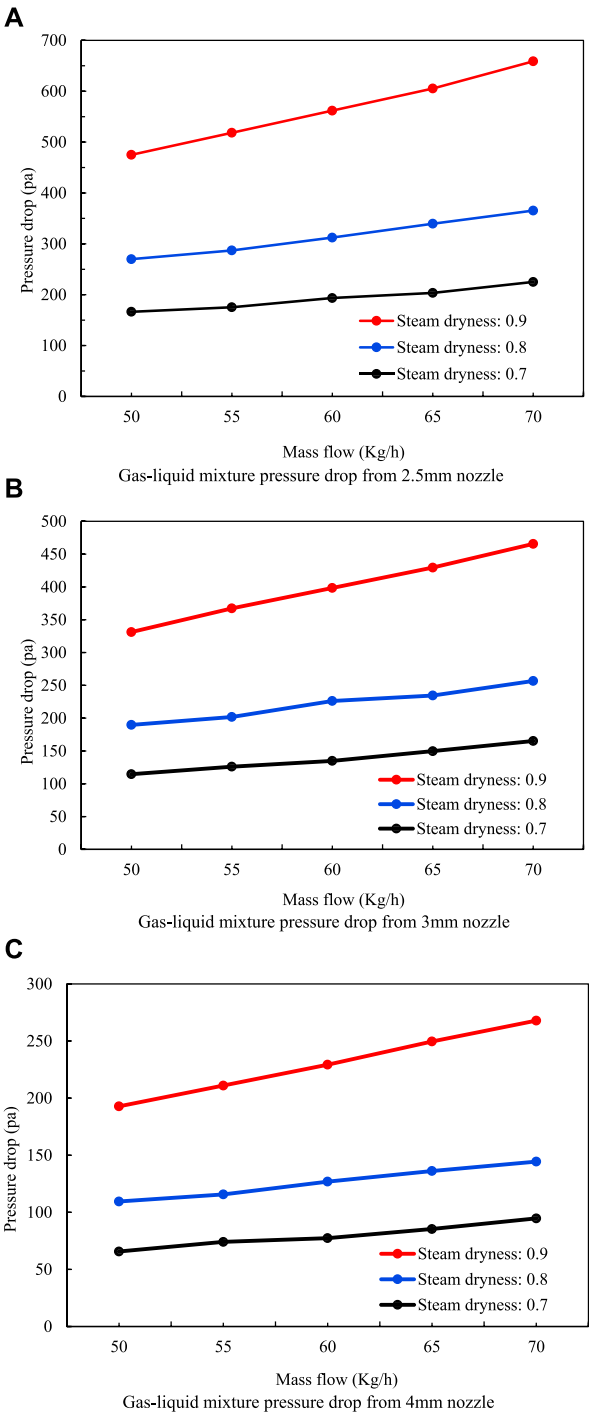

FIGURE 6
Calculation of flow resistance of the gas–liquid two-phase mixture. **(A)** Gas–liquid mixture pressure drop while using a 2.5-mm nozzle. **(B)** Gas–liquid mixture pressure drop while using a 3-mm nozzle. **(C)** Gas–liquid mixture pressure drop while using a 4-mm nozzle.

2.3 Experimental procedure

The experimental procedure is as follows:

(1) Screw pump pumps the fluid in the liquid storage tank after suction and pressurization, with a certain flow and pressure through the flow control device.

TABLE 1 Experimental data of single-phase liquid flow resistance (kPa).

Flow rate (m^3/h)		0.15	0.2	0.25	0.3	0.35	0.4
Nozzle diameter/mm	2.5	25.42	45.20	70.62	101.70	138.42	180.80
	3	12.72	22.61	35.32	50.87	69.23	90.43
	4	4.26	7.58	11.84	17.05	23.20	30.31
	5	1.83	3.25	5.07	7.30	9.94	12.98

TABLE 2 Pressure difference data of the gas–liquid mixture flow resistance through the 2.5-mm simulated nozzle.

Mass flow (kg/h)		50	55	60	65	70
Dryness	0.9	475.0	518.4	561.8	605.3	658.8
	0.8	269.9	287.1	312.3	339.6	365.4
	0.7	166.4	175.4	193.5	203.5	225.1

TABLE 3 Pressure difference data of the gas–liquid mixture flow resistance through the 3.0-mm simulated nozzle.

Mass flow (kg/h)		50	55	60	65	70
Dryness	0.9	331.2	367.3	398.4	429.5	465.6
	0.8	189.7	201.8	226.2	234.5	256.7
	0.7	114.6	126.1	134.9	149.7	165.2

TABLE 4 Pressure difference data of the gas–liquid mixture flow resistance through the 4.0-mm simulated nozzle.

Mass flow (kg/h)		50	55	60	65	70
Dryness	0.9	192.8	211.0	229.3	249.6	267.9
	0.8	109.5	115.7	126.9	136.2	144.4
	0.7	65.7	74.1	77.4	85.4	94.7

(2) The liquid flow rate is measured by the liquid flowmeter, the size of the flow rate is controlled by the motor frequency converter, and the flow rate of the valve is recorded in real time.
(3) The pressure drop of the liquid through the flow control device is reflected and recorded in computer software by the differential pressure meter connected at both ends.
(4) The flow rate and pressure drop are monitored by the computer in real time, such that the pressure drop generated when fluid passes through the control device under a certain flow condition can be obtained.
(5) In the process of a single-phase liquid experiment, the liquid can be returned to the liquid storage tank through the pipeline for recycling.
(6) After the completion of the single-phase liquid experiment, start the compressor, adjust the gas-phase flow rate and liquid-phase flow rate, and when the flow is stable, record the pressure drop and dryness of the gas-liquid mixture in the outflow control device.

3 Results and discussion

3.1 Analysis of single-phase liquid flow resistance

The pressure difference data of single-phase liquid flow resistance through the simulated nozzle are shown in Table 1 and the pressure drop curves under different nozzle diameters are shown in Figure 4. In the general literature, the formula for calculating the pressure drop of the fluid through the orifice plate or nozzle is used to obtain the throttle pressure difference when the fluid flows through the control valve:

$$\Delta p = \frac{1}{2}\left(\frac{G_l}{C_d A_p \rho_l}\right)^2 \rho_l, \tag{1}$$

where Δp is the pressure difference before and after the throttle hole of the control valve, that is, the throttle pressure drop in Pa; A_p is the control valve orifice area in m^2; and C_d is the flow coefficient without dimensionality. G_l is the steam mass flow rate in kg/s, and ρ_l is the fluid density in kg/m^3. The value of C_d in common flow control valves ranges from 0.66 to 1.

According to the method of drawing the nozzle loss curve, the flow coefficient C_d of the fluid passing through the nozzle should not be a constant but a function of the hole diameter. According to the data of the pressure drop, flow rate, and hole diameter, the corresponding relationship between the flow coefficient C_d and hole diameter under different flow rates was obtained, and data fitting was carried out to obtain the fitting relationship between C_d and hole diameter:

$$C_d = 1.3052 d^{-0.11} = \frac{1.3052}{d^{0.11}}. \tag{2}$$

The calculated results of the fitting relationship were compared with the experimental results (Figure 5). The comparison results show that the flow coefficient obtained by fitting can calculate the experimental data more accurately.

3.2 Flow resistance analysis of the gas–liquid two-phase fluid

The Pressure difference data of the gas–liquid mixture flow resistance through the simulated nozzle are shown in Tables 2–4.

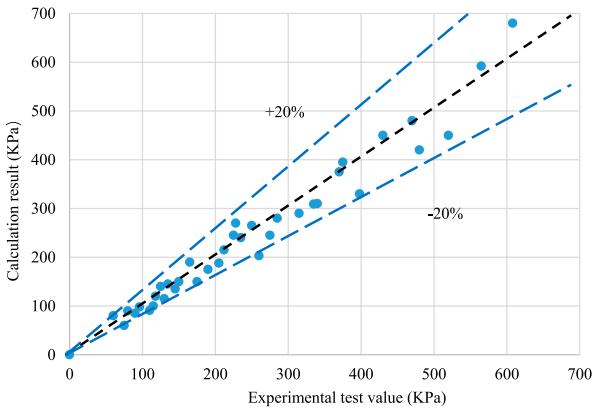

FIGURE 7
Experimental data calculation results of the gas–liquid mixture flow resistance through simulated nozzles.

The calculation method of the pressure drop of gas–liquid mixture flow through the orifice plate proposed by Chisholm was used for data processing. Through the two-phase flow momentum equation analysis, the pressure drop of the fluid flowing through the orifice plate can be calculated as follows:

$$\Delta p_{TP}/\Delta p_{LO} = 1 + \frac{C}{X} + \frac{1}{X^2}, \tag{3}$$

where X^2 is equal to $\triangle p_{LO}/\triangle p_{GO}$; $\triangle p_{TP}$ is the pressure drop of the gas–liquid two-phase mixture through the orifice plate in Pa; $\triangle p_{LO}$ and $\triangle p_{GO}$ are the pressure drop when the liquid and gas phases in the mixture, respectively, pass through the orifice plate alone in Pa; and C is a coefficient related to the pressure and slip ratio.

The following formula was used to calculate X^2:

$$X^2 = \frac{(1-x)^2}{x^2}\frac{\rho_G}{\rho_L}. \tag{4}$$

In 1997, Chisholm suggested the following method for calculating the C values:

When $X < 1$, then

$$C = \left(\frac{\rho_L}{\rho_G}\right)^{1/4} + \left(\frac{\rho_G}{\rho_L}\right)^{1/4}. \tag{5}$$

When $X > 1$, then

$$C = \left(\frac{\rho_m}{\rho_G}\right)^{1/2} + \left(\frac{\rho_G}{\rho_m}\right)^{1/2}. \tag{6}$$

The calculation method proposed by Chisholm was used to calculate the pressure drop data of the gas–liquid mixture flow through the simulated nozzle. The pressure drop changes under the aperture of 2.5 mm, 3 mm, and 4 mm were obtained, as shown in the Figure 6, and the pressure drop decreased significantly when the nozzle size was increased. The greater the steam dryness, the greater the pressure drop and the better the effect of overflow resistance. The flow rate has little influence on the flow resistance effect, and the flow rate is positively correlated with the pressure drop.

The calculated results were compared with the experimental results (Figure 7). The comparison results show that the calculated values using Chisholm's recommended method were consistent with the experimental results of the gas–liquid mixture, and the calculation error is less than ±20%.

3.3 Flow resistance analysis of the gas–liquid two-phase fluid with a large aperture

Since multi-stage OCD completion is usually used in the production process, that is, multiple OCDs are connected in series for steam injection at the same time, this paper designs a variety of large-aperture OCDs to meet production needs and installation on demand. Using the steam dryness of 0.9, steam injection pressure of 2 MPa, large aperture sizes of 20 mm, 50 mm, 80 mm, 110 mm, and 140 mm, the pressure drop and temperature change of steam through a valve under different apertures are calculated; the pressure drop calculation method of the gas–liquid two-phase flow is referred to formulas (3)–(6), and the heat calculation method is as follows:.

The temperature and pressure of saturated steam have a coupling relationship, which is given as follows:

$$T_s = 210.2376 p_s^{0.21} - 30, \tag{7}$$

where T_s is the temperature of steam in °C and p_s is the pressure of steam in MPa.

The heat of the injected wet steam will reach the formation along the radial path through the inner tube of the insulated tubing, the insulation layer of the insulated tubing, the outer tube of the insulated tubing, and the annular space between the tubing and casing and the casing and cement ring. In this process, radial heat loss will be generated, which can be bounded by the outer edge of the cement ring. The former is the steady heat transfer, and the latter is the unsteady heat transfer. Convection heat transfer occurs when the wet steam flows through the inner wall of the insulated tubing, heat transfer occurs when it flows from the inner wall of the insulated tubing to the outer wall of the insulated tubing, convection heat transfer and heat radiation occur when it flows in the annular space between the tubing and casing, and heat transfer occurs when it flows in the annular space between the casing and cement ring; hence, the thermal resistance formula is expressed as follows:

$$R = \frac{1}{2\pi h_1 r_1} + \frac{1}{2\pi\lambda_{tub}}\ln\left(\frac{r_2}{r_1}\right) + \frac{1}{2\pi\lambda_{ins}}\ln\left(\frac{r_3}{r_2}\right) + \frac{1}{2\pi\lambda_{tub}}\ln\left(\frac{r_4}{r_3}\right) + \frac{1}{2\pi(h_c + h_r)r_4} + \frac{1}{2\pi\lambda_{cas}}\ln\left(\frac{r_{co}}{r_{ci}}\right) + \frac{1}{2\pi\lambda_{cem}}\ln\left(\frac{r_h}{r_{co}}\right), \tag{8}$$

where h_1 is the convective heat transfer coefficient of wet steam in W/(m^2·°C) and $r1$ is the inner tube radius of the insulated tubing in m. λ_{tub} is the thermal conductivity of the inner tube of the heat-insulated tubing in W/(m·°C); r_2 is the inner and outer radius of the insulated tubing in m; λ_{ins} is the thermal conductivity of the insulation layer of the insulated tubing in W/(m·°C); r_3 is the outer tube radius of the insulated tubing in m; r_4 is the outer radius of the insulated tubing in m; h_c is the natural convection heat transfer coefficient in the annular space between the tubing and

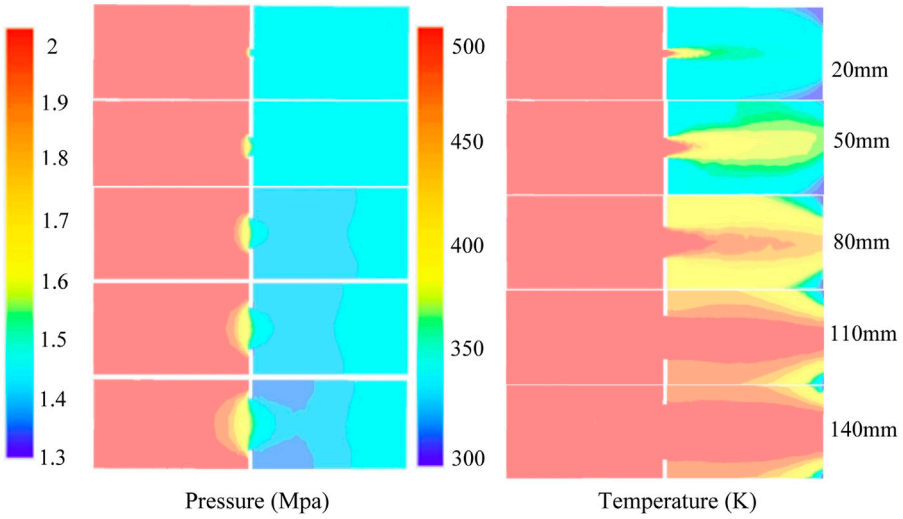

FIGURE 8
Distribution of the pressure field and temperature field of the steam flow in OCD.

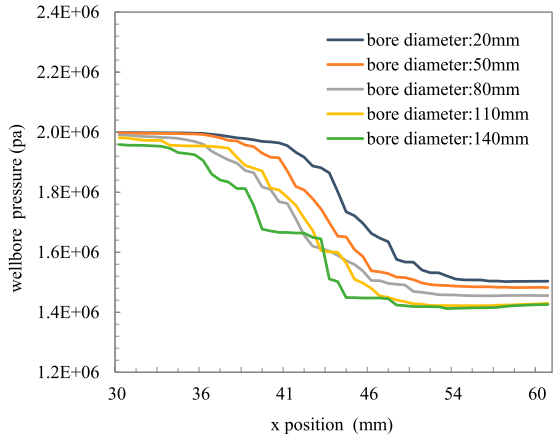

FIGURE 9
Relationship between pressure and pore size in OCD.

casing in W/(m^2·°C); h_r is the radiant heat transfer coefficient in the annular space between the tubing and casing in W/(m^2·°C); λ_{cas} is the thermal conductivity of the casing in W/(m·°C); r_{co} is the outer radius of the casing in m; r_{ci} is the tube radius in m; λ_{cem} is the thermal conductivity of the cement ring in W/(m·°C); and r_h is the outer radius of the cement ring in m.

The section of steam flowing through the nozzle is suddenly reduced, and the formula for calculating overflow resistance is given as follows:

$$F = \frac{P_1 - P_2}{\gamma} + \frac{\alpha_1 V_1^2}{2g} - \frac{\alpha_2 V_2^2}{2g} - F_{1\text{-}2}, \quad (9)$$

where F is the overflow resistance; $F_{1\text{-}2}$ is the resistance loss along the path; α_1 and α_2 are the kinetic energy correction coefficients; γ is the fluid weight; and V_1 and V_2 are the average flow rates at the interface.

It can be observed from Figure 8 and Figure 9 that the pressure drop of the gas–liquid two-phase fluid varies greatly under different apertures. Because the mechanism of the local pressure drop of nozzle-type OCD depends on the minimum flow area, with the increase in the aperture, the pressure drop becomes smaller, the temperature range decreases, the heat transfer speed increases, and the heat loss decreases. When the pore diameter is greater than 110 mm, the effect of the steam pressure drop through the pore is not obvious, and the effect of OCD current limiting is worse.

4 Conclusion

(1) A simulation experimental device was established to carry out the flow resistance experiment of the single-phase liquid and gas–liquid mixture through the nozzle/orifice plate flow control device simulation system.

(2) Data analysis shows that the experimental data of the single-phase liquid flow can reliably be predicted using the formula of the liquid pressure drop through the orifice plate and the flow coefficient obtained by fitting the experimental data, and the prediction accuracy is less than ±10%; the calculation error of the experimental data of the gas–liquid mixture can be less than ±20% by using the method proposed by Chisholm.

(3) The factors affecting the flow resistance effect of the gas–liquid two-phase flow were compared and analyzed, and the overflow pressure drop effect under different pore sizes, steam dryness, and steam flow rates was simulated. It was concluded that the pore size had a significant effect on the pressure drop effect, and the pressure drop amplitude became smaller with the increase in the pore size. In order to achieve an obvious throttling effect, the maximum pore size should not exceed 80 mm; the higher the steam dryness, the more obvious the pressure drop effect is. The flow rate has little influence on the overflow resistance, and the

overflow pressure difference becomes larger with the increase in the flow rate.

Data availability statement

The raw data supporting the conclusion of this article will be made available by the authors, without undue reservation.

Author contributions

QD: conceptualization, data curation, formal analysis, investigation, methodology, project administration, resources, software, supervision, validation, visualization, writing–original draft, and writing–review and editing. ML: methodology, resources, and writing–review and editing. CL: data curation, supervision, and writing–review and editing.

Funding

The author(s) declare that financial support was received for the research, authorship, and/or publication of this article. This study was supported by the National Science and Technology Major Project (No. 2016ZX05031-002) and National Natural Science Foundation of China (No. 51704190).

Acknowledgments

The authors would like to thank ML for fruitful discussions.

Conflict of interest

The authors declare that the research was conducted in the absence of any commercial or financial relationships that could be construed as a potential conflict of interest.

Publisher's note

All claims expressed in this article are solely those of the authors and do not necessarily represent those of their affiliated organizations, or those of the publisher, the editors, and the reviewers. Any product that may be evaluated in this article, or claim that may be made by its manufacturer, is not guaranteed or endorsed by the publisher.

References

Caetano, E. F., Shoham, O., and Brill, J. P. (1992). Upward vertical two-phase flow through an annulus-Part I: single-phase friction factor, taylor bubble rise velocity, and flow pattern prediction. *J. Energy Resour. Technol.* 114, 1–13. doi:10.1115/1.2905917

Caetano, E. F. (1985). *Upward two-phase flow through an annulus*. Tulsa, OK: University of Tulsa.

Chesney, M. R., Felten, F., Hallibuton, H. S., and Edlebeck, J. (2015). Design, testing, and field performance of steam-injection flow-control devices for use in SAGD oil recovery. *SPE*, 174490. doi:10.2118/174490-MS

Dong, X. H., Liu, H. Q., Lu, N., Wu, K., Wang, K., and Chen, Z. (2020a). Steam conformance along horizontal well with different well configurations of single tubing: an experimental and numerical investigation. *SPE Prod. Operations* 35, 549–563. doi:10.2118/195799-pa

Dong, X. H., Liu, H. Q., Pang, Z. X., Wang, C., and Lu, C. (2014b). Flow and heat transfer characteristics of multi-thermal fluid in a dual-string horizontal well. *Numer. Heat. Transf. Part A Appl.* 66, 185–204. doi:10.1080/10407782.2013.873255

Dong, X. H., Liu, H. Q., Zhai, Y., Wang, C., Chen, Z., and Liu, D. (2020b). Experimental investigation on the steam injection profile along horizontal wellbore. *Energy Rep.* 6, 264–271. doi:10.1016/j.egyr.2020.01.005

Dong, X. H., Liu, H. Q., Zhang, Z. X., and Wang, C. (2014a). The flow and heat transfer characteristics of multi-thermal fluid in horizontal wellbore coupled with flow in heavy oil reservoirs. *J. Petroleum Sci. Eng.* 122, 56–68. doi:10.1016/j.petrol.2014.05.015

Gai, P., Du, Y., Lu, G., Li, X., and Li, S. (2010). Uniform steam injection technology used in thermal horizontal wells. *SPE*, 130893. doi:10.2523/130893-MS

Gu, H., Cheng, L., Huang, S., Zhang, H., Lin, M., and Hu, C. (2014b). A new semi-analytical model for predicting steam pressure and temperature in annuli. *SPE*, 170042. doi:10.2118/170042-ms

Gu, H., Cheng, L. S., Huang, S. J., Du, B., and Hu, C. (2014a). Prediction of thermophysical properties of saturated steam and wellbore heat losses in concentric dual-tubing steam injection wells. *Energy* 75, 419–429. doi:10.1016/j.energy.2014.07.091

Gu, H., Cheng, L. S., Huang, S. J., Li, B., Shen, F., Fang, W., et al. (2015). Steam injection for heavy oil recovery: modeling of wellbore heat efficiency and analysis of steam injection performance. *Energy Convers. Manag.* 97, 166–177. doi:10.1016/j.enconman.2015.03.057

Hasan, A. R., and Kabir, C. S. (2005). A simple model for annular two-phase flow in wellbores. *SPE* 95523. doi:10.2118/95523-PA

Hasan, A. R., and Kabir, C. S. (1994). Aspects of wellbore heat transfer during two-phase flow. *SPE Prod. Facil.* 9, 211–216. doi:10.2118/22948-pa

Hasan, A. R., Kabir, C. S., and Wang, X. W. (1998). Wellbore two-phase flow and heat transfer during transient testing. *SPE J.* 3, 174–180. doi:10.2118/38946-pa

Huang, S. J., Cao, M., Xia, Y., Chen, X., and Yang, M. (2018b). Heat and mass transfer characteristics of steam in a horizontal wellbore with multi-point injection technique considering wellbore stock liquid. *Int. J. Heat Mass Transf.* 127, 949–958. doi:10.1016/j.ijheatmasstransfer.2018.07.136

Huang, S. J., Xia, Y., Xiong, H., Liu, H., and Chen, X. (2018a). A three-dimensional approach to model steam chamber expansion and production performance of SAGD process. *Int. J. Heat Mass Transf.* 127, 29–38. doi:10.1016/j.ijheatmasstransfer.2018.06.136

Kumar, A., Oballa, V., and Card, C. (2010). Fully-coupled wellbore design and optimization for thermal operations. *SPE* 137427. doi:10.2118/137427-MS

Least, B., Greci, S., Wilemon, A., and Ufford, A. (2013). Autonomous ICD range 3B single-phase testing. *SPE* 166285. doi:10.2118/166285-MS

Liu, X. J., Ren, J. J., Chen, D. Y., and Yin, Z. Y. (2022). Comparison of SDS and L-Methionine in promoting CO2 hydrate kinetics: implication for hydrate-based CO2 storage. *Chem. Eng. J.* 438, 135504. doi:10.1016/j.cej.2022.135504

Luo, W., Li, H. T., Wang, Y. Q., and Wang, J. C. (2015). A new semi-analytical model for predicting the performance of horizontal wells completed by inflow control devices in bottom-water reservoirs. *J. Nat. Gas Sci. Eng.* 27, 1328–1339. doi:10.1016/j.jngse.2015.03.001

Mozaffari, S., Nikookar, M., Ehsani, M. R., Sahranavard, L., Roayaie, E., and Mohammadi, A. H. (2013). Numerical modeling of steam injection in heavy oil reservoirs. *Fuel* 112, 185–192. doi:10.1016/j.fuel.2013.04.084

Parappilly, R., and Zhao, L. (2009). SAGD with a longer wellbore. *J. Can. Petroleum Technol.* 48 (6), 71–77. doi:10.2118/09-06-71

Prakasa, B., Muradov, K., and Davies, D. (2019). Principles of rapid design of an inflow control device completion in homogeneous and heterogeneous reservoirs using type curves. *J. Petroleum Sci. Eng.* 176, 862–879. doi:10.1016/j.petrol.2019.01.104

Rivas, D. A., and Gates, I. (2018). SAGD circulation phase: thermal efficiency evaluation of five wellbore completion designs in Lloydminster reservoir. *SPE*, 193357. doi:10.2118/193357-ms

Sun, F. R., Yao, Y. D., Li, G. Z., Li, X., Zhang, T., Lu, C., et al. (2018b). An improved two-phase model for saturated steam flow in multi-point injection horizontal wells under steady-state injection condition. *J. Petroleum Sci. Eng.* 167, 844–856. doi:10.1016/j.petrol.2018.04.056

Sun, F. R., Yao, Y. D., Li, G. Z., and Liu, W. (2019). A numerical model for wet steam circulating in horizontal wellbores during starting stage of the steam-assisted-gravity-drainage process. *Heat Mass Transf.* 55, 2209–2220. doi:10.1007/s00231-019-02564-7

Sun, F. R., Yao, Y. D., Li, X. F., Li, G., Liu, Q., Han, S., et al. (2018a). Effect of friction work on key parameters of steam at different state in toe-point injection horizontal wellbores. *J. Petroleum Sci. Eng.* 164, 655–662. doi:10.1016/j.petrol.2018.01.062

Temizel, C., Canbaz, C. H., Palabiyik, Y., Irani, M., Balaji, K., and Ranjith, R. (2019). Production optimization through intelligent wells in steam trapping in SAGD operations. *SPE*, 195361. doi:10.2118/195361-ms

Wang, J., Liu, H. Q., Liu, Y. G., Jiao, Y., Wu, J., and Kang, A. (2016). Mechanism and sensitivity analysis of an inflow control devices (ICDs) for reducing water production in heterogeneous oil reservoir with bottom water. *J. Petroleum Sci. Eng.* 146, 971–982. doi:10.1016/j.petrol.2016.08.007

Yin, Z. Y., Huang L, L., and Linga, P. (2019). Effect of wellbore design on the production behaviour of methane hydrate-bearing sediments induced by depressurization. *Appl. Energy* 254, 113635. doi:10.1016/j.apenergy.2019.113635

Yin, Z. Y., and Linga, P. (2019). Methane hydrates:A future clean energy resource. *Chin. J. Chem. Eng.* 27 (09), 2026–2036. doi:10.1016/j.cjche.2019.01.005

Yu, T. T., Zhang, H. Q., Li, M. X., and Sarica, C. (2010). A mechanistic model for gas/liquid flow in upward vertical annuli. *SPE Prod. Operations* 25, 285–295. doi:10.2118/124181-pa

frontiers | Frontiers in Chemistry

TYPE Original Research
PUBLISHED 20 November 2023
DOI 10.3389/fchem.2023.1279729

OPEN ACCESS

EDITED BY
Jafar Soleymani,
Tabriz University of Medical Sciences, Iran

REVIEWED BY
Tushar Dhanani,
Florida Agricultural and Mechanical University, United States
María Del Rayo Camacho Corona,
Autonomous University of Nuevo León, Mexico

*CORRESPONDENCE
Muhammad Mushtaq,
muhammad.mushtaq@gcu.edu.pk
Saima Sharif,
Saimasharif04@gmail.com

RECEIVED 18 August 2023
ACCEPTED 30 October 2023
PUBLISHED 20 November 2023

CITATION
Shaheen A, Akram S, Sharif S, Rashid A, Adnan A and Mushtaq M (2023), Fractionation of *Xanthium strumarium* L. foliage phenolics, *in-vitro* antioxidant activities, and *in-vivo* anti-diabetic potential.
Front. Chem. 11:1279729.
doi: 10.3389/fchem.2023.1279729

Fractionation of *Xanthium strumarium* L. foliage phenolics, *in-vitro* antioxidant activities, and *in-vivo* anti-diabetic potential

Asma Shaheen[1], Sumia Akram[2], Saima Sharif[3]*, Ayoub Rashid[1], Ahmad Adnan[1] and Muhammad Mushtaq[1]*

[1]Department of Chemistry, Government College University Lahore-Pakistan, Lahore, Pakistan, [2]Division of Science and Technology, University of Education Lahore-Pakistan, Lahore, Pakistan, [3]Department of Zoology, Lahore College for Women University Lahore-Pakistan, Lahore, Pakistan

Introduction: The present research aimed to fractionate *Xanthium strumarium* L. (XSL) foliage phenolics into a set of solvents and evaluate their antioxidant potential and *in-vivo* anti-diabetic activity against Alloxan monohydrate-induced diabetic mice.

Methodology: For this purpose, XSL foliage was fractionated into petroleum ether, ethyl acetate, ethanol, and water *via* orbital type shaking and tested for the presence of phenolics, and their antioxidant and antidiabetic potential.

Results and discussion: The results revealed that the ethyl acetate fraction of XSL foliage contained the highest amount of total phenolics 95.25 mg GAE/g of extract, followed by ethanol (65.14 mg GAE/g), petroleum ether (25.12 mg GAE/g), water (12.20 mg GAE/g), and XSL powder (69.13 mg GAE/g). At the end of treatment time (day 18 of oral administration of 400 mg/kg body weight of mice), the ethyl acetate fraction significantly ($p \leq 0.05$) lowered blood glucose level (353 $\pm$ 10.6 to 220 $\pm$ 25.5 mg/dL) which might due to the elevated level of phenolic compounds in this fraction.

Conclusion: Overall, it can be speculated that ethyl acetate and ethanol may work efficiently for the enrichment of XSL phenolic without compromising their antidiabetic potential.

KEYWORDS

***Xanthium strumarium*, L. Foliage, fractionations, phenolics, antioxidants, antidiabetics**

1 Introduction

Despite the prevalence and widespread use of anti-diabetic medications like metformin, sulfonylureas, thiazolidinediones, and insulin, diabetes ranks as a major global health concern. International Diabetic Federation estimates indicate that the prevalence of diabetes has increased to 463 million in 2019 and figures may rise to 578 (10.2%) and 700 million (10.9%) by 2030 and 2045, respectively (Akhtar et al., 2022). Additionally, it has been predicted that by 2030, diabetes will account for 3.3% of all fatalities worldwide, making it the seventh greatest cause of death (Kokil et al., 2015). For centuries herbs have been used to meet healthcare needs through medical procedures and traditional remedies. Traditional medicine employs at least 1200 different plant species for their potential biological activities and almost half of these have been studied for their phytochemistry, and antioxidant activities (Krupa et al., 2019; Mawoza et al., 2019).

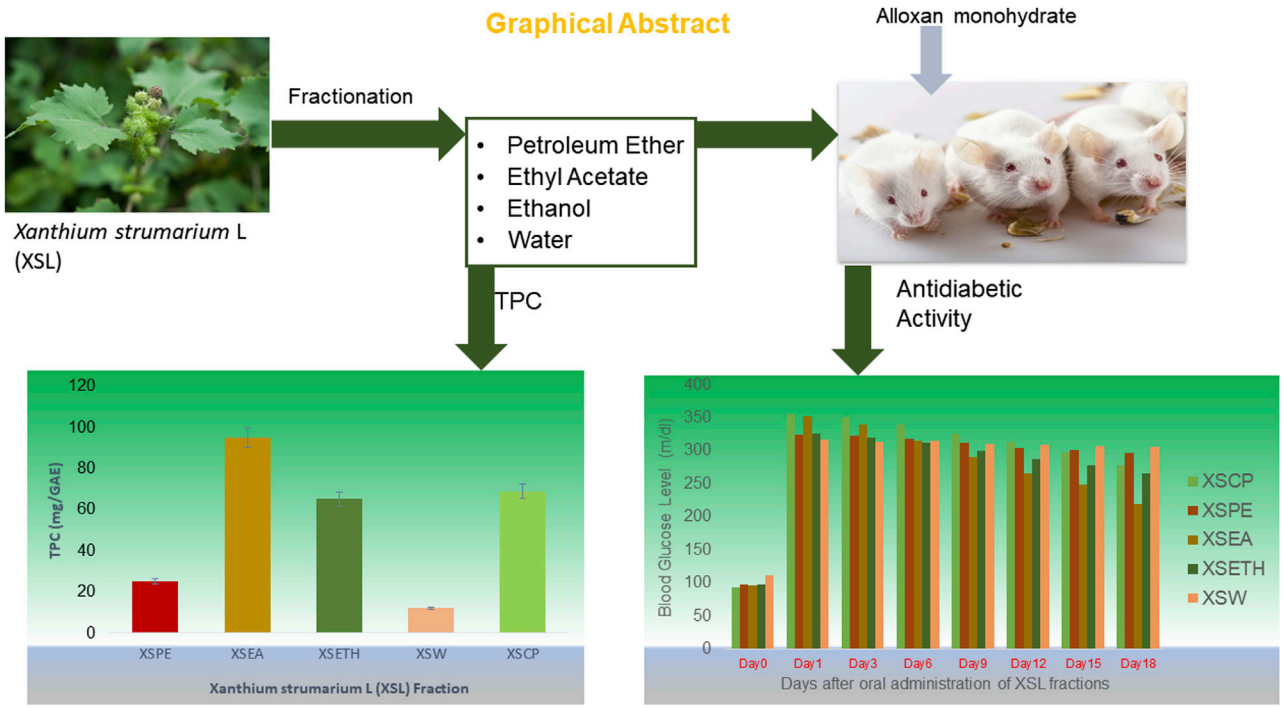

GRAPHICAL ABSTRACT

Xanthium strumarium Linn (hereafter XSL) belongs to the Asteraceae family and is commonly identified as cocklebur, sheep bur, hedgehog bur weed, ditch bur, sea burdock, clot bur, and button bur by different civilizations in the world (Ghahari et al., 2017). The plant has habitats worldwide, but temperate zones are the areas of high prevalence, especially India, Russia, Iran, Australia, North Korea, Japan, Pakistan, America, South Africa, China, Eastern Asia, and some parts of South Asia. It frequently grows along roadsides, and on plains, hills, and mountains. The flowering period starts during July/August whereas fruits are usually ripe in September/October (Fan et al., 2019). The fruit as a whole clings to animal fur for its dispersal and is considered poisonous, however, it possesses cytotoxic, sedative diuretic, antitussive antimalarial, antispasmodic, anti-rheumatic antibacterial, and antifungal properties (Clayton et al., 2020). Few researchers have evaluated the antidiabetic potential of *X. strumarium* L. (XSL), but the majority of these studies utilized aqueous or alcoholic extracts of XSL foliage (Ahmad et al., 2016). An acute review of previously published research regarding phenolics reveals that the solubility of these compounds varies widely and similar can be speculated about the stability and biological functions of these bioactives. Keeping in view these facts, we have planned to fractionate XSL foliage phenolics into a range of solvents including petroleum ether, ethyl acetate, ethanol, and water and each fraction of XSL foliage was subsequently assessed for its total phenolic content (TPC), radical scavenging capacity, *in-vitro* antioxidant activity, and antidiabetic potential (*in-vivo*).

2 Materials and methods

The experimental work regarding the fractionation of XSL foliage was done in the Biochemistry laboratory of Government College University Lahore. The *in-vivo* trials associated with the present research were carried out at the animal house in the Lahore College for Women University's Zoology Department. Formal approval was obtained from the institutional ethical committee (No. GCU-IIB-2596) dated 31 October 2022. Animals (Swiss albino mice) were supplied by F. Z traders, Lahore, Pakistan, and at the time of the experiment the average age and weight ranged from 4 to 8 weeks and 22–24 g, respectively. The chemicals and solvents used during the current study were of analytical grade and acquired from the companies Sigma Aldrich Chemical Co. (United States) and Merck (Germany).

2.1 Sample collection

The XSL foliage was collected during the month of June 2022 from a remote location in Pakistan's District Narowal and was identified as rough cocklebur (voucher no. LCW -1016) by Dr. Shubnam Shaheen Associate Professor, Department of Botany, Lahore College for Women University Lahore.

2.2 Preparation of XSL fractions

The XSL foliage was air dried at 40°C after being cleaned with distilled water to remove dirt and contaminants. The dried XSL foliage was powdered prior to the fractionation with particle mesh sizes ranging from 24 to 60 sorted by electromagnetic vibrator for 15 min, packed in an opaque plastic bag, and stored. Petroleum ether, ethyl acetate, ethanol, and water were

sequentially used as solvents during the fractionation process. A carefully-weighed 25 g of dried XSL foliage powder was placed in a 500 mL Erlenmeyer flask and shaken with 250 mL of petroleum ether for 12 h in an orbital shaker (Gallenkamp, UK) at 250 rpm under ambient conditions 25°C–30°C. The resultant aliquot was filtered using Whatman filter paper 1, and residues were mixed with the second extraction solvent, *i.e.*, ethyl acetate, and shaken under the above-mentioned conditions. The residues of step 2 and step 3 were subsequently subjected to ethanol- and water-based fractionation following the above-mentioned procedure. All four fractions were separately dried using a rotating evaporator (SB-651; EYELA, Tokyo, Japan) operated at 35°C and reduced pressure, weighed to calculate the percent yield of each fraction (g/100 g of XSL powder), and stored at −10°C until the required dosages were made. Finally, the amount of extractable bioactives (total extract) was calculated by adding the percent yield of each fraction.

2.3 Total phenolic content

The TPC in every fraction of XSL foliage powder was measured using Folin-Ciocalteu reagent as documented by (Elagdi et al., 2023). Gallic acid was processed as a positive control to express the results as milligrams of gallic acid equivalent (mg GAE)/g) of extract. The five different concentrations of the gallic acid standard (50, 40, 30, 20, and 10 mg/mL) and 1.0 mg/mL of each XSL foliage powder fraction were introduced into the test tube containing 2.5 mL of 10% (v/v). To the Folin-Ciocalteu reagent was added 2 mL of 7.5% (w/v) Na_2CO_3, and the mixture was allowed to stand in the dark at room temperature for half an hour. The absorbance was measured at 760 nm using a Shimadzu 160-UV spectrophotometer. For each extract, all the calculations were done in triplicates.

2.4 DPPH assay

The radical scavenging potential of each XSL foliage fraction was estimated by using the method described by Villano et al. with minor changes (Villaño et al., 2007). In this assay, 0.1 mM solution of 1,1-diphenyl-2-picrylhydrazyl and 1.0 mg/mL of each XSL extract was prepared in HPLC grade methanol. The equal volumes 2.5 mL of DPPH solution and extract were incubated at room temperature for half an hour under dark, and at 517 nm absorbance was measured and compared with ascorbic acid acting as a standard. The free radical scavenging potential of the XSL fraction was expressed as %inhibition calculated by the following formula where As and Ac stand for the absorbance of the sample and control respectively. The IC_{50} (Conc. providing 50% inhibition) value is used to express the DPPH assay results. IC_{50} value can be measured by plotting a graph between the scavenging effect and the corresponding extract concentration. AAI (Antioxidant activity index) is used to measure the antioxidant potential and can be calculated by dividing the final DPPH concentration (μg/mL) by IC_{50} (μg/mL) (Scherer and Godoy, 2014).

$$\%\text{Inhibition} = [(\text{Ac-As})/\text{Ac}] \times 100$$

2.5 FRAP assay

The ferric-reducing ability of plasma (FRAP) comprising XSL foliage fractions was determined by using the strain and Benzie method with minor changes (Benzie and Strain, 1996). In this method, 300 μL distilled water was mixed in 100 μL of plant extract followed by the addition of 3 mL of frap reagent. The frap reagent was prepared by mixing 25 mL acetate buffer (0.3 M) at PH = 3.6 and 2.5 mL (10 mM) of TPTZ (2, 4, 6- tripyridyl-s-triazine) in hydrochloric acid (40 mM) and 2.5 mL of $FeCl_3$ (20 mM). The mixture was incubated under ambient conditions (30°C) and absorbance was measured at 593 nm by a Shimadzu 160-UV spectrophotometer. Frap assay evaluates the antioxidant activity of plant extract by reducing metal ions using electron donation. Ascorbic acid was used as the standard and the FRAP value was measured by the following equation, Where A_O and A_S are the absorbance of the standard and sample respectively.

$$\text{Frap value } ((\mu\text{mascorbate/g}) = \text{As-Ao/Ao}$$

2.6 Induction of diabetes in mice

For the animal study, 45 male albino mice were selected and were kept for 1 week of acclimatization. With a maximum of six animals per cage, the animals were housed in sterile polypropylene cages and kept at room temperature. The bedding material was sterile rice husk. These animals were housed in a controlled setting with respect to temperature (25°C), humidity (45%–57% range), and light period (12: 12-h dark-light cycle). Alloxan monohydrate was intraperitoneally injected at a dosage of 120 mg/kg to cause hyperglycemia in male albino mice that were more than 8 weeks old and weighed 22–24 g. The blood glucose levels were assessed by tail clip sampling 48 h following alloxan administration. When the blood sugar level exceeded 185 mg/dL, mice were considered diabetic (Nagappa et al., 2003). The animals were divided into seven groups each having six mice and the body weight and blood glucose (using glucometer) level of control and treated groups were monitored on days 1, 3, 6, 9, 12, 15, and 18 of treatment.

C: Mice who had not been given any drug or alloxan monohydrate (Normal control).

DC: Mice were given alloxan monohydrate (Diabetic control).

XSCP: Diabetic mice were administered with crude powder of XSL.

XSPE: Diabetic mice were administered a petroleum ether fraction of XSL.

XSEA: Diabetic mice were administered with ethyl acetate fraction of XSL.

XSETH: Diabetic mice were administered an ethanolic fraction of XSL.

XSW: Diabetic mice were administered with an aqueous fraction of XSL.

2.7 Acute toxicity studies

The process was completed in accordance with OECD (Organization for Economic Co-operation and Development)

TABLE 1 The XSL foliage fraction yield in various solvents and their Total Phenolic Content (TPC).

Fractions	% yield (w/w)	TPC (mg GAE/g)
XSPE[1]	0.033 ± 0.01[a]	25.12 ± 7.06[ab]
XSEA[2]	0.095 ± 0.02[a]	95.25 ± 7.41[c]
XSETH[3]	0.301 ± 0.07[b]	65.14 ± 7.06[b]
XSW[4]	0.402 ± 0.28[bc]	12.2 ± 5.80[a]
Total	0.828 ± 0.38[d]	197.71 ± 27.33[d]
Crude powder (XSCP[5])	----	69.13 ± 6.01[bc]

The values are mean ± SD, of triplicate experiments, the different superscript letters over each range denote the significantly different ($p \leq 0.05$) values.

guidelines to check the toxicity (Ahmad et al., 2016). To investigate the acute toxicity, different doses of XSL foliage fractions were administered to male Swiss albino mice. The control group received the vehicle (normal saline only), whereas the treatment groups orally received plant fractions in dosages of 2 and 5 g/kg. The adverse effects were thoroughly monitored for 2 days after the dose was introduced. The body weight of the mice before and after administration, any sign of toxicity such as changes in the fur, skin, and eyes, as well as changes in the respiratory, circulatory, and central nervous systems, behavior patterns, signs of tumors, salivation, diarrhea, sleep, and coma were also noted.

2.8 Blood collection and determination of blood glucose

To determine the blood glucose level blood samples were collected from fasted mice on days 0, 1, 3, 6, 9, 12, 15, and 18 of the treatment. Blood was collected[1] from the mouse tails by snipping with a sharp razor, and glucose level was measured by glucometer (Accu-Chek Active, Roche Limited, Pakistan)[2] as described by Arya et al. (2012).

2.9 Statistical analysis

All the parameters including extract yield, TPC, and DPPH radical scavenging activity were measured in triplicate and the estimates were compared[3] for significant difference $p \leq 0.05$ by using Duncan's multiple range[4] test (MRT) (Tallarida and Murray, 1987).

3 Results and discussion

Table 1 shows the percentage yield[5] of fractions of XSL foliage depending on the solvent polarity that significantly affected the fraction yield in the order of petroleum ether < ethyl acetate < ethanol < water. Fraction yield depends upon the solvent polarity and the difference in fraction yield in different solvents was due to the solubility of phytochemicals in the respective solvent (Dirar et al., 2019). TPC of different fractions of XSL in ethyl acetate was 95.25 ± 7.41 mg GAE/g, followed by ethanol 65.14 ± 7.06 mg GAE/g, petroleum ether 25.12 ± 7.06 mg GAE/g, and water 12.2 ± 5.80 mg GAE/g. The TPC in crude powder of XSL foliage was found to be 69.13 ± 6.01 mg GAE/g. In the previous studies TPC value of ethyl acetate and aqueous leave extract of XSL extracted by maceration and hot extraction method was 59.98 and 35.92 mg of GAE/g DW, respectively (Pillai and Thebe, 2023). The TPC value of ethanolic extract prepared from the aerial parts of XSL using the cold percolation method was determined 84.86 ± 5.13 mg of GAE/g DW (Ly et al., 2021). Similarly, aqueous and ethyl acetate fractions were obtained from 80% methanolic extract of XSL dried leaves using the cold percolation method, and their TPC values were determined as 75.24 ± 13.31 and 166.26 ± 27.98 mg of GAE/g DW (Guemmaz et al., 2018; Pillai and Thebe, 2023). In other studies ethyl acetate and 80% ethanol extract were extracted from XSL dried leaves by dynamic maceration, static maceration, and soxhlet method, and their TPC values were determined as 70.07 ± 1.6, 64.51 ± 1.0, 69.38 ± 1.3 mg GAE/g DW (Ethanol), 27.19 ± 1.0, 21.98 ± 3.6 and 23.19 ± 0.3 mg GAE/g DW (Ethyl acetate) respectively (Scherer and Godoy, 2014). No literature reported on petroleum ether fraction. The discrepancy in TPC value is due to factors like sample variety, sample quantity, type of extraction techniques, seasonal variation, extracted bioactive components, and geographic location.

3.1 Antioxidant activity

The DPPH assay evaluates the antioxidant's scavenging capacity towards the DPPH radical. DPPH is a stable free radical having a blue color in alcoholic solution, while in the presence of antioxidants its reduction changes color to yellow. DPPH assay depends upon the antioxidant's potential to donate hydrogen or electrons and is spectrophotometrically analyzed. Absorbance is inversely proportional to the antioxidant potential which is directly proportional to % inhibition. Table 2 shows the antioxidant activity of petroleum ether (XSPE), ethyl acetate (XSEA), ethanol (XSETH), and water (XSW) fractions of XSL. The IC_{50} value decreased in the order of 101.20 > 88.02 > 54.60 > 46.11 and the antioxidant index value (AAI) increased in the order of 1.87 > 0.90 > 0.28 > 0.05 respectively. In the present study the ethyl acetate fraction has the lowest IC_{50} value followed by the

1 Petroleum ether fraction of *X. strumarium* L. Foliage.
2 Ethyl acetate fraction of *X. strumarium* L. Foliage.
3 Ethanol fraction of *X. strumarium* L. Foliage.
4 Water fraction of *X. strumarium* L. Foliage.
5 Crude powder of *X. strumarium* L. Foliage.

TABLE 2 DPPH Radical scavenging activity of different fractions of XSL foliage powder.

Fractions	IC_{50} µg/mL	AAI
XSPE	88.02^{c}	0.28^{b}
XSEA	46.11^{a}	1.87^{d}
XSETH	54.60^{b}	0.90^{c}
XSW	101.20^{d}	0.05^{a}

The values are mean ± SD, of triplicate experiments, the different superscript letters over each range denote the significantly different ($p \leq 0.05$) values.

TABLE 3 FRAP Assay of different fractions of XSL foliage powder.

Sample	Absorbance	Frap value (µm ascorbate/g)
XSPE	0.75	0.194 ± 0.04
XSEA	1.19	0.238 ± 0.06
XSETH	0.98	0.212 ± 0.07
XSW	0.59	0.179 ± 0.01

ethanol fraction, while in the previous literature the IC_{50} value of different solvent extracts of *Xanthium strumarium* aerial parts has been determined. IC_{50} values of aqueous and ethyl acetate extracts (obtained by maceration and hot percolation method) have been determined at 2465.21 and 1856.02 µg/mL, respectively (Kim et al., 2005; Guemmaz et al., 2018; Pillai and Thebe, 2023). Similarly Aqueous and ethyl acetate fractions of 80% methanol extract of dried XSL leaves obtained by cold percolation method have demonstrated IC_{50} values 46.00 ± 0.0006, 17.00 ± 0.0004 µg/mL respectively (Pillai and Thebe, 2023). In another study, 80% ethanol and ethyl acetate extract prepared from XSL dried leaves by dynamic maceration, static maceration, and soxhlet method and their IC_{50} values were determined as 53.01 ± 1.20, 47.83 ± 1.40, 53.34 ± 1.52 µg/mL (Ethanol), 369.83 ± 13.58, 346.35 ± 16.50, and 423.97 ± 22.27 µg/mL (Ethyl acetate) in the DPPH assay (Scherer and Godoy, 2014). There was no literature reported on petroleum ether fraction. The variation in the IC_{50} in the present study and previous reports might be due to the above-mentioned factors as discussed before.

FRAP assay evaluates the antioxidant potential of antioxidants in terms of the reduction of ferric to ferrous ions. Ascorbic acid is used as standard and the values of reducing potential of antioxidants are compared to it. With the increase of antioxidant concentration, absorbance increases, and the resulting reducing power also increases. The frap value will be greater the higher the antioxidant potential. Table 3 depicts the Frap values and absorbance of different fractions of XSL foliage. Ethyl acetate has greater absorbance with FRAP value of 0.238 ± 0.06 (µm ascorbate/g) followed by ethanol (0.212 ± 0.07), petroleum ether (0.194 ± 0.04) and water (0.179 ± 0.01) µm ascorbate/g. In the literature cited the ferric reducing capacity of ethyl acetate and water extracts of XSL have been determined to be 0.996 ± 0.101 and 0.412 ± 0.009 µm ascorbate/g at a concentration of 100 µg/mL (Kim et al., 2005; Pillai and Thebe, 2023). While the FRAP value in this research work was measured at 30 µg/mL. The FRAP values of ethanol and petroleum ether fractions were not reported in the literature.

3.2 Body weight

Table 4 elaborates on the difference in body weight between the experimental and control group animals after treatment with different fractions of XSL foliage. The mice administered alloxan monohydrate (120 mg/kg) lost body weight from 1% to 3% which was averted by the treatment of different fractions and powdered samples of the selected plant. The control group animals (C) which use only the vehicle shows an increase in body weight from 21.5 ± 2.12 to 24.75 ± 1.77 (14%) while diabetic control (DC) loss in body weight from 23.50 ± 0.71 to 21.05 ± 0.78 (10%) on day 18 days.

The animals in the XSCP sample lost body weight by 23 ± 2.83 to 22.40 ± 2.69 (3%) on the first day and after receiving with powdered sample increased by 24 ± 2.82 (7%) on the last day of the trial. The XSPE and XSEA animals reduced their body weight from day 1 23.50 ± 0.71 to 23.15 ± 0.50 (1%) and 21.50 ± 0.71 to 21.15 ± 0.64 (2%) respectively and after being treated with petroleum ether and ethyl acetate fractions, the weight of XSPE and XSEA animals increased up to 23 ± 0.57, 24 ± 0.71 (1% and 13%) of their initial body weight. The animals treated with the ethanol and water fractions showed body weight reduction of 23.5 ± 0.71 to 23.05 ± 0.64 (2%), 22.75 ± 1.06 to 22.55 ± 1.06 (1%), and after treatment increased up to 24.15 ± 0.64, 22.70 ± 0.71 (5% and 1%) respectively. The results shown are based on the mean of six mice and the percentage change indicates the change from day 1 to the end of the study (day 18).

3.3 Antidiabetic activity

The blood glucose level of diabetic mice (CD) was significantly ($p \leq 0.05$) higher as compared to normal mice (C) and the effect of powdered sample and different fractions of XSL on diabetic mice was studied. Data assembled in Table 5 shows the blood glucose levels of the control and treatment groups on days 1, 3, 6, 9, 12, 15, and 18 of treatment. The blood glucose level of C (control group), who simply used a vehicle, did not vary significantly ($p \leq 0.05$) during the treatment time (as shown by subscript and superscript letters). However, the blood glucose level of diabetic mice (DC) was significantly ($p \leq 0.05$) higher as compared to the control group. Fasting mean blood glucose level of diabetic control DC and XSCP on day one after being diabetic was 345 ± 7.07 mg/dL, and 355 ± 7.07 mg/dL, respectively. On day 18 the blood glucose level of DC (diabetic control) increased up to 364 ± 2.12 mg/dL, while oral administration of powdered sample to XSCP significantly ($p \leq 0.05$) decreased the blood glucose level to 278 ± 10.6 mg/dL (22%). On day one, blood glucose levels of diabetic-induced mice of XSPE, XSEA,

TABLE 4 Effect of different fractions of XSL on body weight in alloxan-induced diabetic mice.

Groups	Doses (mg/kg)	Days after treatment							
		0	1	3	6	9	12	15	18
C		21.50 ± 2.12	21.65 ± 2.05	21.90 ± 1.98	22.20 ± 1.84	22.55 ± 1.91	22.90 ± 1.84	23.75 ± 1.77	24.75 ± 1.77
DC		23.50 ± 0.71	23.30 ± 0.57	23.25 ± 0.78	22.80 ± 0.85	22.45 ± 0.78	22.00 ± 0.71	21.45 ± 0.78	21.05 ± 0.78
XSCP	400	23.00 ± 2.83	22.40 ± 2.69	22.30 ± 2.69	22.75 ± 2.76	23.05 ± 2.62	23.25 ± 2.62	23.60 ± 2.69	24.00 ± 2.82
XSPE	400	23.50 ± 0.71	23.15 ± 0.50	23.00 ± 0.57	22.50 ± 0.71	22.65 ± 0.64	22.80 ± 0.57	22.90 ± 0.57	23.00 ± 0.57
XSEA	400	21.50 ± 0.71	21.15 ± 0.64	21.60 ± 0.71	21.95 ± 0.64	22.50 ± 0.71	22.85 ± 0.64	23.30 ± 0.71	24.00 ± 0.71
XSETH	400	23.50 ± 0.71	23.05 ± 0.64	22.95 ± 0.64	23.15 ± 0.78	23.55 ± 0.78	23.65 ± 0.78	23.75 ± 0.78	24.15 ± 0.64
XSW	400	22.75 ± 1.06	22.55 ± 1.06	22.30 ± 0.99	22.3 ± 0.71	22.40 ± 0.71	22.45 ± 0.78	22.50 ± 0.71	22.70 ± 0.71

The values are mean ± SD, of triplicate experiments.

TABLE 5 Blood Glucose Level of alloxan-induced diabetic mice at different intervals after XSL fractions administration.

Groups	Dose (mg/kg)	Days after treatment							
		0	1	3	6	9	12	15	18
C		$103 \pm 9.90^{a}_{a}$	$95.5 \pm 0.71^{a}_{a}$	$97 \pm 4.24^{a}_{a}$	$91 \pm 1.41^{a}_{a}$	$94 \pm 2.83^{a}_{a}$	$96.5 \pm 2.12^{a}_{a}$	$93 \pm 4.24^{a}_{a}$	$97 \pm 1.41^{a}_{a}$
CD		$105 \pm 7.07^{a}_{a}$	$345 \pm 7.07^{d}_{d}$	$348 \pm 5.66^{d}_{d}$	$350 \pm 5.66^{d}_{d}$	$355 \pm 7.07^{d}_{d}$	$358 \pm 5.66^{d}_{d}$	$363 \pm 3.54^{d}_{d}$	$364 \pm 2.12^{d}_{d}$
XSCP	400	$93.5 \pm 0.71^{a}_{a}$	$355 \pm 7.07^{d}_{d}$	$350 \pm 7.07^{d}_{d}$	$339 \pm 8.49^{c}_{c}$	$327 \pm 9.20^{c}_{c}$	$313 \pm 11.3^{c}_{c}$	$299 \pm 4.95^{b}_{b}$	$278 \pm 10.6^{b}_{b}$
XSPE	400	$97.5 \pm 3.54^{a}_{a}$	$325 \pm 21.2^{d}_{c}$	$323 \pm 21.9^{cd}_{b}$	$318 \pm 21.9^{cd}_{b}$	$313 \pm 21.9^{cd}_{b}$	$305 \pm 21.2^{c}_{b}$	$301 \pm 22.6^{c}_{b}$	$297 \pm 26.2^{c}_{b}$
XSEA	400	$96 \pm 2.73^{a}_{a}$	$353 \pm 10.6^{d}_{d}$	$341 \pm 10.6^{d}_{cd}$	$316 \pm 7.78^{d}_{b}$	$291 \pm 5.66^{c}_{b}$	$267 \pm 23.3^{b}_{b}$	$250 \pm 23.3^{b}_{b}$	$220 \pm 25.5^{b}_{b}$
XSETH	400	$99 \pm 4.95^{a}_{a}$	$327 \pm 9.2^{d}_{c}$	$320 \pm 7.1^{d}_{bc}$	$312 \pm 4.95^{d}_{c}$	$300 \pm 7.1^{d}_{b}$	$288 \pm 10.6^{c}_{b}$	$278 \pm 13.4^{c}_{b}$	$266 \pm 15.6^{c}_{b}$
XSW	400	$112 \pm 4.24^{a}_{a}$	$316 \pm 8.5^{d}_{d}$	$314 \pm 9.90^{d}_{d}$	$315 \pm 12.73^{d}_{d}$	$310 \pm 14.1^{c}_{b}$	$309 \pm 14.4^{c}_{b}$	$308 \pm 14.1^{c}_{c}$	$306 \pm 14.1^{c}_{c}$

The values are mean ± SD, of triplicate experiments, the different letters over each range denote variation ($p \leq 0.05$) in blood glucose level at various intervals (superscripted letters) and type of fraction administered (subscript letters).

XSETH, and XSW were measured as 325 ± 21.2 mg/dL, 353 ± 10.6 mg/dL, 327 ± 9.2 mg/dL, and 316 ± 8.5 mg/dL, respectively. There was no substantial decrease in the blood glucose level of the XSPE group (treated with petroleum ether) observed and two mice out of six died on days 8 and 13 of the treatment, while on day 18 the mean blood glucose level of the remaining mice decreased upto 297 ± 26.2 mg/dL (9%). Animals treated with ethyl acetate (XSEA) showed a substantial decrease in the blood glucose level from day 1 353 ± 10.6 mg/dL to 220 ± 25.5 mg/dL (38%) on day 18. The blood glucose levels of animals treated with ethanol (XSETH) and water (XSW) fractions on the day 18 were 266 ± 15.6 mg/dL and 306 ± 14.1 mg/dL respectively.

Ethanol fraction lowers the blood glucose level by up to 19% while water fraction decreases it by only 3%. Overall, it can be claimed that the ethyl acetate fraction of XSL (XSEA) contains substantial amounts of phenolic bioactive antioxidants which decreased the blood glucose level of diabetic mice. However, more comprehensive studies with a larger number of mice might be helpful to generalize these findings.

In the previous studies, the aqueous leaf extract of XSL was also used as an antidiabetic agent at a dose of 500 mg/kg and 250 mg/kg body weight respectively in alloxan-induced diabetic mice for 10 days and a significant reduction in blood glucose level was observed at the high dose of XSL aqueous extract (Mouhamad, 2022). Similarly, methanolic extract of XSL leaves prepared by the soxhlet apparatus was used to determine the antioxidant potential (*in-vitro*) and antidiabetic potential (*in-vivo*) in albino rats by oral administration at a dose of 200 mg/kg and 400 mg/kg body weight for 9 days (Umer et al., 2016). In another study hypoglycemic effect of ethanolic extract of XSL and its isolated compound were evaluated in alloxan-induced diabetic mice for 14 days and compared with Glibenclamide 10 mg/kg b. w; an antidiabetic drug (Ahmad et al., 2016). Leaf and fruit methanolic extract of *X. strumarium* obtained by the soxhlet method was used to measure the antidiabetic effect in diabetic mice by oral administration of 400 mg/kg b. w of extract for a period of 24 days (Harikumar et al., 2012). Methanolic extract of XSL stem was used to evaluate the hypoglycemic effect at doses of 100 mg/kg and 200 mg/kg body weight and antidiabetic potential was compared with Glibenclamide 0.6 mg/kg in Streptazocin-induced diabetic rats (Narendiran et al., 2011). By surveying the literature, it can be observed that there is no research work published about crude foliage fractionation and comparison of their antioxidant, antidiabetic potential, and variation in body weight. In the present research work, four fractions of XSL were obtained and their total phenolic content (TPC), antioxidant, and antidiabetic potential were studied. The antidiabetic potential of ethyl acetate fraction (XSEA)

fractions was comparable with standard Glibenclamide. By comparing results observed by all fractions, it has been observed that the XSEA fraction showed high TPC value, antioxidant potential and antidiabetic effect followed by the ethanol, petroleum ether, and aqueous fractions.

4 Conclusion

The aim of the current research was to assess the antidiabetic potential of different fractions of XSL foliage on diabetic mice. After 18 days of constant administration of XSL fractions, the blood glucose level of mice significantly decreased. These verdicts reinforced the traditional usage of the XSL foliage as an antidiabetic mediator as well as for the treatment of a number of ailments (Rahman et al., 2022). In order to boost insulin release from pancreatic cells, the conventional medication Glibenclamide has been used to treat diabetes for several decades. Several plant extracts were reported to exhibit hypoglycemic effects through stimulatory actions on insulin release, which is a possible pathway by which plant extracts lower blood glucose levels. This mechanism involves elevating the pancreatic insulin secretion from islets of Langerhans β cells or through its breakdown from the confined form (IfedibaluChukwu et al., 2020). According to some reports, other plants may also influence blood glucose levels by stimulating insulin release. Some wild herbs have chemical components that have hypoglycemic effects. There is evidence that certain types of plant-derived compounds, including carboxyatractyloside, chlorogenic acid, caffeic acid, and other phenolic compounds lower blood glucose levels. It has been found that plant's extracts and metabolites have pharmacological effects. The results obtained supported the use of XSL in conventional medical system to cure diabetes. To determine the precise pathway of the anti-diabetic activity of the XSL fractions, a more comprehensive pharmacological and chemical research with large number of subjects is required.

Data availability statement

The original contributions presented in the study are included in the article/Supplementary material, further inquiries can be directed to the corresponding authors.

Ethics statement

The animal study was approved by Institute of industrial biotechnology Government College University, Lahore. The study was conducted in accordance with the local legislation and institutional requirements.

Author contributions

AS conducted experiments and prepared the draft, MM conceptualized and supervised this research, and SS, SA, AR, and AA reviewed the draft. All the authors endorsed the final version of the article.

Funding

The authors declare financial support was received for the research, authorship, and/or publication of this article. The authors with affiliation are thankful to the Higher Education Commission of Pakistan for financial support of this research via NRPU project # 17549.

Conflict of interest

The authors declare that the research was conducted in the absence of any commercial or financial relationships that could be construed as a potential conflict of interest.

Publisher's note

All claims expressed in this article are solely those of the authors and do not necessarily represent those of their affiliated organizations, or those of the publisher, the editors and the reviewers. Any product that may be evaluated in this article, or claim that may be made by its manufacturer, is not guaranteed or endorsed by the publisher.

References

Ahmad, S., Wani, S. H., and Lone, S. A. (2016). Biochemical evaluation and hypoglycemic activity of ethanolic extract of *Xanthium strumarium* L. on normoglycemic and alloxan-induced diabetic mice. *Indian J. Appl. Res.* 2(4): 397–402.

Akhtar, S., Nasir, J. A., Ali, A., Asghar, M., Majeed, R., and Sarwar, A. (2022). Prevalence of type-2 diabetes and prediabetes in Malaysia: a systematic review and meta-analysis. *Plos one* 17 (1), 02631399–e263214. doi:10.1371/journal.pone.0263139

Arya, A., Abdullah, M. A., Haerian, B. S., and Mohd, M. A. (2012). Screening for hypoglycemic activity on the leaf extracts of nine medicinal plants: *in-vivo* evaluation. *E-Journal Chem.* 9 (3), 1196–1205. doi:10.1155/2012/103760

Benzie, I. F., and Strain, J. J. (1996). The ferric reducing ability of plasma (frap) as a measure of "antioxidant power": the frap assay. *Anal. Biochem.* 239 (1), 70–76. doi:10.1006/abio.1996.0292

Clayton, M. J., Davis, T. Z., Knoppel, E. L., and Stegelmeier, B. L. (2020). Hepatotoxic plants that poison livestock. *Veterinary Clin. N. Am Food Animal Pract.* 36 (3), 715–723. doi:10.1016/j.cvfa.2020.08.003

Dirar, A., Alsaadi, D., Wada, M., Mohamed, M., Watanabe, T., and Devkota, H. (2019). Effects of extraction solvents on total phenolic and flavonoid contents and biological activities of extracts from Sudanese medicinal plants. *South Afr. J. Bot.* 120, 261–267. doi:10.1016/j.sajb.2018.07.003

Elagdi, C., Bouaouda, K., Rahhal, R., Hsaine, M., Badri, W., Fougrach, H., et al. (2023). Phenolic compounds, antioxidant and antibacterial activities of the methanolic extracts of Euphorbia resinifera and Euphorbia echinus. *Sci. Afr.* 21 (2023), 017799–e1787. doi:10.1016/j.sciaf.2023.e01779

Fan, W., Fan, L., Peng, C., Zhang, Q., Wang, L., Li, L., et al. (2019). Traditional uses, botany, phytochemistry, pharmacology, pharmacokinetics and toxicology of *Xanthium strumarium* L.: a review. *Molecules* 24 (2), 359. doi:10.3390/molecules24020359

Ghahari, S., Alinezhad, H., Nematzadeh, G. A., Tajbakhsh, M., and Baharfar, R. (2017). Biochemical composition, Antioxidant and biological activities of the essential oil and fruit extract of *Xanthium strumarium* Linn. From Northern Iran. *J. Agric. Sci. Technol.* 19 (7), 1603–1616.

Guemmaz, T., Zerargui, F., Boumerfeg, S., Arrar, L., Aouachria, S., Khennouf, S., et al. (2018). Anti-hemolytic, anti-lipid peroxidation, antioxidant properties and acute toxicity of *Xanthium strumarium* leaves extracts. *Annu. Res. Rev. Biol.* 24 (3), 1–12. doi:10.9734/arrb/2018/40024

Harikumar, K., Shavari, S., Harshavardhan, G., Vishnupriya, M., Sandhya, B., and Rekha, B. (2012). Evaluation of antidiabetic activity of xanthium strumarium l.(compositae) in alloxan induced diabetic mice. *Int. J. Pharm. Ther.* 3 (3), 226–231.

IfedibaluChukwu, E. I., Aparoop, D., and Kamaruz, Z. (2020). Antidiabetic, anthelmintic and antioxidation properties of novel and new phytocompounds isolated from the methanolic stem-bark of Vernonia amygdalina Delile (Asteraceae). *Sci. Afr.* 10, 005788–e617. doi:10.1016/j.sciaf.2020.e00578

Kim, I.-T., Park, Y.-M., Won, J.-H., Jung, H.-J., Park, H.-J., Choi, J.-W., et al. (2005). Methanol extract of *Xanthium strumarium* L. possesses anti-inflammatory and anti-nociceptive activities. *Biol. Pharm. Bull.* 28 (1), 94–100. doi:10.1248/bpb.28.94

Kokil, G. R., Veedu, R. N., Ramm, G. A., Prins, J. B., and Parekh, H. S. (2015). Type 2 diabetes mellitus: limitations of conventional therapies and intervention with nucleic acid-based therapeutics. *Chem. Rev.* 115 (11), 4719–4743. doi:10.1021/cr5002832

Krupa, J., Sureshkumar, J., Silambarasan, R., Priyadarshini, K., and Ayyanar, M. (2019). Integration of traditional herbal medicines among the indigenous communities in Thiruvarur District of Tamil Nadu, India. *J. Ayurveda Integr. Med.* 10 (1), 32–37. doi:10.1016/j.jaim.2017.07.013

Ly, H. T., Truong, T. M., Nguyen, T. T. H., Nguyen, H. D., Zhao, Y., and Le, V. M. (2021). Phytochemical screening and anticancer activity of the aerial parts extract of *Xanthium strumarium* L. on HepG2 cancer cell line. *Clin. Phytoscience* 7 (1), 14–18. doi:10.1186/s40816-021-00252-w

Mawoza, T., Nhachi, C., and Magwali, T. (2019). Prevalence of traditional medicine use during pregnancy, at labour and for postpartum care in a rural area in Zimbabwe. *Clin. mother child health* 16 (2), 321. doi:10.24105/2090-7214.16.321

Mouhamad, R. S. (2022). Evaluate the influence of *Xanthium strumarium* L. Extract on blood sugar levels in healthy and diabetic mice. *J. Clin. Cases Rep.* 2022 (2), 72–81.

Nagappa, A., Thakurdesai, P., Rao, N. V., and Singh, J. (2003). Antidiabetic activity of *Terminalia catappa* Linn fruits. *J. Ethnopharmacol.* 88 (1), 45–50. doi:10.1016/s0378-8741(03)00208-3

Narendiran, S., Mohanambal, E., Kumar, P., Shankar, M., Kuttimani, T., and Vijayakumar, B. (2011). Study of anti diabetic and anti oxidant activities of methanolic extract of *Xanthium strumarium* (Linn.) stems on diabetic rats. *J. Pharm. Res.* 4 (10), 3728–3732.

Pillai, M. K., Thebe, P., and Matamane, R. P. (2023). Antioxidant activity of extracts from *Xanthium strumarium* – a medicinal plant from the Kingdom of Lesotho. *Int. J. Plant Based Pharm.* 3 (1), 114–122. doi:10.29228/ijpbp.23

Rahman, M. M., Dhar, P. S., Anika, F., Ahmed, L., Islam, M. R., Sultana, N. A., et al. (2022). Exploring the plant-derived bioactive substances as antidiabetic agent: an extensive review. *Biomed. Pharmacother.* 152 (2022), 1–20.

Scherer, R., and Godoy, H. (2014). Effects of extraction methods of phenolic compounds from *Xanthium strumarium* L. and their antioxidant activity. *Rev. Bras. Plantas Med.* 16 (1), 41–46. doi:10.1590/s1516-05722014000100006

Tallarida, R. J., and Murray, R. B. (1987). *Duncan multiple range test. Manual of pharmacologic calculations: with computer programs*. New York, NY: Springer, 125–127.

Umer, L., Tripathi, J., Muzafar, A., and Waseem, B. (2016). *In-vitro* antioxidant and antidiabetic activity of isolated fraction and methanolic leaf extract of xanthium strumarium. *World J. Pharm. Res.* 5 (7), 950–966.

Villaño, D., Fernández-Pachón, M. S., Moyá, M. L., Troncoso, A., and García-Parrilla, M. (2007). Radical scavenging ability of polyphenolic compounds towards DPPH free radical. *Talanta* 71 (1), 230–235. doi:10.1016/j.talanta.2006.03.050

frontiers | Frontiers in Chemistry

TYPE Original Research
PUBLISHED 04 January 2024
DOI 10.3389/fchem.2023.1298630

OPEN ACCESS

EDITED BY
Citlalli Gaona-Tiburcio,
Autonomous University of Nuevo León, Mexico

REVIEWED BY
José Luis Tristancho Reyes,
Technological University of Pereira, Colombia
Gabriela Roa Morales,
Universidad Autónoma del Estado de México, Mexico

*CORRESPONDENCE
Patricio J. Espinoza-Montero,
pespinoza646@puce.edu.ec

†These authors have contributed equally to this work and share first authorship

RECEIVED 22 September 2023
ACCEPTED 07 December 2023
PUBLISHED 04 January 2024

CITATION
Castillo-Cabrera GX, Pliego-Cerdán CI, Méndez E and Espinoza-Montero PJ (2024), Step-by-step guide for electrochemical generation of highly oxidizing reactive species on BDD for beginners.
Front. Chem. 11:1298630.
doi: 10.3389/fchem.2023.1298630

Step-by-step guide for electrochemical generation of highly oxidizing reactive species on BDD for beginners

G. Xavier Castillo-Cabrera[1†], Caroline I. Pliego-Cerdán[2†], Erika Méndez[2] and Patricio J. Espinoza-Montero[1*]

[1]Escuela de Ciencias Químicas, Pontificia Universidad Católica del Ecuador, Quito, Ecuador, [2]Facultad de Ciencias Químicas, Benemérita Universidad Autónoma de Puebla, Puebla, Mexico

Selecting the ideal anodic potential conditions and corresponding limiting current density to generate reactive oxygen species, especially the hydroxyl radical ($^{\bullet}$OH), becomes a major challenge when venturing into advanced electrochemical oxidation processes. In this work, a step-by-step guide for the electrochemical generation of $^{\bullet}$OH on boron-doped diamond (BDD) for beginners is shown, in which the following steps are discussed: i) BDD activation (assuming it is new), ii) the electrochemical response of BDD (in electrolyte and ferri/ferro-cyanide), iii) Tafel plots using sampled current voltammetry to evaluate the overpotential region where $^{\bullet}$OH is mainly generated, iv) a study of radical entrapment in the overpotential region where $^{\bullet}$OH generation is predominant according to the Tafel plots, and v) finally, the previously found ideal conditions are applied in the electrochemical degradation of amoxicillin, and the instantaneous current efficiency and relative cost of the process are reported.

KEYWORDS

electrochemical oxidation, highly oxidizing reactive species, sampled current voltammetry, boron-doped diamond, Tafel plot, amoxicillin degradation

1 Introduction

When delving into the wide world of advanced oxidation processes (AOPs), we found an overwhelming amount of information that can be frustrating for a beginner. All these technologies mainly seek the generation of the hydroxyl radical ($^{\bullet}$OH) and other highly oxidizing reactive species (HORS) to carry out highly efficient oxidation processes. Advanced electrochemical oxidation (AEO) is one of the most studied AOPs for the oxidation/degradation of organic matter in aqueous media (Martínez-Huitle et al., 2015; Bessegato et al., 2021; Hand and Cusick, 2021; Pierpaoli et al., 2021; Espinoza-Montero et al., 2023). AEO consists of applying a polarization potential to a conductive substrate (metal or semiconductor) to produce HORS, mainly $^{\bullet}$OH if possible, on the electrode–solution interface (Ganiyu et al., 2021; Lee et al., 2022; Xu et al., 2023b). One of the most appreciated electrodes for AEO is the boron-doped diamond (BDD) electrode. BDD is a p-type semiconductor due to the chemical nature of boron, as they are impurity/dopant donors, so in thermal equilibrium, there is an imbalance of charge carriers in the valence and conduction bands, with the positive holes being the majority carriers (Yokoya et al., 2005; Yang et al., 2019). As an electrode, BDD is a very versatile material as it has unique electronic properties. It is a non-active electrode; *i.e.*, its chemical structure is not compromised by the

redox processes to which it may be subjected, although its reticular terminations are susceptible to slight changes during oxidation and reduction (Berenguer et al., 2019). As it has a very wide potential, this electrode has been used for multiple applications in electroanalytical chemistry (Wei et al., 2011b; Joshi et al., 2022), electrosynthesis (Ivandini and Einaga, 2017; Lips and Waldvogel, 2019), and AEO for water treatment (Cisneros-León et al., 2023).

For water treatment, electrochemical oxidation can take advantage of the complexity of mixtures of organic and inorganic species that can be found in typical contaminated water since, depending on the composition of the inorganic electrolyte in the system to be treated, the so-called HORS can be generated (Wen et al., 2017; Xu et al., 2021; Ahmed et al., 2022; Parvulescu et al., 2022; dos Santos et al., 2023; Mousset, 2023). Most HORS are "free" radicals and detrimental to most biological systems; the opposite is true for advanced oxidation processes, where they contribute to the oxidation of organic and inorganic matter (Murphy et al., 2022; Cisneros-León et al., 2023). HORS covers a wide spectrum of inorganic radicals, ions, and neutral molecules in aqueous media whose redox potentials are varied (Ross and Neta, 1982; Armstrong et al., 2015). Directly or indirectly, electrochemical oxidation can generate reactive oxygen species (ROS) such as the superoxide radical ($O_2^{\bullet-}$), singlet oxygen ($^1O_2$), hydrogen peroxide (H_2O_2), and the strongest oxidant, the hydroxyl radical ($^{\bullet}OH$) (Xie et al., 2022). On the other hand, in the presence of nitrates and nitrites, through the reaction of the electrogenerated $^{\bullet}OH$, reactive nitrogen species (RNS) such as mono-, di-, and trioxide nitrogen radicals ($NO^{\bullet}$, $NO_2^{\bullet}$, and $NO_3^{\bullet}$) can be obtained (Wu et al., 2020; Rayaroth et al., 2022). Likewise, in the presence of sulfates, sulfites, and carbonates, sulfate ($SO_4^{\bullet-}$) and sulfite ($SO_3^{\bullet-}$) radicals, the persulfate anion ($S_2O_8^{2-}$), and the carbonate radical ($CO_3^{\bullet}$) can be generated *in situ*, and in the presence of chlorides or chlorites, reactive chlorine species (RCS) are very common, such as the chlorine radical ($Cl^{\bullet}$) and the oxychloride radical ($ClO^{\bullet}$) (Ganiyu and Martínez-Huitle, 2019; Ganiyu et al., 2021; Zhou and Xiao, 2022). In addition, reactive phosphate species (RPS) are generated indirectly by reacting $^{\bullet}OH$ with phosphates, producing phosphate radicals in three acidic forms, the $H_2PO_4^{\bullet}$ radical being the most powerful oxidizing species of this type (Weiss et al., 2008). All these species can contribute greatly to the oxidation of organic and inorganic pollutants, achieving a predominant synergistic effect, or they can have the opposite effect since they all compete in coupled reactions in electrocatalysis.

This work intended to provide a step-by-step guide aimed primarily at beginners in the investigation of electrode properties in common electrolytic systems, with emphasis on the HORS that can be generated in the medium and that compete in catalysis. First, an approach from the existing theory in this field is addressed, and then, a real example is given using the BDD electrode in a known electrolytic environment.

2 Step-by-step electrooxidation on BDD

To experimentally determine the optimal operating conditions at AEO, some fundamental electrochemical tests in known redox environments must be considered. In the following, we will carefully describe the suggested minimum steps that will allow us to develop our understanding of the optimal conditions for electrolysis at larger scales.

2.1 Electrode activation and cleaning (if required)

BDD is a "non-active" electrode when acting as an anode, and the HORS that are generated when a high oxidation overpotential is applied do not drastically change their chemical nature; this property makes it a unique material and is the basis for a large number of applications including in the area of environmental remediation (Sánchez-Montes et al., 2020; Carrera-Cevallos et al., 2021; Cisneros-León et al., 2023; Long et al., 2023). Therefore, studying the surface terminations of the crystal lattice of this material becomes key and is addressed in this section.

Diamond is a purely insulating material since its crystal lattice is composed of hybridized C-sp^3. However, by introducing impurities of boron or nitrogen atoms during its synthesis using controlled methods at high temperatures and pressure, such as chemical vapor deposition (CVD) (Macpherson, 2015; Sun et al., 2021), a conducting, semiconducting, or superconducting material is obtained as a result of two factors; the first is that by introducing boron (or nitrogen) atoms, carriers that previously formed bonds are "released" and move freely through the lattice and participate in conduction in the BDD (Yokoya et al., 2005; Yang et al., 2019). On the other hand, when impurities are introduced to the diamond, it changes the hybridization of certain carbon atoms (from C-sp^3 to Csp^2), which extends to the surface terminations of the crystal lattice. The sp^2 (C-sp^2) hybridization (graphitic carbon) is the one that contributes the most to the conductive properties of BDD. Therefore, the surface termination of the BDD is a mixture of C-sp^3 and C-sp^2. When the surface termination is predominantly C-sp^3, the BDD is said to have an H-termination, while when the surface termination is C-sp^2, it is said that the surface termination is predominantly oxygen or oxygenated organic functional groups (Medeiros De Araújo et al., 2014; Garcia-Segura et al., 2015). Surface modifications of BDD from C-sp^2 to C-sp^3 or *vice versa* are possible through different controlled experimental methods. BDD electrode manufacturers often prefer methods that are as effective as their cost, *e.g.*, oxygen plasma for oxygenated surfaces and hydrogen plasma for hydrogenated surfaces, but these are not practical for use in most laboratories (Kasahara et al., 2017; Einaga, 2022). On the other hand, surface modification of BDD electrochemically is simpler and cheaper; *e.g.*, anodic polarization generates an oxygen surface termination, and cathodic polarization generates a hydrogen surface termination, for which a power source and a two-electrode cell are required (Figure 1A). This simple assay is commonly performed in strong acid media (H_2SO_4, $HClO_4$, and HNO_3) at moderate concentrations. The transitions from H to O or *vice versa*, in addition to the intrinsic equilibrium of adsorption–desorption of the gases produced on the surface—O_2 at the anode and H_2 at the cathode—are achieved as long as the redox potentials of the organic forms present in the lattice are reached; *i.e.,* care must be taken to control the DC density applied to the cell as well as the time for which the electrode is exposed to oxidation or reduction.

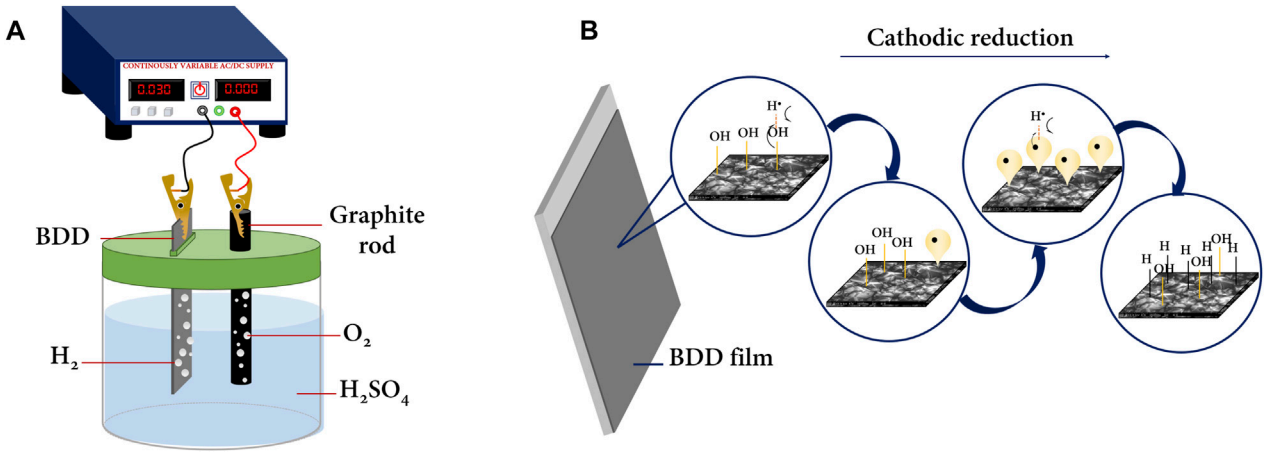

FIGURE 1
(A) Two-electrode cell for electrolysis in an acidic medium performed in lab. **(B)** BDD surface transition by cathodic reduction, adapted from the work of Einaga (2022).

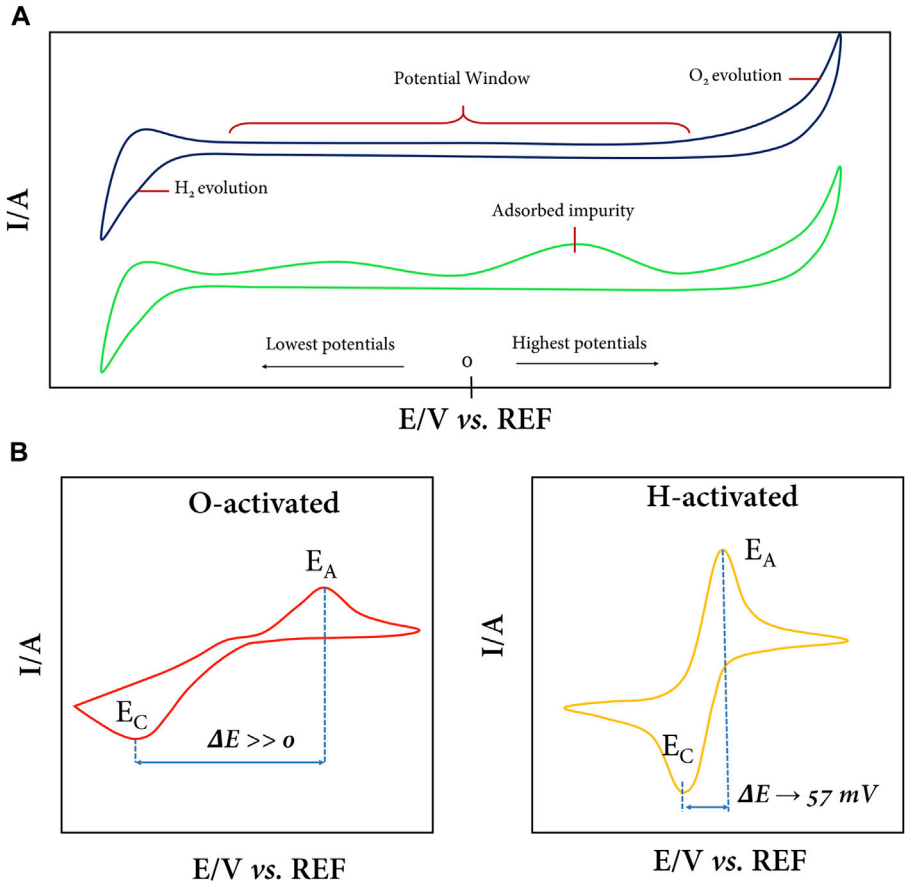

FIGURE 2
(A) Voltammetric profiles of the full potential window of the BDD in the presence of an electrolyte. Without the presence of contaminants or adsorbed impurities, only the oxygen and hydrogen evolution peaks are observed (top), while on a soiled surface, peaks are present in the capacitive zone (bottom). **(B)** Typical BDD CVs in the ferri/ferro-cyanide redox couple for an oxygenated (left) and hydrogenated (right) surface.

Einaga (2022) proposed a mechanism for the transition from oxygenated to hydrogenated BDD terminations. In essence, there is a homolytic contribution of hydrogen and the –O–H group from the BDD surface, yielding a good leaving group (water). In this way, the carbon formerly bonded to the R–CH_2–O–H group leaves a hybrid orbital with an unpaired electron ripe to overlap with another atomic hydrogen and obtain surface groups with hydrogen-bonded carbons (R–CH_2–H) (Figure 1B). In addition, electrolysis in a strong acidic medium serves to clean impurities from BDDs prior to use, if required. It is very common to adsorb carbon impurities generated during the synthesis of the BDD or by the adsorption of contaminants from the environment or from contact with other surfaces. Therefore, it is common that during the manufacture of BDDs, especially bipolar (double-sided modified) BDDs, a thin layer of hybrid material with major impurities remains, and electrochemical cleaning is useful to remove this layer, as recommended by the manufacturers themselves. Cleaning, which should be understood interchangeably as surface activation of the BDD, is a soft electrochemical method that does not compromise the crystalline integrity of the BDD, much less of the substrate on which the doped diamond layer has been deposited, which is commonly Nb or n-type Si.

2.2 Electrode characterization

By cyclic voltammetry (CV), the cleanliness and surface termination of the BDD can be evaluated, as shown in Figure 2A. The BDD has an impurity-free surface (Figure 2A top) when no peak appears in the potential range of the capacitive region, and only the extreme peaks of oxidation evolution (more positive potentials) and hydrogen evolution (more negative potentials) should be detected. However, additional signals characteristic of surface carbon impurities often appear when the electrode is not properly cleaned/activated (Figure 2A bottom). These CV profiles are typically recorded in the presence of the electrolyte only, commonly Na_2SO_4, H_2SO_4, and phosphate buffer solutions, in dilute concentration (0.1 M). Although it is also possible to use strong bases (NaOH or KOH) as the supporting electrolyte to generate these voltammograms, caution must be exercised when using a suitable reference electrode (Zoski, 2007).

CV, in addition to being useful for calculating the electrode area by applying the Randles–Sevcik equation, is also useful for evaluating the predominant surface termination of H or O on BDD after electrochemical treatment. For this purpose, one can use the $[Fe(CN)_6]^{3-}/[Fe(CN)_6]^{4-}$ redox couple (or others) in dilute concentration and in a suitable electrolyte medium, typically KCl in a 1:100 ratio, although it is common to use more concentrated electrolyte solutions to avoid potential losses due to Ohmic drop (Suffredini et al., 2004; Actis et al., 2008; Zanin et al., 2014; Cheah and Chernev, 2021; Bard et al., 2022; Zheng, 2023). Figure 2B shows the typical CVs of BDD electrodes in the ferro/ferri-cyanide redox couple. At an electrode with oxygen surface terminations (Figure 2B left), the $[Fe(CN)_6]^{3-}/[Fe(CN)_6]^{4-}$ redox process becomes very slow, and the separation of anodic potential (E_a) and cathodic potential (E_c) peaks is enormous; *i.e.*, ΔE_p (E_c- E_a) takes large values. On the contrary, in Figure 2B (right), a typical CV of a BDD electrode with H-terminations predominant on the surface is observed, where the redox couple response is fast, chemically and electrochemically reversible, ΔE_p is close to 57 mV, and the width at half on the forward scan of the peak is close to 59 mV (Elgrishi et al., 2018). In practice, it is crucial to define which surface is of interest depending on the intended application of the BDD electrode (Oliveira et al., 2010; Kondo, 2022). For example, if a semiconductor-photocatalyst-modified electrode is required, it is ideal to have an oxidized surface as the physical and chemical interactions are stronger for oxygen with the semiconductor metal. On the other hand, if bare electrode electrocatalysis is what is sought, a predominantly hydrogenated surface is ideal since charge transfer at the solid–liquid interface is favored.

2.3 Selecting parameters

Once BDD is electrochemically characterized to "micro-scale," the next step is the search for the "ideal" parameters to carry out electrochemical oxidation with the greatest efficiency, driven mainly by HORS, which will be discussed in depth later. AEO is a complex process involving the balance of several variables that must be carefully controlled in practice (Ganiyu et al., 2021; Bany Abdelnabi et al., 2022; Lee et al., 2022; Xu et al., 2023a; Zheng, 2023). In this section, we will focus mainly on the potential and/or current density to be applied to the system and how the electrochemical test should be carried out to find it. Our purpose is to systematically relate the Tafel analysis to the different electrolyte species that may be present and their consequent formation of HORS at the BDD electrode. For the construction of the Tafel curves, we will use voltammograms generated by sampled current voltammetry, a very effective and easy-to-apply technique.

2.3.1 Tafel analysis

To monitor an electrochemical process quantitatively and from the point of view of kinetics, the Tafel analysis is often very useful for certain processes (Bard et al., 2022; Shih et al., 2022). The equation that quantitatively relates the potential to the current of a specific system is called the Tafel equation (Eq. 1), and it was first designed to study the hydrogen evolution reaction (HER) (Tafel, 1905; Petrii et al., 2007; Fang and Liu, 2014; Jung et al., 2022).

$$\eta = a - b\ln j \quad or \quad \eta = \frac{RT}{\alpha F}\ln i_0 - \frac{RT}{\alpha F}\ln j, \tag{1}$$

where η is the overpotential, which is calculated from the algebraic subtraction of the potential applied (E_{app}) to the working electrode and the open-circuit potential (E_{OCP}), *i.e.*, the equilibrium potential that is specific for each electrolyte in solution. The Tafel plot is obtained by plotting ln j vs. η, where b is the Tafel slope(s), which is of interest to us because of its kinetic significance (Fang and Liu, 2014).

To study the kinetics of redox processes in electrochemistry, the rotating disk electrode is employed since the speed of revolution is controlled and the diffusional and capacitive influences of the system are eliminated, thus allowing the kinetic parameters and charge transfer constants to be calculated with high reproducibility (Chen et al., 2020). However, not all laboratories have this

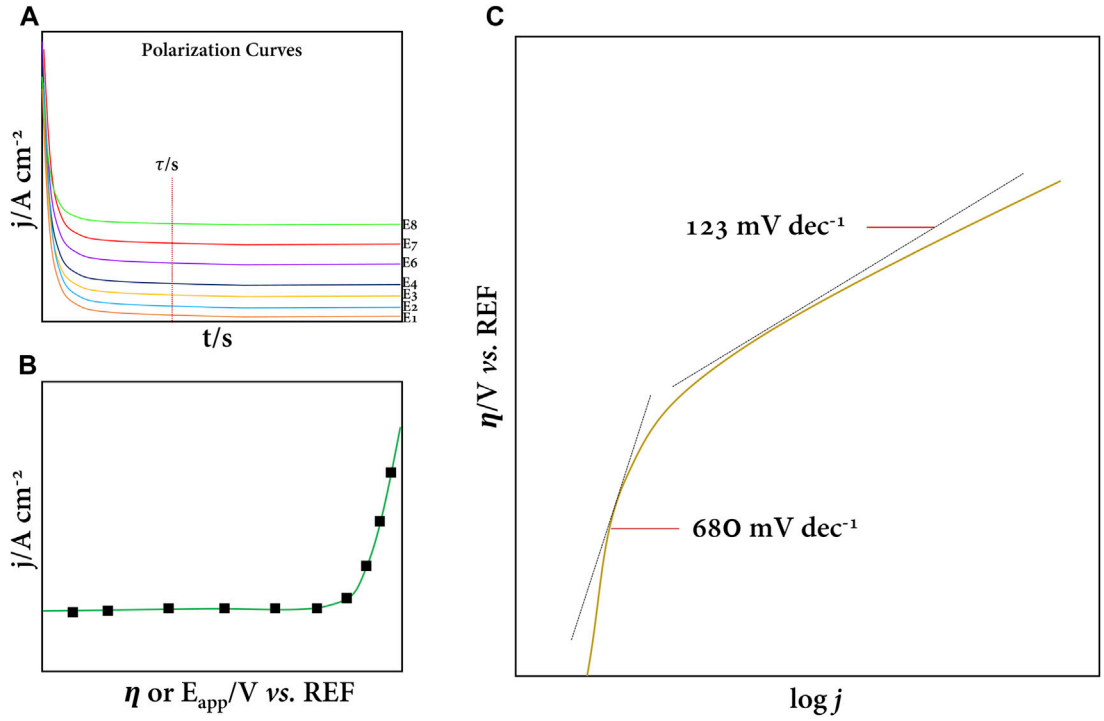

FIGURE 3
(A) Typical polarization curves at oxidation overpotentials in a given electrolyte. **(B)** j vs. η curve corresponding to OER. **(C)** Tafel plot for OER. **(C)** Adapted from the work of Kapałka et al. (2008).

sophisticated system at their disposal. Instead, sampled current voltammetry (SCV) is a useful technique that frees us from this experimental drawback, and the kinetics of reversible or irreversible reactions can be studied with the Tafel analysis without major problems (Soares et al., 2020; Rodríguez and Denuault, 2021).

An SCV assay consists of subjecting the working electrode to various polarization potentials—in a specific range and in the medium of interest—during a specific pulse time (chronoamperometry); in this sense, the so-called polarization curves are obtained (Figure 3A). The polarization curves are used to select the current density corresponding to each potential at a given time constant (τ), thus plotting the η vs. j or E_{app} vs. j curve (Figure 3B) and applying the Tafel analysis to the data obtained.

Kapałka *et al.* (2008) pioneered the study of the kinetics of the oxygen evolution reaction (OER) at a BDD electrode (Figure 3C). They showed that in the Tafel analysis, there were two well-defined slopes corresponding to independent, one-to-one electron transfer processes. For our interest and depending on the electrolyte, the Tafel analysis gives us a hint of the optimal potential to produce HORS before oxygen evolution is favored (thermodynamically). Therefore, this kinetic study will allow us to select a wide range of anodic potentials and evaluate the production of HORS, as discussed below.

2.3.2 HORS at BDD

A further digression is necessary here to address the HORS generated on the BDD. Depending on the electrolyte in which the electrolysis is carried out, different reactive species capable of efficiently oxidizing organic molecules may coexist, some more than others. We cannot begin this discussion without first analyzing the ROS and, in essence, the hydroxyl radical ($^{\bullet}$OH). This radical is the first intermediate of the OER from water splitting (Reaction 1), and it is generated in a process favored by kinetics rather than thermodynamics; i.e., large overpotentials are required for its formation on the BDD surface (Siahrostami et al., 2017; Zhu, 2019; Xie et al., 2022).

$$BDD + H_2O + E_{app} \rightarrow BDD(OH^{*}) + H^{+} + 1e^{-} \quad (1)$$

BDD (OH*) refers to the $^{\bullet}$OH adsorbed on the surface of the BDD, specifically on the active site, which plays a crucial role (Moreira et al., 2017; Vogt and Weckhuysen, 2022). $^{\bullet}$OH is a highly reactive and unstable species whose lifetime is estimated to be a few nanoseconds (Moreira et al., 2017). The high reactivity of the $^{\bullet}$OH is explained by its unpaired electron in an antibonding orbital (π^{*}) of an oxygen atom located at high energy (Figure 4). This instability (in energy) means that its electron easily pairs with an organic species to form covalent bonds in the electrooxidation pathway (Imlay, 2003; Krumova and Cosa, 2016). Its oxidizing power (~2.73 V vs. NHE), second only to fluorine, is due to its high tendency to capture electrons and stabilize the antibonding orbital. Therefore, it is capable of non-selectively oxidizing a wide variety of organic pollutants as long as the redox potential of the target molecules is aligned with the redox potential of the radical at the interface (Armstrong et al., 2015).

On the other hand, molecular oxygen in its fundamental state is triplet ($^3O_2$) and is dissolved in the medium or generated by the electrolysis of water; it can trigger reduction reactions to generate other highly reactive species but with lower oxidizing power than

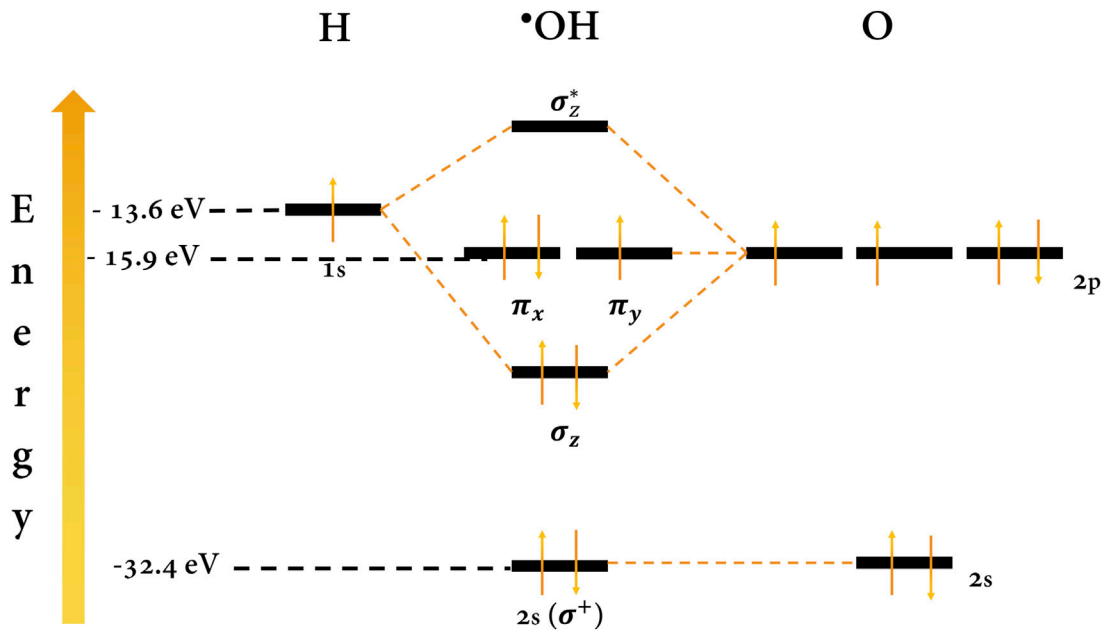

FIGURE 4
Molecular orbital diagram for the •OH. Energy values were taken from the work of Mann et al. (2000).

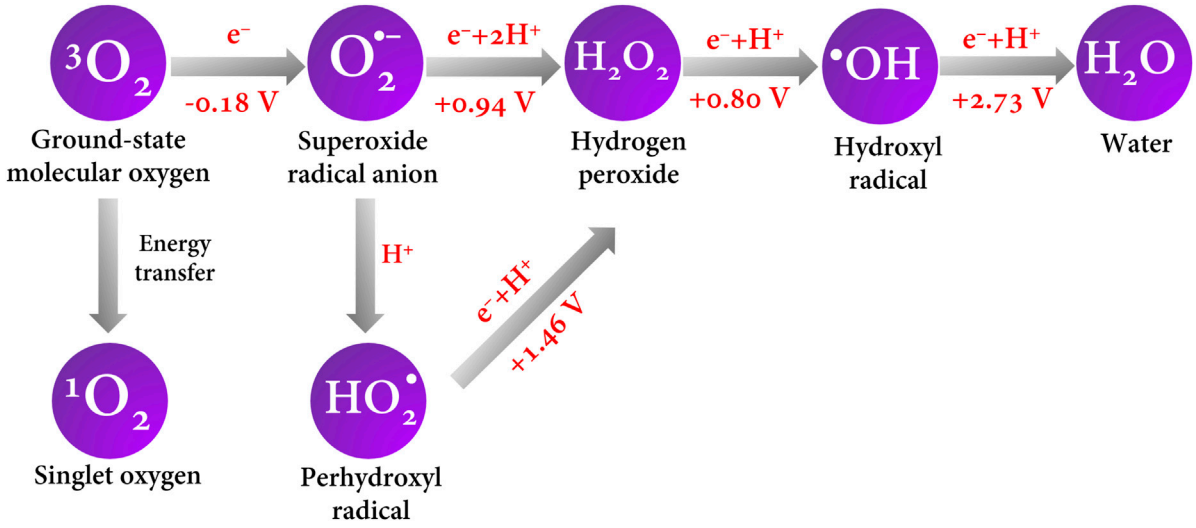

FIGURE 5
ROS formation by electron and energy transfer. Redox potential values are reported vs. NHE and were taken from the work of Armstrong et al. (2015).

the •OH (Krumova and Cosa, 2016). When O_2 is reduced by the conduction band electrons of the BDD, on transfer of a first electron, it produces the superoxide anion radical $O_2^{\bullet-}$ (E^0 = −0.18 V vs. NHE) (Armstrong et al., 2015; Hayyan et al., 2016). In brief, Figure 5 shows a schematic of the ROS generated by electron transfer and their redox potentials.

In short, the •OH, due to its oxidizing power, is the species that is sought to be generated efficiently in AEO, and it will be seen from now on that this radical plays a crucial role in the generation of other highly reactive oxidizing species (Gligorovski et al., 2015). As for pH, it is also a parameter that greatly influences the generation of reactive species and electrocatalysis in general. We said that the •OH production process is kinetically favorable, where pH influences the rate of charge transfer (Tao et al., 2019; Zhang et al., 2020). At low pH, the concentration of H_3O^+ increases, which favors the generation of •OH. H_3O^+ can react with electrons from the electrode (depending on the electrode potential) and produce atomic hydrogen, which is highly reactive and reacts with water to produce •OH (Katsounaros et al., 2014). Very low pH can also be detrimental to the electrode as it can create a passivation layer on the electrode surface that limits charge transfer; in BDD, this is not a

drawback as its high stability in strong acid environments frees it from this issue (Xie et al., 2022). Other considerations must be taken with respect to pH since the stability of the target molecule to be degraded is also a tremendously influential factor, as well as the concentration of the electrolyte species in the solution (Fornaciari et al., 2022).

The utility of ions in a solution is imperative for the vast majority of electrochemical processes (Bard et al., 2022). In the process at stake here, the supporting electrolyte plays a dual role since it is not only responsible for mitigating the migration of the electroactive species and serving as an ionic conductor in the medium but the ions can also react instantaneously with the electrogenerated $^{\bullet}$OH and produce other chemical species of high reactivity and, sometimes, high oxidizing power (Kim et al., 2018; Hand and Cusick, 2021). Many authors refer to this process as the "activation" of a certain species since in the absence of any perturbation, the ions are not a major threat to organic pollutants (Lin and Deng, 2021). In a medium containing sulfate ions, activation of the sulfate radical ($SO_4^{\bullet-}$) and other reactive sulfate species is very likely. This radical anion is mainly produced by the oxidation of (SO_4^{2-}) in the presence of $^{\bullet}$OH adsorbed on the BDD in a 1-electron transfer process (Reaction 2). Another species, the persulfate anion ($S_2O_8^{2-}$), can be generated by direct oxidation on the surface of the BDD or by oxidation of sulfate by the $^{\bullet}$OH in a 2-electron transfer process (Reaction 3) or by direct combination of two sulfate radicals (Reaction 4) (Oh et al., 2016; Lee et al., 2020; Ganiyu et al., 2021; Araújo et al., 2022).

$$\mathrm{BDD(OH^*) + SO_4^{2-} \rightarrow BDD(SO_4^{\bullet-}) + OH^-} \quad (2)$$

$$\mathrm{2BDD(OH^*) + 2SO_4^{2-} \rightarrow BDD(S_2O_8^{2-}) + 2H_2O} \quad (3)$$

$$\mathrm{2BDD(SO_4^{\bullet-}) \rightarrow BDD(S_2O_8^{2-})} \quad (4)$$

In the literature, the vast majority of works that seek to treat polluted water by electrochemical oxidation use sulfate-based electrolytes, typically sodium or potassium sulfate, or sulfuric acid. Why is this? This can be accounted for by the oxidizing power of this radical, which ranges from 2.5 to 3.1 V vs. NHE; these values compete with the oxidizing power of the $^{\bullet}$OH (Ganiyu and Martínez-Huitle, 2019; Ganiyu et al., 2021; Araújo et al., 2022). When comparing these two species, both radicals have an affinity for capturing electrons in redox processes since they have unpaired antibonding molecular orbitals in oxygen, while the electronegativity of S is greater than that of O, and the polarization of the bond is more efficient (Lin and Deng, 2021). Therefore, if these two species can coexist in a moderate "balance," the treatment of contaminated water can be very efficient. Understanding the oxidation power of these species from theory can be a simple issue, but, in practice, it is not so since variables such as pH, applied potential and current density, temperature, and contaminants must be controlled.

Reactive chlorine species (RCS) are produced in an electrolytic chloride environment. Mainly, the chlorine radical ($Cl^{\bullet}$) is the outstanding species of this group with an oxidation power of approximately 2.43 V vs. NHE (Armstrong et al., 2015). It is produced by indirect oxidation, *i.e.*, by the oxidation of Cl^-at the electrode surface by the adsorbed $^{\bullet}$OH (Reaction 5) (Mostafa et al., 2018). On the other hand, the hypochlorite radical ($ClO^{\bullet}$), also a highly reactive species of chlorine, is produced by the same oxidation reaction by the $^{\bullet}$OH (Reaction 6) and has a relatively low oxidation power (1.39 V vs. NHE) (Armstrong et al., 2015). The $^{\bullet}$OH can trigger reactions with chloride in the medium to produce hypochlorite, chlorite, chlorate, and perchlorate anions, but they are not highlighted here since their oxidizing power is overshadowed by their toxicity, and reactions producing these species can be found anywhere (Ganiyu et al., 2021; Choo et al., 2022; Barnum and Coates, 2023).

$$\mathrm{BDD(OH^*) + Cl^- \rightarrow BDD(Cl^{\bullet}) + OH^-} \quad (5)$$

$$\mathrm{BDD(OH^*) + ClO^- \rightarrow BDD(ClO^{\bullet}) + OH^-} \quad (6)$$

Similarly, reactive phosphate species (RPS) are produced by hydroxyl radical chain reactions (Reactions 7–9). The phosphate radical ($PO_4^{\bullet 2-}$) can exist in its three acidic forms, with the radical ($H_2PO_4^{\bullet}$) having the highest oxidizing power, approximately 2.75 V vs. NHE (Armstrong et al., 2015). The other radical species are less reactive for both redox processes and acidic proton capture (Ross and Neta, 1982; Weiss et al., 2008).

$$\mathrm{BDD(OH^*) + H_3PO_4 \rightleftarrows BDD(H_2PO_4^{\bullet}) + H_2O} \quad (7)$$

$$\mathrm{BDD(OH^*)H_2PO_4^- \rightleftarrows BDD(H_2PO_4^{\bullet}/\,H_2PO_4^{\bullet-}) + OH^-/H_2O} \quad (8)$$

$$\mathrm{BDD(OH^*) + HPO_4^{2-} \rightleftarrows BDD(HPO_4^{\bullet-}/\,PO_4^{\bullet 2-}) + OH^-/H_2O} \quad (9)$$

Finally, it is not difficult to imagine that reactive nitrogen and carbon species are produced by the indirect oxidation of the hydroxyl or sulfate radical with nitrates, nitrites, and carbonates to generate nitrogen di- and trioxide radicals ($NO_2^{\bullet}$, $NO_3^{\bullet}$), as well as the carbonate radical ($CO_3^{\bullet-}$) (Reactions 10–12). Among these species, the nitrogen trioxide radical is the strongest oxidant (2.5 V vs. NHE) (Armstrong et al., 2015). Despite being weaker than the hydroxyl radical, they can oxidize on one-electron transfer reactions a wide variety of organic and inorganic molecules, such as phenols, anilines, sulfur compounds, and some metal ions (Ross and Neta, 1982; Fang et al., 2014; Rayaroth et al., 2022).

$$\mathrm{BDD(OH^*) + NO_2^- \rightleftarrows BDD(NO_2^{\bullet}) + OH^-} \quad (10)$$

$$\mathrm{BDD(OH^*) + NO_3^- \rightleftarrows BDD(NO_3^{\bullet}) + OH^-} \quad (11)$$

$$\mathrm{BDD(OH^*) + CO_3^{2-} \rightleftarrows BDD(CO_3^{\bullet-}) + OH^-} \quad (12)$$

In this section, we left for a while the main aim of this work and tried not to digress in exposing all the species that can exist in an electrochemical reaction medium; instead, we emphasized the main highly reactive oxidizing species of each type depending on the electrolyte (Figure 6). In practice, it is obvious that after the ROS and, especially, $^{\bullet}$OH, the other species are the consequence of the redox reaction of the latter with the ions in solution; *i.e.,* the other species can be regarded as trapping hydroxyl radicals. This is because $^{\bullet}$OH is not selective and reacts simultaneously with whoever stabilizes its unpaired electron most quickly and efficiently. All these species highlighted above compete in electrocatalysis, and attributing the major contribution to pollutant degradation to just one of them would be a mistake. Instead, emphasis should be placed on controlling the other variables that take place in electrochemical oxidation.

3 Beyond the lab

3.1 Limiting current and limiting potential

All the previous analyses can be carried out successfully with accuracies that slightly deviate from the theory, but when the

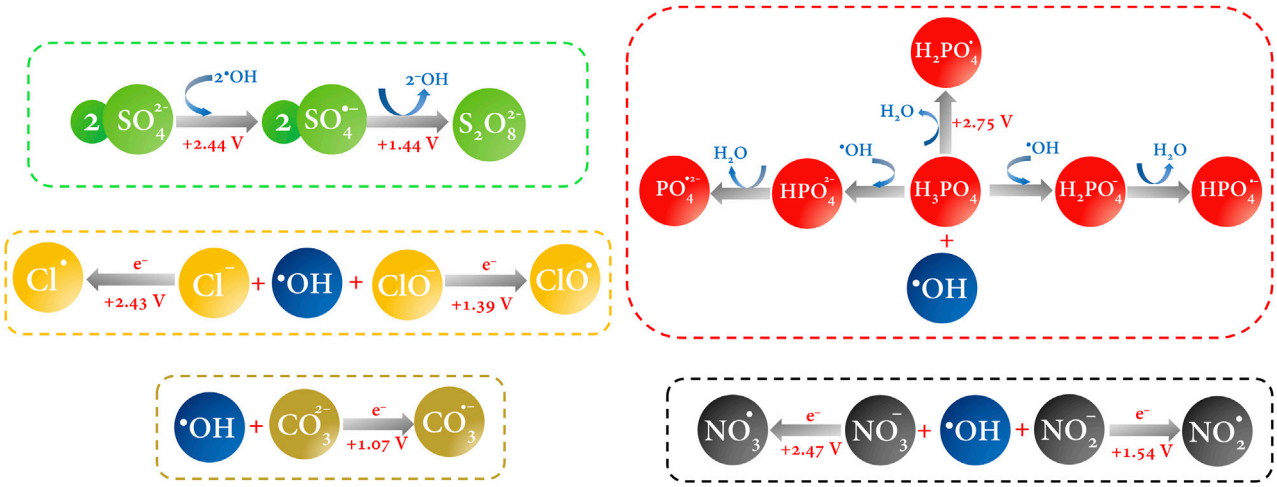

FIGURE 6
HORS generation pathway by reaction of the $^{\bullet}$OH in a one-to-one electron transfer. Redox potential values are reported vs. NHE and were taken from the work of Armstrong et al. (2015).

results are transferred to a scale larger than that of the laboratory, it often involves complications that lead to results that deviate greatly from those predicted at the micro-scale, but are not wrong for the most part. These noticeable differences, which are often found at a real scale, are mainly due to the electrochemical cell and the intrinsic energy consumption. That is, when testing electrode behavior, electrolyte effects, and cell configuration in the laboratory, it is common to use simple systems on account of having known and small electrode areas, solution volumes no larger than 25 mL, and simple cell configurations, usually batch type (Bard et al., 2022). In the pre-pilot scale, all the dimensions of the upstream electrochemical components are increased. This increase has important implications for current and potential density. Thus, at scales larger than the laboratory, it is common to have control of the experimental limiting current, *i.e.*, the current that maximizes the charge transfer efficiency of the redox reaction occurring at the electrode surface. Typically, the limiting current can be found in electrooxidation systems as a function of time in the chemical oxygen demand (COD) (Eq. 2) (Wei J. J. et al., 2011; Ochoa-Chavez et al., 2018).

$$i_{lim} = i_{lim}(t) = 4Fk_mCOD(t), \quad (2)$$

where i_{lim} is the limiting current, F is Faraday's constant, and k_m is the mass transfer coefficient. For microelectrode or rotating disk arrays, the limiting current can be calculated by SCV in known redox systems, and its procedure can be found elsewhere (Soares et al., 2020; Bard et al., 2022).

Then, when scaling a system, it is not strange that current densities or overpotentials reach values higher than those predicted by Tafel curves or voltammetric profiles in various electrolytes (Moreira et al., 2017). This is because the diffusion flow of the species within the solution towards the electrode surface changes and, therefore, the energy barrier to be overcome also increases; on the other hand, the potential loss by Ohmic drop also increases significantly due to the resistance of the solution and the micro- and nano-bubbles that evolve on the surface, as well as the presence of the target molecule to be electrochemically oxidized (Petrii et al., 2007; Lee and Bazylak, 2021; Zheng, 2023). In practice and when disk electrodes are not available, the limiting potential and its limiting current are controlled in a non-analytical way (at least for now); *i.e.*, when the electrooxidation test is carried out, the electrode potential is progressively increased, and the current density circulating in the reactor is controlled, and when the proportionality between the potential and current is lost, the limiting current has been exceeded; in other words, the maximum potential value that the system supports so that the charge transfer is also maximum corresponds to the current limit where the process is optimized.

3.2 Instantaneous current efficiency and energy consumption

Additionally, another parameter of interest when scaling certain processes is the determination of the instantaneous current efficiency (ICE), which gives us information regarding the optimum range of applicability of a process (Comninellis and Pulgarin, 1991; Xing et al., 2018); this can be calculated by the following equation:

$$ICE = \frac{[COD_t - COD_{t+\Delta t}]FV}{8I\Delta t}, \quad (3)$$

where $(COD)_t$ and $(COD)_{t+\Delta t}$ are the chemical oxygen demand at times t and t + Δt (in g O_2 dm^{-3}), F is Faraday's constant, V is the volume of electrolyte (dm^3), and I is the applied current (A).

Furthermore, the energy consumption of the process is also relevant since it gives us a picture of the efficiency from the perspective of energy expenditure and also helps us to optimize

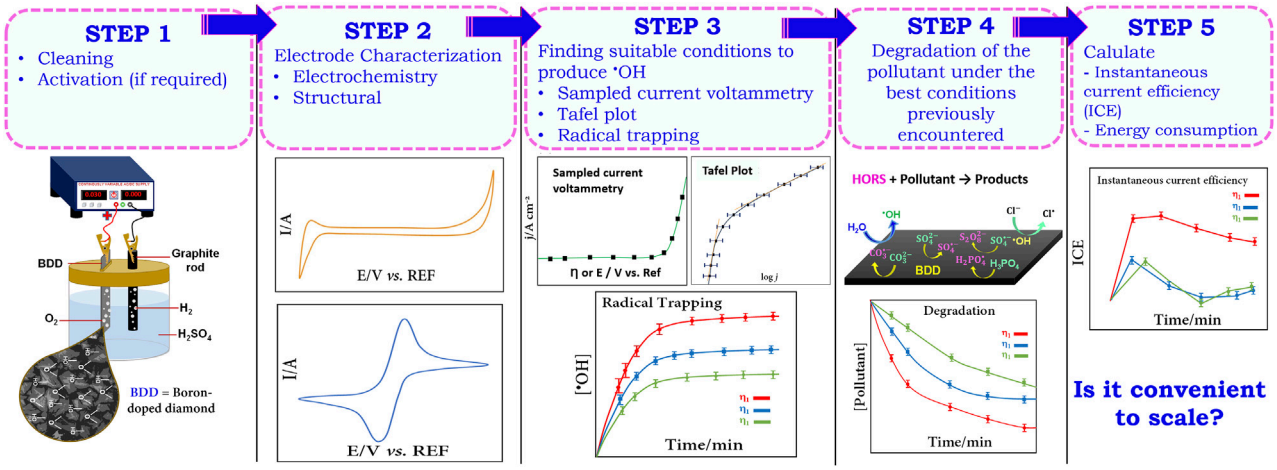

SCHEME 1
Systematic step-by-step approach for the investigation of HORS on BDD.

not only the parameters but also the resources (Brillas et al., 2009). Energy consumption is calculated by the following equation:

$$\text{Energy consumption } (\text{kWh m}^{-3}) = \frac{E_{cell} I t}{V_s}, \quad (4)$$

where E_{cell} is the cell voltage (V), t is the electrolysis time (h), and I is the current passing through the cell (A). Therefore, the cost of the process can be obtained according to the following equation:

$$\text{Cost of process} = \text{Energy consumption} \times \text{Cost per kWh}. \quad (5)$$

In summary, Scheme 1 presents a systematic representation of the steps that we aimed to introduce so far and serves as a guide for the user; we emphasize that this is a preliminary approach to get to know our working electrode in the presence of a suitable electrolyte. We encourage the authors to include new electrochemical and non-electrochemical techniques to gain a deeper understanding of the electrode materials to be investigated.

The following is a specific case study involving BDD in the search for the optimal potential range for the generation of HORS, applying the reasoning that has been shown so far in the search for the prime parameters by carrying out electrochemical tests that can be handled without major problems in any electrochemical laboratory.

4 Case study: BDD in a Na_2SO_4 medium

Quite recently, Lu et al. (2023) highlighted the most recent advances in the effects of electrolytes in a solution for electrochemical processes and discussed their effects on different reactions of interest in electrochemistry, such as oxygen and hydrogen evolution reactions (HER and OER, respectively) and oxygen and CO_2 reduction reactions (ORR and CO_2RR, respectively). Nevertheless, to date, no review has been found in the literature that addresses, in a simplistic fashion and with an experimental approach, the investigation of ionic species in a solution and their participation in electrochemical oxidation as a guide for beginners. In this section, a real experimental example is presented as a case study that evaluates the behavior of BDD in Na_2SO_4 and other electrolytes of interest, emphasizing the steps that should be followed if one wishes to begin in this field.

Anhydrous sodium sulfate (N_2SO_4 99%) was purchased from J.T. Baker, *N*,*N*-Dimethyl-4-nitroso-aniline (for synthesis) was purchased from Merck, and amoxicillin was purchased from Sigma-Aldrich. All chemicals were used without further purification. BDD electrodes were purchased from CONDIAS and were cut into 25 mm × 15 mm rectangular plates, and an effective bipolar electrode area of 6.0 cm^2 in a cell volume of 60.0 mL was used for all experiments. The BDD was previously electrochemically activated by anodic polarization for 10 min in 0.5 mol L^{-1} sulfuric acid (H_2SO_4 95%–97%, Merck) at 0.1 Acm^{-2} in a BK Precision AC/DC power supply. All electrochemical assays were carried out on a BioLogic potentiostat/galvanostat workstation in a typical three-electrode cell. The BDD served as the working electrode, Ag/AgCl served as the reference, and a graphite rod served as the counter electrode. For the degradation of amoxicillin (40 μM), a two-electrode system was used, with a BDD as the anode and a Pt mesh as the cathode.

4.1 Cyclic voltammetry and polarization curves

Once the electrode or electrode material to be evaluated—BDD in this case—has been selected, the electrolyte medium in which the behavior of the electrode is to be investigated is chosen without any additional species in the solution. Therefore, the first step is to perform cyclic voltammetry at oxidative potentials—actually overpotentials—in the chosen medium; our interest is in Na_2SO_4 for reasons already discussed earlier. The CV gives us a first insight into the potential where oxygen evolution is kinetically and thermodynamically predominant. The inflection point of the

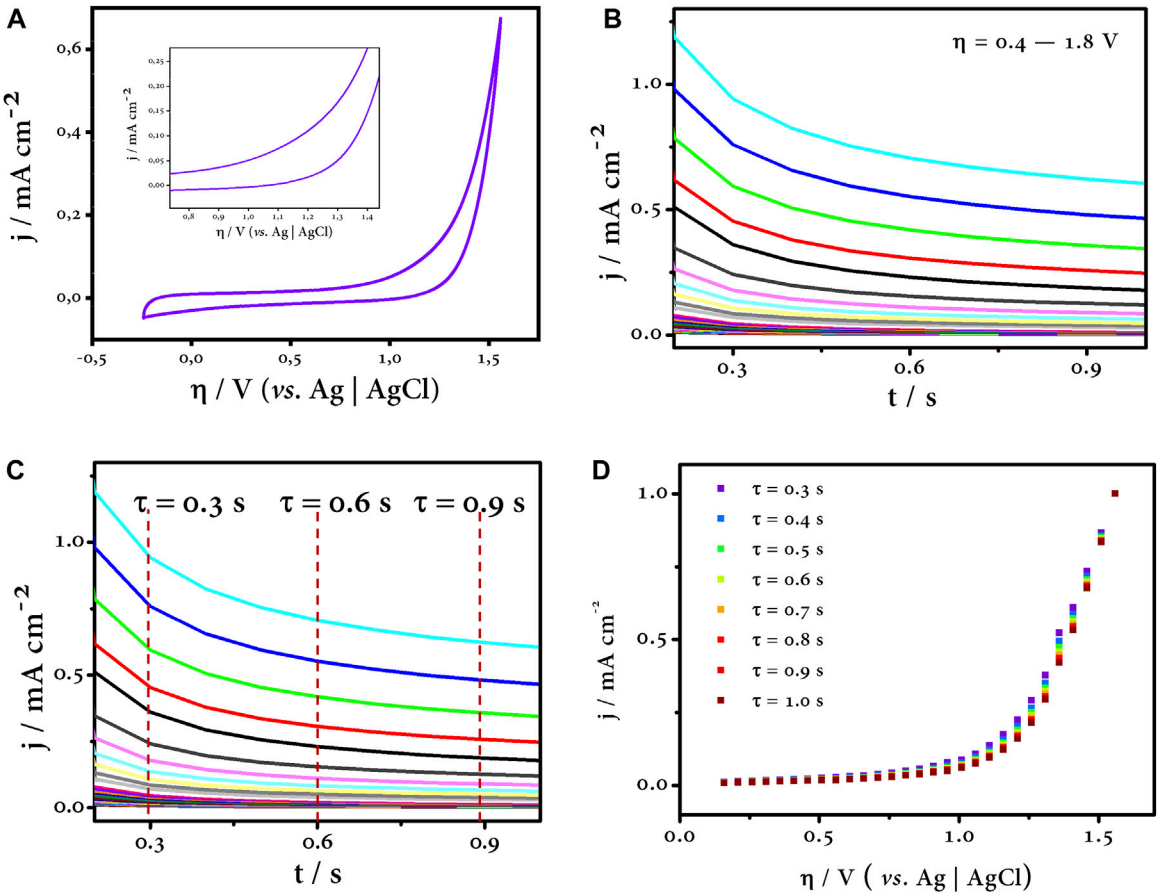

FIGURE 7
CV profile **(A)** and polarization curves **(B)** at oxidation overpotentials. The time constants were selected **(C)** for plotting the η vs. j curve by sampled current voltammetry **(D)**. All assays were carried out on a typical three-electrode system (WE: BDD, CE: graphite rod, and RE: Ag/AgCl in Na_2SO_4 0.1 mol L^{-1}).

oxidation branch of the CV indicates the potential where the transition from one electron transfer process to another is likely to occur and is likely to be the potential where most intermediate reactions compete, which is approximately 1.20 V vs. Ag/AgCl according to Figure 7A. Then, by chronoamperometry, we determine the polarization curves at the oxidation potentials determined in the previous CV profile (Figure 7B).

4.2 Sampled current voltammetry and η vs. j curves

After completing the polarization curves at the oxidation overpotentials, the next step is to choose a time interval, called time constant (τ), in which the process is controlled by charge transfer (Bard et al., 2022). For this purpose, the SCV is a useful tool that allows us to control this phenomenon when a rotating disk electrode is not available (Soares et al., 2020). Typically, it consists of choosing current values at small time constants and constructing η vs. j curves (Figures 7B, C). In this range, the process is kinetic-controlled, and the influence of diffusion, *i.e.*, mass transfer, is limited, so the effect of the electrode capacitance does not affect our test, and all measurements are focused entirely on the Faradaic current (Soares et al., 2020; Rodríguez and Denuault, 2021; Bard et al., 2022). Finally, Figure 7D shows all the η vs. j curves corresponding to different time constants, and all of them fit the same trend.

4.3 Tafel plot

As discussed in previous sections, the Tafel analysis is useful to evaluate the kinetics of an electrochemical process. In this sense, and summarized in the last step of our survey, the Tafel curve is constructed by plotting the logarithmic function of the current *versus* the overpotential (Figure 8). Three zones can be distinguished in this curve (highlighted by the straight lines). Each region of the curve has an associated slope, and this is the Tafel slope. The green line corresponding to the first zone has a slope value of 946 mV dec^{-1}, and this region is purely capacitive (it can be checked with the CV profile). The overpotential values up to about 1.1 V vs. Ag/AgCl are potentials where the double layer of the electrode—at the solid–liquid interface—is charged, and all this charge is stored in this imaginary region of the electrode, the inner Helmholtz plane (Bard et al., 2022). The next region illustrated by the blue line has a Tafel slope of 458 mV dec^{-1}, and this sharp change in slope indicates that another

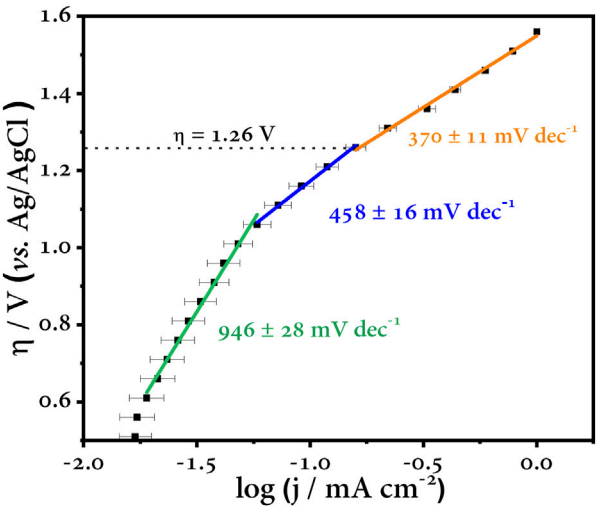

FIGURE 8
Tafel plot and slopes corresponding to the oxygen evolution reaction.

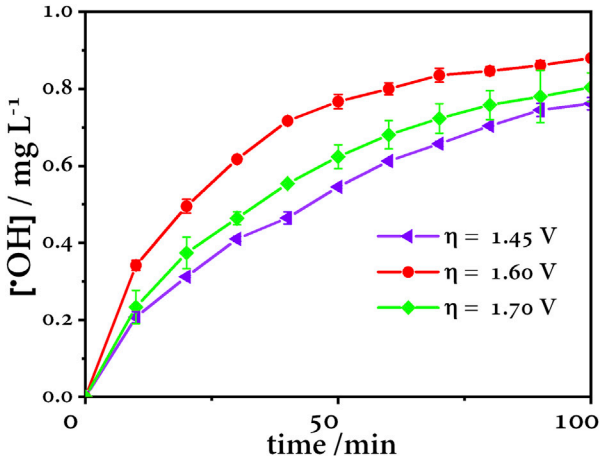

FIGURE 9
Effect of anode overpotential in the production of •OH using a BDD anode, Pt cathode, and Ag/AgCl reference electrode.

process(es) is taking place at the electrode surface. Finally, the last zone highlighted by the orange line has a slope of 370 mV dec^{-1}. This region plotted at overpotentials above 1.3 V vs. Ag/AgCl refers to the last process. This zone is distinctive as oxygen evolution reaction is predominant (Kapałka et al., 2008). This is self-evident as the error bars in this last region are almost undistinguishable, *i.e.*, the current and potential values do not oscillate to a large extent as long as the test is run again. The opposite is true for the previous zones. The intermediate zone is of interest to us as the former is easily discarded because of its capacitive contribution. The intermediate zone allows us to have an overview of the processes that can take place at these potential values. Since we know the chemical nature of the medium in which the test was carried out, we can say that this region is dominated by the generation of HORS that compete with the •OH, our main oxidant.

However, despite our efforts, we cannot be certain of the exact potential at which the most highly oxidizing species can be harnessed for any given process, and to do so would be a tremendous mistake. Instead, these steps allow us to determine a wide range of potentials and discriminate those that do not contribute to our process to save us errors, time, and costs of unnecessary laboratory testing. Quantitative assays such as the quantification of reactive species or degradation of a known contaminant should be added to this procedure to extend this assumption and have a more adequate approach to our purpose; with this, we will have approached our search for the optimal experimental conditions to achieve adequate efficiencies in our advanced electrochemical oxidation process. To experimentally verify the overpotential region where the highest amount of •OH is generated, a radical trapping study was performed, as shown below.

4.4 Trapping of radicals

The •OH concentration was quantified by the N,N-Dimethyl-4-nitroso-aniline (RNO) method (Ochoa-Chavez et al., 2018). Anode overpotentials were chosen based on the Tafel plot at values above 1.26 V vs. Ag/AgCl, according to Figure 8. At an anodic overpotential value of 1.60 V vs. Ag/AgCl, the highest concentration of •OH is generated, while at 1.45 V vs. Ag/AgCl, the concentration is lower because the applied potential is not enough to generate the maximum concentration of •OH. On the other hand, at 1.70 V, the concentration decreases because OER is the predominant reaction (Figure 9).

4.5 Amoxicillin degradation

vIn order to verify that the higher •OH radical production matches a maximum degradation efficiency, the electrooxidation of amoxicillin (AMX 40 μM) was tested. The electrochemical degradation of amoxicillin was evaluated under the best •OH production conditions, as discussed above. The degradation was followed by UV–Vis spectroscopy and chemical oxygen demand (COD). According to Figure 10A, at η = 1.40 V, the competition between the •OH electrogeneration (E° = 2.43 V vs. SHE) and formation of sulfate species $SO_4^{\bullet-}$ (E° = 2.44 V vs. SHE) and $S_2O_8^{2-}$ (E° = 1.44 V vs. SHE) is expected to be carried out (Armstrong et al., 2015); this agrees with the first minutes of electrolysis where amoxicillin degradation decreases rapidly and then remains unchanged. This is because sulfate species are not able to completely mineralize highly stable small organic molecules such as formic acid and oxalic acid (k = 1.3×10^8 and 1.4×10^6 L mol^{-1} s^{-1}, respectively), reaching 24.1% AMX concentration removal and 55.8% COD removal in 360 min of electrolysis (Figure 10B). On the other hand, at η = 1.60 V, the highest amoxicillin removal is achieved; this potential corresponds to the highest mineralization, and these removals decrease linearly until reaching 39.9% and 77.9%, respectively; therefore, this overpotential obtains the highest •OH production. Whereas, when overpotential increases, at η = 1.80 V, the removal behavior is similar as that at 1.40 V, and in this case, the OER is predominant, obtaining only 36% amoxicillin removal and 54% COD removal.

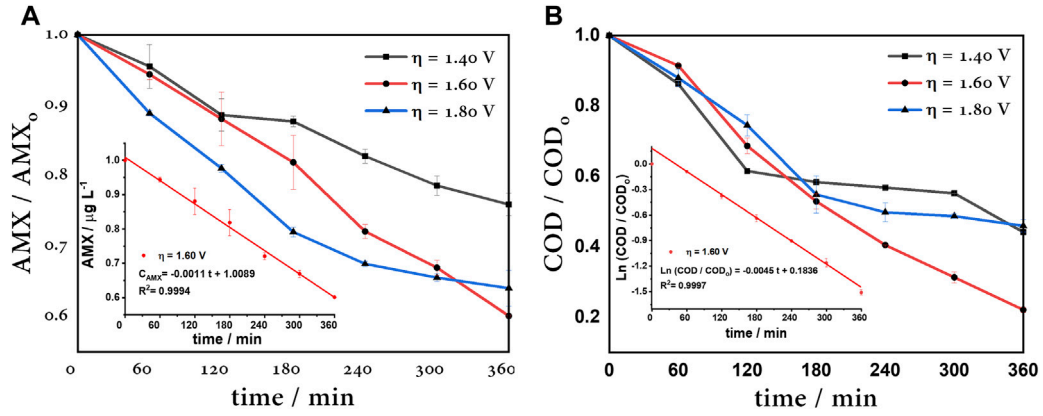

FIGURE 10
(A) 40 μM AMX degradation at different overpotentials. Inset: zero-order kinetic of amoxicillin removal. **(B)** COD of 40 μM AMX degradation at different overpotentials. Inset: pseudo-first-order kinetic of COD removal, using a BDD anode, Pt cathode, and Ag/AgCl reference electrode.

TABLE 1 Kinetic parameters of amoxicillin degradation.

η/V vs. Ag/AgCl	AMX remotion (%)	k_{amx}/min × 10^{-3}	COD remotion (%)	k_{COD}/min^{-1} × 10^{-3}
1.4	24.1	0.7	55.8	2.0
1.6	39.9	1.1	77.9	4.5
1.8	36.0	1.0	54.0	2.3

AMX, amoxicillin; η, overpotential; COD, chemical oxygen demand; k_{AMX}, zero-order kinetic constant; k_{COD}, pseudo-first-order kinetic constant.

In summary, Table 1 shows the kinetic parameters, where rate constants for amoxicillin degradation were adapted to a zero-order kinetic model and a pseudo-first-order kinetic model to COD removal. The COD constant rate of 1.60 V was almost two times greater than others' overpotentials; therefore, this is considered the optimal anode overpotential. In this case, this is the overpotential corresponding to the limit current, *i.e.*, the current associated to the maximum capacity to degrade AMX.

4.6 Instantaneous current efficiency and energy consumption

Figure 11 shows the evolution of the instantaneous current efficiency (ICE) with respect to electrolysis time, where maximum values of ICE are reached in the first hours, after which it decays due to the oxidation process and the formation of organic compounds. In the case of 1.60 V, it can be observed that after 2 h, the ICE remains stable, so the generation of $^{\bullet}$OH is continuous and allows progressive degradation, as it was discussed previously. Nevertheless, the ICE of the other overpotentials decreases drastically.

On the other hand, Table 2 shows the energy consumption and operating cost for the degradation of amoxicillin at different overpotentials. The cost of operation was calculated based on the cost per kilowatt-hour in Ecuador, which is 0.096 USD until March 2023 (Global Petrol Prices, 2023).

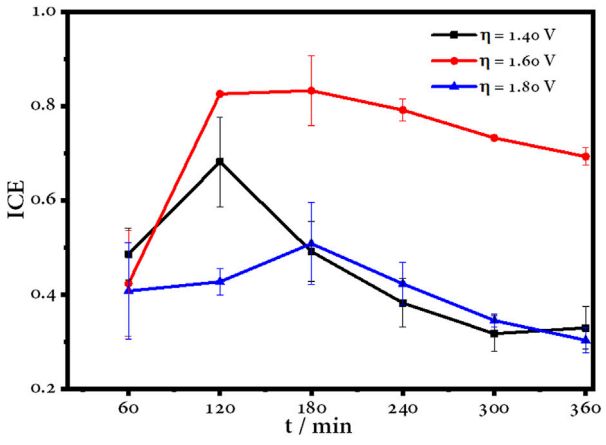

FIGURE 11
Instantaneous current efficiency over time for the electrochemical degradation of amoxicillin using a BDD electrode.

The results showed that the energy used during the electrolysis under the optimal overpotential was 0.224 kWh m^{-3}, and the operation cost was 0.022 USD m^{-3}, which represents the lowest cost among the other potentials tested and is in mutual agreement with the most efficient potential of the degradation process.

TABLE 2 Parameters of efficiency for the amoxicillin electrooxidation during a 6 h reaction.

η/V vs. Ag/AgCl	ICE	Energy consumption/kWh m^{-3}	Cost/USD m^{-3}
1.40	0.33	0.252	0.024
1.60	0.69	0.224	0.022
1.80	0.30	0.324	0.031

η, overpotential; ICE, instantaneous current efficiency.

5 Conclusion and outlook

Properly understanding the behavior of an electrode in a specific system can sometimes be a complicated endeavor, even more so when one does not know the charge transfer processes that may or may not take place in the medium under study and when this medium is a complicated mixture of organic and inorganic species. Electrochemical oxidation is a useful and efficient technology for many remediation applications if applied correctly, *i.e.*, having adequate knowledge and control over the parameters that influence the process, both internal and external. In this sense, this work attempted to provide a step-by-step guide, particularly for beginners, on the tests to be considered in the investigation of electrodes and new electrode materials for advanced electrochemical oxidation processes, with emphasis on the range of anodic potentials where the generation of highly reactive oxidizing species predominates, which are priceless in these processes. It is not our intention that this guide should be followed rigorously, but rather that it should serve as a support for those who wish to get started in this field, adjusting these steps to their research objectives. The study of the kinetic behavior of BDD in different electrolytes by SCV, the Tafel plot, and trapping of radicals is essential to achieve results of this magnitude. A detailed study of the effect of the electrolyte is in progress in our research group.

Although this guide is particularly focused on the BDD, it is not limited to this electrode. This guide can be followed to investigate a new electrode material from an electrochemical point of view at first glance. In addition to the steps proposed here, the reader is free to implement other electrochemical techniques that suit his or her research. For example, electrochemical impedance spectroscopy is important when specific reaction mechanisms need to be studied and can provide valuable information about a particular electrode; however, this technique is beyond the scope of this work.

Data availability statement

The original contributions presented in the study are included in the article/Supplementary Material; further inquiries can be directed to the corresponding author.

Author contributions

GC-C: formal analysis, investigation, methodology, and writing–original draft. CP-C: data curation, formal analysis, investigation, methodology, and writing–original draft. EM: funding acquisition, investigation, validation, and writing–review and editing. PE-M: conceptualization, data curation, funding acquisition, investigation, methodology, project administration, resources, supervision, validation, writing–original draft, and writing–review and editing.

Funding

The authors declare financial support was received for the research, authorship, and/or publication of this article. This work was funded by the Pontificia Universidad Católica del Ecuador through the project: Degradation of Microplastics by Photoelectrocatalysis Using a Titanium Dioxide-Modified Boron-Doped Diamond Photoanode (TiO_2/BDD). Code: 030-UIO-2023.

Acknowledgments

The authors would like to thank the School of Chemical Sciences of the Pontificia Universidad Católica del Ecuador for lending them part of the equipment for the development of this work.

Conflict of interest

The authors declare that the research was conducted in the absence of any commercial or financial relationships that could be construed as a potential conflict of interest.

Publisher's note

References

Actis, P., Denoyelle, A., Boukherroub, R., and Szunerits, S. (2008). Influence of the surface termination on the electrochemical properties of boron-doped diamond (BDD) interfaces. *Electrochem. Commun.* 10 (3), 402–406. doi:10.1016/j.elecom.2007.12.032

Ahmed, M., Mavukkandy, M. O., Giwa, A., Elektorowicz, M., Katsou, E., Khelifi, O., et al. (2022). Recent developments in hazardous pollutants removal from wastewater and water reuse within a circular economy. *npj Clean. Water* 5 (1), 12–25. doi:10.1038/s41545-022-00154-5

Araújo, K. C., dos Santos, E. V., Nidheesh, P. V., and Martínez-Huitle, C. A. (2022). Fundamentals and advances on the mechanisms of electrochemical generation of persulfate and sulfate radicals in aqueous medium. *Curr. Opin. Chem. Eng.* 38, 100870. doi:10.1016/j.coche.2022.100870

Armstrong, D. A., Huie, R. E., Koppenol, W. H., Lymar, S. V., Merényi, G., Neta, P., et al. (2015). Standard electrode potentials involving radicals in aqueous solution: inorganic radicals (IUPAC Technical Report). *Pure Appl. Chem.* 87 (11–12), 1139–1150. doi:10.1515/pac-2014-0502

Bany Abdelnabi, A. A., Al Theeb, N., Almomani, M. A., Ghanem, H., and Rosiwal, S. M. (2022). Effect of electrode parameters in the electro-production of reactive oxidizing species via boron-doped diamond under batch mode. *Water Environ. Res. a Res. Publ. Water Environ. Fed.* 94 (12), e10830. doi:10.1002/wer.10830

Bard, A. J., Faulkner, L. R., and White, H. S. (2022). *Electrochemical methods fundamentals and applications*. Hoboken, New Jersey: John Wiley and Sons, Ltd.

Barnum, T. P., and Coates, J. D. (2023). Chlorine redox chemistry is widespread in microbiology. *ISME J.* 17 (1), 70–83. doi:10.1038/s41396-022-01317-5

Berenguer, R., Quijada, C., La Rosa-Toro, A., and Morallón, E. (2019). Electro-oxidation of cyanide on active and non-active anodes: designing the electrocatalytic response of cobalt spinels. *Sep. Purif. Technol.* 208, 42–50. doi:10.1016/j.seppur.2018.05.024

Bessegato, G. G., Cooke, M., Christensen, P., Wood, D., and Zanoni, M. (2021). Synthesis and electrochemical characterization of Si/TiO2/Au composite anode: efficient oxygen evolution and hydroxyl radicals generation. *Electrochimica Acta* 370, 137742. doi:10.1016/J.ELECTACTA.2021.137742

Brillas, E., Sirés, I., and Oturan, M. A. (2009). Electro-fenton process and related electrochemical technologies based on fenton's reaction chemistry. *Chem. Rev.* 109 (12), 6570–6631. doi:10.1021/cr900136g

Carrera-Cevallos, J. V., Prato-Garcia, D., Espinoza-Montero, P. J., and Vasquez-Medrano, R. (2021). Electro-oxidation of a commercial formulation of glyphosate on boron-doped diamond electrodes in a pre-pilot-scale single-compartment cell. *Water, Air, Soil Pollut.* 232 (2), 69. doi:10.1007/s11270-020-04941-z

Cheah, M. H., and Chernev, P. (2021). Electrochemical oxidation of ferricyanide. *Sci. Rep.* 11 (1), 23058–23067. doi:10.1038/s41598-021-02355-3

Chen, W., Xu, M. L., Li, M. F., Wei, Z., Cai, J., and Chen, Y. X. (2020). Quantifying intrinsic kinetics of electrochemical reaction controlled by mass transfer of multiple species under rotating disk electrode configuration. *J. Electroanal. Chem.* 872, 114042. doi:10.1016/j.jelechem.2020.114042

Choo, Z. S., Hsieh, M. C., Lin, H. H. H., Yang, J. S., and Lin, A. Y. C. (2022). Reactive chlorine species in the enhanced degradation of UV stabilizers during the sunlight/free chlorine process. *Chemosphere* 309, 136677. doi:10.1016/J.CHEMOSPHERE.2022.136677

Cisneros-León, D. G., Espinoza-Montero, P. J., Bolaños-Mendez, D., Alvarez-Paguay, J., Fernández, L., Saavedra-Alulema, P. F., et al. (2023). Electrochemical degradation of surfactants in domestic wastewater using a DiaClean® cell equipped with a boron-doped diamond electrode. *Front. Chem.* 11, 1–10. doi:10.3389/fchem.2023.900670

Comninellis, C., and Pulgarin, C. (1991). Anodic oxidation of phenol for waste water treatment. *J. Appl. Electrochem.* 21 (8), 703–708. doi:10.1007/BF01034049

dos Santos, A. J., Barazorda-Ccahuana, H. L., Caballero-Manrique, G., Chérémond, Y., Espinoza-Montero, P. J., González-Rodríguez, J. R., et al. (2023). Accelerating innovative water treatment in Latin America. *Nat. Sustain.* 2023, 349–351. doi:10.1038/s41893-022-01042-z

Einaga, Y. (2022). Boron-doped diamond electrodes: fundamentals for electrochemical applications. *Accounts Chem. Res.* 55, 3605–3615. doi:10.1021/acs.accounts.2c00597

Elgrishi, N., Rountree, K. J., McCarthy, B. D., Rountree, E. S., Eisenhart, T. T., and Dempsey, J. L. (2018). A practical beginner's guide to cyclic voltammetry. *J. Chem. Educ.* 95 (2), 197–206. doi:10.1021/acs.jchemed.7b00361

Espinoza-Montero, P. J., Martínez-Huitle, C. A., and Loor-Urgilés, L. D. (2023). Technologies employed for carwash wastewater recovery. *J. Clean. Prod.* 401, 136722. doi:10.1016/J.JCLEPRO.2023.136722

Fang, J., Fu, Y., and Shang, C. (2014). The roles of reactive species in micropollutant degradation in the UV/free chlorine system. *Environ. Sci. Technol.* 48 (3), 1859–1868. doi:10.1021/es4036094

Fang, Y. H., and Liu, Z. P. (2014). Tafel kinetics of electrocatalytic reactions: from experiment to first-principles. *ACS Catal.* 4 (12), 4364–4376. doi:10.1021/cs501312v

Fornaciari, J. C., Weng, L. C., Alia, S. M., Zhan, C., Pham, T. A., Bell, A. T., et al. (2022). Mechanistic understanding of pH effects on the oxygen evolution reaction. *Electrochimica Acta* 405, 139810. doi:10.1016/J.ELECTACTA.2021.139810

Ganiyu, S. O., and Martínez-Huitle, C. A. (2019). Nature, mechanisms and reactivity of electrogenerated reactive species at thin-film boron-doped diamond (BDD) electrodes during electrochemical wastewater treatment. *ChemElectroChem* 6 (9), 2379–2392. doi:10.1002/celc.201900159

Ganiyu, S. O., Martínez-Huitle, C. A., and Oturan, M. A. (2021). Electrochemical advanced oxidation processes for wastewater treatment: advances in formation and detection of reactive species and mechanisms. *Curr. Opin. Electrochem.* 27, 100678. doi:10.1016/j.coelec.2020.100678

Garcia-Segura, S., Vieira Dos Santos, E., and Martínez-Huitle, C. A. (2015). Role of sp3/sp2 ratio on the electrocatalytic properties of boron-doped diamond electrodes: a mini review. *Electrochem. Commun.* 59, 52–55. doi:10.1016/j.elecom.2015.07.002

Gligorovski, S., Strekowski, R., Barbati, S., and Vione, D. (2015). Environmental implications of hydroxyl radicals (●OH). *Chem. Rev.* 115 (24), 13051–13092. doi:10.1021/cr500310b

Global Petrol Prices (2023). Ecuador electricity prices. Available at: https://www.globalpetrolprices.com/Ecuador/electricity_prices/.

Hand, S., and Cusick, R. D. (2021). Electrochemical disinfection in water and wastewater treatment: identifying impacts of water quality and operating conditions on performance. *Environ. Sci. Technol.* 55 (6), 3470–3482. doi:10.1021/acs.est.0c06254

Hayyan, M., Hashim, M. A., and Alnashef, I. M. (2016). Superoxide ion: generation and chemical implications. *Chem. Rev.* 116 (5), 3029–3085. doi:10.1021/acs.chemrev.5b00407

Imlay, J. A. (2003). Pathways of oxidative damage. *Annu. Rev. Microbiol.* 57, 395–418. doi:10.1146/annurev.micro.57.030502.090938

Ivandini, T. A., and Einaga, Y. (2017). Polycrystalline boron-doped diamond electrodes for electrocatalytic and electrosynthetic applications. *Chem. Commun.* 53 (8), 1338–1347. doi:10.1039/c6cc08681k

Joshi, P., Riley, P., Goud, K., Mishra, R. K., and Narayan, R. (2022). Recent advances of boron-doped diamond electrochemical sensors toward environmental applications. *Curr. Opin. Electrochem.* 32, 100920. doi:10.1016/j.coelec.2021.100920

Jung, O., Jackson, M. N., Bisbey, R. P., Kogan, N. E., and Surendranath, Y. (2022). Innocent buffers reveal the intrinsic pH- and coverage-dependent kinetics of the hydrogen evolution reaction on noble metals. *Joule* 6 (2), 476–493. doi:10.1016/j.joule.2022.01.007

Kapałka, A., Fóti, G., and Comninellis, C. (2008). Determination of the Tafel slope for oxygen evolution on boron-doped diamond electrodes. *Electrochem. Commun.* 10 (4), 607–610. doi:10.1016/j.elecom.2008.02.003

Kasahara, S., Natsui, K., Watanabe, T., Yokota, Y., Kim, Y., Iizuka, S., et al. (2017). Surface hydrogenation of boron-doped diamond electrodes by cathodic reduction. *Anal. Chem.* 89 (21), 11341–11347. doi:10.1021/acs.analchem.7b02129

Katsounaros, I., Cherevko, S., Zeradjanin, A. R., and Mayrhofer, K. J. J. (2014). Oxygen electrochemistry as a cornerstone for sustainable energy conversion. *Angew. Chem. - Int. Ed.* 53 (1), 102–121. doi:10.1002/anie.201306588

Kim, S., Kim, C., Lee, J., Kim, S., Lee, J., Kim, J., et al. (2018). Hybrid electrochemical desalination system combined with an oxidation process. *ACS Sustain. Chem. Eng.* 6 (2), 1620–1626. doi:10.1021/acssuschemeng.7b02789

Kondo, T. (2022). Recent electroanalytical applications of boron-doped diamond electrodes. *Curr. Opin. Electrochem.* 32, 100891. doi:10.1016/J.COELEC.2021.100891

Krumova, K., and Cosa, G. (2016). "Overview of reactive oxygen species," in *Singlet oxygen: applications in biosciences and nanosciences*, 3–21. doi:10.1039/9781782620389-00001

Lee, J., Von Gunten, U., and Kim, J. H. (2020). Persulfate-based advanced oxidation: critical assessment of opportunities and roadblocks. *Environ. Sci. Technol.* 54 (6), 3064–3081. doi:10.1021/acs.est.9b07082

Lee, J. K., and Bazylak, A. (2021). Bubbles: the good, the bad, and the ugly. *Joule* 5 (1), 19–21. doi:10.1016/j.joule.2020.12.024

Lee, K. M., Lee, H. J., Seo, J., Lee, T., Yoon, J., Kim, C., et al. (2022). Electrochemical oxidation processes for the treatment of organic pollutants in water: performance evaluation using different figures of merit. *ACS ES T Eng.* 2 (10), 1797–1824. doi:10.1021/acsestengg.2c00228

Lin, Q., and Deng, Y. (2021). Is sulfate radical a ROS? *Environ. Sci. Technol.* 55 (22), 15010–15012. doi:10.1021/acs.est.1c06651

Lips, S., and Waldvogel, S. R. (2019). Use of boron-doped diamond electrodes in electro-organic synthesis. *ChemElectroChem* 6 (6), 1649–1660. doi:10.1002/CELC.201801620

Long, X., Huang, R., Li, Y., Wang, J., Zhang, M., and Zhang, I. Y. (2023). Understanding the electro-cocatalytic peroxymonosulfate-based systems with BDD versus DSA anodes: radical versus nonradical dominated degradation mechanisms. *Sep. Purif. Technol.* 309, 123120. doi:10.1016/j.seppur.2023.123120

Lu, X., Tu, W., Zhou, Y., and Zou, Z. (2023). Effects of electrolyte ionic species on electrocatalytic reactions: advances, challenges, and perspectives. *Adv. Energy Mater.* 13, 2300628. doi:10.1002/AENM.202300628

Macpherson, J. V. (2015). A practical guide to using boron doped diamond in electrochemical research. *Phys. Chem. Chem. Phys.* 17 (5), 2935–2949. doi:10.1039/c4cp04022h

Mann, J. B., Meek, T. L., and Allen, L. C. (2000). Configuration energies of the main group elements. *J. Am. Chem. Soc.* 122 (12), 2780–2783. doi:10.1021/ja992866e

Martínez-Huitle, C. A., Rodrigo, M. A., Sirés, I., and Scialdone, O. (2015). Single and coupled electrochemical processes and reactors for the abatement of organic water

pollutants: a critical review. *Chem. Rev.* 115 (24), 13362–13407. doi:10.1021/acs.chemrev.5b00361

Medeiros De Araújo, D., Cañizares, P., Martínez-Huitle, C. A., and Rodrigo, M. A. (2014). Electrochemical conversion/combustion of a model organic pollutant on BDD anode: role of sp3/sp2 ratio. *Electrochem. Commun.* 47, 37–40. doi:10.1016/j.elecom.2014.07.017

Moreira, F. C., Boaventura, R. A., Brillas, E., and Vilar, V. J. (2017). Electrochemical advanced oxidation processes: a review on their application to synthetic and real wastewaters. *Appl. Catal. B Environ.* 202, 217–261. doi:10.1016/j.apcatb.2016.08.037

Mostafa, E., Reinsberg, P., Garcia-Segura, S., and Baltruschat, H. (2018). Chlorine species evolution during electrochlorination on boron-doped diamond anodes: *in-situ* electrogeneration of Cl2, Cl2O and ClO2. *Electrochimica Acta* 281, 831–840. doi:10.1016/j.electacta.2018.05.099

Mousset, E. (2023). Electrochemical hydrogenation for water purification made easy. *Nat. Water* 1 (1), 28–29. doi:10.1038/s44221-022-00011-2

Murphy, M. P., Bayir, H., Belousov, V., Chang, C. J., Davies, K. J. A., Davies, M. J., et al. (2022). Guidelines for measuring reactive oxygen species and oxidative damage in cells and *in vivo*. *Nat. Metab.* 4 (6), 651–662. doi:10.1038/s42255-022-00591-z

Ochoa-Chavez, A. S., Pieczyńska, A., Fiszka Borzyszkowska, A., Espinoza-Montero, P., and Siedlecka, E. (2018). Electrochemical degradation of 5-FU using a flow reactor with BDD electrode: comparison of two electrochemical systems. *Chemosphere* 201, 816–825. doi:10.1016/j.chemosphere.2018.03.050

Oh, W.Da, Dong, Z., and Lim, T. T. (2016). Generation of sulfate radical through heterogeneous catalysis for organic contaminants removal: current development, challenges and prospects. *Appl. Catal. B Environ.* 194, 169–201. doi:10.1016/j.apcatb.2016.04.003

Oliveira, B., and Oliveira-Brett, A. M. (2010). Voltammetric and electrochemical impedance spectroscopy characterization of a cathodic and anodic pre-treated boron doped diamond electrode. *Electrochimica Acta* 55 (15), 4599–4605. doi:10.1016/j.electacta.2010.03.016

Parvulescu, V. I., Epron, F., Garcia, H., and Granger, P. (2022). Recent progress and prospects in catalytic water treatment. *Chem. Rev.* 122 (3), 2981–3121. doi:10.1021/acs.chemrev.1c00527

Petrii, O. A., Nazmutdinov, R. R., Bronshtein, M. D., and Tsirlina, G. A. (2007). Life of the Tafel equation: current understanding and prospects for the second century. *Electrochimica Acta* 52 (11), 3493–3504. doi:10.1016/j.electacta.2006.10.014

Pierpaoli, M., Jakobczyk, P., Sawczak, M., Łuczkiewicz, A., Fudala-Książek, S., and Bogdanowicz, R. (2021). Carbon nanoarchitectures as high-performance electrodes for the electrochemical oxidation of landfill leachate. *J. Hazard. Mater.* 401, 123407. doi:10.1016/j.jhazmat.2020.123407

Rayaroth, M. P., Aravindakumar, C. T., Shah, N. S., and Boczkaj, G. (2022). Advanced oxidation processes (AOPs) based wastewater treatment - unexpected nitration side reactions - a serious environmental issue: a review. *Chem. Eng. J.* 430, 133002. doi:10.1016/j.cej.2021.133002

Rodríguez, O., and Denuault, G. (2021). The electron transfer kinetics of adsorbed species derived by sampled current voltammetry. *J. Electroanal. Chem.* 882, 115021. doi:10.1016/j.jelechem.2021.115021

Ross, A. B., and Neta, P. (1982). Rate constants for reactions of inorganic radicals in aqueous solution. *Natl. Stand. Ref. Data Ser.* 17 (3), 1027–1284. doi:10.1063/1.555808

Sánchez-Montes, I., Pérez, J. F., Sáez, C., Rodrigo, M. A., Cañizares, P., Aquino, J. M., et al. (2020). Assessing the performance of electrochemical oxidation using DSA® and BDD anodes in the presence of UVC light. *Chemosphere* 238, 124575. doi:10.1016/J.CHEMOSPHERE.2019.124575

Shih, A. J., Monteiro, M. C. O., Dattila, F., Pavesi, D., Philips, M., da Silva, A. H. M., et al. (2022). Water electrolysis. *Nat. Rev. Methods Prim.* 2 (1), 84–91. doi:10.1038/s43586-022-00164-0

Siahrostami, S., Li, G. L., Viswanathan, V., and Nørskov, J. K. (2017). One- or two-electron water oxidation, hydroxyl radical, or H2O2 evolution. *J. Phys. Chem. Lett.* 8 (6), 1157–1160. doi:10.1021/acs.jpclett.6b02924

Soares, C. O., Rodríguez, O., Buvat, G., Duca, M., Garbarino, S., Guay, D., et al. (2020). Sampled current voltammetry for kinetic studies on materials unsuitable for rotating discs or microelectrodes: application to the oxygen reduction reaction in acidic medium. *Electrochimica Acta* 362, 136946. doi:10.1016/j.electacta.2020.136946

Suffredini, H. B., Pedrosa, V. A., Codognoto, L., Machado, S. A., Rocha-Filho, R. C., and Avaca, L. A. (2004). Enhanced electrochemical response of boron-doped diamond electrodes brought on by a cathodic surface pre-treatment. *Electrochimica Acta* 49, 4021–4026. doi:10.1016/j.electacta.2004.01.082

Sun, L., Yuan, G., Gao, L., Yang, J., Chhowalla, M., Gharahcheshmeh, M. H., et al. (2021). Chemical vapour deposition. *Nat. Rev. Methods Prim.* 1 (1), 5. doi:10.1038/s43586-020-00005-y

Tafel, J. (1905). Über die Polarisation bei kathodischer Wasserstoffentwicklung. *Z. für Phys. Chem.* 50U (1), 641–712. doi:10.1515/zpch-1905-5043

Tao, H. B., Zhang, J., Chen, J., Zhang, L., Xu, Y., Chen, J. G., et al. (2019). Revealing energetics of surface oxygen redox from kinetic fingerprint in oxygen electrocatalysis. *J. Am. Chem. Soc.* 141 (35), 13803–13811. doi:10.1021/jacs.9b01834

Vogt, C., and Weckhuysen, B. M. (2022). The concept of active site in heterogeneous catalysis. *Nat. Rev. Chem.* 6 (2), 89–111. doi:10.1038/s41570-021-00340-y

Wei, J. J., Zhu, X. -P., Lü, F. -X., Ni, J. R., et al. (2011a). Comparative study of oxidation ability between boron-doped diamond (BDD) and lead oxide (PbO2) electrodes. *Int. J. Minerals, Metallurgy Mater.* 18 (5), 589–593. doi:10.1007/s12613-011-0482-1

Wei, M., Liu, Y., Gu, Z. -Z., and Liu, Z. -D. (2011b). Electrochemical detection of catechol on boron-doped diamond electrode modified with Au/TiO2 nanorod composite. *J. Chin. Chem. Soc.* 58 (4), 516–521. doi:10.1002/JCCS.201190015

Weiss, E., Sáez, C., Groenen-Serrano, K., Cañizares, P., Savall, A., and Rodrigo, M. A. (2008). Electrochemical synthesis of peroxomonophosphate using boron-doped diamond anodes. *J. Appl. Electrochem.* 38 (1), 93–100. doi:10.1007/s10800-007-9405-2

Wen, Y., Schoups, G., and Van De Giesen, N. (2017). Organic pollution of rivers: combined threats of urbanization, livestock farming and global climate change. *Sci. Rep.* 7 (1), 43289–9. doi:10.1038/srep43289

Wu, Y., Bu, L., Duan, X., Zhu, S., Kong, M., Zhu, N., et al. (2020). Mini review on the roles of nitrate/nitrite in advanced oxidation processes: radicals transformation and products formation. *J. Clean. Prod.* 273, 123065. doi:10.1016/j.jclepro.2020.123065

Xie, J., Zhang, C., and Waite, T. D. (2022). Hydroxyl radicals in anodic oxidation systems: generation, identification and quantification. *Water Res.* 217, 118425. doi:10.1016/j.watres.2022.118425

Xing, X., Ni, J., Zhu, X., Jiang, Y., and Xia, J. (2018). Maximization of current efficiency for organic pollutants oxidation at BDD, Ti/SnO2-Sb/PbO2, and Ti/SnO2-Sb anodes. *Chemosphere* 205, 361–368. doi:10.1016/j.chemosphere.2018.04.090

Xu, J., Zheng, X., Feng, Z., Lu, Z., Zhang, Z., Huang, W., et al. (2021). Organic wastewater treatment by a single-atom catalyst and electrolytically produced H2O2. *Nat. Sustain.* 4 (3), 233–241. doi:10.1038/s41893-020-00635-w

Xu, T., Fu, L., Zhang, M., Wang, W., Hu, B., Zhou, Y., et al. (2023a). Electrochemical oxidation degradation of rhodamine B dye on boron-doped diamond electrode: input mode of power attenuation. *J. Clean. Prod.*, 116544. doi:10.1016/j.jclepro.2023.136794

Xu, Y., Mao, Z., Qu, R., Wang, J., Yu, J., Luo, X., et al. (2023b). Electrochemical hydrogenation of oxidized contaminants for water purification without supporting electrolyte. *Nat. Water* 1 (1), 95–103. doi:10.1038/s44221-022-00002-3

Yang, N., Yu, S., Macpherson, J. V., Einaga, Y., Zhao, H., Zhao, G., et al. (2019). Conductive diamond: synthesis, properties, and electrochemical applications. *Chem. Soc. Rev.* 48 (1), 157–204. doi:10.1039/c7cs00757d

Yokoya, T., Nakamura, T., Matsushita, T., Muro, T., Takano, Y., Nagao, M., et al. (2005). Origin of the metallic properties of heavily boron-doped superconducting diamond. *Nature* 438 (7068), 647–650. doi:10.1038/nature04278

Zanin, H., May, P. W., Fermin, D. J., Plana, D., Vieira, S. M. C., Milne, W. I., et al. (2014). Porous boron-doped diamond/carbon nanotube electrodes. *ACS Appl. Mater. Interfaces* 6 (2), 990–995. doi:10.1021/am4044344

Zhang, J., Tao, H. B., Kuang, M., Yang, H. B., Cai, W., Yan, Q., et al. (2020). Advances in thermodynamic-kinetic model for analyzing the oxygen evolution reaction. *ACS Catal.* 10 (15), 8597–8610. doi:10.1021/acscatal.0c01906

Zheng, W. (2023). iR compensation for electrocatalysis studies: considerations and recommendations. *ACS Energy Lett.* 8, 1952–1958. doi:10.1021/acsenergylett.3c00366

Zhou, H., and Xiao, D. (2022). Role of NOM in the photolysis of chlorine and the formation of reactive species in the solar/chlorine system. *ACS Omega* 7 (9), 7769–7776. doi:10.1021/acsomega.1c06616

Zhu, R. C. (2019). Fish the oxygen intermediates. *Joule* 3 (6), 1408–1409. doi:10.1016/j.joule.2019.05.024

Zoski, C. G. (2007) *Handbook of electrochemistry*. Amsterdam, Netherlands: Elsevie. doi:10.1016/B978-0-444-51958-0.X5000-9

Frontiers in Chemistry

Explores all fields of chemical science across the periodic table

Advances our understanding of how atoms, ions, and molecules come together and come apart. It explores the role of chemistry in our everyday lives - from electronic devices to health and wellbeing.

Discover the latest Research Topics

See more →

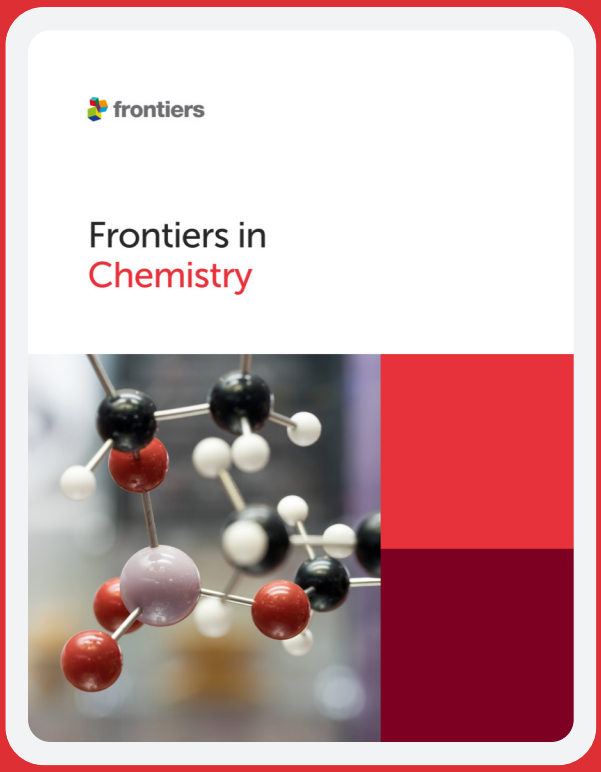

Frontiers

Avenue du Tribunal-Fédéral 34
1005 Lausanne, Switzerland
frontiersin.org

Contact us

+41 (0)21 510 17 00
frontiersin.org/about/contact